TOPICS IN MOLECULAR ORGANIZATION AND ENGINEERING

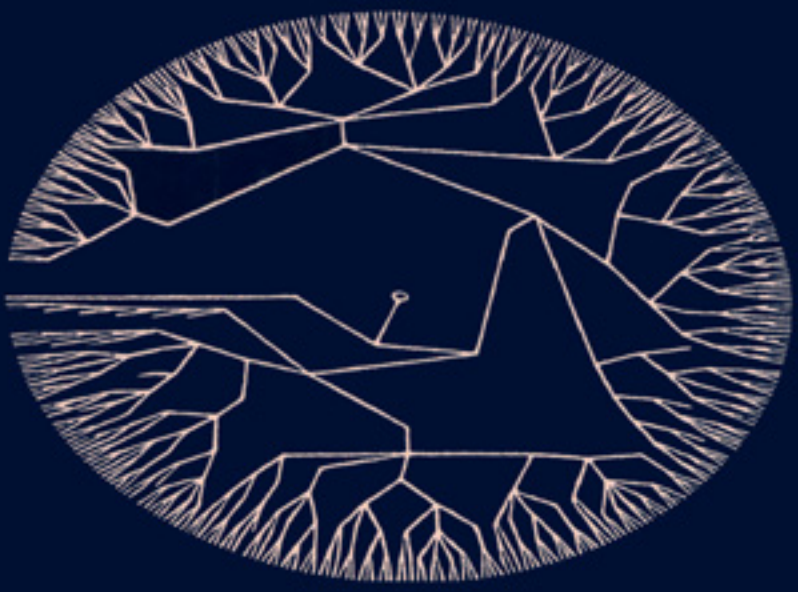

Modelling of Minerals and Silicated Materials

edited by

BERNARD SILVI and PHILIPPE D'ARCO

KLUWER ACADEMIC PUBLISHERS

Modelling ofMinerals and Silicated Materials

TOPICS IN MOLECULAR ORGANIZATION AND ENGINEERING

Volume 15

Modelling of Minerals and Silicated Materials

edited by

Bernard Silvi

Laboratoire de Chimie Théorique,
Université Pierre et Marie Curie,
Paris, France

and

Philippe D'Arco

Laboratoire de Géologie,
Ecole Normale Supérieure,
Paris, France

KLUWER ACADEMIC PUBLISHERS
NEW YORK / BOSTON / DORDRECHT / LONDON / MOSCOW

eBook ISBN: 0-306-46933-2
Print ISBN: 0-792-34333-6

Created in the United States of America

Visit Kluwer Online at: http://www.kluweronline.com
and Kluwer's eBookstore at: http://www.ebooks.kluweronline.com

TABLE OF CONTENTS

INTRODUCTION vii

* J. R. CHELIKOWSKY, N. R. KESKAR and N. BINGGELI / The Structural Properties of Silica Using Classical and Quantum Interatomic Forces 1-37

* R. M. WENTZCOVITCH and G. D. PRICE / High Pressure Studies of Mantle Minerals by *Ab initio* Variable Cell Shape Molecular Dynamics 39-61

* R. G. GORDON and D. J. LACKS / Calculation of Mineral Properties with the Electron Gas Model 63-79

* M.S.T. BUKOWINSKI, A. CHIZMESHYA, G.H. WOLF and H. ZHANG / Advances in Electron-Gas Potential Models : Applications to some Candidate Lower Mantle Minerals 81-112

* M. CATTI and A. PAVESE / Quantum-Mechanical and Classical Simulations of Mg-Ca Carbonates 113-156

G. V. GIBBS, F. C. HILL and M. B. BOISEN Jr. / The SiO Bond and Electron Density Distributions 157-177

B. SILVI, A. SAVIN and F. R. WAGNER / The Nature of Silicon-Oxygen Bonds in Silica Polymorphs 179-199

* S. TSUNEYUKI / Molecular Dynamics Simulation of Silica with a First-Principles Interatomic Potential 201-226

* A. N. CORMACK and YUAN CAO / Molecular Dynamics Simulation of Silicate Glasses 227-271

M. HENRY / Application of the partial charge model to the aqueous chemistry of silica and silicates 273-334

INDEX 335-341

* Contributions marked with an asterisk also appear in the journal *Molecular Engineering,* Volume 6, 1996.

This page intentionally left blank.

Introduction

The modeling of minerals and silicated materials is a. difficult challenge faced by Solid State Physics, Quantum Chemistry and Molecular Dynamics communities. The difficulty of such a modeling is due to the wide diversity of elements, including heavy atoms, and types of bonding involved in such systems. Moreover, one has to consider infinite systems: either perfect crystals or glasses and melts. In the solid state a given chemical composition gives rise to numerous polymorphs, geometrically closely related. These polymorphs have very similar energies and related thermodynamical properties which explain the complexity of their phase diagrams.

The modeling of silicates and minerals covers a wide field of applications ranging from basic research to technology, from Solid State Physics to Earth and Planetary science. The use of modeling techniques yields information of different nature. In the case of chemical studies, we can mention investigations on catalytic processes occurring on surfaces and in zeolite cages. These calculations find possible applications in chemical engineering, in particular in the oil industry.

Physical properties, such as elastic constants, are currently investigated in order to get better insights on their relationships to the structure and chemistry. In this respect, the understanding of the phase transition mechanisms is of primary importance. The estimation of thermodynamical properties under extreme conditions of pressure and temperature supplies the difficulty of performing experimental measurements. In Earth and Planetary Science, the deep internal pressure and temperature are very high (at Earth core-mantle boundary P$\sim$ 300 GPa, T$\sim$ 3000 K). Our knowledge of Earth interior is mainly inductive. The principal sources of information are seismic data from which models have been built. The validation of the hypothesis underlying the construction of interior models relies on difficult high pressure and temperature experiments as well as on the results of calculations. In this field, the calculations are expected to be as accurate as the experiments which are not always technically feasible.

Another important field of application directly related to technology is the design of new materials such as ceramics. The prediction of their physical properties, at least the order of magnitude, allows the selection of those systems for which investments in further investigations are justified.

The basic tools for the modeling of the solid and liquid states belong to three main categories. We can mention first the Molecular Mechanics which rely on site-site or covalent potentials and which are used to study in particular defect formations, to calculate accoustic and optical phonon modes by lattice dynamics and to estimate mechanical and thermodynamical properties. The easy implementation of the Molecular Mechanics scheme supports its intensive use in the past and its success in commercial softwares.

Molecular Dynamics and Monte Carlo simulations also rely on site-site potentials, but the point of view is now that of Statistical Mechanics which allows to explicitly account for temperature and pressure. The price to be paid in order to include the temperature is that the sampling must be statistically significant. This implies that a large number of particles ($\sim$ 700) and a much more larger number of configurations (typically > 10000) have to be considered.

In Quantum Mechanical calculations, the energy is computed from the exact hamiltonian. It is then possible to build a Born-Oppenheimer energy surface which can be used later to perform lattice dynamics or to study the reaction path of a displacive phase transition. These methods give access to the electron density, the spin density and the density of states which are useful to predict electric and optical properties as well as to analyze the bonding. Recently, methods combining a quantum mechanical calculation of the potential and the Molecular Dynamics scheme have been developed after the seminal work of R. Car and M. Parrinello.

The quality of the potential is the key of a reliable simulation. Historically, the first potential were derived from experimental data and with simple assumptions on the bonding. These potentials are basically of the Born-Mayer type and polarization effects can be accounted for by a shell model. A new trail to derive potentials is to fit the parameters to the *ab initio* Born-Oppenheimer energy surfaces of prototype molecules such as $Si(OH)_4$ and $(OH)_3SiOSi(OH)_3$.

The first principle calculations on minerals have been pioneered by geochemists : G. V. Gibbs, J. A. Tossel, M. O'Keefe. They began to perform semi-empirical calculations on prototype molecules derived from mineral fragments in the early seventies. With the advent of efficient user friendly *ab initio* codes they evolved towards more accurate calculations in the eight-

ies. The prototype molecule technology provided significant results, but it is very limited because the same prototype molecule represents several polymorphs. Moreover, the periodicity is not taken into account and the dangling bonds are saturated by hydrogens in order to neutralize the system. These methods are now replaced by periodic schemes working either within the Hartree-Fock theory or within the density functional theory. In both cases core pseudopotentials are very useful to represent heavy atoms. In spite of the increase in the performances of the available computational facilities such periodic calculations remain extremely intensive both in CPU time and storage requirements. This prevents from the study of compound with large unit cell and low symmetry. An approximate scheme has been derived from the Electron Gas Approximation of Gordon and Kim which allows to consider large cells.

The bonding in silicates has been first investigated by Pauling. In particular it is difficult to decide the multiplicity of the SiO bond and its mostly ionic or covalent Character through a series of polymorphs. The advent of new tools of analysis which rely on the topology of local functions are shown to be useful to bring a more objective information on a controversial subject.

Molecular Dynamics of solids have made considerable progress during the ten past years. It is now possible to reproduce order-disorder phase transitions as well as the local structure of glasses.

The chapters in this book address the different points briefly sketched above. Our goal is to present the most efficient and reliable modeling approaches and to give the present state of the art.

Though the prediction of the structure and properties of *any* solid material is still out of reach, it is now possible to make reliable predictions on moderately complex structures. Therefore, the "scandal" revealed by John Maddox in 1988 is ending.

Bernard SILVI and Philippe D'ARCO

This page intentionally left blank.

THE STRUCTURAL PROPERTIES OF SILICA USING CLASSICAL AND QUANTUM INTERATOMIC FORCES

JAMES R. CHELIKOWSKY, NITIN R. KESKAR
Department of Chemical Engineering and Materials Science, Minnesota Super computer Institute, University of Minnesota, Minneapolis, MN 55455 USA

AND

NADIA BINGGELI
Institut Romand de Recherche Numérique en Physique des Matériaux (IRRMA), PHB-Ecublens, 1015 Lausanne, Switzerland

1. Introduction

It is well known that SiO_2 exists in amorphous or glassy phases as well as in numerous crystalline polymorphs. What is not well known are the structural details of amorphous silica, or the driving forces which produce numerous polymorphs. The crystal chemistry of silica in some ways is analogous to organic chemistry. Not only do numerous SiO_2 structures occur which differ only slightly in terms of the free energies, but nature of the $Si-O$ bond is such that multiple coordination states can occur. This analogy while useful cannot be taken too literally as silica chemistry (geology) is quite different from organic chemistry (biology). Nonetheless, the theoretical obstacles which one faces in modeling silica are almost as challenging as biological systems. There are a number of theoretical methods available for the description of condensed matter systems. One would like such methods to be accurate, yet computationally simple, but the complex nature of the chemical bond in silica places stringent conditions on the available methods. Since the $Si-O$ bond cannot be viewed as a purely ionic bond, it is not apparent that complete descriptions of silica can be handled by *pairwise* interatomic potentials.

A more rigorous approach to modeling silica centers on *quantum* descriptions of condensed matter systems. These methods can adequately describe

B. Silvi and P. D'Arco (eds.),Modelling of Minerals and Silicated Materials, 1-37.

structural energies, e.g. a typical error in the equilibrium bond length might be less than ~1%. Unfortunately, these methods tend to be computationally intensive. This problem can be compounded by large number of atoms in the unit cell of silica, *e.g.,* the coesite crystal form of silica contains 48 atoms in the unit cell. If one wishes to examine models for amorphous solids, the number can exceed several hundred atoms in the unit cell. At present, it is decidedly nontrivial to perform quantum calculations on cells which contain more than a few dozen atoms.

Perhaps a sensible procedure is to consider an approach which incorporates both interatomic potentials (classical forces) and fully quantum mechanical methods. One can compute the properties of smaller systems with quantum mechanical approaches and establish the accuracy, or inaccuracy, of interatomic potentials. For example, some elastic anomalies have been reported for α-cristobalite. These elastic anomalies indicated the presence of a negative Poisson ratio in this crystalline form of silica. With the use of interatomic potentials, it is a trivial matter to compute these properties. If the anomalies are confirmed via such calculations, it is likely that the experimental measurements are accurate, and more computationally intense calculations with quantum forces are merited. Another useful role of interatomic potentials is to perform molecular dynamics simulations, *e.g.,* to examine the amorphization of quartz under pressure. One can easily compute the free energy of large systems as a function of both temperature and pressure via interatomic potentials. Such calculations can be useful as guides if interpreted in a judicious fashion.

Given an accurate method for determining the energy (structural or free energies) of a condensed matter system, a number of important issues can be addressed. If accurate theoretical phase diagrams can be obtained, then hypothetical high pressure forms of silica can be examined. It may be that a low density form of silica, under geologic pressures may be unstable against a high pressure form of silica. Direct calculations of the free energy of hypothetical forms of silica can give guidance to establishing a realistic picture of the interior of the Earth. At a more fundamental level, questions concerning the structural nature of silica glass can be addressed. For example, it is possible to create high pressure forms of silica glass by different routes. Consider two cases. In the first case, one quenches liquid silica, and subjects the resulting glass to high pressure. In the second case, one subjects quartz to a high pressure to create amorphous silica. Are the resulting forms of silica in these two cases the same, or are they fundamentally different in their structural attributes?

2. Classic Forces from Pairwise Interatomic Potentials

An elementary approach for determining the structural energies of a solid is to construct an algebraic representation of the interatomic force field. There are numerous obstacles to constructing such potentials. For example, changes in coordination, re-hybridization, charge transfer, and Jahn-Teller distortions are very difficult to incorporate in classical potentials. However, if the Coulomb forces play a dominant role in the chemical bonds present, it may be possible to obtain some useful results with interatomic potentials. This may be the case for materials subjected to high pressure situations.

One of the more successful attempts at constructing an interatomic potential is from Tsuneyuki, *et al.* [1] who proposed a new interatomic potential for silica. They employed Hartree-Fock self-consistent-field calculations to examine clusters of SiO_2. From these calculations, they fit pairwise interatomic potentials to the structural energies of the clusters. The form of the interatomic potentials they employed is given by

$$U_{ij} = \frac{q_i q_j}{R_{ij}} + g_o(b_i + b_j)\exp[\frac{(a_i + a_j - R_{ij})}{(b_i + b_j)}] - \frac{c_i c_j}{R_{ij}^6} \qquad (1)$$

where R_{ij} is the interatomic distance between the i- and j-th species, q_i is the charge on the i-th species. The parameters (a_i, b_i, c_i, g_o) are fixed to replicate the structural energy of the SiO_2 clusters. Once the potentials are fixed, they may be used to calculate the structural energies of other forms of silica. For example, these potentials were used to examine known polymorphs of silica: α-quartz, α-cristobalite, coesite and stishovite. Using molecular dynamic simulations, Tsuneyuki, *et al.* found stable structures at normal pressures and temperatures. This was true despite large differences in the coordination numbers, and the densities of the structures considered. Moreover, they could reproduce the equilibrium structural parameters of the silica polymorphs. Earlier studies of silicon dioxide clusters had suggested that interatomic potentials would describe qualitatively, and sometimes quantitatively, the *Si - O* bond in the solid state. The Tsuneyuki, *et al.* work showed for the first time that dynamic stability in silica polymorphs could be achieved with simple pairwise potentials.

The use of accurate pairwise forces would greatly enhance our ability to use molecular dynamics simulations to describe melting and glass formation of the silica polymorphs. Recent proposals for high pressure forms of silica which could be examined by accurate pairwise forces,

The successful application of pairwise forces to silica is counter intuitive. SiO_2 has traditionally been viewed as a covalent material. Tetrahedral units of SiO_4 dominate the structural properties for those structures containing four-fold coordinated silicon. Pairwise potentials would not be expected to

reproduce angular forces present the tetrahedral bonds. Other workers have found it necessary to include three body forces in their description of silicas to replicate the ground state structural parameters[2,3,4]. The use of three body forces can greatly complicate the simulations for melting or crystal stability. Hence, the creation of an accurate pairwise potential would be quite useful and have widespread applications.

3. Quantum Interatomic Forces from Pseudopotentials

Despite the utility of interatomic potentials, these potentials cannot provide a "complete" description. Such potentials cannot provide a description of electronic properties, and may be suspect for situations involving coordinate changes, *e.g.,* defects, and surfaces. Quantum mechanical methods can provide a complete description of matter. Once the spatial and energetic distributions of the electrons are known, the electronic energy of a system is determined. Given the Hamiltonian of a system, the remainder of the work involves a numerical solution of the Schrödinger equation. In practice, it is simply not possible to describe a system with 10^{23} electrons. Fortunately, there are some sensible approximations which allow one to solve a Schrödinger-like equation with sufficient accuracy for useful comput tations.

Three approximations are commonly invoked. The first is the Born-Oppenheimer approximation. This approximation allows one to separate the electronic degrees of freedom from the nuclear degrees of freedom. For a material like silica, this is a superb approximation. A second approximation is the one-electron approximation within the local density approximation[5, 6, 7]. The one-electron approximation allows us to consider an electronic potential which takes many-body effects into account in an average sense. In the local density approximation the exchange-correlation potential at a point $\vec{r}$ depends only on the electron density $\rho(\vec{r})$ at that point. This approximation has proven to be a powerful approach for solid state systems. The error one makes is probably significant in terms of the exchange-correlation energy, but if one considers *relative* energies often the cancellation of errors between two similar states is nearly complete. For example, suppose one considers two crystalline forms of silica. For each crystal, the error incurred via the local density approximation may be significant, but the relative energy difference between the crystalline states may be reproduced accurately. The third approximation commonly made is to use *pseudopotentials*[8] to describe the interactions between the outer (valence) electrons with the inner (core) electrons. The pseudopotential concept rests on the orthogonality requirement of the valence states to core states. The orthogonality condition imposes a nodal structure on solutions

to the Schrödinger equation. For the valence states, the nodal structure reflects a high kinetic energy state. The valence state can be made nodeless by effectively transforming the kinetic energy of the state to potential energy. The eigenvalue of the state remains unaltered, but the transformed state (a pseudo-wavefunction state) is altered. The pseudo-wavefunction differs from the "all electron" wavefunction within the core region, *e.g.*, for an atom it is usually nodeless. Outside the core region the pseudo-wavefunction matches the original state. The transformed potential, *i.e.*, the pseudopotential, is also different from the original potential. Unlike the "all electron" potentials, the pseudopotential is angular-momentum dependent, *e.g.*, the pseudopotential has a different form for an $s-$ versus a p-state.

Of the three approximations outlined, the one-electron approximation, *i.e.*, the local density approximation, is the weakest. This approximation fails to replicate features such as image charges at a surface. Also, it fails to describe excited states properly, but this is not a concern for structural energies. Despite such shortcomings, the local density remains one of the most successful approaches to calculating many-body energies in solids.

Within the local density-pseudopotential approximation, the total electronic potential for the valence electrons is written as

$$V_{total}(\vec{r}) = V_{ion}(\vec{r}) + V_H(\vec{r}) + V_{xc}[\rho(\vec{r})] \tag{2}$$

V_{ion} corresponds to the interaction potential between the valence electrons and the ion core formed by the nucleus and tightly bound core electrons, *i.e.*, the "ion-core" pseudopotential. V_H corresponds to the electrostatic interactions between the valence electrons, and V_{xc} corresponds to the effective exchange-correlation potential between the valence electrons. The ionic pseudopotential is a *nonlocal* operator. It can be written as

$$V_{ion}(\vec{r}) = \sum_{l=0}^{\infty} \mathcal{P}_l^{\dagger}\, V_{ion,l}\,(\vec{r})\, \mathcal{P}_l \tag{3}$$

where P_l projects out the l-component of the pseudowave function. The sum over angular components is over all l values, in principle. However, in practice, only the $s-$, and $p-$ (and sometimes $d-$) components are important for silica.

The replacement of the "all electron" potential with a pseudopotential has a number of advantages. Core states are not considered, and only the properties of the chemically active valence states are reproduced. Moreover, the ion-core pseudopotentials are highly transferable. The same potentials can be used in clusters, molecules, solids or the liquid state. In the case of silica, the $1s^2$, $2s^2$, $2p^6$ states in silicon are treated as chemically inert

as are the $1s^2$ states in oxygen. Only the valence states are replicated by pseudopotentials, the resulting wavefunctions are smooth and slowly varying. A simple plane wave basis will be efficient in this circumstance. Such a basis possesses a number of positive attributes: the basis is complete, no shape approximations are made, the set is orthogonal/orthonormal, and the electrostatic potential can be trivially evaluated with a plane wave basis.

Several procedures exist for constructing pseudopotentials. One of the most efficient methods produces "soft" pseudopotentials, *i.e,* pseudopotentials which rapidly converge in terms of the number of plane waves [8, 9, 10]. Pseudopotentials have been constructed for both oxygen and silicon, and have been widely used in the literature[11, 12, 13, 14, 15, 16]. The oxygen ion core pseudopotential is usually generated from the atomic valence $2s^2 2p^4$ ground state configuration. The size of the core is determined by the outermost node of the 2*s* state, *e.g.* the core radius might be taken as 1.45*a.u.* (1 a.u.= 0.529Å) The oxygen pseudopotential is not adjusted to replicate the unoccupied 3*d*-states, as these states do not contribute significantly to the chemical bond. For silicon, s-, *p-,* and *d*-components of the potential are included. A typical value for the radial cut-off for all three components is 1.80*a.u.*

Given an ion core pseudopotential, the valence electrons are allowed to respond to the potentials to form a self-consistent total potential. Initially, an approximate potential is used to solve the one-electron Schrödinger equation. The wavefunctions from the solution of this approximate potential are then used to construct a new potential which in turn can generate new wave functions from which the potential can be updated again. When the "input" potential agrees with the "output" potential, a self-consistent. field has been obtained.

In summary, the one electron Schrödinger equation for a crystal has the form :

$$[\frac{-\hbar^2\nabla^2}{2m} + V_{ion} + V_H + V_{xc}]\psi_{n,\vec{k}}(\vec{r}) = E_n(\vec{k})\psi_{n,\vec{k}}(\vec{r}) \tag{4}$$

where $\vec{k}$ represents the wave vector quantum number. This equation can be solved using a. fast iterative diagonalization method[17, 18]. One advantage of this method is that it does not require a calculation of the full Hamiltonian matrix. Rather, only $H\psi$ is calculated. This procedure leads to dramatic reduction in storage, and a considerable reduction in computing time.

Within a plane wave basis, the wave functions can be written in the Bloch form as

$$\psi_{n,\vec{k}}(\vec{r}) = \sum_{\vec{G}} \alpha_n(\vec{k},\vec{G}) \exp(i(\vec{k}+\vec{G})\cdot\vec{r}) \tag{5}$$

where $\vec{G}$ is a reciprocal lattice vector. Normally one terminates the sum by considering only $\vec{G}$'s such that $|\vec{k} + \vec{G}|^2 < G^2_{max}$. A typical energy cut-off might be $64Ry$. Even for a relatively simple form of crystalline silica., such as α-quartz, this entails a few thousand plane waves in the basis.

Once the Schrödinger equation is solved, the energy and spatial distributions of the valence electrons are known[19]. The total electronic energy can be obtained from terms of the form:

$$E_{tot} = E_{c-c} + [E_{kin} + E_{c-e} + E_{e-e}] \tag{6}$$

The first term, $E_{c\text{-}c}$, corresponds to the Coulomb interactions of the ion cores. Since the cores are treated as rigid, this term can be evaluated by an Ewald summation. The remaining terms are evaluated using the electronic pseudo-wave functions. The kinetic energy, E_{kin} is evaluated trivially in a plane wave basis. The ion core-electron term, $E_{c\text{-}e}$, is evaluated from the valence charge density and a knowledge of the ion core pseudopotential. The most complicated term is the electron-electron term, $E_{e\text{-}e.}$ This term contains Coulomb terms from the Hartree potential, V_H, which must he included in an Ewald summation with the core-core interactions. The energy of this term corresponds to each valence electron moving in an average potential generated by the other electrons. The term also includes exchange-correlation energies resulting from V_{xc} .Within the local density approximation, these terms can be evaluated once a self-consistent charge density has been constructed.

The goal of a total energy calculation is to determine the electronic energy for a given structure, or structures. For example, one might consider a number of candidate structures for SiO_2. Since crystalline silica often condenses in complex structures with a number of internal parameters, it is nontrivial to evaluate the structural energy. For example, the α-quartz structure has three molecular units in the hexagonal unit cell. The cell shape is determined by $\frac{c}{a}$ ratio, and four internal parameters fix the positions of the silicon and oxygen atoms within the cell. At each volume, the shape and internal structure of the crystal must be optimized by minimizing the total energy. It is possible to expedite this procedure by calculating the forces on each atom using the Hellman-Feynman theorem. The atoms can then be moved according to the computed forces to minimize the structural energy. One can use the energy versus volume calculations to determine the enthalpy of the structure as a function of volume, or pressure. This type of calculation can be used to predict which phase of silica will be most stable as a. function of pressure. Moreover, the results can be used to predict such ground state properties as the cohesive energy, ambient structural parameters, and bulk moduli of virtually any crystalline form of matter[8].

The accuracy of the local density-pseudopotential method is quite adequate for most studies. The structural properties are often replicated to within ~1-2%. The cohesive energies are not so accurately determined; the binding energy is usually overestimated by 5-10%. However, the relative energy differences between solid state structures are more accurately calculated . Structural energy differences as small as ~0.01 eV/atom can be reliably predicted.

4. Crystalline silica under pressure

A useful classification for crystalline silica is the coordination number of the silicon cation. The most stable forms of crystalline silica contain four-fold coordinated cations: these structures consist of SiO_4 tetrahedral units. Within these units, the O-Si-O bond angles are close to the ideal tetrahedral angle of 109.5°. The tetrahedral units are linked via bridging oxygen atoms. The Si-O-Si bond angles center near ~140° with a range of ±20°. These bond angles are quite pliant and the differences between four-fold coordinated crystals of SiO_2 can be traced to how the tetrahedral units are linked together.

When subjected to pressure, the coordination number of the cations, and anions, increases. In the case of silica, this has been an area of some conjecture. Some thirty years ago, a new phase of SiO_2 was discovered, *i.e.,* stishovite. Stishovite can be formed from silica under pressure, yet it can exist in a metastable state under ambient conditions. In this form of crystalline silica,, silicon is six-fold coordinated. Questions as to the denser forms of silica beyond stishovite have been raised in the context of mineral physics.

In Figure 1, some of the common forms of crystalline silica along with possible high pressure forms are illustrated. The structures with SiO_2 tetrahedral units include α- and β–quartz. Dense phases of silica include stishovite which corresponds to the rutile structure. Possible high density phases of silica include fluorite, and a distortion of the fluorite structure, the $Pa\bar{3}$ structure. In particular, it might seem that a "fluorite-like" structure would be an appropriate candidate for a high pressure form of silica as the cation in such a structure is eight fold coordinated. In Figure 2, the total energy of the structures as a function of volume are illustrated.

These curves were generated by fitting a standard equation of state to computed energies as a function of volume. Consistent with experiment, the lowest energy phase is the α-quartz structure which is a distortion of the β-quartz structure. The stishovite structure is nearly as stable as the α-quartz structure, but the equilibrium molecular volume is considerably smaller owing to the higher coordination in the stishovite structure. The $CaCl_2$

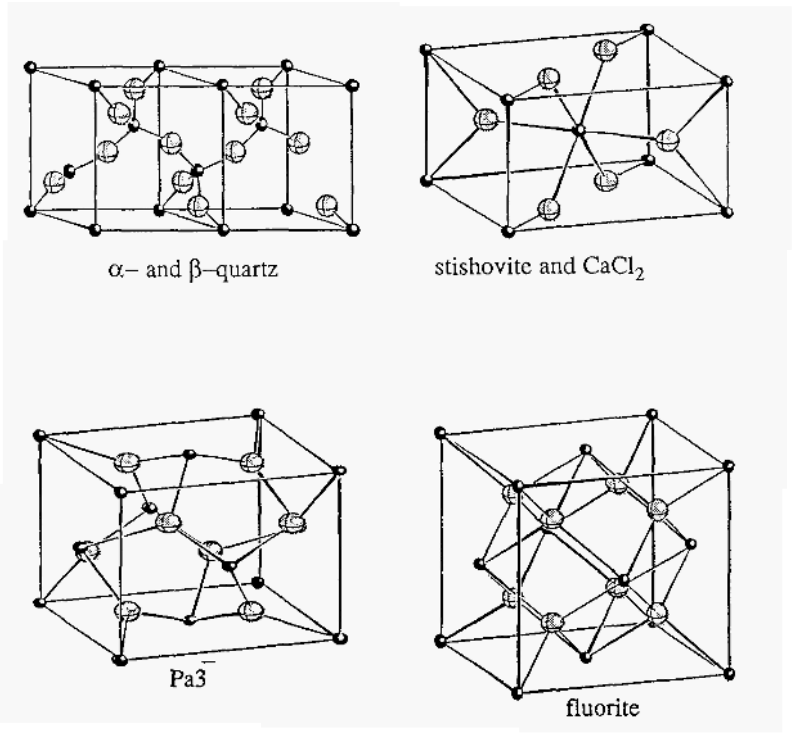

Figure 1. Ball and stick models for several crystalline forms of silica. The smaller spheres represent the silicon cations. α- and β-quartz possess four-fold silicon cations. The stishovite and the $CaCl_2$ structures possess six-fold coordinated cations. Hypothetical forms of silica include the $Pa\bar{3}$ structure and the fluorite structure. These latter structures have eight-fold coordinated cations.

structure, which corresponds to a distorted stishovite structure[20, 21]. is nearly degenerate in energy with stishovite in our calculations.

An interesting aspect of Figure 2, is the prediction that, the $Pa\bar{3}$ structure should be stable under high pressure whereas the fluorite structure is not. Pseudopotential calculations predict that the density of fluorite is slightly lower than the density of the $Pa\bar{3}$ and the stishovite structure. From thermodynamics, it is not possible to convert a dense structure into a less dense structure with the application of isotropic pressure. The inclusion of temperature is unlikely to alter our calculations and this conclusion. Despite theoretical predictions indicating the high pressure stability of the $Pa\bar{3}$ structure, it has not been observed at pressures up to ~100GPa. There may be kinetic barriers which inhibit the transformation of the stishovite, or $CaCl_2$ structure to the $Pa\bar{3}$ structure.

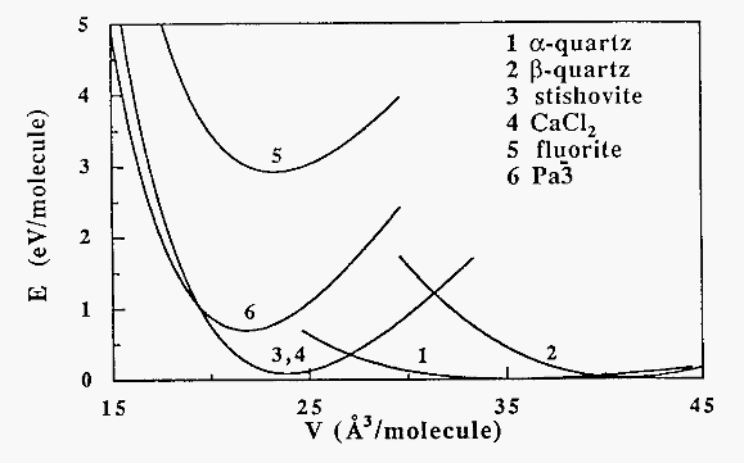

Figure 2. Equations of state for several polymorphs of crystalline silica.

TABLE 1. Calculated structural parameters for several forms of crystalline silica.

	Equilibrium energy (eV/SiO2)	V_0(Å^3/SiO_2) expt.	theory	*Bo* (GPa) expt.	theory
α-quartz [23, 24]	0(0)	37.710	37.86	37.1	38.1
β-quartz [25]	0.017	39.634	41.05		135.1
Stishovite[26, 27]	0.086	23.308	22.82	313.0	292.0
Fluorite	2.914	–	23.29	–	300.1
Pa3	0.699	–	21.82	–	347.0

In Table 1, the calculated structural parameters are listed: the equilibrium energy and volume, and the bulk modulus. The equilibrium energy of α-quartz is taken as the zero of energy. Relative to isolated pseudo-atoms of silicon and oxygen, quartz is over bound by about 15%, *i.e.,* the cohesive energy of quartz is calculated to be ~22.2 eV/molecular unit as compared to an experimental value of 19.2 eV/molecular unit. This is consistent with the local density approximation. The *relative energies* of the silica phases to a-quartz should be much more accurate. As expected owing to the small structural differences, the energy difference between α- and β-quartz is only

~0.02eV/molecular unit. Such a small energy difference is at the limit of pseudopotential methods. Stishovite is slightly higher in energy than a-quartz. This small energy difference is consistent with the observation that stishovite can coexist as a metastable phase with quartz. The equilibrium volumes for the five phases in Table 1 are in good agreement with experiment. The largest error is ~3%.

Ambient structural parameters from pseudopotential calculations are listed in Table 2 For comparison purposes, interatomic potentials have been used to compute the properties of these forms of silica and several other polymorphs. In general, the interatomic potentials do a surprisingly good job of replicating the structural properties.

5. Elastic Anomalies and the Structural Stability of Crystalline Silica

5.1 ELASTIC CONSTANTS

The elastic or mechanical properties of a perfect crystal can be related to changes in the structural energy when the crystal is subjected to a strain field. It is possible to determine such properties by direct calculations using either quantum, or classical methods. The elastic constants of a solid at ambient pressure can be determined from:

$$\sigma_i = \sum_j c_{ij}\epsilon_j + \mathcal{O}(\epsilon^2) \tag{7}$$

where

$$\sigma_i(\epsilon) = \frac{1}{V(\epsilon)}\left(\frac{\partial E(\epsilon,\epsilon')}{\partial \epsilon'}\right)_{\epsilon'=0} \tag{8}$$

σ_i is the stress tensor, E and V are the total energy and volume of the system, and E and ϵ' are the symmetric strain tensors. Using Voigt's notation[30] $\epsilon_1 = \epsilon_{xx}, \epsilon_2 = \epsilon_{yy}, \epsilon_3 = \epsilon_{zz}, \epsilon_4 = 2\epsilon_{yz}, \epsilon_5 = 2\epsilon_{xx}$ and $\epsilon_6 = \epsilon_{xy}$. By a judicious choice of strains, one can calculate the stresses and determine the elastic constants.

It is a computationally intensive task to compute elastic constants from quantum methods. To obtain accurate structural energies, one requires a highly converged basis set. Conversely, interatomic potentials may be trivial to implement and are cornputationally simple. To compute the elastic constants, one can consider the limit of $\vec{q} \to 0$ with respect to lattice vibrations, *i.e.,* the long wavelength limit. In this approach, the dynamical matrix is computed along with the first and second derivatives from the pairwise potentials.

In Table 3, the elastic constants obtained from the pair potential calculations are given for two low density forms of crystalline silica: α-quartz and

TABLE 2. Structural parameters of silica polymorphs. The numbers within parentheses are the results of our pseudopotential calculations. The other theoretical results are obtained using pair potentials. The reference numbers in the first columns indicate the source of the experimental data. The lattice constants (c, a) are in Å

Crystal	Symmetry	Lattice Parameters (Expt.)	(Theory)
α-quartz[23]	Hexagonal	a = 4.9160	5.02(4.89)
	($P3_121$)	c = 5.4054	5.53(5.49)
		u = 0.4697	0.461(0.469)
		x = 0.4135	0.425(0.418)
		y = 0.2669	0.280(0.274)
		z = 0.1191	0.119(0.118)
β-quartz[28]	Hexagonal	a = 5.01	5.17
	(P6222)	c = 5.47	5.73
		u = 0.197	0.217
α-cristobalite[29]	Tetragonal	a = 4.9570	4.96
	(P41212)	c = 6.8903	6.68
		u(Si) = 0.3047	0.330
		x = 0.2381	0.231
		y = 1109	0.140
		z = 0.1826	0.190
β-cristobalite[28]	Cubic	a = 7.16	7.07
	(Fd3m)	u(Si, 1) = 0.255	0.298
		u(Si, 2) = −0.008	0.032
		u (O) = 0.125	0.164
		x = 0.66	0.634
		y = 0.66	0.669
		z = 0.06	0.022
β-tridymite[28]	Hexagonal	a = 5.03	5.37
	(P63/mmc)	c = 8.22	8.75
		u = 0.44	0.438
Stishovite[26]	Tetragonal	a = 4.1801	4.26(4.14)
	(P42/mnm)	c = 2.6678	2.75(2.67)
		u = 0.3062	0.304(0.305)
Fluorite	Cubic	–	a = 4.52(4.53)
Pa3	Cubic	–	a = 4.55(4.43)
	(Pa3)		u = 0.337(0.344)

α-cristobalite. Elastic constants can provide insights into the stability of the crystal, and point to any anomalies which might occur in its mechan-

TABLE 3. Single crystal elastic constants (in GPa) of α-quartz and α-cristobalite.

	α-quartz		α-cristobalite	
	Experiment[32]	Theory	Experiment[33]	Theory
c_{11}	87.103	71.5	59.4	51.5
c_{33}	106.552	99.1	42.4	35.3
c_{44}	59.215	42.4	67.2	59.0
c_{66}	38.339	30.9	25.7	17.5
c_{12}	10.425	9.7	3.8	6.0
c_{13}	12.894	15.5	-4.4	-3.1
c_{14}	-17.206	-13.1	–	–

ical properties. Crystalline forms of silica often possess unusual structural properties owing to the existence of "rigid" tetrahedral units.

5.1.1. *Negative Poisson Ratio in Crystalline Silica*

The Poisson ratio can be used to characterize the mechanical property of a solid. It is defined as the negative quotient of the strain in the transverse direction to the strain applied in the longitudinal direction. For a uniaxial loading along the *c*-axis:

$$\nu = -\frac{\Delta a/a}{\Delta c/c} \tag{9}$$

Most solids contract laterally when subjected to a uniaxial stress. This response acts to conserve the crystal volume and reflects a positive Poisson ratio. However, α-cristobalite, a low density form of silica has been reported to have a negative Poisson ratio: when subjected to a uniaxial compression, α-cristobalite *contracts* in the transverse direction[33]. This response is not prohibited by any thermodynamic constraints. The requirement that the strain energy for an elastic isotropic solid be non-negative only leads to the restriction that $-1 \leq \nu \leq \frac{1}{2}$ However, other low-density forms of silica have been measured to have positive Poisson ratios. This is a surprising situation. α-cristobalite has a similar structural and chemical environment as other low density forms of crystalline silica such as α- or β quartz. This situation reinforces the need for a theoretical determination of the Poisson ratio. Experimental measurements of a negative Poisson ratio can be difficult, and spurious reports exist in the literature.

It is possible to gain insights into this anomalous phenomenon using either interatomic potentials, or quantum methods such as the pseudopotential method. One can fix the *c*-parameter and find the optimal *a*-parameter.

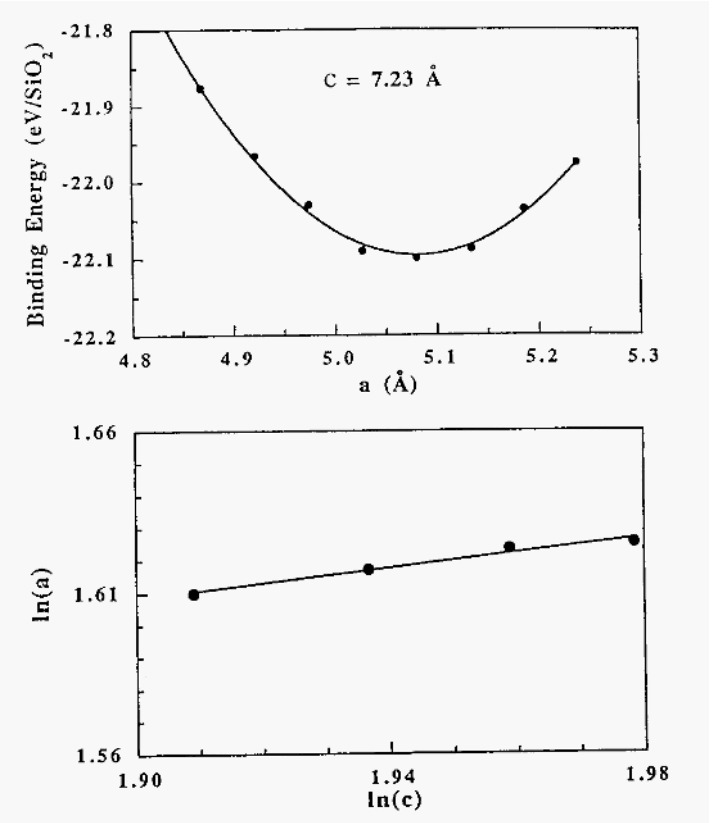

Figure 3. Determining the Poisson ratio. The top figure shows the variation of the total energy of a-cristobalite as a function of the lattice parameter a at c = 7.23Å. The minimum energy of this curve fixes the equilibrium value of a for the given value of c. The bottom figure illustrates a *as* a function of c on a logarithmic scale. The negative of the slope of this curve yields the Poisson ratio. The structural energy is determined from *ab initio* pseudopotential calculations.

If one does this for a number of values for c, then a plot of $ln(a)$ versus $ln(c)$ can be made. The first derivative of this curve determines the Poisson ratio at the c-value of interest. This procedure is illustrated in Figure 3. In Figure 4, the Poisson ratio for α-cristobalite and α-quartz is illustrated as a function of the uniaxial strain. Pseudopotential calculations were performed in the limit of small strains, whereas interatomic potentials were performed for a wide range of strains. In agreement with experiment, both the pseudopotential and interatomic potentials confirm the existence of a negative Poisson ratio in α-cristobalite. The value of the Poisson ratio calculated from a pseudopotential calculation is -0.20; the value calculated

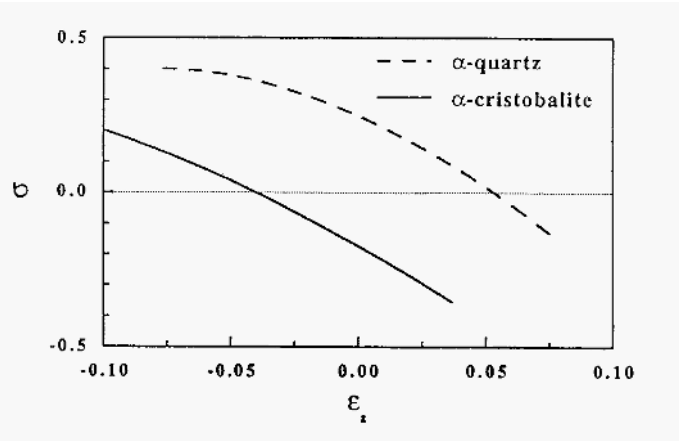

Figure 4. The variation of the Poisson ratio from interatomic potentials as a function of the uniaxial strain along the *c*-axis. Note that a *positive* strain occurs for a material under *tension.*

from interatomic potentials is -0.17. The measure isotropic average value, i.e., $\sigma_{ave} = (3B - 2G)/2(3B + G)$ where B is the bulk modulus and G is the shear modulus, is -0.163[33]. The interatomic potential calculations suggest both crystals will exhibit a positive value for the Poisson ratio for large compressive strains. For large tensile strains, both crystals are predicted to exhibit a *negative* ratio. The main difference is that a-cristobalite has a negative ratio at small strains whereas α-quartz does not. The most interesting feature of this work is the prediction of a negative ratio for α-quartz under large tensile strains.

It is possible to perform uniaxial loading along arbitrary directions. For some directions, it is possible to have a crystal exhibit a negative ratio while the average ratio is positive. An analysis for α-quartz indicates a small negative ratio may exist for specific directions. For α-cristobalite the ratio is negative for any loading direction.

The origin of a negative Poisson ratio is subtle. An unanticipated conclusion is that angular forces *per se* are not required for reproducing the negative Poisson ratio. Pairwise forces alone can reproduce the negative Poisson ratio in these materials. A simple model has been proposed for the occurrence of a negative Poisson ratio based solely on interatomic distances. If the nearest neighbor $O - O$ distances are held fixed, then the tetrahedral units of SiO_4 are absolutely rigid. In the "rigid" tetrahedral limit, the Poisson ratio is strongly negative for the α-cristobalite crystal. On the other hand, this model shows that tetrahedral units cannot be absolutely rigid

for other silica crystals if the *c/a* ratio changes. It is not possible to maintain the rigidity of a SiO_4 units in β-quartz while maintaining it symmetry. This model predicts β-quartz will never exhibit a negative Poisson ratio when a uniaxial stress is applied along the *c*-axis.

Motion of the SiO_4 tetrahedra is illustrated explicitly in Figure 5 for α- and β-quartz and α-cristobalite crystals when subjected to a uniaxial tension.. The atomic positions are determined from interatomic pair potential calculations. As the *c*-axis is extended the SiO_4 units in α-cristobalite rotate "outward" by increasing the *Si - O - Si* bridging angle. From quantum mechanical calculations, as well as from interatomic potentials computations[4], this angle between the units is known to be soft. The tetrahedral rotation of the SiO_4 units allows the *a* lattice parameter to increase along with the volume of the unit cell, and a negative Poisson ratio occurs. This behavior does not follow for high compressive strains as the SiO_4 unit eventually distorts. α-cristobalite, and α-quartz under tension, are similar. If sufficient distance occurs between the tetrahedral units, then the stain can be accommodated by a reduction in the intertetrahedral distances while preserving the SiO_4 units. This situation appears necessary for a negative Poisson ratio.

5.1.2. *Mechanical Stability of Quartz Under Pressure: The Origin of Pressure Induced Amorphization*

Another area where structural energy calculations can be of great utility concerns the solid-state order-disorder transformation. Such transformations can be induced by pressure. At high pressures, α-quartz subsists as a metastable phase which gradually transforms to an amorphous form and, subsequently to a rutile-like crystalline structure[34]. Evidence for the onset of the amorphization has been reported at about 15 GPa from single crystal analysis[35]. In powder measurements[36], the transition is observed to be complete by ~35 GPa. Experiments performed on powered samples at pressures above 60 GPa indicate a crystalline structure which is thought to resemble the stishovite structure[37].

One advantage of structural energy calculations is that one can examine the theoretical evolution of the α-quartz crystalline phase at pressures above the amorphization transformation. It has been proposed that α-quartz would evolve under pressure to a structure in which the oxygen anions are arranged in a body-centered-cubic (bcc) stacking, were it not for the fact that the crystal first amorphizes. The bcc arrangement of oxygen anions was proposed[38] by an extrapolation of the trends observed during the compression of α-quartz and its low pressure isomorphic counterpart: – GeO_2.

This hypothesis can be tested by examining the arrangement of oxy-

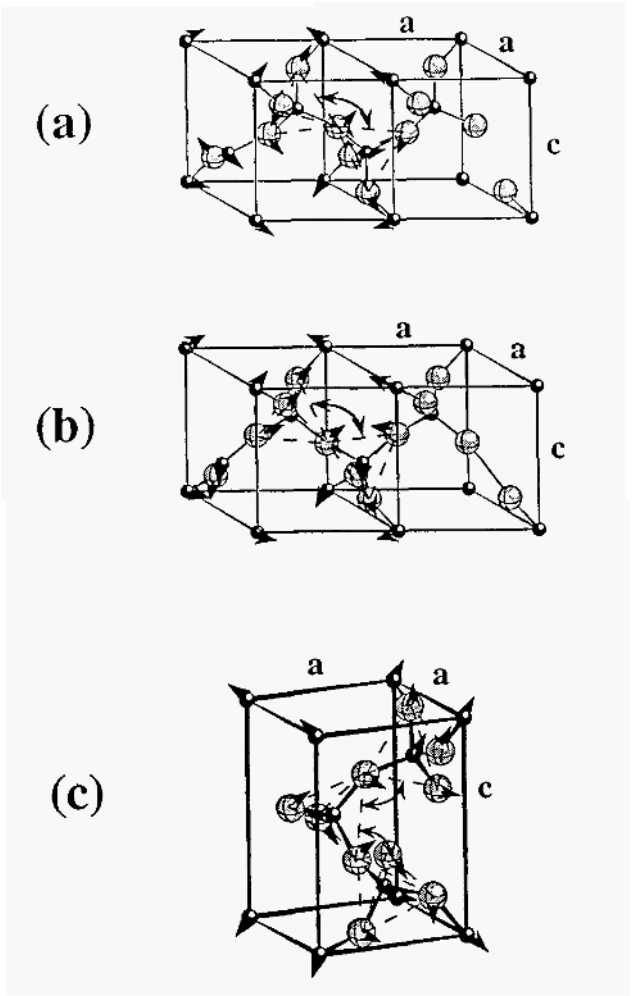

Figure 5. Motion of the SiO_4 tetrahedra under uniaxial *tension* for α-quartz (a), β-quartz (b) and α-cristobalite (c).

gen anions in α-quartz as a function of pressure[14]. At fairly high pressures, *e.g.,* above ~50 GPa, the oxygen positions are clearly tending toward a bcc arrangement. For an ideal bcc arrangement of oxygen anions, $x = y = \frac{1}{3}$ and $z = 1/12$ in the Wyckoff notation[28] and the lattice ratio $c/a = \sqrt{\frac{3}{2}} \approx 1.225$. Assuming ideally centered SiO_4 tetrahedra, $u = 5/12 \simeq 0.417$ where u determines the position of the silicon cation. At ambient pressure, these parameters are $x = 0.418, y = 0.274, z = 0.118, u = 0.469$

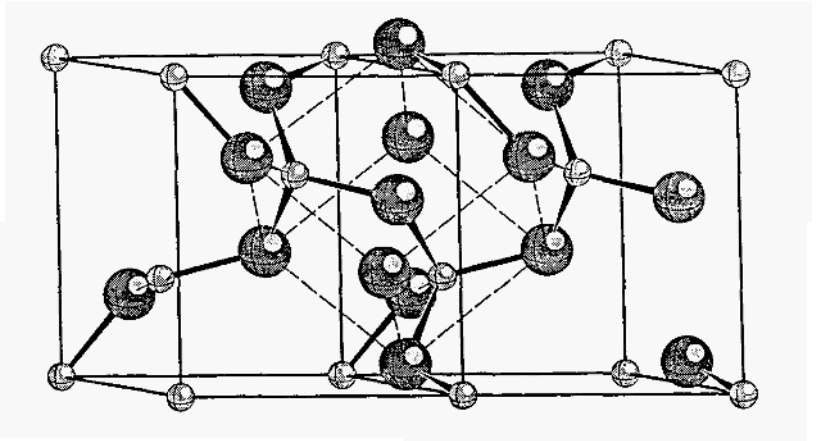

Figure 6. Theoretical high pressure form for the α-quartz structure. The silicon cations are shown by the small spheres, oxygen anions by the large spheres. Note how the oxygen anions form a bcc packing at high pressure.

and c/a = 1.125. At a pressure near ~ 50GPa, total energy calculations yield $x = 0.350$, $y = 0.339$, $z = 0.077$, $u = 0.406$ and c/a = 1.149, and confirm a pressure-induced tendency of the oxygen anions toward the bcc structure. The bcc arrangement is not ideal as the c/a ratio is smaller than expected. The bcc arrangement of oxygen anions at high pressure in the a-quartz structure is illustrated in Figure 6 .

Although bcc packing is achieved at pressures significantly larger than the amorphization pressure, the main features associated with the bcc packing already occur at pressures of the order of ~30 GPa. Oxygen bcc packing will promote the diffusion of the silicon cations. The body centered cell has 12 equivalent tetrahedral sites and 6 octahedral sites. Only one of the tetrahedral sites is occupied in the α-quartz structure. Diffusion of silicon between the tetrahedral sites, or to a nearby octahedral site along "tunnels" formed by the columns of oxygen anions may be a key process in the transformation to the amorphous state and the further transformation to the crystalline Si six-fold coordinated structure. As a function of pressure, one of the independent 0-Si-0 angles, which is equal to ~ 110° at ambient pressure, increases to ~ 127° in the bcc environment. This angle opening provides a pathway for enhanced diffusion of the silicon cations from the four-fold to six-fold sites.

A closely related issue to the formation of the bcc oxygen anion packing concerns the mechanical stability of α-quartz under pressure. It has been suggested that such an instability could drive the amorphization process[36, 39], *i.e.,* bcc packing could be inherently unstable against a shear. Total energy calculations allow one to test such a hypothesis. One can understand, at least qualitatively, strain induced nonlinearities in α-quartz by examining changes in the bond angles with pressure[41]. In Figure 7, the Si-O-Si and O-Si-O bond angles are plotted as a function of pressure. Experiment 1 is from Levien *et al.* [23] Experiment 2 is from Glinnemann *et al.*[43] Except at very elevated pressures, the O-Si-O bonds remain near the tetrahedral angle of 109.5°. However, the Si-O-Si bridging bond angle is quite pliant. This angle is equal to 145° at ambient pressure; at ~20GPa it is reduced to 125°. From roughly ambient pressures to 10 GPa, this angle varies linearly with pressure. Above 10 GPa, the angle exhibits a nonlinear behavior with pressure. This nonlinearity is indicative a strained bond angle. Such a conclusion is consistent with quantum chemistry calculations on molecular fragments. These calculations suggest that Si-O-Si angles below ~120° are very unfavorable in terms of generating a large strain[41].

Another structural feature which exhibits a large strain is the interpolyhedral O-O distance. For modest pressures, *e.g.,* less than ~10GPa, the decrease in interpolyhedral distances can accommodate the compression in α-quartz as opposed to a compression of the $Si-O$ bond length. An anomalous feature of the pseudopotential calculations is that a small *expansion* of the $Si-O$ bond length is found to occur at low pressures[11]. This feature has also been suggested by Raman studies of quartz under pressure[42]. The smallest O-O interpolyhedral distance at ambient pressure is 3.4Å. This value decreases to ~2.GÅ at 20GPa. In naturally occurring silicates, the smallest known interpolyhedral distance is 2.75Å which occurs in Be2SiO4[44]. This suggests that the α-quartz structure may becoming unstable at pressures greater than ~20GPa as the minimum interpolyhedral distance approaches the smallest known value. Moreover, the behavior of this distance with pressure exhibits nonlinear behavior above 15 GPa.

While the Si-O-Si angles and the interpolyhedral O-O distances exhibit nonlinearities with pressure, these do not provide a quantitative measure for mechanical instability. With total energy methods, it is possible to calculate the elastic constants directly as a function of pressure. Under initial hydrostatic pressure, the elastic constants, C_{ij}, are related to the energy variation, ΔE, to second order in the strains, ϵ_{ij}, through[31]

$$\frac{\Delta E}{V_o} = -p\frac{\Delta V}{V_o} + \frac{1}{2}\sum_{ij} c_{ij}\,\epsilon_i\,\epsilon_j \qquad (10)$$

where p, V are the initial pressure and volume, respectively, and ΔV =

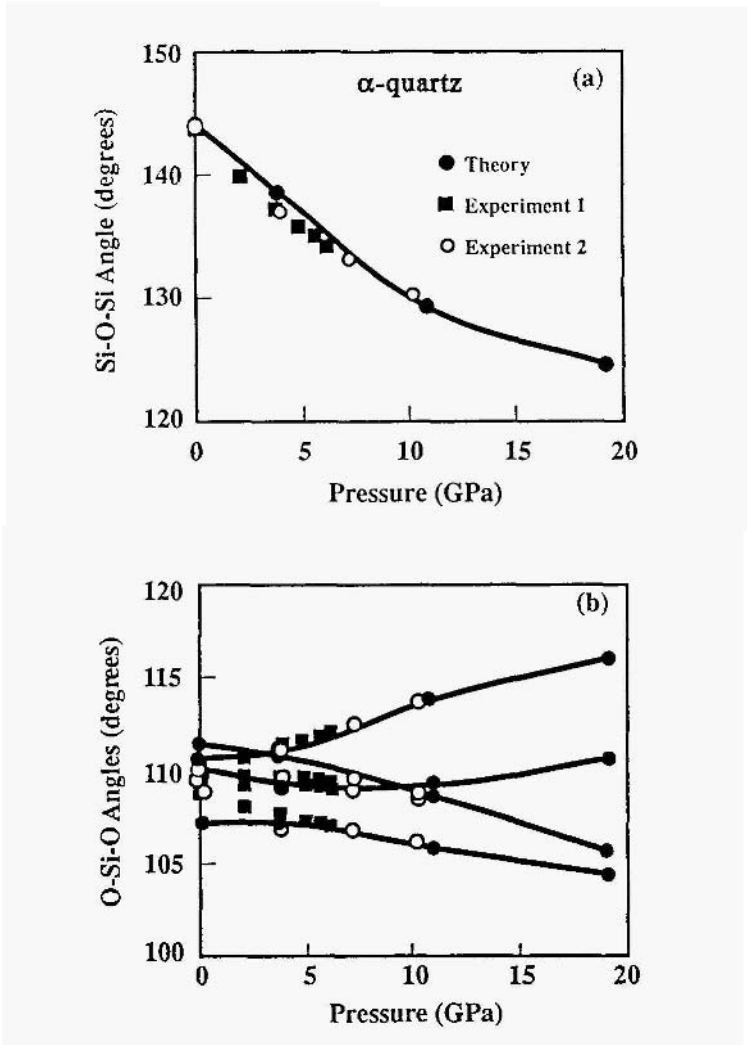

Figure 7. Bond angles in α–quartz as a function of pressure.

V – V0is the volume change to second order in the strain:

$$\frac{\Delta V}{V0} = \epsilon_1 + \epsilon_2 + \epsilon_3 + \epsilon_2\epsilon_3 + \epsilon_3\epsilon_1 + \epsilon_1\epsilon_2 - (\epsilon_4^2 + \epsilon_5^2 + \epsilon_6^2)/4 \tag{11}$$

For a-quartz, it is possible using symmetry to reduce the number of independent elastic constants to six[31]: $c_{11}, c_{12}, c_{13}, c_{14}, c_{33}, c_{44}$. The elastic energy must be positive. This condition imposes the following constraints, the Born criteria:

$$\mathrm{Bl} = c_{11} - |c_{12}| > 0 \tag{12}$$

$$B_2 = (c_{11} + c_{12})\, c_{33} - 2c_{13}^2 > 0 \tag{13}$$

$$B_3 = (c_{11} - c_{12})\, c_{44} - 2c_{14}^2 > 0 \tag{14}$$

for the *a*-quartz crystal to be mechanically stable. The first criterion, Eq.(12), insures that the squared velocity of a transverse elastic wave in the plane perpendicular to the *c*-axis is positive. The second criterion, Eq.(13) corresponds to positive bulk modulus. The third criterion, Eq.(14), ensures stability with respect to shear waves in planes different from the quartz hexagonal plane. As illustrated in Figure 8, the first two criteria are met at ambient conditions and for pressures well above the amorphization transformation. However, the third criterion is violated at a pressure of ~30Gpa which is consistent with the collapse of the crystalline phase observed experimentally at that pressure.

The microscopic nature of this instability appears to be associated with the formation of the bcc anion packing at high pressure. Our analysis suggests that the instability is intimately related to the coordination change of the silicon cation from a four-fold to a six-fold site. In the picture suggested by first-principles calculations, as pressure is applied to *a*-quartz structure a mechanical strain builds. This strain is confirmed by the small Si-O-Si bond angle and the interpolyhedral O-O distances. The nonlinearity of the angle and distance changes with pressure above ~15GPa reinforces the picture of large mechanical strains near the amorphization transformation. Near this transformation the α-quartz structure assumes a bcc packing of the anions. Moreover, this bcc packing is accompanied by a mechanical instability in which one of the Born criteria is violated. In this unstable arrangement, silicon cations may diffuse from tetrahedral to octahedral sites. At high pressures, the silicon cations occupy primarily octahedral sites, and a rutile-like, *i.e.,* stishovite, structure occurs.

The existence of a mechanical instability in quartz subjected to high pressures suggests anomalies might also occur in the vibrational spectrum of quartz. Since the pairwise interatomic potentials yield trends in the mechanical properties which are consistent with quantum calculations, one might expect these potentials to yield "reasonable" vibrational spectra, especially for long wavelength modes. Using the potentials of Tsuneyuki et al., one can determine the phonon spectra throughout the Brillouin zone. An soft-mode does appear as a function of pressure. The first negative eigenvalue of the dynamical matrix is found near 18.5 GPa, at the Brillouin zone-edge *K*-point[47]. In Figure 10, the lowest eigenvalues $v^2(q)$ at zero and 19 GPa along the Γ-*K* direction is presented. The quartz lowest acoustic branch softens under pressure. At 18.5 GPa, the width of the soft acoustic branch along Γ-*K* is ~3.5 meV, i.e., less than 50 K The maximum width of this branch is about 7 meV, at the A-point. The same

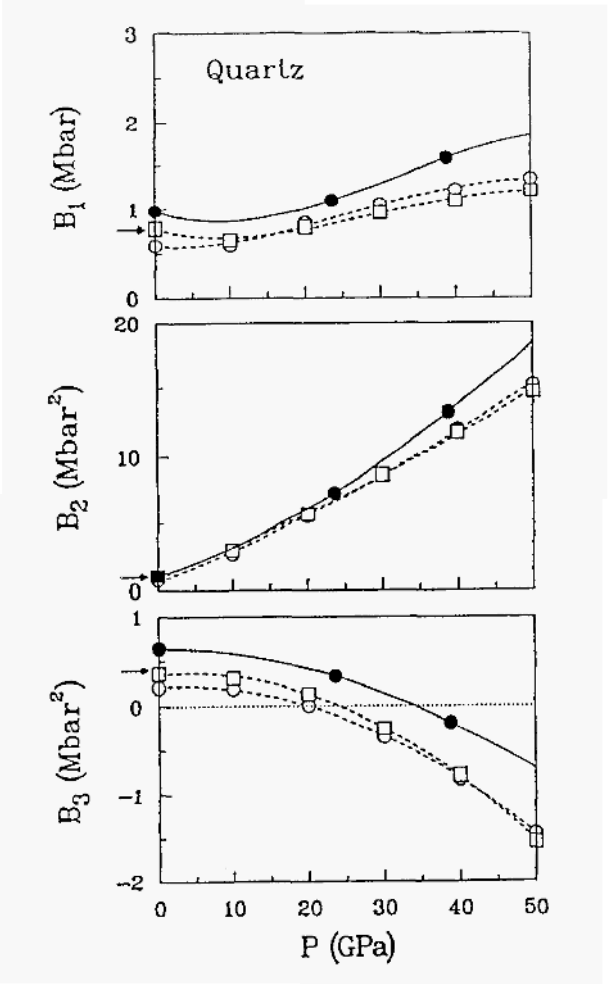

Figure 8. Born criteria for mechanical stability. Three calculations are illustrated. The black dots are from a pseudopotential calculation. The open circles and squares are from interatomic potential calculations. Note how the third criterion, B_3, is violated at high pressures.

general pressure behavior is found using other interatomic potentials, *e.g.* the potential by van Beest *et al.*[48] With the latter potentials, the phonon instability occurs at about 21.5 GPa.

The curvatures of the two lowest branches near Γ, in Figure 10, are

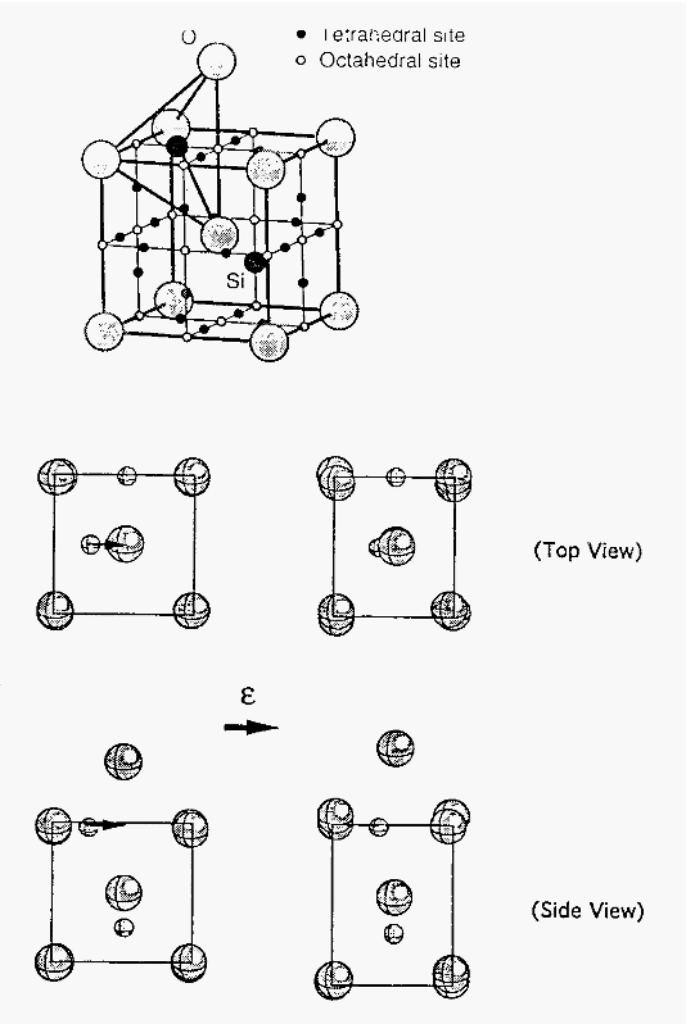

Figure 9. Idealized high pressure form for the α-quartz structure (top) illustrating tetrahedral and octahedral sites. Under a B_3 strain the cations are displaced toward the octahedral sites.

proportional to:

$$\lambda\pm = \frac{c_{66} + c_{44}}{2} \pm \sqrt{\frac{(c_{66} - c_{44})^2}{4} + c_{14}^2} \qquad (15)$$

where $c_{66} = (c_{11} - c_{12})/2$. The phonon modes associated with these two

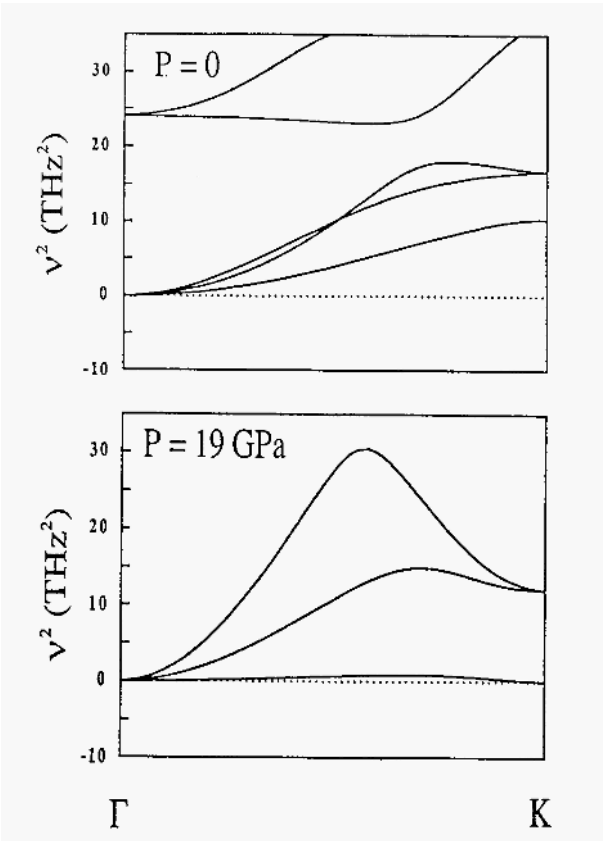

Figure 10. Phonon dispersion curves for the Γ-*K* direction in α-quartz. A soft mode appears along this direction under pressure.

branches are purely transverse in the limit $\vec{q} \rightarrow 0$, and the corresponding elastic-wave velocities are: $v_{\pm} = \sqrt{\lambda_{\pm}/\rho}$, where ρ stands for the density. B_3 is given by the product: $\lambda_{-} . A+ = \frac{1}{2} B_3$. The flattening of the quartz lowest branch under pressure, $\lambda_{-} \rightarrow 0$, reflects the fact that $B_3 \rightarrow 0$. At these pressures, the silicon cations reside in four-fold sites within a bcc-like arrangement of the oxygen anions. The lowest mode at K corresponds to oscillations of the cations between two six-fold sites. Therefore, the K mode is directly related to a change in Si coordination. The soft K mode by itself, however, is not sufficient to drive a change in Si coordination. The enthalpy minimum along the soft mode corresponds to a configuration where the Si lie close to their four-fold site, *i.e.,* at most at 10% of the tetrahedral-octahedral intersite distance. Anharmonic effects, and in particular coupling

to the mechanical instability strain, are necessary to overcome the energy barrier and induce a change in Si coordination. This change in coordination is observed in simulations of the quartz transformation, and occurs at a pressure slightly below the instabilities in the acoustic branch.

A soft zone-edge mode is expected to induce a crystalline-to-crystalline transition. Such a transition has been reported recently from a detailed x-rays diffraction study of quartz, just below the amorphization pressure[45, 46]. The transformed material appears to involve a microstructure, and the amorphous phase seems to nucleate and grow as the sample is pressurized[45]. In view of the small width for the whole acoustic branch at such pressure, these results are not too surprising.

Disorder is also found in pair-potential simulations [22, 39, 40, 47, 49] of the quartz transformation. Unfortunately, the pair-potentials simulations performed to date do not yield definitive results on the nature of the final state. The algorithms employed in the finite cell simulations are in fact inappropriate to simulate a strongly first-order transformation as found in these studies. A densified arid poorly crystallized α-PbO_2-like structure is the resulting structure[49]. While nucleation and growth are clearly beyond such simulations, the simulations are likely to yield a reasonable description of the type of short-range atomic order in the transformed material. In particular, the change in cation coordination related to the soft acoustic branch is expected to be present in the high-pressure material obtained from the quartz solid-state transformation.

6. Calculating the thermal properties of silica

There is an important issue which has yet to be addressed within this chapter: the role temperature plays on the structural properties of silica. Computing the structural properties and the phase stability of a. solid as a function of temperature is a difficult, and largely unresolved problem. In the simplest approach, one can consider the entropic contributions derived solely from vibrational contributions. A simple method of computing thermodynamic properties of solids at *low* temperatures is based on the harmonic approximation [50, 51]. Within this approximation, one can compute the vibrational spectrum of a solid by truncating a series expansion of the potential energy of the crystal as a function of atomic displacements. Typical vibrational energies in solids are tens of meV, which correspond to a few hundred K. Therefore one can expect that the vibrational spectra will not change significantly between 0 K and several hundred degrees K. An harmonic effects due to thermal expansion of the solid may be important at high temperature. To take into account full anharmonicity one can resort to statistical methods such as Monte-Carlo sampling, or molecular dynam-

ics. Such methods can be difficult to apply, and they are computationally intensive[52, 53]. Moreover, determining the absolute entropies or absolute free energies is a problematic issue in such calculations. Free energies are related to the accessible volume of the phase space, not the entire volume of the phase space. As a result, traditional Monte Carlo methods are usually impractical in the computations of absolute free energy[54]. Another approach frequently used is to construct an artificial reversible "path" in the phase space from a system with *known* free energy to the system of interest. Constructing such a path may not always be possible. Moreover, there are only a few thermodynamic states for which the free energy is known, *e.g.,* a harmonic lattice is one such state.

Only a few attempts have been made to compute vibrational modes from first principles. For example, an *ab initio* calculation of the *complete* phonon spectrum has been only recently reported for stishovite[55]. In principle, such methods could be applied towards calculating thermodynamic properties of silica. At present, however, applying interatomic potentials is a more practical route, especially for polymorphs like coesite which have a large number of atoms in the unit cell.

Calculations for thermodynamic properties of three important silica polymorphs: α–quartz, stishovite and coesite are illustrated within this Chapter. These calculations have been carried out in the harmonic approximation[50, 51].

6.1. PHONON SPECTRA OF QUARTZ, STISHOVITE AND COESITE

The phonon spectrum of a crystal can be calculated easily from interatomic potentials by constructing the dynamical matrix. Results of pair potential calculations for the phonon spectrum of α–quartz are shown in Figure 11; the acoustic and the lowest optic modes are displayed. The calculated dispersion for the three lowest (acoustic) branches is in very good agreement with the inelastic neutron scattering data. Higher branches (optic modes) agree only qualitatively with experiment[56]. The largest overestimation of the optic frequencies occurs at the Γ-point. Given the pairwise form of the interatomic potentials, it is not surprising that the optic modes are not accurately replicated. The calculated phonon spectrum for stishovite is shown in 12. For stishovite, experimental data are available only at the Γ-point[57, 58, 59] and are indicated in the figure by solid circles. Given the limited experimental data, it is difficult to assess the accuracy of the results obtained from pair potential calculations. *Ab initio* calculations based on a variational density-functional perturbation technique have recently been published for the phonon spectrum of stishovite[55] across the entire Brillouin zone. The interatomic potential calculations are in fair agreement

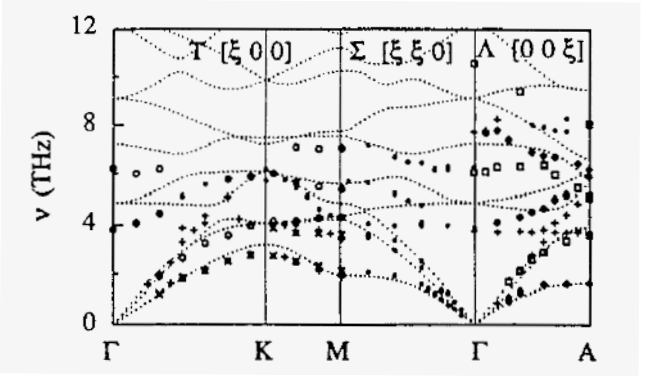

Figure 11. The phonon spectrum of α-quartz at ambient pressure. The dotted lines are the results of our pair potential calculations. The symbols represent different sets of inelastic neutron scattering data.

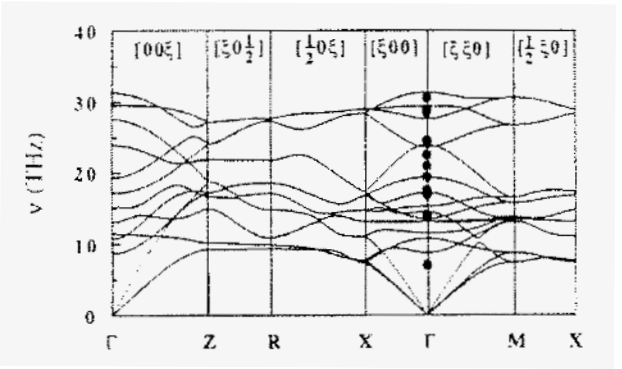

Figure 12. The phonon spectrum for stishovite calculated at ambient pressure from interatomic pair potential calculations. The solid circles are from experiment.

with these calculations.

The vibrational spectrum for coesite is shown in Fig. 12. To date, no experimental phonon data are available for coesite. The coesite spectrum is complicated owing to the presence of 144 phonon branches. Given the large number of atoms in the unit cell, a detailed analysis of this spectra is decidedly non-trivial.

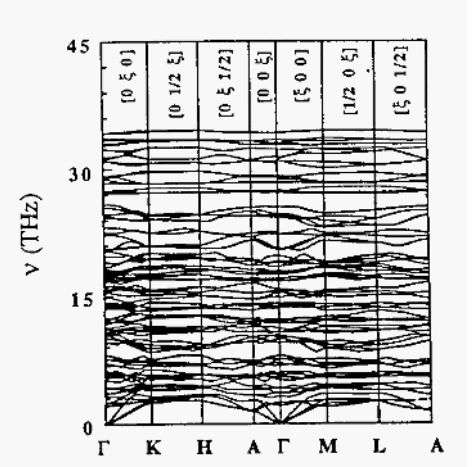

Figure 13. The phonon spectrum of coesite at ambient pressure. Coesite is a complex form of crystalline silica with 16 molecular units of SiO_2 in the unit cell.

6.2. COMPUTATION OF THE FREE ENERGY

TABLE 4. Calculated thermochemical properties for the between quartz to stishovite, and quartz to coesite transitions.

	Theory	Experiment[63]	Experiment[61]
Quartz→stishovite			
ΔV^0_{298}	-8.58	-8.68	-8.68
ΔH^0_{298} (kcal/mol)	10730	11790±300	12400±400
ΔH^0_{975} (kcal/mol)	11018	–	–
ΔS^0_{298} (cal/mol-K)	-2.36	-3.24	-1.7±0.5
ΔS^0_{975} (cal/mol-K)	-1.87	–	–
Quartz→coesite			
ΔV^0_{298}	-1.89	-2.05	-2.05
ΔH^0_{298} (kcal/mol)	-3928	1210±150	700 ± 70
A H^0_{975} (kcal/mol)	-3768	700±150	320 ± 70
ΔS^0_{298} (cal/mol-K)	-0.35	-0.23	-0.7±0.2
ΔS^0_{975} (cal/mol-K)	-0.10	–	-1.2±0.1

To obtain an accurate estimate of thermodynamic properties for crystalline silica polymorphs, one needs an accurate description of the phonon *density of states*. Given the complexity of the problem, this is tractable only with several assumptions. For example, it is often assumed that the calculated phonon spectra are not strongly dependent on temperature. Certainly this will be a satisfactory assumption in the absence of any thermal expansion, and any changes in the interatomic potentials as a function of temperature. In this case, the force constants, and consequently the dynamical properties like phonon frequencies and density of states, will be independent of temperature.

Another common assumption concerns the electronic degrees of freedom and the corresponding entropic contributions. For crystalline forms of silica, the electronic degrees of freedom have very high excitation energies as compared the vibrational energy levels, *e.g.,* the band gap of quartz is on the order of ~10 eV. Therefore, at modest temperatures, *e.g.,* temperatures well below the melting point, it is safe to assume that the electronic energy (U_{el}) of the solid does not change significantly with temperature. The total internal energy, U, of the crystal is computed as follows:

$$U(\beta) = U_{el} + U_{vib}(\beta) \tag{16}$$

where $\beta = 1/k_B T$, k_B is the Boltzmann constant, U_{el} is the electronic contribution and U_{vib} is the vibrational contribution.

Such assumptions have been used successfully to calculate the free energy between metallic crystalline phases. For example, Lam *et al.*[60] computed the temperature-pressure phase diagram of beryllium. They predicted the static lattice energy using *ab initio* pseudopotentials and estimated the phonon energy and entropy from the second order elastic constants. Since the electronic contribution to the entropy varies less for insulators than it does for metals, one would expect a better description of the thermodynamics for the materials here than for beryllium.

Figure 14 depicts the density of states for β-quartz, stishovite and coesite. The low energy part of the phonon density of states of stishovite shows pronounced Debye-like behavior This is in contrast to the low density polymorphs of quartz and coesite. The high frequency regions (~ 30 THz) for α-quartz and coesite exhibit some strong Einstein-like optic modes.

Using the calculated phonon density of states for the polymorphs of interest, one can implement standard Bose-Einstein statistics to determine the partition function, Q_{NVT}, of the crystal and compute the temperature dependence of thermodynamic properties (on a molar basis) as follows:

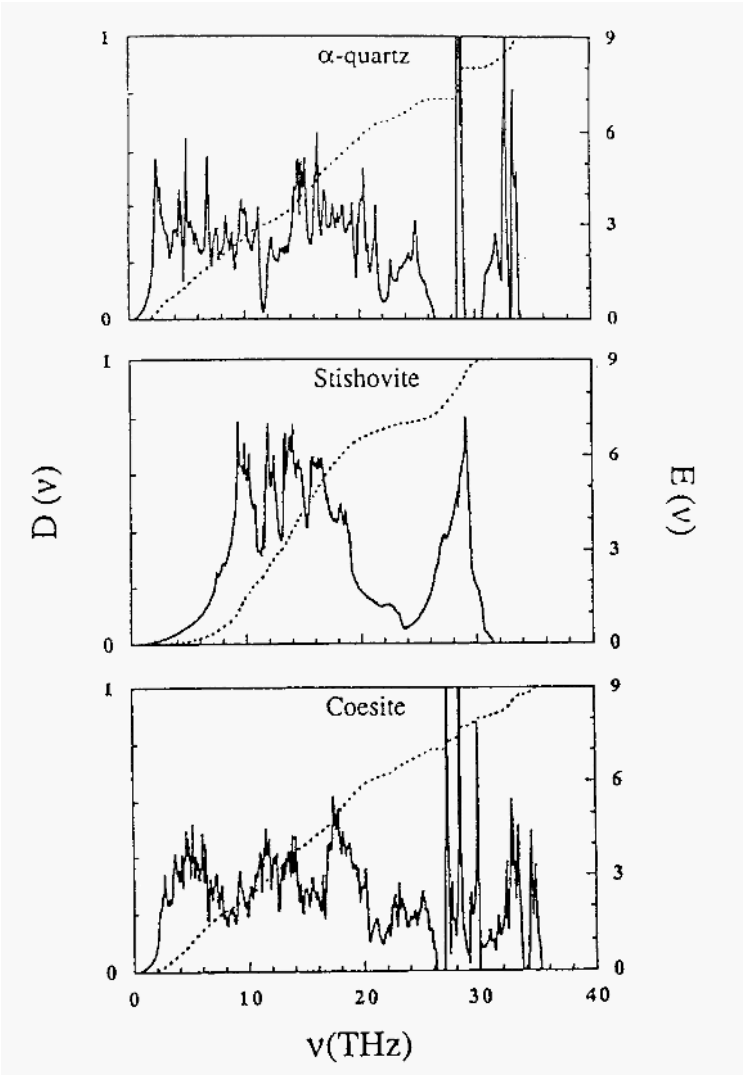

Figure 14. The phonon density of states per molecular unit (D(ν)) and the integrated density of states per molecular unit (E(ν)) (dotted line) for several silica polymorphs.

$$Q_{NVT} = \prod_{j=1}^{3\mathcal{N}_A N_{atom}} \frac{\exp(-\beta h\nu_j/2)}{1-\exp(-\beta h\nu_j)} \exp(-\beta U_{pe}(0,p))$$

$$= \psi \times \prod_{i=1}^{\mathcal{N}_A} \left[\prod_{j=1}^{3N_{atom}} \times \frac{\exp(-\beta h\nu_j/2)}{1-\exp(-\beta h\nu_j)} \right] \tag{17}$$

where h is Planck's constant, N_A is Avogadro's number, N_{atom} is the number of atoms per molecular unit, $U_{pe}(0,p)$ is the equilibrium potential energy per molecule at pressure, p, and $\psi = \exp(-\beta U_{pe}(0,p))$. $U_{pe}(0,p)$ merely serves as a reference and does not affect the remaining discussion.

The following definitions are used for the vibrational contributions to the internal energy(U), enthalpy (H), the isochoric heat capacity (C_V), and the entropy (S),:

$$\begin{aligned}
U(\beta) &= -\frac{\partial lnQ}{\partial \beta} \\
&= U(0,p) + \mathcal{N}_A \left[\int_0^\infty h\nu \{ \frac{1}{2} + I(\beta h\nu) \} D(\nu) d\nu \right] \\
H(\beta) &= U(\beta) + pV \\
C_v(\beta) &= \mathcal{R} \left[\int_o^\infty \{ (\beta h\nu)^2 \frac{I(\beta h\nu)}{[1-\exp(-\beta h\nu)]} \} D(\nu) d\nu \right] \\
S(\beta) &= k_B \left[lnQ - \beta \frac{\partial lnQ}{\partial \beta} \right] \\
&= \mathcal{R} \left[\int_0^\infty \{ \beta h\nu I(\beta h\nu) - ln[1-\exp(-\beta h\nu)] \} D(\nu) d\nu \right]
\end{aligned} \tag{18}$$

where $I(x) = \exp(-x)/(1-\exp(-x))$, $D(\nu)$ is the phonon density of states per molecular unit and R is the gas constant.

The computed temperature variations of the isochoric heat capacity and the absolute entropy of silica polymorphs are compared with experimental data in Figures 15 and 16 respectively. In Figure 15, the experimental data is from Akaogi and Navrotsky[61]. In Figure 16, experiments 1-3 are from Richet *et al.* [62], Holm *et al.* [63] and Robie *et al.* [64], respectively. Particularly good agreement with experiment is achieved at low temperatures. The agreement at higher temperature, although not as good, is still satisfactory. Deficiencies in the interatomic pair potentials as well as anharmonic effects will play an increasingly important role at higher temperatures.

Although the entropy difference between coesite and stishovite is small over the temperature range of interest, this difference acts to stabilize coesite versus stishovite. As a function of increasing temperature the pressure required to transform coesite to stishovite increases. The transformation

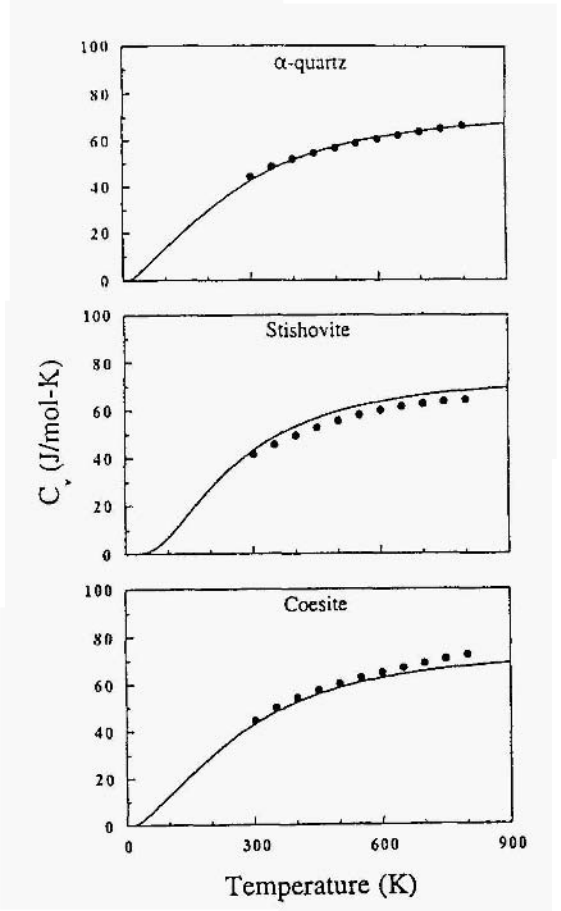

Figure 15. The variation of the constant volume heat capacity (C_v) for α-quartz, stishovite, and coesite. The solid circles indicate calculations based on the experimental data.

pressure at 300 K is approximately 8 GPa while at 1500 K the required pressure is over 9 GPa [61, 65]. One of the main obstacles to calculating accurate free energies is the small entropic differences between competing phases. In Figure 16, the calculated S versus T appear qualitatively the same for all three polymorphs. In Table 4 calculations are presented for the entropy and enthalpy of transformations for the quartz → stishovite and

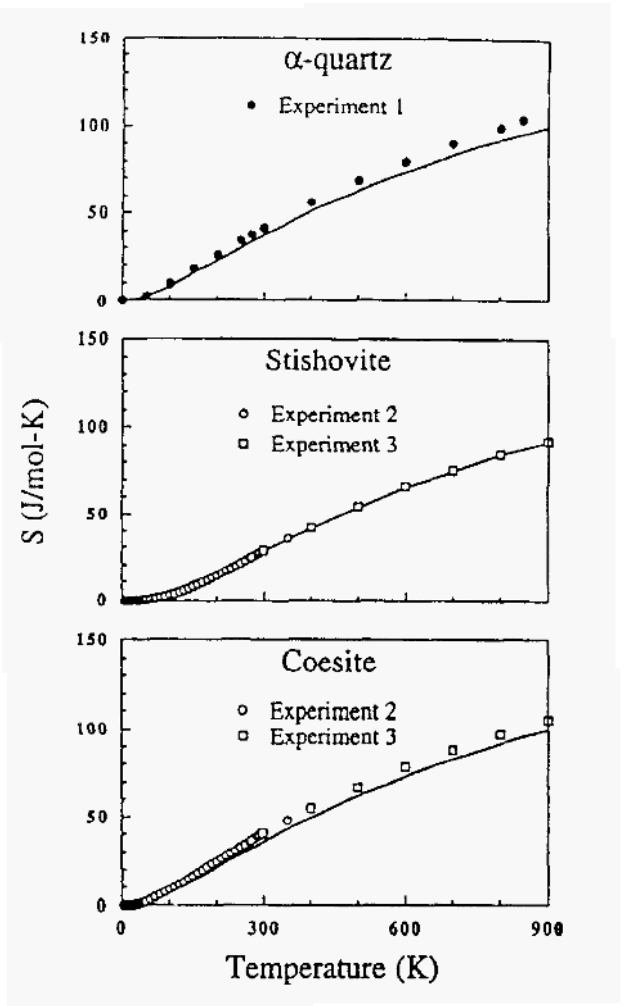

Figure 16. The variation of the absolute entropy (S) for α-quartz, stishovite, and coesite.

quartz → coesite transitions. α–quartz undergoes a transition to β–quartz at 847 K. However, the thermochemical changes during this transformation are known to be small [62, 66]. Thus, one often assumes negligible entropy and enthalpy differences between α– and β–quartz. The measured values are reproduced reasonably well by the interatomic pair potential calculations. The enthalpy change for quartz → stishovite transition is calculated within about 10%. However, the interatomic potential does not reproduce

the enthalpy of the quartz→coesite transition. According to this potential, coesite is more stable than α quartz. This is in contradiction with the experimental data. The failure of the interatomic potential to yield the correct values for the enthalpy differences is a significant problem in terms of generating a comprehensive pressure -temperature phase diagram for these oxides.

Acknowledgments

We would like to acknowledge support, for this work by the U.S. Department of Energy under Grant No. DE-FG02-89ER45391, and the Minnesota Supercomputer Institute.

References

1. Tsuneyuki, S., Tsukada, M., Aoki, H., and Matsui, Y. (1988) First principles interatomic potential of silica applied to molecular dynamics, *Phys. Rev. Lett.,* **61**, 869-872.
2. Lasaga, A.C., and Gibbs, G.V. (1987) Applications of quantum mechanical potential surfaces to mineral physics calculations, *Phys. Chem. Mineral.,* **14**, 107-117.
3. Stisrude, L., and Bukowinski, M.S.T. (1991) Atomic structure of SiO_2 glass and its response to pressure, *Phys. Rev.,* **B44**, 2523-2533.
4. Chelikowsky, J.R., King Jr., H.E., and Glinnemann, J. (1990) Interatomic potentials and the structural properties of silicon dioxide under pressure, *Phys. Rev.,* **B41**, 10866-10871.
5. Kohn, W., and Sham, L. (1965) Self-consistent equations including exchange and correlation, *Phys. Rev.,* **A140**, 1133-1143.
6. Hohenberg, P., and Kohn, W. (1964) Inhomogeneous electron gas, *Phys. Rev.,* **136**, 864-872.
7. Lundqvist, S., and March, N.H. (1987) *Theory of the Inhomogeneous Electron Gas,* Plenum, New York.
8. Chelikowsky, J.R., and Cohen, M.L. (1992) Ab initio pseudopotentials for semiconductors, in P. Landsberg, (ed.), *Handbook on Semiconductors, Vol. 1,* Elsevier, Amsterdam, p. 59.
9. Troullier, N., and Martins, J.L. (1991) Efficient pseudopotentials for plane wave calculations, *Phys. Rev.,* **B43**, 1993-2006.
10. Troullier, N., and Martins, J.L. (1991) Efficient pseudopotentials for plane wave calculations II. operators for fast iterative diagonalization, *Phys. Rev.,* **B43**, 8861-8869.
11. Chelikowsky, J.R., King Jr., H.E., Troullier, N., Martins, J.L., and Glinnemann, J. (1990) Structural properties of cy-quartz near the amorphous transition,, *Phys. Rev. Lett.,* **65**, 3309-3312.
12. Chelikowsky, J.R., Troullier, N., Martins, J.L., and King Jr., H.E. (1991) Pressure dependence of the structural properties of *a*-Quartz near the amorphous transition, *Phys. Rev.,* **B44**, 489-497 .
13. Binggeli, N., Troullier, N., Martins, J.L., and Chelikowsky, J.R. (1991) Electronic properties of *a*-quartz under pressure, *Phys. Rev.,* **B44**, 4771-4778.
14. Binggeli, N.,, and Chelikowsky, J.R. (1991) Structural transformation of quartz at high pressures, *Nature,* **353**, 344-346.
15. Keskar, N.R., and Chelikowsky, J.R. (1992) Structural properties of nine silica polymorphs, *Phys. Rev.,* **B46**, 1.

16. Chelikowsky, J.R., Binggeli, N., and Keskar, N.R. (1993) First principles methods for structural trends in oxides: Applications to Crystalline Silica, *J. of Compounds and Alloys,* **197**, 137-144.
17. Martins, J.L., and Cohen, M.L. (1988) Diagonalization of large matrices in pseudopotential calculations: dual space formalism, *Phys. Rev.,* **B37**, 6134-6138.
18. Martins, J.L., Troullier, N., and Wei, D.S.-H. (1991) Pseudopotential calculations for ZnS, *Phys. Rev.,* **B43**, 2213-2217.
19. Ihm, J., Zunger, A., and Cohen, M.L. (1979) Momentum space formalism for the total energy of solids, *J. Phys. C,* **12** 4409-4422.
20. Keskar, N.R., Troullier, N., Martins, J.L., and Chelikowsky, J.R. (1991) Structural properties of SiO_2 in the stishovite structure, *Phys. Rev.,* **B44**, 4081-4086.
21. Cohen, R.E. (1991) Bonding and elasticity of stishovite (SiO_2) at high pressure-linearized augmented plane wave calculations, *Amer. Mineral.,* **76**, 733-742.
22. Tsuneyuki, S., Matsui, Y., Aoki, H., and Tsukada., M. (1989) New pressure induced structural transformations in silica obtained by computer simulation, *Nature,* **339**, 209-211.
23. Levien, L., and Prewitt, C.T. (1980) Structural and elastic properties of quartz at pressure, *Amer. Mineral.,* **65**, 920-930.
24. Bass, J.D., Libermann, R.C. ,Weidner, D.J., and Finch, S.J. (1981) Elastic properties from acoustic and volume compressibility experiments, *Phys. Earth Planet. Inter.,* **25**, 140-158.
25. Zubov, V.G., and Firsova, M.M. (1956) The elastic properties of high β-quartz, *Kristallographia,* **1**, 546-552.
26. Ross, N.L., Shu, J., Hazen, R.M., and Gasparik, T. (1990) High pressure crystal chemistry of stishovite, *Amer. MIneral.,* **75**, 739-747.
27. Sugiyama, M., Endo, S., and Koto, K. (1987) Crystal structure of stishovite under pressure up to 6 GPa, *Mineral. J.,* **13**, 455-460.
28. Wyckoff, W.G. (1974) *Crystal Structures,* 4th edition, Interscience, New York.
29. Pluth, J.J., Smith, J.V., and Faber Jr., J. (1985) Crystal structure of low cristobalite at 10, 293 and 473 K: variation of framework geometry with temperature, *J. Appl. Phys.,* **57**, 1045-1049.
30. Barron, T.H.K., and Klein, M.L. (1965) Second order elastic constants of a solid under stress, *Proc. Phys. Soc.,* **85**, 523-533.
31. Fedorov, F.I. (1968) *Theory* of *Elastic Waves in Crystals,* Plenum, New York.
32. Smagin, A.G., and Mil'shtein, B.G. (1975) Internal friction of in quartz crystals at low temperatures, *Sou. Phys. Crystal.,* **19**, 514-516.
33. Yeganeh-Haeri, A., Weidner, D.J., and Parise, J.B. (1992) Elasticity of α-cristobalite-a silicon dioxide with a negative poisson ratio, *Science,* **257**, 650-652.
34. Williams, Q., Hemley, R.J., Kruger, M.B.) and Jeanloz, R. (1993) High pressure infrared spectra of a-quartz, coesite, stishovite, and silica glass, *J. Geophys. Res.,* **98**, 22157-22170.
35. Hazen, R.M., Finger, L.W., Hemley, R.J., and Mao, H.-K. (1988) High pressure crystal chemistry and amorphization of a-quartz, *Solid State Commun.,* **72**, 507-511.
36. Hemley, R.J., Jephcoat, A.P., Mao, H.-K., Ming, L.C., and Manghnani, M.H. (1988) Pressure induced amorphization of crystalline silica, *Nature,* **334**, 52-54.
37. Tsuchida, Y., and Yagi, T. (1990) New pressure-induced transformations of silica at room temperature, *Nature,* **347**, 267-269.
38. Sowa, H. (1988) The oxygen packing of low quartz and ReO_3 under high pressure, *Z. Kristallogr.,* **184**, 257-268.
39. Tse, J.S., and Klug, D.D. (1991) High pressure densification of amorphous silica, *Phys. Rev.,* **B46**, 5933-5938.
40. Tse, J.S., Klug, D.D., and Le Page, Y. (1992) Novel high pressure phase of silica, *Phys. Rev. Lett.,* **69**, 3647-3649.
41. Navrotsky, A., Geisinger, K.L., McMillan, P., and Gibbs, G.V. (1985) The tetra-

hedral framework in glasses and melts-inferences from molecular orbital calculations and implications for structure, thermodynamics, and physical properties, *Phys. Chem. Mineral.,* **11**, 284-298.
42. Hemley, R.J. (1987) Pressure dependence of Raman spectra of SiO_2 polymorphs: *a*-quartz, coesite, and stishovite, in M.H. Manghnani, and Y. Syono, (eds.), *High Pressure Research in Minearl Physics,* Terra Scientific Publishing Company (TERRAPUB), Tokyo, pp. 347-359.
43. Glinnemann, J., King Jr., H.E., Schulz, H., Hahn, T., Lapaca, S.J., and Dcaol, F. (1992) Crystal structure of the low temperature quartz type phases of SiO_2 and GeO_2 at elevated pressure, Z. *Kristall.,* **198**, 177-212.
44. Zemann, J. (1986) The shortest known Interpolyhedral *O-O* distance in a silicate, Z. *für Kristall.,* **175**, 299-303.
45. Kingma, K., Hemley, R.J., Mao, H.-K., and Veblen, D.R. (1993) New high pressure transformation in *a*-quartz, *Phys. Rev. Lett.,* **70**, 3927-3931.
46. Kingma, K., Meade, C., Hemley, R.J., Mao, H.-H., and Veblen, D.R. (1993) Microstructural observations of *a*-quartz amorphization, *Science,* **259**, 666-669.
47. Chaplot, S.L., and Sikka, S.K. (1993) Molecular-dynamics simulation of pressure induced crystalline-to-amorphous transition in some corner-linked polyhedral compounds, *Phys. Rev.,* **B47**, 5710-5715.
48. van Beest, B.W.H., Kramer, G.J., and van Santen, R.A. (1990) Force fields for silicas and aluminophospates based on *ab initio* calculations, *Phys. Rev. Lett.,* **64**, 1955-1958.
49. Binggeli, N., and Chelikowsky, J.R. (1993) Is simulated 'amorphous' silica really amorphous?, in S.C. Schmidt, J.W. Shaner, G.A. Samara, and M. Ross, (eds.), *Proceedings of the AIRAPT/APS High Pressure Science and Technology Conference, High Pressure Science and Technology 1993,* American Institute of Physics, Woodbury, New York, p. 397-400.
50. Maradudin, A., Montroll, E.W., Weiss, G.H., and Ipatova, I.P. (1971) *Theory of Lattice Dynamics in the Harmonic Approximation,* Academic Press, New York.
51. Bruesch, P. (1982) *Phonons: Theory and Experiment I.,* Springer-Verlag, Berlin.
52. Catlow, C.R.A., and Mackrodt, W.C., (eds.) (1982) *Computer Simulations of Solids,* Springer-Verlag. Berlin.
53. Ciccotti, G., Frenkel, McDonald, I.R., (eds.) (1987) *Simulation of Liquids and Solids,* North Holland, Amsterdam.
54. Allen, M.P., and Tildesley, D.J. (1987) *Computer Simulations of Liquids,* Oxford Press, Oxford.
55. Lee, C., and Gonze, X. (1994) Lattice dynamics and dielectric properties of SiO_2 stishovite, *Physical Review Letters,* **72**, 1686-1689.
56. Barron, T.H.K., Huang, C.C., and Pasternak, A. (1976) Interatomic forces and lattice dynamics of a-quartz, *J Phys C,* **9**, 3925-3940.
57. Hemley, R.J., Mao, H.-K., and Chao, E.C.T. (1986) Raman spectrum of natural and synthetic stishovite, *Phys. Chem. Minerals,* **13**, 285-290.
58. Vigasina, M.F., Gusea, E.V., and Orlov, R.Y. (1989) Vibrational spectrum of stishovite and analysis of its crystal lattice dynamics, *Soviet Physics-Solid State,* **31**, 747-749.
59. Hofmeister, A.M., Xu, J., and Akimoto, S. (1990) Infrared spectroscopy of synthetic and natural stishovite, *Am. Mineral.,* **75**, 951-955.
60. Lam, P., Chou, M.Y., and Cohen, M.L. (1984) Temperature and pressure induced crystal transitions in Be, *J. Phys. C,* **17**: 2065-2073.
61. Akaogi, M., and Navrotsky, A. (1984) The quartz-coesite-stishovite transformations: new calorimetric measurements and calculation of phase diagrams, *Phys Earth Planet. Int.,* **36**, 124-134.
62. Richet, P., Bottinga, Y., Danielou, L., Petitet, J.P., and Tequi, C. (1982) Thermodynamic properties of quartz, cristobalite, and amorphous SiO_2: Drop calorimetry measurements between 1000K and 1800K and review from 0 to 2000K. *Geochim.*

Cosmochim. Acta, **46,** 2639-2658.
63. Holm, J.L., Kleppa, O.J., and Westrum, E.F. (1967) Thermodynamics of polymorphic transformations in silica: Thermal properties from 5-1070 K and pressure-temperature stability fields for coesite and stishovite, *Geomchim. Cosmochim. Acta*, **31**, 2289-2307.
64. Robie, R.A., Hemingway, J.R., and Fisher, J.R. (1978) Thermodynamic properties of minerals and related substances at 298.15K and 1b pressure and higher temperatures, *Geol Surv Bull,* **1452**, 216-221.
65. Navrotsky, A. (1980) Lower mantle phase transitions may generally have negative pressure temperature slope, *Geophys. Res. Lett.,* **7,** 709-711.
66. Cohen, L.H., and Klement, W. (1967) High-low quartz inversion: Determination to 35 Kbar, *J. Geophys. Res.,* **72**, 4245-4253.

This page intentionally left blank.

HIGH PRESSURE STUDIES OF MANTLE MINERALS BY *AB INITIO* VARIABLE CELL SHAPE MOLECULAR DYNAMICS

RENATA M. WENTZCOVITCH
Department of Chemical Engineering and Materials Sciences, Minnesota Super computer Institute University y of Minnesota, Minneapolis, MN 55455, USA

AND

G. DAVID PRICE
Research School for Geological and Geophysical Sciences, Birbeck College, University College London,, London, WC1E 6BT, U.K.

1. Introduction

The Earth's Mantle is predominantly composed of magnesium-iron silicates. This is known from direct sampling of Upper Mantle material, seismic velocity - density systematics, and from inferences based upon solar abundances. The Upper Mantle is largely composed of the forsteritic olivine ($(Mg.Fe)_2SiO_4$), and both orthorhombic and monoclinic pyroxene ($(Mg,Fe)SiO_3$). The forsterite structure is characterized by having isolated SiO_4 tetrahedra,,while the pyroxene structures have linear chains of corner sharing SiO_4 tetrahedra. At a depth of about 400 km, the Upper Mantle minerals become unstable, and transform to denser polymorphs that make up the Mantle Transition Zone. Forsterite transforms first to wadsleyite (or the beta-phase) and subsequently to ringwoodite (which has the spinel structure). Silicon remains in four-fold coordination in both of these phases. In contrast, pyroxenes transform either to majorite (which has the garnet structure) or to a polymorph with the ilmenite structure. Both of these phases have silicon in octahedral (or sixfold) coordination. The 670 km seismic discontinuity marks the boundary of the Lower Mantle. It is believed that this discontinuity coincides with the breakdown reaction of ringwoodite to magnesium silicate perovskite ($MgSiO_3$) and magnesiowustite ($(Mg,Fe)O$). Under about the same pressure-temperature conditions, gar-

B. Silvi and P.D'Arco (eds.),Modelling of Minerals and Silicated Materials, 39-61.

net also transforms to perovskite. In fact over 70% of the Lower Mantle, and over 40% of the entire planet is composed of magnesium silicate perovskite. Perovskite is a simple structure, based on the corner sharing of SiO_6 octahedra. Magnesium silicate perovskite appears to be orthorhombically distorted at lower pressures, with silicon in the octahedral sites and the magnesium ion sitting in an 8-fold distorted environment.

In order to be able to interpret new, seismic tomographic data, it is essential to determine the high pressure (over 25 GPa) and high temperature (over 2000 K) behavior of these Lower Mantle phases. However, such pressure and temperature conditions are experimentally very difficult to achieve, and so one of the major goals of computational mineral physics has been to describe fully the structural properties of Earth-forming phases under the conditions found in the Earth's interior.

The computational approaches currently used to study thermoelastic properties of minerals, generally employ either lattice dynamics (LD) or molecular dynamics (MD) techniques. Traditionally these studies have been carried using interatomic potentials (e.g. Catlow and Price[1]) or the Potential Induced Breathing model (PIB)[2]. These model potentials are now invariably successful in reproducing known structural properties of mantle silicates. This success has led to the extension of these studies to the prediction of properties under conditions currently beyond experimental reach.

Lattice dynamics within the quasi-harmonic-approximation (QHA) provides phonon spectra from which all thermodynamical properties can be derived[3]; however the validity of this approach is limited to "low" temperatures. At high temperatures, unharmonicities become non-negligible and ionic motion can be more properly treated by classical MD. These approaches therefore are complementary and a complete study of thermoelasticity of minerals requires the use of both within their respective regimes of validity, usually delimited by the Debye temperature. Unfortunately the wide range of pressures ($\approx$ 20 to 100 GPa) existent in the mantle, makes such temperature demarcation less obvious. This point has recently been investigated by Matsui *et al*[4], who performed a parallel set of LD and MD calculations on $MgSiO_3$-perovskite at a wide range of thermodynamical conditions. At lower mantle conditions, unharmonicities were shown to affect significantly properties like the thermal expansion coefficient.

Some successful examples of the use of MD to study mantle phases are: 1) the simulation of structural and thermodynamical properties of six $MgSiO_3$ polymorphs[5], which reproduced experimental results to within a few percent. They investigated the existence of a post-protoenstatite high temperature phase and a C2/c high pressure phase. Their predicted coordinates and structure for the high pressure C2/c phase were subse-

quently used by Angel *et al* [6] to solve the single crystal X-ray data for that phase, when it was later unambiguously synthesized; 2) Investigation of sub-lattice melting and ionic conductivity in $MgSiO_3$-perovskite[7]. The constant pressure and constant temperature calculations predicted the onset of oxygen sublattice melting and an orthorhombic to cubic phase transition above 10 GPa, just prior to melting. They showed that the cubic phase exhibits solid electrolytic behavior with an electrical conductivity comparable with that inferred for the lower mantle. A parallel study using different model potentials[8] confirmed the high temperature solid electrolyte behavior but predicted an orthorhombic to tetragonal phase transition in $MgSiO_3$-perovskite, due to precession of SiO_6 octahedra, at 2600 K and 31 GPa. If ionic conductivity in $MgSiO_3$-perovskite is really significant, then it plays an important role in the behavior of the Earth's lower mantle.

Although MD calculations resorting of interatomic potentials have been successful in many instances, the major shortcoming associated with this type of study, is the reliance of the quantitative precision of the predicted property upon the accuracy of the empirical potential used to model interatomic interactions when interatomic distances are substantially different from those used to "fit," the model potential. *Ab initio* MD circumvents entirely this problem and will play a decisive role in the study of mantle phases under pressure. In the next section we outline the theory behind a new *ab initio* constant pressure MD with variable cell shape (VCS). The following section illustrates its use as an efficient structural optimizer for two mantle phases: $MgSiO_3$-perovskite and C2/c enstatite. Although these were 0 K calculations, finite temperature studies are similarly possible, the current limitation being simply computational power.

2. The method

The technique utilized here is an *ab initio* molecular dynamics (MD) with variable cell shape (VCS)[9]. It combines a fully self-consistent approach to *ab initio* MD[10] with a VCS dynamics which includes strains as dynamical variables[11]. Together these features make this method ideally suited to predict the behavior of solids at high pressures and temperatures.

Ab initio MD is a powerful simulational technique which emerged in the last decade[12]. It allows us to investigate atomic motion in the presence of complex electronic bonding. The original approach consisted of a fictitious dynamics in an extended space of ionic coordinates and electronic wave-functions. This method has undergone numerous modifications aiming to improve its efficiency. In the past few years, alternative *ab initio* MD methods departing substantially from the original approach have been proposed. Most of them no longer make use of *fictitious electron dynam-*

ics, but instead, keep the electrons in the ground state while the ionic dynamics strictly follows the Born-Oppenheimer surface. The current approach[10, 13], is the earliest of these methods and is based on a quite conventional approach to the electronic structure problem.

In common with other *ab initio* MD methods, the present one is based on a tractable total energy scheme which makes use of 1) density functional theory and the one electron approximation[14];2) pseudopotentials to describe the interaction between valence electrons and the core[15]; 3) iterative improvement of trial electronic valence wave-functions, which are expanded in plane-waves. In contrast with previous methods, this one obtains: 1) fully converged LDA energies and forces at every step of the dynamics which proceeds with the large time scale typical of classical MD; 2) the LDA energy minimization is based on a conventional (iterative) diagonalization/self-consistency cycle (charge mixing). More references to these techniques can be found in previously published work.

The VCS-MD used here[11] is based on a Langragian formulation very similar to the original dynamics[16]; however it uses strains as dynamical variables, instead of the Cartesian coordinates of the simulation cell vectors. This new choice of dynamical variables makes the Lagrangian (and the trajectories) invariant with respect to the choice of simulation cell vectors. It also gives a more physical strain/stress relationship which preserves throughout the trajectories the space group symmetry of the initial condition. This latter property *is* physical and does not imply in any constraints. This point will be further discussed when presenting examples in the next section.

The VCS-MD is generated by promoting the components of the strain tensor (ϵ) to dynamical variables and rescaling the ionic coordinates $\vec{r}_i$ by $(1+\epsilon)\vec{q}_i$. The new variables $(\vec{q}_i)$ are the particles coordinates referred to this breathing coordinate system.

$$L = \sum_{i=1}^{N} \frac{m_i}{2} \dot{\vec{q}}_i g(\epsilon) \dot{\vec{q}}_i + \frac{w}{2} Tr(\dot{\epsilon}\dot{\epsilon}^T) - U(\epsilon, \vec{q}_i) - P\Omega(\epsilon). \tag{1}$$

Here $g(\epsilon) = (1 + \epsilon)^T(1+\epsilon)$ is the metric tensor, $U(\epsilon, \vec{q}_i)$ is the Kohn-Sham energy, P is the constant *applied* external pressure, and $\Omega(\epsilon)$ is the variable cell volume. The first and second terms on the r.h.s. are the kinetic energies associated with internal and strain variables (w is a *fictitious* mass usually adjusted to optimize the dynamical coupling with the other variables). The third and fourth terms combined, correspond to the enthalpy in the thermodynamical limit. This plays the role of a generalized potential energy. Equations of motion (EM) for coordinates and strains can be derived by

applying Lagrange's equations to Eq. (1):

$$\ddot{\vec{q}}_i = -\frac{1}{m_i}(1+\epsilon)^{-1}\vec{f}_i - g^{-1}\dot{g}\dot{\vec{q}}_i \qquad (2\text{ - a})$$

$$\ddot{\epsilon} = \frac{\Omega}{w}(\Pi - P)(1+\epsilon^T)^{-1} \qquad (2\text{ - b})$$

In Eq. (2-a), $\vec{f}_i$'s are the Hellman-Feynmann forces, and in (2-b), Π is the total stress:

$$\Pi = \sum_{i=1}^{N}\frac{1}{\Omega}m_i\vec{v}_i\vec{v}_i^T + \Sigma \qquad (3)$$

where $\vec{v}_i(\epsilon, \dot{\vec{q}}_i) = (1+\epsilon)\dot{\vec{q}}_i$ and Σ is the quantum mechanical stress tensor.

This is the conceptual framework of the present technique. It is a completely general *ab initio* VCS-MD which can be used to simulate solids at finite temperatures and pressures. Subjected to small modifications, and in the limit of isotropic fluctuations, it maps into Andersen's dynamics[17], whose averages over trajectories correspond to those of the isoenthalpic isobaric (N,P,H) ensemble.

This method has been used recently to simulate the pressure induced *hcp* to *bcc* transformation in magnesium at finite temperatures[18], and to study the behavior of solids other than silicates[19, 20]. Except for the study in Mg, all others addressed phases at T = 0 K. In these studies, the focus was the optimization of structures (stress and force minimization) at high pressures. In practice these calculations involved the utilization of a *damped* version of this VCS-MD algorithm: when certain force components (Eq.'s 2-a,b) changed sign the corresponding velocity components were zeroed. This strategy can be quite efficient if the normal modes have similar frequencies, which can be approximately achieved by equating the ionic masses, and choosing the fictitious cell mass to produce approximately the same cell oscillation period. Once the period is established, the time step can be chosen to be approximately half of this value, which insures a fast damping rate. The performance of such algorithm for $MgSiO_3$ and $CaSiO_3$ will be demonstrated below.

3. Applications to mantle minerals

Understanding the compressive behavior of Earth forming phases is important for several reasons[21]. From the practical point of view the knowledge of their equations of state is fundamental to aid the interpretation of seismic velocity data and sort out the precise mineralogical mantle composition. From the purely mineralogical point of view, there is interest in understanding how different classes of silicates adapt to conditions found

in planetary interiors. The array of Si-O bonds forms a "skeleton" and the way this one articulates might indicate how the transformations between phases occur.

Below we exemplify the application of the *ab initio* VCS-MD to some of the most important mantle mineral phases. $MgSiO_3$-perovskite is by far the most important of them and was the first application of this technique. The viability of the method was established with this calculation [9]. The precise behavior of this mineral up to pressures which exceed the highest values reached in the Earth's mantle was predicted. Since the compressive behavior is related to the elastic moduli, we have obtained the latter as well[22] in order to present a reliable and consistent description of $MgSiO_3$-perovskite's compressive behavior. In order to further substantiate the conclusions on this phase, we performed similar calculations on $CaSiO_3$[22], which is another relevant lower mantle mineral. $CaSiO_3$ is a cubic perovskite at high pressures, in contrast to $MgSiO_3$, which is an orthorhombically distorted perovskite.

The structural complexity of mantle minerals increases quite rapidly as we attempt to address other phases. The upper mantle is dominated by olivine, spinel, pyroxene, and garnet type minerals. In some mineralogical models, pyroxene type minerals comprise nearly 25% in volume of the upper mantle. A vast family of minerals is described under this name. There are chemical and structural variations among pyroxene phases. Here we investigate $MgSiO_3$-C2/c enstatite[23] for a couple of reasons: 1)it is a polymorph of $MgSiO_3$-perovskite and direct comparison of results in both phases can bring insight on the nature of these calculations. 2) C2/c enstatite is the simplest stable (at high pressures) pyroxene form, containing 40 atoms per cell and 18 structural parameters. This is still a relatively small level of complexity compared to that of other mineral phases, but until recently this level of complexity was not possible in *ab initio* high pressure studies. To our knowledge, this is the most complex *ab initio* zero temperature study of a mineral phase with the largest unit cell studied so far. 3) Detailed experimental data at high pressures on this phase had recently been acquired [6],and we could readily compare with our theoretical predictions. These are quite challenging calculations and experimental guidance is not to be underestimated.

3.1. $MGSIO_3$ AND $CASIO_3$-PEROVSKITES

The structure of $MgSiO_3$-perovskite is shown in Fig. 1. This is the most abundant mineral on our planet[24]. Latest estimates suggest that at least 85% of the Earth's lower mantle consists of pure perovskite $Mg_{1-x}Fe_xSiO3$ ($x \leq 0.2$). This is the largest single region of the planet and accounts for $\simeq$

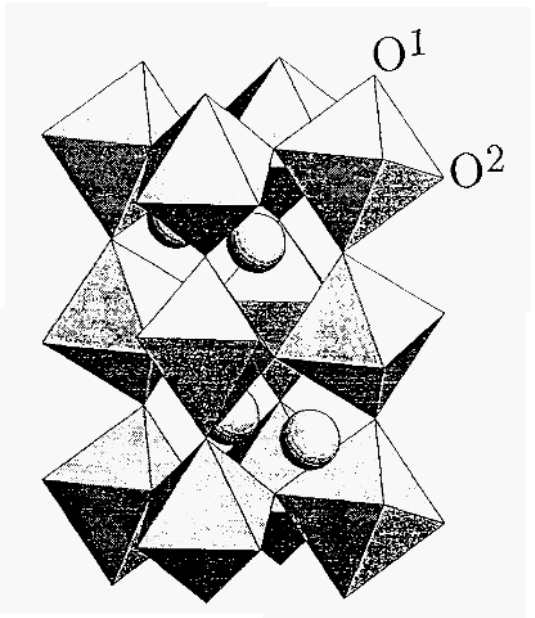

Figure 1. Orthorhombic (*Pbnm*) phase of $MgSiO_3$-perovskite. There are two crystallographically distinct oxygen sites (O^1 and O^2) at octahedral corners. Silicons are near the octahedral centers. Spheres represent magnesium cations.

55% of its volume, however the precise behavior of this mineral under this region's extreme conditions is as yet unknown. We apply this algorithm to perform symmetry conserving structural optimizations and predict the zero temperature behavior of this mineral up to pressures which exceed the highest values reached in the mantle (150 GPa).

This phase is stable above 23 GPa, which is the typical pressure at the upper/lower mantle boundary. At low pressures it is metastable, the stabler phases being pyroxenes. The orthorhombic phase is obtained from the cubic perovskite phase (*Pm3m*) by superposing rotations ofnearly-rigid oxygen octahedra to an anti-ferroelectric displacement of Mg ions perpendicular to the *c*-axis. This brings to twenty and ten the number of atoms per cell and structural parameters respectively.

Because of the implications for the structure of the Earth's lower mantle, the behavior of $MgSiO_3$ under compression has been an issue of great concern. A precise determination of this mineral's equation of state up to pressures typical of this region can have important Geophysical implications. The possible existence of other stable phases at high pressures is another related issue. Besides experimental evidence to the contrary, com-

parative crystal chemistry suggests the possibility of a stable *Pm3m* phase at very high pressures. The argument is based on a "cavity filling effect": whether perovskites are either cubic or distorted, depends on the relative size of cations (spheres in Fig. 1) and octahedra. For instance, if Mg is replaced by Ca, a larger cation, the structure becomes cubic. It is possible that under compression Mg occupies a larger fraction of cavity volume and will drive the structure into cubic. This phenomenon is observed in $SrZrO_3$ under pressure[25]. Besides, MD simulations using ionic force field models suggest the *Pbnm* phase might undergo a temperature induced transition to the *Pm3m* before melting and at high pressures[7]. These evidences indicate the cubic phase is probably one of the most sensible alternative structures at high pressures and temperatures.

We have proceeded and performed structural optimizations at arbitrary pressures according to the *damped* VCS-MD algorithm outlined in the previous section. Fig. 2 illustrates a typical dynamical evolution of the structural parameters in MgSiO3 and $CaSiO_3$. A comparison of algorithm performance in these two cases is relevant because: 1) it shows how well the algorithm can distinguish between these structures, and 2) establishes that indeed it is possible to find structures of high symmetry out of initial conditions with low symmetry. For instance the internal structural parameters in CaSiO3 converge to 0, 1/4, and 1/2, while the lattice parameters converge to $a = b$, and $c = \sqrt{2}a$, which is clearly the cubic phase.

Although the initial space group symmetry is preserved in this dynamics, this example demonstrates this is not a restrictive property. It is possible to obtain structures with any space group out of structures with no symmetry. Specific details of these calculations can be found in Wentzcovitch *et al* [22].

The zero pressure structural parameters in $MgSiO_3$ obtained this way are displayed in Table 1. The agreement with experimental values can be considered excellent, with theoretical lattice parameters a, *b,* and *c* smaller by about 1%. Detailed analizes of the theoretical zero pressure structure, reveals that all bond lengths are within 1% of the experimental values, and the octahedral tilting angles are about 1 degree larger. These trends are to be expected from zero temperature calculations.

The predicted behavior of $MgSiO_3$-perovskite under compression is summarized in Fig.'s 3 and 4. These results reveal the several trends. The orthorhombic axes have different compressibilities (Fig. 3-c,d,e), among which the *a*-axis is the most compressible followed by *c* and *b,* as observed in single crystal measurements. The internal parameters vary continuously (Fig. 3-a,b) and no change in trend is observed under compression. These imply in increasing anti-ferroelectric displacements of Mg ions, increasing octahedral tilt angles, and a decreasing degree of octahedral distortions.

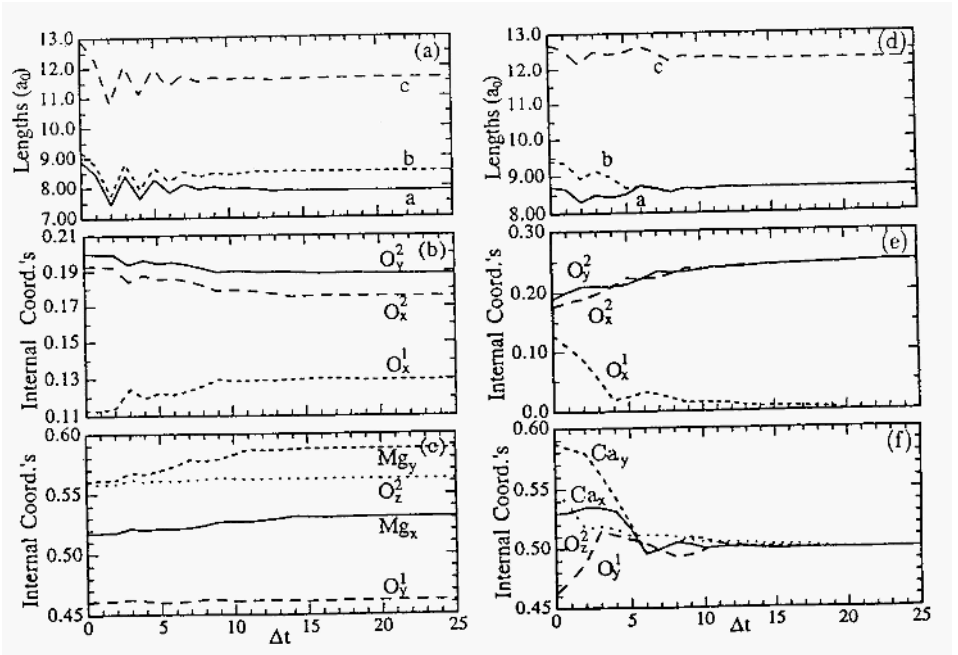

Figure *2*. Typical dynamical evolutions of structural parameters for $MgSiO_3$ ((a), (b), and (c)), and $CaSiO_3$ ((d), (e), and (f)). The initial configurations are the zero pressure structure and a general Pbnm configuration for $MgSiO_3$ and $CaSiO_3$ respectively. The final configurations (*Pbnm* and *Pm3m* symmetries for $MgSiO_3$ and $CaSiO_3$ respectively) are the equilibrium ones at 150 GPa.

The stability of the *Pbnm* phase with respect to the cubic *Pm3m* perovskite increases with pressure from 1.50 eV/molecule at zero pressure, to 3.54 eV/molecule at 150 GPa (Fig. 3.1.4-b). Although this is a zero temperature calculation, it seems unlikely that vibrational entropy differences between these phases would be so large as to stabilize the cubic phase even at the highest bounds of the mantle geotherm.

Table 2 shows the bulk modulus (K_o) and its pressure derivative obtained by a third order fit to the Birch-Murnaghan's equation of state, of the calculated volume versus pressure relation for the orthorhombic (*Pbnm*) and cubic (*Pm3m*) phases. The *Pbnm's* K_o is within the range spanned by inter-laboratory measurements.

We have also calculated the elastic constants of $MgSiO_3$-perovskite (Table 3). They give further support to our conclusions about the structural distortion under pressure. They were obtained by direct calculations of

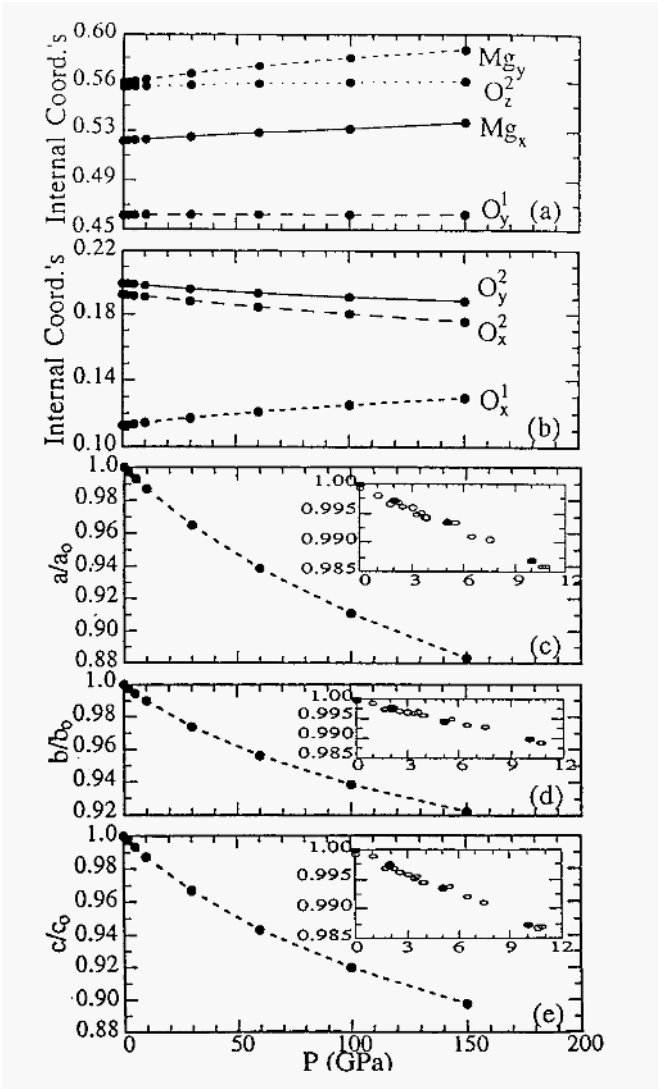

Figure 3. Pressure dependence of structural parameters for the *Pbnm* phase. a) and b) show the internal ones, while c), d) and e) show the rescaled Bravais lattice parameters a/a_o, b/b_o, and c/c_o, where a_o, b_o, c_o are zero pressure values. The insets show experimental results of Ross and Hazen [28] (o) and ours (•).

TABLE 1. Theoretical (first column) and experimental (Horiuchi *et al*[26]) parameters of the zero pressure *Pbnm* phase. The primitive vectors are respectively: $\vec{a} = a\hat{x}, \vec{b} = b\hat{y}, \vec{c} = c\hat{z}$. This phase ($4MgSiO_3$) has Si atoms located at (1/2, 0, 0), (1/2, 0, 1/2), (0, 1/2, 0), and (0, 1/2, 1/2), Mg's at ±(Mgx, Mgy, 1/4; 1/2-Mgx, Mgy+1/2, 1/4), and two sets of inequivalent O's at ±(0lx, *0ly,* 1/4; 1/2-02, $O_y^1+1/2$, 1/4) and ±(O_x^2, O_y^2, O_z^2; 1/2-O_x^2, $O_y^2+1/2$, 1/2-02; O_x^2, O_y^2, $O_y^2+1/2$; 1/2+O_x^2, 1/2-O_y^2, O_z^2). The calculated zero pressure lattice parameter of the cubic phase (*Pm3m*) is a'. Alternatively, this phase can be described in terms of a supercell four times larger with *Pbnm* symmetry (third column). Lengths are in Å . (+ is from Cohen *et al*, [27]).

	Calc.(Pbnm)	Exp.(Pbnm)	Calc.(Pm3m)
a	4.711	4.7787(4)	4.909
b	4.880	4.9313(4)	4.909
c	6.851	6.9083(8)	6.942
Mg_x	0.5174	0.5141(1)	0.500
Mg_y	0.5614	0.5560(1)	0.500
O_x^1	0.1128	0.1028(*2*)	0.000
O_y^1	0.4608	0.4660(2)	0.500
O_x^2	0.1928	0.1961(1)	0.250
O_y^2	0.1995	0.2014(2)	0.250
O_z^2	0.5582	0.5531(1)	0.500
	Calc.(Pm3m)		
a'	3.472		
a'	3.48+		

the stresses[36] generated by small deformations of the zero-pressure orthorhombic cell and simultaneous relaxation of the internal parameters.

These constants are in very close accord with those measured by Yeganeh-Haeri *et al*[33], but are generally slightly stiffer, as would be expected for constants evaluated at T = 0 K. It is interesting to note that, in contrast with previous estimates, we find $C_{11} < C_{33} < C_{22}$. This is consistent with the overall predicted distortion pattern under pressure. The linear compressibilities of the unit cell axes are $\beta_a=0.00137$ GPa^{-1}, $\beta_b=0.00110$ Gpa-1, and $\beta_c=0.00127$ GPa^{-1}. This study supports the result from experimental studies that the b-axis of $MgSiO_3$ perovskite is the least compressible axis, and the findings of Ross and Hazen[28] that the a-axis is more compressible than the c-axis; however, this overall pattern of distortion is in conflict with the data of Yeganeh-Haeri *et al*[33], and the Hartree-Fock calculations of D'Arco *et al*[35], which suggest that $\beta_c > \beta_a$.

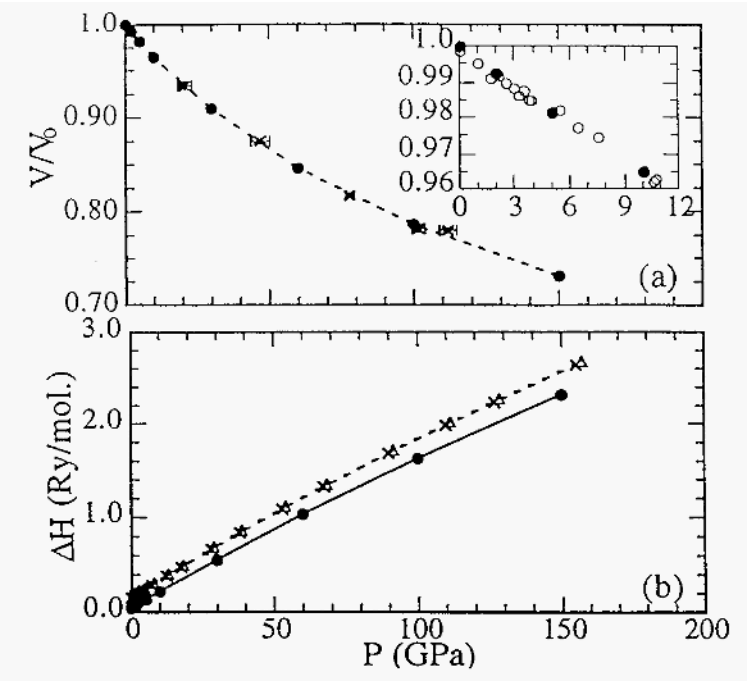

Figure 4. a) Pressure dependence of the *Pbnm* phase's rescaled volume V/V_0 where V_0 is the zero pressure value. (x) with error bars are from Knittle and Jeanloz [29], while those in the inset are from Ross and Hazen [28], (o) and ours (•). b) Change in enthalpy (H - Ho), where Ho is the zero pressure value for the *Pbnm* phase (•). (x) and (?) are results for the cubic phase obtained using 1 and 4 special *k*-points respectively.

We have also used the elastic constants to calculate a Voigt-Reuss-Hill average shear modulus of 178 ± 1 GPa. The value is significantly smaller than the 196 ± 8 calculated by Cohen[2], but is close to the 184 GPa measured by Yeganeh-Haeri *et al*[33].

Table 4 summarizes the structural properties of cubic $CaSiO_3$. Our K_o is smaller than that preferred by Mao *et al*[38], because our Ko', 4.4, is greater than 4 as assumed by them. Since $CaSiO_3$'s K_0 is similar to $MgSiO_3$'s, it is likely that a Ca enrichment of the lower mantle would not have a significant effect on the average K's. Bulk modulus alone cannot therefore be used to establish a bound on the $CaSiO_3$-perovskite content of the lower mantle. This will require the estimation of the shear modulus of this phase at high pressures.

TABLE 2. Bulk modulus of $MgSiO_3$-perovskite: a) This work, b) Knittle and Jeanloz [29], c) Ross and Hazen [28], d) Kudoh et al [30], e) Yagi *et* al [31], f) Mao et al [32], g) Yeganeh-Haeri *et al* [33] h) Stixrude and Cohen [34], i) D'Arco *et al* [35], j) Cohen et al [27].

Pbnm	K_o	K_o'
a	259	3.9
b	266	3.9
c	254	4.0
d	247	4.0
e	258	4.0
f	272	4.0
g	246	
h	266	4.2
i	309	
Pm3m	K_o	K_o'
a	258	4.0
i	291	
j	279	3.74

TABLE 3. Elastic constants of MgSiO3-perovskite. a) This work, b) Cohen [2], c) Matsui et al [37], d) Yeganeh-Haeri [33].

	Calc.[a]	Calc.[b]	Calc.[c]	Exp.[d]
C_{11}	496	548	460	520
C_{22}	560	551	506	510
C_{33}	504	441	378	437
C_{44}	151	241	162	181
C_{55}	198	253	159	202
C_{66}	171	139	112	176
C_{12}	132	54	139	114
C_{13}	136	153	184	118
C_{23}	156	175	177	139

3.2. MGSIO3 C2/C ENSTATITE

Pyroxene phases are characterized by the presence of single tetrahedral ($(Si03)^{2-}$) chains arranged in layers parallel to (100). Within these layers, each tetrahedron shares two corners with adjacent ones to form infinite chains parallel to the c-axis. Tetrahedral layers are separated by octahedral

TABLE 4. Structual properties of $CaSiO_3$-perovskite: a) This work, b) Hemley et al [39], c) Mao et al [38],d) Tarrida and Richet [40], e) Yagi et al [41], f) Liu and Ringwood [42].

		Calc.	Exp.
a (Å)	0 GPa	3.587[a]	3.565[c]
		3.568[b]	3.573[d]
			3.572[e]
	16 GPa	3.518[a]	3.486[f]
		3.530[b]	
K_o(GPa)		254[a]	281[c]
		247[b]	275[d]
			288[e]
K_o'		4.4[a]	4.0[c]
		5.3[b]	4.0[d]
			4.0[e]

layers containing 6 to 8 coordinated cations (Mg's in this case). Different symmetries arise from different stacking sequences of the octahedral layers and from symmetrically distinct tetrahedral chains. (For a detailed description of structural variations, see Cameron and Papike[43], and Putnis[44]). Besides space group variations, there are chemical subdivisions (compatible with these space groups). Enstatite, $MgSiO_3$, with ferrosilite, $FeSiO_3$, orthopyroxenes, $(Mg,Fe2+)_2 Si2O_6$, and pigeonite $(Mg,Fe^{2}+,Ca)_2si2O_6$, constitute one of these major subdivisions, the Magnesium-Iron pyroxenes. Together these pyroxenes comprise almost 25% by volume of some mineralogical models of the earth's upper mantle[45].

Among these pyroxenes, only the Ca-rich pigeonites were known to exist in the orthopyroxene (space group Pbca) structure, as well as in clinopyroxene $P2_1/c$ phase, even though evidence for the stability of low-Ca C2/c phases has been available for many years (e.g. [46, 47]). Petrological experiments on the $MgSi0_3$ system in the pressure-temperature range 7-10 GPa and 900-1700 °C[48 49] in combination with *in situ* single crystal diffraction experiments to 8 GPa.at room temperature [6]have confirmed the true stability of a clinopyroxene phase with C2/c symmetry at high pressures. A recent single-crystal diffraction study of low-clinoferrosilite by Hugh-Jones and Angel[50] has also demonstrated the stability at high pressures of the same C2/c structure type for $FeSiO_3$ composition.

C2/c pyroxenes contain 40 atoms per cell and are described by 18 free parameters. The Bravais lattice is monoclinic with a β angle around

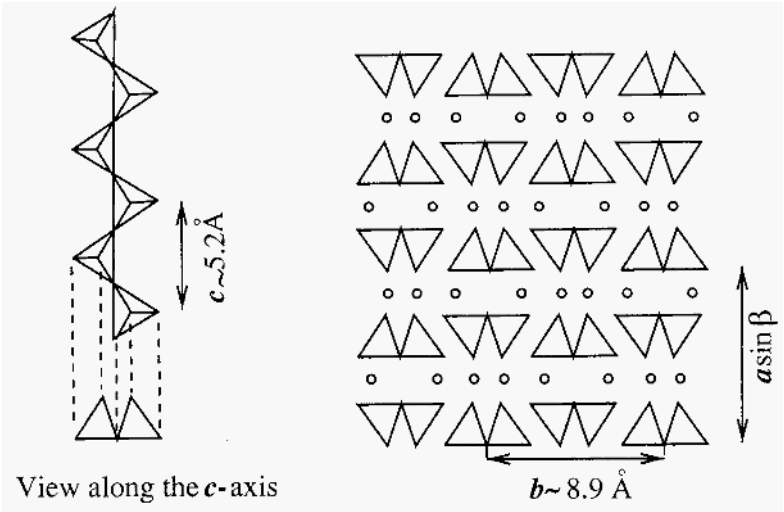

Figure 5. Schematic representation of the structure of high-pressure C2/c clinoenstatite viewed down (001).

106 degrees (hence the name clinopyroxene). The chains are all equivalent and symmetrically related to one another. Tetrahedral chains ($(SiO_3)_n^{2n-}$) stretch along the c-axis and have a periodicity of two tetrahedra. The basic topology of this structure, when viewed along the c-axis, is shown in Fig. 5.

There are two symmetrically distinct cation sites, both occupied by Mg in enstatite. The M1 site lies between the apices of opposing tetrahedra; the M2 site lies between their bases. The M1 sites are smaller and almost regular octahedra, while the M2 sites are larger, more distorted, and the local coordination may be nearly 8-fold when that site is occupied by larger cations such as Na or Ca (see review by Cameron and Papike[43]). The polyhedral linkage in this structure is shown in Fig. 6, where the M1 sites are surrounded by oxygen-octahedra, while the M2 sites are represented by spheres.

The way this structure reacts to heat, pressure, and cation substitution, reflects the basic linkage between tetrahedral chains and the linking polyhedra. Tetrahedra are more rigid than the cation polyhedra. The cation sites are the ones which respond the most to external conditions, while the

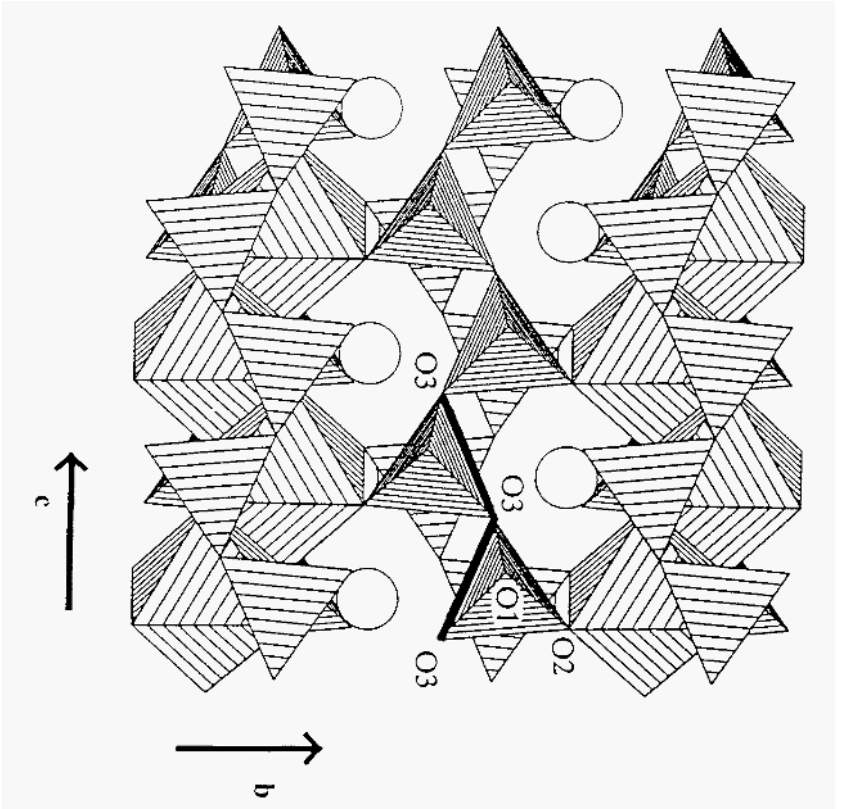

Figure 6. The structure of high-pressure C2/c clinoenstatite viewed down (100). Si'S are located at the center of oxygen tetrahedra; the M I cation sites are represented by octahedra, while the M2 sites are represented by spheres.

chains expand or contract mainly by means of tetrahedral rotations.

C2/c-enstatite is known to be thermodynamically stable above 7.9 GPa at room temperature. At lower pressures the structure distorts into another form of clinoenstatite with $P2_1/c$ symmetry, with chains differentiated into "O-rotated" and "S-rotated". The precise pressure range of mechanical stability of the C2/c phase is uncertain, but it has been held metastable down to 5.3 GPa [6].

Here we summarize our investigation on $MgSi0_3$ C2/c enstatite[23]. We optimized structures under pressure from 0 to 30 GPa, and have found dynamically stable structures with C2/c symmetry in almost all cases; however, at 8 GPa we found large dynamical fluctuations. The amplitude of these fluctuations is reported in parenthesis in Table 5.

TABLE 5. Theoretical (this work) and experimental (Angel *et al*,[6]) parameters for $C2/c$ clinoenstatite. The primitive vectors are respectively: $\vec{a} = (a\sin\beta\hat{x} + a\cos\beta\hat{z}$, $\vec{b} = b\hat{y}$, $\vec{c} = c\hat{z}$. This phase ($8MgSiO_3$) has Si's and three crystallographic distinct O's, O(1,2,3), at sites generally described as (x, y, z); (-x, -y, -z); (-x, y, 1/2-z); (x,-y, 1/2+z); (1/2+x, 1/2+y, z); (1/2-x, 1/2-y, -z); (1/2-x, 1/2+y, 1/2-z); (1/2+zx 1/2-y, 1/2+z), and two distinct, Mg's, Mg(1,2), at (0, y, 1/4); (0, -y, 3/4); (1/2, 1/2+y, 1/4); (1/2, 1/2-y, 3/4). The lattice parameters are given in Å and the monoclinic β angle in degrees. Numbers in parentheses are uncertainties in the last significant digit.

	Calc.(8 Gpa)	Exp. (7.9 GPa)
a	9.12(1)	9.201(3)
b	8.19(1)	8.621(1)
c	4.904(5)	4.908(1)
β	101.32)	101.50(3)
$Mg1_y$	0.912(1)	0.9057(6)
$Mg2_y$	0.277(1)	0.2742(5)
Si,	0.2987(5)	0.2988(4)
Si,	0.0959(5)	0.0915(3)
Si,	0.2137(5)	0.2112(4)
$O1_x$	0.0121(1)	0.1215(9)
$O1_y$	0.0953(5)	0.0914(8)
$O1_z$	0.133(1)	0.139(1)
$O2_x$	0.378(2)	0.380(1)
$O2_y$	0.2474(5)	0.2376(7)
$O2_z$	0.377(1)	0.367(1)
$O3_x$	0.356(5)	0.357(1)
$O3_y$	0.061(1)	0.0613(6)
$O3_z$	0.917(1)	0.915(1)

Despite the presence of dynamical fluctuations (structural instability), which we discuss below, a detailed comparison with the experimental structure at 7.9 GPa reveals interesting trends and a successful description of subtle structural features (see Wentzcovitch *et al*[23]). The calculated O3-O3-O3 chain extension angle of 135.6 compares with the experimental value of 135.5±0.5. The monoclinic angle β is correctly found to be in the range 100-102 degrees. This is typical of high pressure $C2/c$ phases, as opposed to high temperature C2/c phases in which this angle is around 106 degrees. The overall distortion pattern of tetrahedra and cation polyhedra are also correctly reproduced with the correct sequence of long, medium, and short bonds (see Wentzcovitch *et al*[23]).

An intriguing effect is observed in the longer and weaker Mg-O bonds. They have their lengths underestimated by an average of 2.4%, resulting

in polyhedral volumes that are 7% (M1) and 8% (M2) too small compared with experimental values. This effect is apparent in the calculated unit cell parameters. The c-axis, which is parallel to the strongly bonded tetrahedral chains, is reproduced correctly to within 0.1%, and the a-axis, approximately perpendicular to the pseudo-close-packed planes of oxygen atoms within the structure (Fig. 6), is calculated to within 0.8% of the experimental value. But the b-axis, which is the weakest bonded direction within the structure, as evidenced by structural voids (Fig. 6) and its high compressibility[51], underestimated by 4.9% at 8 GPa (For a more extensive account of this deficiency, see Wentzcovitch *et al*[23]). This behavior contrasts with that of $MgSiO_3$-perovskite ([9, 19]),in which the skeleton of strong Si-O bonds forms a completely connected array that determines the lattice parameters, which were calculated to be about 1% smaller than experimental values. The origin of the present deficiency is likely to be related to the use of the LDA[14]. Lately, we have seen accumulating evidences suggesting that Gradient-Corrected LDA (GC-LDA)[52, 53, 54] might help to account for this trend (see for instance the study case of ice under pressure by Lee *et al*[55]).

The trends in cell parameters under pressure agree well with experimental data which is limited to the pressure range from 5.3 to 7.9 GPa[51]. At 8 GPa, the calculation correctly reproduces the observed trend of axial compressibilities, $c/c_o > a/a_o > b/b_o$. The magnitude of changes in monoclinic angle with pressure, $d\beta/dP$ is also correctly described (-0.09 ± 0.02 compared with -0.11 ± 0.01 degrees/GPa in the experiments).

We also analize further the nature of the dynamical fluctuations at 8 GPa. The most significant of these fluctuations involves the silicate chains, in particular, the movement of the bridging oxygens (O3). This oscillation is accompanied by a sudden change in tetrahedra tilting and chain extension angles (Fig. 7). Below and above 8 GPa these angles decrease steadily, but around 8 GPa there is an abrupt change in behavior.

The origin of this phenomenon is not clear, but it could be an artifact of this symmetry conserving dynamics, which holds the C2/c structure metastable when it is mechanically unstable. It might have turned into $P2_1/c$ in the presence of symmetry breaking fluctuations. Although we did not investigate further this phenomenon, in principle it is possible to answer this question by performing structural optimizations with initial conditions of space groups which are simultaneous sub-groups of $P2_1/c$ and C2/c.

The other possibility is that the low pressure behavior reflects the existence of another truly metastable C2/c configuration. There are several mineralogical examples of this type of behavior[30, 50] and the most recently documented case is $MgSiO_3$ orthopyroxene[50]. That phase is very closely related to the present one, and the structural anomaly under pres-

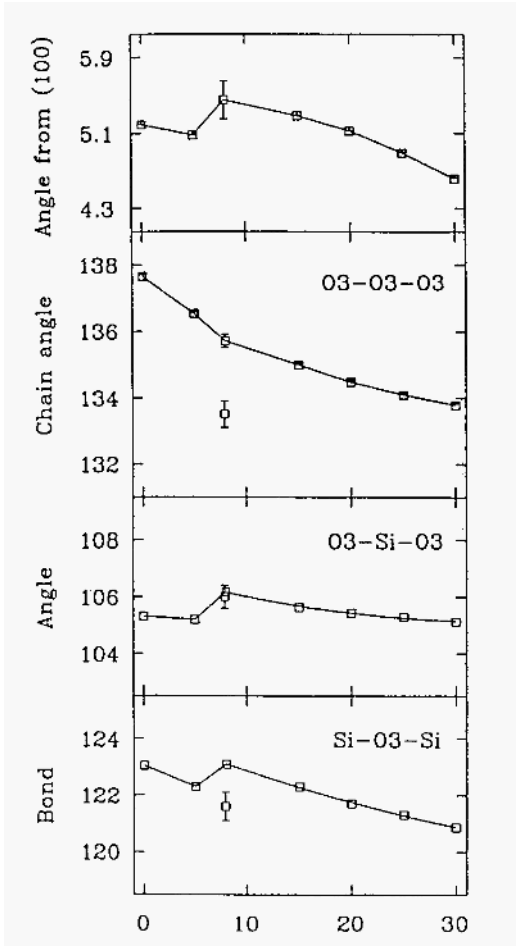

Figure 7. Variation of tetrahedral chain configuration with pressure. Filled error-bars represent experimental data points at 7.9 GPa.

sure involves a change in polyhedral compressibilities around 4 GPa.

The present case also involves changes is polyhedral compressibilities across the structural anomaly (for a detailed account, see Wentzcovitch *et al*[23]). Since the cation polyhedra link the tetrahedral chains, this behavior

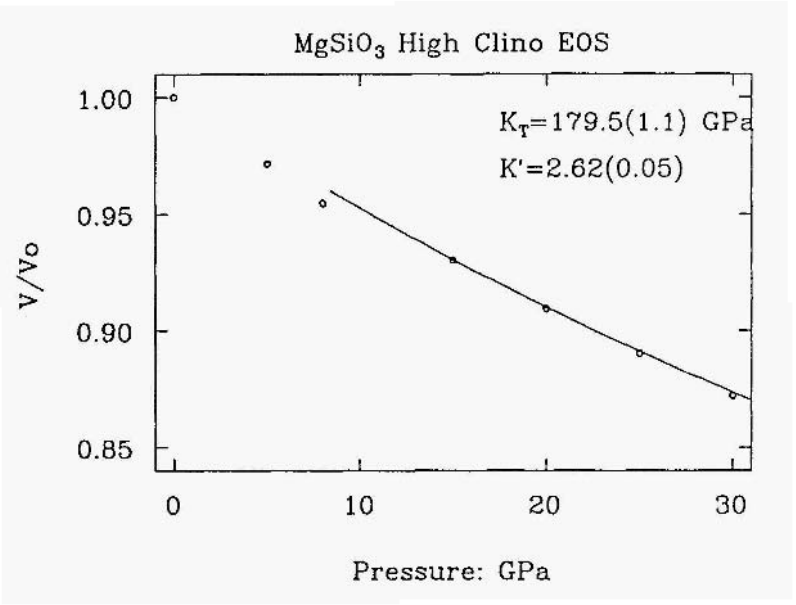

Figure 8 Variation of the cell volume with pressure.

is obviously related to the change in chain configuration. Figure 7 displays the subtler volume anomaly across the calculated structural instability at 8 GPa in C2/c enstatite.

The bulk modulus obtained by fitting the calculated unit cell volumes in the range of 15 to 30 GPa to a third-order Birch-Murnaghan equation of state (EOS) (but excluding the result at 8 GPa) is 180 ± 1 GPa, with $K'_o = 2.3 \pm 0.5$ The experimental data for C2/c-enstatite[51] is insufficient to allow a similar fit, but we note that K_o calculated here is significantly larger than the values of 123 ± 17 GPa and 111 ± 3 GPa of other pyroxene polymorphs of $MgSiO_3$[51].

4. Conclusions

We presented a summary of the theory and of applications of an *ab initio* constant pressure variable cell shape molecular dynamics (VCS-MD) algorithm to the study of Earth forming mineral phases. The applications discussed here demonstrated the use of the technique as an efficient structure

optimizer at arbitrary pressures and at T = 0 K. The symmetry conservation property of this dynamics in the absence of thermal fluctuation is particularly useful to this type of problem because it helps to speed up considerably these calculations by allowing the use of k-point sampling in the irreducible Brillouin Zone wedge only. We demonstrated this property is not restrictive by showing that structures of higher symmetry can be obtained as special cases of structures of lower symmetry.

Although we have used this algorithm only as a structure optimizer, finite temperature calculations are also possible. We expect that adaptation of this algorithm to parallel architectures will enable this methodology to be applied to give finite temperature estimates of the properties and behavior of other major Earth-forming phases as well.

References

1. Catlow, C. R. A. and Price G. D. (1990) Computer Modelling of Solid State Inorganic Materials, *Nature* **347**, 243-248.
2. Cohen, R. E., (1987) Elasticity and Equation of State of $MgSiO_3$-Perovskite, *Geophys. Res. Lett.* **14**, 1053-1056.
3. Parker, S. C. and Price, G. D., (1989) Computer Modelling of Phase Transition in Minerals, *Ad. Solid State Chem.* **5**, 295-327.
4. Matsui, M., Price, G. D., and Patel. A., (1994) Comparison Between the Lattice Dynamics and Molecular Dynamics Methods: Calculations Results for $MgSiO_3$-perovskite, *Geophys. Res. Lett.* **21**, 1659-1662.
5. Matsui, M. and Price, G. D., (1992) Computer Simulation of $MgSiO_3$ Polymorphs, *Phys. Chem. Min.* **18**, 365-372.
6. Angel, R. J., Chopelas, A., and Ross, N. L., (1992) Stability of High-Density Clinoenstatite at Upper-Mantle Pressures, *Nature* **358**, 322-324.
7. Matsui, M. and Price, G. D., (1991) Simulation of the Pre-melting Behavior of $MgSiO_3$ Perovskite at High Pressures arid Temperatures, *Nature* **351**, 735-737.
8. Kapusta, B. and Guillope, M., (1993) Molecular Dynamics of the Perovskite $MgSiO_3$ at High Temperature: Structural, Elastic, and Thermodynamical Properties, *Phys. Earth Planet. Int.* **75**, 205-224.
9. Wentzcovitch, R. M., Martins, J. L., and Price, G. D., (1993) *Ab initio* Molecular Dynamics with Variable Cell Shape: Application to $MgSiO_3$-Perovskite, *Phys. Rev. Lett.* **44**, 2-5.
10. Wentzcovitch, R. M. and Martins, J. L., (1991) First Principles Molecular Dynamics of Li: Test of a New Algorithm, *Sol. Stat. Comm.* **78**, 831-834.
11. Wentzcovitch, R. M., (1991) Invariant Molecular Dynamics Approach to Structural Phase Transitions, *Phys. Rev.* **B44**, 2358-2361.
12. Car, R. and Parrinello, M., (1985) Unified Approach for Molecular Dynamics and Density Functional Theory, *Phys. Rev. Lett.* **55**, 2471-2474.
13. Wentzcovitch, R. M., Martins, J. L., and Allen, P. B. (1992) Energy Versus Free Energy Conservation in *ab initio* Molecular Dynamics, *Phys. Rev. B* **45**, 11372-11375.
14. Lundqvist, S. and March, N. H., (1987) *Theory of the Inhomogeneous Electron Gas,* Plenun Press, London.
15. Troullier, N. and Martins, J. L., (1991) Efficient Pseudopotentials for Plane-Wave Calculations, Phys. *Rev. B* **43**, 1993-2003.
16. Parrinello, M. and Rahman, A., (1980) Crystal Structure and Pair Potentials: A Molecular Dynamics Study, Phys. *Rev. Lett.* **45**, 1196-1199.

17. Andersen, H.C. (1980) Molecular Dynamics Simulations at Constant Pressure and/or Temperature, *J. Chem. Phys.* **72,** 2374-2393.
18. Wentzcovitch, R. M., (1994) The hcp to bcc Pressure Induced Transition in Mg Simulated by *ab initio* Molecular Dynamics, *Phys. Rev. B* **50**, 10358-10361.
19. Wentzcovitch, R. M., Schulz, W., and Allen, P. B., (1994) VO2: Peierls or Mott, Hubbard? A View from Band Theory, Phys. *Rev. Lett.* **72**, 3389-3392.
20. Wentzcovitch, R. M. and Liu, A. Y., (1994) Stability of Carbon Nitride Solids, *Phys. Rev. B* **50,** 10362-10365.
21. Woodhouse, J. H. and Dziewonski, A. M., (1989) Seismic Modeling of Earth's Large-Scale Three-Dimensional Structure, *Phil. Trans. R. Soc. Lond.* **A328**, 291-308.
22. Wentzcovitch, R. M., Ross, N. L., and Price, G. D., (1994) *Ab initio* Study of $MgSiO_3$ and $CaSiO_3$-Perovskites at Lower Mantle Pressures, *Phys. Earth Planet. Int.,* in press.
23. Wentzcovitch, R. M., Hugh-Jones, D. A., Angel, R. J., and Price, G. D., (1995) *Ab Initio* Study of $MgSiO_3$ C2/c Enstatite, *Phys. Chem. Min.,* in press.
24. Hemley, R. and Cohen, R., (1992) Silicate Perovskite, *Annu. Rev. Earth Planet. Sci.* **20,** 553-601.
25. Andrault, D. and Poirier, J. P., (1991) Evolution of the Distortion of Perovskites Under Pressure: An EXAFS Study of $BaZrO_3$, , $SrZrO_3$, . and $CaGeO_3$, *Phys. Chem. Minerals* **18**, 91-105.
26. Horiuchi, H., Ito, E., and Weidner, D., (1987) Perovskite Type $MgSiO_3$: Single Crystal X-ray Diffraction Study, *Am. Mineral.* **72**, 357-360.
27. Cohen, R. E., Boyer, L. L., Mehl, M. J., Pickett, W. E., and Krakauer, H., (1989) Electronic Structure and Total Energy Calculations For Oxide Perovskite and Superconductors. See Navrotsky and Weidner[56], 55-66.
28. Ross, N. L. and Hazen, R. M., (1990) High Pressure Crystal Chemistry of $MgSiO_3$ Perovskite, *Phys. Chem. Minerals* **17**, 228-237.
29. Knittle, E. and Jeanloz, R., (1987) Synthesis and Equation of State of $(Mg,Fe)SiO_3$ to over 100 GPa, *Science* **235**, 668-670.
30. Kudoh Y., Ito, E., and Takeda, H., (1987) Effect of Pressure on the Crystal Structure of Perovskite Type $MgSiO_3$, *Phys. Chem. Minerals* **14**, 350-354.
31. Yagi, T., Mao, H. K., and Bell, P. M., (1982) Hydrostatic Compression Perovskite-Type $MgSiO_3$, in *Advances in Physical Geochemistry,* Ed. by S. K. Saxena, Springer, Berlin, 317-25.
32. Mao, H. K., Hemley, R. J., Shu, J., Chen, L. C., and Jephcoat, A. P., (1988-1989b) The Effect of Pressure, Temperature, and Composition on Lattice Parameters and Density of $(Fe,Mg)SiO_3$-Perovskites to 30 GPa, *Ann. Rep. Div. Geophys. Lab.,* 82-89.
33. Yeganeh-Haeri, A., Weidner, D. J., and Ito, E., (1989) Single Crystal Elastic Moduli of Magnesium Metasilicate Perovskite. See Navrotsky and Weidner [56], 13-25.
34. Stixrude, L. and Cohen, R. E., (1993) Stability of Orthorhombic $MgSiO_3$-Perovskite in the Earth's Lower Mantle, *Nature* **364**, 613-616.
35. D'Arco, P., Sandrone, G., Dovesi, R., Orlando, R., and Saunders, V. R., (1993) A Quantum Mechanical Study of the Perovskite Structure type of $MgSiO_3$, *Phys. Chem. Minerals* **20**, 407-414.
36. Nielsen, O. H. and Martin, R., (1985) Quantum Mechanical Theory of Stress and Force, *Phys. Rev. B* **32**, 3780.
37. Matsui, M. and Akaogi, M., and Matsumoto, T., (1987) Computational model of the structural and elastic properties of the ilmenite and perovskite phases of $MgSiO_3$, *Phys. Chem. Minerals* **14**, 101-106.
38. Mao, H. K., Chen, L. C., Hemley, R. J., Jephcoat, A. P., and Wu, Y., (1989) Stability and Equation of State of $CaSiO_3$ Perovskite to 134 GPa, *J. Geophys. Res.* **94**, 17889-17894.
39. Hemley, R. J., Jackson, M. D., and Gordon, R. G., (1987) Theoretical Study of the Structure, Lattice Dynamics, and Equations of State of Perovskite-type $MgSiO_3$

and $CaSiO_3$, *Phys. Chem. Minerals* **14**, 2-12.
40. Tarrida. M. and Richet, P., (1989) Equation of State of $CaSiO_3$-Perovskite to 96 GPa, *Geophys. Res. Lett.* **16**, 1351-1354.
41. Yagi, T.,Kusanaga, S., Tsuchida, Y., Fukai, Y., (1989) Isothermal Compression and Stability of Perovskite-type $CaSiO_3$, *Proc. Jpn. Acad. Ser. B* **65**, 129-132.
42. Liu, L.-G and Ringwood, A. E., (1975) Synthesis of a Perovskite-Type Polymorph of $CaSiO_3$, *Earth Planet. Sci. Lett.* **28**, 209-211.
43. Cameron, M. E. and Papike, J. J., (1980) Crystal Chemistry of Silicate Pyroxenes, M. S. A. *Reviews in Mineralogy* **7**, 5-92.
44. Putnis, A., (1992) *Introduction to Mineral Science,* Cambridge Press, Cambridge.
45. Ringwood, A. E., (1975) *Composition and Petrology of the Earth's Mantle,* McGraw-Hill, New York.
46. Yamamoto, K. and Akimoto, S., (1977) The System MgO-SiO_2-H_2O at High Pressures and Temperatures: Stability Field for Hydroxyl-Hondrodite, Hydroxyl-Clinohumite and the 10 Å Phase, *Amer. J.* Sc., **277**, 288-312.
47. Akaogi, M. and Akimoto, S., (1977) Pyroxene-garnet solid solution equilibria in the system $Mg_4Si_4O_{12}$ - $Mg_3Al_30_{12}$ and $Fe_4Si_4O_{12}$ - $Fe_4Al_2Si_3O_{12}$ at, high-pressures and temperatures, *Phys. Earth and Planet. Sc.* **15**, 90-106.
48. Pacalo, R. E. G. and Gasparik, T., (1990) Reversals of the Orthoenstatite-Clinoenstatite Transition at High-Pressures and High-Temperatures, *J. Geophys. Res.* **95**, 15853-15858.
49. Kanzaki, M., (1991) Ortho-clinoenstatite transition, *Phys. Chem. Min.* **17**, 726-730.
50. Hugh-Jones, D. A. and Angel, R. J., (1994) A Compressional Study of $MgSiO_3$ Orthoenstatite to 8.5 GPa, *Amer. Mineral.* **79**, 405-410.
51. Angel, R. J. and Hugh-Jones, D. A., (1994) Equations of State of Enstatite Pyroxenes, *J. Geophys. Res.,* in press.
52. Langreth, D. C., and Mehl, M. J., (1981) Easily implementable non-local exchange-correlation energy functionals, *Phys.* Rev. *Lett.* **46,** 446-449.
53. Perdew, J. P . and Wang, Y., (1986) Accurate and Simple Density Functional for the Electronic Exchange Energy: Generalized Gradient Approximation, *Phys. Rev. B* **33**, 8822-8825.
54. Becke, A. D., (1988) Density Functional Exchange Energy Approximation with Correct Asymptotic Behaviour, *Phys. Rev. A* **38**, 3088-90.
55. Lee, C., Vanderbilt, D., Lasoonen, K., Car, R., and Parrinello, M., (1992) *Ab Initio* studies of high pressure phases of ice, *Phys. Rev. Lett.* **69**, 462-465.
56. Navrotsky, A. and Weidner, D. J., (1989) *Perovskite a Structure* of *Great Interest for Geophysics and Materials Science,* Washington D. C., Am. Geophys. Union.

This page intentionally left blank.

CALCULATION OF MINERAL PROPERTIES WITH THE ELECTRON GAS MODEL

ROY G. GORDON
Department of Chemistry Harvard University Cambridge, MA 02138

AND

DANIEL J. LACKS†
Department of Chemistry Harvard University Cambridge, MA 02138
† *present address: Department of Chemical Engineering, Tulane University, New Orleans, LA 70118*

1. Introduction

An understanding of the thermodynamic and mechanical properties of minerals is necessary to explain the structure and dynamics of the earth's interior. Because of the difficulty in determining these properties experimentally at the extreme pressures and temperatures which exist within the earth, computer modeling can yield much information and insight.

The most rigorous methods of calculating the properties of a crystal involve solving the Hartree-Fock or Kohn-Sham equations for the periodic system, and have recently been applied to minerals such as MgO periclase [1, 2], SiO_2 quartz [3], SiO_2 stishovite [4, 5, 6, 7], Mg_2SiO_4 spinel [8, 9], and $MgSiO_3$ perovskite [10, 11]. However the difficulty of these calculations increases rapidly with the size of the unit cell, and for more complex crystals the calculation times prohibit the use of large basis sets and full structure optimizations. Another method of calculating crystal properties uses parameterized force fields, where the parameters are obtained from Hartree-Fock calculations on small molecules or clusters. Such calculations have been carried out for silica and silicates by Tsuneyuki et al. [12] and van Beest et al. [13]. A disadvantage of this method is the ambiguity in

B. Silvi and P. D'Arco (eds.), Modelling of Minerals and Silicated Materials, 63-79

determining certain parameters (such as atomic charges) which can vary considerably with the atomic environment [13].

The electron gas model is an alternative, non-empirical, method for the calculation of crystal properties. The electron gas model has the advantages that it is more computationally efficient than the periodic Hartree-Fock or Kohn-Sham calculations, and does not have the ambiguity of the force field calculations. In the electron gas model the crystal is assumed to be made up of ions: The total crystal energy is obtained as the interaction energy of the ions in the crystal plus the self-energy of the ions. The self-energies of the ions are obtained by accurate Hartree-Fock or Kohn-Sham methods, and the interaction energy is obtained approximately with density functionals.

The present paper focuses on the application of the electron gas model to the calculation of mineral properties, particularly crystal structures, cohesive energies, electron densities, compressibilities, and pressure-induced phase transitions. The effects of partial covalent bonding, or equivalently the non-spherical distortions of the ions, on these properties are addressed.

2. Computational Method

2.1. THEORY

The electron gas model is characterized by three assumptions [14]:

1. The interaction energy DE is calculated with energy functionals of the electron density,

$$\Delta E = \int \left\{ \epsilon[\rho(\mathbf{r})] - \sum_i \epsilon[\rho_i(\mathbf{r} - \mathbf{r}_{oi})] \right\} \tag{1}$$

where ϵ is the density functional, p is the electron density of the total system, p_i is the electron density of the ion centered at $\mathbf{r}_{oi}$, and the sum is over the interacting ions in the system. This calculation of the interaction energy would be exact if the exact density functional was known; however, only approximate density functionals are known.

2. The total electron density $p(\mathbf{r})$ is the sum of the electron densities of the ions p_i in the system:

$$\rho(\mathbf{r}) = \sum_i \rho_i(\mathbf{r} - \mathbf{r}_{oi}) \tag{2}$$

This additive density approximation does not correspond to the antisymmetrized product of the ionic wavefunctions which give the densities p_i; however, the resulting electron density does correspond to some antisymmetrized (although unknown) wavefunction, and thus does not violate the Pauli exclusion principle [15]. If there were full variability

in the p_i, any total electron density p could be constructued and the additive density approximation would not limit the accuracy of the calculation. In practice, however, the limited variability in the ionic densities restricts the possibilities for the total electron density and thus the accuracy of the calculation.

3. The electron densities of the ions, p_i, are obtained from accurate quantum mechanical calculations, such as Hartree-Fock or Kohn-Sham calculations, on the isolated ions. Changes in the ionic densities p_i due to the crystal environment can be incorporated by including a perturbative potential in the ionic calculation. The self-energy of the ion is calculated as the energy of the ion with the perturbed density (the energy does not include the perturbation energy) minus the energy of the gas phase, stable ion (For oxides, since O_2^- is unstable in the gas phase, the reference ion is O^-).

2.2. APPROXIMATIONS

The electron gas model would give exact results if an exact density functional were used for the interaction energy, the ionic densities were fully variable so that any total density could be obtained by summing the ionic densities, and the calculation of the ionic self-energies were exact. In practice these conditions cannot be met and approximations must be used.

2.2.1. *Density functionals for interaction energy*

The exact density functionals for arbitrary electron densities are not known. The simplest approximate density functionals are those which are exact for the uniform electron gas [16, 17] (the correlation energy functional is known exactly for the uniform electron gas only in the limits of high and low electron densities; the correlation energy for intermediate densities can be obtained by interpolation between these limits [14]). To improve upon the uniform electron gas functionals, Waldman and Gordon introduced scaling coefficients which depend on the number of electrons in the system [18]. Although these scaled functionals increase the accuracy of electron gas model calculations, this increased accuracy is due somewhat to a cancellation of the error due to the approximate electron density [19]. Accurate non-local density functionals have recently been developed [20, 21, 22], which lead to more accurate calculations of interaction energies [19, 22].

2.2.2. *Electron densities*

In the simplest formulations of the electron gas model, gas phase ionic densities are used for the crystalline ionic electron densities [23]. However, to

increase the accuracy of the model, changes in the ionic densities in response to the crystalline environment must be incorporated. The changes in ionic density are non-spherical in general, although a spherical ion approximation is valid when the ion is in a high symmetry position. Most of the earlier electron gas model calculations assumed spherical ions for simplicity; more recent work has been directed towards non-spherical distortions.

The changes in the ionic electron densities have been incorporated in three ways:

1. An electrostatic perturbation is included in the ionic calculation, the parameters of which are chosen to reproduce the electrostatic environment of the ion in the crystal. The electrostatic perturbation is a charged spherical shell for spherical ion calculations [24, 25], and a series of point charges for non-spherical ion calculations [26].
2. An electrostatic perturbation is included in the ionic calculation, the parameters of which are varied to minimize the total crystalline energy. By varying the parameters to minimize the total crystal energy, rather than to reproduce the electrostatic environment of the ion in the crystal, all factors which affect the electron density - including short range repulsions caused by overlap of the ionic densities - are taken into account, rather than just the electrostatic factors. These variational calculations have been carried out both for spherical [27] and non-spherical ions [28].
3. The effects of the other ions in the crystal are included directly in the Hamiltonian for the electronic structure calculation for the ion; the electron densities of the ions are obtained self-consistently as those which minimize the total crystalline energy. This method, which corresponds to the variational electrostatic perturbation method with an infinite number of variational parameters, has been applied in both the spherical ion approximation [29, 30] and the general non-spherical case [31].

In practice, since the cation electrons are more tightly bound than the anion electrons, the changes in the cation densities are small compared to the changes in the anion densities and are generally neglected [24].

2.2.3. *Ionic self energies*

When the Hartree-Fock method is used for the ionic calculation, the error due to the neglect of electron correlation is significant if the number of electrons in the crystal ion is different from that in the reference gas phase ion (this occurs for oxides, where the crystal ion is O_2^- and the reference gas phase ion is 0-). Earlier electron gas calculations estimated the self-energy due to electron correlation [24], but in more recent calculations an

accurate non-local correlation energy functional [32] was used to evaluate this part of the self-energy [28].

The basis set superposition error must also be accounted for when small basis sets are used (small basis sets are used in the distorted ion calculations [28, 31]; the basis sets are large enough so that this effect is neglible in the spherical ion calculations). A counterpoise method, in which the energy of the gas phase ion is calculated with a basis set similar to that used in the crystal calculation, is used to minimize this error [28].

3. Spherical ion calculations of mineral properties

Many calculations of mineral properties have been carried out with spherical ion electron gas models. For example, early investigations of CaO predicted that the B1 phase would transform to the B2 phase at approximately 1 megabar [33]; later experiments substantiated this prediction [34]. Results for silica predicted that stishovite would transform to the $CaCl_2$ structure at megabar pressures [35]; subsequent experimental evidence suggested that this phase transition does in fact occur at approximately 1 megabar [36,37]. Temperature and pressure dependences of the structural and elastic properties of simple oxide minerals have also been calculated [27, 38, 39, 40].

The spherical ion models, however, give poor results for crystals in which the anions occupy low symmetry positions, such as the silica polymorphs quartz and cristobalite, the silicate diopside, and the zeolite sodalite [41, 42, 43]. The non-spherical distortions are expected to be significant for anions in low symmetry positions; For example, in the quartz structure the oxygen anion has two neighboring silicon cations at an angle of 143° and the oxygen electron density is significantly distorted towards the silicon cations [44]. To obtain meaningful results for such crystals, non-spherical distortions of the ionic electron densities must be incorporated.

4. Distorted ion calculations of mineral properties

The results discussed below were obtained with a variational electrostatic perturbation for calculating the anion electron densities, and the scaled density functionals for calculating the interaction energies. These results have been presented in more detail elsewhere [28, 45, 46].

4.1. STRUCTURES AND COHESIVE ENERGIES

Results for structural parameters and the cohesive energies of several partially covalent crystals are given in Table I (For the open structures, the most sensitive structural parameter is the cation-anion-cation bond angle; for close-packed systems, these angles are constrained by the packing, and

the cation-anion bond length is the most sensitive parameter). For systems with open crystal structures, the structures and energies calculated with distorted ions are in much better agreement with experiment than those calculated with spherical ions. The improved structural results are due to smaller and more accurate cation- anion-cation bond angles, and the improved energetic results are due to the stronger bonds formed when charge density moves into the bonding regions. For systems with close- packed structures, the structures are modeled well with both the distorted and spherical ion models, but the energies are calculated more accurately with the distorted ions.

TABLE 1. Structural Results. Calculated results are from reference 28; experimental results are quoted from reference 28.

Open Structures	Cation-Anion-Cation Angle (°)			Cohesive Energy (kJ/mol)		
	exper.	distorted	spherical	exper.	distorted	spherical
SiO_2 Quartz	142	143	163	-11530	-11470	-11080
SiO_2 Cristobalite	145	150	180	-11530	-11470	-11110
$Na_4ClSi_3Al_3O_{12}$ Sodalite	138	137	156	_	-57550	-56160
BeF_2 Quartz	–	145	161	_	-3730	-3390
Close-Packed Structures	**Cation-Anion-Cation Angle (°)**			**Cohesive Energy (kJ/mol)**		
	exper.	distorted	spherical	exper.	distorted	spherical
SiO_2 Stishovite	1.81[a]	1.77	1.75	-11470	-11450r	-10880
	1.76[b]	1.76	1.74			
$Mg2SiO_4$ spinel	1.66[c]	1.67	1.60	-17620	-17670	-17040
	2.07[d]	2.01	2.08			
$MgSiO_3$ perovskite	1.79[e]	1.73	1.74	–	-14440	-13970
TiO_2 Rutile	1.98[a] 1.95	1.91	-10400	-10080	-9910	
	1.94'	1.96	1.94			

[a] 1 bond per oxygen ion

[b] 2 bonds per oxygen ion

[c] Si-O bond

[b] Mg-O bond

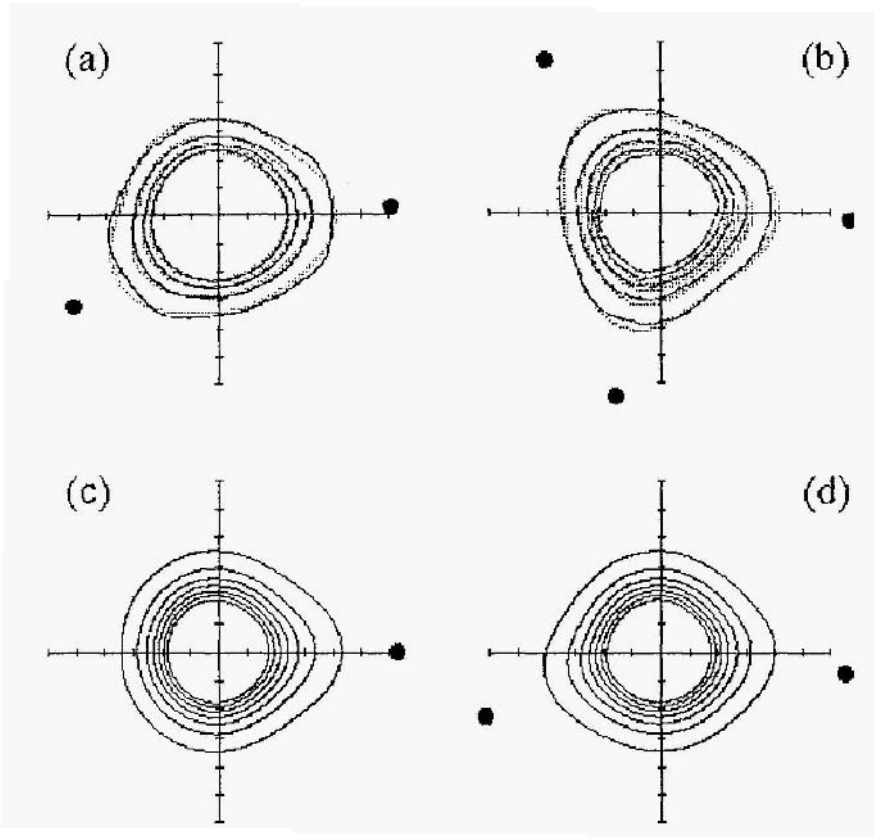

Figure 1. Valence electron distributions, in the plane of the oxygen anion and the neighboring cations. The oxygen anion is centered at the origin, and the filled circles are the positions of the neighboring silicon cations. Contour lines are spaced at 0.5 electrons/Å3, and the length of the axes are 1.588 Å.
(a) Cristobalite, (b) Stishovite. Solid lines: crystalline Hartree-Fock calculation; Dotted lines: Electron gas model.
(c) Spinel, (d) Perovskite. Solid lines: Electron gas model.

4.2. ELECTRON DISTRIBUTIONS

The valence electron density distributions of cristobalite, stishovite, spinel and perovskite are shown in Figure 1 (the electron distribution of quartz, which is not shown, is essentially identical to that of cristobalite). The non-spherical distortions are significant, and agree well with the results of crystalline Hartree-Fock calculations [47]. In general, there are approximately 0.3-0.5 electrons in the bonding regions, by Mulliken population analysis.

The non-spherical distortions are as large in the close-packed stishovite structure as in the open cristobalite structure; therefore, stishovite is not significantly more ionic than cristobalite (or quartz). However, the distortions are smaller in the perovskite structure than in the cristobalite, stishovite or spinel structures, and so the bonding in perovskite can be considered more ionic than in these other structures.

The oxygen electron density in spinel is found to be polarized much more towards the silicon ion than towards the magnesium ions (the three neigboring magnesium ions are in the direction opposite to the silicon ion). This result occurs because the extent ofpolarization is proportional to the electric field at the anion, and the electric field from a silicon ion (with a charge of+4 and at a distance of1.66) is significantly greater that from a magnesium ion (with a charge of +2 and at a distance of 2.07).

4.3. STRUCTURAL CHANGES AT HIGH PRESSURES

As discussed above, whereas for open structures the zero-pressure structures are calculated more accurately with the distorted ion model than with the spherical ion model, for close-packed systems the zero-pressure structures are calculated just as well with the spherical ion model. In the same way, the distorted ion model leads to improvements in the compression at high pressures for open structures but not for close-packed structures. Although the agreement with experiment is reasonable for calculated changes in volume with pressure, the calculated structures are generally less compressible than observed experimentally (i.e., the bulk moduli are too high).

For example, Figure 2 shows the change in volume with pressure for quartz. The large compressibility is reproduced well with the distorted ion model, but poorly with the spherical ion model, because the change in volume is due primarily to the decrease in the Si-O-Si angle (the bond length varies only slightly) [48, 49, 50]. The bulk modulus, K, and its pressure derivative, K', for quartz are K=47 GPa and K'=7.9 with the distorted ion model, K=229 GPa, and K'=7.5 with the spherical ion model, and K=34-37 GPa and K'=5.7-6.2 experimentally [49, 50]. Therefore, the distorted ion model greatly improves the bulk modulus relative to the spherical ion model, but still overestimates the bulk modulus somewhat.

4.4. PRESSURE-INDUCED PHASE TRANSITIONS

4.4.1. *Quartz to stishovite phase transition*

As the pressure is increased, silica undergoes a phase transition from quartz to coesite at 3 GPa, which in turn transforms to stishovite at, 8 GPa (for temperatures of 1000 K) [51]. Stishovite differs from quartz and coesite in that the silicon ions are coordinated to six oxygen ions in stishovite, as

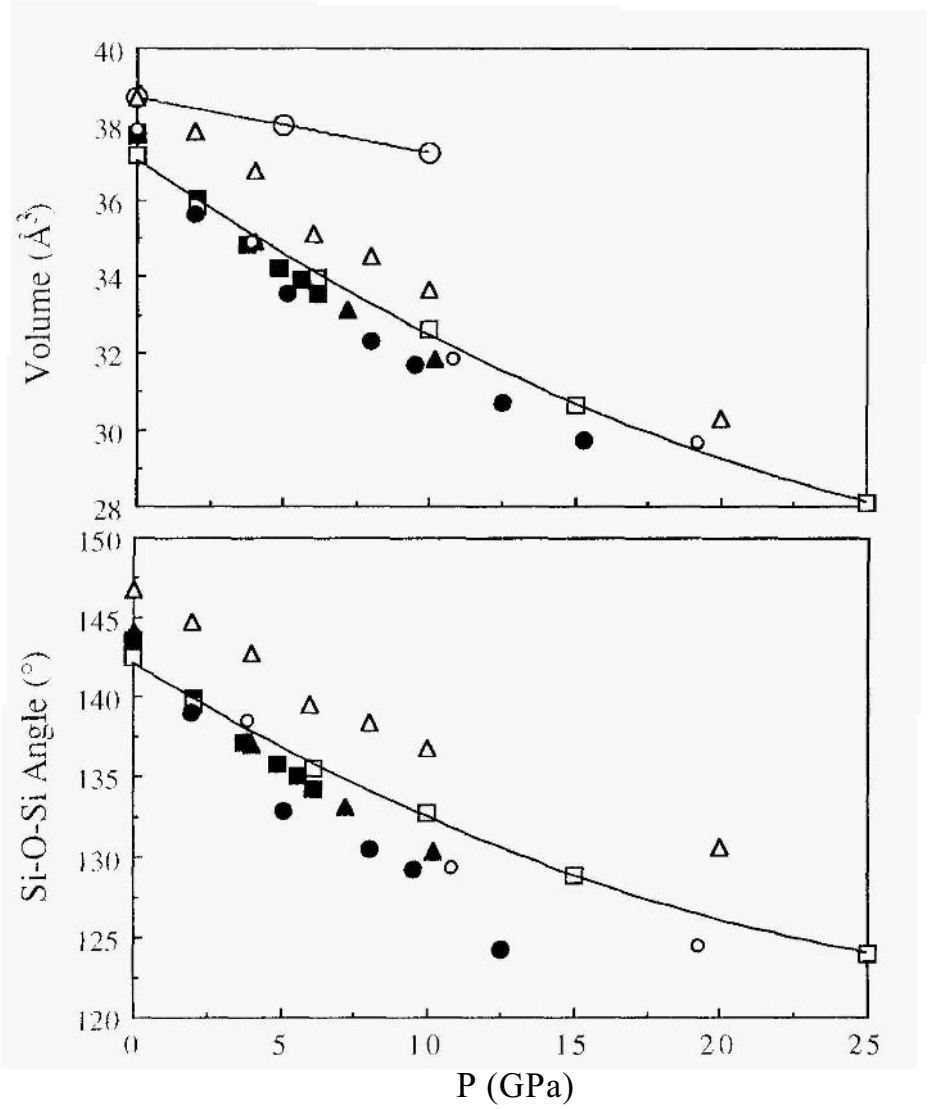

Figure 2. *a*-Quartz structure as a function of pressure. Open squares: distorted ion electron gas model; open large circles: spherical ion electron gas model; open triangles: I'I' A M model: open small circles: pseudopotential plane wave calculations of Chelikowsky et al. [3]; filled triangles: experimental results of Glinneman et al. [48]; filled squares: experimental results of Levien et al. [49]; filled circles: experimental results of Hazen et al. [50]. The spherical ion electron gas model Si-O-Si angles are all greater than 160 degrees.

compared to only four oxygen ions in quartz and coesite. This increase in the coordination of the silicon ion allows a much denser structure, with an associated volume decrease of about 38% [52]. Although the equilibrium transformation of quartz to stishovite proceeds through the coesite intermediate phase, the coesite phase is ignored in the present calculations for simplicity.

The calculated enthalpies for silica in the quartz and stishovite phases are shown in Figure 3 as a function of pressure. The stishovite structure becomes more stable than the quartz structure at 3.5 GPa with the distorted ion model, and at 21 GPa with the spherical ion model. In comparison, the experimental zero temperature transition pressure for the quartz to stishovite phase transition is estimated to be 5.5 GPa from thermodynamic data [53], and the transition pressure for the similar cristobalite to stishovite phase transition is calculated to be 6 GPa by periodic Hartree-Fock methods [54]. The non-spherical distortions improve the modeling of this phase transition by stabilizing stishovite with respect to quartz; the greater stabilization of stishovite occurs because the distortions strengthen three bonds per anion in stishovite, and only two bonds per anion in quartz (the bonds are significantly covalent in both structures, as shown above in the plots of the electron density distributions).

4.4.2. *Stishovite* to *$CaCl_2$-type structure phase transition*

Upon further compression, stishovite is believed to undergo further phase transitions, although these are not well understood. Analogous systems showed transitions from the stishovite-type (rutile) structure to the $CaCl_2$-type structure [55], which is a slight distortion of the stishovite structure; the stishovite structure is a special case of the $CaCl_2$ structure in which the lattice parameters a and b, and the oxygen position parameters x and y, are equal. Spherical ion electron-gas calculations first predicted that stishovite would transform to the $CaCl_2$ structure at megabar pressures [35], and evidence from subsequent experiments suggest that this phase transition occurs at approximately 100 GPa [36, 37].

The changes in the lattice parameters and the oxygen position parameters with pressure are shown in Figure 4. The distorted ion model predicts the phase transition to occur at slightly under 200 GPa, and although not shown, the spherical ion model predicts the phase transition to occur at 500 GPa. The distortion of the oxygen ions decreases the calculated transition pressure considerably, due to the interaction of the dipoles that form when the distorted anion moves out of the plane of the silicon ions. We note that the transition pressure with the distorted ion model is still somewhat larger than the pressure suggested by experiment [36, 37], and the pressures of 45 to 80 GPa obtained in periodic electronic structure calculations [4, 5].

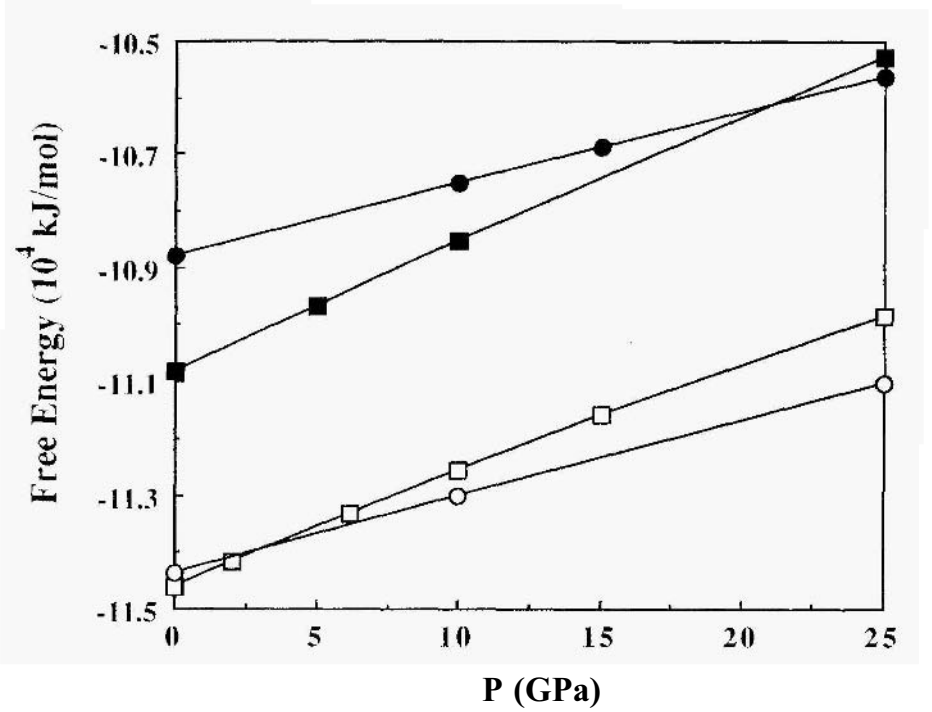

Figure 3. Enthalpy of silica in quartz and stishovite structures as a function of pressure Key: squares: quartz, circles: stishovite; open symbols: distorted ion electron gas model closed symbols: spherical ion electron gas model.

4.4.3. *Spinel to perovskite phase transitions in $MgSiO_3$ and Mg_2SiO_4*

The seismic discontinuity occuring in the earth's mantle at a depth of 670 km is attributed to the phase transition from the spinel phase to the perovskite phase. and it is this discontinuity which marks the separation between the upper and lower mantle. Calculations were carried out of this phase transition in the $MgSiO_3$ and Mg_2SiO_4 systems, which approximately model the composition of the mantle

The results of the distorted ion calculations for the enthalpies relevant to this phase transition are shown in Figure 5a. At zero pressure, spinel is the most stable phase. At 24.5 GPa, the two-oxide assemblage (MgO periclass + SiO_2 stishovite) becomes stable, and remains stable to 31.5 GPa, at which point the perovskite phase becomes stable. The spinel to perovskite phase transition occurs at 26.0 GPa for the Mg_2SiO_4 stoichiom-

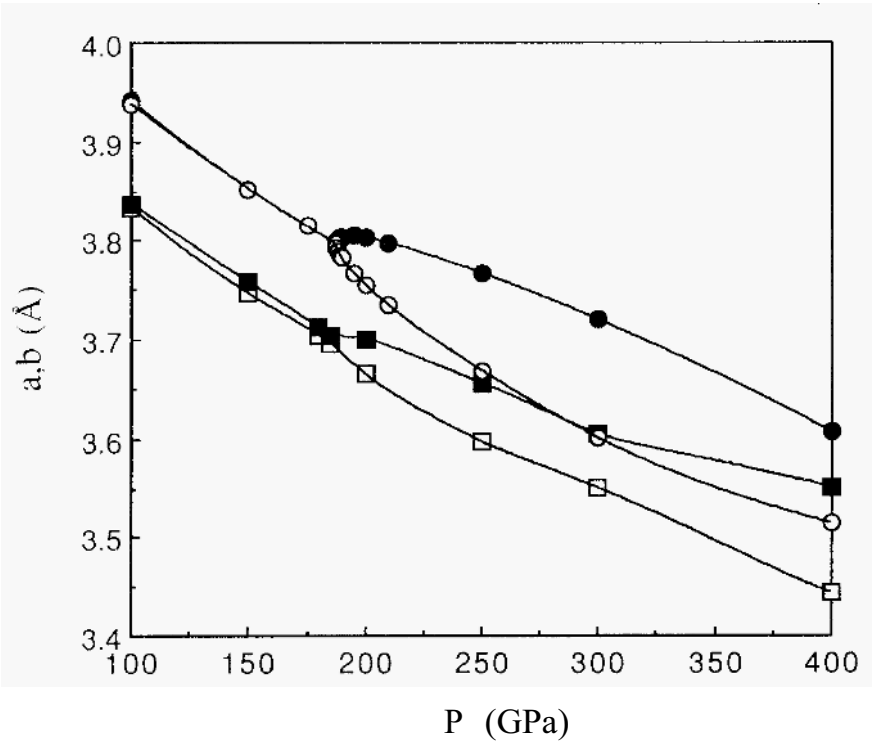

Figure 4. $CaCl_2$ *a, b* lattice parameters as a function of pressure. When $a = b$, the $CaCl_2$ structure reduces to stishovite. Square: distorted ion electron gas model; circles: TTAM model.

etry, and at 27.0 GPa for the $MgSiO_3$ stoichiometry. These results are in good agreement with extrapolations to zero temperature of experimental results. which find the spinel to perovskite phase transition to occur at 27.4 GPa for the Mg_2SiO_4 stoichiometry and at 27.7 GPa for the $MgSiO_3$ slochiometry. and also that the two-oxide assemblage is the most stable form in the pressure range 26.7 GPa to 28.0 GPa [56]. In contrast, the spherical ion results, shown in Figure 5b, are in poor agreement with the experimental extrapolations. The inclusion of covalent bonding effects improves the results by stabilizing the spinel and stishovite structures relative to the perovskite and periclase structures – the anions were shown above to be significantly more distorted in spinel and stishovite than in perovskite.

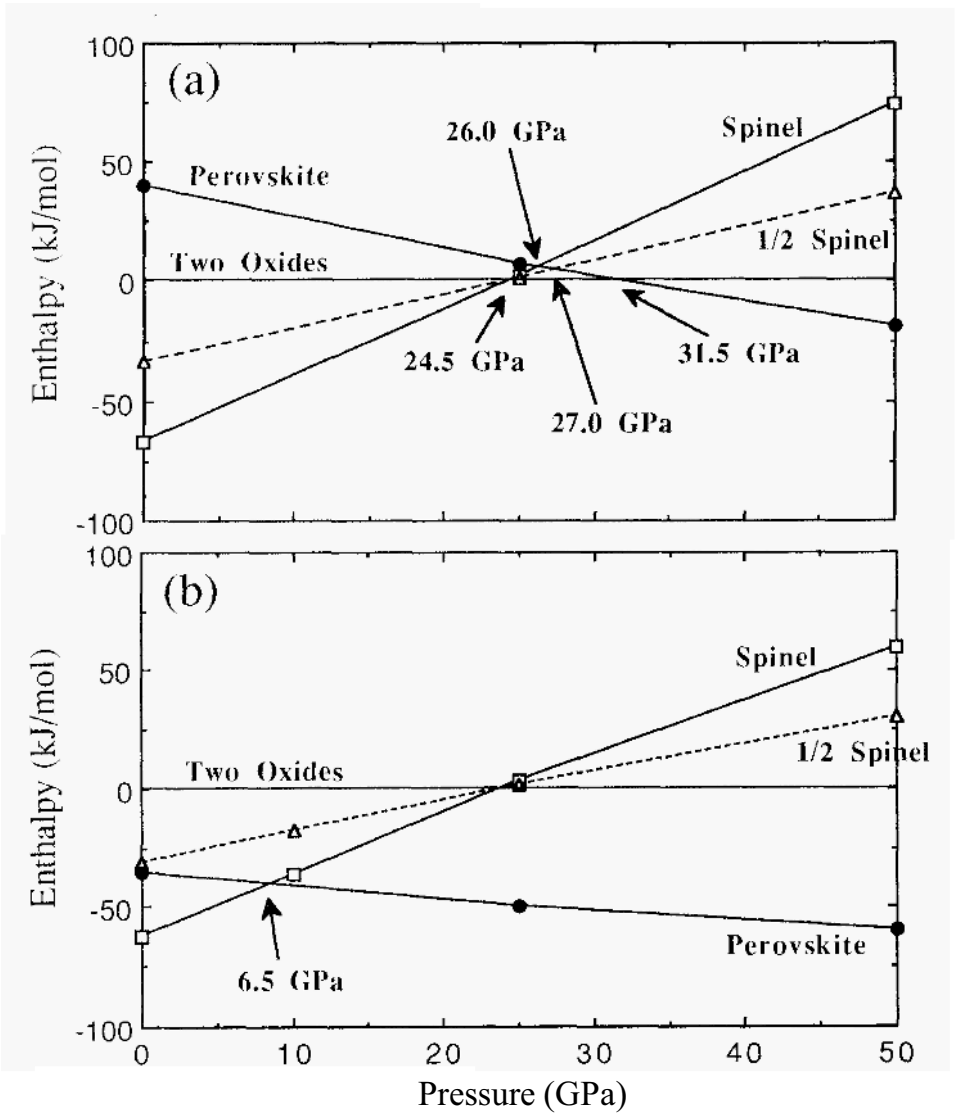

Figure 5. Enthalpies of phases in Magnesium Silicate system as a function of pressure, relative to the binary oxides (stishovite and periclase). (a) distorted ion electron gas model; (b) spherical ion electron gas model.

5. Conclusions

The inclusion of non-spherical distortions of the ions, or equivalently covalent bonding effects, in the electron gas model leads to improved results for the properties of minerals. For crystals which have open structures, the structures, energies and compressibilities calculated with the distorted ion model are in much better agreement with experiment than those calculated with spherical ion model; the improved structures are due mainly to smaller and more accurate cation-anion-cation bond angles and the improved energies are due to the stronger bonds formed when charge density moves into the bonding regions. For crystals which have close-packed structures, the structures and compressibilites are modeled well with the spherical ion model, but the energies are calculated more accurately with the distorted ion model. The distorted ion model leads to improved modeling of pressure-induced phase transitions, due to the more accurate calculation of the crystal structures, compressibilities and energies.

The effects of covalency on the quartz to stishovite phase transition in silica and the spinel to perovskite phase transition in magnesium silicates can be compared. Both of these phase transitions are from a phase based on tetra-coordinated silicon ions to a phase based on hexa-coordinated silicon ions. For the phase transition in silica, the inclusion of covalent effects reduces the transition pressure by over 15 GPa: stishovite is stabilized relative to quartz because it has more bonds, and the bonds are significantly covalent in both structures. In contrast, for the magnesium silicate phase transition, the inclusion of covalent effects increases the transition pressure by 20 GPa: although there are more bonds in perovskite than in spinel, spinel is stabilized more because the bonds are more covalent in spinel than in perovskite.

Acknowledgements

We thank Dr. Harry Hummel for many valuable discussions and the use of his program for the spherical ion calculations, and Dr. Bernard Silvi for plotting the electron density curves from his crystalline Hartree-Fock calculations. This work was supported in part by the National Science Foundation and the National Renewable Energy Laboratory.

References

1. Bukowinski, M.S.T. (1985) First principles equations of state of MgO and CaO, *Geophys. Res. Lett.* **12**,536-539.
2. Mehl, M.J., Cohen, R.E. and Krakauer, H. (1988) Linearized augmented plane wave electronic structure calculations for MgO and CaO *J. Geophys. Res.* **93**, 8009-8022.

3. Chelikowsky, J.R., King, H.E., Troullier, B., Martins, J.L. and Glinnemann, J. (1990) Structural properties of a-quartz near the amorphous transition Phys. *Rev. Lett.* **65**,3309-3312.
4. (a) Cohen, R.E. (1991) Bonding and elasticity of stishovite Sio2 at high pressure: linearized augmented plane wave calculations *Am. Miner.* **76**, 733-742.; (b) Cohen, R.E. (1992) First principles predictions of elasticity and phase transitions in high pressure SiO_2 and geophysical applications, in Y. Syono and M.H. Manghnani (eds.), *High-Pressure Research: Application to Earth and Planetary Sciences,* Terra Scientific, Tokyo, pp 425-431.
5. (a) Jolly, L-H., Silvi, B.and D'Arco Ph. (1994) Periodic Hartree-Fock study of minerals: Hexacoordinated SiO_2 and GeO_2 polymorphs *Eur. J. Mineral.* **6**, 7-16.; (b) Jolly, L-H., Silvi, B. and D'Arco Ph. (1993) Periodic Hartree-Fock investigation of the stishovite $CaCl_2$-like phase transition of silica *J. Chim. Phys.* **90**,1887-1895.
6. Keskar, N., Troullier, N., Martins, J.L. and Chelikowsky, J.R. (1991) Structural properties of SiO_2 in the stishovite structure *Phys. Rev.* **B44**, 4081-4088.
7. Sherman, D.M. (1993) Equation of state and high-pressure phase transitions of stishovite (SiO_2): ab initio (periodic hartree-fock) results *J. Geophys. Res.* **98**, 11865-11873.
8. D'Arco, Ph., Silvi, B., Roetti, C. and Orlando, R. (1991) Comparative study of spinel compounds: a pseudopotential periodic Hartree-Fock Calculation of Mg_2SiO_4, Mg_2GeO_4, Al_2MgO_4 and Ga_2MgO_4 *J. Geophys. Res.* **96**,6107-6112.
9. Silvi, B., Bouaziz, A., and D'Arco Ph., Pseudopotential periodic Hartree-Fock study of Mg_2SiO_4 polymorphs: olivine, modified spinel and spinel *Phys. Chem. Minerals* **20**,333-340.
10. Wentzcovitch, R.M., Martins, J.L. and Price, G.D. (1993) Ab initio molecular dynamics with variable cell shape: application to $MgSiO_3$ *Phys. Rev. Lett.* **70**, 3947-3950.
11. D'Arco, Ph., Sandrone, G., Dovesi, R., Orlando, R. and Saunders, V.R. (1993) A Quantum mechanical study of the perovskite structure type of $MgSiO_3$ *Phys. Chem. Minerals* **20**, 407-414.
12. Tsuneyuki, S., Tsukada, M., Aoki, H. and Matsui, Y. (1988) First principles interatomic potentials of silica applied to molecular dynamics *Phys. Rev. Lett.* **61**,869-872.; Tsuneyuki, S., Matsui, Y., Aoki, H. and Tsukada, M. (1989) New pressure induced structural transformations in silica obtained by computer simulation *Nature* **339**, 209-211.
13. van Beest, B.W.H., Kramer, G.J. and van Santen, R.A. (1990) Force fields for silica and aluminophosphates based on ab initio calculation *Phys. Rev. Lett.* **64**, 1955-1958.
14. Gordon, R.G. and Kim, Y.S. (1972) Theory for the forces between closed shell atoms and molecules *J. Chem. Phys.* **56**, 3122-3133.
15. Gilbert, T.L. (1975) Hohenberg-Kohn theorem for nonlocal external potentials *Phys. Rev.* **B12**, 2111-2120.
16. Thomas, L.H. (1927) The calculation of atomic fields *Proc. Camb. Phil. Soc.* **23**,542-548.; Fermi, E. (1927) Un metodo statistice per la determinazione di alcune proprieta dell'atomao *Rend. Accad. Lincei* **6**, 602-607.
17. Dirac, P.A.M. (1930) Note on exchange phenomena in the Thomas atom, *Proc. Camb. Phil. Soc.* **26**, 376-385.
18. Waldman, M. and Gordon, R.G. (1979) Scaled electron gas approximation for intermolecular forces *J. Chem. Phys.* **71**,1325-1329.
19. Lacks, D.J. and Gordon, R.G. (1994) Tests of non-local kinetic energy functionals *J. Chem. Phys.* **100**, 4446-4452.
20. 20. Perdew, J.P., Yue, W. (1986) Accurate and simple density functional for the electronic exchange energy: Generalized gradient approximation *Phys. Rev.* **B33**, 8800-8802.
21. Lee, H., Lee, C. and Parr, R.G. (1991) Conjoint gradient correction to the Hartree-

Fock kinetic- and exchange-energy density functionals *Phys. Rev.* **A44,** 768-771.
22. Lacks, D.J. and Gordon, R.G. (1993) Pair Interactions of Rare Gas Atoms as a Test of Exchange Energy Density Functionals in Regions of Large Density Gradients *Phys. Rev.* **A47,** 4681-4691.
23. Kim, Y.S. and Gordon, R.G. (1974) Theory of binding in ionic crystals: Application to alkali-halide and alkaline-earth dihalide crystals *Phys. Rev.* **B9,** 3548-3554.
24. Muhlhausen, C. and Gordon, R.G. (1981) Electron gas theory of ionic crystals, including many-body effects *Phys. Rev.* **B23,** 900-923; Muhlhausen, *C.* and Gordon, R.G. (1981) Density-functional theory for the energy of crystals: test of the ionic model *Phys. Rev.* **B24,** 2147-2160.
25. Boyer, L.L., Mehl, M.J., Feldman, J.L., Hardy, J.R., Flocken, J.W., Fong, C.Y. (1985) Beyond the rigid-ion approximation with spherically symmetric ions *Phys. Rev. Lett.* **54,** 1940-1943.
26. LeSar, R. and Gordon, R.G. (1982) Electron gas model for molecular crystals. Application to the alkali and alkaline earth hydroxides *Phys. Rev.* **B25,** 7221-7237.
27. Wolf, G.H. and Bukowinski, M.S.T. (1988) Variational stabilization of the ionic charge densities in the electron-gas theory of crystals: applications to MgO and CaO Phys. *Chem. Minerals,* **15,** 209 -220.
28. Lacks, D.J. and Gordon, R.G. (1993) Crystal structure calculations with distorted ions *Phys. Rev.* **B48,** 2889-2908.
29. LeSar, R. (1983) Ground- and excited-state properties of solid argon under pressure *Phys. Rev.* **B28,** 6812-6820; LeSar, R. (1988) Equation of state of dense helium *Phys. Rev. Lett.* **61,** 2121-2124.
30. Zhang, H. and Bukowinski, M.S.T. (1991) Modified potential-induced-breathing model of potentials between closed shell ions *Phys. Rev.* **B44,** 2495-2503.
31. Hummel, H.H (1993) Density functional theory of ionic solids: theory and application, Ph.D. Thesis, Harvard University.
32. Perdew, J.P., Cevary, J.A., Vosko, S.H., Jackson, K.A., Pederson, M.R., Singh, D.J., and Fiolhais, C. (1992) Atoms, molecules, solids and surfaces: applications of the generalized gradient approximation for exchange and correlation *Phys. Rev.* **B46,** 6671-6687.
33. Cohen, A.J. and Gordon, R.G. (1976) Modified electron-gas study of the stability, elastic properties, and high-pressure behavior of MgO and CaO crystals Phys. *Rev.* **B14,** 4593-4605.
34. Jeanloz, R., Ahrens, T.J., Mao, H.K., Bell, P.M. (1979) B1-B2 transition in calcium oxide from shock-wave and diamond-anvil experiments *Science* **206,** 829-830.
35. Hemley, R.J., Jackson, M.D. and Gordon, R.G. (1985) Lattice dynamics and equations of state of high-pressure mineral phases studied with electron gas theory *EOS Trans. AGU* **66,** 357.
36. Hemley, R.J. (1987) Pressure dependence of Raman spectra of SiO_2 polymorphs: α-quartz, coesite, and stishovite, in M. H. Manghnani and Y. Syono (eds.), *High-Pressure Research in Mineral Physics,* American Geophysical Union, Washington, pp. 347-359.
37. Tsuchida, Y. and Yagi, T. (1989) A new, post stishovite high pressure polymorph of silica *Nature* **340,** 217-220.
38. Hemley, R.J., Jackson, M.D. and Gordon, R.G. (1985) First,-principles theory for the equations of state of minerals at high pressures and temperatures: Application to MgO *Geophys. Res. Lett.* **12,** 247-250.
39. Cohen, R.E. (1987) Calculation ofelasticity and high pressure instabilities in corundum and stishovite with the potential induced breathing model *Geophys. Res. Lett.* **14,** 37-40.
40. Isaak, D.G., Cohen, R.E and Mehl, M.J. (1990) Calculated elastic and thermal properties of MgO at high pressures and temperatures *J. Geophys. Res.* **95,** 7055-7067.
41. Post, J.E. and Burnham, C.W. (1986) Ionic modeling of mineral structures and

energies in the electron gas approximation: TiO_2 polymorphs, quartz, forsterite, diopside *Am. Miner.,* **71**, 142-150.
42. Jackson, M.D. and Gordon, R.G. (1988) MEG investigation of low-pressure silica: Shell model for polarization *Phys. Chem. Minerals* **16**, 212-220.
43. Hummel, H.H. and Gordon, R.G. (1989) in J. Tersoff, D. Vanderbilt and V. Vitek (eds.), *Atomic Scale Calculations in Materials Science,* M.R.S Symposia Proceedings No. 141, Materials Research Society, Pittsburgh (1989).
44. Stewart,, R.F. and Spackman, M.A. (1981) Charge density distributions, in M. O'Keefe and A. Navrotsky (eds.), *Structure and Bonding in Crystals, Vol II.,* Academic Press, Orlando, pp. 279-278.
45. Lacks, D.J. and Gordon, R.G. (1993) Calculations of pressure induced phase transitions in silica *J. Geophys. Res.* 98, 22147-22155.
46. Lacks, D.J. and Gordon, R.G. (1994) Calculations of pressure induced phase transitions in mantle minerals *Phys. Chem. Minerals,* submitted.
47. Silvi, B. (1992) personal communication; Silvi, B., Allavena, M., Hannachi, Y. and D'Arco, Ph. (1992) Pseudopotential periodic Hartree-Fock study of the cristobalite phases of silica and germanium dioxide, J. Amer. Ceram. Soc. **75**, 1239-1246.
48. Glinneman, J., King, H.E., Schulz, H., Hahn T., LaPlaca, S.J. and Dacol F. (1992) Crystal structures of the low-temperature quartz-type phases of SiO_2 and GeO_2 at elevated pressure *Z. Krist.* **198**, 177-212.
49. Levien, L., Prewitt, C.T. and Weidner, D.J. (1980) Structure and elastic properties of quartz at pressure *Am. Miner.* **65**, 920-930.
50. Hazen, R.M., Finger LW, Hemley, R.J. and Mao, H.K. (1989) High pressure crystal chemistry and amorphization of α-quartz *Solid State Comm.* **72**,507-511.
51. Akimoto, S., Yagi, T. and Inoue, K. (1977) High temperature-pressure phase boundaries in silicate systems using in situ x-ray diffraction, in M. H. Manghnani and S. Akimoto (eds.), *In High-pressure Research: Applications to Geophysics,* Academic Press, New York, pp. 585-602.
52. Jamieson, J.C., Manghnani, M.H. and Ming, L.C. (1981) Crystal chemical effects on geophysical equilibrium, in M. O'Keefe and A. Navrotsky (eds.), *Structure and Bonding in Crystals, Vol II.,* Academic Press, Orlando, pp. 95-106.
53. Robie, R.A., Hemingway, B.S., and Fisher, J.R. (1979) Thermodynamic properties of minerals and related substances at 298.15 K and 1 bar (105 pascals) pressure and at higher temperatures, p. 21, Geological Survey Bulletin 1452.
54. Silvi, B., Jolly, L-H. and D'Arco, Ph. (1992) Pseudopotential periodic Hartree-Fock study of the cristobalite to stishovite phase transition *J. Mol. Struct.* **260**, 1-9.
55. Worlton, T.G. and Beyerlein, R.A. (1975) Structure and order parameters in the pressure induced continuous transition in TiO_2 *Phys. Rev.* **B12**, 1899-1907.
56. Gasparik, T. (1992) Melting experiments on the enstatite-pyrope join at 80-152 kbar *J. Geophys. Res.* **97,** 15181-15188.

This page intentionally left blank.

ADVANCES IN ELECTRON–GAS POTENTIAL MODELS: APPLICATIONS TO SOME CANDIDATE LOWER MANTLE MINERALS

M.S.T. BUKOWINSKI §, A. CHIZMESHYA†, G.H. WOLF† AND H. ZHANG§
§*Department of Geology and Geophysics, University of California at Berkeley, Berkeley, California 94 720, USA*
† *Department of Chemistry, Arizona State University, Tempe, Arizona 85287, USA*

1. Introduction

The earth's lower mantle, extending from a depth of about 670 km to the core-mantle boundary at 2890 km, is the earth's largest repository of silicate and oxide minerals. Arguments based on cosmochemical abundances and observations of near surface rocks show that minerals derived from SiO_2, MgO, FeO, Al_2O_3, and CaO make up over 99% of the mantle's mass. Reactions among these components can produce numerous phase assemblages. Fortunately, high-pressure experiments and the demands of consistency with seismologically derived density and elasticity profiles, restrict the class of likely abundant minerals. Peridotite, composed primarily of olivine, clinopyroxene, orthopyroxene and garnet dominates the upper mantle. As we enter the transition zone between 400 and 670 km, various chemical reactions and phase transformations occur that may significantly increase the number of minerals present [1]. Deeper still, pressure favors structures with efficient atomic/ionic packing and hence high coordination numbers. Model assemblages of $(Mg,Fe)SiO_3$ perovskite with some magnesiowüstite are compatible with seismic observations in the lower mantle; because of their relatively low abundance Ca and Al are commonly presumed to have negligible effect on the density and elastic properties [2, 3, 4].

The fine details of lower mantle chemical and mineral composition models remain in dispute, however. Notwithstanding the apparent adequacy of the $(Mg,Fe)SiO_3$ perovskite plus magnesiowüstite models of the lower mantle, petrological experiments on peridotite-like assemblages yield phases that contain Ca and Al [5, 6] which, barring an improbable efficient seg-

B. Silvi and P. D'Arco (eds.), Modelling of Minerals and Silicated Materials, **81-112.**

regation into the upper mantle, requires that some such phases be present in the lower mantle. Minor seismic discontinuities in the lower mantle [7, 8] may implicate additional minerals, pressure and/or temperature induced phase changes and/or changes in chemical composition. Experiments and model computations suggest that Ca and Al have low solubility in $(Mg,Fe)SiO_3$ perovskite and instead form separate Ca- and Al-rich phases [5, 9, 10, 11]. Apart from the room temperature equations of state of $(Mg,Fe)SiO_3$ and $CaSiO_3$ perovskites, and magnesiowüstite, very little is known about the high-pressure thermoelastic properties of potential lower mantle constituents. Consequently, despite some contrary claims, it is not yet possible to establish with any certainty whether the composition of the lower mantle differs from that of the upper mantle [2, 4, 12], nor is it possible to assess whether a particular model agrees quantitatively with observed radial velocity profiles, lateral velocity changes and surface gravity data.

Thus, in addition to the obvious need for more experimental data - none of which is easy to obtain - there is also ample motivation to develop theoretical and computational models of silicates and oxides that are accurate at extreme pressure and temperature conditions. Given the scarcity of data, it is difficult to develop reliable phenomenological models. Furthermore, oxides present the modeler with some fundamental difficulties: since O^{2-} ions are unstable in the gas state, their existence in condensed materials relies on the stabilizing effect of the field generated by the surrounding ions [13, 14, 15]. The consequent sensitivity of the valence electrons of O^{2-} to the structure of the material gives rise to many-body effects. This presents no difficulty to modern band structure techniques, which often yield very accurate properties of oxide crystals (*e.g.,* [16, 17, 18, 19, 20, 21, 22, 23, 24]). However, the complexity that is responsible for the success of the band structure methods also limits their application to relatively simple materials (i.e., few structural parameters and few distinct ions/atoms per cell). Electronic structure methods do not readily yield thermal and dynamic properties, except through rather complex *ab initio* molecular dynamics methods and relatively simple materials (*e.g.*, [25]). In contrast, models based on atomic/ionic interactions are very efficient: quite complex structures can be simulated and their dynamical properties can be obtained readily through lattice dynamics, Monte Carlo or molecular dynamics techniques. *Ab initio* pair potentials, derived from electron gas theory, offer the advantages of high computational speed and a usefully accurate representation of the energetics of complex materials that are otherwise very difficult to study.

Indeed, recent computations demonstrate that approximate *ab initio* electron-gas pair potential methods can generate mineral structures and thermodynamic properties that are in very good quantitative agreement

with experiment [26]. While older models based on rigid ions (ie. the MEG model) generally underestimate crystal densities, those that allow ionic charge relaxation give results that differ from data and each other by at most a few percent. The accuracy of the calculated equations of state and crystal structures often rivals those derived from first principles band structure calculations. Although calculated elastic shear constants exhibit errors as large as 20%, the many- body effects implicit in the non- rigid- ion models cause violations of the Cauchy relationships that closely parallel those observed experimentally [27, 28, 29], and their calculated temperature derivatives compare well with available data [30].

The purpose of this article is to report on some of our recent work based on electron gas potentials. We summarize the theoretical concepts in section 2. Starting with a summary of the principles that underlie all *ab initio* density functional potential models, we follow with the specific assumptions that define the Modified Potential Induced Breathing (MPIB) and Variationally Induced Breathing (VIB) models. We then give a very brief review of the methods used to generate model mineral structures and their properties, including finite temperature effects. In section 4 we present a few applications of geophysical interest. These examples serve to point out some successes as well as shortcomings of the present models. We conclude with a brief summary and discussion of possible improvements.

2. Electron Gas Potential Models

2.1. GENERAL DESCRIPTION

Electron–gas potential models start with the assumption that electrons in condensed matter are localized around well defined units which can be molecules, atoms or ions [31]. Since our aim here is to describe materials that are largely ionic, in what follows we shall refer to the interacting units as ions . The total electron density is then taken to be a superposition of the electron densities of the component ions:

$$n(\mathbf{r}) = \sum_{i=1}^{N} n_i(\mathbf{r}) \tag{1}$$

where N is the number of ions in the system, and $n_i(\mathbf{r})$ is the electron density of the i^{th} ion. The total energy of the system is given exactly by a functional of the electron density [32, 33]:

$$E[n] = E_{ee} + E_{ext} + E_{NN} + G[n] \tag{2}$$

where E[n] is the total energy, E_{ee} and E_{NN} are the electron–electron and nucleon–nucleon Coulomb energies (in Rydbergs)

$$E_{ee} = \int d\mathbf{r} \int d\mathbf{r}' \frac{n(\mathbf{r})n(\mathbf{r}')}{|\mathbf{r} - \mathbf{r}'|} \quad , \tag{3}$$

$$E_{NN} = \sum_{i \neq j} \frac{Z_i Z_j}{|\mathbf{R}_i - \mathbf{R}_j|} \quad , \tag{4}$$

where Z_i and $\mathbf{R}_i$ are the charge and position of the i^{th} nucleus, respectively. Eext is the energy contributed by any external potential V_{ext} acting on the electrons:

$$E_{ext} = \int d\mathbf{r} n(\mathbf{r}) V_{ext}(\mathbf{r}) \quad . \tag{5}$$

V_{ext} includes the Coulomb potential due to the nuclei, V+(r) $= 2\sum_i \frac{Z}{|\mathbf{r}\text{-}\mathbf{R}_i|}$ but may also contain any other potential not due to the electrons, *e.g.,* a magnetic or electric field applied to the material. $G[n]$ is a functional of the electron density that contains the quantum mechanical contributions to the energy: the kinetic, exchange and correlation energies of the electrons. Although this functional is known to exist, its exact form is not known [32]. According to the local density approximation (LDA), we may write [33]

$$G[n] = T[n] + E_{xc}[n] \tag{6}$$

where $T[n]$ is the kinetic energy functional, and $E_{xc}[n]$ is the local exchange–correlation energy of the electrons

$$T[n] = \int d\mathbf{r} n(\mathbf{r}) \epsilon_k[n(\mathbf{r})] \tag{7}$$

$$E_{xc}[n] = \int d\mathbf{r} n(\mathbf{r}) \epsilon_{xc}[n(\mathbf{r})] \tag{8}$$

where ϵ_k and ϵ_{xc} are the kinetic and exchange–correlation energies per electron, respectively. We discuss their explicit forms later.

2.2. POTENTIALS

We define an electron–gas pair potential between ions i and j as the energy of the combined pair less the sum of the isolated ion energies [31]:

$$\phi_{ij}(r) = E[n_i + n_j] - E[n_i] - E[n_j] \tag{9}$$

where r is the distance between the ions. The total energy of the material is then given by

$$U = \frac{1}{2} \sum_{i \neq j} \phi_{ij}(|\mathbf{R}_i - \mathbf{R}_j|) + \sum_i \phi_i^S \tag{10}$$

U includes a sum over ionic self energies, ϕ_i^S, that account for changes in the ionic energies arising from distortions of the site charge densities induced by changes in the material's configuration. The effect of all other ions in the material on a given ionic charge density is represented by a potential $W(\mathbf{r})$. The self–energy includes only intra–ionic interactions since interactions with other ions are accounted for in the pair potentials.

Models that include ionic distortions are much more accurate than those based on rigid ions [26]. In particular, the many–body effects introduced by the distortions are necessary to account for the observed violations of the Cauchy relations among elastic constants [27, 28]. Since the form of $W(\mathbf{r})$ is model dependent, we defer its discussion until the following section.

It is convenient to separate into the long range point Coulomb interaction between the ions, and the short range overlap contributions:

$$\phi_{ij}(r) = \frac{q_i q_j}{r} + \phi_{ij}^e + \phi_{ij}^k + \phi_{ij}^{xc} \tag{11}$$

q_i are the ionic charges, while superscripts e, k and xc indicate contributions from the electrostatic, kinetic, and exchange–correlation overlap electronic energy, respectively. The electrostatic short range potential is given exactly by

$$\begin{aligned}\phi_{ij}^e(r) &= 2\left(\frac{Z_i Z_j - q_i q_j}{r}\right) + \int d\mathbf{r}_1 \int d\mathbf{r}_2 \frac{n_i(\mathbf{r}_1) n_j(\mathbf{r}_2)}{r_{12}} \\ &- 2Z_j \int d\mathbf{r}_1 \frac{n_i(\mathbf{r}_1)}{r_{1j}} - 2Z_i \int d\mathbf{r}_2 \frac{n_j(\mathbf{r}_2)}{r_{1i}} \ .\end{aligned} \tag{12}$$

where $r_{\alpha i}$ is the distance between electron α and ion i, and $r_{\alpha\beta}$ is the distance between electrons α and β. According to equations (7) and (8) the non–electrostatic overlap potentials are

$$\phi_{ij}^{\Gamma} = \int d\mathbf{r} \Big[(n_i + n_j)\epsilon_{\Gamma}(n_i + n_j) - n_i \epsilon_{\Gamma}(n_i) - n_j \epsilon_{\Gamma}(n_j) \Big] \ , \tag{13}$$

where Γ stands for k or xc.

2.3. SPECIFIC MODELS

Practical applications require an explicit form for ϵ_k and ϵ_{xc}, and a choice of ionic electron densities $n_i(\mathbf{r})$. Early formulations of the theory used electronic charge densities derived from Hartree–Fock atomic codes. For a review of the various implementations of electron gas potentials we refer the reader to Wolf and Bukowinski [28], Gordon and LeSar [34] and Chizmeshya *et al.* [29]. In the remainder of this report we concentrate on topics relevant to applications of the VIB [28, 35] and MPIB [36] models. Both models

attempt to capture, in an approximate way, the response of ionic charge densities to changes in crystal configurations. In its original version, then called VSMEG, the VIB model also used Hartree–Fock charge densities. Our current versions of VIB and MPIB are based entirely on density functional theory. This has a number of advantages: highly converged ionic charge densities are easily and efficiently obtained, the polarizability and van der Waals interactions among ions are rigorously obtainable from LDA theory [37] and, from an esthetic perspective, it is more satisfying to have models that are based entirely on LDA theory, rather than a mix of LDA and Hartree–Fock.

2.3.1. *Charge Densities*

To obtain ionic charge densities we follow Kohn and Sham[33] and introduce single electron orbitals in terms of which $n_i(\mathbf{r}) = \sum \psi^*_{i\alpha}(\mathbf{r})\psi_{i\alpha}(\mathbf{r})$, where α denotes a specific eigenstate of the i^{th} ion, and the kinetic energy

$$T_{KS} = \int d\mathbf{r} \sum_{\alpha} \nabla\psi^*_{i\alpha}(\mathbf{r}) \cdot \nabla\psi_{i\alpha}(\mathbf{r}) \tag{14}$$

which is recognized as equation (8) with $\epsilon_k = \sum \nabla\psi^*_{i\alpha}(\mathbf{r}) \cdot \nabla\psi_{i\alpha}(\mathbf{r})$, the non–interacting–particle kinetic energy density. Application of the variational theorem to equation (2) with (3),(5),(7) and (14), including $W(\mathbf{r})$ in $V_{ext}(\mathbf{r})$, and requiring that orbital normalization be conserved, yields

$$\left[-\nabla^2 - 2\sum_i \frac{Z_i}{|\mathbf{r} - \mathbf{R}_i|} + 2\int d\mathbf{r}_1 \frac{n(\mathbf{r}_1)}{|\mathbf{r}_1 - \mathbf{r}|} + V_{xc}(\mathbf{r}) + W(\mathbf{r})\right]\psi_{i\alpha} = \epsilon_{i\alpha}\psi_{i\alpha} \tag{15}$$

with

$$V_{xc}(\mathbf{r}) = \frac{\delta E_{xc}}{\delta n} = \left(\frac{\partial(n\epsilon_{xc})}{\partial n}\right)_{n=n(\mathbf{r})} \tag{16}$$

Several useful approximations to ϵ_{xc}, or V_{xc}, have been proposed (see Jones and Gunnarson [38], for review). The fact that most of them give very similar total energies suggests that the essence of ϵ_{xc} is reasonably well known. We adopted the Hedin and Lundqvist [39] form for the potential:

$$V_{xc}[n(\mathbf{r})] = \left[1 + Bx\ln\left(1 + \frac{1}{x}\right)\right]\mu_x[n(\mathbf{r})] \tag{17}$$

where

$$\mu_x[n(\mathbf{r})] = -\frac{2}{\pi}(2\pi^2 n(\mathbf{r}))^{1/3} \tag{18}$$

is the Kohn–Sham exchange potential, $x = \frac{r_s}{A}$ and r_s is the mean electron separation given by $4\pi r_s^3 n/3 = 1$. A and B are constants determined

by approximate calculations for the interacting electron gas. We used and $A = 24.3$ and $B = 0.7679$, as suggested by Lundqvist and Lundqvist [40]. Integration (16) with (17) and (18) gives

$$\epsilon_{xc} = \left[\frac{3}{4} + Bx\left((x^3 + 1)ln(1 + \frac{1}{x}) + x(\frac{1}{2} - x) - \frac{1}{3}\right)\right]\mu_x[n] \tag{19}$$

for the exchange–correlation energy per electron. We use equation (19) to calculate the contribution of exchange and correlation to the ionic self energies and the overlap potentials.

To approximate the kinetic energy contribution to the short–range overlap potential, equations (11) and (13), we follow Gordon and Kim [31] in using the Thomas-Fermi expression for the kinetic energy of a uniform electron gas with electron density n

$$\epsilon_k[n] = \frac{3}{5}(3\pi^2 n)^{2/3} \tag{20}$$

The Thomas–Fermi expression underestimates the kinetic energy relative to Hartree–Fock and Kohn–Sham theory [41]. To reduce this discrepancy, Waldman and Gordon [41] introduced constant scaling factors that depend only on the atomic number. We use a more dynamic scaling that depends on the local charge density and is thus sensitive to the configuration of the ions, and approaches the local ionic scaling when the overlap is small:

$$\phi_{ij}^k = \int d\mathbf{r}\left[(n_i + n_j)s_{ij}\epsilon_k[n_i + n_j] - n_i s_i \epsilon_k[n_i] - n_j s_j \epsilon_k[n_j]\right] \tag{21}$$

where

$$s_i = \frac{T_{KS}[n_i]}{T_{TF}[n_i]} \tag{22}$$

and

$$s_{ij} = \frac{n_i s_i + n_j s_j}{n_i + n_j} \tag{23}$$

T_{TF} is the Thomas–Fermi kinetic energy given by equations (8) and (20).

The justification of scaling schemes ultimately lies in the accuracy of the calculations. Scaling can produce total ionic kinetic energies that agree with those obtained through Hartree–Fock or Kohn–Sham calculations, which are superior to the Thomas–Fermi model. However, there is no rigorous justification for scaling the contribution of electronic kinetic energy to interionic potentials in the manner given by equation (21). A more fundamental approach must recognize gradients in the charge density. However, more rigorous corrections, including generalized gradient methods, vitiate the simplicity of the electron–gas models without a commensurate improvement

in calculated properties [42, 43, 44]. We therefore adopt a flexible attitude towards scaling and do not always scale every ion's kinetic energy.

2.3.2. *Stabilizing Potentials*

It remains to specify $W(\mathbf{r})$. As stated earlier, $W(\mathbf{r})$ represents the interaction of an ion's electrons with the rest of the material. The most important contribution to $W(\mathbf{r})$ in ionic materials is the long range Coulomb potential. Around an anion site such as O^{2-}, this potential has the form of an attractive well that helps to contract, and hence stabilize, the valence electrons. In the SSMEG model [45, 461, and the PIB model [47, 27], $W(\mathbf{r})$ is approximated by a Watson shell with a surface charge Q_w equal to the negative of the charge of the ion at its center, and a radius R_w chosen such that the constant potential inside the sphere, Q_w/R_w, equals the site Coulomb potential. Total charge densities obtained from ionic densities thus stabilized closely approximate self- consistent charge densities derived from band structure calculations [21]. One might expect further improvements on allowing the ionic charge densities to relax so as to minimize the total energy. Minimization of the energy with respect to the Watson shell radius is a simple step in that direction [45]. Wolf and Bukowinski [28] implemented this idea in the VSMEG model. Applications to MgO and CaO showed that, provided that careful optimization of the Hartree- Fock ionic wave functions are performed for each structure, the method gives better agreement with experimental equations of state and elastic constants. However, the calculated compressibilities were underestimated by about 10–15%.

2.3.3. *MPIB and VIB models*

The MPIB and VIB [35] models attempt to improve the accuracy of the earlier models and to overcome some of the difficulties associated with the use of Hartree–Fock wave functions. We have already stated some of the advantages of using the density functional approach to obtain ionic wavefunctions; they were amply demonstrated by the PIB model which replaced the Hartree–Fock equation with a density functional implementation of the Dirac equation [21]. The MPIB is so called because it also adopts the density functional approach to obtain ionic charge densities (specifically a non–relativistic version derived from the Herman–Skillman [48],but replaces the potential inside the Watson shell with the spherical average of the potential due to the rest of the material, $W_s(r)$ [36]:

$$W_s(r) = \left\langle W_c(\mathbf{r}) + W_{xc}(\mathbf{r}) \right\rangle \tag{24}$$

where

$$W_c(\mathbf{r}) = 2 \int d\mathbf{r}' \sum_{i \neq 0} \frac{Z_i \delta(|\mathbf{r}' - \mathbf{R}_i|) - n_i(|\mathbf{r}' - \mathbf{R}_i|)}{|\mathbf{r} - \mathbf{r}'|} \tag{25}$$

is the Coulomb potential due to all ions except the one at $r = 0 (i = 0)$, and

$$W_{xc}(\mathbf{r}) = V_{xc}[n(\mathbf{r})] - V_{xc}[n_0(r)] \tag{26}$$

is an approximation to the exchange potential contributed by charge overlap from other ions. <...> indicates spherical averaging around $r = 0$.

The potential outside the shell retains the electrostatic, form of the Watson shell. However, the charge on the shell, Q_s, is that of the local ion's electrons found outside a sphere centered on it and with radius equal to that at which the spherically averaged total crystal potential is maximum, this being taken as a rough measure of the extent of the "sphere of influence" of the ion. The potential outside the shell is then Q_s/r, and the radius of the shell, R_s, is chosen such that this potential is continuous with $W_s(R_s)$. Calculations are started with ionic charge densities stabilized by Watson spheres, and are then iterated until the ionic charge densities satisfy a self–consistency criterion [36]. No scaling is applied to the kinetic energy functionals in the ionic interaction terms.

The MPIB model gives very accurate equations of state, binding energies and phase transformation pressures for alkali–halides and alkaline–earth oxides [36]. It appears to he the only electron gas potential model to give a good account of the B1 *and* B2 phases of CaO. We show in section 4 that it also gives excellent results when applied to more complex minerals. However, this success is attained at a considerable increase in computational complexity. Furthermore, there is no simple way to implement lattice dynamics with MPIB potentials.

The VIB model (called MVIB by Zhang, [35]), which differs from the VSMEG model only in that is uses equation (15) in place of the Hartree - Fock equation to obtain charge densities, gives up some of the accuracy of the MPIB model, but retains much of the simplicity of earlier models for both static and dynamic calculations. It too uses a Watson shell to approx - imate the effect of the crystal on ionic charge densities, but R_w is chosen to minimize the total energy. Variation of R_w allows an approximate relaxation of the ionic wave functions in response to changes in crystal configuration. For a fixed lattice, the overlap energy decreases with contraction of the charge densities, whereas self energies increase. This tradeoff produces an optimal value of R_w at which the total energy is a minimum. The relaxation also introduces coupling between atomic displacements and charge density breathing, which in turn yields many - body effects in both static and dynamic properties. A detailed discussion of the VIB model, and its application to the calculation of static lattice energies and lattice dynamics is given by Clizmeshya. *et al.* [29].

3. Calculation of Mineral Structures and Properties

We obtain mineral structures and equations of state by minimizing the Gibbs free energy with respect to structural parameters and, in the case of VIB, the Watson shell radius:

$$G(T,P) = \min_{\mathbf{R}}\left[\min_{\zeta}[\Phi(\mathbf{R};\zeta)] + G_{th}(\mathbf{R},T;\zeta_{ad}) + PV(\mathbf{R})\right] . \quad (27)$$

where $E(\mathrm{R}, \zeta)$ is the internal static energy as given by equation (2), except that here we make explicit its dependence on atomic coordinates **R** and, in the case of VIB, the set of Watson sphere radii ζ . ζ_{ad} is the set of radii that minimizes $E(\mathbf{R},\zeta)$. $G_{\mathrm{th}}(\mathbf{R}, T; \zeta_{ad})$ is the contribution of the quasiharmonic lattice vibrations to the free energy. In MPIB calculations this is approximated according to a Debye model with parameters derived from the static equation of state [49]. In VIB calculations it is obtained from the calculated phonon spectrum as prescribed by statistical mechanics:

$$G_{th}(\mathbf{R},T;\zeta_{ad}) = \sum_{i}\left[\frac{1}{2}\hbar\omega_i + k_BTln(1-e^{-\hbar\omega_i/k_BT})\right] \quad (28)$$

kB is Boltzmann's constant and $\mathrm{w_i}$ is the frequency of the i^{th} quasiharmonic mode corresponding to structure **R** and shell radii ζ_{ad}. Details of the dynamical matrix used to compute the ω_i are given in Chizmeshya *et al.* [29]. The primary difference between the VIB and PIB implementations of lattice dynamics (LD) is that the energy of the equilibrium static lattice on which the harmonic expansion is based, is optimized with respect to both structural and breathing degrees of freedom. This leads to a simplification of the equations of motion in the VIB treatment and "shell–model"–like dynamical equations for the atomic displacements *u:*

$$-\ddot{u} = M^{-1}\left[D^{RR} - D^{R\zeta}(D^{\zeta\zeta})^{-1}D^{\zeta R}\right]u . \quad (29)$$

The first term in the square brackets is the usual "rigid–ion" dynamical matrix while the second term is the VIB correction that accounts for the coupling between ionic positions and the Watson sphere radii [29]. Implicit in the derivation of this expression is an adiabatic constraint on the breathing degrees of freedom. In practice this constraint is enforced by minimizing the static crystal energy, for a fixed set of atomic positions, with respect to the breathing parameters. The dynamical matrix in the preceding expression is then diagonalized and the resulting phonon spectrum is populated using a Boltzmann distribution. An estimate of the thermal free energy is thus obtained and used to contruct the Gibbs free energy for a fixed P and

T, as given by equation (27). Using this procedure we obtain directly the $V(P)$ equation of state, an "athermal" phonon spectrum, and elastic constants. The only input to the computational procedure is the set of nuclear charges and lattice structure information.

Other thermodynamic parameters like thermal expansivity and compressibility follow directly from standard relationships (e.g., [50]. Elastic constants are readily calculated from the acoustic phonon branches of the VIB model (e.g., Chizmeshya, *et al.,* [29]). MPIB elastic constants have not yet been calculated.

4. Sample Applications

As illustrations, we present results from calculations on a few silicates and oxides selected from those discussed in the introduction. Our intent here is to illustrate some of the strenghts and weaknesses of the VIB and MPIB models. We do not attempt to present complete modeling results for any given material. Since our primary interest is the reliable simulation of high pressure properties, we mostly limit the examples to those properties for which there are some relevant high pressure data.

Unless otherwise noted, all calculations are done with identical functionals. In particular, in VIB and PIB calculations, only the oxygen Thomas-Fermi kinetic energy density was scaled according to equation (22). For cations, the scaling parameter is set equal to 1. Our experience indicates that full scaling tends to give anion-cation interactions that are too repulsive. Being an ad–hoc feature of the calculations it is not very satisfying, but it does seem to yield the most accurate equations of state in most cases. As already noted, no scaling is ever used in the MPIB model.

4.1. MgO AND CaO

MgO and CaO provide a convenient platform for the testing of models. Their simple structures allow easy energy minimizations for even the most numerically intensive methods, and yet the many–body effects introduced by oxygen renders the task of simulating their properties rather nontrivial. Electron–gas models based on rigid ions give equations of state that are at best semiquantitative in their accuracy [51, 28]. Until recently, full band structure calculations [18, 21], or empirical models that incorporate many–body effects [14, 15], were necessary to accurately reproduce the known equations of state of alkaline–earth oxides in both B1 and B2 structures. *Ab initio* electron gas models with deformable ions have changed all that.

Figures 1a and 1b show calculated and experimental equations of state of MgO. MgO is an exception to the rule that oxygen–only scaling of the kinetic energy works best for the VIB model. As figure 1a shows, the

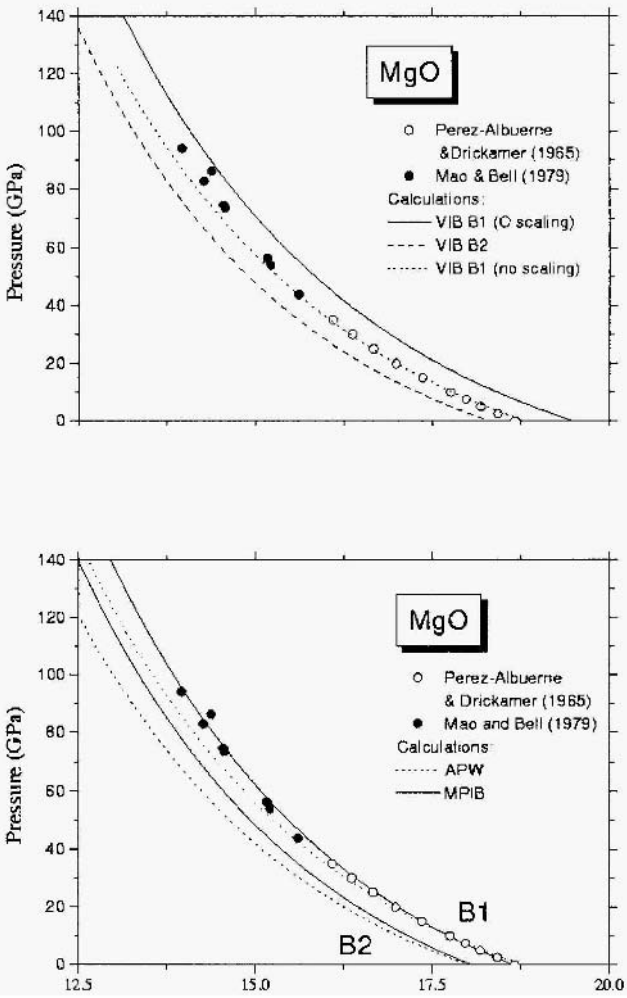

Figure 1. a) MgO equation of state. VIB model calculations; the calculated B1 equation of state without scaling is from Chizmeshya *et al.* [29]. The other calculations include oxygen scaling in the kinetic energy density. b) MPIB room temperature equation of state compared to date and a band structure derived equation of state (APW).

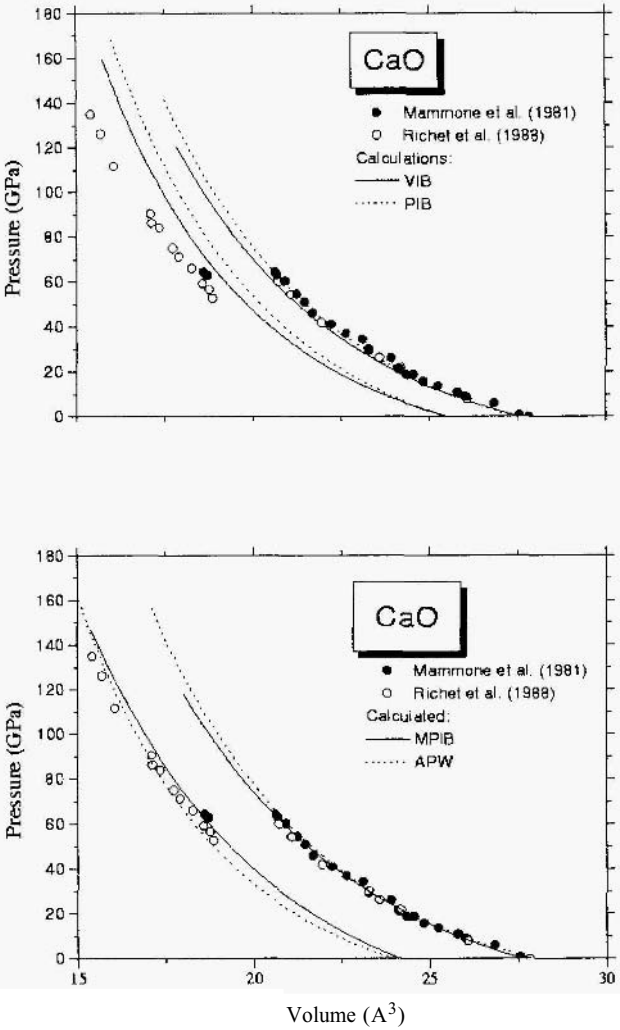

Figure 2. CaO equation of state. a) VIB and PIB calculations with **O** scaling in kinetic energy density. Both methods underestimate the density change associated with the B1− B2 phase transformation. b) The MPIB method compares with data somewhat better than the APW calculation [18]. MPIB predicts a phase transformation at 61 GPa, while APW predicts about 30 GPa.

B1 equation of state without any scaling is very accurate, while oxygen–only scaling gives densities that are in error by as much as 4%. Figure 1b compares the MPIB and APW equations of state with the same data. Both calculations give almost identical densities at zero pressure, but have different compressibilities. Although the MPIB equation of state for B1 MgO appears to agree better with the data, its zero pressure isothermal bulk modulus is 180 GPa, compared to the observed 160±2 GPa [52] and the APW value of 155± 5. Nevertheless, in terms of the whole equation of state, it can be said that the MPIB densities are competitive with those obtained from the band structure calculation.

The predicted B1–B2 transformation pressures are 500 GPa and 580 GPa with the VIR and MPIB methods, respectively. These values agree closely with previous estimates [27, 14]. We note that no phase transformation has been observed in MgO up to the highest pressures attempted [53].

CaO has proven to be a difficult challenge for electron gas models. Figures 2a and 2b compare equation of state data with several theoretical curves. There is a pressure induced phase transformation from the B1 to the B2 structure at approximately 60 GPa, with a density decrease of about 10% [54, 55]. As shown in figure 2a, neither the VIB or PIB model accurately reproduces both phases. We stress that the PIB calculation was carried out with the exact same functionals as the VIB calculations, including identical scaling of the kinetic energy. Changing the kinetic, energy scaling shifts the equations of state without significantly affecting the B1–B2 density difference, which remains close to 7%, in agreement with an earlier PIB calculation that included no scaling [27]. Only the MPIB method is able to reproduce both equations of state (figure 2b). It yields a transformation pressure of 61 GPa with a density decrease of 10%, in excellent agreement with data. It gives equally satisfying results for SrO and alkali halides [36]. The APW equation of state is the most accurate of those derived from hand structure calculations 55]. However, its predicted transition pressure is about 30 GPa [18], and the B1-B2 density difference is somewhat overestimated.

4.2. Al_2O_3

The structure of Al_2O_3 is considerably more complicated than that of MgO and CaO. Corundum is the equilibrium phase of Al_2O_3 at ambient conditions. The symmetry of this structure is $R\bar{3}c$; it has 6 formula units in the unit cell and four independent structural parameters. Although no other phase of Al_2O_3 has ever been observed, several structures are possible at high pressure conditions. Of these, only the perovskite (Pnma)

and Rh_2O_3(II) (Pbcn) structures appear to have low enough energies at geologically interesting pressures [57]. First principles electronic structure calculations with full optimization of these crystal structures make heavy demands on computer resources and may be impractical (e.g., Marton and Cohen [58]. However, such optimizations are well within the capabilities of electron gas theories [59, 60, 57, 61, 62]. With nothing more than desktop workstations, fully optimized structures may be obtained that agree quite closely with available data.

Earlier electron–gas calculations suggested that corundum should transform to the Rh_2O_3(II) structure somewhere between 6 and 60 GPa [57]. More recently, Marton and Cohen [58] used the LAPW band structure approach to predict that this transformation should occur at around 91 GPa, in agreement with an early VIB calculation [11]. This agreement is probably fortuitous, however. The VIB calculation used a somewhat crude form of kinetic energy scaling, while the LAPW calculations did not optimize the energy with respect to structural parameters, but instead used a scaled PIB structure (so as to agree with the experimental density) for the corundum calculation and the actual PIB structure for the Rh2O3(II) phase [58].

TABLE 1. Equation of state parameters for α–Al_2O_3. Experimental values of K_0 and K_0' were obtained with a third order finite strain fit to the combined data of Finger and Hazen [65] and Richet *et al.* [55, 56].

	V_0 (Å^3)	K_0(GPa)	K_0'
VIB	42.42	263	4.24
MPIB	42.03	286	3.85
data	42.2 ± 0.1	282 ± 23	3.83 ± 1.06

Recent VIB and MPIB model calculations suggest that the transformation from corundum to the Rh_2O_3(II) structure occurs at a higher pressure [63]. Figures 3a and 3b show calculated VIB and MPIB static equations of state, respectively, as well as the measured equation of state for corundum. As before, the VIB calculation included O kinetic energy scaling only. The MPIB equation of state for corundum is more accurate, since addition of zero point vibrations and thermal contributions would bring it into virtual coincidence with data, while the same correction would obviously yield VIB volumes that slightly exceed the experimental ones. However, both equations of state compare favorably to those obtained with band structure calculations [58]. Some calculated equation of state parameters for corundum are compared with data in Table 1. Experimental values of K_O and K_O' were obtained with a third order finite strain fit to the combined data

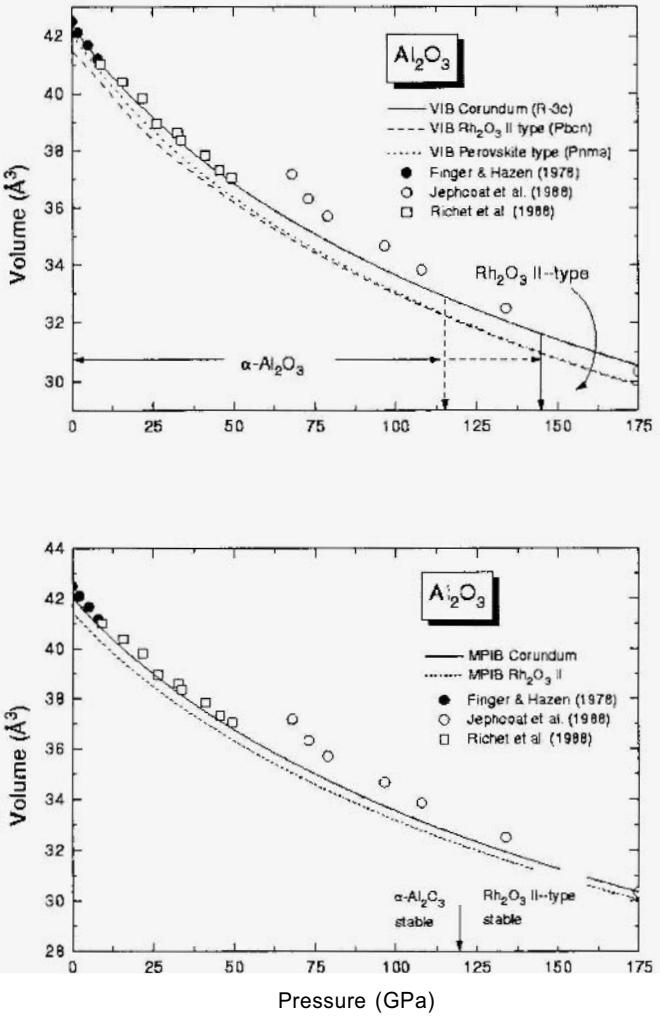

Figure 3. Equation of state data for Al_2O_3 and theoretical predictions for possible high pressure phases. See text for details. Jephcoat *et al.* data [76?] are anomalous and are shown only for completeness. a) MVIB predicts that corundum transforms to the Rh_2O_3 (II) structure at a pressure between the two vertical arrows. The perovskite phase is predicted to be thermodynamically unstable throughout the earth's lower mantle. b) MPIB calculations also indicate a phase transformation to the Rh_2O_3 (II) structure. A complete equation of state for the perovskite structure was not carried out, but perovskite was found to be unstable relative to the other phases within pressures of interest.

TABLE 2. Structural parameters of α–Al_2O_3. Experimental data is from Finger and Hazen [65].

	a(Å)	c/a	z(Al)	x(O)
VIB	4.7642	2.71	0.357	0.306
MPIB	4.7600	2.70	0.357	0.304
data	4.7607	2.73	0.352	0.306

of Finger and Hazen [64] and Richet [55, 56]. As shown in Table 2, the calculated structures also agree with data very nicely.

Table 3 summarizes predicted equation of state parameters for the perovskite and Rh_2O_3(II) phases. These phases are predicted to be only slightly denser than corundum, a result that is consistent with the earlier determinations [57, 58] and may account for the lack of unambiguous experimental evidence for any phase transformations.

TABLE 3. Calculated equation of state parameters for Rh_2O_3(II) and perovskite phases of Al_2O_3. ΔV_{trans} is the volume change at the transition pressure.

	V_0(Å^3)	K_0(GPa)	K_0'	ΔV_{trans} (%)
Pnma(VIB)	42.06	256	4.03	
Rh_2O_3(II) (VIB)	41.51	278	3.91	2.2
Rh_2O_3(II) (MPIB)	41.44	292	3.87	1.0

Also shown in figure 3a and 3b are the estimated pressures at which the α–Al_2O_3 to Rh_2O_3(II) phase transformation takes place. The pressures were determined by comparing Gibbs free energies for the static lattices. Since the choice of electron kinetic energy scaling in the VIB model is influenced by phenomenological considerations, we calculated the phase transformation pressure for the extreme cases of no scaling and full scaling, in addition to O-only scaling. This yields pressures in the range 112-148 GPA (see figure 3a). The MPIB method yields 120 GPa for the transformation pressure (figure 3b). The consistency of these results and the mounting evidence that the MPIB method yields accurate equations of state and phase transformation pressures [11, 61], lead us to believe that any pressure–induced change in the crystallographic structure of Al_2O_3 is likely to occur well above 100 GPa. However, given the sensitivity of phase transformation pressures to very small energy changes, it is unwise to give these predic-

tions much weight in analyses of mantle mineralogy, for example. Rather, we consider the value of these predictions to reside in their potential verification by future experiments, and consequent objective validation of the models. We note in passing that we found the perovskite phase of Al_2O_3 not to be thermodynamically stable below pressures of at least 400 GPa.

4.3. $(Mg_{1-x}Ca_x)SiO_3$ PEROVSKITE–LIKE MINERALS

$MgSiO_3$ and $CaSiO_3$ perovskites offer a sensitive test of the accuracy of the VIB and MPIB models. All electron gas models appear to give the correct structures: cubic $CaSiO_3$ and orthorhombic $MgSiO_3$ [68, 65, 69, 60]. Figures 4a and 4b show calculated equations of state for $CaSiO_3$ and $MgSiO_3$ perovskites. While the rigid–ion MEG calculation underestimates the density of $MgSiO_3$, models that allow ions to breathe are in very satisfactory agreement with data and band structure methods. VIB and MPIB yield accurate $CaSiO_3$ equations of state. The predicted ambient bulk moduli are 292 GPa and 300 GPa for the VIB and MPIB models, respectively. Experimental values range from 281 to 325 GPa [70, 10, 71]. One of the remaining unresolved issues in our understanding of $MgSiO_3$ concerns the stability of the orthorhombic (Pbnm) phase at high temperatures. It has been suggested, on the basis of theoretical work with rigid ionic models [68] that ortho-$MgSiO_3$ approaches the cubic structure at high temperature. Molecular dynamics simulations with parametric potentials exhibit similar behavior [72]. Recent experimental work (Meade *et al.,* [73]) seems to lend some support to this notion. Naturally any conclusion about the phase stability of $MgSiO_3$ has obvious geophysical significance since it is the most prevalent mantle mineral.

The resolution of the stability question has been addressed theoretically in essentially two ways. One approach is to carry out elaborate first principles band structure calculations for the equilibrium orthorhombic phase and the constrained cubic phase. Although the effects of thermal pressure are neglected, the underlying static lattice energy surface can be accurately charted, and the total energies of the phases compared [81, 23, 75]. The magnitude of the calculated energy barriers can then be used to estimate the relative stability of various phases. A potentially more realistic picture might emerge upon examination of the dynamic stability of the lattice within a first principles context. It is therefore of interest to examine the question of stability from both perspectives but on the same theoretical footing. Here we describe the results of VIB calculations on $MgSiO_3$ perovskite in which the effects of thermal pressure are consistently incorporated in the description *via* quasi-harmonic lattice dynamics [29]. In figure 5 we compare our thermal equations of state with available data. As can

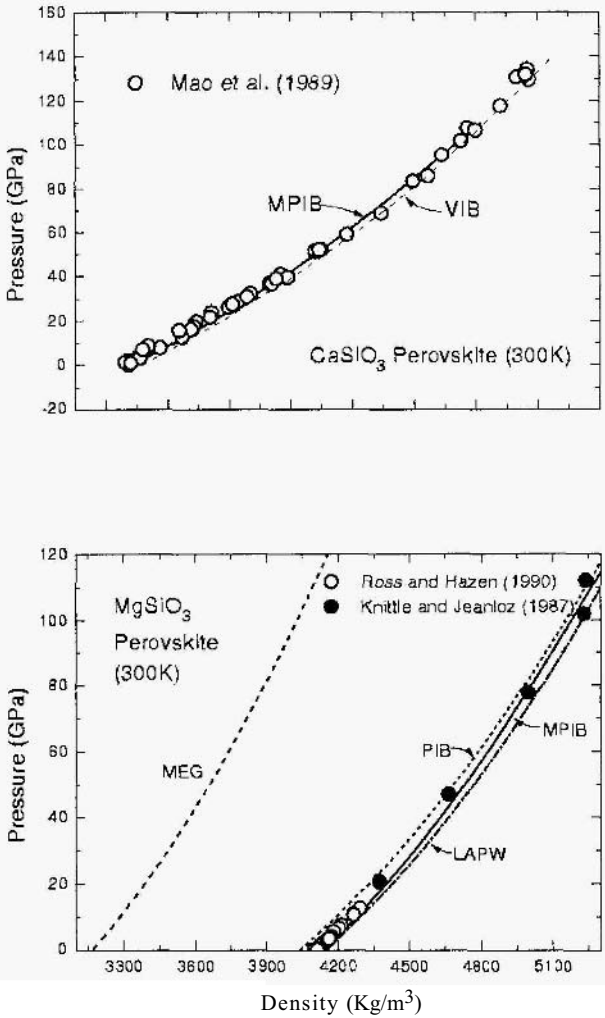

Figure 4. Equation of state for silicate perovskites. a) Both VIB and MPIB models give a good account of the compressibility and density of $CaSiO_3$ perovskite, which is predicted to be cubic, in accord with data. b) Calculated $MgSiO_3$ equations of state compared with data. The MEG calculation [66] used rigid ions; it gave poor absolute densities but excellent compressibility and thermal expansivity. The breathing ion methods (MPIB and PIB) fare much better. R&H and K&J stand for Ross and Hazen [67] and Knittle and Jenaloz [68], respectively. LAPW calculation from Stixrude and Cohen [23].

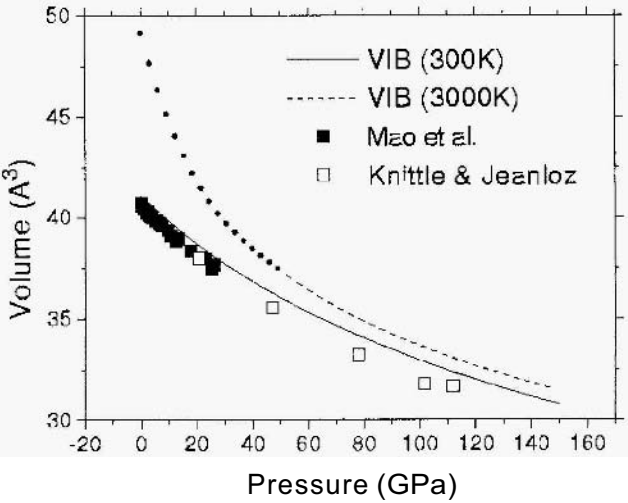

Figure 5. Thermal VIB equation of state for $MgSiO_3$ perovskite. The dotted line in the 3000K isotherm indicates that the structure is dynamically unstable; see text for details.

be seen from the plot, VIB somewhat overestimates the volume of $MgSiO_3$ perovskite. Also shown in this figure is the equation of state at 3000K, which exhibits the expected volume expansion at high temperature over the calculated pressure range. The high–T equation of state was generated by reducing the pressure from 150 GPa and studying the lattice stability at each step. At 50 GPa a zone center soft mode was detected signaling a dynamic instability. Below this pressure we continued to calculate the thermal free energy by folding the modulus of the imaginary frequencies back into the frequency integrals. The state points below 50 GPa (indicated by bold dots) are therefore physically meaningless but provide a useful indication of the thermal instability.

We also carried out a suite of lattice dynamics calculations as a function of temperature, at ambient pressure and 50 GPa, in order to explore thermal expansion and the temperature dependence of the stability field. Our preliminary results for the volume expansion (normalized to the volume at room temperature) are shown in figure 6. Also plotted in this figure are the single crystal data of Ross and Hazen [76] and Knittle *et al.* [77]. The calculated expansivity follows the data closely, and thus inspires some confidence

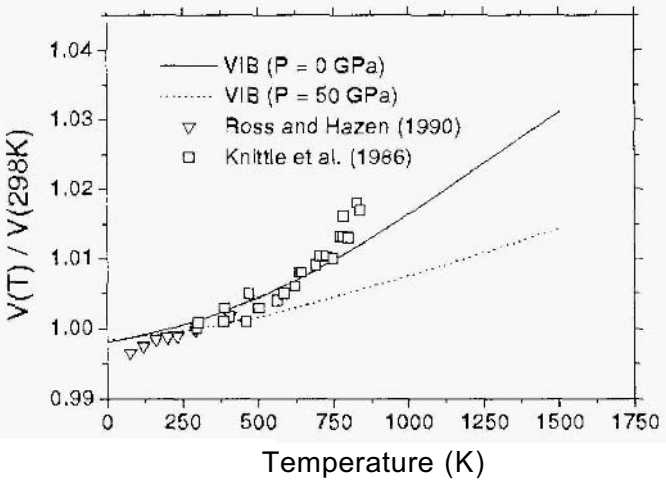

Figure 6. Thermal expansivity data and calculations for $MgSiO_3$ perovskite. See text for details.

in the quasi-harmonic VIB description. The most significant discrepancies seem to occur below 200K — a regime in which the thermal data exhibits a dubious trend toward smaller volume, and with a somewhat unphysical curvature. The dashed line in the figure illustrates the thermal expansion at 50 GPa, also obtained from quasi-harmonic lattice dynamics. As expected, the thermal expansivity is substantially reduced by the application of pressure. Our results are also consistent with the earlier calculations of Wolf and Bukowinski [68], who used a rigid ion MEG potential with a thermal pressure prescription identical to the one described above.

In order to make contact with existing work, we have also performed static lattice calculations in the constrained cubic and the fully relaxed orthorhombic structures. We find that the static energy of cubic perovskite exceeds that of orthorhombic perovskite by 0.017 Hartrees per formula unit at ambient pressure. This value is similar to that found by Hemley *et al.* [69] with a different electron gas model. Both estimates are roughly three times smaller than those based on independent *ab initio* electronic structure calculations, all of which give an energy difference of about 0.05 Hartrees [23, 81, 75]. Evidently, the electron gas theories underestimate the energy

needed to rotate the SiO_6 octahedra towards a cubic structure.

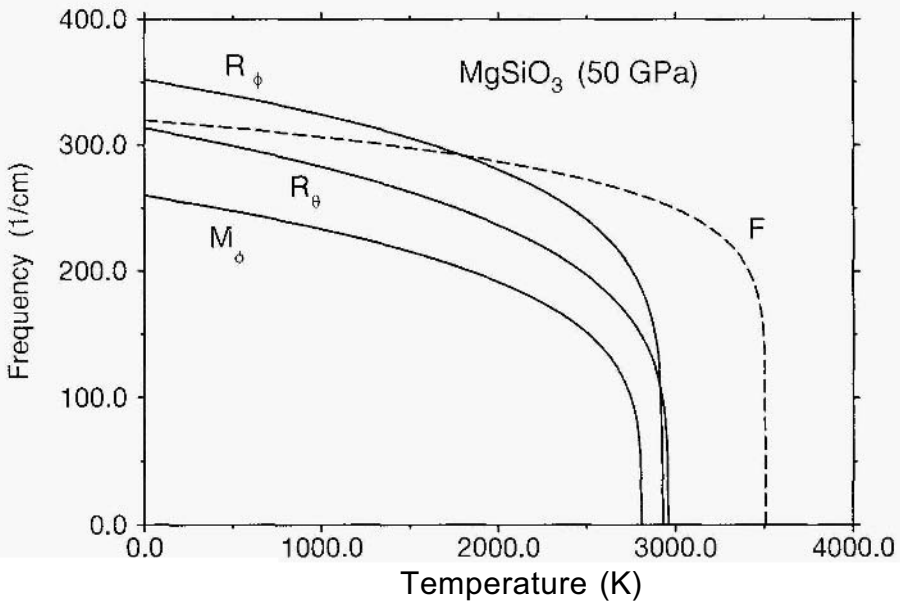

Figure 7. $MgSiO_3$ perovskite soft modes, according to VIB. The plots were obtained by fitting the phonon frequencies to a Landau–type function.

The orthorhombic structure of $MgSiO_3$ arises from a deep well in the energy surface generated by rotations of rigid SiO_6 octahedra corresponding to the M and R vibrational modes in the cubic structure [23]. We have examined the effect of temperature on the zone center modes of the orthorhombic lattice that derive from the M and R cubic modes by folding of the Brillouin zone [68]. For simplicity we denote these branches by M_ϕ, R_ϕ and R_θ. The results of our VIB calculation are summarized in figure 7 which clearly illustrates the soft mode behavior at 50 GPa as a function of temperature. The dashed curve (labeled with an F) represents the lowest lying ferroic mode. The displacement pattern associated with this latter branch involves out-of-phase cation motion. The in–phase counterpart to this branch (not shown for clarity) is observed at a slightly higher frequency and exhibits the same temperature dependence. At ambient pressure we find that the modes described in figure 7 exhibit a qualitatively similar behavior, but with the M_ϕ condensing out at 1500K. The critical temperatures obtained from the soft–mode behavior scale roughly by a factor of two in going from ambient pressure to 50 GPa.

An examination of the structural parameters near these critical (P,T) points reveals a strong tendency toward cubic symmetry. In particular, the internal distortions tend to decrease (relative to their values at P=0 and T=300K) and the lattice parameter ratios and approach cubic ratios (figure 8). It shouald be emphasized that a tetragonal distortion originating from a softening of the F mode in figure 7 cannot be excluded on the basis of our calculations. We have applied our procedure to *bona fide* ferroelectric compounds ($BaTiO_3$, $SrTiO_3$) and find that VIB typically overestimates the ferroic mode frequencies by a few hundred wave numbers. This is not surprising in view of the fact that polarization effects and non–spherical distortion effects have not been incorporated in the present formalism. The implications for $MgSiO_3$ are that the ferroic mode frequencies are also overestimated. In a recent study we have shown, *via* lattice dynamics and molecular dynamics, that the ferroic mode plays a central role in initiating the sequence of transitions leading to an amorphous state [78]. Nevertheless, within the context of the present discussion, the important point is that the VIB lattice dynamics provides an upper bound on the critical temperatures for ferroelectric transitions.

Since the phonon frequencies were derived from the quasiharmonic approximation, the critical temperatures for the soft modes are almost certainly underestimated. Hence, at zero pressure, the VIR critical temperature is larger than 1500K, and might be two to three times larger for an energy surface that is more consistent with the electronic structure calculations. This result supports Stixrude and Cohen's contention that the Pbnm structure of $MgSiO_3$ is very stable.

Encouraged by the reliability of the MPIB model, Zhang and Bukowinski[61] used it to estimate the properties of solid solutions of the type $(Mg_{1-x}Ca_x)SiO_3$. As described in that paper, while some experimental evidence suggests that $MgSiO_3$ and $CaSiO_3$ are essentially immiscible at high pressures, other data indicate the presence of a perovskite phase with diopsidic composition, that is $(Mg,Ca)SiO_3$. Zhang and Bukowinski [61] found two perovskite–like structures with diopsidic composition. Both structures are shown in figure 9. In one structure, space group symmetry $Pmn2_1$, the Mg and Ca. ions are regularly distributed in distorted NaCl like manner. The other structure, $Pmc2_1$, has Mg and Ca ions in alternating planes perpendicular to the c axis. However, neither structure is found to be thermodynamically stable relative to a mechanical mixture of orthorhombic $MgSiO_3$ and cubic $CaSiO_3$, suggesting that the phases are immiscible. The miscibility at finite temperatures and arbitrary concentrations of Ca was estimated with an averaged atom model based on work by Ottonello [79]. Averaged atom potentials were constructed by first generating a concentration weighed charge density from those of the Mg and Ca ions. Interactions

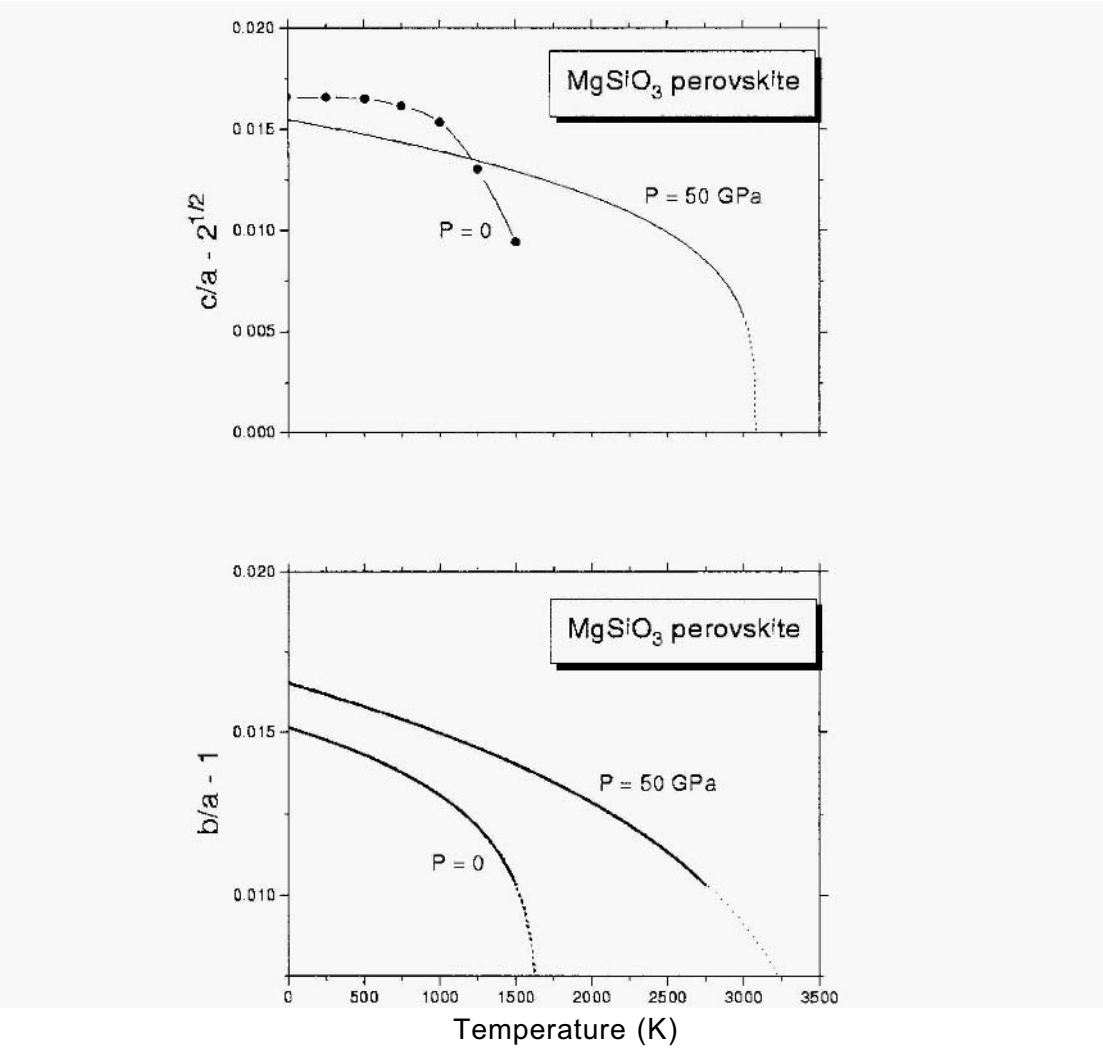

Figure 8. Pressure and temperature dependence of the deformation of $MgSiO_3$ perovskite, as measured by lattice constant rations. a) c/a relative to its cubic value,2. b) b/a relative to its cubic value, 1. The solid lines are Landan–type fits; dots indicate extrapolation.

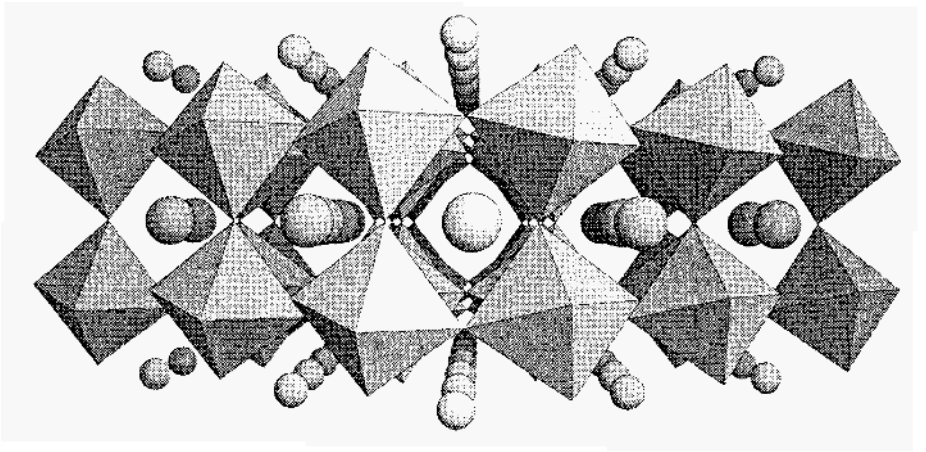

(a)

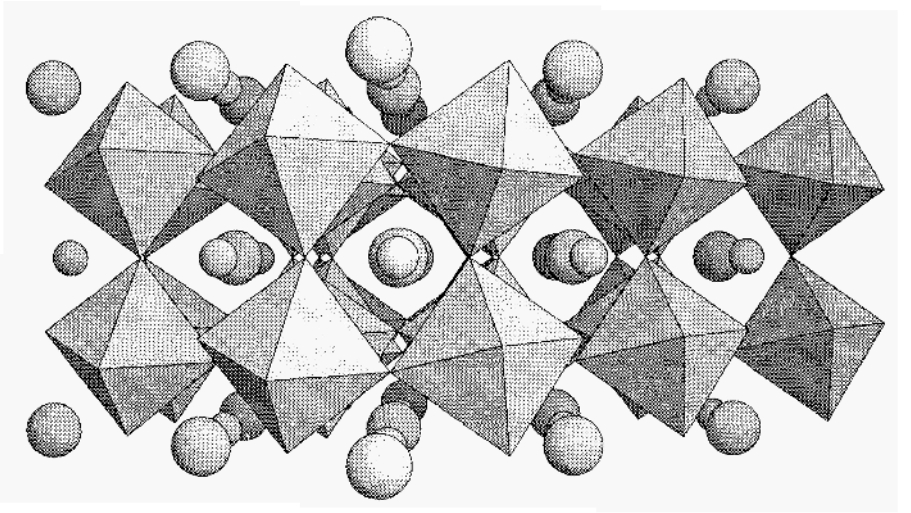

(b)

Figure 9. Structures of two ordered perovskite–like polymorphs of $MgCaSi_2O_3$. Small and large spheres represent Mg and Ca, respectively. The polygons are SiO_6 octahedra. a) Lattice symmetry $Pmc2_1$. b) Lattice symmetry $Pmn2_1$.

and self–energies were then obtained with the MPIB procedure. The mixing entropy was taken as that of a completely random distribution of the cations. Figure 10 shows solvus curves at P=0 and P=25 GPa. Evidently, the model perovskites exhibit very little miscibility under geologically interesting conditions, thus suggesting that most calcium in the lower mantle is likely to be present in a separate perovskite–type phase. These results are consistent with the findings of Irifune *et al.* [9].

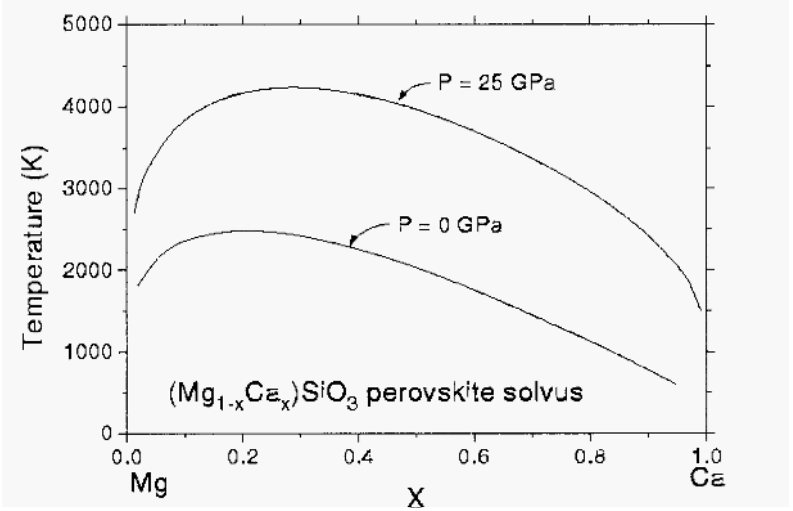

Figure 10. Estimated solubility between $MgSiO_3$ and $CaSiO_3$ perovskites. The solvus curves are estimates based on an MPIB averaged atom model [62]. At temperatures below the curves, the solution decomposes into two perovskites with compositions indicated by the intercepts of the solvus curves with the corresponding constant temperature line.

The average atom model also affords an examination of the effect of Ca concentration on the structure of silicate perovskite. Given that $CaSiO_3$ is cubic, we expect $(Mg_{1-x}Ca_x)SiO_3$ to become cubic for some value of x, even for a static lattice, and to lower the temperature of the predicted temperature induced orthorhombic to tetragonal/cubic transformation. Figure 11 shows the b/a and c/a lattice ratios as functions of. At the low concentrations that are compatible with our miscibility estimates (figure 10), Ca is unlikely to have a substantial effect on the structure of the static lattice. However, the effect of Ca on the critical temperature remains unknown. A full assessment of calcium's effect on the structure of silicate

perovskite requires a lattice dynamics/molecular dynamics simulation of $(Mg_{1-x}Ca_x)SiO_3$, and should also consider the effect of Fe. Should Ca

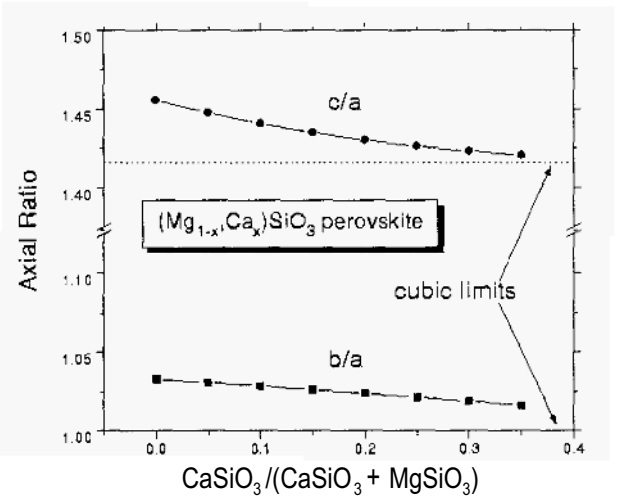

Figure 11. Effect of Ca on distortion of $(Mg_{1-x}Ca_x)SiO_3$ perovskite. Results based on MPIB averaged atom model [62].

significantly lower the critical temperature, structural changes in silicate perovskite may yet offer an explanation for minor seismic discontinuities that have been proposed in the 900 to 1200 km depth range [7,8].

5. Discussion

Ab initio electron gas potential models produce accurate equations of state and crystal structures for complex minerals, including oxides. They do so at a fraction of the cost and effort of first principles band structure and molecular dynamics methods. The VIB model, like the PIB model, offer reasonably simple *ab initio* approaches to quasiharmonic lattice dynamics, and appears to generate realistic values of thermal expansivity. It is not always as accurate as the MPIB model, but has the advantage of greaater simplicity. The calculations presented here suggest a practical compromise: accurate static properties may be calculated with the MPIB model, and VIB phonon contributions may be added to obtain reasonable thermal properties. In any case, our experience encourages us to believe that the models

presented here offer an efficient and frequently very accurate *ab initio* approach to the thermoelastic properties of minerals under diverse pressure and temperature environments. Detailed structural properties, such as the effect of temperature on the distortion of $MgSiO_3$, and the associated ferroelastic transformations, are not represented with comparable accuracy. The VIB model underestimates the energy necessary to rotate the SiO_6 octahedra. The MPIB method, which appears to yield static properties that are usually as good as those derived from first principles calculations, did not fare quite as well when applied to stishovite (Zhang and Bukowinski, 1991). These discrepancies are most likely due to a degree of covalency in the Si–O bonds. Hence the next step towards improved ionic models needs to at least include the polarizability of the ions, the effect of the latter on phonon frequencies, and possibly dispersion forces. We say *possibly* in the sense that dispersion forces are in many cases likely to be small compared to the errors due to covalent effects, as well as other errors inherent in electron gas potentials (e.g., Francisco *et al.,* [80]). Fortunately, polarizabilities and dispersion effects can be readily calculated within the density functional approach to ionic properties [37]. We have carried out some preliminary *ab initio* calculations that indicate that the effect of van der Waals interactions is small but non negligible in CaO and $CaSiO_3$ perovskite. However, the practical significance of these corrections in the electron gas context remains to be explored. In summary, we are persuaded that electron gas potentials have proven accurate enough to warrant further developments. What must be some very fortunate cancellation of errors endows a crude approximation to quantum mechanical interactions with unexpected accuracy. Although more fundamental methods based on modern electronic structure calculations offer high accuracy, electron gas models can often yield added insights and are orders of magnitude more efficient, and are often comparably accurate. Therefore we expect them to continue playing a significant role in studies of mineral properties subjected to the conditions of deep planetary interiors.

References

1. Ita, J. J., and Stixrude, L. (1992) Petrology, elasticity and Composition of the mantle transition zone, *J. Geophys. Res.,* **97**, 6849-6866.
2. Jackson, I. (1983) Some geophysical constraints on the chemical composition of the earth's lower mantle, *Earth Planet. Sci. Lett.* **62,** 91-103.
3. Jeanloz, R. and Thompson, A.B. (1983) Phase transitions and mantle discontinuities, *Revs. Geophys. Sp. Phys.* **21,** 51-74.
4. Bukowinski, M.S.T. and Wolf, G.H. (1990) Thermodynamically consistent decompression: implications for lower mantle composition, *J. Geophys. Res.* **95,** 12583-12593.
5. Irifune, T. and Ringwood, A.E. (1987) Phase transformations in primitive MORB and pyrolite compositions to 25 GPa and some geophysical implications. In M. H.

Manghnani and Y. Syono, (eds.), *High-Pressure Research in Mineral Physics,* AGU, Washington.
6. O'Neill, B. and Jeanloz, R. (1990) Experimental petrology of the lower mantle: A natural peridotite taken to 54 GPa, *Geophys. Res. Lett.* **17,** 1477-1480.
7. Petersen, N.,Gossler, J.,Kind, R.,Stammler, K. and Vinnik, L. (1993) Precursors to SS and structure of transition zone of the northwest Pacific, *Geophys. Res. Lett.* **20,** 281-284.
8. Kawakatsu, H. and Niu, F. (1994) Seismic evidence for a 920-km discontinuity in the mantle, *Nature* **371,** 301-305.
9. Irifune, R.,Susaki, J.,Yagi, T. and Sawamoto, H. (1989) Phase transformations in diopside $CaMgSi_2O_6$ at pressures up to 25 GPa, *Geophys. Res. Lett.* **16,** 187-190.
10. Tamai, H. and Yagi, T. (1989) High-pressure and high-temperature phase relations in $CaSiO_3$ and $CaMgSi_2O_6$ and elasticity of perovskite-type $CaSiO_3$, *Phys. Earth Planet. Int.* **54,** 370-377.
11. Zhang, H. and Bukowinski, M.S.T. (1992) Possible high pressure phases of Al_2O_3 and Mg-Ca-AI silicates, *EOS* **73,** 521.
12. Zhao, Y. and Anderson, D.L. (1994) Mineral physics constraints on the chemical composition of the Earth's lower mantle, *Phys. Earth Planet. Int* **85,** 273-292.
13. Boyer, L.L. (1983) Bonding and equation of state of MgO, *Phys. Rev.* **B27,** 1271-1275.
14. Agnon, A. and Bukowinski, M.S.T. (1988) High pressure Shear moduli-A many-body model for oxides, *Geophys. Res. Lett.* **15,** 209-212.
15. Agnon, A. and Bukowinski, M.S.T. (1990) Thermodynamic and elastic properties of many-body model for simple oxides, *Phys. Rev.* **B141,** 7755-7766.
16. Bukowinski, M.S.T. (1980) Effect of pressure on bonding in MgO, *J. Geophys. Res.* **85,** 285-292.
17. Bukowinski, M.S.T. (1982) Pressure effects on bonding in CaO: Comparison with MgO, *J. Geophys. Res.* **87,** 303-310.
18. Bukowinski, M.S.T. (1985) First principles equation of state of MgO and CaO, *Geophys. Res. Lett.* **12,** 536-539.
19. Cohen, R.E. (1991) Bonding and elasticity of stishovite SiO_2 at, high pressures: Linearized augmented Plane Wave calculations, *Am. Mineral.* **76,** 733-742.
20. Cohen, R.E. (1992) First-principles predictions of elasticity and phase transitions in high pressure SiO_2 and geophysical implications, In Y. Syono and M. H. Manghnani, (eds.), *High-Pressure Research: Applications to Earth and Planetary Sciences,* Terra Scientific Publishing Company (TERRAPUB), Tokyo, 425-431.
21. Mehl, M.J.,Cohen, R.E. and Krakauer, H. (1988) Linearized Augmented Plane Wave electronic structure calculations for MgO and CaO, *J. Geophys. Res.* **93,** 8009-8022.
22. Sherman, D.M. (1993) Equation of state and high-pressure phase transitions of stishovite (SiO_2): *Ab initio* (periodic Hartree-Fock) results, *J. Geophys. Res.* **98,** 11865-11874.
23. Stixrude, L. and Cohen, R.E. (1993) First pnciples investigation of the electronic structure and physical properties of solid iron at core pressures (abstract) , *EOS* **74,** 305.
24. Stixrude, L. and Cohen, R.E. (1993) Stability of orthorhombic $MgSiO_3$ perovskite in the Earth's lower mantle, *Nature* **364,** 613-616.
25. Car, R. and Parrinello, M. (1985) Unified approach for molecular dynamics and density-functional theory, *Phys. Rev. Lett.* **55,** 2471-2474.
26. Bukowinski, M.S.T. (1994) Quantum Geophysics, *Annu. Rev. Earth Planet. Sci.* **22,** 167-205.
27. Mehl, M.J.,Hemley, R.J. and Boyer, L.L. (1986) Potential-induced breathing model for the elastic moduli and high-pressure behavior of the cubic alkaline-earth oxides, *Phys. Rev.* **B33,** 8685-8695.
28. Wolf, G.H. and Bukowinski, M.S.T. (1988) Variational stabilization of the ionic charge densities in the electron-gas theory of crystals: Applications to MgO and

CaO, *Phys. Chem. Minerals* **15,** 209-220.
29. Chizmeshya, A.,Zimmermann, F.M.,La Violette, R.A. and Wolf, G. (1994) Variational charge relaxation in ionic crystals: An efficient treatment of statics and dynamics, *Phys. Rev. B* **50,** 15559-15574.
30. Isaak, D.G.,Cohen, R.E. and Mehl, M.J. (1990) Calculated elastic and thermal properties of MgO at high pressures and temperatures, *J. Geophys. Res.* **95,** 7055-7067.
31. Gordon, R.G. and Kim, Y.S. (1972) A theory for the forces between closed shell atoms and molecules, *J. Chem. Phys.* **56,** 3122-3133.
32. Hohenberg, P.C. and Kohn, W. (1964) Inhomogeneous electron gas, *Phys. Rev.* **B136,** 864-871.
33. Kohn, W. and Sham, L.J. (1965) Self-consistent equations including exchange and correlation effects, *Phys. Rev.* **140,** 1133-1138.
34. Gordon, R.G. and LeSar, R. (1990) Local density functional theories of ionic and molecular solids, *Adv. Quantum Chem.* **21,** 341-363.
35. Zhang, H. (1993) A study of lower mantle mineralogy by *ab initio* potential methods, PhD thesis, University of California at Berkeley.
36. Zhang, H. and Bukowinski, M.S.T. (1991) Modified potential-induced breathing model of potentials between closed-shell ions, *Phys. Rev.* **B44,** 2495-2503.
37. Mahan, G.D. and Subbaswamy, K.R. (1990) *Local Density Theory of Polarizability,* Plenum Press, New York.
38. Jones, R.O. and Gunnarson, O. (1989) The density functional formalism, *Rev. Mod. Phys.* **61,** 689-746.
39. Hedin, L. and Lundqvist, B.I. (1971) Explicit local exchange-correlation potentials, *J. Phys. C* **4,** 2064-2083.
40. Lundqvist, B.I. and Lundqvist, S. (1972) Local excange-correlation potentials, in F. Herman, L. Dalton, and T. Koehler., (eds.), *Computational Solid State Physics,* Plenum Press, New York.
41. Waldman, M. and Gordon., R.G. (1979) Scaled electron gas approximation for intermolecular forces, *J. Chem. Phys.* **71,** 1325-39.
42. Clugston, M.J. (1978) The calculation of intermolecular forces. A critical examination of the Gordon-Kim model, *Adv. phys.* **27,** 893-912.
43. Pearson, E.W. and Gordon, R.G. (1985) Local asymptotic gradient corrections to the energy functional of an electron gas, *J. Chem. Phys.* **82,** 881-889.
44. Plumer, M.L. and Stott, M.J. (1985) Approximate kinetic energy functionals for atoms in extended systems, *J. Phys. C: Sol. St. Phys.* **18,** 4143-4163.
45. Muhlhausen, C. and Gordon, R.G. (1981) Density-functional theory for the energy of crystals: test of the ionic model, *Phys. Rev.* **B24,** 2147-2160.
46. Hemley, R.J. and Gordon, R.G. (1985) Theoretical study of solid NaF and NaCl at high pressures and temperatures, *J. Geophys. Res.* **90,** 7803-7813.
47. Boyer, L.L.,Mehl, M.J.,Feldman, J.L.,Hardy, J.R.,Flocken, J.W. and Fong, C.Y. (1985) Beyond the rigid-ion approximation with spherically symmetric ions, *Phys. Rev. Lett.* **54,** 1940-1943.
48. Herman, F. and Skillman, S. (1963) *Atomic Structure Calculations,* Prentice-Hall, Englewood Cliffs (New Jersey).
49. Aidun, J.,Bukowinski, M.S.T. and Ross, M. (1984) Equation of state and metallization of CsI, *Phys. Rev.* **B29,** 2611-2621.
50. Wallace, D.C. (1972) Thermodynamics of Crystals, Wiley and Sons, New York.
51. Cohen, A.J. and Gordon, R.G. (1976) Modified electron-gas study of the stability, elastic properties, and high-pressure behavior of MgO and CaO crystals, *Phys. Rev.* **B14,** 4593-4605.
52. Jackson, I., and Niesler, H. (1982) The elasticity of periclase to 3 GPa and some geophysical implications." In High-pressure Research in Geophysics, in S. Akimoto and M. H. Manghnani, (eds.), *High-pressure Research in Geophysics,* Center for Academic Publications Japan with Reidel Publishing Company, Tokyo.

53. Vassiliou, M.S. and Ahrens, T.J. (1981) Hugoniot equation of state of periclase to 200 GPa, *Geophys. Res. Lett.* **8,** 729-733.
54. Mammone, J.F.,Mao, H.K. and Bell, P.M. (1981) Equation of state of CaO under static pressure conditions, *Geophys. Res. Lett* **79,** 140-143.
55. Richet, P.,Mao, H.K. and Bell, P.M. (1988) Static compression and equation of state of CaO to 1.35 Mbar, *J. Geophys. Res* **93,** 15279-15288.
56. Richet, P.,Xu, J.-A. and Mao, H.-K. (1988) Quasi-hydrostatic compression of ruby to 500 Kbar, *Phys. Chem. Minerals* **16,** 207-211.
57. Cynn, H.,Isaak, D.G.,Cohen, R.E.,Nicol, M.F. and Anderson, O.L. (1990) A high-pressure phase transition of corundum predicted by the potential induced breathing model, *Am. Mineral.* **75,** 439-442.
58. Marton, F.C. and Cohen, R.E. (1994) Prediction of a high-pressure phase transition in Al_2O_3, *Amer. Mineral.* **79,** 789-792.
59. Cohen, R.E. (1987) Calculation of elasticity and high pressure instabilities in corundum and stishovite with the potential induced breathing model, *Geophys. Res. Lett.* **14,** 37-40.
60. Cohen, R.E. (1987) Elasticity and equation of state of $MgSiO_3$ perovskite, *Geophys. Res. Lett.* **14,** 1053-1056.
61. Zhang, H. and Bukowinski, M.S.T. (1995) Electron-gas model properties of $MgSiO_3$ and $CaSiO_3$ perovskites and their perovskite-like solid solutions, *Phys. Chem. Minerals* (submitted).
62. Bukowinski, M.S.T., and Zhang, H. (1995)
63. Bukowinski, M.S.T., and Zhang, H. (1995) to be published.
64. Finger, L.W. and Hazen, R.M. (1978) Crystal structure and compression of ruby to 46 kbar, *J. Appl. Phys.* **49,** 5823-5826.
65. Wolf, G.H. and Bukowinski, M.S.T. (1987) Theoretical study of the structural properties and equations of state of $MgSiO_3$ and $CaSiO_3$ perovskites: Implications for lower mantle composition, in M. H. Manghnani and Y. Syono.a, (eds.), *High-Pressure Research in Mineral Physics,* Terra Scientific Company (TERRAPUB), Tokyo.
66. Ross, N.L. and Hazen, R.M. (1990) High-pressure crystal chemistry of $MgSiO_3$ perovskite, *Phys. Chem. Minerals* **17,** 228-237.
67. Knittle, E. and Jeanloz, R. (1987) Synthesis and equation of state of $(Mg,Fe)SiO_3$ perovskite to over 100 GPa, *Science* **235,** 669-670.
68. Wolf, G.H. and Bukowinski, M.S.T. (1985) *Ab initio* structural and thermoelastic properties of orthorhombic $MgSiO_3$ perovskite, *Geophys. Res. Lett.* **12,** 809-812.
69. Hemley, R.J.,Jackson, M.D. and G., G.R. (1987) Theoretical study of the structure, lattice dynamics, and equations of state of perovskite-type $MgSiO_3$ and $CaSiO_3$, *Phys. Chem. Minerals* **14,** 2-12.
70. Mao, H.K.,Chen, L.C.,Hemley, R.J.,Jephcoat, A.P.,Wu, Y. and Bassett, W.A. (1989) Stability and equation of state of $CaSiO_3$-perovskite to 134 GPa, *J. Geophys. Res.* **94,** 17889-17894.
71. Tarrida, H. and Richet, P. (1989) Equation of state of $CaSiO_3$ perovskite to 96 GPa, *Geophys. Res. Lett.* **16,** 1351-1354.
72. Kapusta, B. and Guillope, M. (1993) Molecular dynamics study of the perovskite $MgSiO_3$ at high temperature: structural, elastic and thermochemical properties, *Phys. Earth Planet. Int.* **75,** 205-224.
73. Hu, J., Meade, C., and Mao, H.K. (1994) High temperature phase transition and dissociation of (Mg,Fe)SiO3 perovskite at lower mantle pressures, *EOS* **75,** 605.
74. D'Arco, P.,Sandrone, G.,Dovesi, R.,Orlando, R. and Saunders, V.R. (1993) A quantum mechanical study of the perovskite structure type of $MgSiO_3$, *Phys. Chem. Minerals* **20,** 407-414.
75. Wentzcovitch, R.M.,Martins, J.L. and Price, G.D. (1993) *Ab initio* molecular dynamics with variable cell shape: applications to $MgSiO_3$, *Phys. Rev, Lett.* **70,** 3947-3950.

76. Ross, N.L. and Hazen, R.M. (1989) Single crystal X-ray diffraction study of $MgSiO_3$ perovskite from 77 to 400 K, *Phys. Chem. Minerals* **16,** 415-420.
77. Knittle, E., Jeanloz, R., and Smith, G. L. (1986) Thermal expansion of silicate perovskite and stratification of the earth's mantle, *Nature,* **319,** 214-216.
78. Hemmati, M. ,Chizmeshya, A.,Wolf, G.H., Poole, P.H.,Shao, J. and Angell, C.A. (1995) Crystalline-amorphous transition in silicate perovskites, *Phys. Rev.* **B51,** (in press).
79. Ottonello, C. (1987) Energies and interactions in binary (*Pbmn*) orthosilicates: a Born parametrization, *Geochim. Cosmochim. Acta,* **51,** 3129-3135.
80. Francisco, E.,Recio, J.M.,Blanco, M.A.,Pendas, A.M. and Pueyo, L. (1995) Derivation of electron-gas interatomic potentials from quantum-mechanical description of ions in crystals, *Phys. Rev.* **B51,** 2703-2714.
81. Jephcoat, A.P.,Hemley, R.J. and Mao, H.K. (1988) X-ray diffraction of ruby (Al_2O_3:Cr3+) to 175 GPa, *Physica* **B150,** 115-121.
82. Mao, H.-Kand Bell, P.M. (1979) Equations of state of MgO and Fe under static pressure conditions, *J. Geophys. Res.* **84**, 4533-4536.
83. Perez-Albuerne, E.A. and Drickamer, H.G. (1965) Effect of high pressure on the compressibility of seven crystals having the NaCl or CsCl structure, *J. Chem. Phys.* **43,** 1381-1387.
84. Yagi, T.,Mao, H.K. and Bell, P.M. (1978) Structure and crystal chemistry of perovskite-type $MgSiO_3$, *Phys. Chem. Minerals* **3,** 97-110.

QUANTUM-MECHANICAL AND CLASSICAL SIMULATIONS OF MG-CA CARBONATES

MICHELE CATTI
Dipartimento di Chimica Fisica ed Elettrochimica, Università di Milano, via Golgi 19, 20133 Milano, Italy

AND

ALESSANDRO PAVESE
Dipartimento di Scienze della Terra (Sez. Mineralogia), Università di Milano, via Botticelli 23, 20133 Milano, Italy

1. Introduction

Carbonates of alkaline-earth and other divalent metals are crystalline phases of noteworthy importance both in the earth sciences, as rock-forming minerals, and in chemical technology, as raw materials for a number of industrial processes. In particular, the calcite polymorph of $CaCO_3$ and dolomite, $CaMg(CO_3)_2$, are present in huge quantities in the earth's crust as main constituents of limestones (sedimentary rocks), and are also important minerals of several metamorphic rocks.

From the structural point of view, most of these carbonates are either rombohedral (space group $R\bar{3}c$) or orthorhombic (Pmcn) phases, corresponding to the structures of calcite and aragonite, respectively, the two most important polymorphs of $CaCO_3$. Carbonates of smaller divalent cations, like $MgCO_3$ (magnesite), show the rombohedral structure[1], while the orthorhombic one is observed in the case of larger cations[2]. The calcite-type crystal structure has a primitive rombohedral unit-cell containing two formula units (Z=2), but is more often described in the triple hexagonal cell (Z=6). There is a single atomic coordinate unconstrained by symmetry, x of the oxygen atom. The aragonite-type structure, on the other hand, is more complicated, as nine independent atomic coordinates instead of one are present (Z=4 in the primitive unit-cell). Other carbonates, like dolomite $CaMg(CO_3)_2$, have a rombohedral structure slightly less symmet-

B. Silvi and P. D'Arco (eds.), Modelling of Minerals and Silicated Materials **113-156.**

rical (space group $R\bar{3}m$, three independent atomic coordinates) than that of calcite.

The crystal-chemical behaviour of carbonates is interesting and significantly different from that of silicate systems. In particular, the C-O bond is much more covalent than Si-O, so that the CO_3 group forms a real molecular unit. Thus carbonates are good examples of oxysalts containing a covalently bonded molecular ion (the CO_3^{2-} anion), which interacts mainly ionically with the metal cations. In this respect they share features of ionic, covalent and molecular crystals, and are thus a challenge for theoretical and computational simulations of properties related to chemical bonding. The molecular carbonate anion is planar in the calcite structure, and very slightly pyramidal in those of aragonite and dolomite. Divalent cations are surrounded by oxygen atoms of carbonate groups with coordination numbers of 6 and 8, respectively, in the two structure types. A particularly intriguing feature is the complex polymorphism displayed by $CaCO_3$, which shows not only the calcite and aragonite phases, but also the metastable, not well characterized vaterite modification, and two high-pressure monoclinic distortions of the calcite structure[3]. Further, transformations of calcite have been reported also at high temperature, and these seem to involve a rotational disordering of the CO_3 group over different orientations. Other carbonates, like magnesite, seem to have a simpler behaviour, but they have been investigated less thoroughly.

Although for some of the phases of the carbonate group (e.g., calcite) a very rich set of experimental results is available, for many others of great importance the data are scarce and difficult to obtain[4]. Thus outstanding questions related to detailed structural knowledge at non-ambient conditions, relative stabilities of phases vs. pressure and temperature, mechanisms of solid-state transformations and careful characterization of chemical bonding are still open and particularly suited to be tackled by theoretical methods. The aim of this work is to present a part of the contributions which have appeared recently in this field, with limitation to studies concerning magnesite $MgCO_3$[5] and the polymorphs of $CaCO_3$ calcite and aragonite[6, 7, 8].

Two types of theoretical and computational methods will be considered. The first one is the quantum-mechanical ab initio approach, in the particular version based on the Hartree-Fock approximation extended to periodic system[9]. This, as all first-principles theoretical schemes, is very attractive because does not require any kind of empirical knowledge. In the last years, it has proved to be able to account for the structural and electronic behaviour of a number of crystalline solids and minerals quite successfully[10, 11, 12]. The Hartree-Fock approach is particularly reliable and efficient, in this respect. The hypersurface of the ground-state total en-

ergy of the crystal is evaluated as a function of the lattice geometry and of the atomic positions in the unit-cell. Several physical properties can thus be derived: the equilibrium crystal structure at 0 K, its dependence on volume and pressure (hence the static equation of state), the elastic constants, and some features of the phonon dispersion curves. The case of divalent metal carbonates with the calcite structure is particularly attractive, in this respect, because different kinds of chemical bonding are present in the same crystal. Further, the rhombohedral calcite-type crystal structure has only three independent geometrical parameters, so a detailed study of lattice and electron properties is feasible.

However, the drawback of ab initio calculations is that they usually refer to the athermal limit ($T = 0$ K), so that pressure but not temperature effects are included in the simulation. Although in principle the ab initio molecular dynamics approach[13] is able to overcome this limitation, at the present state of the art no temperature-dependent quantum-mechanical simulations are feasible yet for mineral systems. Thus thermal properties have to be dealt with by methods based on empirical interatomic potential functions, containing parameters to be fitted to experimental quantities[14, 15, 16]. The computational scheme applied here to carbonates is that based on the quasi-harmonic approximation for representing the atomic motion[17].

Early simulation work on calcite and aragonite was aimed either to reproduce the equilibrium structures using Born-type potentials[18], or to fit purely empirical force-constant models to elastic and dynamic data[19]. These phases have also been studied by deriving thermodynamic data from spectroscopic measurements[20]. The aim of recent studies, on the other hand, is to devise a potential model fully consistent with the chemical bonding in calcium carbonates, and able to reproduce the variety of their physical behaviour, including thermodynamic and equation-of-state properties. Some observables (equilibrium structural variables, elastic constants, some vibrational frequencies) are included in the fitting process, while others (thermodynamic quantities and non-ambient structural variables) are predicted by the quasi- harmonic equilibration. One of the purposes of this work is to assess the reliability of the quasi-harmonic lattice-dynamical model to account for the thermal properties of complex crystals such as calcite and aragonite. Further, different types of interatomic potentials are tested with respect to their transferability between polymorphs, and to their ability to reproduce thermodynamic behaviour.

2. Computational methods

2.1. AB INITIO CALCULATIONS

All quantum-mechanical computations were performed by the CRYSTAL program, based on the all-electron ab initio Hartree-Fock linear combination of atomic orbitals formalism applied to periodic systems[21]. Every atomic orbital is expressed as a linear combination of Gaussian-type functions, consisting of a radial Gaussian multiplied by a real solid harmonic function. The basis sets utilized for Mg and Ca contain 18 and 22 atomic orbitals and are denoted as 8-511G* and 8-6-511G*, respectively, according to the conventional notation in quantum-chemistry[22]. For the O and C atoms, 18 and 14 orbitals were used, respectively, and the corresponding basis sets are indicated as 8-411G* and 6-21G*. The exponents of the outermost shells were optimized distinctly for magnesite and calcite, by minimization of the corresponding total crystal energies. Details of the atomic basis sets used are reported in Table 1. With respect to the basis set of magnesite, the external valence shells of O and C appear to be significantly more diffuse in calcite. Inclusion of d orbitals in the basis sets of O and C was shown to lower the crystal energy and to affect the properties of $MgCO_3$ and $CaCO_3$ substantially.

The computational conditions employed in the CRYSTAL calculations were the following. A value of 10^{-6} e was assumed for the overlap and penetration threshold of Coulomb and exchange integrals, while 10^{-8} and 10^{-14} e were the pseudo-overlap thresholds for the exchange series. The truncated bipolar expansion was used to approximate bielectronic integrals with very small reciprocal penetration (less than 10^{-14} and 10^{-10} for Coulomb and exchange integrals, respectively). The irreducible Brillouin zone was sampled at 6 points for diagonalization of the Fock matrix. An estimate of the residual error introduced by these stringent computational conditions was obtained by removing the bipolar expansion approximation and increasing the number of sampled points in the Brillouin zone to . In the case of magnesite, the total energy per formula unit decreased by 2×10^{-4} hartrees.

For every structural configuration considered, the total electronic energy of the crystal unit-cell and the full wave function were obtained.

2.2. EMPIRICAL POTENTIALS AND QUASI-HARMONIC MODEL

Calcite and aragonite typically share chemical bonding features of both ionic and molecular crystals, owing to the strong covalent interactions inside the CO_3 units and to the presence of Ca^{2+} ions. This situation is also met in many mineral oxysalts, like orthosilicates, and needs to be taken into account in the design of the interatomic potential by modelling inter- and

TABLE 1. Exponents ($bohr^{-2}$) and contraction coefficients of the Gaussian functions adopted for the study of $MgCO_3$, magnesite (m) and $CaCO_3$, calcite (c). The contraction coefficients multiply individually normalized Gaussians. $y[\pm z]$ stands for $y \times 10^{\pm z}$.

Shell type	Exponents	Coefficients s	Coefficients s, p	Exponents	Coefficients s	Coefficients p, d
		Carbon			Oxygen	
1s	3.048[+3]	1.826[-3]	4.000[+3]	1.440[-3]		
	4.564[+2]	1.406[-2]	1.356[+3]	7.640[-3]		
	1.037[+2]	6.876[-2]	2.485[+2]	5.370[-2]		
	2.923[+1]	2.304[-1]	6.953[+2]	1.682[-1]		
	9.349	4.685[-1]	2.389[+1]	3.604[-1]		
	3.189	3.628[-1]	9.276	3.861[-1]		
			3.820	1.471[-1]		
			1.235	7.105[-2]		
2sp	3.665	-3.959[-1]	2.365[-1]	5.219[+1]	-8.730[-3]	9.220[-3]
	7.705[-1]	1.216	8.606[-1]	1.033[+1]	-8979[-2]	7.068[-2]
				3 210	-4.079[-2]	2.043[-1]
				1.235	3.767[-1]	3.496[-1]
3sp	0.260(m	1.0	1.0	4.790[-1]	1.0	1.0
3sp	0.235 (c)	1.0	1.0			
4sp				0.2300(m)	1.0	1.0
4sp				0.1850(c)	1.0	1.0
3d	08		1.0	0.8		1.0
		Magnesium			Calcium	
1s	6.837[+4]	2.226[-4]		1.913[+5]	2.204[-4]	
	9.699[+3]	1.898[-3]		2.697[+4]	1.925[-3]	
	2.041[+3]	1.105[-2]		5.696[+3]	1.109[-2]	
	5.293[+2]	5.006[-2]		1.489[+3]	4.995[-2]	
	1.592[+2]	1.691[-1]		4.483[+2]	1.701[-1]	
	5.468[+1]	3.670[-1]		1.546[+2]	3.685[-1]	
	2.124[+1]	4.004[-1]		6.037[+1]	4.034[-1]	
	8.746	1.499[-1]		2.509[+1]	1.452[-1]	
2sp	1.568[+2]	-6.240[-3]	7.720[-3]	4.486[+2]	-5.750[-3]	8470[-3]
	3.103[+1]	-7.882[-2]	6.427[-2]	1.057[+2]	-7.670[-2]	6.027[-2]
	9.645	-7.992[-2]	2.104[-1]	3.469[+1]	-1.122[-1]	2.124[-1]
	3.711	2.906[-1]	3.431[-1]	1.350[+1]	2.537[-1]	3.771[-1]
	1.611	5.716[-1]	3.735[-1]	5.820	6.880[-1]	4.010[-1]
				1.819	3.4901-1]	1.980[-1]
3sp	0.68	1 0	1.0	2.075[+1]	-2.000[-3]	-3.650[-2]
				8 40	-1.255[-1]	-6.850[-2]
				3 537	-6.960[-1]	1.570[-1]
				1.408	1.029	1.482
				7.260[-1]	9.440[-1]	1.025
4sp	0.28	1.0	1.0	4.530[-1]	1.0	1.0
5sp				2.620[-1]	1.0	1.0
3d	0.8		1.0	3.191		1.60[-1]
				8.683[-1]		3.13[-1]
				3.191[-1]		4.06[-1]

intra-molecular interactions appropriately. Thus a conventional two-body Born-type potential $e^2 z_i z_j / r_{ij} + A_{ij} e^{(-r_{ij}/\rho_{ij})}$ has been used to express the interaction energy for O-O, Ca-O and C-O atom pairs, adding a dispersive term $-c_{ij}/r_{ij}^6$ in the O-O case only (e is the electron charge, z_i the charge of the i-th atom in e units, r_{ij} the interatomic distance, A_{ij} and p_{ij} the

coefficient and hardness parameter of the repulsive energy, c_{ij} the coefficient of the dispersive energy for the ij atom pair). The covalent, directional bonding in the CO_3 molecular ion is accounted for by a harmonic angular potential $1/2k_\Theta(\Theta - \Theta_0)^2$, where Θ is the actual O-C-O bond angle and its equilibrium value of 120°. An additional term $k_\Phi(1-\cos 2\omega)$ expresses the energy increase of the CO_3 unit due to out-of-plane displacements of the C atom; Φ is the torsional angle between the OCO' and OCO" planes. The z_{Ca} charge was either fixed at its fully ionic value +2 or allowed to vary, while fractional charges were always assumed on C and O atoms and constrained by the electroneutrality relation $z_C + 3z_O = -z_{Ca}$. Thus the following independent potential parameters were considered as unknowns to be determined by an optimization process: z_O, $A_{O\text{-}O}$, $A_{Ca\text{-}O}$, $A_{C\text{-}O}$, $\rho_{O\text{-}O}$, $\rho_{Ca\text{-}O}$, $\rho_{C\text{-}O}$, $c_{O\text{-}O}$, k_Θ and k_Φ; z_{Ca} was included in some cases only.

The above potential is based on a rigid-ion-model (RIM), as no effect of atomic polarization is taken into account. A shell model (SM) was also developed, which considers a split core-shell structure for polarizable O atoms. As usual [23], core and shell are coupled by an elastic spring of force constant k_s, and are characterized by different electric charges z_{Oc} and z_{Os}. In addition to k_s and z_{Os}, also the core-shell displacement, d_{cs} is to be optimized, and contributes three positional parameters (unless reduced by symmetry) for each O atom in the asymmetric unit. When an O atom is involved in the two-body interaction, the repulsive and, possibly, dispersive energy is computed by reference to the O shell position. All other atoms and interactions are treated as for the RIM case.

The energy parameters were fitted to equilibrium structural data (cell constants and atomic fractional coordinates), elastic constants, vibrational frequencies at the centre of the Brillouin zone (wave vector K=0) and, for the SM case only, dielectric tensor components, using the THBFIT program[24]. The input data are all the experimental quantities referred to above, and initial trial values for the energy parameters to be optimized. At first specific potentials were fitted in this way separately on calcite and aragonite; then some of them were used to compute properties of the other polymorph, so as to check their generality and transferability.

By using explicit expressions for the interatomic potential energy, the lattice dynamical problem can be solved straightforwardly within the harmonic approximation, obtaining the spectrum of vibrational eigenfrequencies. Then the usual formulas of statistical mechanics are used for the contribution of each normal mode of vibration to the vibrational part of the Helmholtz free energy, entropy, energy and heat capacity. The total value of each thermodynamic function is evaluated either by direct sum over all normal modes or by integration over the frequency range after multiplying

by the density of vibratioanal states. In this respect, an important computational problem lies with the sampling of the first Brillouin zone at a minimum but sufficient number of wave vectors: 64 points have been used in the present case.

According to the quasi-harmonic approach, an explicit volume dependence is assumed for each vibrational frequency, from which the mode Grüneisen parameters can be defined. Thus it is possible to calculate the vibrational pressure and thermal expansion coefficient of the crystal. The quasi-harmonic equilibration is performed by an iterative process. In the first iteration, the experimental volume V is assumed, the atomic positions are relaxed to minimize the static energy, and the total pressure $p(V_0) = p_{st}(V_0) + p_{vib}(V_0,T) = [-dE_{st}/dV - (\Delta F_{vib}/\Delta V)_T]_{V=V_0}$ is computed by considering a small volume increase ΔV to approximate the derivatives numerically. The elastic bulk modulus B_T is also obtained, approximated by its static component; its temperature dependence is neglected. Then the volume change $V - V_0$ necessary to move the pressure from p to p_0 is computed as $V - V_0 = -(p-p_0)V/B_T$. As the linear relationship between ΔV and Δp holds to a first approximation only, the whole procedure has to be repeated for a number of times, until the computed pressure p differs from p_0 by less than a chosen value. However, in subsequent cycles only the static pressure is recalculated, while p_{vid} is kept fixed at the first computed value. At each cycle an atomic relaxation step is run after updating the volume. Then the second iteration starts, and the total pressure including a new p_{vib} term is calculated on the basis of the last volume value; subsequent cycles recalculating pst only follow. A number of iterations of this kind are performed, until convergence to the required p value is attained. Only at that stage has the crystal structure been equilibrated consistently with the quasi-harmonic equation of state, and then the final vibrational frequencies and thermodynamic properties can be computed.

This simplified equilibration process holds strictly for a cubic crystal; in a general non-cubic case, the volume, static pressure and bulk modulus have to be replaced by the strain components (related to unit-cell parameters), stress components and elastic constants, respectively. The computer program PARAPOCS[17] performs the lattice-dynamical, thermodynamical and quasi-harmonic calculations in the general tensorial formalism, and has been used to obtain all results reported below for calcite and aragonite.

3. Quantum-mechanical results for magnesite and calcite

3.1. ATHERMAL EQUATIONS OF STATE

The structure of magnesite and calcite (Fig.1) has three geometrical

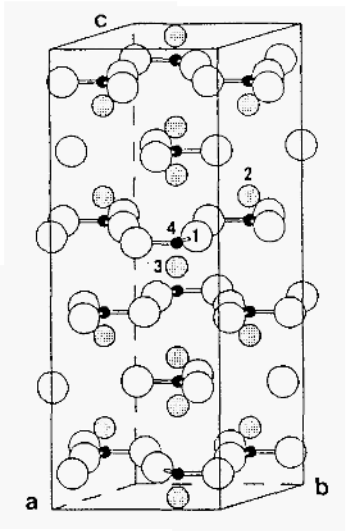

Figure 1. Hexagonal unit-cell of the calcite and magnesite structure. Black, grey and open circles represent C, Ca (or Mg) and O atoms, respectively. The labelled atoms appear in the maps of Figs. 12 and 13.

degrees of freedom. With reference to the triple hexagonal unit-cell (containing six formula units of ACO_3, where A is Mg or Ca), these are the edges a and c, and the fractional coordinate x of the O atom. The corresponding experimental values at room temperature are reported in Table 2 for each of the two crystals from different literature sources; extrapolation to 0 K was performed by a parabolic fitting of data measured in the range 300 - 773 K[25]. We have preferred to choose three other structural variables related to the previous ones: the volume of the hexagonal unit-cell $V = (\sqrt{3}/2)a^2c$, the ratio $q = c/a$ and the C-O bond length $r_{C-O} = ax$. The total (electronic + nuclear) crystal energy is a function $E(V, q, r_{C-O})$ of all three variables, but only V *is* independent, as the least-energy conditions $(dE/dq)_{V,r} = 0$ and $(dE/dr_{C-O})_{V,q} = 0$ lead to $q = q(V)$ and $r_{C-O} = r_{C-O}(V)$ functional dependencies: thus at equilibrium $E = E(V)$.

The procedure used for magnesite is described in detail; for calcite, the same scheme was used. At first the energy was computed keeping q and r_{C-O} fixed at their experimental values, and changing V in the range -9% to +6% with respect to the experimental volume. Then the q ratio was relaxed for six of the thirteen V values considered (- 9%, -6%, -3%, 0%, +3%, +6%), by computing $E(q, V)$ and finding the optimum $q(V)$ numeri-

TABLE 2. Experimental structural data and elastic constants of magnesite and calcite (300 K) from different literature sources, and structural values extrapolated to 0 K. The estimated uncertainties are given in parentheses. For calcite, the dielectric tensor components are given, too.a; Markgraf and Reeder [25]; b: Goettlicher and Vegas [39]; c: Effenberger et al. [59]; d: Humbert and Plicque [61]; e: Maslen et al. [62]; f: Dandekar and Ruoff [31]; g: Vo Thanh and Lacam [63]; h: Deer et al. [43]; i: Kaye and Laby [44]; *: extrapolation to 0 K from data of ref. a.

$MgCO_3$ a(Å)	c(Å)	V(Å^3)	x(O)	r_{C-O}(Å)	r_{Mg-O}(Å)		Ref.
4.635(2)	15.019(3)	279.3(2)	0.2778(2)	1.288(1)	2.1018(4)		*a*
4.636(1)	15.026(2)	279.6(1)	0.2775(1)	1.286(1)	2.1031(3)		*b*
4.6328(2)	15.0129(5)	279.05(3)	0.27740(7)	1.2851(4)	2.1017(1)		*c*
4.632	14.991	278.5	0.2778	1.285	2.100		*
C_{11}	C_{12}	C_{13}	C_{14}	C_{33}	C_{44}	C_{66}	Ref.
258.7	75.6	58.8	-19.1	155.5	54.8	91.6	*d*
$CaCO_3$ a(Å)	c(Å)	V(Å^3)	x(O)	r_{C-O}(Å)	r_{Ca-O}(Å)		Ref.
4.988(1)	17.061(1)	367.6(1)	0.2567(2)	1.280(1)	2.3595(5)		a
4.991(2)	17.062(2)	368.1(3)	0.2573(2)	1.284(1)	2.3590(8)		e
4.9896(2)	17.061(1)	367.85(5)	0.2568(1)	1.2813(6)	2.3598(3)		c
4.995	16.920	365.6	0.2567	1.283	2.354		*
C_{11}	C_{12}	C_{13}	C_{14}	C_{33}	C_{44}	C_{66}	Ref.
148.1	55.9	54.6	-20.6	85.6	32.7	46.1	f
145.7	55.9	53.5	-20.5	85.3	33.4	44.9	f
$\epsilon(0)_{11}$	$\epsilon(0)_{33}$	$\epsilon(\infty)_{11}$	$\epsilon(\infty)_{33}$				
8.5	8.0	2.75	2.21				*h, i*

cally from the minimum energy condition. With the optimized q values, the r_{C-O} bond length was relaxed in its turn for $V/V_0 = -9\%, -6\%, 0\%, +6\%$; the $E(r_{C-O}, V)$ surface was calculated and the best r_{C-O} lengths were

determined by the condition $(dE/dr_{C\text{-}O})_V = 0$, yielding the linear fit:

$$r_{C\text{-}O} = 1.1896 + 2.8150 \times 10^{-4} V$$

Eventually, the q ratio vs. V was optimized again by using the above computed $r_{C\text{-}O(V)}$ distance instead of its fixed experimental value, and the results were least-squares interpolated according to a cubic polynomial.

By computing the energy for each volume with the optimized $r_{C\text{-}O}$ and q quantities, instead of the fixed equilibrium experimental values, the $E(V)$ curve for the fully relaxed structure was obtained (Table 3). By polynomial interpolations, the equilibrium least-energy volume V_0 was derived, and by substitution into the above $q(V)$ and $r_{C\text{-}O(V)}$ relations all other structural parameters were determined and compared to experimental values (Table 4). The calculated volume is in excellent agreement with that extrapolated to 0 K from X-ray data; neglecting the structure relaxation, a slightly larger volume (281.1 Å^3) would be obtained. On the other hand, the equilibrium c/a ratio and $r_{C\text{-}O}$ bond length are somewhat over- and underestimated, respectively, by comparison with measured values.

In order to assess the importance of polarization functions for reproducing the equilibrium geometry, the whole calculation was repeated omitting the d orbitals from the basis sets of all three atoms Mg, C and O. The equilibrium C-O distance turns out to be larger, and the c/a ratio smaller with respect to the values computed with the larger basis set. Thus inclusion of d orbitals in the atomic basis sets produces a shortening of the C-O bond length in the CO_3 group, consistently with Hartree-Fock calculations on molecular systems containing C-O bonds[22].

The dependence of the energy on volume, if interpolated by a suitable analytical formula, yields all relevant information on the equations of state of magnesite at 0 K. The Murnaghan equation[26], widely used in solid state thermodynamics, is based on the assumption of a linear dependence of the elastic bulk modulus on pressure ($B = B_0 + B'p$):

$$E(V) = B_0 V_0 \left[\frac{1}{B'(B'-1)} \left(\frac{V_0}{V} \right)^{(B'-1)} + \frac{1}{B'} \frac{V}{V_0} - \frac{1}{B'-1} \right] + E_0 \qquad (1)$$

By interpolation of the computed $E(V)$ points, the Murnaghan parameters reported in Table 3 were obtained. By differentiation of the $E(V)$ function, the pressure $p(V) = -dE/dV$ can be computed, and thus a full representation of the thermodynamical behaviour at 0 K is derived.

The same computational scheme was followed for calcite. The values obtained for E, c/a and x(O) as functions of V/V_0 are reported and compared to the corresponding quantities of magnesite in Table 3. By substituting V_0 for V in least-squares polynomial interpolations of $q(V)$ and $x(V)$, and

TABLE 3. Hartree-Fock energies (including relaxation contribution), and relaxed c/a ratios and oxygen fractional coordinates vs. V/V_0 for magnesite and calcite. The $V_0/6$ (least-energy volume per formula unit), $E_0 = E(V_0)$, B_0 (zero-pressure bulk modulus) and B' = $(dB/dp)_0 = 0$ quantities have been fitted to a Murnaghan equation of state.

$MgCO_3$			
V/V_0	E(hartree)	c/a	x(O)
0.9117	462.3615	3.1918	0.27927
0.9418	462.3650	3.2184	0.27762
0.9718	462.3669	3.2470	0.27614
1.0019	462.3674	3.2748	0.27461
1.0319	462.3667	3.3021	0.27313
1.0620	462.3651	3.3241	0.27153
$V_0/6 = 46.53$ Å^3		$E_0 = 462.3674$ hartree	
$B_0 = 124.73$ GPa		$B' = 3.08$	
$CaCO_3$			
V/V_0	E(hartree)	c/a	x(O)
0.8674	939.5235	3.2359	0.25574
0.8960	939.5289	3.2974	0.25512
0.9246	939.5327	3.3528	0.25436
0.9532	939.5350	3.3995	0.25335
0.9818	939.5361	3.4446	0.25243
1.0104	939.5363	3.4830	0.25128
1.0390	939.5355	3.5178	0.25018
$V_0/6 = 64.32$ Å^3		$E_0 = 939.5363$ hartree	
$B_0 = 75.27$ GPa		B' = 4.63	

using the relationships between a, c, r_{C-O}, r_{M-O} and q, x, the theoretical equilibrium values (at zero pressure and temperature) of unit-cell constants and relevant bond lengths were obtained (Table 4). These results are compared to experimental values extrapolated to $T = 0$ K reported in Table 2. Two main features appear by inspection of Table 4. First, the theoretical unit-cell volume of calcite is significantly overestimated, while that of magnesite reproduces the experimental value very closely. This result is related to a lengthening of the computed vs. observed Ca-O bond distance, which does not occur appreciably in the Mg-O case. A similar effect has been observed in many instances, and seems to be due to the intrinsic Hartree-Fock error increasing sharply in compounds of fourth- vs. third-row atoms: see the case of CaO[27] compared to MgO[28]. The corrections for electron

TABLE 4. Structural data (units as in Table 1) of magnesite and calcite, calculated by minimizing their quantum-mechanical ab initio energies. The percentage errors with respect to experimental values extrapolated to 0 K (Table 1) are reported.

	$MgCO_3$		$CaCO_3$	
a_o		-0.3		+1.0
	4.618 Å		5.045	
c_o		+0.8		+3.5
	15.114 Å		17.504	
c_o/a_o		+1.1		+2.4
	3.273		3.469	
V_0	279.2 Å^3	+0.2	385.9	+5.5
x_0		-1.0		-2.0
	0.2746		0.2517	
r^0_{C-O}		-1.3		-1.0
	1.268 Å		1.270	
r^0_{M-O}		+0.4		+2.5
	2.109 Å		2.412	

correlation based on the local density functional theory, which are presently available (cf. Perdew et al.,[29]), account satisfactorily for the equilibrium energy but not for its volume dependence. Thus more work in this field is needed to solve that problem. The second feature is the elongation distortion (parallel to **c**) of the calculated vs. experimental unit-cell, which is larger for calcite but appreciable in magnesite as well. As a result, the computed c edge of calcite appears to be substantially overestimated. No simple explanation can be given for this result, unless it is ascribed to neglect of polarization and dispersion effects which is intrinsic in the Hartree-Fock approximation, and which could play a larger role for inter-layer interactions affecting specifically the normal direction [001]. On the other hand, it is interesting to remark that an even larger elongation distortion of the calcite unit cell ($c/a = 3.564$) is produced by the classical simulation based on empirically optimized interatomic potentials discussed below, though the computed volume fitted the experimental one very closely. Eventually, a very similar shrinking of the C-O bond length appears in the computed structures of both carbonates.

As experiments are usually done at constant pressure, rather than at constant volume, it can be useful to transform the computed dependences

on volume of structural parameters of the two carbonates into pressure dependences. This is done by the $p(V)$ Murnaghan relation

$$p = -\frac{dE}{dV} = \frac{B_0}{B'}\left[\left(\frac{V_0}{V}\right)^{B'} - 1\right] \tag{2}$$

using the optimized parameters (Table 3). The values obtained for the unit-cell constants and for the C-O, Ca-O and Mg-O bond distances, referred to the corresponding values at $p = 0$, are plotted against pressure in Figs. 2, 3, 4 for calcite and magnesite. Least-squares parabolic interpolations were carried out for the pressure dependence of a/a_0, c/c_0, r_{C-O}/r^0_{C-O}, r_{Ca-O}/r^0_{Ca-O} and r_{Mg-O}/r^0_{Mg-O} of both minerals; the coefficients obtained are reported in Table 5. The pressure dependences of ratios r/r_0 (where r is any of the above structural variables) are believed to be reasonably independent of errors in the r_0 parameters. The unit-cells appear to be compressed in a remarkably anisotropic way, with a larger shrinking of the c with respect to the a edge. This is clearly related to the presence of (001) layers of nearly uncompressible CO_3 triangular groups in the structures, as shown by the behaviour of the C-O bond length in Fig. 4 and in Table 5. On the other hand, this anisotropy is more pronounced for calcite than for magnesite, consistently with the larger compressibility of the Ca-O vs. Mg-O bond distance.

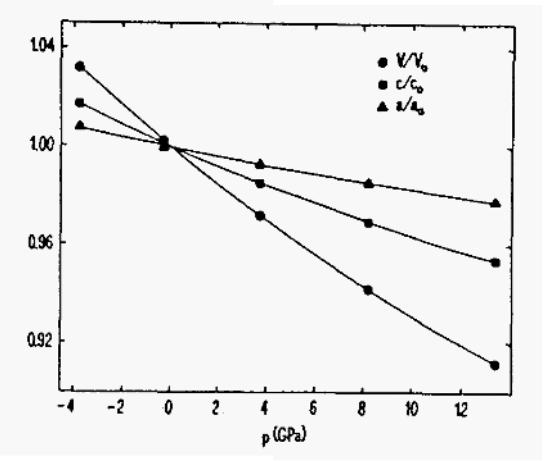

Figure 2. Computed hexagonal unit-cell constants of magnesite versus pressure.

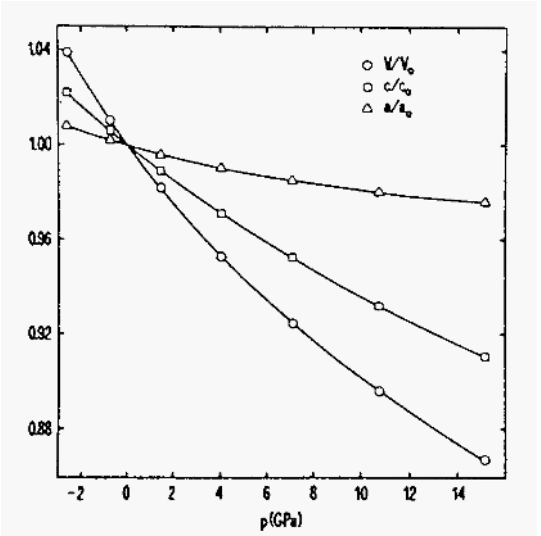

Figure 3. Computed hexagonal unit-cell constants of calcite, divided by the least-energy values ($p=0$) of Table 4, plotted versus pressure.

While no data are reported in the literature on the pressure dependence of the crystal structure of magnesite, calcite is well known to undergo a reversible phase transition (at 1.5 GPa) to the monoclinic polymorph $CaCO_3$-II, followed by a further transformation at 2.2 GPa into the $CaCO_3$-III phase[30]. Moreover, both modifications are considered to lie within the equilibrium stability range of aragonite. Thus, the results obtained for calcite are useful to characterize a hypothetical high-pressure metastable state of the rombohedral polymorph of $CaCO_3$; this is important for thermodynamical evaluations concerning the calcite/aragonite phase transition. The other rombohedral carbonates studied at high pressure are dolomite, $CaMg(CO_3)_2$, and ankerite, $CaFe(CO_3)_2$. Their crystal structures were refined up to 4.7 and to 4.0 GPa in the first and in the second case, respectively, without observing any phase transitions[31]. The case of dolomite is particularly relevant here, because its structure, containing CaO_6 and MgO_6 coordination octahedra, shares features of both calcite and magnesite, so that its experimental pressure dependence can be usefully compared to our theoretical results concerning individual $CaCO_3$ and $MgCO_3$. The mean linear compressibilities of the a and c cell edges of dolomite are 1.92 and 5.82 TPa^{-1}, respectively; these values are intermediate between those computed for the Ca and Mg carbonates, but closer to the latter. Thus the stiffer MgO_6 octahedron seems to condition the unit-cell compression

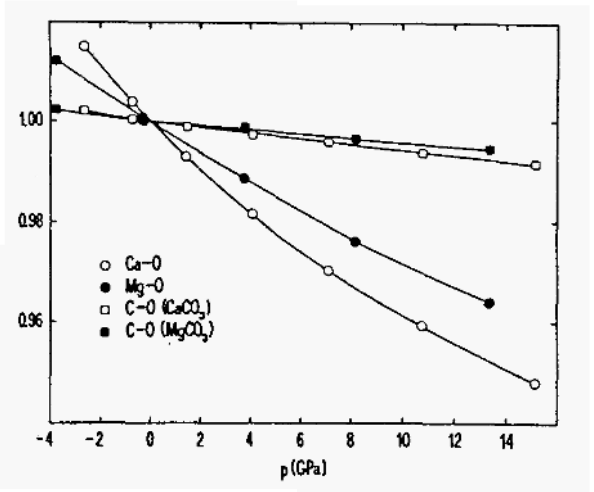

Figure 4. Computed interatomic distances of calcite and magnesite, divided by the values at p=0 (Table 4), plotted versus pressure.

of the mixed carbonate. On the other hand, the linear compressibilities of the Ca-O and Mg-O bonds obtained by quadratic interpolations of the dolomite data reported by Ross and Reeder[31] are 4.43 and 3.04 TPa^{-1}, respectively, which compare very well with the theoretical results for calcite and magnesite (Table 5).

3.2. ELASTIC AND VIBRATIONAL PROPERTIES

For both magnesite and calcite, the elastic bulk modulus $B_0 = V_0(\frac{d^2E}{dV^2})v=v_0$ was computed straightforwardly by the Murnaghan interpolation formula, while of the elasticity tensor only the C_{33} component and the $C_{11} + C_{12}$ linear combination could be calculated in a simple way. The relations used are $C_{33} = (1/V_0)c^2(d^2E/dc^2)_{c=c_0}$ and $C_{11} + C_{12} = (1/2V_0)a^2(d^2E/da^2)_{a=a_0}$: the deformations involved preserve the full symmetry of the crystal structure. To derive other elastic constants, the symmetry must be lowered with a consequent need of complex calculations for structural relaxation. A detailed account of how to compute the full tensor of crystal elasticity by use of simple lattice strains and structure relaxation was given previously[10, 11]. For the present deformations only the r_{C-O} (V) relaxation need be considered. The results are reported in Table 6, together with the corresponding values extrapolated to 0 K from experimental data (Table 2). For calcite, the mea-

TABLE 5. Least-squares interpolation coefficients of the quadratic pressure dependence $1 + D_1 \times p + D_2 \times p^2$ for unit-cell constants and bond lengths. The corresponding linear compressibilities are given by minus D_1.

$MgCO_3$		
	D_1	D_2
a/a_0	-1.98 TPa^{-1}	24 TPa^{-2}
c/c_0	-4.16	51
r_{C-O}/r^0_{C-O}	-0.46	
r_{Mg-O}/r^0_{Mg-O}	-3.20	40
$CaCO_3$		
	D_1	D_2
a/a_0	-2.58 TPa^{-1}	68 TPa^{-2}
c/c_0	-7.63	116
r_{C-O}/r^0_{C-O}	-0.57	
r_{Ca-O}/r^0_{Ca-O}	-4.94	103

surements of elastic constants at variable temperature of Dandekar[32] and Dandekar and Ruoff[33] (298-523 and 160-300 K, respectively) were used for the extrapolation. For magnesite, owing to the lack of thermal data the same temperature coefficients derived for the elastic constants of calcite were employed, too.

All calculated values are overestimated with respect to experimental data in the case of $MgCO_3$, and the effect is larger for the C_{33} constant. For $CaCO_3$ the error is smaller or even negative, because the overestimate of the unit-cell volume leads to a smaller rigidity. However, also in this case the C_{33} component has a positive error. This means that the MgO_6 and CaO_6 coordination octahedra are not only more elongated, but also stiffer with respect to compression along the threefold axis, by comparison to experimental behaviour.

As a by-product of computing the relaxation energy of the C-O bond length, the vibrational frequency C-O of the Raman-active total-symmetrical A_{1g} mode (symmetrical stretching of the CO_3 group) can be obtained. Since there are three C-O bonds per formula-unit, the force constant is given by

$$k_{C-O} = (1/3)(d^2E/dr^2_{C-O})_0$$

TABLE 6. Theoretical and experimental (extrapolated to $T = 0$ K, cf. Table 2) elastic and vibrational properties of magnesite $MgCO_3$ and calcite $CaCO_3$. ν_{C-O} and γ_{C-O} are the frequency and the mode Grüneisen parameter, respectively, of the A_{1g} C-O stretching in calcite. a: Liu and Mernagh, [33].

	exp	calc		(%)
$MgCO_3$				
B_0	117	125	GPa	+6.8
C_{33}	159	187	GPa	+17.6
$C_{11}+C_{12}$	361	392	GPa	+8.6
$CaCO_3$				
B_0	80	75	GPa	-5.8
C_{33}	90	96	GPa	+6.5
$C_{11}+C_{12}$	230	224	GPa	-2.9
ν_{C-O}	32.6[a]	36.3	THz	+11.3
γ_{C-O}	0.4[a]	0.3		-25.0

hence the frequency

$$\nu_{C-O} = (1/2\pi)(k_{C-O}/M(O))^{1/2}$$

is derived, where $M(O)$ is the mass of the O atom. In Table 7 the results obtained for different volumes in the case of $CaCO_3$ are reported. The frequency at equilibrium volume V_0 is shown and compared to the measured Raman value[34] in Table 6: a moderate overestimate is observed, consistent with the systematic Hartree-Fock positive error of computed vibrational frequencies in molecular systems[22]. Also the mode Grüneisen parameter for the C-O stretching can be obtained, by differentiating the

TABLE 7. Force constant of the C-O bond (N m^{-1}) and vibrational frequency of the C-O stretching mode (THz) computed for calcite as functions of volume.

V/V_0	k_{C-O}	ν_{C-O}
0.8674	1480	37.6
0.8960	1469	37.4
0.9246	1434	37.0
0.9532	1413	36.7
0.9818	1389	36.4
1.0104	1365	36.1
1.0390	1333	35.7

volume dependence of the frequency: $\gamma_{C-O} = -(V/\nu_{C-O})d\nu_{C-O}/dV$. The computed value compares reasonably (Table 6) with that determined by Raman spectroscopy at high pressure[35,36].

3.3. BINDING ENERGIES

The difference between total crystal energy per formula unit (computed for the optimized equilibrium structure) and energies of isolated atoms gives E_B(HF), the Hartree-Fock approximation to the binding energy of magnesite and calcite (Table 8). The atomic energies were calculated with

TABLE 8. Total energies per formula unit for individual atoms and for $MgCO_3$ and $CaCO_3$ (calcite), and binding energies of magnesite and calcite (energy unit: hartree $= 4.35975\times10^{-18}$ J). Hartree-Fock and electron correlation (Perdew et al., [27]) corrected values are reported. Δ(%) is the percentage error of binding energy with respect to the experimental value (from thermochemical cycle).

	calc.			exp.
	HF	correl.	HF+correl.	
E(O)	-74.7943	-0.2552	-75.0495	—
E(C)	-37.6648	-0.1582	-37.8230	—
E(Mg)	-199.6042	-0.4480	-200.0522	—
E(Ca)	-676.7258	-0.8436	-677.5694	—
$E(MgCO_3)$	-462.3674	-1.6150	-463.9824	—
$E_B(MgCO_3)$	-0.716	-0.244	-0.960	-1.038
(%)	-31.0		-7.5	
$E(CaCO_3)$	-939.5363	-2.0093	-941.5455	—
$E_B(CaCO_3)$	-0.763	-0.242	-1.005	-1.087
Δ(%)	-29.8		-7.5	

the basis sets of Table 1, omitting the *d* orbitals and adding two diffuse *sp* shells for Mg and Ca (8-51111G and 8-651111G, respectively), and a single shell for O (8-4111G) and for C (6-211G). In this way the more diffuse character of atomic wavefunctions in the absence of chemical bonds was accounted for. The exponents of the outer shells were optimized. The contribution of electron correlation to the binding energy was estimated by the density-functional formula of Perdew et al.[29], applied to the Hartree-Fock charge densities of the crystal and of the isolated atoms.

For a comparison, the experimental values of the binding energies of magnesite and calcite were computed from the corresponding formation enthalpies at 298 K, by applying a conventional Born-Haber thermochemical cycle. Solid Mg, Ca, C, $MgCO_3$ and $CaCO_3$, and gaseous O_2 were

ideally cooled down to 0 K; sublimation of Mg, Ca and C and dissociation of O_2 molecules followed. Because no heat capacity data could be found for $MgCO_3$, its cooling energy was estimated from the corresponding result of calcite $CaCO_3$. The zero-point vibrational energies of the two carbonates was evaluated by the Debye model, using values Θ_D = 469K for calcite[37], and 739 K for magnesite obtained by application of Anderson's[38] method to the elastic constants. All other data involved are taken from Weast[39].

The HF theory substantially underestimates the binding energy (in absolute value), as expected. It should be noticed that omitting the d orbitals from the atomic basis sets in the two carbonates would increase the error to -40% . On the other hand, we believe that the values of E_B(HF) reported in Table 8 is close to the true HF limit. A large improvement is observed by including the corrections for electron correlation. The residual errors may be partly related to the approximations in the correlation correction, partly to some residual inadequacy of the HF variational basis set, and partly to approximations in the thermochemical data used to obtain the experimental binding energies.

3.4. CHEMICAL BONDING AND CHARGE DENSITY

The charge distribution on individual atoms and on chemical bonds in the two carbonate phases can be estimated by means of a Mulliken population analysis based on the corresponding Hartree-Fock wavefunctions (Table 9). Significant contributions are observed from the d shells of all atoms, but that of C is an order of magnitude larger than the other ones. This confirms the importance of d orbitals for a correct account of the C-O bonding. The net atomic charges indicate not only a strong back-transfer of electrons in the covalent C-O bond (consistently with the large overlap population), but also a substantial deviation from ionicity for the Mg-O interaction, and a smaller one but not negligible for Ca-O, too. The Mg charge is lower than those computed in MgO (1.95 *e*) and in MgF_2 (1.80 *e*) by Causà et al.[28] and Catti et al.[11], respectively, with similar orbital basis sets. The Mg-O overlap appears to be populated by a small but significant fraction of electrons, again pointing to the partially covalent bonding between Mg and the carbonate ions. The cation-oxygen interaction in the two carbonates scales reasonably for the Mg-Ca pair, according to the corresponding net atomic charges. This scaling can be compared to that observed by similar calculations on CaF_2 (z_{Ca} = 1.868 *e*) and MgF_2 (z_{Mg} = 1.803 *e*)[10, 11]. It should also be noticed the relevant antibonding population of the O-O interaction, due to strong repulsion between oxygen atoms belonging to the same CO_3 group.

TABLE 9. Mulliken charges and bond populations (e units) for individual atoms and for atomic pair overlap in $MgCO_3$.

	Mg	O	C	Ca	O	C
1*s*	2.000	1.997	1.997	2.000	1.997	1.997
2*sp*	6.456	2.704	1.671	8.077	2.675	1.705
3*sp*	1.448	2.471	0.944	4.564	2.764	1.048
4*sp*	0.327	1.791		2.440	1.513	
5*sp*				0.946		
3*d*	0.019	0.023	0.180	0.120	0.023	0.185
total	10.250	8.986	4.793	18.146	8.973	4.936
net charge z	+1.750	-0.986	+1.207	+1.854	-0.973	+1.064
	Mg-O	O-O	C-O	Ca-O	O-O	C-O
total	+0.029	-0.065	+0.389	-0.010	-0.110	+0.378

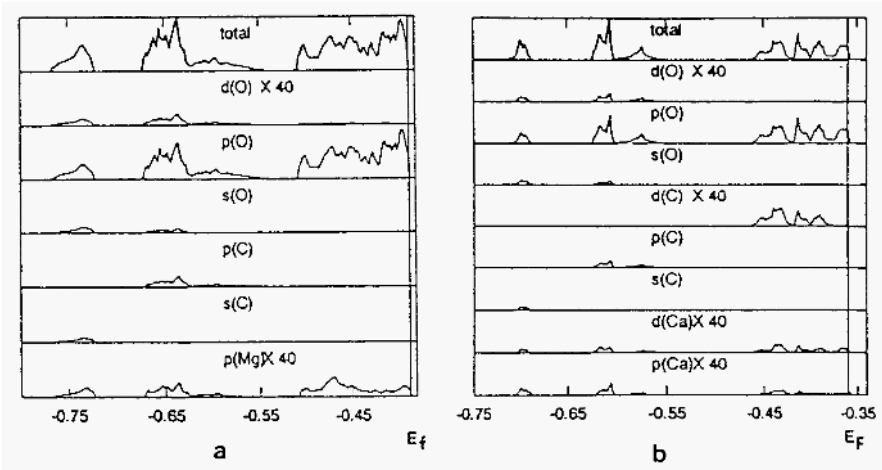

Figure 5. Total and projected densities of states (DOS) of MgCO3 (a) and CaCO3 (b). A Mulliken partition scheme was used to obtain atomic orbital contributions.

A more complete picture of the electron energy distribution is given by the density of states (DOS), reported in Fig. 5 for both magnesite and aragonite. In particular, by projecting the total DOS onto contributions of specific atomic orbitals, it is possible to interpret the band structure of

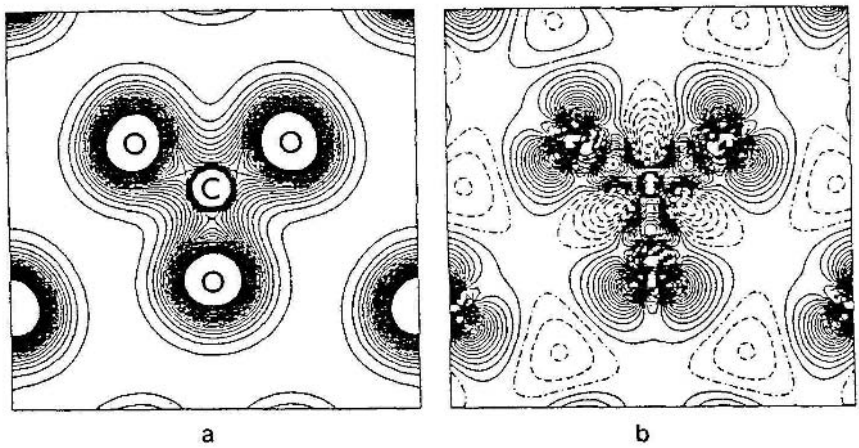

Figure 6. Total (a) and difference (crystal minus atomic superposition) (b) electron density maps on the plane of the CO_3 molecular unit for magnesite and calcite. Continuous, dashed-dotted and dashed lines indicate positive, zero and negative values, respectively. Contour lines are separated by 0.025 (a) and 0.005 e $Bohr^{-3}$ (b).

valence electrons. All three upper bands, starting from the Fermi energy downwards, are contributed by the *p* orbitals of O, plus *s*(O) and *p*(C) in the second band and *s*(O) and *s*(C) in the third one. Thus the first band is related to excess p electrons on O giving rise to the mainly ionic interaction with Mg or Ca. The second band, on the other hand, and to a lesser extent the third one as well, correspond to *sp* overlap in the C-O covalent bonding. This finely structured DOS of magnesite and calcite should be compared to the much simpler ones found for MgO and MgF_2, where the upper valence band gives a single sharp peak due to *p*(O) or *p*(F) electrons only.

The steric and anisotropic character of chemical bonding in magnesite and calcite is well represented by maps of total and difference (between crystal and atomic superposition) electron density. Results of this computation on the plane of the CO_3 group are shown in Fig. 6. The deformation of O atoms from spherical shape can be noticed even in the total map, but is very evident from the difference density. Three main features appear in Fig. 6b: the build up of bonding electron density along the C-O directions, the peculiar two-lobe shape of charge distribution around the O atoms, and the withdrawal of electrons from the angular sectors between C-O directions. These results are fully confirmed by inspection of the deformation density map[40] computed as difference between experimental X-ray data and data calculated by spherical atomic scattering factors. Similar features are also

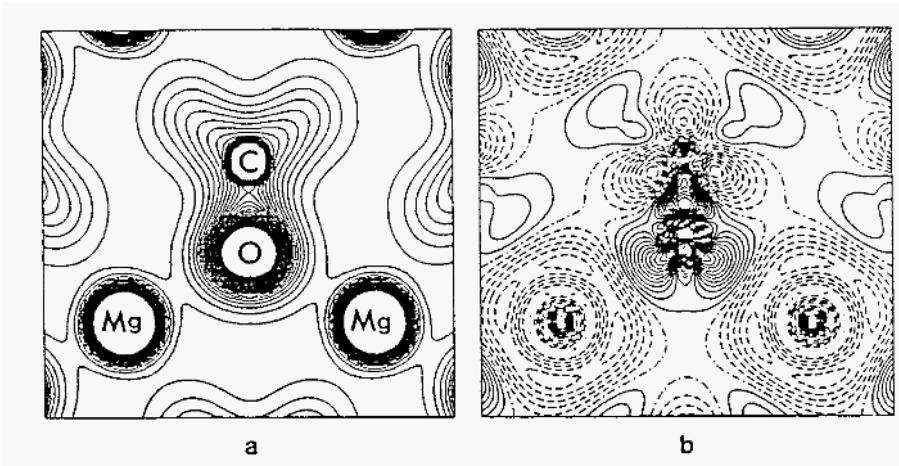

Figure 7. Total (a) and difference (b) electron density maps of magnesite on the plane 1-2-3-4 in Fig. 1, showing the coordination environment of the O atom. Symbols and scale as in Fig. 6.

observed in a difference density map computed for the isolated CO_3 ion, starting from 4-31G basis sets[41]. Thus the two-lobe shape of the extra electron charge on the oxygen atoms should not be ascribed to intermolecular interactions in the crystal, but rather to the bonding pattern of the carbonate ion.

Charge density maps were also calculated on the plane determined by atoms 1, 2 and 3 in Fig. 1, in order to show bonding features in the coordination shell of the O atom (Fig. 7). The latter is ionically bonded to two Mg or Ca atoms, and attains, with the covalent C-O bond, a planar triangular coordination. The total map for magnesite shows a small but significant electron density build up along the Mg-O direction, indicating a covalent contribution to the bonding, consistently with the Mulliken population analysis discussed above. The maps on the central section of the MgO_6 octahedron are shown in Fig. 8. An appreciable density is localized along the four Mg-O bonds, so that significant deviations from pure ionic bonding can be inferred. On the other hand, the difference map shows clearly the net electron charge on oxygen due to ionic charge transfer, and the typical contraction of the electron cloud with respect to free atoms already observed in other cases[10, 11].

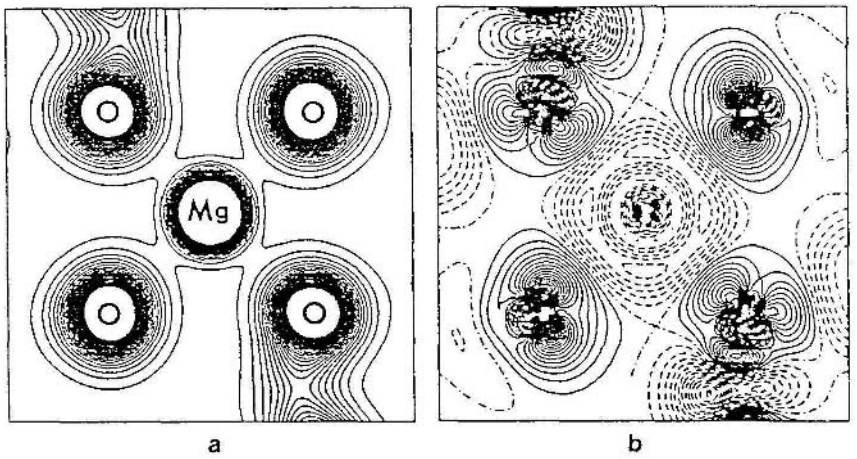

Figure 8. Total (a) and difference (b) electron density maps on a central section of the MgO_6 coordination octahedron in calcite symbols and scale as in Fig. 6.

4. Semiclassical results for calcite and aragonite

4.1. INTERATOMIC POTENTIALS

4.1.1. *Calcite*

The experimental static properties of calcite used in the fitting are reported in Table 2. The spread of values from different sources gives an idea of the real experimental uncertainty of these quantities.

A unit cell group analysis of the total vibrational representation of calcite (K=0) leads to the decomposition $A_{1g}+3A_{2g}+4E_g+2A_{1u}+3A_{2u}+5E_u$, corresponding to 27 optical normal modes (9 one- and 9 two-dimensional). Of these, 12 are internal modes of the two CO_3 molecular groups in the primitive cell, and 15 are external modes of these groups and of the two Ca atoms. The *g* and *u* modes are Raman and infrared active, respectively, with the exception of A_{2g} and A_{1u} modes which are forbidden for both. Experimental single crystal Raman[34] and IR[42] vibrational frequencies, together with the frequency of one of the A_{2g} modes from inelastic neutron scattering measurements[43], were used for the fitting of potentials, and they are reported extensively by Pavese et al.[6]. IR active frequencies show the TO-LO splitting effect; LO values were determined by Hellwege et al.

citeref41 by the minima of the dielectric function $\epsilon(\omega)$. The values of the dielectric tensor components (Table 2) come from Deer et al.[45] for $\omega = \infty$ and from Kaye and Laby[44] for $\omega = 0$.

Two potentials (RIM and SM) were optimized for calcite, with the calcium charge fixed at $z_{Ca} = 2e$ in both cases. In developing the SM potential we took as a starting point the parameters obtained in the RIM case, supplemented by values of the k_s force constant and of the z_{Os}/z_{Oc} charge separation. In addition, the crystal structure was relaxed statically to allow the O core and shell to reach an equilibrium distance, so as to provide the starting value of the dcs vector. Twelve parameters characterize the SM potential instead of nine (RIM), bearing in mind that the dispersive coefficient $c_{O\text{-}O}$ was kept fixed. The optimized parameters obtained at convergence for the RIM and SM potentials are reported in Table 10. The computed least-energy lattice constants are reported in Table 11 (static values), and can be compared to experimental values of Table 2. A slightly smaller cell, more elongated along the trigonal axis coinpared to the X-ray data is obtained with both potentials. However, the stretching effect is larger in the SM than in the RIM case, which show increases of 6.3 and 4.2%, respectively, of the c/a ratio. Consistent results are observed for the diagonal elastic constants (Table 12): the computed values of C_{11} and C_{33} are slightly larger and smaller, respectively, than experimental data (Table 2), so as to simulate more/less rigidity along the shortened/lengthened unit cell edges. Except for the C_{14} component, all other elastic constants give a good agreement between RIM and observed values (average relative deviation of 5.5%), while the SM results are slightly worse (a.r.d. 8.5%) because the C_{44} component is significantly underestimated. In addition, the dielectric behaviour of calcite appears to be simulated by the shell model rather poorly, particularly for the limit $\epsilon(\infty)$ at very high frequencies. The sign of the computed C_{14} elastic constant does not match that of the experimental value: this might be due to a different orientation of the Cartesian with respect to the crystallographic reference frame in the two cases.

As for the vibrational data, the internal frequencies of the CO_3 unit are nearly reproduced within the limits of experimental error (the average relative deviation is 2.4 and 1.5% for RIM and SM, respectively), except for the ν_{2u}(T) (-12.4% for RIM) and ν_{3u}(L) (-7% for SM) values, which show the largest deviations. The agreement is less good for the lattice modes, giving average errors of 15.1 and 8.6% for frequencies computed by the RIM and SM potentials, respectively. It should be remarked that frequencies not included in the fitting do not show significantly larger errors than those used in the fitting.

As expected, the shell model proves to be superior for simulating the lattice dynamics of calcite, while static properties (cell geometry and elastic constants) are reproduced better with the rigid ion model. However, the overall difference between RIM and SM results is comparatevely modest, and that can be considered to be a good performance for the simpler RIM

TABLE 10. Parameters of the RIM, RIM1, RIM2 and SM potentials (first, second, third and fourth line) used for calcite (RIM and SM) and aragonite (RIM, RIM1 and RIM2).

z_O (e)	-0.995	z_{Ca}(e)	2.000
	-0.939		2.000
	-0.794		1.515
	-1.095	(zos= -2.662, zoc= 1.567)	2.000
	O-O	Ca-O	C-O
A_{ij}(eV)	14683.5	1870.3	54129.5x10 ^{8}
	1563461	2043.2	14461.0 x10^{7}
	6106.3	83062.8	314629.3x10 ^{8}
	20431.8	1605.4	13258.3x10 ^{8}
p_{ij} (Å)	0.2107	0.2893	0.0402
	0.1366	0.2886	0.0458
	0.2326	0.1856	0.0370
	0.2127	0.2965	0.0415
c_{ij} (eV Å^6)	3.47	0	0
	3.47		
	3.47		
	3.47		
k_Θ (eVrad^{-2})	2.550	k_ϕ(eV)	0.092
	4.040		0.156
	17.752		0.334
	2.881		0.113
k_s (eV Å^{-2})	0		
	0		
	0		
	177.4		

potential. On the other hand, the shell model appears somehow unsatisfactory in fitting the dielectric behaviour.

4.1.2. *Aragonite*

The orthorhombic unit-cell of aragonite contains 20 atoms instead of 10 as for calcite, so that the amount of static and dynamic crystal data avail-

	4.908	17.493	364.9	static	
0					
	4.922	17.639	370.1		
0					
300	4.926	17.678	371.5		RIM
500	4.932	17.739	373.7		
	4.873	17.718	364.4	static	
0					
	4.884	17.825	368.2		
0					
300	4.888	17.861	369.6		SM
500	4.894	17.917	371.6		

able and the amount of computation, needed to optimize potentials, is much larger. The structural variables are nine independent atomic coordinates and three cell edges; a slight pyramidal deformation of the CO_3 group is observed, with respect to the planar configuration present in calcite. **A** single very old set of elastic data[46] is available and is reported by Hearmon[47]. The symmetry of optical phonons at the centre of Brillouin zone is described by the group-theoretical set of irreducible representations $9A_g+6B1g+6B2g+9B3g+6Au+8B1u+8B2u+5B3u$ giving the required number of 57 one-dimensional normal modes of vibration (24 are internal and 33 external modes). All g phonons are Raman active, while u phonons are IR active except for those of type A,. Infrared frequencies were measured by Schaefer and Matossi[48] and are reported by later authors[49, 19], while Raman data come from Couture[50]. This set of experimental frequencies (set I) is not complete, and assignments can only be done unambiguously for internal modes, as external frequencies are quite close to one another in a fairly narrow range. A more recent spectroscopic study of aragonite[51], concerning Raman data for internal and external modes, and IR data for internal modes only, provides the set II of data. The agreement with the former set of measurements is good, except for some inconsistencies concerning the symmetry assignments of two Raman and one IR phonon. The

TABLE 12. Elastic constants (GPa) and dielectric tensor components of calcite computed by RIM and SM potentials. Pecentage deviations with respect to some of the experimental values reported in Table 2 are given.

	RIM	(%)	SM	(%)
C_{11}	152.7	+3.9	152.6	-0.0
C_{33}	77.8	-9.0	79.0	-7.6
C_{44}	30.4	-8.2	24.4	-26.3
C_{66}	48.0	+5.5	47.6	+4.6
C_{12}	56.8	+1.6	57.3	+2.5
C_{13}	53.9	-0.4	50.8	-6.1
C_{14}	10.8		7.3	
$\epsilon(0)_{11}$			5.7	
$\epsilon(0)_{33}$			8.5	
$\epsilon(\infty)_{11}$			1.37	
$\epsilon(\infty)_{33}$			1.33	

first potential studied (RIM1) has the same analytical form as RIM of calcite. However, as its performance turned out to be worse, the constraint $z_{Ca} = +2e$ was relaxed by optimizing a second potential (RIM2) with z_{Ca} as tenth parameter to be fitted. The parameters obtained for both potentials are reported in Table 10. No shell model-type potential (cf. SM of calcite) was tried for aragonite, because it would have nearly doubled the number of parameters. In addition, results on calcite show that the improvement of the SM over the RIM potential was not significant. The values of unit-cell edges and elastic constants, computed by the RIM1 and RIM2 potentials, are compared to measured data in Table 13. The unit-cell simulated by RIM1 appears to be slightly elongated parallel to **c** and contracted along the other two axes; this resembles the behaviour observed in calcite, taking into account that for both structures the **c** direction is normal to planes of CO_3 groups. The average relative deviation of lattice constants is similar in the two cases, while the RIM2 potential nearly exactly reproduces the unit-cell geometry of aragonite with no distortion. As for the elastic constants, the a.r.d.'s obtained for RIM1 (18.5%) and RIM2 (10.0%) cases, excluding the off-diagonal components, are clearly less satisfactory than those found for calcite; the C_{12}, C_{13} and C_{23} terms appear to be quite incorrect. However, there are some reasons to believe that these very old experimental values may be affected by significant errors: in particular, the off-diagonal components are much smaller than the corresponding ones of calcite, while this is not the case for diagonal terms.

TABLE 13. Experimental unit-cell data (De Villiers, 1971) and elastic constants[45] of aragonite compared to values calculated by RIM1 and RIM2 (optimized on aragonite) and RIM (optimized on calcite) potentials. Quantities with asterisks were not included in the fitting of RIM1 and RIM2.

	exp.	RIM1	RIM2	RIM	
a	4.961	4.875	4.972	4.951	Å
b	7.967	7.904	7.979	7.940	
c	5.740	5.896	5.730	5.736	
V	226.9	227.2	227.3	225.5	Å^3
C_{11}	159.6	164.4	157.7	194.2	GPa
C_{22}	87.0	112.0	100.9	117.1	
C_{33}	85.0	59.2	68.3	71.3	
C_{44}	41.3	40.5	36.0	44.1	
C_{55}	25.6	33.9	24.1	34.5	
C_{66}	42.7	49.0	41.1	43.8	
C_{12}	36.6'	65.3	58.0	65.9	
C_{13}	2.0'	39.0	34.1	35.7	
C_{14}	15.9'	48.2	50.4	50.2	

The agreement observed between calculated vibrational frequencies and the set I of experimental data is surprisingly good, not only for internal (a.r.d. 1.7 and 2.7% for RIM1 and RIM2, respectively) but also for external (10.3 and 11.0%) modes, taking into account that the latter were not included in the fitting and that their number is large. These results are even better than those obtained by the rigid ion model for calcite. However, it is surprising that the more flexible RIM2 potential gives a slightly worse agreement with vibrational data than RIM1; this is probably related

to the significant superiority of RIM2 over RIM1 in describing the lattice and elastic properties. Thus relaxing the calcium electric charge from its formal value proves to affect the static properties of aragonite much more than the dynamic ones. As for the set II of measured data, they compare similarly with computed results.

4.1.3. *Discussion*

It would he highly desirable to obtain a single potential that accounts simultaneously for the properties of both polymorphs of $CaCO_3$. Optimizing a rigid ion model for both calcite and aragonite was indeed attempted, but unfortunately failed because of the excessive number of physical constraints. Thus a different approach was tried, i.e. exchanging the potentials between the two polymorphs. This could only be done for the rigid ion models (RIM for calcite, and RIM1 and RIM2 for aragonite), since a shell model was not developed for aragonite for the reasons discussed above.

The results of using the RIM potential to model aragonite are reported in Table 13. The most direct comparison should be done with results pertaining to RIM1 rather than to RIM2, where the z_{Ca} charge was varied as well. The overall agreement between calculated and experimental data is similar for both RIM and RIM1. For the unit-cell geometry, the results of RIM are even better than those of RIM1, while for the elastic constants a slightly worse agreement is observed, with an average relative deviation of 19.4 against 18.5%. External and internal vibrational frequencies give a.r.d.'s of 11.8 and 2.5%, respectively, against 10.3 and 1.7% for RIM1. These results can be considered as satisfactory, taking into account that none of the aragonite data was included in the fitting of the RIM potential. The weak point of simulations for aragonite are the elastic constants, the measured values of which may not be fully reliable as argued above.

The RIM1 and RIM2 potentials, fitted to aragonite, were used to compute the properties of calcite. However, in this case the results (which are not reported in detail for shortness) are definitely less satsfactory than those obtained by the RIM potential optimized on calcite itself. The unit-cell volume increases by 6.2 and 3.9% for RIM1 and RIM2, respectively, against -0.8% for RIM. The elastic constants show a.r.d.'s of 12.4 and 21.2% against 5.5%. On the other hand, the RIM1 potential produces an agreement between calculated and observed optical phonons for the zone centre comparable to that of RIM, while RIM2 is clearly worse. This seems to confirm again that the real difficulty in optimizing a unique potential for both polymorphs lies in the correct, reproduction of the elastic constants of aragonite. Thus, both potentials RIM and RIM1 simulate the vibrational behaviour of calcite and aragonite. However, for the static properties RIM

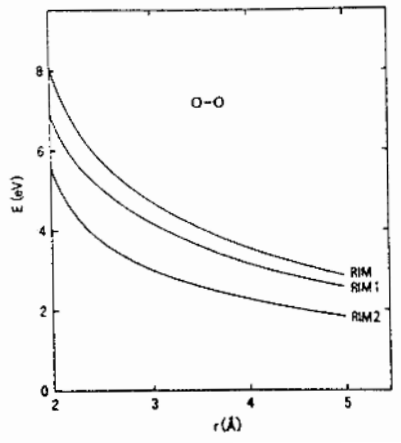

Figure 9. Born-type potential energy of O-O interactions vs. interatomic distance, computed using the RIM, RIM1 and RIM2 parameters (cf. Tables 3 and 4).

gives comparable results to RIM1 on aragonite, while RIM1 works decidedly less well than RIM for calcite. The RIM2 potential, with its fractional charge on Ca, is even more specific to aragonite and even less transferable to calcite than is RIM1.

The three rigid-ion potentials RIM, RIM1 and RIM2 are compared by plotting the energy vs. interatomic distance $E(r)$ for the O-O (Fig. 9) and Ca-O (Fig. 10) atom-atom pairs. A common trend is observed: the two-body potential energy decreases (in absolute value) from RIM to RIM1, and to a greater extent from RIM1 to RIM2. Such an effect may be ascribed to two causes. First, the aragonite structure is characterized by a smaller molar volume and shorter interatomic distances than calcite. This would lead on the average to stronger Ca-O attraction and O-O repulsion energies, which are balanced by lowering the interaction potentials RIM1 and RIM2 fitted to aragonite with respect to RIM fitted to calcite. Second, by decreasing the interaction strength the errors of poorly reproduced properties (like some elastic constants of aragonite) are lowered significantly, thus improving the fitting of aragonite. This behaviour is enhanced for the RIM2 potential because the reduction of z_{Ca} charge allows for a larger decrease of all charges, such that the two-body potentials are lowered much more.

As for the C-O interaction, the most evident effect is given by the increase of the angular force constant k_Θ in the sequence RIM RIM1 RIM2 (Table 10). In the RIM2 case, the value attained by k_Θ seems to be really too large to be physically reasonable. The effect balances the decrease of

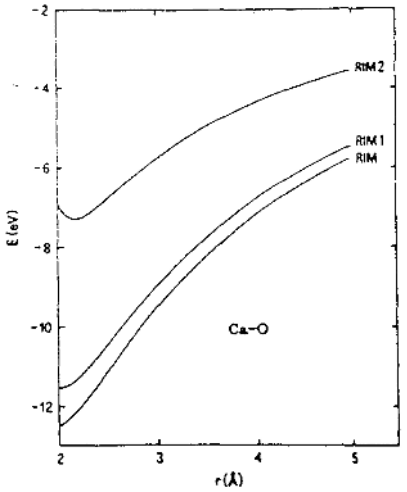

Figure 10. Born-type potential energy of Ca-O interactions vs. interatomic distance, computed using the RIM, RIM1 and RIM2 parameters (cf. Tables 3 and 4).

O-O repulsion, which would bring about too weak a O-C-O bending term.

It can be concluded that a rigid ion model supplemented by bond-bending harmonic interactions within CO_3 (RIM potential), fitted to calcite properties, is able to account for structural, elastic and vibrational data of both aragonite and calcite. The slight improvement obtained by a specific fitting to aragonite (RIM1) might be related to the poor quality of some experimental data of that phase. The RIM potential is believed to be transferable to other $CaCO_3$ polymorphs, and thus will be the basis for theoretical studies of thermodynamics and phase equilibria in the calcium carbonate system.

4.2. QUASI-HARMONIC EQUILIBRATION

4.2.1. *Calcite*

Quasi-harmonic equilibrations were performed at $p = 1$ bar and $T = 0$, 300 and 500 K. The unit-cell constants obtained are reported in Table 11 for each of the two potentials, together with results of the purely static equilibration (at 0 K). The most interesting feature concerns the volume behaviour, which shows a strong increase from its static value at 0 K by including the zero-point contribution of vibrational energy. This amounts to 46.6 or 47.5 kJ mol^{-1} for the RIM or SM potential, respectively, and produces a vibrational expansion of 1.4%, i. e. larger than the thermal

expansion occurring from 0 to 500 K. The corresponding zero-point vibrational pressure is reported in Table 14. It appears crucial, therefore, to con-

TABLE 14. Some thermodynamic quantities of calcite computed from quasi-harmonic equilibrations. First and second lines report calculatd RIM and SM results, respectively; in the third lines (where present) experimental values are shown for comparison. a: Stavely and Linford [35]; b: Jacobs et al. [51]; c: Dandekar and Ruoff [31]; d: Interpolation of data by Rao et al. [53] and Chessin et al. [52]. *: Derived from the relation $\gamma = V\alpha B_T/C_v$ using experimental values.

T	0	300	500	K
	0.830	0.841	0.845	
	0.725	0.798	0.776	
		0.624*	0.509*	
P^{vib}	1.030	1.303	1.717	GPa
	0.784	1.049	1.441	
C_v	0.0	16.03	19.91	J K^{-1} g $atom^{-1}$
	0.0	15.89	19.70	
		16.69 [a]	20.56 [b]	
C_p	0.0	16.13	20.17	
	0.0	16.05	19.91	
		16.75 [a]	20.66 [b]	
B_T	72.07	71.59	69.92	GPa
	73.52	72.91	71.29	
		73.1 [c]	67.9 [c]	
α	0.0	2.51	3.19	10^{-5} K^{-1}
	0.0	2.34	2.86	
		1.93 [d]	2.08 [d]	

sider the lattice dynamics at 0 K to account correctly for absolute crystal volumes. The computed unit-cell is more elongated than the experimental one (particularly in the shell-model case), and this distortion is maintained through the temperature range. The same effect is observed in the purely static calculation at 0 K by Dove et al. [8]. The absolute value of the volume at room temperature reproduces the observed result satisfactorily, or with a slight overestimate (most marked for the RIM potential).

A better insight into the quality of the quasi-harmonic calculation and corresponding equation of state is obtained by considering the other ther-

modynamic quantities reported in Table 14. A good agreement between computed and observed values (where available) is found in all cases, except for the average Grüeneisen parameter γ and the related thermal expansion coefficient α: this is overestimated by 30% (RIM) or 21% (SM) at 300 K, and the discrepancy tends to increase with temperature. It may be worthwhile to look at some selected mode Grüneisen parameters (Table 15) for which experimental results have been obtained by high-pressure Raman spectroscopy[35]. In the case of the internal modes, the RIM computed γ_n

TABLE 15. Vibrational frequencies (THz) and mode Grüneisen parameters γ_n for five Raman active modes of calcite. a: Liu and Mernagh [33].

		exp[a]	RIM	SM
ν_{13}	Eg	4.68	4.07	3.67
γ_n		1.18	0.91	0.97
ν_{14}	Eg	8.48	7.66	7.33
γ_n		1.38	2.11	2.05
ν_{4g}	Eg	21.38	21.07	21.25
γ_n		0.24	0.32	0.17
ν_{1g}	A1g	32.53	30.54	32.23
γ_n		0.41	0.71	0.29
ν_{3g}	Eg	42.99	38.64	40.78
γ_n		0.47	1.01	0.69

values are systematically larger than the SM ones, while the experimental values lie in-between. On the other hand, the experimental value of γ is even smaller than the corresponding SM result (Table 14). Thus, the reason for the error in γ appears to be related to a systematic overestimate of γ_n values of most external modes by both the RIM and SM models, as indicated by the case of the γ_{14} mode. Indeed most modes with frequencies in the range 6 to 9 THz show calculated n parameters larger than 2, and these are all probably too large. This error is probably not related to the neglect of intrinsic anharmonicity, but rather to inadequacies either in the potentials (cf. the improvement of SM over RIM results) or in the approximations used to simplify the quasi-harmonic model. In particular, our neglect of the temperature dependence of the bulk modulus may play an important role, and we believe that future calculations including the explicit vibrational component of B_T would improve the results significantly.

Let us now examine the thermodynamic quantities computed over a range of temperatures, based on the structure equilibrated at 300 K. The density of vibrational frequencies is shown in Fig. 11 for the RIM and SM potentials. Some differences concerning the internal modes of the CO_3

groups can be remarked upon: the shell model produces a significant increase of frequencies, decreasing the dispersion of modes as well, so that the corresponding peaks approach the shape of Dirac's delta functions. The heat capacity at constant volume C_v has been calculated in the range 0 to 750 K. For comparison, two sets of experimental C_p data have been considered: from 0 to 300 K[37] and from 300 to 750 K[52]. The first set comes from very accurate measurements by adiabatic calorimetry, while the second one is based on less reliable DSC (differential scanning calorimetry) results. All these values were transformed into C_v data by the equation $C_p - C_v = a^2 B_T V T$. The adiabatic compressibility $\beta_s = 1/B_s$ of calcite was measured between 160 and 523 K by Dandekar and Ruoff[33]; we used the quadratic fit of these data $\beta_s = 12.515 + 0.003039T + 0.2562 \times 10^{-5} T^2 (10^{-3} \mathrm{GPa}^{-1})$ over the whole temperature range considered. The unit-cell edges of calcite are available as a function of temperature in the ranges 110 to 300 K[53] and from 300 to 800 K[54]. The low temperature results underestimate sys-

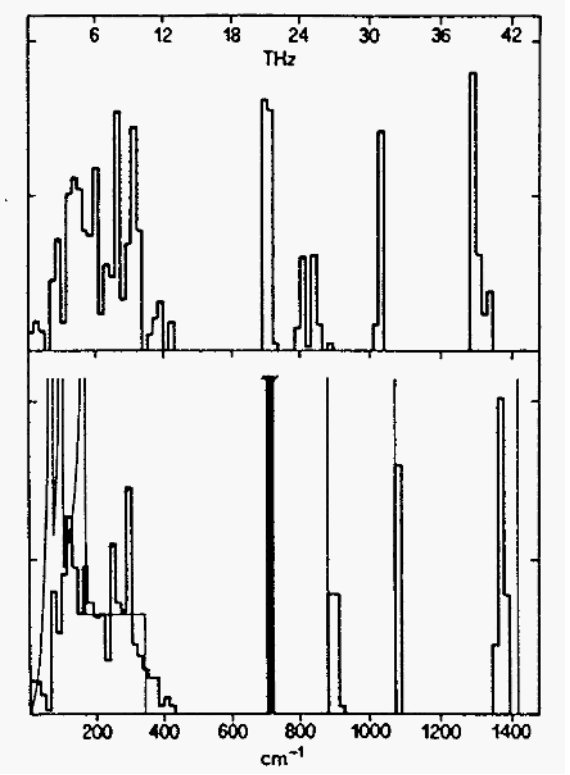

Figure 11. Density of vibrational frequencies of calcite, computed by the RIM (rigid-ion-model) potential (above), by the SM (shell model) potential and by Kieffer's model (below, thick and thin lines, respectively).

tematically the c value, as discussed by Rao et al[54]; so we increased all low-T values of V by 1.1 Å3 in order to join them smoothly to the high-T volumes. Then a parabolic interpolation of all data gave the relation $V = 365.68 + 0.006199T + 0.1468 \times 10^{-5}T^2$, which was used to derive the coefficient of thermal expansion $\alpha(T)$ to be put into the above formula. In Fig. 12, the $C_v(T)$ curves corresponding to experimental and calculated results are shown. The values of C_v computed by the RIM model appear to be systematically underestimated by 2 - 4 higher temperatures. The shell model values, on the other hand, are overestimated at low temperature (below 160 K), while for $T > 260$ K they are affected by a negative error larger than that of RIM results. It should be noted that a comparison of computed vs. measured C_p values would have shown a smaller error than in the C_v case, because the coefficient of thermal expansion a is overestimated by the calculation, and so the $C_p - C_v$ term partly compensates for the C_v error. On the other hand, using the crystal structure unit-cells equilibrated at 100 K and at 500 K to com pute C_v at low and at high temperatures, respectively, improves the results by only a small fraction of the error observed with respect to experimental data.

It is also interesting to examine the C_v results obtained for calcite by using the empirical and purely harmonic Kieffer's model[55, 56, 57]. A density of states function was built up by considering three acoustic modes with sin-like dispersion and cut off frequencies of 76, 102 and 173 cm^{-1}

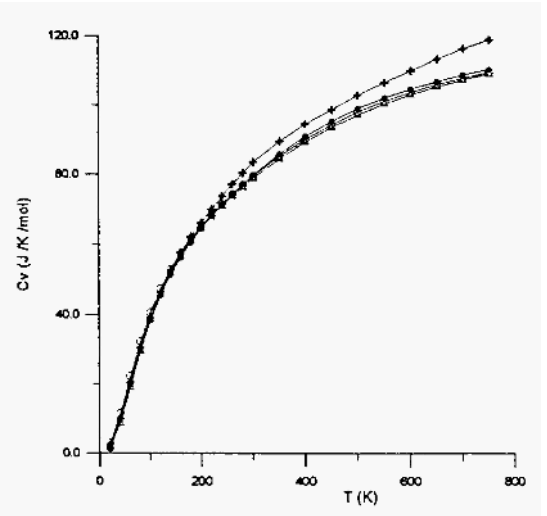

Fig. 12. Curves of C_v versus T for experimental (crosses, from C_p results of Stavely and Linford[35] and Jacobs et al.[51]) and computed (dots: RIM; circles: SM; triangles: Kieffer's model) data of calcite.

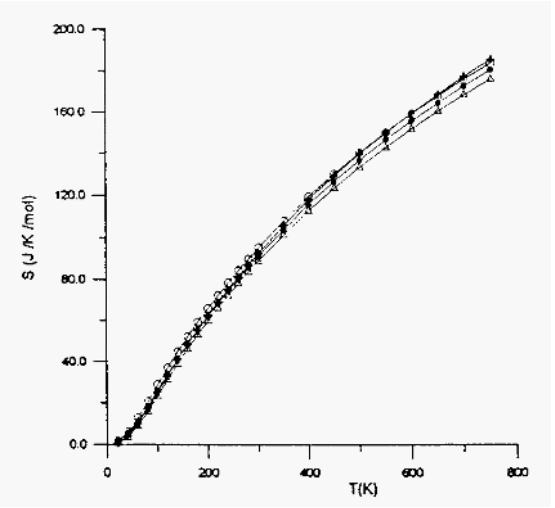

Figure 13. Curves of entropy S versus T for experimental and computed data of calcite. Symbols as in Fig. 12.

(derived from elastic constants), four Einstein oscillators at 714, 881, 1076 and 1455 cm^{-1} representing, with appropriate weights, the internal optical modes, and an optic continuum ranging from 113 to 345 cm^{-1} (Fig. 11). The computed C_v values are plotted against T in Fig. 12 and compared to those obtained by the full lattice- dynamical calculations and to the experimental values. The results of Kieffer's model (KM) are surprisingly good below 250 K, where they compare well with RIM and SM data; at higher temperatures, however, they show significantly smaller, though still reasonable, values.

In Fig. 13 the entropy curves are shown. The RIM and SM data have been computed by the relation $S = \int_0^T (C_p/T)\,dT$, while for the KM C_p has been replaced by C_v in the integration formula.The agreement is very good for the RIM results at low temperature; at high temperatures, a slight underestimation is observed. The SM data behave similarly as in the C_v case, i.e. they show positive and negative errors at low and high temperatures, respectively. KM results are always underestimated, probably as a consequence of neglecting the $C_p - C_v$ anharmonic term.

4.2.2. *Aragonite*

The crystal structure of aragonite was equilibrated statically at $T = 0$ K, and quasi-harmonically at room temperature (Table 16). By examination of data at 300 K, for which a direct comparison with experimental results[58] is possible, the computed unit-cell volume appears to be signifi-

TABLE 16. Unit-cell edges and volume of aragonite calculated by static (0 K) and quasi-harmonic (300 K) equilibrations (RIM and RIM1 potentials).

T (K)	0	300	
a (Å)	4.951	4.982	RIM
	4.875	4.894	RIM1
b(Å)	7.940	8.021	RIM
	7.904	7.954	RIM1
c(Å)	5.736	5.864	RIM
	5.896	5.986	RIM 1
V(Å^3)	225.5	234.3	RIM
	227.2	233.0	RIM1

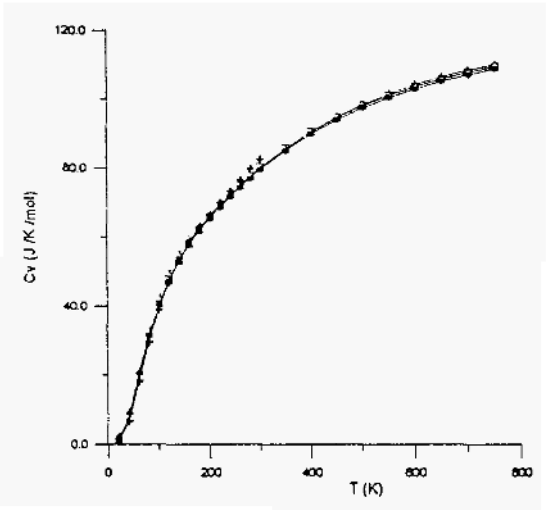

Figure 14. Curves of experimental C_p (crosses, from results of Stavely and Linford [35] and computed C_v (dots: RIM; squares: RIM1; triangles: Kieffer's model) data of aragonite versus T.

cantly overestimated both by the RIM (+3.3%) and RIM1 (+2.7%) potentials. This effect is mainly contributed by the **c** edge, which is correlated with the distance between (001) layers of CO_3 triangles. The same effect, though to a lesser extent, was obtained for calcite as well. An explanation is easily found by considering that for both phases the potentials were fitted

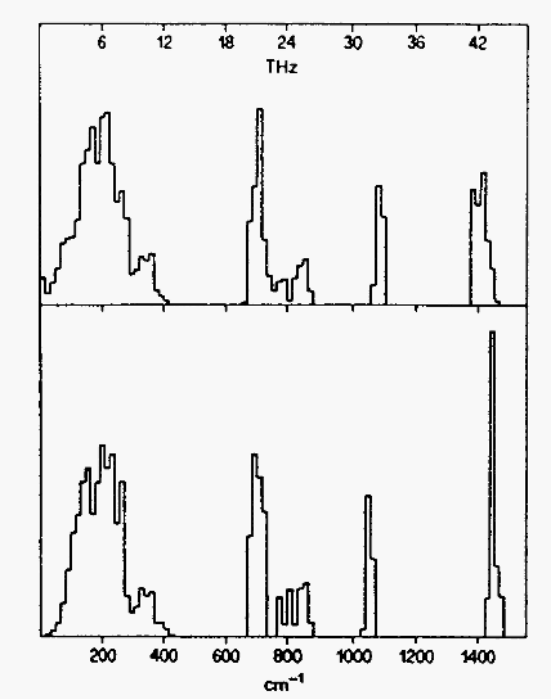

Figure 15. Density of vibrational frequencies of aragonite, calculated by the RIM (above) and RIM1 (below) potentials.

to the room temperature experimental lattice constants, but using purely static methods which are appropriate, in principle, for the absolute zero only. Thus computed volumes at 0 K resemble those measured at 300 K, while those calculated at 300 K are obviously overestimated. This weak point would be hard to remove, because the optimization of the potential is too complex a process to include a quasi-harmonic equilibration step in a self-consistent way, at least with the present computational state of the art. The RIM1 potential gives a slightly smaller volume error than RIM, but at the cost of a larger anisotropy error of the unit cell, as the computed *c/a* ratio is larger by 5.7% (RIM1) and 1.7% (RIM) than the measured value.

As for the quantities related directly to the quasi-harmonic model, i.e. Grüneisen parameter and thermal expansion coefficient, the only data derived from measurements are, to our knowledge, those reported in diagrams by Salje and Viswanathan[20]: $\gamma = 1.80$ and $\alpha = 6.5 \times 10^{-5}$ K^{-1} at room temperature. These should be compared with the values computed by the RIM ($\gamma = 2.61$, $\alpha = 11.5 \times 10^{-5}$ K^{-1}) and RIM1 ($\gamma = 1.50$, $\alpha = 5.8 \times 10^{-5}$

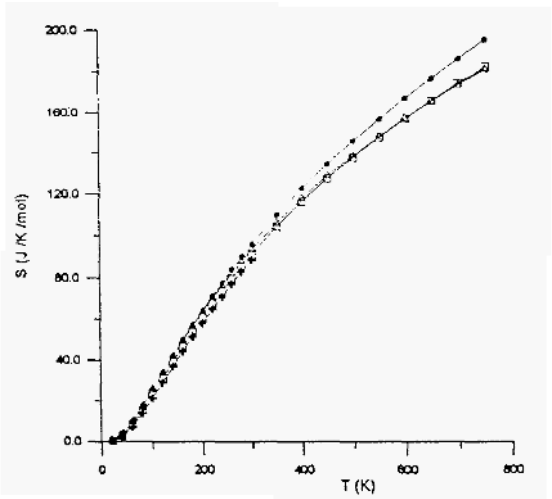

Figure 16. Curves of entropy S versus T for experimental and computed data of aragonite. Symbols as in Fig. 14.

K^{-1}) potentials, which turn out to be substantially over- and slightly underestimated, respectively. The difference between these results is remarkable considering the similarity of the potentials. In Fig. 14 the C_v values calculated by the full lattice dynamical method (RIM and RIM1 potentials, equilibration at 300 K) and by the empirical Kieffer's model are reported and compared to the experimental C_p up to 300 K[37]. No conversion from C_p to C_v was attempted, because insufficient data on thermal expansion vs. temperature was available. However, the difference $C_p - C_v$ can be estimated from the corresponding one for calcite (Table 14), which turns out to be much smaller than deviations between measured and theoretical C_v values; thus C_p can be safely used for the sake of comparison with computed C_v in the case of aragonite. Calculated results are systematically underestimated (by about 3% at 300 K) above 150 K for RIM and RIM1 and above 200 K for KM; the Kieffer's model appears to give as good results as the RIM potential, while the RIM1 data are slightly better.

The densities of vibrational states for the two potentials (Fig. 15) are actually very similar, except for a somewhat wider gap for RIM1 between the two peaks at higher frequencies, corresponding to inner modes of CO_3. As for the Kieffer's model, the cut off frequencies of acoustic modes were derived from elastic constants by the Voigt-Reuss-Hill approximation[38], amounting to 51, 66 and 90 cm^{-1}. An optic continuum ranging from 113 to 287 cm^{-1} was used, and four Einstein oscillators at 708,867, 1042 and 1470 cm^{-1} with appropriate weights represented the internal optical modes. The

values of the acoustic cut off frequencies appear surprisingly low, by comparison with the corresponding frequencies found for calcite and also with the RIM and RIM1 densities of states of Fig. 12. Nevertheless, KM results for C_v are very satisfactory, confirming the importance of error cancelling in this simple model based on empirical spectroscopic data. The calculation of entropy seems to be a more severe test with respect to heat capacity (Fig. 16). The RIM error has an opposite sign and is substantially larger than in the case of calcite, while results are more satisfactory with the RIM1 potential, which is specific for aragonite.

5. Conclusions

The $MgCO_3$ and $CaCO_3$ phases with rombohedral calcite structure have been studied by first-principles quantum-mechanical techniques. A detailed picture of structural relaxation as a function of volume has been established, in good agreement with experimental data at room pressure. These results, together with the evaluation of some relevant elastic properties, allow the prediction of the static equations of state at the athermal limit from ab initio calculations of these carbonates. The covalent bonding inside CO_3 molecular units and the prevalently ionic Mg-O and Ca-O interactions have been fully characterized: a non negligible electron transfer between the divalent cation and CO_3 ions, reflecting partial covalency between these two entities, appears. The Ca-O bond length is slightly overestimated, while Mg-O is not, consistently with results for simple oxides. The high-pressure simulation shows a significantly larger compressibility of the calcite structure with respect to magnesite, according to thermodynamic instability of the former phase against denser polymorphs. These results can be useful for modelling pressure- dependent phase transitions and ion-exchange reactions in the carbonate system, taking also into account their consistency with the behaviour of the mixed Ca-Mg phase dolomite.

The calcite and aragonite polymorphs of $CaCO_3$ have also been investigated by use of empirical interatomic potentials including two-, three- and four-body terms, in the frame of a point-charge model supplemented by covalent angular contributions. In particular, by fitting the parameters to structural, elastic and vibrational properties, a charge distribution within the CO_3 molecular ion has been obtained which compares favourably with the ab initio results. The partial atomic charges from different sources are reported in Table 17. In model (b) ([18] Yuen et al., 1978) the energy parameters were fitted solely to the equilibrium structure, whereas in (c) ([6] Pavese et al., 1992; cf. also RIM in Table 10) and (d) ([8] Dove et al., 1992) the elastic and vibrational properties were included in the op-

TABLE 17. Atomic charges (e units) in calcite and magnesite. MP = Mulliken net charges from ab initio Hartree-Fock results; EF = empirical fitting to physical properties. a: Catti et al., [60]; b: Yuen et. al., [18]; c: Pavese et al., [7]; d: Dove et al. [8]; e: Catti et al., [5]

	MP	EF		
	a	b	c	d
Ca	1.865	2.00	2.00	1.642
O	-0.980	-0.98	-0.995	-0.894
C	1.075	0.95	0.985	1.041
	e			
Mg	1.750			
O	-0.986			
C	1.207			

timization process. In (b) and (c) the calcium charge was kept fixed at the formal $+2e$ value. By inspection of Table 17, a surprising consistency appears among charge distributions on the CO_3 molecular group obtained by different methods. On the other hand, the Hartree-Fock charge on Ca is intermediate between the formal and the fitted value obtained in model (d). These results support the belief that point-charge models with fractional charges, if properly treated, may have a quite unambiguous physical meaning in the atomistic simulation of crystals.

The optimized potentials for calcite and aragonite have allowed us to simulate the full thermodynamic behaviour of both phases, by use of the quasi-harmonic model. The quality of results obtained is very satisfactory for heat capacity and entropy data, but less good for thermal expansion. Use of a shell model (SM) for calcite seems to improve somewhat the thermal expansion results, but not those of heat capacity and entropy. On the other hand, the RIM potential optimized on calcite is not as good for aragonite, because both the entropy and the thermal expansion of this phase are overestimated significantly, while C_v is reproduced in a satisfactory way. Use of an "ad hoc" aragonite potential (RIM1) is necessary to obtain better results. The poor quality of some experimental data (e.g. the elastic constants) of aragonite may contribute to difficulties in fitting a fully transferable potential. Further, it should be stressed how critical it is to simulate the correct value for the thermal expansion coefficient: the relation between mode Grüneisen parameters and details of the interatomic potential is poorly understood, in spite of its crucial role. These points should be investigated more deeply, in order to be able to model fully equation-of-state behaviour and phase equalibria of crystalline phases by atomistic

calculations.

References

1. Goldsmith, J.R. (1983) Phase relations of rombohedral carbonates, in R.J. Reeder (ed.), Carbonates: Mineralogy and Chemistry, *Rev. Mineral.* vol. **11**, Mineralogical Society of America, Washington, pp. 49-76.
2. Speer, J.A. (1983) Crystal chemistry and phase relations of orthorhombic carbonates, in R.J. Reeder (ed.), *Carbonates: Mineralogy and Chemistry,* Rev. Mineral. vol. **11,** Mineralogical Society of America, Washington, pp. 145-189.
3. Carlson, W.D. (1983) The polymorphs of $CaCO_3$ and the aragonite- calcite transformation, in R.J. Reeder (ed.), Carbonates: *Mineralogy and Chemistry, Rev. Mineral.* vol. **11**, Mineralogical Society of America, Washington, pp. 191-225.
4. Williams, Q., Collerson, B., and Knittle, E. (1992) Vibrational spectra of magnesite ($MgCO_3$) and calcite-III at high pressures, *Am. Mineral.* **77,** 1158-1165.
5. Catti, M., Pavese, A., Dovesi, R., and Saunders, V.R. (1993) Static lattice and electron properties of $MgCO_3$ (magnesite), by ab initio periodic Hartree-Fock calculations, *Phys. Rev.* **B 47,** 9189-9198.
6. Pavese, A., Catti, M., Price, G.D., and Jackson, R.A. (1992) Interatomic potentials for $CaCO_3$ polymorphs (calcite and aragonite), fitted to elastic and vibrational data, *Phys. Chem. Minerals* **19,** 80-87.
7. Catti, M., Pavese, A., and Price, G.D. (1993) Thermodynamic properties of $CaCO_3$ calcite and aragonite: a quasi-harmonic calculation, *Phys. Chem. Minerals* **19**, 472-479.
8. Dove, M.T., Winkler, B., Leslie, M., Harris, M.J., and Salje, E.K.H. (1992) A new interatomic potential model for calcite: applications to lattice dynamics studies, phase transition, and isotope fractionation, *Am. Mineral.* **77,** 244-250.
9. Pisani, C., Dovesi, R., and Roetti, C. (1988) Hartree-Fock Ab Initio Treatment of Crystalline Solids, Vol. 48 of Lecture Notes in Chemistry, Springer-Verlag, Berlin.
10. Catti, M., Dovesi, R., Pavese, A., and Saunders, V.R. (1991) Elastic constants and electronic structure of fluorite (CaF_2): an ab initio Hartree-Fock study, *J. Phys.: Condens. Matter* **3,** 4151- 4164.
11. Catti, M., Pavese, A., Dovesi, R., Roetti, C., and Causà, M. (1991) Quantum-mechanical Hartree-Fock self-consistent-field study of the elastic constants and chemical bonding of MgF_2 (sellaite), *Phys. Rev.* **B 44,** 3509-3517.
12. Catti, M., Valerio, G., Dovesi, R., and Causà, M. (1994) Quantum-mechanical calculation of the solid-state equilibrium $MgO+\alpha\text{-}Al_2O_3$ $MgAl_2O_4$ (spinel) versus pressure. *Phys. Rev.,* **B 49,** 14179-14187.
13. Car, R. and Parrinello, M. (1985) Unified approach for molecular dynamics and density-functional theory. *Phys. Rev. Lett.* **55,** 2471-2474.
14. Catti, M. (1986) Theoretical computation of physical properties of mantle minerals, in S.K. Saxena (ed.), *Chemistry and Physics of Terrestrial Planets, Advances in Physical Geochemistry,* Vol. **6,** Springer Verlag, Berlin, pp. 224-250.
15. Price, G.D. and Parker, S.C. (1988) The computer simulation of the lattice dynamics of silicates, in E.K.H. Salje (ed.), *Physical properties and thermodynamic behaviour of minerals,* NATO ASI Series C, Vol. **225,** Reidel, Boston, pp. 591-618.
16. Winkler, B., Dove, M.T., and Leslie, M. (1991) Static lattice energy minimization and lattice dynamics calculations on alumino-silicate minerals, *Am. Mineral.* **76,** 313-331.
17. Parker, S.C. and Price, G.D. (1989) Computer modelling of phase transitions in minerals, *Advances in Solid State Chemistry* **1,** 295-327.
18. Yuen, P.S., Lister, M.W., and Nyburg, S.C. (1978) The four-center charge distribution of the carbonate ion and the lattice energies of calcite and aragonite, *J. Chem. Phys.* **68,** 1936-1941.

19. Yamamoto, A., Shiro, Y., and Murata, H. (1974) Optically-active vibrations and elastic constants of calcite and aragonite, *Bull. Chem. Soc. Japan* **47,** 265-273.
20. Salje, E. and Viswanathan, K. (1976) The phase diagram calcite- aragonite as derived from the crystallographic properties, *Contrib. Mineral. Petrol.* **55,** 55-67.
21. Dovesi, R., Saunders, V.R.S., and Roetti, C. (1992) CRYSTAL92. User's Manual, Gruppo di Chimica Teorica, Universitá di Torino.
22. Hehre, W.H., Radom, L., Schleyer, P.R., and Pople, J.A. (1986) Ab Initio Molecular Orbital Theory, Wiley, New York.
23. Dick, B.G. and Overhauser, A.W. (1958) Theory of the dielectric constants of alkali halide crystals, *Phys. Rev.* **112,** 90-103.
24. Leslie, M. (1985) A three-body potential model for the static simulation of defects in ionic crystals, *Physica* **131B,** 145-150.
25. Markgraf, S.A. and Reeder, R.J. (1985) High-temperature structure refinements of calcite and magnesite, *Am. Mineral.* **70,** 590-600.
26. Murnaghan, F.D. (1944) The compressibility of media under extreme pressures, *Proc. Nat. Acad. Sci. USA* **30,** 244-247.
27. D'Arco, P., Jolly, L.H., and Silvi, B. (1992) Periodic Hartree- Fock study of B1-B2 reactions: phase transition in CaO, *Phys. Earth Planet. Inter.* **72,** 286-298.
28. Causà, M., Dovesi, R., Pisani, C., and Roetti, C. (1986) Electronic structure and stability of different crystal phases of magnesium oxide, *Phys. Rev.* **B 33,** 1308-1316.
29. Perdew, J.P., Chevary, J.A., Vosko, S.H., Jackson, K.A., Pederson, M.R., Singh, D.J., and Fiolhais, C. (1992) Atoms, molecules, solids, and surfaces: applications of the generalized gradient approximation for exchange and correlation. *Phys. Rev.* **B 46,** 6671-6687.
30. Merrill, L. and Bassett, W.A. (1975) The crystal structure of $CaCO_3$(II), a high-pressure metastable phase of calcium carbonate, *Acta Crystallogr.* **B31,** 343-349.
31. Ross, N.L. and Reeder, R.J. (1992) High-pressure structural study of dolomite and ankerite, *Am. Mineral.* **77,** 412-421.
32. Dandekar, D.P. (1968) Variation in the elastic constants of calcite with temperature, *J. Appl.* Phys. **39,** 3694-3699.
33. Dandekar, D.P. and Ruoff, A.L. (1968) Temperature dependence of the elastic constants of calcite between 160 and 300 K, *J. Appl. Plays.* **39,** 6004-6009.
34. Porto, S.P.S., Giordmaine, J.A., and Damen, T.C. (1966) Depolarization of Raman scattering in calcite, *Phys. Rev.* **147,** 608-611.
35. Liu, L.G. and Mernagh, T.P. (1990) Phase transitions and Raman spectra of calcite at high pressures and room temperature, *Am. Mineral.* **75,** 801-806.
36. Gillet, Ph., Biellmann, C., Reynard, B., and McMillan, P. (1993) Raman spectroscopic studies of carbonates, part I: high-pressure and high-temperature behaviour of calcite, magnesite, dolomite and aragonite, *Phys. Chem. Minerals* **20,** 1-18.
37. Stavely, L.A.K. and Linford, R.G. (1969) The heat capacity and entropy of calcite and aragonite, and their interpretation, *J. Chem. Thermodynamics* **1,** 1-11.
38. Anderson, O.L. (1963) A simplified method for calculating the Debye temperature from elastic constants. *J. Phys. Chem. Solids* **24,** 909-917.
39. Weast, R.C. (ed.) (1987) Handbook of Chemistry and Physics, Chemical Rubber Company, Boca Raton, Florida.
40. Goettlicher, S. and Vegas, A. (1988) *Acta Crystallogr.* **B44,** 362-367.
41. Tossel, J.A. (1985) Electron deficient anions and ion pairs, *Physica* **131B,** 283-289.
42. Hellwege, K.H., Lesch, W., Plihal, M., and Schaack, G. (1970) Zwei-Phononen-Absorptionsspektren und Dispersion der Schwingungszweige in Kristallen der Kalkspatstruktur, *Z. Physik* **232,** 61-86.
43. Cowley, E.R. and Pant, A.K. (1973) Lattice dynamics of calcite, *Phys. Rev.* **B 8,** 4795-4800.
44. Kaye, G.W.C. and Laby, T.H. (1982) Tables of physical and chemical constants, Longman, London.
45. Deer, W.A., Howie, R.A., and Zussman, J. (1966) An introduction to rock forming

minerals, Longmans, London.
46. Voigt, W. (1910) Lehrbuch der Kristallphysik (reprinted 1928), Teubner, Leipzig.
47. Hearmon, R.F.S. (1946) The elastic constants of anisotropic materials, *Rev. Mod. Phys.* **18,** 409-440.
48. Schaefer, C. and Matossi, F. (1930) Das ultrarote Spektrum, Springer, Berlin.
49. Bhagavantam, S. and Venkatarayudu, T. (1939) Raman effect, in relation to crystal structure. *Proc. Indian Acad. Sci. Sect. A* **9,** 224-258.
50. Couture, L. (1947) Etude des spectres de vibrations de monocristaux ioniques, *Ann. Physique Ser. 12,* **2,** 5-94.
51. Frech, R. and Wang, E.C. (1980) The i.r. and Raman spectra of $CaCO_3$ (aragonite), *Spectrochim. Acta* **36A,** 915-919.
52. Jacobs, G.K., Kerrick, D.M., and Krupka, K.M. (1981) The high- temperature heat capacity of natural calcite ($CaCO_3$), *Phys. Chem. Minerals* **7,** 55-59.
53. Chessin, H., Hamilton, W.C., and Post, B. (1965) Position and thermal parameters of oxygen atoms in calcite, *Acta Crystallogr.* **18,** 689-693.
54. Rao, K.V.K., Naidu, S.V.N., and Murthy, K.S. (1968) Precision lattice parameters and thermal expansion of calcite, *J. Phys. Chem. Solids* **29,** 245-248.
55. Kieffer, S.W. (1979) Thermodynamics and lattice vibrations of minerals I, *Rev. Geophys. Space Phys.* **17,** 1-19.
56. Kieffer, S.W. (1979) Thermodynamics and lattice vibrations of minerals II, *Rev. Geophys. Space Phys.* **17,** 20-34.
57. Kieffer, S.W. (1979) Thermodynamics and lattice vibrations of minerals III, *Rev. Geophys. Space Phys.* **17,** 35-58.
58. De Villiers, J.P.R. (1971) Crystal structures of aragonite, strontianite, and witherite, *Am. Mineral.* **56,** 758-767.
59. Effenberger, H., Mereiter, K., and Zeman, J. (1981) Crystal structure refinements of magnesite, calcite, rhodochrosite, siderite, smithsonite and dolomite, with discussion of some aspects of the stereochemistry of calcite-type carbonates, *Z. Kristallogr.* **156,** 233-243.
60. Humbert, M.M.P. and Plicque, F. (1972) Proprietés élastiques de carbonates rhomboédriques monocristallins: calcite, magnésite, dolomie, *C. R. Acad. Sc. Paris* **275,** Série B, 391-394.
61. Catti, M., Pavese, A., Aprá, E., and Roetti, C. (1993) Quantum- mechanical Hartree-Fock study of calcite ($CaCO_3$) at variable pressure, and comparison with magnesite ($MgCO_3$), *Phys. Chem. Minerals* **20,** 104-110.
62. Maslen, E.N., Streltsov, V.A., and Streltsova, N.R. (1993) X-ray study of the electron density in calcite, $CaCO_3$, *Acta Crystallogr.* **B49,** 636-641.
63. Vo Thanh, D. and Lacam, A. (1984) Experimental study of the elasticity of single crystalline calcite under high pressure (the calcite I- calcite II transition at 14.6 kbar), *Phys. Earth Planet. Inter.* **34,** 195-203.

THE SiO BOND AND ELECTRON DENSITY DISTRIBUTIONS

G. V. GIBBS, F. C. HILL AND M. B. BOISEN JR.
Department of Geological Sciences,
Material Science and Engineering and Mathematics
Virginia Tech, Blackburg, VA 24061

If an experimental and a theoretical deformation map agree, then the most probable interpretation is that they are both wrong. –William N. Lipscomb

1. Introduction

A mapping of the electron density distribution, $p(\mathbf{r})$, of a molecule as revealed in an X-ray diffraction analysis of a crystal, usually displays well-defined peaks interspersed in a field of low-lying ridges, saddle-shaped depressions and valleys. By locating the positions of the peaks and correcting them for series termination error, early workers found that they could determine the positions of the atoms and the equilibrium structure of a molecule with an accuracy of ~0.01Å [1]. They also found that a rough count could be made of the number of electrons that "belong" to a given atom together with its relative charge by integrating the electron density distribution over a definite region of a molecule. At that time, it was not clear whether the remaining features of the distribution such as the saddle-shaped depressions and the low lying ridges of electron density that connect the peaks of bonded atoms could provide additional information about the bonded interactions that obtain when atoms combine and form a molecule.

To gain insight into these interactions from the topography of $p(\mathbf{r})$, Roux and Daudel [2] recommended the use of the deformation electron density distribution, $\Delta\rho(\mathbf{r}) = p_m(\mathbf{r}) - \rho_p(\mathbf{r})$, as a tool for probing the changes that can occur in the electron density distribution of a molecule upon its formation from a set of atoms. A map of $\Delta p(\mathbf{r})$ can be constructed by subtracting from the observed or theoretical electron density distribution of a molecule, $p_m(\mathbf{r})$, the electron density distribution of a promolecule, $p_p(\mathbf{r})$, usually constructed by superimposing a set of spherically averaged electron density distributions of non-interacting, ground state atoms at the

B. Silvi and P. D'Arco (eds.), Modelling of Minerals and Silicated Materials, 157- 177

positions that they occupy in the molecule. A $\Delta p(\mathbf{r})$ distribution provides a map of the changes that can occur in the electron density distribution of a promolecule when its atoms combine, interact and form a molecule. The application of the deformation map for studying deformed electron density distributions and structure was not new. Actually, X-ray crystallographers had been generating and using these maps (referred to as Fourier difference synthesis maps) for some time for determining and refining crystal structures, for locating H atoms and for determining temperature and scale factors [3, 4, 5]. Such maps have also been used to study the effects of bonding on electron density distributions. For instance, they have provided corroborating evidence for Bragg's suggestion [6] that the electron density distribution of the C atom in diamond is deformed from a spherical distribution towards the center of each of its four CC bonds, producing a tetrahedral deformation of the electron distribution about each C atom [7].

With the advent of the automated single crystal diffractometer and the computer during the late 1950's, the determination of crystal structures and the mapping of electron density distributions became more commonplace with the development of ever more creative and precise strategies for collecting and processing diffraction data. In an effort to relate the properties of a molecule to the character of its bonds, workers constructed deformation density distributions for a large number of molecules and crystals with experimental diffraction data to learn how $p(\mathbf{r})$ is redistributed upon bond formation relative to that of the promolecule. Later, with the writing and development of SCF-MO software like that provided by GAUSSIAN Inc., comparisons were made between experimental distributions and one-electron density distributions generated with the wave functions of molecules calculated with relatively robust basis sets. When corrected for thermal motion effects, the theoretical maps were found at times to be in close agreement with the experimental $\Delta\rho(\mathbf{r})$ distributions, particularly when molecules consist of light atoms [8, 9, 10]. In interpreting these distributions, it was assumed by some workers that a build-up of deformation electron density in the intermolecular region between a pair of bonded atoms can be related to the ionic/covalent character of the bond, the greater the build-up, the more covalent the bond. With some notable exceptions, such arguments are consistent with Feynman's observation [11] that the strongest and the most important attractive forces arise in a molecule when there is an accumulation of electron density between its bonded atoms. In point of fact, both theory and experiment indicate that a build-up of electron density between a pair of nuclei is a necessary condition if two atoms are to be bonded to one another [12]. Despite their qualitative nature, $\Delta\rho(\mathbf{r})$ maps have, nonetheless, provided useful pictures of these build-ups [13] as well as features that have been ascribed to covalent

and multiple SiO bonding effects and lone pair electrons [14, 15].

However, the unexpected absence of a significant build-up of the $\Delta p(\mathbf{r})$ density in interatomic regions reported by Dunitz and Sieler [16] for a number of covalent systems with NN, CN and CO bonds led Spackman and Maslen [17] to assert that a build-up in interatomic regions is not a necessary condition to satisfy the requirements for bonded interactions to obtain between atoms, although such a build-up is often observed. Moreover, they were unable to establish a direct link between the magnitude of the build up and the ionic/covalent character of a bond. One serious problem with a deformation density distribution is that the promolecule density distribution is not unique. As is well known, it can be defined in several different ways resulting in as many different reference state promolecule distributions [18]. For example, in addition to constructing the promolecule as a superposition of spherically averaged atomic electron distributions, a promolecule can also be constructed either with the superposition of oriented atomic electron density distributions or with the superposition of the electron density distributions of those states to which the molecule dissociates. Thus, the derivation of a unique and unambiguous deformation density distribution that represents the true difference between $p_m(\mathbf{r})$ and an appropriate promolecule may only be obtainable in a few special cases. In light of these caveats, Cremer [19] has stated that there is no way of obtaining a consistent description of the interactions between bonded atoms by mapping experimental or theoretical densities (also see Low and Hall [20]. He continued by asserting that a consistent description can be obtained only if one analyzes the total electron density distribution free of any artificial constructs such as reference state densities. Because of these drawbacks and the qualitative nature of $\Delta p(\mathbf{r})$ maps, Bader and Essén [21] and Bader *et al* [22] developed a more quantitative method for evaluating atomic interactions and bond type that is based on the one-electron density distribution alone. In the method, the value of the electron density distribution and the eigenvalues of the Hessian of $p(\mathbf{r})$, evaluated at a stationary point along a bond, together with a mapping of the Laplacian field of $p(\mathbf{r})$, are used to quantify atomic interactions and to determine whether a bond is predominantly ionic or covalent or a bond of intermediate type.

According to Bader [12], a chemical bond can be pictured as existing between a pair of atoms only if they are connected by a ridge of electron density that adopts a saddle-shaped depression in $p(\mathbf{r})$ in the region between their peaks. When these features are absent, a bonded interaction between the pairs is considered to be nonexistent. The line that runs along the top of the ridge between a pair of bonded atoms, referred to as the atomic interaction line, or simply the bond path in a bound system, is special in that it passes through regions where $p(\mathbf{r})$ adopts a saddle point where

the gradient of the electron density distribution, $\nabla p(\mathbf{r}) = 0$. The point, denoted $\mathbf{r}_c$, referred to as a bond critical point by Bader [12] is the point at which the electron density is at a minimum value with respect to any displacement along the bond path. But, $p(\mathbf{r})$ is at a maximum value with respect to any radial displacement perpendicular to the path. Thus, the Hessian of the electron density distribution ($H_{ij} = \partial^2\rho(\mathbf{r}_c)/\partial x_i \partial x_j$), when evaluated at $\mathbf{r}_c$, has one positive eigenvalue (the positive curvature of $p(\mathbf{r}_c)$ along the bond path) denoted λ_3 and two negative eigenvalues (the negative curvature of $p(\mathbf{r}_c)$) perpendicular to the bond path) denoted λ_1 and λ_2 (see Bader [12]).

As the eigenvectors assiciated with λ_1 and λ_2 are both perpendicular to the bond path, Bader [12] has indicated that the electron density distribution has a tendency to be progressively enhanced (concentrated) toward the critical point as the values of λ_1 and λ_2 become more negative [23]. In addition, as the eigenvector associated with λ_3 parallels the bond path, the electron density is assumed to have a tendency to be progressively dissipated (depleted) in the interatomic region with a concomitant enhancement of the distribution away from the critical point toward each of the bonded atoms as λ_3 increases in value. Overall, the electron density distribution is expected to be increased at $\mathbf{r}_c$ when the enhancements of the distribution perpendicular to the bond path exceed that along the path toward the nucleus of each of the bonded atoms. Accompanying these changes, the length of the bond is expected to shorten as the magnitude of the electron density, $p(\mathbf{r}_c)$, at the critical point increases [11, 12].

As observed by Bader and Essén [21], the magnitude of $p(\mathbf{r}_c)$ and the magnitude and the sign of the Laplacian $\nabla^2\rho(\mathbf{r}_c) = \lambda_1 + \lambda_2 + \lambda_3$ can be used to characterize atomic interactions and bond type. If the interaction between a pair of bonded atoms involves a sharing of electrons as in the case of a covalent bond (a shared interaction), then there should not only be a build-up of electron density at $\mathbf{r}_c$ (roughly between 2 and $4e/\text{Å}^3$), but also the sum $|\lambda_1 + \lambda_2|$ is expected to exceed λ_3 so that $\nabla^2 p(\mathbf{r})$ has a negative value. In contrast, if the interaction between the bonded atoms is ionic (a closed-shell ionic interaction), then the magnitude of the electron density at the bond critical point is expected to be relatively small in value (roughly $\sim 0.5/\text{Å}^3$ and smaller) and $p(\mathbf{r})$ is expected to be enhanced along the bond path towards the directions of the ions comprising the bond. In this case, λ_3 is expected to be large in value while $|\lambda_1 + \lambda_2|$ is expected to become smaller in value so that the value of $\nabla^2 p(\mathbf{r})$ is positive for bonds involving closed-shell ionic interactions. Bonds exhibiting values of $p(\mathbf{r}_c)$ and $\nabla^2 p(\mathbf{r})$ intermediate between those exhibited by ionic and covalent bonds are pictured as being bonds of intermediate character.

Equally important, the interactions between the atoms of a molecule can also be characterized in terms of the Laplacian field, $\nabla^2 p(\mathbf{r})$ of an electron density distribution [21]. As shown by Bader [12], $\nabla^2 p(\mathbf{r})$ is related to the kinetic energy density $G(\mathbf{r})$ and the potential energy $V(\mathbf{r})$ by the expression $\frac{1}{4}\nabla^2 p(\mathbf{r}) = 2G(\mathbf{r}) + V(\mathbf{r})$. As $V(\mathbf{r})$ is everywhere negative and as $2G(\mathbf{r})$ is everywhere positive, the sign of $\nabla^2 p(\mathbf{r})$ determines which of these two energy terms is larger in magnitude at a given point $\mathbf{r}$. In a regions where $\nabla^2 p(\mathbf{r}) < 0$, not only is the electron density locally enhanced, but also $|V(\mathbf{r})|$ locally exceeds the average value of $2G(\mathbf{r})$. By mapping those regions where $\nabla^2 p(\mathbf{r})$ is negative, regions are delineated where $p(\mathbf{r})$ is enhanced and where the potential energy density makes a dominant contribution over the kinetic energy in lowering the total energy of the molecule. On the other hand, by mapping of those regions where $\nabla^2 p(\mathbf{r})$ is positive, molecular regions are delineated where $p(\mathbf{r})$ is dissipated and where the kinetic energy density makes a dominant contribution over the potential energy density in lowering the energy of the system [12]. For purposes of discussion, a surface that separates regions of enhanced and dissipated $p(\mathbf{r})$ in a molecule (where $\nabla^2 p(\mathbf{r}) = 0$) is referred to as a nodal surface.

In shared covalent atomic interactions, the electron density distribution is pictured as being relatively large in magnitude at $\mathbf{r}_c$ and enhanced in the binding region between a pair of bonded atoms. The region where $\nabla^2 p(\mathbf{r})$ is negative not only includes the critical point, but it is contiguous over the region between and within the valence shells of the two atoms involved in the interaction [21] with $\mathbf{r}_c$ being located relatively far from a nodal surface. On the other hand, in case of a closed-shell ionic interaction, the magnitude of $p(\mathbf{r}_c)$ is observed to be relatively small in magnitude with the region of enhancement being confined, at least in part, to the valence shell of the anion. The curvature of $p(\mathbf{r}_c)$ perpendicular to the bond path, albeit negative in sign, are expected to be smaller in magnitude than those observed for shared interactions such that $\nabla^2 p(\mathbf{r})$ is positive. Because the region of enhancement is largely confined to the valence shell of the anion and to the basins of the atoms, the spatial distribution of $\nabla^2 p(\mathbf{r})$ in the vicinity of the ions is strikingly similar to that displayed by the individual atoms or ions with the critical point expected to be located relatively far from the nodal surfaces of both ions. For an intermediate interaction, the critical point is located in closer proximity to a nodal surface than in the case of the shared interaction at one extreme and those characterized as a closed-shell at the other [21]. Also, the magnitude of $p(\mathbf{r}_c)$ is of intermediate value, $\nabla^2 p(\mathbf{r})$ is expected to be positive and there is an increased polarization enhancement of the electron density distribution of the anion along the bond path in the direction of the cation as the covalent character of the bond increases.

In this study, $p(\mathbf{r})$ and $\nabla^2\rho(\mathbf{r})$ of the SiO bond is mapped and explored in terms of the environment and structural variants of several molecules containing such bonds. Using GAUSSIAN92/DFT software, SCF-MO calculations have been completed on the molecules $Si^{I}O$, $Si^{II}O_2$, $H_2Si^{III}O_3$, $H_4Si^{IV}O_4$, $H_6Si_2^{IV}O_7$, $H_8Si^{VI}O_6$, $H_{10}Si_2^{VI}O_{10}$ and $H_{12}Si^{VIII}O_8$ where the Roman number denotes the coordination number of the Si atom. The structure of these molecules were either fully or partially optimized using a triple zeta 6-311++G** basis set. The geometries of SiO and SiO_2 (C_{∞} point symmetry), H_2SiO_3 (C_{2v}) H_4SiO_4 (S_4), H_4Si2O_6 (D_{2h}), $H_6Si_3O_3$ (D_{3h}), $H_6Si_2O_7$ (a staggered conformer with C_s symmetry), H_8SiO_6 (O_h) and $H_{12}SiO_8$ (D_{4h}) were fully optimized within the constraints of their assumed point group symmetries while that of $H_{10}Si_2O_{10}$ (C_s) was only partially optimized. Ball and stick model drawings of several of these molecules are given in Figure 1. Electron density distributions were calculated with the wave functions generated in the MO calculations and Hessian matrices were computed at bond critical points of the molecules using the software PROAIM/AIMPAC, kindly supplied by Professor Richard Bader of the Chemistry Department at McMaster University. The electron density distribution and Hessian matrices were also calculated for the H_8SiO_6 (O_h) molecule with its SiO bond lengths fixed at 1.76Å, a value observed, on average, for silicates and siloxane molecules with 6-coordinate Si. The minimum energy SiO bond lengths, R(SiO), the bonded radii of the oxide ion and the eigenvalues of the Hessian matrices obtained in the calculation are given in Table 1. The distance between the nucleus of the oxide ion and the critical point, $\mathbf{r}_c$ that lies along the path of the SiO bond is defined to be the bonded radius of the oxide ion, r_b(O). In this study, the properties of $p(\mathbf{r})$ of the SiO bonds for coesite and for a number of molecules are modeled, the correlations between SiO bond length and electronic properties are studied and maps of the Laplacian of $p(\mathbf{r})$ are examined and discussed as they relate to the electronic structure of the SiO bond.

2. A modeling of the properties of $p(\mathbf{r})$ for the SiO bonds of coesite.

Coesite is a high pressure structure-type of silica that is stable at pressures somewhat in excess of ~4 GPa that is observed to persist metastably at pressures as low as one atmosphere. It contains two nonequivalent SiO_4 silicate tetrahedra with a total of eight nonequivalent SiO bond lengths that range between 1.595Å and 1.621Å. The tetrahedra are linked together into a framework structure of corner sharing SiO_4 tetrahedra with five nonequivalent SiOSi angles that range between 137 and 180°. The trends between these bond lengths have been explored rather extensively in evaluating the

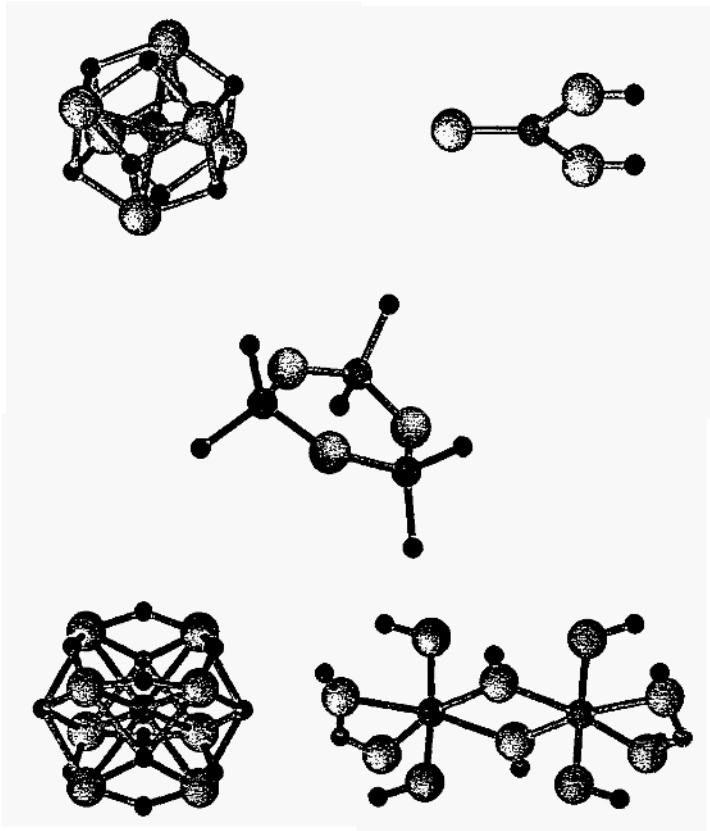

Figure 1. Ball and stick model drawings of the molecules H_2SiO_3 (upper left), H_8SiO_6 (upper right), $H_6Si_3O_3$ (middle), $H_{10}Si_2O_{10}$ (lower left) and $H_{12}SiO_8$ (lower right). The small black spheres represent H atoms, the large light gray spheres represent O atoms and intermediate-sized darker gray spheres represent Si atoms. No significance is attached to the relative sizes of the spheres. The drawings were constructed with software written by Drs R. T. Downs and K. L. Bartlemehs who are currently at The Geophysical Laboratory, Carnegie Institution at Washington, D. C. and at The University of Texas at Austin, Texas, respectively.

role played by the 3*d*-AOs in the formation of a (p -d)π–bond between Si and O [24, 25]. But, because similar trends have been generated in MO calculations for the $H_6Si_2O_7$ molecule, completed with and without 3*d*-type polarization functions, it can be argued that little can be inferred about the role played by these functions in the bond formation other than their

TABLE 1. Electronic properties of the SiO bond

Molecule	SiO	R(SiO)	r_b(O)	$\rho(r_c)$	$\nabla^2\rho(r_c)$	λ_1	λ_2	λ_3	$\frac{\lvert\lambda_1\rvert}{\lvert\lambda_3\rvert}$
SiO	SiO	1.486	0.865	1.316	47.602	-9.427	-9.427	66.456	0.142
SiO_2	SiO	1.478	0.857	1.359	45.388	-8.689	-8.689	62.766	0.138
H_2SiO_3	SiO	1.487	0.864	1.340	44.533	-9.166	-8.551	62.249	0.147
	SiOH	1.602	0.946	0.976	28.184	-7.452	-6.664	42.299	0.176
$H_6Si_3O_3$	SiO	1.639	0.970	0.870	24.300	-6.102	-5.945	36.342	0.170
H_4SiO_4	SiOH	1.623	0.962	0.944	26.005	-7.067	-6.586	39.658	0.178
$H_4Si_2O_6$	SiOSi	1.656	0.987	0.897	23.060	-6.031	-5.996	35.088	0.172
	SiOH	1.608	0.952	0.978	27.471	-7.451	-6.823	41.746	0.178
$H_6Si_2O_7$	SiOSi	1.589	0.933	0.958	29.333	-7.085	-7.083	45.500	0.163
	SiOH	1.627	0.966	0.928	25.400	-6.889	-6.482	38.771	0.178
H_8SiO_5	SiO	1.690	1.013	0.846	21.212	-5.259	-5.259	31.930	0.165
H_8SiO_6 D	SiO	1.760	1.062	0.737	15.779	-4.016	-4.016	23.811	0.169
$H_{12}SiO_8$	SiO	1.960	1.199	0.495	6.159	-1.920	-1.879	9.958	0.193
$H_{12}Si_2O_{10}$	SiOSi	1.885	1.141	0.472	9.105	-2.591	-2.354	14.049	0.184
	SiOSi	1.866	1.128	0.498	9.668	-2.844	-2.435	14.948	0.190
	SiOH	1.788	1.074	0.591	13.531	-3.764	-3.428	20.724	0.182
	SiOH	1.693	1.016	0.863	18.877	-5.970	-5.548	30.395	0.196

inclusion in a basis set results in shorter SiO bond lengths and narrower SiOSi angles in better agreement with observed values.

The electron density distribution of coesite has been mapped and explored by Geisinger *et al* [26] with the goal of covering and learning more about the electronic structure and properties of the SiO bond. Deformation maps calculated through the SiOSi skeletal units of the mineral show a significant accumulation (peak heights of $\sim 0.5e/\text{Å}^3$) of electron density between Si and O along each of the SiO bonds with the accumulation being displaced slightly off the line between the two atoms and towards the interior of the SiOSi angle and towards the more electronegative oxide ion. In addition, theoretical deformation maps, calculated for the SiOSi skeletal unit of the $H_6Si_2O_7$ molecule and for the ring in a $H_8Si_4O_4$ molecule, were found to be similar to the $\Delta\rho(\mathbf{r})$-maps observed for coesite with the peak heights in the bonds being smaller ($\sim 0.35e/\text{Å}^3$) than observed. Tsirelson *et al* [14] concluded from an examination of the deformation density distributions for coesite and quartz that the SiO bonds in the silica polymorphs with 4-coordinate Si are predominantly covalent in character with a significant double bond component (See also, Stuckenschmidt *et al* [15]. On the other hand, Cohen [27] has concluded on the basis of the deformation maps

calculated for quartz by Binggeli *et al* [28] that silica is clearly very ionic and that it consists of nearly fully charged Si^{4+} and O^{2-} ions.

As the lengths of the SiO bonds in coesite decrease, it is expected that the heights of the peaks in the bonds n the $\Delta\rho(\mathbf{r})$ maps should increase, particularly in light of Feynman's elegant examination of the forces in molecules [11]: the results of his study indicate that the length of such a bond should be highly dependent on the build-up of $\rho(\mathbf{r})$ due to the migration of the electron density towards the bond, the greater the build-up, the shorter the bond. An examination of the deformation maps observed for coesite and those calculated for the molecular models provides little or no support for such a correlation [26]. The $\Delta\rho(\mathbf{r})$-maps calculated for the $H_6Si_2O_7$ molecules show that the heights of the peaks in the SiO bonds actually decrease as the SiOSi angle widens and the bond shortens rather than increasing as expected. In addition, the value of the Mulliken overlap populations calculated for the bonds increases as the angle widens despite the fixing of the SiO bond lengths of the molecule at 1.62Å[29]. In light of the absence ofan accumulation of $\Delta\rho(\mathbf{r})$ density in the NN, CN and NO bonds for several covalently bonded systems as discussed above, a meaningful correlation between bond length and peak height may not be expected to be revealed by a deformation map.

In an examination of whether the total electron density distribution of the "Si_2O_7 dimers" in coesite varies as expected as its SiO bonds shorten, $\rho(\mathbf{r})$ and $\nabla^2\rho(\mathbf{r})$ model maps for the mineral were generated in a calculation completed on five $H_6Si_2O_7$ molecules. The geometry of each Si_2O_7 dimer was adjusted to match that observed for each of the five nonequivalent "dimers" in coesite. The hydrogen atoms used to neutralize each dimer and to mimic the local field of the crystal were placed at 0.97Å from each nonbridging oxide ion of the dimer in the directions of the nearest neighbor Si atoms in coesite external to the dimer. The Laplacian, $\nabla^2\rho(\mathbf{r}_c)$ of the distributions and the λ_i-values $(i = 1,2,3)$ evaluated at each SiO bridging bond critical point are plotted in Figures 2a, 2b and 2c as functions of the SiO bond lengths observed for coesite. As observed, the electron density is expected to be progressively enhanced in a direction perpendicular to the bond as the SiO bond shortens. The systematic increase in both λ_1 and λ_2 also indicates that the potential energy density makes a progressively greater contribution to the energy of the system in the region of the SiO bond as the bond lengths shorten and the angle widens (see Bader [12]). Collectively, this evidence suggests that the covalent character of the SiO bond increases as the bond length decreases (and the SiOSi angle widens). This observation is borne out by Figure 2d, in which it is seen that the magnitude $\rho(\mathbf{r}_c)$ increases from ~0.92 $e/Å^3$ to ~0.95$e/Å^3$ as R(SiO) shortens from 1.621Å to 1.595Å and the angle widens from 137° to 180°. As

the magnitude of $p(\mathbf{r}_c)$ increases, the R(SiO) vs. $G(\mathbf{r}_c)/p(\mathbf{r}_c)$ plot in Figure 2e indicates that the polarity of the bond increases as well where $G(\mathbf{r}_c)$ is the kinetic energy density at the critical point [19, 12]. This result can be

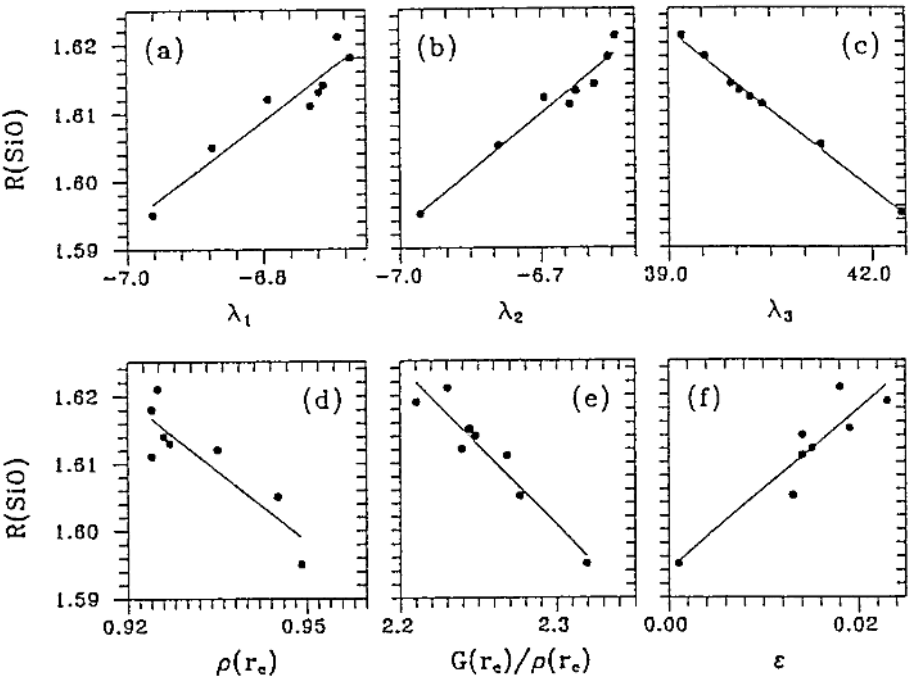

Figure 2. A summary of the properties of the electron density distribution for the skeletal SiOSi dimers in a set of $H_6Si_2O_7$ molecules with geometries fixed at those observed for the "Si_2O_7 dimers" in coesite. In (a), (b) and (c), respectively, the individual SiO bond lengths, R(SiO), observed for coesite are plotted against λ_1, λ_2 and λ_3, the curvatures of the electron density distribution calculated for the molecules at their saddle points $\mathbf{r}_c$. In (d), R(SiO) is plotted against the magnitude of the electron density, $p(\mathbf{r}_c)$. In (e) R(SiO) is plotted against $G(\mathbf{r}_c)/p(\mathbf{r}_c)$ where $G(\mathbf{r}_c)/p(\mathbf{r}_c)$ is the kinetic energy density and in (f) R(SiO) is plotted vs. ellipticity, ϵ, of the bonds.

ascribed to either an increase in the ionicity of the bond or to an increase in the participation of the *p*- and the *d*-AOs on Si in the π–bond formation as the SiO bond shortens. If the latter is important, then the ellipticity of the SiO bond, $\epsilon = |(\lambda_1 - \lambda_2)/\lambda_3|$ should be zero when the SiOSi angle is straight and both π–systems are predicted to be involved in bond formation [30,31, 32]. Moreover, the ellipticity should increase in a regular way as the SiOSi angle narrows and as one of the π–systems becomes more dominant [32]. A plot of ϵ vs. R(SiO) shows that $\epsilon = 0$ when the SiOSi angle is straight and that it increases in a regular way as the angle narrows (Fig. 2f). These

results indicate that the increases polarization and shortening of the SiO bond accompanying the widening of the SiOSi angle can be interpreted, at least in part, in terms of the formation of a weak π–system [33, 34].

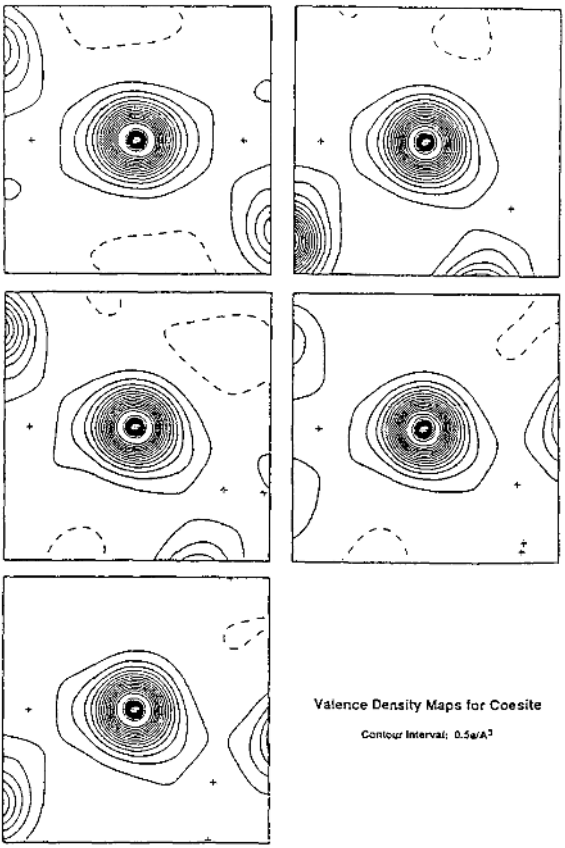

Figure 3. Maps of the valence electron density distribution measured for coesite constructed through its five nonequivalent SiOSi dimers. The position of the Si atoms in each dimer is indicated by a plus sign. The diffraction data used to construct the maps was measured by Geisinger *et al* [26]

Deformation electron density distributions calculated through the planes of the SiOSi angles of H_6Si_2O, $H_6Si_2O_7$ and $H_8Si_4O_4$ molecules and those recorded for coesite, as observed above, show peaks along the SiO bonds that are displaced toward the interior of each bent SiOSi angle [26]. This evidence suggests that the bond paths that connect the nuclei of Si and

O and the bond critical point are curved away from the line connecting Si and O, indicating strained SiO bonds. In an examination of the strained character of the bonds, the bond path lengths for the SiO bridging bonds in each of the five $H_6Si_2O_7$ molecules were calculated. In each case they were found to match the SiO bond lengths of the molecules to within 0.0005Å. With these results and similar results obtained in an analysis of the electron density for coesite [35], it can be concluded that the bond paths in the SiOSi dimers follow the line between each pair of Si and O atoms rather closely in both the molecule and the crystal, suggesting that the SiO bonds are largely strain free [33, 34].

Relief and level line contour maps of $\nabla^2 p(\mathbf{r})$ for each of the $H_6Si_2O_7$ molecules were calculated to learn where the electron density in the vicinity of each bond is locally enhanced and where it is locally dissipated. Each map displays nodes that correspond to the K- and L-shells for both Si and O with the nodes of the valence L-shells on the oxide ions being prominent features in the maps. Because of the very diffuse nature of the valence electrons of the Si atoms, the nodes corresponding to the M-shell of Si are not prominent features in the maps [34]. In fact, a mapping of the valence electron density distribution for coesite, using the data recorded by Geisinger *et al* [26], shows peaks of electron density centered at the position of each oxide ion with little or no density in the vicinity of the Si atoms (Fig. 3), with a polarization of $p(\mathbf{r})$ along the SiO bonds toward each Si cation. The $\nabla^2 p(\mathbf{r})$ maps for the five molecules show a dissipation of the L-valence shell electron density for each oxide ion where the shell crosses the SiO bond, with electron density being locally enhanced away from the shell along the bond in the direction of the Si cation. Figure 4 displays a relief map and a level line contour map of $-\nabla^2 p(\mathbf{r})$ for the molecular model of the Si(1)O(5)Si(2) dimer in coesite. The negative of the Laplacian is displayed in Figure 4 so that the reader can more readily assess the effects of chemical bonding on the valence shells of Si and O. Fig. 4 shows that the electron density distribution of the O(5) oxide ion is polarized in its enhancement in the directions of Si(1) and Si(2). It also shows that electron density is locally enhanced in the valence shell of the anion on the external side of the SiOSi angle [33]. This site of local enhancement of the valence shell is considered to be a site of potential electrophilic activity and attack, say by the protons of a water molecule [34]

All the features seen in Figure 4 are displayed by the molecular models for the remaining four nonequivalent SiOSi dimers in coesite. Several of the features exhibited by the SiO bonds in the $H_6Si_2O_7$ molecules are observed for coesite, but the trends are more poorly developed [34, 35]. In particular, negative correlations obtained between $p(\mathbf{r}_c)$ and $\nabla^2 p(\mathbf{r}_c)$ and between $p(\mathbf{r}_c)$ and $|\lambda_1|/\lambda_3$. The average values for $p(\mathbf{r}_c)$ ($1.05e/Å^3$),

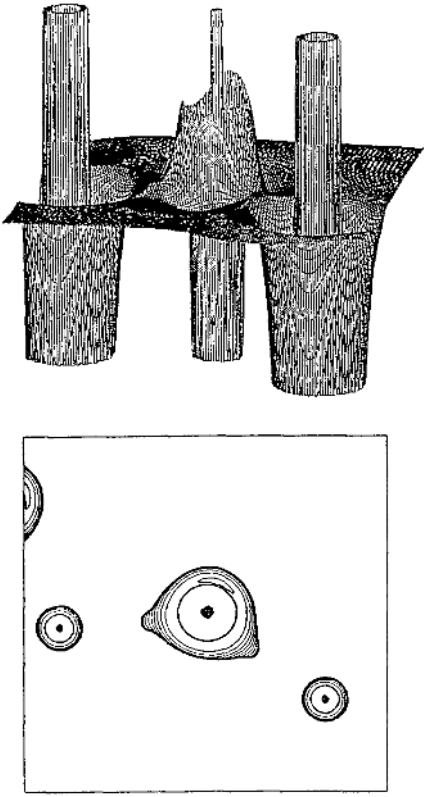

Figure 4. (a) A relief map of $-\nabla^2 p(\mathbf{r})$ and (b) a map of the positive level line contours of $-\nabla^2 p(\mathbf{r})$ passing through the SiOSi plane of a $H_6Si_2O_7$ molecule [33]. The negative rather than the positive Laplacian of $p(\mathbf{r})$ is presented in this figure and in Fig. 7 so that the reader can more readily assess the effects of chemical bonding on the valence shells of Si and O.

($20.4e/Å^5$), λ_1 ($-7.2e/Å^5$), λ_2($-6.8e/Å^5$) and λ_3($34.4e/Å^5$) observed for coesite [35] are in rough agreement with the values calculated for the dimers ($0.93e/Å^3$, $26.9e/Å^5$, $-6.8e/Å^5$, $-6.7e/Å^5$ and $37.8e/Å^5$, respectively). This agreement, albeit rough, indicates that the electron density distribution of the SiOSi dimers in coesite are similar to that in $H_6Si_2O_7$. The agreement in these parameters has been shown to improve dramatically when the wave functions for the molecule are calculated with a model that includes electron correlation and exchange effects [36].

3. SiO bond length and electron density variations.

Knop *et al* [37] have observed well-developed correlations between bond length and the magnitude of $p(\mathbf{r}_c)$ for a variety of XA bonds underscoring Feynman's assertion [11] that the strength of a bond should increase and that its length, R(XA), should decrease in a systematic way as the value of the electron density at the bond critical point increases. In a study of CC, CN and SS bonds, the bond length data was found to vary in a similar fashion with $p(\mathbf{r}_c)$ with an r^2-value of ~0.99 (see also Cremer [19]). Bond length data for OO, AlF and BeCl bonds was also found to vary linearly with $p(\mathbf{r}_c)$, but the correlations are not as well-developed with an r^2-value of ~0.95. As observed by Knop *et al* [37], the power law is the simplest model equation that is consistent with the constraint that $p(\mathbf{r}_c) \rightarrow 0.0$ as $R(XA) \rightarrow \infty$. Application of such an equation to the OO, AlF and BeCl bond length data resulted in a model power equation of the form $R(XA) = \alpha \times \rho(\mathbf{r}_c)^{-\beta}$. Statistical analyses indicate that this model results in a better fit to the data, as argued by Knop *et al* [37], than that provided by a linear model. The SiO bond length data for coesite, plotted in Figure 2d against $p(\mathbf{r}_c)$, seems to obey a linear rather than a power equation model. A statistical analysis of the data fails to provide evidence for the power model relationship: a linear model was accepted given the small number of bond length data observed for coesite and their small range of values. Because the data set in Table 1 is much larger in number and because it shows a much wider range of SiO bond lengths, it was added to the coesite data set and subjected to a regression analysis using a power model expression. The data was also explored to assess whether the correlations presented in Fig. 2 between R(SiO) and the λ-values and r_b(O)hold and whether they conform with a linear or a power model relationship.

A regression analysis of the data in Table 1 together with that calculated for the dimers in coesite indicates that the power equation $R(SiO) = 1.588p(\mathbf{r}_c)^{-0.25}$ explains more than 97 per cent of the variation of R(SiO) in terms of linear dependence on $p(\mathbf{r})$. As this expression explains more than 50 per cent of variation left unexplained by a linear model, it can be concluded that a power equation provides a better model for the correlation between bond length and $p(\mathbf{r})$. An examination of data shows that SiO bonds with a Pauling bond strength [38] of 1.0 have ~$0.95e/Å^3$ at their bond critical points, on average, while those with a bond strength of 2/3 have ~$0.67e/Å^3$, on average, and those with 1/2 have ~$0.5e/Å^3$, on average (Table 1). The relationship between the strengths of these SiO bonds and the values of the electron density evaluated at their critical points corresponds with a similar relationship established between the bond orders of the CC bonds in the hydrocarbons ethane, benzene, ethylene and acetylene

and $p(\mathbf{r}_C)$ [12].

The MO calculations for the molecules used to model the dimers in coesite indicate that both λ_1 and λ_2 become more negative in value and $p(\mathbf{r}_c)$ increases as the SiO bond decreases in length. But, rather than decreasing with increasing $p(\mathbf{r}_c)$, λ_3 actually increases, indicating a progressive enhancement of electron density toward Si and O as R(SiO) decreases. Because the rate at which λ_3 increases exceeds the rate at which $\lambda_1 + \lambda_2$ decreases, the Laplacian $\nabla^2\rho(\mathbf{r}_c)$, increases with $p(\mathbf{r}_c)$, Similar trends have been observed to obtain between $\nabla^2\rho(\mathbf{r}_c)$, $p(\mathbf{r}_c)$ and R(XO) for a variety of first row (Be, B, C and N) and second row X-cations (X = Mg, Al, S, P and C1) [33] and for the bonds in hydrocarbon molecules with single, double and triple CC bonds [12].

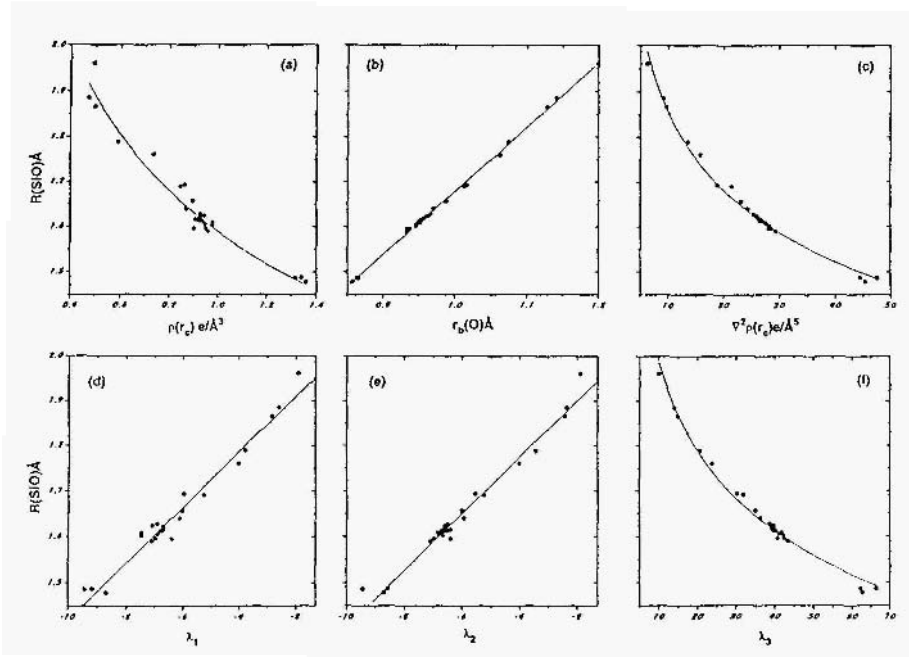

Figure 5. The properties of $p(\mathbf{r}_C)$ for the SiO bonds of the molecules given in Table 1 plotted against SiO bond length, R(SiO).

The properties calculated for the molecules in Table 1 show the same sort of trends as observed for the dimers used to model the electronic properties of coesite. The SiO bonds are indicated to increase in length linearly with λ_1 and λ_2 with the largest curvatures at $p(\mathbf{r}_c)$ perpendicular to the

bond paths involving the shortest bonds with largest values of $p(\mathbf{r}_c)$ (Figure 5). Cross-sections of $p(\mathbf{r})$ constructed perpendicular to the SiO bonds in the molecules SiO_2, H_4SiO_4 and $H_{12}SiO_8$ and passing through $\mathbf{r}_c$, reveal a progressive build-up of $p(\mathbf{r})$ together with a progressive increase in the sharpness (curvature) of maximum in $p(\mathbf{r})$ at $\mathbf{r}_c$ as the SiO bond shortens (Fig. 6). This conforms with Bader's arguments that the electron density distribution becomes more enhanced in the internuclear surface at the critical point between Si and O as the bond length shortens. The data in the table also shows that λ_3 increases as $p(\mathbf{r}_c)$ increases in magnitude (Fig. 5). Cross-sections in $p(\mathbf{r})$ passing through $\mathbf{r}_c$ and parallel to the SiO vectors of the three molecules are displayed in figure 6. As λ_3 increases in value, not only does $p(\mathbf{r}_c)$ increase in magnitude from $0.5e/Å^3$ to $1.36e/Å^3$, but also the sharpness of the minimum of $p(\mathbf{r})$ at $\mathbf{r}_c$ increases progressively. Like λ_3, $\nabla^2\rho(\mathbf{r}_c)$ also increases in value as $p(\mathbf{r}_c)$ increases in value (Fig. 5). Glasser [39] has suggested in a study of hydrated structure that their "constitutional formulae" are such that basicity differences between oxide ions are minimized and that SiOSi bonds are more stable than the more basic SiOH bonds. The optimized geometry of $H_6Si_2O_7$ agrees with her suggestion with the value of $p(\mathbf{r}_c)$ for the SiOSi bonds of the molecule, $0.96e/Å^3$, being larger than its SiOH bonds, $0.93e/Å^3$,, implying that the SiOSi bonds are more stable than the SiOH bonds. To gain further insight into the interaction between Si and O and the nature of the SiO bond, a mapping of $\nabla^2 p(\mathbf{r})$ was undertaken to learn whether the features of the resulting maps are those of a closed-shell ionic or of an intermediate bond type interaction.

4. Bonded interactions between Si and O as inferred from a mapping of the Laplacian of $p(\mathbf{r})$

Relief and level line contour maps of $\nabla^2\rho(\mathbf{r})$, calculated for SiO_2, H_4SiO_4, H_8SiO_6 and $H_{12}SiO_8$ are displayed in Figure 7. These molecules were selected for the calculation because their $p(\mathbf{r}_c)$-values range between $0.5e/Å^3$, a value of a predominately ionic type bond, to $1.36e/Å^3$. The maps calculated through the SiO bonds of the H_4SiO_4 molecule display features that are consistent with an intermediate type of bond (Fig. 7b). They reveal an enhancement of $p(\mathbf{r})$ away from the valence shell of the oxide ion in the direction of the Si atom (as observed for the $H_6Si_2O_7$ molecule in Fig. 4) with the nodal surface located ~0.15 Å from the critical point on the side of the oxide ion. Consistent with the greater covalent, character of the SiO bonds in SiO_2, the electron density of both of its oxide ions (Fig. 7a) not only shows a greater enhancement away from the valence shells of the ions towards the Si atom, but the enhancement occurs over a broader do-

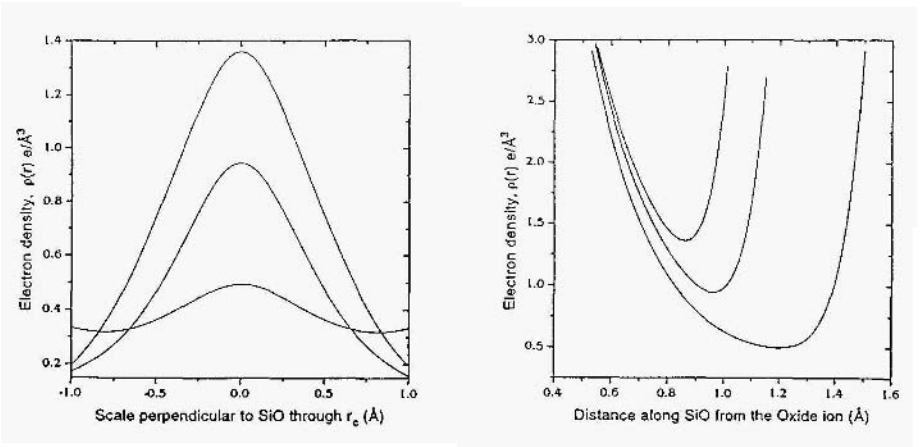

Figure 6. Profiles of the electron density distributions passing through the bond critical point calculated in a plane perpendicular (left three curves) and parallel (right three curves) to the SiO bonds in the molecules H_4SiO_4 (upper set of curves), H_6SiO_6 (middle curves) and H_8SiO_8 (lower set of curves).

main in the internuclear region than displayed for the bonds of the H_4SiO_4 molecule. In addition, the map shows a greater dissipation of the valence shells of the oxide ions where each shell crosses the bond than displayed for the H_4SiO_4 molecule.

The maps calculated for the bonds in $H_{12}SiO_8$ display features that are typical of a closed-shell ionic interaction (Fig. 7d). The enhancement of $p(\mathbf{r})$ in this case is localized almost entirely within the region of the valence shell of the oxide ion with the bond critical points being at a larger distance (~0.60Å) from the nodal surface with $\nabla^2 p(\mathbf{r})$ being negative over much of the valence shell region of the oxide ion. As a consequence, the valence shell of each oxide ion displays little dissipation where the shell crosses the bond. The $\nabla^2 p(\mathbf{r})$ maps calculated for the 6-coordinate Si in the H_8SiO_6 molecule (Fig. 7c) show a somewhat larger polarization of the valence shell of the oxide ion with a somewhat larger enhancement of $p(\mathbf{r})$ in the direction of Si with the critical point being situated ~0.40Å from

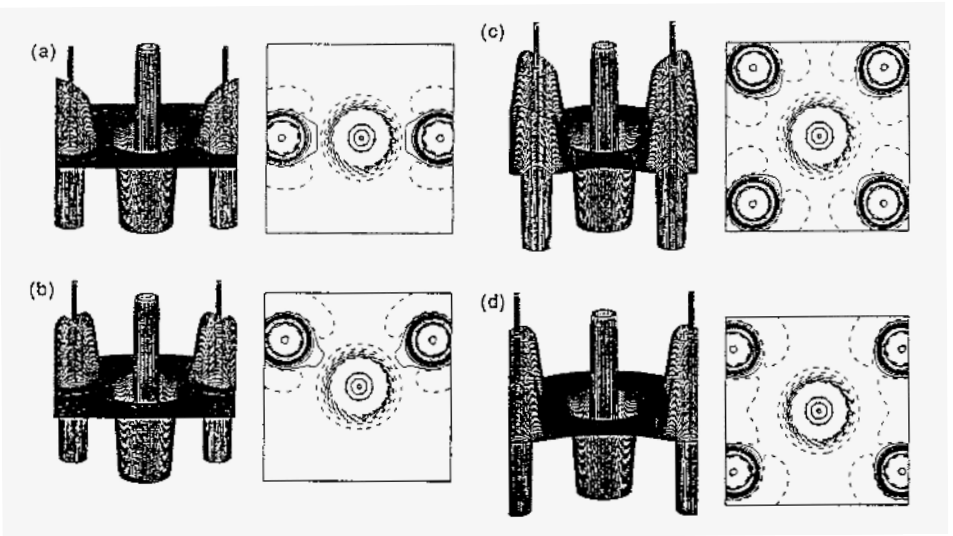

Figure 7. Relief and level line contour maps of $-\nabla^2\rho(\mathbf{r})$ calculated through the SiO bonds of the molecules (a) SiO_2, (b) H_4SiO_4, (c) H_8SiO_6 with R(SiO) = 1.75Å and (d) $H_{12}SiO_8$. The solid contours represent positive values of $-\nabla^2\rho(\mathbf{r})$ and the dashed contours represent negative values for $-\nabla^2\rho(\mathbf{r})$. The maps are truncated as $\pm 150e/Å^5$ (See legend of Fig. 4).

a nodal surface, intermediate between those calculated for the H_4SiO_4 and the $H_{12}SiO_8$ molecules. The enhancement of the valence shell of the oxide ions in $H_{12}SiO_8$ appears to be largely unaffected by Si and to have the configuration of a free atom or ion (cf. Gibbs *et al* [34]). This result agrees with the predominantly ionic character of the bond. Thus, the enhancement of the electron density toward the critical point in a $Si^{VI}O$ bond is less than that of $Si^{IV}O$ bond but greater than that of $Si^{VIII}O$ bond, indicating that

$Si^{VI}O$ bond has a relatively large component of ionic character intermediate between that of a Si^{IV} and a Si^{VIII} bond.

The evidence provided by the mapping of $\nabla^2\rho(\mathbf{r})$ and $p(\mathbf{r})$ indicate that the interaction between Si and O in a molecule like H_4SiO_4 is intermediate in character as determined by Pauling [40] from electronegativity considerations. Also, the ionic character of the bond is indicated to increase in a regular way with increasing coordination number and $r_b(O)$ and decreasing $p(\mathbf{r}_c)$. The distance between a pair of bonded atoms and a bond critical point (defining their bonded radii) has been related to the relative electronegativities of the atoms. For example, Bader and Laidig [41] have observed that the location of $\mathbf{r}_c$ along a bond parallels the electronegativities of the atoms comprising the bond with the point being closer to the more electronegative atom. As the position of $\mathbf{r}_c$ determines the bonded radius and the atomic charge of an atom, it can be argued that the radius of an ion like the oxide ion in an XO bond can be used as a measure of the ionicity of a bond, the larger radius, the more ionic the character of the bond and the greater the atomic charge of the ion. As discovered by Feth *et al* [42], the promolecule radius of an oxide ion correlates with the electronegativity of the metal atom to which it is bonded, varying from ~0.60Å when bonded to a highly electronegative atom like N^{+5} to 1.35Å when bonded to a highly electropositive cation like K^{+1}. Using the bonded radii for the oxide ion recorded in a mapping of the experimentally determined electron density distributions for coesite (SiO_2), stishovite (SiO_2), danburite ($CaB_2Si_2O_8$), phenakite (Be_2SiO_4) and bromellite (BeO) [35, 43, 44, 45, 46], Gibbs *et al* [34] derived the expression

$$f_i(\mathrm{XO}) = (1.0 - \exp(-1/4(-0.85 + 2.64 \times r_b(\mathrm{O}))^2) \quad (1)$$

which relates the fractional amount of ionic character, f_i (XO), of an XO bond to the bonded radius of the oxide ions, r_b(O). With this expression, f_i(SiO) for the SiO bonds of each of the four molecules can be estimated using the bonded radii given in Table 1. As the atoms in these molecules have space-filling requirements that are governed by a range of external forces as well as their average $p(\mathbf{r})$-values, a given atom cannot be expected to exhibit a constant value for its bonded radius. As displayed in Figure 5, the bonded radius of the oxide ion is not constant but increases linearly with R(SiO) from ~0.86Å for the SiO bonds in the SiO_2 molecule to ~0.96Å in H_4SiO_4 to ~1.06Å in H_8SiO_8 to ~1.20Å in $H_{12}SiO_8$. When inserted into Eq. 1, these radii indicate the fractional ionic character of the SiO bond increases in a regular way with the coordination number of the Si atom from ~0.40 for a $Si^{II}O$ bond with a $p(\mathbf{r}_c)$ value of $1.36e/Å^3$ to ~0.50 for a Si^{IV} bond with a $p(\mathbf{r}_c)$ value of $0.96e/Å^3$ to ~0.60 for a $Si^{VI}O$ bond with a $p(\mathbf{r}_c)$ value of ~$0.67e/Å^3$ to ~0.75 for a $Si^{VIII}O$ bond with a $p(\mathbf{r}_c)$ value of

~0.50e/Å$_3$. Similar estimates have been made of the fractional ionic character of the SiO bonds in coesite, stishovite and the fluorite structure type of SiO_2 using Equation 1 and the bonded radii obtained from experimental and theoretical electron density maps [34].

In summary, an analysis of the total electron density distribution of a molecule, unlike a deformation electron density distribution, provides values of $p(\mathbf{r}_c)$ that relate to both the strength and the length of a bond. The curvatures of $p(\mathbf{r}_c)$ increase in a regular way with increasing $p(\mathbf{r}_c)$ reflecting an increased sharpness of the profile of the electron density distribution with increased $p(\mathbf{r}_c)$. The position of the critical point along the bond not only determines the bonded radius of the oxide ion, but it also correlates with the electronegativities of the metal atoms to which the oxide ion is bonded and the fractional ionic character of the bond. The bonded radii calculated for the SiO bonds in a variety of molecules indicate that the fractional ionic character of the SiO bond increases in a regular way with increasing coordination number and bond length. Finally, the agreement between the properties of $p(\mathbf{r}_c)$ for the SiO bonds measured for coesite and those calculated for model $H_6Si_2O_7$ molecules suggests that the electron density distributions in the two systems are rather similar [34]. A study currently underway of the electron density distributions for a number of hydroxyacid molecules composed of first- and second-row X-cation containing polyhedra show that the trends presented in Figure 2 for the SiO bond hold in general for the bonds in these molecules [33]

ACKNOWLEDGEMENTS

The National Science Foundation is thanked for supporting this study with grant EAR-9303589 and France C. Hill with research assistantship. Dr. R. T. Downs of the Geophysical Laboratory, Carnegie Institution is thanked for critically reading the manuscript and Sharon Chiang is thanked for skillfully drafting one of the figures.

References

1. Robertson, J. M. (1953) *Organic crystals and molecules.* Cornell University Press, Ithaca, New-York.
2. Roux, M. and Daudel, R. (1955) Effect of chemical bonding on the electronic density case of the molecule Li_2, *Compt. Rend.* 24090-92.
3. Brindley, G. W. (1929) The distribution of charge in the chlorine ion in rock salt, *Phil. Mag.,* **7,** 616-623.
4. Booth, A.D. (1948) Fourier refinement technique, *Nature,* **161,** 765-766.
5. Cochran, W. (1951) Some properties of the (F_o-F_c)-synthesis, *Acta Cryst.,* **4,** 408-411.
6. Bragg, W.H. (1921) The intensity of X-ray reflection by diamond, *Proc. Roy. Soc. London,* **33,** 304-311.

7. Brill, R. (1950) The covalent bond in diamond and the X-ray scattering factor of covalent,-bonded carbon. *Acta Cryst.,* **3,** 333-337.
8. Becker, P. (1978) *NATO advanced study institute on electron and magnetization densities in Molecules and crystals.* Plenum Press, New-York.
9. Coppens, P. and Hall, M. B. (1982) *Electron distributions and the chemical bond.* Plenum Press, New-York.
10. Hirshfeld, F. L. (1985) Accurate electron densities in molecules, *J. Mol. Struct.* **130,** 125-141.
11. Feynman, R. P. (1929) Forces in molecules, *Phys. Rev.,* **56,** 340-343.
12. Bader, R. F. W. (1990) *Atoms in molecules,* Oxford Science Publications, Oxford.
13. Hirshfeld, F. L. (1992) The role of electron density in X-ray crystallography, in A. Domenicano and I. Hargittai, (eds.), *Accurate molecular structures,* Oxford Science Publications, New-York.
14. Tsirelson, V. G., Evdokimova, O. A., Belokoneva, E. L., Urusov, V. S. (1990) Electron density distribution and bonding in silicates: A review of recent data, *Phys. Chem. Minerals,* **17,** 275-292.
15. Stuckenschmidt, E., Joswig, W. and Baur, W. H. (1994) Natrolite. Part 11: Determination of the deformation electron densities by X-X method, Phys. *Chem. Minerals,* **21,** 309-316.
16. Dunitz, J. D. and Sieler, P (1983) The absence of bonding electron density in certain covalent bonds as revealed by X-ray analysis, *J. Am. Chem. Soc.,* **105,** 7056-7058.
17. Spackman, M. A. and Maslen, E. N. (1985) Electron density and the chemical bond. Reappraisal of Berlin's theorem. *Acta Cryst,* **A41,** 347-353.
18. Cremer, D. and Krakar, E. (1984) Chemical bonds without electron density-Does the difference electron-density analysis suffice for a description of the chemical bond?, *Angew. Chem. Int. Engl.,* **23,** 627-628.
19. Cremer, D. (1987) New ways of analyzing chemical bonding, in Z. B. Macsic (ed.), *Modelling* of *structure and properties* of *molecules,* 128-144.
20. Low, a. A. and Hall, M. B. (1994) Electron deformation densities and chemical bonding in transition metal complexes. **110,** 544-591.
21. Bader, R.F.W. and Essén, H. (1984) The characterization of atomic interaction, *J. Chem. Phys.* **80,** 1943-1960.
22. Bader, R. F. W., McDougall, P. J. and Lau, C. D. H. (1984) Bonded and nonbonded charge concentrations and their relation to molecular geometry and reactivity, *J. Am. Chem. Soc.,* **106,** 1594-1605.
23. Morse, P. M. and Feschbach, H. (1953) *Methods* of *theoreticalphysics,* McGraw Hill Book Company, New York.
24. Gibbs, G. V., Prewitt, C. T. and Baldwin, K. J. (1977) A study of the structural chemistry of coesite, *Zeit. Kristallog.,* **145,** 108-123.
25. Boisen, M. B., Gibbs, G. V., Downs, R. T. and D'Arco, Ph. (1990) The dependence of the SiO bond length on structural parameters in coesite, the silica polymorphs and the clathrasils, *Ani. Mineralogist,* **75,** 748-754.
26. Geisinger, K. L., Spackman, M. A. and Gibbs, G. V. (1987) Exploration of structure, electron density distribution and bonding in coesite with Fourier and Pseudoatom refinment methods using single crystal X-ray diffraction data, *J. Phys. Chem.,* **91,** 3237-3244.
27. Cohen, R. E. (1994) Theory of Crystalline SiO2. *Rev. in Mineralogy,*
28. Binggeli, N., Troullier, N., Martins, J.L., and Chelikowsky, J.R. (1991) Electronic properties of α-quartz under pressure, *Phys. Rev.,* **B44,** 4771-4778.
29. Newton, M. D. and Gibbs, G. V. (1980) Ab initio calculated geometries and charge distributions for H_4SiO_4 and $H_6Si_2O_7$ compared with experimental values for silicates and siloxanes, Phys. *Ghem. Minerals,* **6,** 221-246.
30. Pauling, L. (1952) Interatomic distances and bond character in the oxygen acids and related substances, *J. Phys. Chem.,* **56,** 361-365.
31. Pauling, L. (1980) The nature of silicon-oxygen bonds. *Am. Mineralogist,* **65,** 321-

323.
32. Cruickshank, D. W. J. (1961) The role of 3*d*-orbitals in π–bonds between (a) silicon, phosphorus, sulphur, or chlorine and (b) oxygen or nitrogen, *J. Chem.* Soc., 1961, 5486-5504.
33. Hill, F. C. (1995) PhD dissertation (in preparation), Virginia Polytechnic Institute and State University, Blackburg, Va.
34. Gibbs, G. V., Downs, J. W. and Boisen, Jr. M. B. (1994) The elusive SiO bond. *Rev. Mineral.,* **29**, 331-368.
35. Downs, J. W. (1995) The electron density and electrostatic potential of coesite, *J. Phys. Chem.* **99**, 6849-6856.
36. Gibbs, G. V., Boisen, M. B. and Downs, R. T., In preparation.
37. Knop, O., Boyd, R. J. and Choi, S. C. (1988) S-S bond lengths, or can a bond length be estimated from a single parameter?, *J. Am. Chem Soc.* , **110**, 7299-7301.
38. Pauling, L. (1929) The principles determining the structure of complex ionic crystals, *J. Am. Chem. Soc.,* **51**, 1010-1026.
39. Glasser, L. D. (1979) Non-existent silicates. *Zeits. Krist.,* **149**, 291-305.
40. Pauling, L. (1939) *The nature* of *the chemical bond,* Cornell University Press, Ithaca, NY.
41. Bader, R. F. W. and Laidig, K. F. (1993) Analysis and classification of the charge distribution using quantum mechanics, *Trans. Am. Crystal Assoc.,* **26**, 1-21.
42. Feth, S., Gibbs, G. V., Boisen, M. B. and Myers, R. H. (1983) Promolecule radii for nitrides, oxides and sulfides. A comparison with effective ionic and crystal radii, *J. Phys. Chem.* **97**, 11445-11450.
43. Spackman, M. A., Hill, R. J. and Gibbs, G. V. (1987) Exploration of the structure and bonding in stishovite with Fourier and pseudoatom refinement methods using single crystal and powder x-ray diffraction data, *Phys. Chem. Minerals,* **14**, 139-150.
44. Downs, J. W. and Swope, R. J. (1992) The Laplacian of the electron density and the electrostatic potential of danburite, $CaB_2Si_2O_8$, *J.* Phys. *Chem.,* **96**, 4834-4840.
45. Downs, J. W. (1990) Electrostatic properties of minerals from X-ray diffraction data: A guide for accurate atomistic models, in J. Ganguly (ed.), *Diffusion, Atomic Ordering, and Mass Transport, Advances in Physical Geochemistry, Vol. 8,* Springer-Verlag, Berlin.
46. Downs, J. W. and Gibbs, G. V. (1987) An exploratory examination of the electron density and electrostatic potential for phenakite, *Am. Mineralogist,* **72**, 769-777.

THE NATURE OF SILICON-OXYGEN BONDS IN SILICA POLYMORPHS

B. SILVI, A. SAVIN AND F. R. WAGNER*
Laboratoire de Chimie Théorique,
Université Pierre et Marie Curie,
4, Place Jussieu, 75232 Paris cedex (France)
* *present address: Institut für Anorganische und Analylische Chemie und Radiochemie,*
Universität des Saarlandes Im Stadtwald,
66123 Saarbrücken (Germany)

1. Introduction

Quantum chemists have devoted considerable effort in order to understand the nature of the chemical bond in silicated minerals. The pioneering work of Linus Pauling[1, 2, 3] provides a first example in which the valence bond concept is used in order to explain why the SiO bond length in silicates is less than the sum of the single bond radii of the two atoms. Moreover, this interpretation emphasizes the role of $3d$ orbitals through a sp^3d^2 hybridization of the silicon. With the advent of efficient computational facilities and of molecular *ab initio* softwares, several leading groups have published reliable calculations performed within the cluster, or more precisely prototype molecule framework. Information provided by such calculations concern several important domains. Born-Oppenheimer energy surfaces allow to set up site-site or covalent potentials to be used in further lattice dynamics or molecular dynamics studies. Important advances in this area are due to Gibbs *et al*[4], Lasaga *et al*[5], Tsuneyuki *et al*[6] and Kramers *et al*[7]. Interaction of such prototype silicated molecules with other reactant molecules, such as water or ammonia,, allows to model the catalytic properties of zeolite[8, 9, 10]. Finally, the study of the electronic structure is of primary importance for understanding the bonding. One important result of the earlier *ab initio* calculations was to discard the possible contribution of silicon *d* orbitals to the bonding. Most calculations on prototype

B. Silvi and P. D'Arco (eds.), Modelling of Minerals and Silicated Materials, **179-199.**

on prototype molecules performed either with minimal or split, valence basis sets[11], as well as periodic Hartree-Fock calculations of quartz[12,13], cristobalite and tridymite[12, 14] correctly reproduce the experimental Si-O bond length. Improvement brought by 3*d* function is less important in this respect and are of the order of what is expected from polarization functions. G. V. Gibbs and his team have been continuously concerned by the understanding of the nature of the SiO bond. They started their analysis with the available quantum chemical tools such as the Mulliken population analysis and electron density difference maps. However, they rapidly realized the limitations of these techniques which rely too much upon the approximations made in the actual calculations of electronic structures. A better "trail toward the Grail"[15] is provided by the theory of Atoms in Molecules of Richard Bader[16]. In a chapter of the present book, Gibbs *et al* discuss in details the limitations of electron density difference maps and show how efficient Bader's analysis is. However, the information carried by the electron density alone is not sufficient to clearly characterize the nature of the bonds. In a recent paper[17], we have shown that the topological analysis of a local function, which is related to the local kinetic energy excess due to the Pauli repulsion, can be used to characterize and define chemical bonds. The topological analysis of the so-called electron localization function (ELF), originally proposed by Becke and Edgecombe[18], provides a set of mathematizable definitions of the bond type.

In this chapter, the main lines of this new theory of chemical bond are presented in details and then it is applied to representative tetracoordinated and hexacoordinated silica polymorphs, namely low quartz, low cristobalite stishovite, the recently discovered $CaCl_2$-like high pressure phase and a prototype fluorite structure in which silicons are octacoordinated.

2. The topological classification of chemical bonds

The conventional tools used in Quantum Chemistry to characterize the bonding (population analysis, orbital localization) mostly rely on concepts related to the approximate treatment of many electron systems such as orbitals, valence-bond structures, atomic basis. In their spirit, they give an illegitimate physical content to mathematical objects which appear as intermediates along the calculation. This transgression of the interpretative postulates of Quantum Mechanics is done in order to conciliate the "atoms in molecules" and localized bonds of the chemical common sense with the impossibility of partitioning the molecular hamiltonian into atomic and bonding contributions. Their reliability is very questionable and results are highly method dependent. Moreover, these methods only apply in a LCAO framework and therefore are useless for calculations performed

within plane-wave basis functions, one-center expansions, numerical functions, quantum Monte Carlo and correlated basis function frameworks. The necessary information cannot be extracted neither from experiment nor from an exact wavefunction.

In order to design a more rigorous theory of chemical bonds consistent with both Quantum Mechanics and chemical experience it is necessary to invoke an external mathematical theory able to extract qualitative information from quantitative. The topological analysis of the gradient vector field of a local function which carries the physical information is the well-established mathematical approach to handle this problem[19].

2.1. KINETIC ENERGY RELATED LOCAL FUNCTIONS

The formation of a chemical bond from fragments is the result of a competition between the potential and kinetic energies which leads to an optimal lowering of the total energy. As pointed out by Ruedenberg[20] : "Delocalization of the valence electrons from one atom to several atoms leads to a lowering of the kinetic energy pressure and, as a consequence there results a firmer attachment of these electrons to the nuclei with a concomitant lowering of the total energy." The importance of the kinetic energy contribution to the bonding is specifically a quantum effect which can be interpreted as a consequence of the uncertainty principle[20]. Once again, we will quote Ruedenberg who states :"The wave mechanical kinetic behavior, which differs typically from the classical behavior and is characterized by the cue *uncertainty principle,* is a fundamentally essential element of covalent binding. Any explanation of chemical binding based essentially on electrostatics, or any other nonkinetic concept, misses the very reason why quantum mechanics can explain chemical binding, whereas classical mechanics cannot".

The study of the chemical bond from a local kinetic energy point of view, is therefore expected to bring a deeper insight into the understanding of its nature. For this purpose we need to calculate and to analyze the one particle kinetic energy density. In principle, this function, $K(\mathbf{r})$ should be calculated from its classical analog :

$$K(\mathbf{r}) = \int F(\mathbf{r}, \mathbf{p})\left(\frac{\mathbf{p}^2}{2m}\right)d\mathbf{p} \qquad (1)$$

in which, m is the mass of the particle and $F(\mathbf{r}, \mathbf{p})$ stands for the joint distribution of position and momentum. Unfortunately, a true joint distribution cannot be defined in Quantum Mechanics. It is nevertheless possible to introduce the so-called phase-space quasi distributions, such as the Wigner function, in order to get an expression which has the property when integrated over all space, yields the proper expectation value of the kinetic

energy. The quasi distributions are build up from correspondence rules and are required to yield the correct marginal distributions. As discussed by Shewell[21], the joint operators derived from the correspondence rules may not fulfill the requirement of uniqueness (i.e different operators for one physical quantity) or yield results in contradiction with the current interpretation of quantum mechanics. Moreover, there is no reason to use one rule rather than another. Cohen has shown[22] that all the possible phase-space distribution functions which obey the correspondence rules and yield correct marginal distributions belong to a given class of analytical functions of the form :

$$F(\mathbf{r},\mathbf{p}) = \left(\frac{1}{6}\right)^6 \int \exp[-i\tau\cdot\mathbf{p} + i\theta\cdot(\mathbf{u}-\mathbf{r})] f(\theta,\tau) \times \psi^*(\mathbf{u}-\frac{1}{2}\tau)\psi(\mathbf{u}+\frac{1}{2}\tau) d\theta d\tau d\mathbf{u} \tag{2}$$

where $f(\theta,\tau)$ is any function which satisfies

$$f(0,\tau) = f(\tau,0) = 1. \tag{3}$$

The relevance of quasi-distributions in physical applications has been discussed by Dahl [23] who has shown that the Wigner function is the only one which satisfies strong requirements such as being the expectation value of the so-called Wigner operator and therefore to be a description based on observables in the sense of Dirac [24]. For one particle, the corresponding possible form of the kinetic energy density is thus given by[25] :

$$K(\mathbf{r}) = \frac{1}{2}|\nabla\psi|^2 - \frac{1}{8}\nabla^2|\psi|^2 - \left(\frac{1}{2\pi}\right)^3 \int \exp[i\theta\cdot(\mathbf{u}-\mathbf{r})] \left\{ \frac{|\psi(\mathbf{u})|^2}{2} \nabla_\tau^2 f(\theta,\tau)|_{\tau=0} + i\nabla_\tau f(\theta,\tau)|_{\tau=0}\cdot J(\mathbf{u}) \right\} d\theta d\mathbf{u} \tag{4}$$

where J is the quantum mechanical current

$$J = \frac{i}{2}(\psi\nabla\psi^* - \psi^*\nabla\psi) \tag{5}$$

Generalization to a many particle system is straightforward.

$K(\mathbf{r})$ appears to be the sum of two contributions : the first one $T(\mathbf{r}) = \frac{1}{2}|\nabla\psi|^2$ yields the expectation value of the kinetic energy when integrated over all space. This contribution is always positive, it is called the definite positive kinetic energy density. The integral over space of the remaining contribution vanishes. For either a real wavefunction or a stationary state the quantum mechanical current is zero and therefore this remaining term

can be expressed in terms of the $f(\theta, \tau)$ function, of the density and of their derivatives.

For a quantum system with a given one particle density, $T(\mathbf{r})$ is the only term which is sensitive to the nature (fermion or boson) of the particles. For a many-fermion system, $T(r)$ can be formally expressed as the sum of two contributions, one of which accounting for the Pauli principle and the other not. However, another paatition scheme in which the total kinetic energy is written as the sum of the von Weizsäcker term $T_W(\mathbf{r})$[26] and of a remaining non-von Weizsäcker term $T_{nW}(\mathbf{r})$ term has been generally adopted[27, 28, 29, 30]. The von Weizsäcker term :

$$T_W(\mathbf{r}) = \frac{1}{8}\frac{|\nabla\rho(\mathbf{r})|^2}{\rho(\mathbf{r})} \tag{6}$$

corresponds to the definite positive kinetic energy density of a system of independent particles with the density $p(\mathbf{r})$. The non-von Weizsäcker term includes the Coulomb and Fermi correlation contributions to the kinetic energy density, its expression involves therefore quantities related to the second order density matrix. Tal and Bader[27] have established that $T_{nW}(\mathbf{r})$ is a true lower bound to the definite positive kinetic energy density, i.e :

$$T_{nW}(\mathbf{r}) = \frac{1}{2}|\nabla\psi|^2 - \frac{1}{8}\frac{|\nabla\rho(\mathbf{r})|^2}{\rho(\mathbf{r})} \geq 0 \tag{7}$$

Moreover, this term is the difference of the kinetic energy density of the actual system and of that of a system of spin-free independent particles both with identical one-particle densities $p(\mathbf{r})$.For real wavefunctions or for stationary states, it is simply the difference of the definite positive kinetic energies since the (unwanted) remaining contributions cancel one another. Another attractive property of the non-von Weizsäcker contribution is that it appears to be the trace of the Fisher's Information matrix[28].

For practical applications, we will not consider $T(\mathbf{r})$ itself but rather the definite positive kinetic energy density of independent particles $T_s(\mathbf{r})$ which appears in the exact density functional theory[31]. Within this framework, the non-von Weizsäcker term accounts only for the Fermi correlation and is usually referred to as Pauli kinetic energy density[32]. Another propery of $T_{nW}(\mathbf{r})$ is its relationship to the conditional probability $P^{\sigma\sigma}_{cond}(\mathbf{r}, \mathbf{r}')$ for electrons of parallel spin in the single determinental approximation :

$$T_{nW}(\mathbf{r}) = \nabla^2_{\mathbf{r}'} P^{\sigma\sigma}_{cond}(\mathbf{r}, \mathbf{r}')\Big|_{\mathbf{r}'=\mathbf{r}} \tag{8}$$

In the original definition of *ELF,* given by Becke and Edgecombe [18], $P^{\sigma\sigma}_{cond}(\mathbf{r}, \mathbf{r}')$ was used.

The definite positive kinetic energy density has received a considerable attention in order to build approximate kinetic energy functionals to be used in a density functional theory not based on orbitals (for a review of such functionals see Lacks and Gordon[33]). Among the most promising routes to this goal, we can mention the approximation proposed by Lee, Lee and Parr[34]:

$$T_s(\mathbf{r}) \approx C_F \rho^{5/3}(\mathbf{r}) F(s(\mathbf{r})) \tag{9}$$

in which $C_F = \frac{3}{10}(3\pi^2)^{2/3}$, $F(s(\mathbf{r}))$ is a function which accounts for the deviation from uniformity and homogeneity and $s(\mathbf{r})$ the scaled density gradient defined by :

$$s(\mathbf{r}) = \frac{|\nabla \rho(\mathbf{r})|}{2(3\pi^2)^{2/3}\rho^{4/3}(\mathbf{r})} \tag{10}$$

For slowly varying densities, the kinetic energy functional can be represented by one of its gradient expansions. The gradient expansion of the kinetic energy density is not unique since it relies upon different derivations techniques [35], which yield or not a contibution of the laplacian of the density in the second order correction. In the following we will consider the expansion expression which does not involve $\nabla^2 p(\mathbf{r})$:

$$T_s(\mathbf{r}) = C_F \rho^{5/3}(\mathbf{r}) + \frac{1}{72}\frac{|\nabla \rho(\mathbf{r})|^2}{\rho(\mathbf{r})} + \ldots = C_F \rho^{5/3}(\mathbf{r}) \left(1 + \frac{5}{27} s^2(\mathbf{r}) + \ldots\right) \tag{11}$$

A similar expression can be derived for the non-von Weizsäcker contribution :

$$T_{nW}(\mathbf{r}) = C_F \rho^{5/3}(\mathbf{r}) - \frac{1}{9}\frac{|\nabla \rho(\mathbf{r})|^2}{\rho(\mathbf{r})} + \ldots = C_F \rho^{5/3}(\mathbf{r}) \left(1 - \frac{40}{27} s^2(\mathbf{r}) + \ldots\right) \tag{12}$$

The scaling by $p^{5/3}$ is made in order to minimize as well as possible the density dependence of the measure of the deviation from uniformity and homogeneity.

We consider now the class of parametrized local functions :

$$G(\mathbf{r}; a) = C_F^{-1} \rho^{-5/3} (T_s(\mathbf{r}) - a T_W(\mathbf{r})) \tag{13}$$

in which the parameter a lies in the interval [0,1]. All these functions are positive. It is possible to make a transformation in order to confine them in the range [0,1],either with the scheme proposed by Becke and Edgecombe for ELF[18]:

$$\eta_a(\mathbf{r}) = \left(G(\mathbf{r}; a)^2 + 1\right)^{-1} \tag{14}$$

or with :

$$\vartheta_a(\mathbf{r}) = \exp\left(-G(\mathbf{r}; a)\right) \tag{15}$$

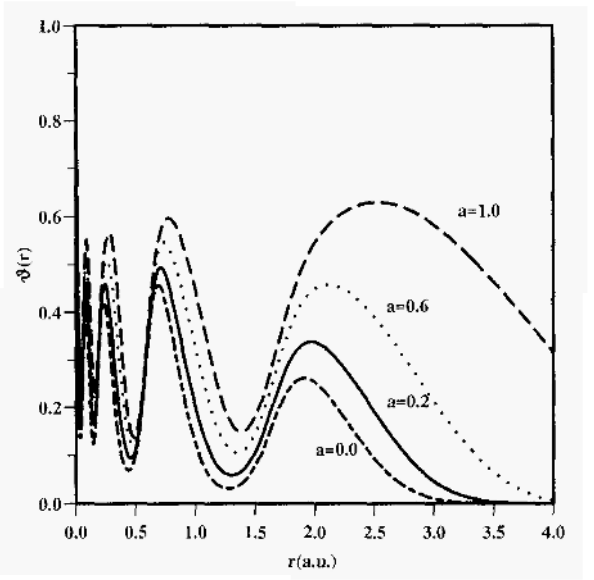

Figure 1. Radial localization functions $\vartheta_a(\mathbf{r})$ for xenon.

$\eta_1(\mathbf{r})$ is the original ELF function. For a given value of a both $\eta_a(\mathbf{r})$, $\vartheta_a(\mathbf{r})$ and $G(\mathbf{r}; a)$ have their extrema at identical positions. These functions display the shell structure of atoms up to the O shell as shown for xenon on figure 1. The increase of the a parameter slightly shifts the locations of the maxima nad minima of ϑ_a towards larger values of r. It is worthy to note, that in contrast with the usual orbital model there is no subshell structure, although the curves were generated from a Hartree-Fock wavefunction.

These functions provide a local measure of the effect of the Pauli repulsion on the kinetic energy density. In the region of space where the Pauli repulsion is weaker than in a uniform electron gas of identical density, we should say where the local parallel pairing is lower, $\eta_a(\mathbf{r})$ and $\vartheta_a(\mathbf{r})$ are respectively larger than 0.5 and 0.36. In the regions where the local parallel pairing is higher (and therefore the Pauli repulsion strongly active) they are lower than these latter values. Up to now, only η_1 (i.e. ELF) has been extensively used.

2.2. SKETCH OF THE TOPOLOGICAL ANALYSIS OF DYNAMICAL SYSTEMS

The topological analysis of local function provides a partition of the space, for our purpose the molecular space, which is analogous to the more familiar partition made in hydrology in river basins delimited by watersheds. In this

paragraph we intend to provide the definitions of the essential concepts for those of the readers who are not trained in this part of mathematics.

By definition a *dynamical system* is a field of bound vectors X on a manifold M. For each and every point of M of coordinates {m} the equations $dm/dt = X(m)$ determine a unique trajectory $h(m)$. Although the analogy with a velocity field is purely formal, the method has been widely used to model the time evolution of many phenomena. The trajectories begin and end in the neighbourhood of points for which $X(m) = 0$. For a given point p belonging to M, $\alpha(p)$ and $w(p)$ denote the limit-sets of $p(t)$ in M corresponding respectively to $t \rightarrow \infty$ and to $t \rightarrow -\infty$.

A *gradient dynamical system* is a dynamical system for which the vector field X derives from a scalar function V, called the *potential* function, that is $X = \nabla V$. The word potential is here somehow confusing because it has not exactly the same meaning as in Mechanics where minus the gradient field of the potential energy is not the velocity field but the force field and therefore is proportional to the acceleration field. For a gradient dynamical system, the *critical points* (i.e those for which $\nabla V = 0$) are single points in the most general case. Exceptions may occur if the system belongs to a continuous symmetry group, in such case those critical points which are not located on the infinite order symmetry element form (in $\mathbb{R}^3$) either a sphere ($SO(3)$ group) or a circle (C_∞ group). A convenient choice of the coordinate system allows to exploit the symmetry in order to reduce the dimensions and to remove the degeneracy of the critical points.

The *stable manifold* or *inset* of a critical point is the set of all the points for which this critical point is an ω-limit, the *unstable manifold* or *outset* the set of those for which it is an α-limit. The critical points of a gradient dynamical system are classified according to the number of positive *critical exponents,* here the eigenvalues of the hessian matrix, the *index* which is also the dimension of its unstable manifold. The index of a critical point m of the vector field X is denoted by $I(X, m)$. They are also denoted by a pair of integers (r,s), the rank (number of non-zero eigenvalues) and the signature (number of positive minus negative eigenvalues) of the hessian matrix. In the euclidian 3-dimensional space, there are four kinds of critical points : the *repellors* of index 3, noted $(3,3)$, which are the local minima of the potential function; the saddle points (3,1) and $(3,-1)$ of index respectively 2 and 1; the *attractors* $(3,-3)$ of index 0 which are the local maxima of the potential function. Attractors are only ω-limits, repellors only α-limits whereas saddle points are both. The stable manifold of an attractor is called the *basin* of the attractor. The *separatrices* are the boundary points, lines or surfaces of two or more basins. They are the stable manifolds of the saddle points. The number of *hyperbolic* critical points (i.e. without zero critical exponent) satisfies the phase-rule type relationship which is given by the

Poincaré-Hopf theorem :

$$\sum(-1)^{I(X,m)} = \chi(M) \tag{16}$$

The sum runs over the critical points of the vector field X bound on the manifold M and $\chi(M)$ is the Euler characteristic of the manifold. For finite and periodic systems in R^q, $q \leq 3$, the Euler characteristic is 1 and 0 respectively.

Another very helpful concept is that of domain. Let M' a subset of the manifold M, if for any couple of points a and b there exists a path joining a and b totally contained in M' then M' is a domain. In the case of the gradient field analysis, volumes bounded by a given isosurface of the potential function form domains. For a given potential function the number of domains depends upon the value defining the isosurfaces. We have been led to consider two types of domains according to the number of attractors lying within them. A domain contains at least one attractor. In this case it is said to be irreducible because the increase of the value defining its bounding isosurface below the value of the potential function at the attractor cannot give rise a splitting into several new domains. If a domain contains more than one attractor, it is reducible because it is possible to get new domains by increasing the value of the bounding isosurface. The values of the bonding isosurface which correspond to domain separation are those taken by the potential function at the critical points located on the separatrix surface between two basins.

2.3. THE TOPOLOGICAL ANALYSIS OF ELF

The localization functions described previously are scalar functions the gradient field analysis of which allows to locate attractors and basins with a clear chemical signification[17]. Usually, the attractors of a gradient field are single points as it is the case for the gradient field of the density. However, for the ELF function, they can also be circles and spheres if the system belongs to a continuous symmetry group (here, cylindrical and spherical symmetry respectively).

2.3.1. *Classification of basins*

There are basically two types of basins. On the one hand are core basins organized around nuclei (with $Z > 2$) and on the other are valence basins in the remaining space. The structure provided by the core basins closely matches the inner atomic shell structure. A valence basin is characterized by its synaptic order which is the number of cores to which it is connected [36]. To be connected to a core a valence basin must fulfill the three following conditions :

i) It is bounded to the core basin by a part of a common separatrix.
ii) The valence attractor lies within the smallest (reducible or irreducible) valence *f*-localization domain which totally surrounds another *f*-localization domain which contains one or more core attractors.
iii) The proton is counted as a formal core.

In principle, a core is always totally encapsulated by at least one valence basin and therefore propositions i) and ii) are redundant when *f* tends to zero unless the valence localization domains and a core domain have already merged into a single domian. In our description of the chemical bond a basin which contains a proton is considered as a valence basin except for the peculiar case of the very strong hydrogen bond for which a pseudo core shell is found around the bridging proton. The valence basins are therefore divided into mono-, di- and polysynaptic ones. As an example, a C-H bond is characterized by a disynaptic basin which encompasses the proton and shares a common separatrix with the carbon core basin. The nomenclature adopted to label core and valence attractors and basins is given in table 1. The attractors and basins are labeled as $T_{[i]}$(atom labels). T denotes

TABLE 1. Nomenclature of attractors and basins.

synaptic order	nomenclature	symbol
0	core	$C(X_i)$
1	monosynaptic	$V(X_i)$
2	disynaptic	$V(X_i, Y_j)$
≥ 3	polysynaptic	$V(X_i, Y_j, \ldots)$

the type of attractor, V for valence, C for core ; *i* is an optional running number in the case of multiple attractors related to the same atom(s). For example, in the water molecule there is one core attractor for the oxygen *K*-shell labeled C(O), two protonated disynaptic attractors $V(H_1, O)$ and $V(H_2, O)$, and two monosynaptic attractors corresponding to the lone pairs $V_1(O)$ and $V_2(O)$. In ethane, the disynaptic attractor of the C-C bond will be named $V(C_1, C_2)$ accordingly.

The classification of bonds proposed previously remains valid with this new nomenclature. The shared electron interaction (a more consistent name is shared valence basin interaction) is characterized by a di or polysynaptic basin. The lone pairs give rise to monosynaptic basins. It is important to note that this picture of the chemical bond implies a somehow different point of view than that currently adopted in Chemistry. In the standard pictures a bond is considered as a link joining an atom to another one.

Here, what is important is the number of cores a given piece of glue (the valence basin) is stuck on.

2.3.2. *The hierarchy of localization basins*

Another criterion of discrimination between basins is provided by the reduction of reducible domains. The reduction of a reducible localization domain occurs at a critical value of the bounding isosurface, over which the domain is split into domains containing fewer attractors. The localization domains are then ordered with respect to the ELF critical values yielding bifurcations. Starting at a very low ELF value, we find only one localization domain (the whole space for $\eta(\mathbf{r}) = 0$.) upon increase of the isosurface defining value, we meet a first separation between valence and core domains, at higher ELF values the valence reducible domain is split in its turn. The value of the localization function at the saddle points lying on the separatrix provides a quantitative information to order the basins. The hierarchy of the bifurcation can be visualized by a tree-diagram [36].

2.3.3. *Integrated density over the localization basins*

The partition of the molecular space into basins of attractors allows the calculation of related properties by integration of the property densities over the basins[37]. In particular, for a basin labeled Ω_A, one can define the average population as :

$$\bar{N}(\Omega_A) = \int_{\Omega_A} \rho(\mathbf{r}) d\mathbf{r} \tag{17}$$

Within the framework of our theory, these average populations are referred to as core, di- or polysinaptic and monosynaptic (i.e. lone pair) populations according to the type of attractor which defines the basin. Such average populations over ELF basins have been first calculated by us[36, 38, 39] and recently by Häussermann *et al.* for intermetallic solids[40]. They are not expected to have integral values and the bond populations would be about twice the topologically defined bond orders[41, 42].

The RMS deviation $\sigma(\bar{N};\Omega_A))$ is defined by[43, 44] :

$$\sigma^2(\bar{N};\Omega_A)) = \langle N^2\rangle_{\Omega_A} - \langle N\rangle^2_{\Omega_A} \tag{18}$$

It represents the quantum mechanical uncertainty on $\bar{N}(\Omega_A)$. The variance (or fluctuation) σ^2 has been investigated by Bader in the framework of atomic basins[45]. The variance is expressed in terms of the diagonal elements of the first (p(x)) and second order $(\pi(\mathbf{x}_1,\mathbf{x}_2))$ density matrices[46] as :

$$\sigma^2(\bar{N};\Omega) = \int_{\Omega} d\mathbf{x}_1 \int_{\Omega} d\mathbf{x}_2 \pi(\mathbf{x}_1,\mathbf{x}_2) + N(\Omega) - [N(\Omega)]^2 \tag{19}$$

in which $\mathbf{x}_i$ denotes the space and spin coordinates of the electron labeled i. For a single determinental wavefunction (i.e. Hartree-Fock or Kohn-Sham) $\sigma^2(\bar{N};\Omega)$ is the difference between the basin population and the integral over the basin of the exchange part of the second order density matrix :

$$\sigma^2(\bar{N};\Omega) = \bar{N}(\Omega) - B(\Omega,\Omega) \tag{20}$$

In terms of the orbitals $\phi_i(\mathbf{r})$ and of the occupations n_i^α, n_i^β, $B(\Omega,\Omega)$ is given by :

$$B(\Omega,\Omega) = \sum_i \sum_j (n_i^\alpha n_j^\alpha + n_i^\beta n_j^\beta)\langle\phi_i|\phi_j\rangle_\Omega\langle\phi_j|\phi_i\rangle_\Omega \tag{21}$$

in which

$$\langle\phi_i|\phi_j\rangle_\Omega = \int_\Omega d\mathbf{r}\phi_i^*(\mathbf{r})\phi_j(\mathbf{r}) \tag{22}$$

It is also convenient to define the interbasin integrated exchange density :

$$B(\Omega_A,\Omega_B) = \sum_i \sum_j (n_i^\alpha n_j^\alpha + n_i^\beta n_j^\beta)\langle\phi_i|\phi_j\rangle_{\Omega_A}\langle\phi_j|\phi_i\rangle_{\Omega_B} \tag{23}$$

The fluctuation in a superbasin $\Omega_A \cup \Omega_B$ is :

$$\sigma^2(N;\Omega_A \cup \Omega_B) = \sigma^2(\bar{N};\Omega_A) + \sigma^2(\bar{N};\Omega_B) - 2B(\Omega_A,\Omega_B) \tag{24}$$

and for the whole space

$$\sigma^2(\bar{N};\Omega_A \cup \Omega_B \cup \ldots) = 0 \tag{25}$$

It follows from eq. 24 that for independent basins σ^2 is an extensive quantity. Following Bader[45], it is useful to introduce the relative fluctuation

$$\lambda(\Omega) = \sigma^2(\bar{N};\Omega)/\bar{N}(\Omega) \tag{26}$$

which is positive and also expected to be less than 1.

3. The Bonding in SiO_2 polymorphs

In crystalline silica the silicon coordination is four for quartz ($P3_221$), tridymite ($F1$ and Cc), cristobalite ($P4_12_12$), coesite ($C2/c$) and keatite ($P4_12_12$), six in stishovite (rutile type structure $P4_2/mnm$) and in the recently high pressure phase with a $CaCl_2$ structure ($Pnnm$) and eight in a fluorite type ($Fm3m$) model structure which is one of the hypothetical post-stishovite modifications investigated by modeling techniques. Of course, the

coordination number of oxygen is always half of that of silicon. The conventional discussion of the Si-O bond is focused on the silicon coordination rather than on the oxygen one. Accordingly, in Pauling's representation of the silicon oxygen bond [3], each oxygen donates one electron to the silicon which is then enabled to form at most six single bonds. The silicon has six valence electrons and is essentially of the sp^3d^2 type. In this picture, the ionic character of the bond deduced from the electronegativity rule is 50%. In tetracoordinated polymorphs, each silicon forms two double bonds and two single bonds, the resonance between the limit structures yields a double bond character of about 55% for the Si-O bond. This temptatively explains why the observed bond length is larger than the sum of the covalent raddi and also why the $\angle$Si-O-Si bond angles observed in low-quartz and low-cristobalite are much more wider than the value expected between single bonds. Though stishovite is not discussed in Pauling paper's, it is worthy to note that this picture accounts for the larger SiO distance observed in this modification.

Another popular description of the chemical bond is provided by the VSEPR model of Gillespie [47, 48]. This model partly explains the geometries of the silica polymorphs investigated here. For Si it cannot give much insight as Si has no lone pairs. The polyhedron with the largest number of staggered bond pairs is preferred for CN 4 (tetrahedron) and CN 6 (octahedron) while for CN 8 the fluorite structure yields a cubic coordination instead of an expected quadratic antiprism. For oxygen the VSEPR model runs into difficulties : for 2-coordinated oxygens, the observed structure is neither consistent with an AX2E (1 double bond, 1 single bond and 1 lone pair) or AX_2E_2 model (2 single bonds and 2 lone pairs) because the angle $\angle XAX \sim 146^\circ$ is too wide. In stishovite, the three O-Si bonds around the oxygen are coplanar, corresponding to the AX_3E_2 model, but the electron count (4 electron pairs) only allows for an AX_3E model.

Though there is no striking contradiction between the pictures provided by Pauling and by the VSEPR model, the topological approach is expected to give more reliable answers. From the preceeding discussion, it appears that the questions concern more the oxygen side than the silicon one in both Pauling's and VSEPR approaches. The calculation of the wavefunctions have been performed at the all-electron level with the periodic software CRYSTAL92 [49] A polarized split-valence basis set has been used. The valence part is that described by Jolly *et al* [50] whereas the core orbitals are the standard 6-31G ones [51]. The integration over the electron density and *ELF* function basins has been carried out numerically on a rectangular grid. This technique is less accurate than that designed by Biegler-König *et al* [37]. The estimated error on basin populations is about ten times larger (0.1 *e* instead of 0.01). However, it is enough accurate to provide reliable

information on the dominant features and on the trends along the series of polymorphs.

3.1. BADER'S ANALYSIS

The values of the oxygen charge $q(O)$, of the laplacian, of the ratio of the perpandicular and parallel components of the hessian matrix and of the bond ellipticity ϵ at the bond critical point are reported in table 2 for the structures investigated here. In Bader's theory a positive value of the laplacian of the density, $\nabla^2\rho(\mathbf{r})$, is a criterion of the closed-shell interaction. Another criterion is ratio $\frac{|\lambda_1|}{\lambda_3}$ which takes larger values (> 1.0) for electron shared interaction than for the closed shell one (< 0.5) and allows a discussion of intermediate cases. The bond ellipticity, $\epsilon = \lambda_1/\lambda_2 - 1$ where λ_1 and λ_2 are the smallest eigenvalues of the hessian matrix, gives an indication of the double bond character. For example, the ellipticity of the C-C bond is respectively 0.0, 0.23 and 0.45 in ethane, benzene and ethylene [16]. The oxygen charges of α-quartz and $CaCl_2$ type structures cannot be accurately computed because technical difficulties (such as hexagonal cell in quartz) downgrade the accuracy of the results. Though the calculated values are rather close to those of α-cristobalite and stishovite, it is not possible to take them into account in reliable comparisons.

TABLE 2. Characterization of atomic interactions in silica polymorphs. All quantities in atomic units. The second entry for stishovite and $CaCl_2$-type structures correspond to the larger Si-O bond. The estimated error on the oxygen charge in quartz amd $CaCl_2$ structure is about $0.2e$.

	$q(O)$	$\nabla^2\rho$	$\frac{\lvert\lambda_1\rvert}{\lambda_3}$	ϵ
α-quartz	-0.7	1.270	0.15	0.015
α-cristobalite	-0.7	1.216	0.16	0.0
stishovite	-1.1	0.652	0.18	0.010
		0.514	0.18	0.0
$CaCl_2$-type	-1.1	1.076	0.16	0.011
		0.918	0.15	0.0
fluorite-type	-1.55	0.326	0.18	0.0

The oxygen net charge increases with the oxygen coordination and the ionic character is ~ 35% for coordination 2, ~ 55% for coordination 3 and ~ 75 % for 4. The values provided by the Bader's analysis for quartz and cristobalite are significantly lower those that assumed from electronegativity. In both cases the Laplacian of the density is positive and the $\frac{|\lambda_1|}{\lambda_3}$

ratio very small which corresponds to Bader's closed-shell interaction. This result is not fully consistent with the rather moderate ionic character of the Si-O bond in quartz and cristobalite. However, the links between the sign of the laplacian or the magnitude of the $\frac{|\lambda_1|}{\lambda_3}$ ratio and the interaction type are rather speculative. The bond ellipticity is always negligible and, accordingly, there is no indication for a partial double bond character in quartz and cristobalite.

3.2. TOPOLOGICAL ANALYSIS OF *ELF*

The picture provided by the *ELF* function displays silicon cores and oxygen cores surrounded by a valence shell [52]. The oxygen valence shell as shown on figure 2 contains 3, 5 and 4 basins for the 2, 3 and 4 oxygen coordinations respectively. The pictures for quartz and $CaCl_2$ structures have not been reported because they are almost identical to those of cristobalite and stishovite. There is no additional valence domain on the silicon side, this latter atom only gives rise to a spherical *L*-shell core domain enclosing the *K*-shell one.

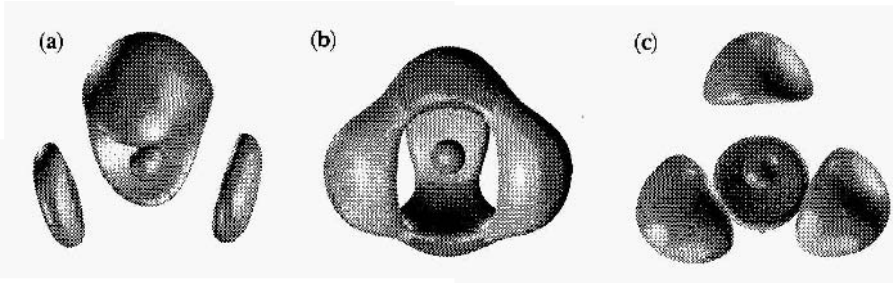

Figure 2. Oxygen *ELF* = 0.85 localization domains of oxygen atoms in (a) cristobalite, (b) stishovite and (c) fluorite-type prototype structure. The bond directions which are not indicated on the figure are along the lines joining the oxygen core domain (the small sphere at the center of the pictures) and the disynaptic domains. In cristobalite the disynaptic domains are the two discs on both side of the core. In stishovite the valence domain is not fully resolved in irreducible domains, the disynpatic attractors are located within the three bulges lying in the horizontal plane. In fluorite-type structure, the four disynaptic domains form a tetrahedron.

In quartz and cristobalite the oxygen atom forms two bonds with the silicons which correspond to the two disynaptic domains on both side of the oxygen core. The oxygen lone pairs give rise to a single monosynaptic basin instead of two as expected from the Lewis structure. This discrepancy from chemical intuition is not an artefact due to the basis set but rather a consequence of the large fluctuation of the electron density within the

valence shell around electronegative atoms. In stishovite, there are three disynaptic basins the attractors of which lie in the plane defined by the nuclei of the silicons bonded to the oxygen and two monosynaptic basins on both sides of this plane. In this case, the $\eta(\mathbf{r}) = 0.85$ isosurface does not achieve the reduction of the valence domain. Finally, the fluorite-type prototype structure is characterized by four disynaptic domains disposed at the vertices of a tetrahedron.

The value of the ELF function at the saddle points between the disynaptic basin and the silicon core is always lower than that between the disynaptic basin of two nearest neighbour oxygens. The difference between such values decreases as the coordination increases. Within a given oxygen valence shell, the ELF value at the saddle point between basins is always close to the attractor value, respectively 0.83 and 0.88 in quartzi for example, indicating a large fluctuation of the electron density between theses basins [36]. This is particularly the case for stishovite and $CaCl_2$-like structures.

The basin population of α-cristobalite, stishovite and fluorite structures are listed in table 3.

TABLE 3. Basin population of oxygen core, disynaptic and monosynaptic attractors.

	core	disynaptic	monosynaptic
α-cristobalite	2.15	1.9	4.0
stishovite	2.15	1.6	1.5
fluorite-type	2.15	1.95	

The oxygen core population has been calculated with a fine grid in order to achieve a better accuracy, it is not structure dependent. Though a population of 2 is expected from a Lewis picture, it has been shown by Kohout and Savin that the K-shell population is around $2.2e$ for atoms beyond Ne. [39]. In quartz and cristobalite, there are three valence basins. Two of them are disynaptic with a population slightly less than 2.0, and the remaining is a crescent-shaped monosynaptic basin. It corresponds to the two conventional lone pairs of the Lewis structure and its population is therefore 4.0. In stishovite, each of the three disynaptic basins contains ~ 1.6 electrons whereas a ~ 1.5 electronic population is assigned to each of the monosynaptic ones. In the $CaCl_2$ structure, the monosynaptic basins are dissymmetric because the nuclei of the oxygen and of the three bonded silicons are not in the same plane. As the pyramidization of the OSi_3 fragment is increased, the population of the monosynaptic basin which is on the silicon side is transferred to that on the other side and to the disynaptic

basins. One can expect a structure with three disynaptic basins and one monosynaptic for a large distorsion from the rutile structure. Finally, in the fluorite structure prototype the disynaptic basin populations are ~ 2.0.

In all systems, there is always only one disynaptic attractor with a population ≤ 2 for each Si-O bond. The interaction clearly belongs to the shared disynaptic basin class (electron-shared interaction in Bader's terminology). Moreover, the basin populations indicate single bonds for 2-fold coordinated oxygens rather than a resonance between a single and a double bond as suggested by Pauling. The larger Si-O bond lengths observed in stishovite are explained by the smaller basin population. In the case of the tetracoordinated oxygens, the origin of the lengthening is probably due to the repulsion between nearest neighbour oxygens. In this structure, in spite of a large SiO bond distance (1.918 Å), the oxygen-oxygen distance is much more smaller than in cristobalite (i.e 2.21 Å instead of 2.6 Å).

The location of the disynaptic attractor in the bonding direction provides some information related to the ionic character. In homopolar bonds its position is roughly given by the covalent radii and small deviations may occur due to substituents whereas in heteropolar bonds it is shifted towards the electronegative centre. The monosynaptic attractors are generally closer to the electronegative centre. Distances of attractors from the oxygen nucleus are listed in table 4 together with Bader's bond critical point distances and estimated cationic radii. The distance of the bond critical point to the nucleus defines the atomic radius (in the sense of the covalent radius). In a similar fashion it is possible to define an effective cationic radius as the distance between the nucleus and the core-valence separatrix which is nearly spherical. It is not possible to define an anionic radius in a similar fashion because the envelope of the oxygen valence shell has a rather intricate shape.

TABLE 4. Distances (in Å) of monosynaptic (R_M), disynaptic (R_D) attractors from the oxygen nucleus, atomic (R_A) and cationic radii (R_+) for α-quartz, α-cristobalite, stishovite and fluorite structures.

	quartz	cristobalite	stishovite	fluorite
R_M	0.58	0.58	0.70	
R_D	0.63	0.63	0.69	0.65
R_A(Si)	0.66	0.67	0.67	0.75
R_A(O)	0.94	0.94	1.08	1.17
R_+(Si)	0.60	0.59	0.62	0.64

The valence attractor-nucleus distances increase with the coordination

and decrease as the basin population increases. In stishovite the nucleus-monosynaptic attractor distance is larger than the nucleus-disynatic one, which is probably due to the lower population of the monosynaptic basin with respect to the disynaptic one. The atomic and ionic radii always increase with the coordination. The silicon atomic and ionic radii vary less than the oxygen ones. The increase of the oxygen atomic radius is consistent with the increase of the ionic character of the bond. In high pressure polymorphs, the packing of the oxygen network explains why the SiO_2 units occupy smaller volumes than in quartz and cristobalite in spite of the increase of the atomic radii.

Another interesting feature provided by the *ELF* analysis is its connection with the VSEPR model. The valence basin is the analogue to the electron domain of Gillespie but with the difference that the former can contain both more than 2 and less than 2 electrons. For instance, in stishovite there are respectively 80% and 75% of a true pair in the disynaptic and monosynaptic domains, whereas in cristobalite even 4 electrons are contained in one monosynaptic basin. In tetracoordinated polymorphs, an AX_2E structure is found around the oxygen atoms. The $\angle SiOSi$ is, however, wider than the value expected by Gillespie for this structure [48] because the monosynaptic basin tends to form a ring around the oxygen core. In molecular prototypes such as $H_3SiOSiH_3$ and $(OH)_3SiOSi(OH)_3$ this angle is always calculated to be greater than 140°. The geometry of stishovite is consistent with AX_3E_2 oxygens in which the electronic domains are partially filled. The transition to the $CaCl_2$ type structure corresponds to a rearrangement towards the local AX_3E type involving an electron transfer from one lone pair domain to the three other domains. Finally, the fluorite-type structure obviously belongs to AX_4.

4. Conclusion

The topological analysis of the density and of the *ELF* function provides new information to understand the nature of the Si-O bond. On the one hand, the atomic population and the bond ellipticities tell us that the SiO bond is partly ionic and also that there is no evidence for a partial double bond character. This latter point is confirmed by the analysis of the *ELF* function since there is only one attractor between the oxygen and silicon cores and that its basin population is always less than or equal to 2 electrons. Moreover, it appears more important to consider the oxygen than the silicon to discuss the bonding in silica. The Si-O bond is found to belong to the electron shared interaction by the *ELF* analysis.

The structural stability of the *ELF* gradient field warrants the reliability of the qualitative information presented here. In fact, lower quality

wavefunctions used in preliminary calculations yield the same number of basins of each type. The noticeable differences which concern the quantitative aspects of this work, i.e. the basin populations, are of the order of magnitude of the error due to the approximate numerical integration. These two errors have the same origin, namely the difficulty of determining precisely the separatrices.

The discussion of the Si-0 chemical bond presented in this chapter provides some guidelines to improve interatomic potentials. On the one hand, the analysis of the density gives support to two-body potentials such as those designed by Tsuneyuki [6] and Kramer *al* [7] insofar as the attractors of the valence basins remain rather close to the oxygen centres and because the value of ELF at the saddle points between these basins is rather high. Covalent potential [5] are also successful, because they take into account the mutual repulsion of the valence basins. A trail to improve two-body potentials may be to treat the electrostatic and dispersion interactions as true two-body potentials and to allow more flexibility for the repulsive potential. This can be done by considering that the repulsive interaction occurs between the silicon centre and the core and valence attractors of oxygen. It should be also possible in this way to model the variation in the number of valence attractors occurring with a change of the oxygen coordination.

References

1. Pauling, L. (1939) *The nature of the chemical bond,* Cornell University Press, Ithaca, NY.
2. Pauling, L. (1952) Interatomic distances and bond character in the oxygen acids and related substances, *J. Phys. Chem.,* **56,** 361-365.
3. Pauling, L. (1980) The nature of silicon-oxygen bonds. *Am. Mineralogist,* **65,** 321-323.
4. Gibbs, G. V., Downs, J. W. and Boisen, Jr. M. B. (1994) The elusive SiO bond. *Rev. Mineral.,* **29,** 331-368.
5. Lasaga, A. C., and Gibbs, G. V. (1987) Application of Quantum Mechanical Potential Surfaces to Mineral Physics Calculations. *Phys. Chem. Minerals*, **14,** 107-117.
6. Tsuneyuki, S., Matsui, Y., Tsukada, M., and Aoki, H. (1988) First-Principles Interatomic Potential of Silica Applied to Molecular Dynamics, *Phys. Rev. Lett.,* **61,** 869-872.
7. Kramer, G.J., Farragher, N.P., van Beest, B.W.H., and van Santen, R.A. (1991) Interatomic Force Fileds for Silicas, Alluminophosphates, and zeolites: Derivation Based on Ab Initio Calculations, *Phys. Rev.,* **B43,** 5068-5080.
8. Kassab, E., Seiti, K. and Allavena, M. (1991) Theoretical Determination of Relative Acidity in Zeolite (Faujasite). *J.* Phys. *Chem.,* **95,** 9425-9431.
9. Allavena, M. and Kassab, E. (1993) Molecular interactions in solid state and quantum chemistry : A model problem, the proton transfer in zeolites. *Solid State lonics,* **61,** 33-39.
10. Sauer, J. (1994) Structure and reactivity of zeolite catalysts Atomistic modeling usin ab initio techniques, in J. Weitkamp et al (eds.), *Zeolithes and Related Microporous materials : State of the Art, Studies in Surface Science and Catalysis, vol. 84,* Elsevier, Amsterdam, pp. 2039-2057.

11. Gibbs, G. V., Meagher, E. P., Newton, M. D., and Swanson, D. K. (1981) A comparison of experimental and theoretical bond length and angle variations for minerals, inorganic solids, and molecules, in M. O'Keefe and A. Navrotsky (eds.), *Structure and Bonding in Crystals,* Academic Press, New York, Vol. 1 pp. 195-225.
12. Silvi, B., D'Arco, Ph., Saunders, V. R., and Dovesi, R. (1991) Periodic Hartree-Fock study of Minerals: Tetracoordinated Silica Polymorphs. *Phys. Chem. Minerals,* **17,** 674-680.
13. Silvi, B., D'Arco, Ph., and Causá, M. (1990) Periodic Pseudo-potential Hartree-Fock Study of a-quartz structure SiO_2 and GeO_2. *J. Chem.* Phys., **93,** 7225-7230.
14. Silvi, B., Allavena, M., Hannachi, Y., and D'Arco, Ph. (1992) Pseudopotential periodic Hartree-Fock study of the cristobalite phases of SiO_2 and GeO_2. *J. Am. Ceram. Soc.,* **75,** 1239-1246.
15. Bachrach, S. M. (1994) Population analysis and Electron Densities from Quantum Mechanics. in K. B. Lipkowwitz and D. B. Boyd (eds.), *Computational Chemistry,* VCH, New York, Vol. 5. pp. 171-227.
16. Bader, R. F. W. (1990) *Atoms in molecules,* Oxford Science Publications, Oxford.
17. Silvi, B. and Savin, A. (1994) Classification of chemical bonds based on topological analysis of electron localization function. *Nature,* **371,** 683-686.
18. Becke, A., and Edgecombe, K. E. (1990) A simple measure of electron localization in atomic and molecular systems. *J. Chem. Phys.,* **92,** 5397-5403.
19. Thom, R. (1972) *Stabilité Structurelle et Morphogénèse.* Intereditions, Paris.
20. Ruedenberg, K. (1962) The Physical Nature of the Chemical Bond. *Rev. Mod. Phys.,* **34,** 326-376.
21. Shewell, J. R. (1959) On the Formation of Quantum-Mechanical Operators. *Am, J. Phys.,* **27,** 16-21.
22. Cohen, L. (1966) Generalized Phase-Space Distribution Functions. *J. Math. Phys.,* **7,** 781-786.
23. Dahl, J. P. (1982) The Wigner Function. *Physica,* **114A,** 439-444.
24. Dirac, P. A. M. (1958) *The Principles of Quantum Mechanics,* Oxford University Press, Oxford.
25. Cohen, L. (1979) Local kinetic energy in quantum mechanics. *J. Chem. Phys.,* **70,** 788-789.
26. von Weizsäcker, C. F. (1935) Zur Theorie der Kernmassen. *Z. Phys.,* **96,** 431-458.
27. Tal, Y., and Bader, R. F. W. (1978) Studies of the Energy Density Functional Approach. I. Kinetic Energy. *Int. J. Quant. Chem.,* **S12,** 153-168.
28. Sears, S. B., Parr, R. G., and Dinur, U. (1980) On the Quantum-Mechanical Kinetic Energy as a Measure of the Information in a Distribution. *Israel J. Chem.,* **19,** 165-173.
29. Gázquez, J. L., and Ludeña, E. V. (1981) The Weizsacker term in Density Functional Theory. *Chem. Phys. Lett.,* **83,** 145-148.
30. Ludeña, E. V. (1982) On the nature of the correction to the Weizsacker term. *J. Chem. Phys.,* **76,** 3157-3160.
31. Kohn, W. and Sham, L. J. (1965) Self-Consistent Equations Including Exchange and Correlation Effects. *Phys. Rev.,* **140,** 1133-1138.
32. Savin, A., Jepsen, O., Flad, J., Andersen, O. K., Preuss, H., and von Schnerring, H. G. (1992) *Angew. Chem. Int. Ed. Engl.,* **31,** 323-324.
33. Lacks, D. J., and Gordon, R. G. (1994) Tests of nonlocal kinetic energy functionals. *J. Chem. Phys.,* **100,** 4446-4452.
34. Lee, H., Lee, C., and Parr, R. G. (1991) Conjoint gradient correction to the Hartree-Fock kinetic-and exchange-energy density functionals. *Phys. Rev.,* **A44,** 768-771.
35. Yang, W. (1986) Gradient correcttion in Thomas-Fermi theory. *Phys. Rev.,* **A34,** 4575-4585.
36. Savin, A., Silvi, B. and Colonna, F. (1996) Topological analysis of the electron localization function applied to delocalized bonds. *Can. J. Chem.,* **74,** 1088-1096.
37. Biegler-König, F. W., Bader, R. F. W., and tang, T. H. (1982) Calculation of the

Average properties of Atoms in Molecules. II. *J. Comput. Chem.,* **3,** 317-328.
38. Savin, A. (1993) Electron Localization Function (ELF) in molecules and solids. *Second International Conference on Inorganic Chemistry,* Stuttgart, Germany.
39. Kohout, M., and Savin, A. (1996) Influence of the core-valence separation on the Electron Localization Function. *Int. J. Quant. Chem.* (in press)
40. Häussermann, U., Wengert, S. and Nesper, R. (1994) Unequivocal Partitioning of Crystal Structures, Exemplified by Intermetallic Phases Containing Aluminium. *Angew. Chem. Id. Ed. Engl.,* **33,** 2073-2076.
41. Cioslowski, J. and Mixon, S. T. (1991) Covalent Bond Orders in the Topological Theory of Atoms in Molecules. *J. Am. Chem. Soc.,* **113,** 4142-4145.
42. Ángyán, J. G., Loos, M. and Mayer, I. (1994) Covalent Bond Orders and Atomic Valence Indices in the Topological Theory of Atoms in Molecules. *J. Phys. Chem.,* **98,** 5244-5248.
43. Messiah, A. (1962) *Mécanique Quantique, Tome I.,* Dunod, Paris, p. 113.
44. Claverie, P. and Diner, S. (1976) Statistical and Stochastic Aspects of the Delocalization Problem in Quantum Mechanics. in O. Chalvet, R. Daudel, S. Diner and J. P. Malrieu (eds.) *Localization and Delocalization in Quantum Chemistry,* Reidel Publishing Company, Dordrecht, Vol. 2 pp. 395-448.
45. Bader, R. F. W. (1975) Comparison of Loge and Virial Methpds of Partitioning Molecular Charge Distributions. in O. Chalvet, R. Daudel, S. Diner and J. P. Malrieu (eds.) *Localization and Delocalization in Quantum Chemistry,* Reidel Publishing Company, Dordrecht, Vol. 1 pp. 15-38.
46. McWeeny, R. (1989) *Methods of Molecular quantum Mechanics,* Academic Press, London, pp. 119-124.
47. Gillespie, R. G. (1972) *Molecular Geometry,* Van Nostrand Reinhold, London.
48. Gillespie, R. G., and Robinson, E. A. (1996) Electron Domains and the VSEPR Model of Molecular Geometry. *Angew. Chem. Int. Ed. Engl.,* **35,** 495-514.
49. Dovesi, R., Saunders, V. R., and Roetti, C. (1992) *CRYSTAL 92, an ab-initio Hartree-Fock LCAO program for periodic systems,* Theoretical Chemistry Group, University of Turin and SERC Daresbury Laboratory.
50. Jolly, L-H., Silvi, B., and D'Arco, Ph. (1994) Periodic Hartree-Fock study of minerals : Hexacoordinated SiO_2 and GeO_2 polymorphs. *Eur. J. Mineral.,* **6,** 7-16.
51. Hehre, W. J., Ditchfield, R., and Pople, J. A. (1972) Self-consistent molecular-orbital methods. XII. Further extensions of gaussian-type basis sets for use in molecular orbital studies of organic molecules. *J. Chem. Phys.,* **38,** 2257-2261.
52. Pepke, E., Murray, J., and Hwu, T.-Z. (1993) *SciAn,* Supercomputer Computations Research Institute, Florida State University, Tallahassee, Florida.

This page intentionally left blank.

MOLECULAR DYNAMICS SIMULATION OF SILICA WITH A FIRST-PRINCIPLES INTERATOMIC POTENTIAL

SHINJI TSUNEYUKI
lnstitute for Solid State Physics, University of Tokyo Roppongi, Minato-ku, Tokyo 106, Japan

1. Introduction

Prediction of the structures and properties of materials from a knowledge of their chemical composition has been a longstanding problem of materials science. The Molecular Dynamics method (MD, hereafter) has been one of the most powerful techniques to simulate both static and dynamical properties of materials starting from atomistic information, i.e. an interatomic potential, which we *expect* not to be affected by a small change in environment of the atoms

In the study of silica and silicates, MD was primarily used to simulate molten and vitreous states using ionic and pairwise interatomic potentials [1, 2, 3, 4], where the interatomic potential was obtained empirically by trial and error. Although the fourfold oxygen coordination of silicon atoms and non-linear Si-O-Si angle widely observed in silica and silicates seem to suggest covalent character of the Si-O bonds, it has been shown that these structural properties are roughly reproduced by pairwise interatomic potentials.

When the application was extended to simulation of crystalline silica and silicate, however, we encounter the fact that these interatomic potentials does not necessarily reproduce important structural properties such as bulk moduli, elastic constants or sometimes even dynamical stability of the crystalline symmetry. Thus some efforts have been made to incorporate crystal structures and their elastic properties into the process of empirical determination of the interatomic potentials by means of a static energy minimization technique [5, 6, 7, 8, 9].

Since these methods are essentially empirical, one cannot but move on to more sophisticated but more complicated interatomic potentials as he

B. Silvi and P. D'Arco (eds.), Modelling of Minerals and Silicated Materials, **201-206.**

tries to reproduce more experimental data. A typical example is found in simulations of silica. Silica can be regarded as a generic material for the most abundant class of minerals. Despite its simple chemical composition, silica is known to assume various crystal structures (polymorphs) which have a wide range of densities varying from 2.3 (low-cristobalite) to 4.3 g/cm^3 (stishovite) and bulk moduli from 18 to 300 GPa. As is evident from this variation, silica is not a close-packed system, and is in fact typical of framework structures in which units (SiO_4 tetrahedra in this case) form networks with various unit-unit (Si-O-Si) angles. Thus a sensitive test of the interatomic potential may be made for this material. Until recently, even the structure and bulk modulus of low-quartz (α-quartz) could not be reproduced by pairwise interatomic potentials, and it had been believed that for this material one needs three-body interatomic potential appropriate for covalent bonds and the shell model representing deformation of oxygen charge density [10, 11].

The inclusion of covalency and charge deformation is physically reasonable, while the potential parameters are still determined empirically. Moreover, increase of the number of parameters causes arbitrariness in their determination. Now we need to revise the interatomic potential from a different standpoint apart from experimental observations.

In this context, we performed first-principles electronic structure calculations of a small cluster (SiO_4) and analyzed potential energy surfaces (PES's) corresponding to some deformation modes of the cluster. The interatomic potential derived from the PES's, which is ionic and pairwise, has been found to reproduce most structural properties of silica minerals quite satisfactorily against expectation.

In this article, I briefly review our works on the interatomic potential of silica. Results by the cluster calculations are shown in section 2. MD results at ambient temperature and moderate pressure are summarized in section 3. Dynamical simulations at high temperature and/or high pressure are the most interesting and important application of the MD method, whose results are briefly introduced in section 4. Section 5 is devoted to the concluding remarks.

2. Interatomic Potential

2.1. CLUSTER CALCULATIONS

We start from the total energy calculation of a tetrahedral SiO_4^{4-} cluster, which exists in most crystalline silica and its melt [12, 13]. We regard the cluster as embedded in a crystal, so that we add four point charges, e^+, as shown in the inset of Fig. 1, which guarantee the charge neutrality and also mimic the Madelung potential arising from the rest of the crystal. The

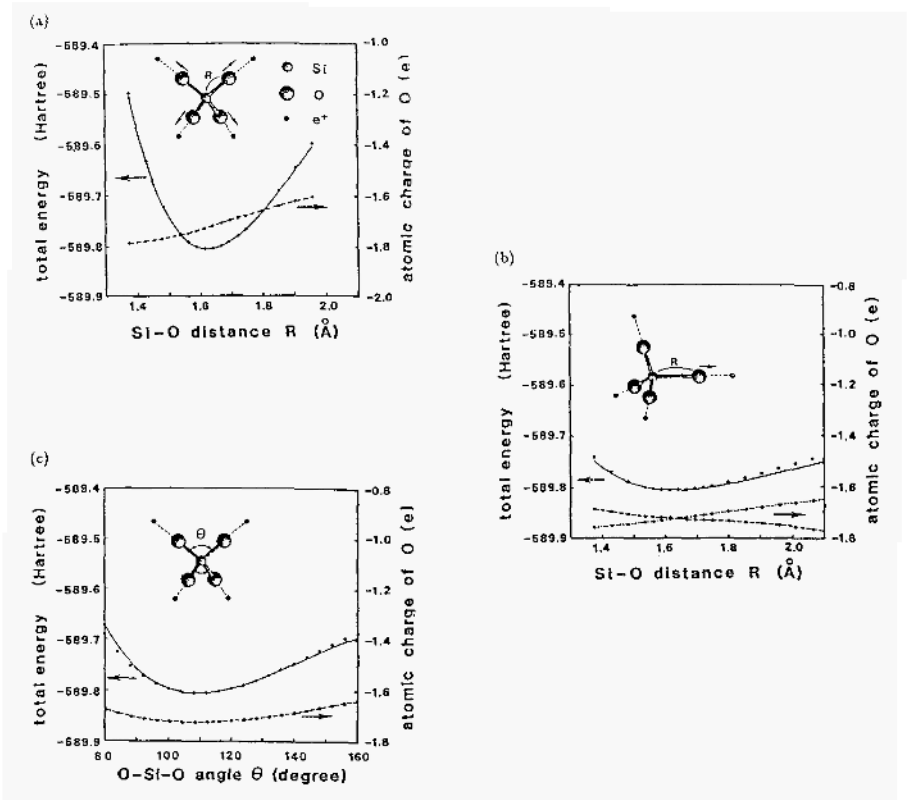

Figure 1. Total energy and the Mulliken charge on an oxygen atom of an SiO_4^{4-}-$4e^+$ cluster for (a) T_d, (b) C_{3v} and (c) D_{2d} deformation modes. The Si-O-e^+ angle is set to 180°. Solid circles represent the cluster calculation, solid lines are the fitted potentials, and the broken lines are guides to the eye. In (b) the Mulliken charge shown by the dashed line is for the oxygen ion moved during the calculation, while that shown by the dotted line is for the fixed oxygen ions. 1 Hartree = 2.6255 x 10^3 kJ/mol.

distance between an oxygen atom and the adjacent point charge is set to 1.65Å, which is close to usual Si-O distance in silicate. Effect of changing the distance will be discussed later in this section.

We performed Hartree-Fock self-consistent-field (HF-SCF) calculation and obtained PES's corresponding to T_d, C_{3v} and D_{2d} deformation modes of the cluster as shown in Fig. 1(a)-(c). Double-zeta basis functions, which express each valence orbital of the atom with two functions, are employed with two *d* functions for silicon and *p* functions for the negative ion state of oxygen. We assume no electron orbitals around the point charges.

It has turned out that all of these PES's can be well fitted by a sum of

pairwise interatomic potentials. We have employed the functional form

$$U_{ij}(r) = U_{ij}^{\text{Coulomb}}(r) + f_0(b_i + b_j)\exp\left[\frac{a_i + a_j - r}{b_i + b_j}\right] - \frac{c_i c_j}{r^6}, \quad (1)$$

which consists of Coulomb interaction with some corrections discussed below, Born-Mayer-type repulsion, and a correction to the repulsive term expressed by a power-law interaction. Here r is the distance between atoms and a_i (b_i) is the effective radius (softness parameter) of the i-th atom with the standard force $f_0 = 1\text{kcal}\text{Å}^{-1}\text{mol}^{-1}$. Note that the last term refines the details of the repulsion and does not necessarily represent dispersion interaction, which is not included in the HF-SCF method. We also include Coulomb interactions of ions with the point charges.

As Si-O bonding is not totally ionic, we have to assign fractional charges for Si and O. Hence a caution must be made in evaluating Coulomb interaction in the cluster, since the effective charge in the bulk, Q_i, is different from that in a SiO_4^{4-} cluster, $\tilde{Q}_i$. In terms of the fractional number of electron, Δn, transferred from a Si atom to an O atom per Si-O bond, we have $Q_O = -2\Delta ne$ and Qsi $= 4\Delta ne$, while we have $\tilde{Q}_O = -(1 + \Delta n)e$ and $\tilde{Q}_{Si} = 4\Delta ne = Q_{Si}$. We describe the Coulomb interaction in the cluster as a sum of long-range and short-range parts as

$$U_{ij}^{\text{Coulomb}}(r) = \tilde{Q}_i\tilde{Q}_j[1 - g_{ij}(r)]/r + Q_iQ_jg_{ij}(r)/r, \quad (2)$$

$$g_{SiO}(r) = (1 + \zeta r)\exp(-2\zeta r) \quad (3)$$

$$g_{OO}(r) = [1 + 11(\zeta r)/8 + 3(\zeta r)^2/4 + (\zeta r)^3/6]\exp(-2\zeta r). \quad (4)$$

The correction, $g_{ij}(r)$, in the long-range part involving $\tilde{Q}_i$ reflect the distribution of the excess charge of oxygen, for which we assume a hydrogen-like orbital with a typical ionic radius of oxygen, $1/\zeta = 1.4$Å. Since the remaining short-range part is expected to be insensitive to the environment, we use the bulk Q_i there. Once the parameters a_i, b_i and c_i are optimized by fitting the cluster PES'S, we switch $\tilde{Q}_i$ back into Q_i (i.e., $U_{ij}^{\text{Coulomb}}(r) = Q_iQ_j/r$) in the MD simulation of the bulk. Thus the final interatomic potential has the same functional form as used by many authors.

From the Mulliken analysis, Δn is ~ 0.7 for the equilibrium bond length, while it depends of the Si-O distance and O-Si-O angles in a complicated manner (e.g., compare Fig. 1(a) and (b)). This clearly indicates the many-body character of the interatomic potential in the covalent system. It should be noted, however, that the PES's are well reproduced by a pairwise potential eq.(1) with fixed charges. As regards the nearest neighbor interaction, the variation of the charge transfer is already included in eq.(1) as a first approximation, though it might affect the interaction with the ions out of the cluster.

It is interesting to compare the above PES's with those calculated with doubly elongated O-e^+ distances (d(O-e+)). In Fig. 2 *net* PES's of T_d mode are shown with a solid line (d(O-e^+) = 1.65Å) and a dashed line (d(O-e^+) = 3.3Å), where the "*net* PES" is obtained by subtracting the Coulomb interaction related with the point charges (e^+) from the total energy of the cluster. We used two different method of estimating the contribution of the point charges. First we used the following expression,

$$U_e(Q) = \sum_{\langle \mu\nu \rangle} \frac{e^2}{r_{\mu\nu}} + \sum_{i\mu} \frac{\tilde{Q}_i e}{r_{i\mu}}, \tag{5}$$

where $r_{\mu\nu}$ is the distance between the μ-th and ν-th point charges, and $r_{i\mu}$ is that between the μ-th point charge and the i-th ion. We did not use eqs.(2)-(4), since the nearest O-e^+ distances are always fixed. The *net* PES's for the different Si-O distances obtained in this way are shown in Fig. 2(a). The energy difference between the two PES's are also shown by a dotted line, which slightly but clearly depends on the Si-O distance. This is nothing but a manybody character of the interatomic potential of silica.

Since the electron charge density in the cluster is available from the HF-SCF calculation, we secondly estimated the contribution of the point charges by

$$U_e(Q) = \sum_{\langle \mu\nu \rangle} \frac{e^2}{r_{\mu\nu}} + \sum_{i\mu} \frac{Z_i e}{r_{i\mu}} + \sum_{\mu} \int d\mathbf{r} \frac{e\rho(\mathbf{r})}{|\mathbf{r} - \mathbf{r}_\mu|}, \tag{6}$$

where Z_i is the atomic number of each ion, and $\rho(\mathbf{r})$ is the electron charge density. The *net* PES's in this case shown in Fig. 2(b) surprisingly coincide with each other except that there remains a constant shift of the energy, which probably comes from the non-Coulombic character of the nearest O-e^+ interaction. This result suggests that the interatomic potential beyond the nearest neighbor atoms are essentially Coulomb interaction and that the manybody character could be renormalized into the ionic charges (Q_i) changing according to the local deformation of the cluster. Note that such manybody character is not incorporated even in the shell model.

2.2. POTENTIAL PARAMETERS

For the present it seems difficult to find an efficient method of determining Q_i's at each configuration of MD runs, so that we do not use eq.(6) below but fit the potential parameters using eqs.(2)-(5). Thus the pairwise interatomic potential obtained in this work has an intrinsic error of neglecting the manybody character mentioned above, although it seems not so significant when the distance to the second nearest neighbor atoms is not so much changed.

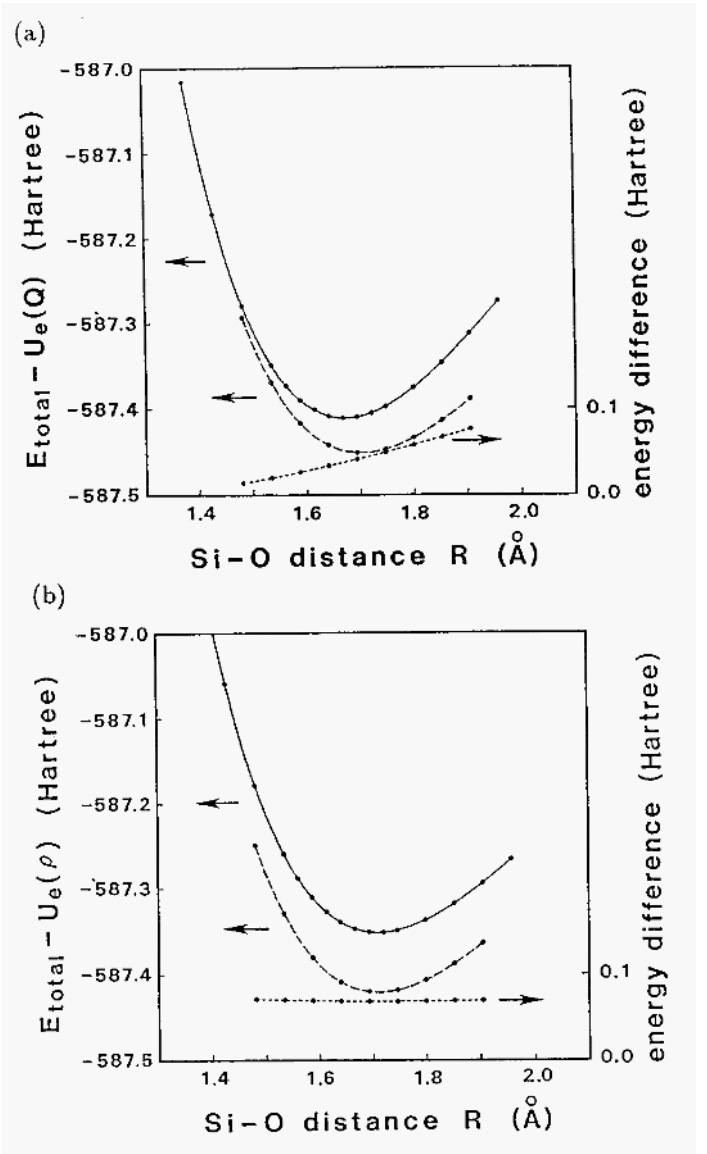

Figure 2. *Net* potential energy surfaces for T_d deformation of an SiO_4^{4-}-$4e^+$ cluster calculated using (a) fixed charges Q_i, and (b) electron charge density $\rho(r)$. The full circles are the cluster calculation. The solid line is for the O-e^+ distances of 1.65Å, and the dashed line is for 3.30Å. The energy difference of these two *net* potential energy surfaces is shown with dotted lines.

TABLE 1. Potential parameters obtained in this study.

	Q/e	a(Å)	b(Å)	c (kcal$^{1/2}$ Å^{3}mol$^{-1/2}$)
O	−1.2	2.0474	0.17566	70.37
Si	+2.4	0.8688	0.03285	23.18

Since small cluster results are insufficient to determine long-range Coulomb interaction, and because the absolute value of the Mulliken charge itself depends on the choice of basis functions for the HF-SCF calculation, we have not included Δn in the fitting procedure. Instead we tried several fixed values of Δn around the Mulliken charge. Moreover, since the least-square fitting procedure for a_i, b_i and c_i is nonlinear, more than one set of parameters are obtained. We have chosen the one (Table 1) which optimizes the structure and compressibility of low-quartz in a static simulation [5]. The potential energy surfaces best fitted by the pair potential are shown in Fig. 1 with solid lines. Interesting is that the PES corresponding to the O-Si-O bending mode (D_{2d} mode in Fig. 1(b)) is remarkably reproduced here by the pairwise O-O interaction. It should also be mentioned that the best-fit potential reproduces the potential surface in a wide range of Si-O or O-O distances, which corresponds to large deformations. Specifically, this guarantees the reliability of the pairwise potential even for states at high pressures, in which small atomic distances are encountered.

So far we have investigated the PES of an SiO_4 cluster, so that the PES for the Si-O-Si bending is not incorporated in the fitting procedure. Previous quantum chemical calculations [14] show that the PES of an $H_6Si_2O_7$ cluster has a slight minimum at around $\angle$Si-O-Si$\sim$ 144° in harmony with experimental observations that the angle is around 140° – 150° in most silica and silicates, which seems to suggest covalent nature of the Si-O-Si bonding. On the contrary, as will be shown later, our pairwise interatomic potential reproduces the Si-O-Si angle quite well not only in crystals but also in the vitreous state.

To check the validity of the interatomic potential, we have also performed HF-SCF calculation of the PES of the bending mode of an $(Si_2O_7)^{6-}$ $6e^+$ cluster as shown in Fig.3(a). The PES is very flat for a wide range of the Si-O-Si angle, although it does not has minima at bent configurations perhaps because the Si-O-e^+ angle is set to 180° in this cluster. The interatomic potential parameterized above has been shown to give a very similar PES for the bending mode (a solid line in Fig.3) and somewhat guarantees its reliability as regards the Si-O-Si bending deformation. Interestingly the *net* PES for this cluster shown in Fig.3(b) gives a distinct minimum at

around $\angle$Si-O-Si= 180°, suggesting that the Coulomb interaction beyond the second-nearest-neighbor ions is important for this flat PES. Another message here is that it is probably dangerous to discuss the subtle potential minimum on the Si-O-Si angle only within the cluster approach.

3. Simulations of polymorphs of silica

Once interatomic potentials are obtained, they are applicable to the static energy minimization or the MD simulation. As we have mentioned in the previous section, we performed static energy minimization of low-quartz to choose the best parameter set, since computational time needed for the static simulation is shorter than MD. On the other hand the MD could be more stringent test for the potential, because dynamical stability of crystals is examined by the method.

We performed MD simulations of low-quartz, low-cristobalite, coesite and stishovite, i.e., virtually all the natural polymorphs of silica so far known. These polymorphs correspond to different pressure-temperature regimes but can also exist at normal pressure and temperature. Our interests are: (1) whether the interatomic potential derived from the cluster calculation is applicable to bulk crystals, (2) whether various physical properties of polymorphs are reproduced by the same interatomic potentials, and (3) whether pair-potential approximation is valid for silica.

In the present MD study, we have used Parrinello and Rahman's constant pressure algorithm [15] combined with the constant temperature algorithm by Nosé [16]. Periodic boundary condition is assumed for typically five hundreds of atoms. The Ewald sum method is used for evaluating the long-range Coulomb interactions. The $1/r^6$ term is calculated by direct summation within a certain cut-off length ($\sim$ 7Å), while the interaction beyond the cut-off length is integrated by continuum approximation. We start from an initial condition in which all the atoms begin to move with random velocities from the ideal positions of the crystal structure. If the interatomic potential were inappropriate, the initial crystalline structure would disintegrate immediately, or in some cases after retaining the structure as a thermal fluctuating state for some period.

The MD results show that at room temperature the four polymorphs are dynamically stable, despite the fact that the polymorphs have large differences in their topologies of atomic configurations and densities [12, 13]. The obtained densities agree with the experimental results within 10% error. The structural parameters are summarized in table 2 and the atomic configurations are shown in Fig. 4.

We have also performed MD simulations under high pressure. Pressure dependence of the cell parameters polymorph is also reproduced quanti-

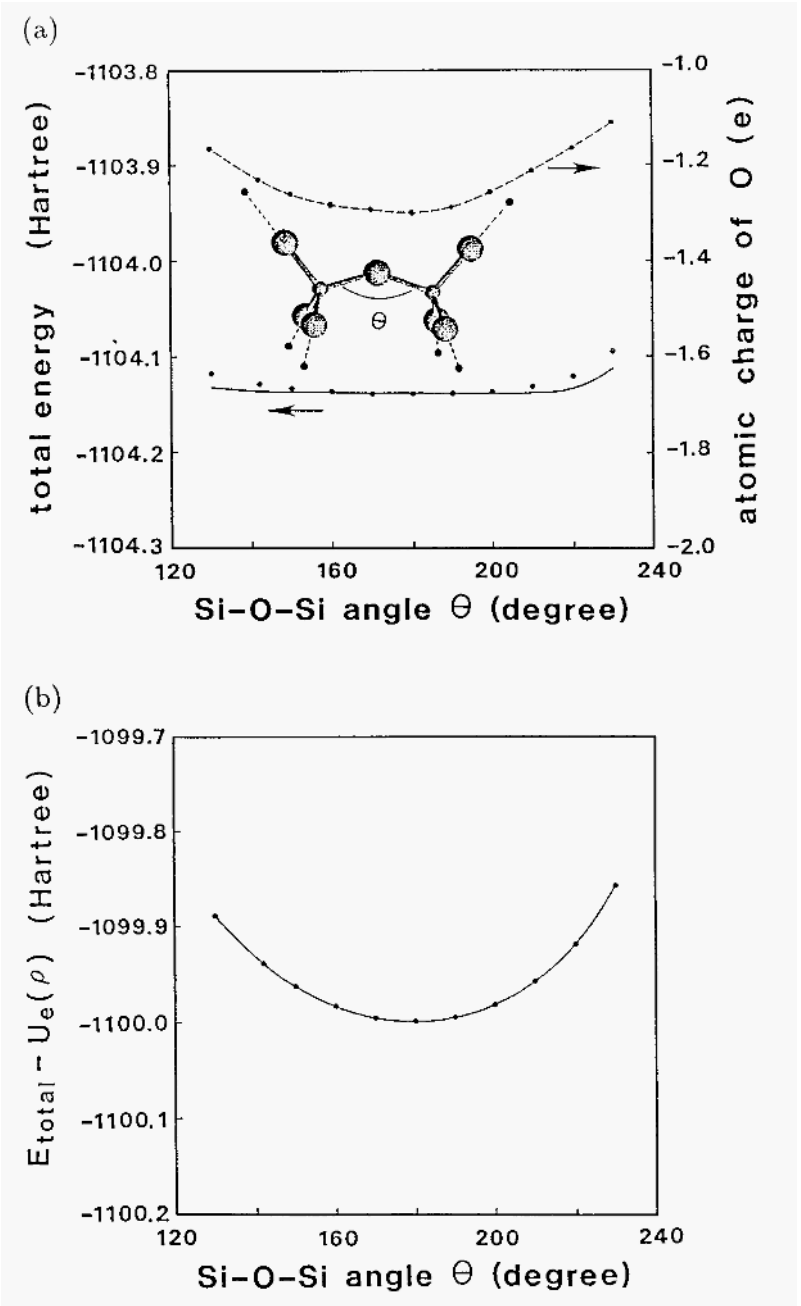

Figure 3. (a) Total energy (PES) and the Mulliken charge on the bridging oxygen atom for the Si-O-Si bending of an $(Si_2O_7)^{6-}6e^+$ cluster. The full circles are obtained by the cluster calculation, the solid line by the interatomic potential in table 1, and the dashed line is a guide to the eye. (b) The *net* PES calculated using electron-density distribution p.

TABLE 2. Structural parameters obtained here by MD simulations as compared with experimental results (or results by the FLAPW band calculation) for various polymorphs of silica.

	low-quartz		low-cristobalite		coesite	
	Obs.[a]	MD	Obs.[b]	MD	Obs.[d]	MD
Space Group	$P3_121$	$P3_121$	$P4_12_12$	$P4_12_12$	$C2/c$	$C2/c$
Z	3	3	4	4	16	16
a (Å)	4.916	5.02	4.979	5.00	7.1356	7.22
b (Å)	4.916	5.02	4.979	5.00	12.3692	12.76
c (Å)	5.4054	5.55	6.950	6.66	7.1736	7.42
α, β, γ	$\gamma = 120°$	120.0°			$\beta = 120.34°$	120.6°
Density (g/cm^3)	2.6458	2.47	2.316	2.41	2.9213	2.72
K_0 (GPa)	38(3)	33.7	18[c]	17.4	96(3)	108
Si-O (Å)	1.605(1)	1.627	1.605(2)	1.644	1.5945(4)	1.609
	1.614(1)	1.640	1.613(2)	1.625	— 1.619(1)	— 1.655
Si-O-Si	143.73(7)°	147.3°	146.4(1)°	142.7°	180.°	180.0°
					137.36(9)°	143.9°
					— 149.64(9)°	— 155.3°

[a]Reference 17. [b]Reference 18. [c]Reference 19. [d]Reference 20.

	stishovite		$Pa\bar{3}$ silica	
	Obs.[e]	MD	FLAPW[g]	MD
Space Group	$P4_2/mnm$	$P4_2/mnm$	$Pa\bar{3}$	$Pa\bar{3}$
Z	2	2	4	4
a (Å)	4.1773(1)	4.27	4.47	4.56
b (Å)	4.1773(1)	4.27	4.47	4.56
c (Å)	2.6655(1)	2.75	4.47	4.56
Density (g/cm^3)	4.2902	3.97	4.46	4.20
K_0 (GPa)	296(5)[f]	312(2)	335	328.4(2)
Si-O (Å)	1.7572(1)	1.813	1.827	1.863
	1.8087(2)	1.840		
Si-O-Si	98.66(1)°	98.8°	119.8°	120.0°
	130.67(1)°	130.6°		

[e]Reference 21. [f]Reference 22. [g]Reference 23.

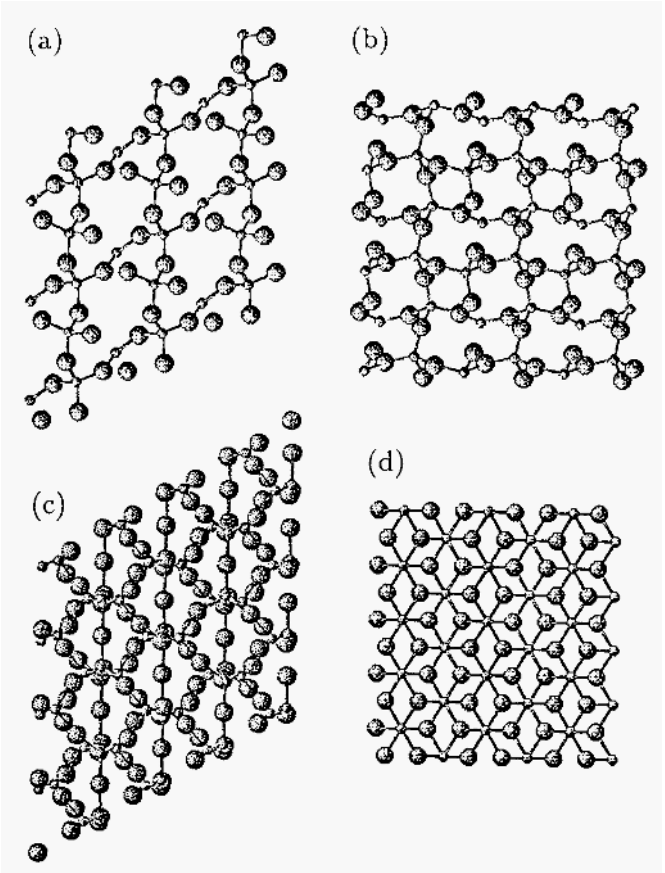

Figure 4. Atomic configurations averaged over time steps obtained in the MD simulation of low-quartz (a), low-cristobalite (b), coesite (c) and stishovite (d).

tatively by the present interatomic potential [13]. The bulk moduli obtained by fitting the pressure-volume result to the Birch-Murnaghan equation of state also agree with experimental results within roughly 10% error. Recently it has also been reported that a negative Poisson ratio of low-cristobalite is successfully reproduced with this interatomic potential [24].

Besides these four polymorphs, we have tested low-tridymite, which has not been fully established as a polymorph of pure silica [25]. Starting from the conjectured low-tridymite structure, we have obtained an equilibrium structure that preserves the exceptionally low symmetry of space group *Cc,* although the structure is different from that in the latest reports [26, 27]. Since the unit cell of low-tridymite is reported to be very large (48 SiO_2 units) and complicated, further investigation will be necessary for both MD

and experimental studies.

We have also performed a simulation of $Pa\bar{3}$-silica, which is first obtained by an MD simulation [28] and predicted to be ~6 % denser than stishovite at ambient pressure and thermodynamically more stable above 60 GPa by the first-principles total-energy-calculation [23]. This phase could have great geophysical implications, because $MgSiO_3$-perovskite, which is widely accepted as the major constituent within the Earth's deep interior, should be less stable than ($Pa\bar{3}$-silica+MgO) at high pressure if the $Pa\bar{3}$ does exist. Although a high-pressure experiment [29, 30] and further theoretical investigation [31, 30] suggest that the preceding rutile-to-$CaCl_2$ structural phase transition suppresses appearance of the $Pa\bar{3}$ phase up to the highest pressure in the Earth, it is noteworthy that this phase is thought to be stable at ambient pressure if it were once formed. The simulated $Pa\bar{3}$ phase at room temperature and normal pressure has a density 5.5 % higher than that of simulated stishovite and a bulk modulus similar to that of stishovite. These results agree very well with the prediction of the full-potential linear augmented plane wave (FLAPW) method [23].

Although the present interatomic potential is derived from an SiO4 cluster, we have found that it also gives good results for stishovite and $Pa\bar{3}$-silica with SiO_6 coordination beyond our expectation. This is partly because oxygen atoms are more closely packed in the sixfold coordinated systems giving higher densities and more rigidity.

4. Dynamical Simulations

In this section I briefly introduce some applications of our interatomic potential to study of dynamics and structural transformation in silica. They are the phase transition of quartz, pressure-induced structural transformations of the polymorphs of silica, and atomic diffusion in silica melt.

4.1. THE α TO β PHASE TRANSITION OF QUARTZ

There is a long history of experimental study on the phase transition in quartz. At room temperature, quartz assumes a low-temperature phase of space group $P3_121$, which is called low-quartz or α-quartz, while it transforms into a high-temperature phase of space group $P6_222$ (high-quartz or β-quartz) when it is heated above 846K. The soft mode of the phase transition was first detected by Raman scattering [32] below T_c and by inelastic neutron scattering [33] above T_c. An incommensurate phase is also observed within a narrow temperature range (~ 2 K) between the α and β phases [34]. There has been a controversy as to the structure of β-quartz: the question is whether the atoms in the β phase vibrate around the idealized position [35, 36] or fluctuate between the α_1 and α_2 phases [37, 38].

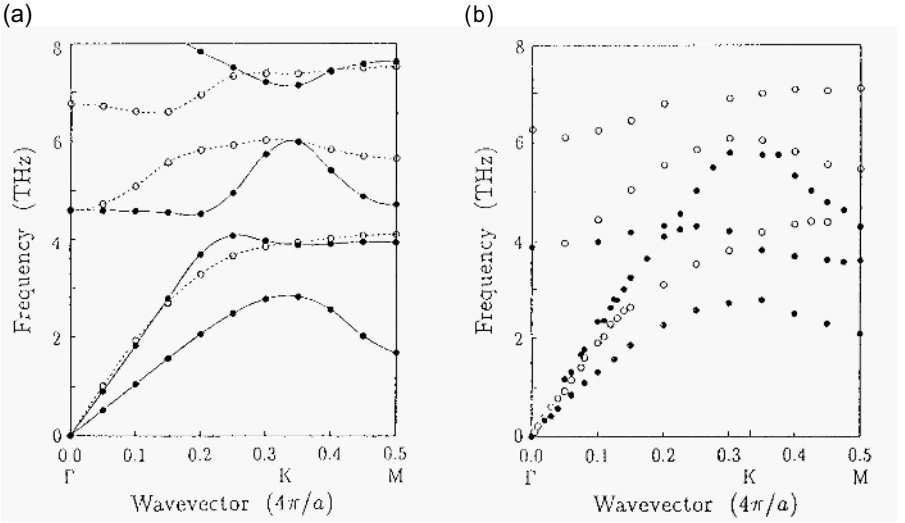

Figure 5. Phonon dispersions of α-quartz (low-quartz) at room temperature: (a) calculated results using the present interatomic potential and (b) experimental data by Dorner *et al.* (Reference 40). Full (open) circles and full (dotted) lines represent antisymmetric (symmetric) modes.

We firstly calculated the phonon dispersion of low-quartz with our interatomic potential [39,40] and found that it reproduces rough features of experimental data [41] as shown in Fig. 5. In this lattice dynamics calculation, we used thermally averaged cell parameters and atomic coordinates at room temperature obtained by an MD simulation. When we used cell parameters obtained at 700 K, we found an appreciable softening of an A_1 (symmetric) phonon mode at the zone center, whose frequency is −6.8 THz by our calculation, together with the softening of the lowest antisymmetric acoustic mode in all the wavevector range and the second antisymmetric acoustic mode at the zone boundary. This is in harmony with experimental results and a previous lattice dynamics study with empirical force constants [42]. Above 800 K, on the other hand, the thermally averaged positions of atoms are no longer stable and simple diagonalization of the dynamical matrix gives imaginary frequencies.

Secondly, we performed an MD simulation of heating quartz up to 1300 K. We have mainly used a system of 432 particles for the periodic boundary condition, while 324- and 576-particle systems have also been studied for comparison. MD results for the temperature dependence of the molar volume and cell parameters shows quite good agreement with experimental data (Fig. 6) [43]. The volume expansion coefficient abruptly

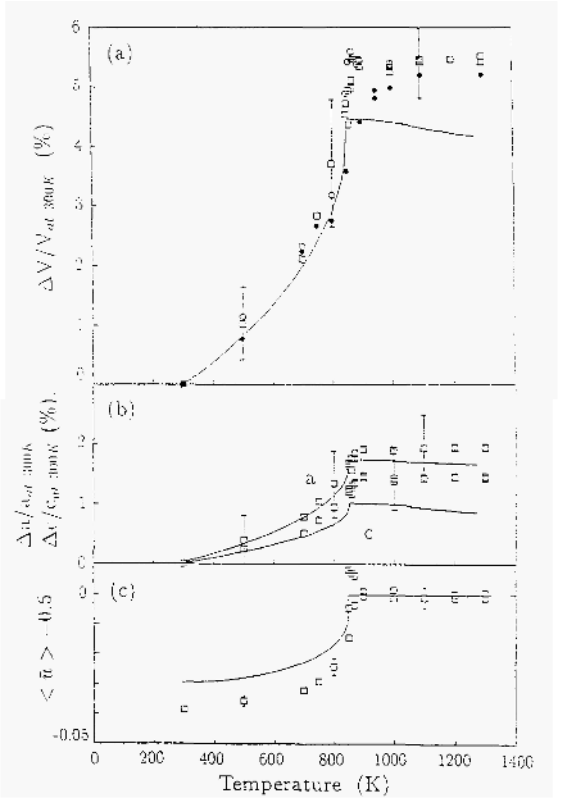

Figure 6. The MD results for the thermal expansion of the volume (a) and cell parameters (b) of quartz, and the temperature dependence of the u parameter of silicon. Open squares represent the 432-particle system with typical magnitude of the fluctuation, while full circles and open circles represent the 324- and the 576-particle systems. The solid line shows show experimental data.

changes at $T_c = 850 - 900$ K and clearly indicates a phase transition, while the system-size dependence shows that the 324-particle system is too small to reproduce the distinct shoulder of the volume-temperature relation.

The character of the transition can be made clear if we look at the fractional coordinate of silicon, u, in the space group of α-quartz, $P3_121$. In the low-temperature phase, there are two equivalent phases called α_1 and α_2, where $u = 0.4705$ and $u = 1 - 0.4705 = 0.5295$, respectively. In the idealized β phase, on the other hand, we have exactly $u = 1/2$ from symmetry restriction. Since the other positional parameters are highly correlated with u to preserve SiO_4 tetrahedra, we can choose $u - 1/2$ as an order parameter of the phase transition. In the MD simulation, we have

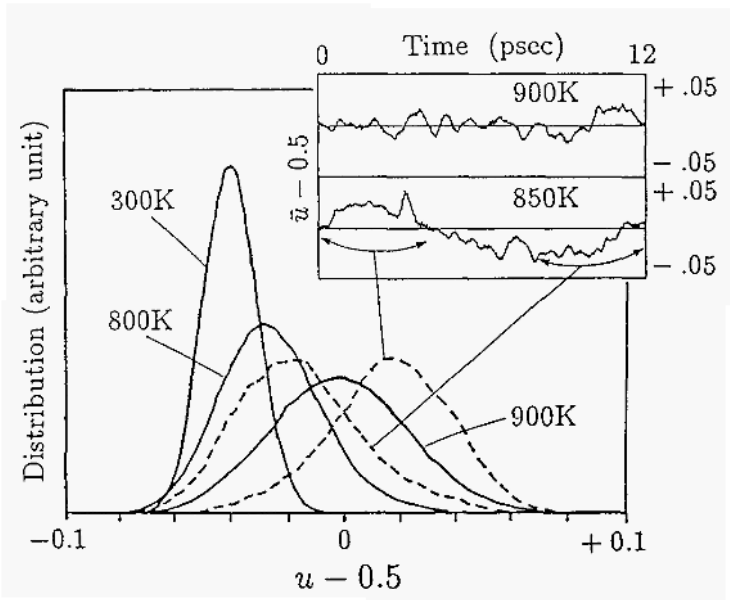

Figure 7. The distribution of the u parameter of silicon. The data were accumulated over 12 ps (full lines) or 4 ps at different intervals at 850 K (dashed lines). The inset shows a typical trace of the u parameter, averaged over all the cells, against the MD step.

monitored the u parameter averaged for the three silicon atoms in each unit cell at each time step. We denote the u parameter averaged over all the unit cells in the system by $\bar{u}$, which is a function of time, while the u parameter averaged over all the cells and all the time steps is denoted by $\langle \bar{u} \rangle$. The temperature dependence of the averaged order parameter, $\langle \bar{u} \rangle - 1/2$ is shown in Fig. 6, which shows that $\langle \bar{u} \rangle - 1/2$ indeed vanishes above T_c.

We can further characterize the structure by the distribution function of u in Fig.7. At low temperature the motion of each particle is nearly harmonic, so that the distribution function is Gaussian. As the temperature increases, the distribution becomes asymmetric, and above T_c it is symmetric again and almost independent of temperature. At 850 K we have found a phase alternation between the a_1 and a_2 phases, which correspond to the experimental observation that the domain boundary between the two phases is constantly vibrating just below T_c [37]. We cannot tell exactly whether T_c is below or above 850 K in this simulation because the system size is too small. At 900 K the MD-synthesized quartz is clearly in the β

phase, where we can no longer find such alternation. When seen locally, however, the α_1 and α_2 structures switch to each other. Thus, although the atomic distribution function shows a single peak like a displacive transition, and though the softening of phonon modes are also confirmed by the lattice dynamics calculation, the β-quartz structure has an order-disorder character at the same time, i.e., the β structure is interpreted as a spatio-temporal average of the α_1 and α_2 structures.

In the present MD simulation, an important driving force for the phase transition is, together with the increase in kinetic energy, the thermal expansion of the lattice, which suppresses the potential barrier between the α_1 and α_2 structures [44]. It might be interesting to study pressure effect, which is likely to increase the barrier height.

4.2. PRESSURE-INDUCED STRUCTURAL TRANSFORMATIONS

Structural transformation of silica at high pressure is not only geophysically important but also interesting for their variety due to the flexibility of the framework structure. Hemley *et al.* have found that polymorphs of silica undergoes amorphization under pressure, even at room temperature, just like H_2O ice does at low temperature [45]. We have investigated the microscopic mechanism of this pressure-induced structural transformation by an MD simulation.

Structural transformation of materials at high pressure is technically one of the most challenging problems for MD, since we need an interatomic potential reliable for variety of atomic configurations with various densities, i.e., various interatomic distances and coordination. As we have shown in the previous section, the present interatomic potential reproduces structures and bulk moduli of polymorphs of silica including high-pressure phases. On the other hand, a drawback with the cluster approach for obtaining the potential is that, as the approach concentrates on the curvature of potential surfaces, it does not necessarily reproduce the exact enthalpy difference between phases. For example, the observed enthalpy of formation of sixfold-coordinated stishovite is $\sim$10 kcalmol^{-1} higher than that of fourfold-coordinated low-quartz, as compared with the calculated difference of $\sim$1 kcalmol^{-1}. As we are interested in pressure-induced structure transformation, which involve changes of the Si-O coordination number, we slightly modify the potential parameters to reproduce the enthalpy difference of stishovite and low-quartz. Merely a reduction of the atomic radius a_{Si} by 1 % (0.01Å) is sufficient to accomplish this.

Using these potentials, we apply a hydrostatic pressure to each polymorph of silica at room temperature. The equations of state obtained at room temperature [46] are shown in Fig. 8 together with those obtained ex-

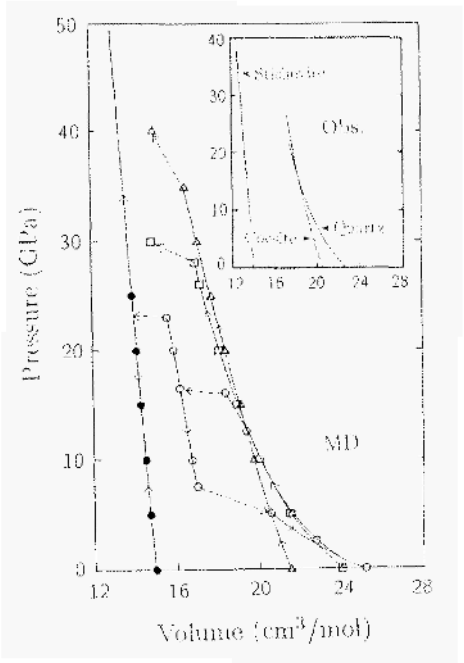

Figure 8. Pressure-volume relation for low-quartz (□), coesite (△), stishovite (•) and low-cristobalite (o) obtained by MD. Solid lines represent continuous change and broken lines discontinuous change of volume due to pressure-induced structural transformation. Hysteresis is indicated by arrows. Pressure-volume relation obtained by an experiment is shown in the inset (from Hemley *et al.* Reference 45).

perimentally [45]. In good agreement with the experiment, MD-synthesized low-quartz and coesite undergo structural transformation with discontinuous volume reduction at pressures of 28-30 GPa and 35-40 GPa, respectively.

By compression of low-quartz, we have found two novel high-pressure structures, depending on the MD runs. One is the α-PbO_2 structure with only sixfold Si-O coordination, which has been proposed [47] but not established. Another structure we obtained is shown in Fig. 9(a). In this structure, 1/3 of Si atoms have fourfold coordination, while the rest have sixfold coordination. Moreover, it contains a number of bond defects at $\sim$30 GPa so that peaks in the radial distribution function are shown to be broadened as in the glass. We confirmed that the bond defects disappears if we further compress the structure up to 50 GPa [48].

Another novel crystalline structure is derived from low-cristobalite at $\sim$17 GPa (Fig. 9(b)). The new structure has a space group of *Cmcm* and

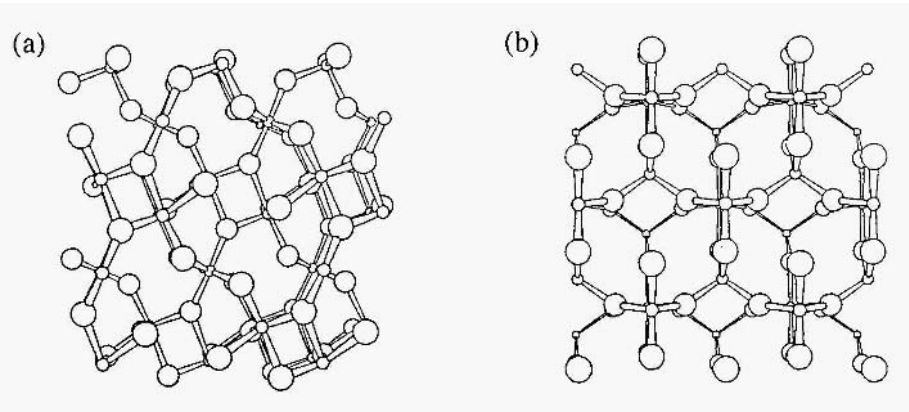

Figure 9. Novel structures of silica obtained by compression of known polymorphs. (a) The $C2$ phase from low-quartz, and (b) the *Cmcm* phase from low-cristobalite.

contains an equal number of fourfold and sixfold silicon atoms. The *Cmcm* phase is not quenchable and all the sixfold silicon atoms return to fourfold after decompression. The decompressed phase is similar to low-cristobalite but contains topological disorder, though the SiO_4 network is complete. The *Cmcm* phase undergoes the second structural transformation at $\sim$23 GPa into stishovite, in which all the silicon atoms have sixfold coordination. If we increase pressure rapidly, the first transformation is not observed and low-cristobalite directly transforms into stishovite above 20 GPa. Once stishovite is formed, it is stable up to the highest pressure (250 GPa) except that it becomes slightly orthorhombic above $\sim$160 GPa [49].

Although the *Cmcm* phase of silica has not been found by *real* experiments, it has been shown that low-cristobalite in fact undergoes pressure-induced structural transformations at room temperature [19, 50]. Very recently it was also confirmed that the displacive transformation from low-cristobalite structure to the *Cmcm* structure really occurs in case of *c*-$GaPO_4$, which probably has larger ionicity than silica. It should also be mentioned that Ga atoms easily turn into sixfold coordination, while P preserves fourfold coordination at high pressure. This tendency is in harmony with the alternate arrangement of the fourfold and sixfold coordinated cations in the *Cmcm* phase.

Interestingly, these structural transformations occur without atomic diffusion in the sense that no isolated atoms or disordered states appear at the transition. The mechanism of these diffusionless transformation is illustrated in Fig. 10. When the pressure is increased the framework of corner-

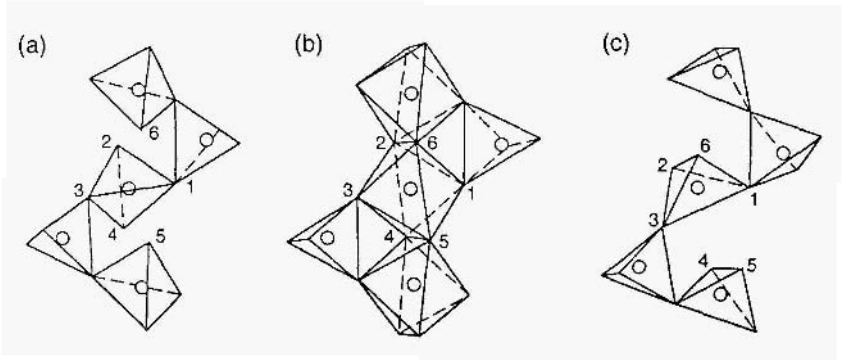

Figure 10. Pressure-induced structural transformation obtained by MD simulations at room temperature. (a) A framework of corner-shared SiO_4 tetrahedra in a low-pressure phase (low-cristobalite), where silicon atoms are shown with circles. Oxygen atoms related with the structural transformation are numbered. (b) The framework structure deformed under pressure. (c) The framework structure after released pressure.

shared SiO_4 tetrahedra in Fig. 10(a) transforms displacively into the the structure shown in Fig. 10(b). This structure can be regarded as comprising a sixfold Si-O coordination on the basis of the Si-O distance. Thus the Si-O coordination number increases smoothly by neither breaking any Si-O bonds nor introducing global atomic diffusion. This mechanism for compression is essentially the same as that suggested by Stolper and Ahrens for amorphous silicate [51] and is thought to occur in silica glass [52]. In case of decompression, the way of unfolding sixfold coordination into fourfold coordination is locally not unique. For example, the sixfold-coordinated structure in Fig. 10(b) does not always resume the structure in (a) but also transforms into a new framework structure in (c). This leads to the topological disorder in the decompressed phase mentioned above.

In summary, we have obtained a microscopic picture of the pressure-induced structural transformation of the polymorphs of silica at room temperature. In most cases the high-pressure phases highly retain structural order since the transformation occurs without diffusion process, although the tendency might be enhanced by the restricted size of the MD cell for the periodic boundary condition. It is conceivable that compression of a macroscopic sample produces small domains of ordered phases with random crystalline directions. The present result also suggest that the application of high pressure at room temperature may provide routes to new polymorphs, which cannot be obtained under equilibrium conditions.

4.3. PRESSURE ENHANCEMENT OF ION MOBILITIES IN LIQUID SILICA

Melts of many silicates are known to have an anomalous transport property that the viscosity (diffusivity of oxygen atoms) drastically decreases (increases) with pressure [53, 54]. This interesting phenomenon is considered to be closely related with the mechanism of the pressure-induced structural transformation. We have stressed that the transformation is diffusionless. However, this is in a specified meaning of the word, in which a diffusive transition is defined as the one accompanied by appearance of isolated atoms. The diffusionless transformation modes contribute to the mechanism of diffusion in the following sense. When the low-pressure structure in Fig. 10(a) is compressed into the high-pressure structure in (b) and then decompressed to the structure in (c), the framework of the corner-shared SiO_4 is topologically rearranged, although no isolated atoms appear during the process. The coordination of silicon atoms changes from fourfold to sixfold and then to fourfold again with different oxygen atoms. If we envisage a process in a disordered phase in which the compressions and decompressions are repeated, this could result in diffusion of atoms. Since local pressure or stress is thought to fluctuate in a melt, we can expect such diffusion in a liquid phase. Sixfold coordination is then realized as a local and transient state for diffusion. Note that the diffusion considered here does not accompany isolated atoms but is regarded as continuous changes of Si-O coordination numbers, which will require much less energy than that needed for stripping an oxygen atom from a fourfold coordinated silicon atom.

The crucial factor for atomic diffusion in the present model is the activation energy needed for forming sixfold coordination from fourfold coordination locally. Then the activation energy is considered to be highly correlated with the enthalpy difference between fourfold and sixfold coordinated phases. As is well known, low-pressure phases of silica allow only fourfold coordination and have relatively small bulk moduli, while the high-pressure phase is characterized by sixfold coordination and large bulk modulus. So the enthalpy of the fourfold coordinated phase and that of the sixfold coordinated phase have different pressure dependence and coincide with each other at a certain critical pressure P_C. Thus the activation energy decreases up to P_C and the diffusion coefficient will have a maximum there. Above P_C, the activation energy for diffusion will be the energy required to make a fourfold coordination in a sixfold coordinated system, which is an increasing function of pressure, so that the diffusion coefficient now decreases with pressure. Although in real situations the average coordination number should be somewhere between four and six, the present picture still holds.

The model for the anomalous diffusion process may be confirmed by demonstrating a correlation between the diffusivity and the enthalpy dif-

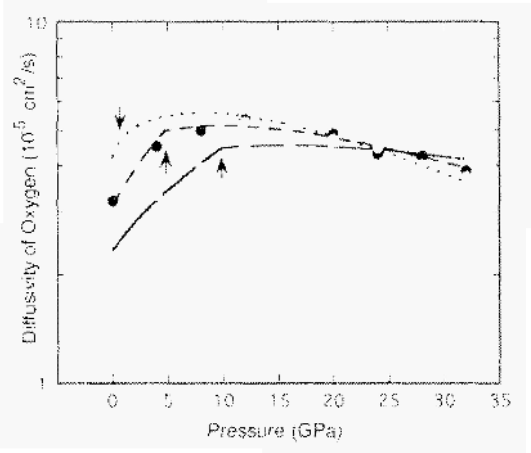

Figure 11. Pressure dependence of the diffusivity of oxygen atoms at 4000 K. Three kinds of symbols and lines correspond to three types of potential parameters: type I (□, a solid line), type II (•, a dashed line) and type III (o, a dotted line), where the size of the symbols approximates the error bars. The lines are the results of the least-square fitting with eq.(8). P_C's for each potential are denoted with arrows.

ference. The interatomic potential we have developed has two virtues for this purpose. First, the potential reproduces the structures and bulk moduli of both fourfold and sixfold coordinated polymorphs of silica.. Second, we can tune the relative stability of fourfold and sixfold coordinated polymorphs by a slight modification of a potential parameter a_{Si} without losing the first virtue. Thus we consider three sets of potential parameters where a_{Si} = 0.86 Å(type I), 0.87 Å(type 1l) and 0.88 Å(type III), which give the critical pressure P_C of 9.9 GPa, 4.7 GPa and 0.7 GPa, respectively.

The key results for the pressure dependence of the diffusivity of oxygen at 4000 K for the three types of parameter sets are shown in Fig. 11 [55]. The results for silicon are qualitatively very similar to those for oxygen. A common characteristic for the three parameter sets is that the diffusion coefficients show maxima as reported for silicate by Angell *et al.* [56, 57]. This is exactly the anomalous diffusion property. Moreover, a new finding here is that there exists a conspicuous correlation between the pressures which give the highest diffusivity and the P_C*'s* estimated before.

The activation volume ΔV defined by $D(P) \propto \exp(-P\Delta V/k_B T)$ is about $(-3) - (-5)$ cm^3/mol around 0 GPa. This is very close to the difference of the molar volume per oxygen in a fourfold coordinated polymorph (coesite) and a sixfold coordinated polymorph (stishovite), and comparable with -6.3 ± 1.2cm^3/mol for jadeite obtained experimentally [53].

Diffusivity of an atom can be written approximately as

$$D \sim a^2 \nu \exp\left(-\frac{\Delta E}{k_B T}\right), \tag{7}$$

where a is a typical length-scale for the elementary process of diffusion, ν is a trial frequency, and ΔE is an activation energy for diffusion. a is proportional to $V(P)^{1/3}$ where $V(P)$ is the molar volume at pressure P known from the simulation of melt. Along the present mechanism, we postulate that ΔE is proportional to $|H_{coe}(P)-H_{st}(P)|$, except for a constant independent of pressure, where $H_{coe(st)}(P)$ is the enthalpy of coesite (stishovite) obtained from simulations at room temperature with some extrapolation. Finally we assume that ν is proportional to $K(P)^{1/2}$, where $K(P)$ is the bulk modulus of the melt at each pressure derived from the simulations of melt. It should be noted that, if we do not include the pressure dependence of $a^2\nu$,D is symmetrical below and above P_C. Thus we obtain [55]

$$\ln D = \frac{2}{3}\ln V(P) + \frac{1}{2}\ln K(P) - \frac{c_1}{k_B T}|H_{coe}(P) - H_{st}(P)| + c_2. \tag{8}$$

We found two fitting parameters (c_1,c_2) for each type of potentials are sufficient to reproduce the tendency of the pressure dependence of D as shown by lines in Fig. 11. This serves as clear evidence that the mechanism for the atomic diffusion in silica melt presented in the above is indeed in action.

Finally it should be stressed that the interatomic potential, which is reliable enough to reproduce the pressure dependence of the enthalpy of the polymorphs of silica, is an essential ingredient of the present investigation. The realistic interatomic potential combined with moderate control of the potential parameter has first enabled us to clarify the close relation between the diffusivity of oxygen atoms in molten state and the relative stability of the polymorphs of silica.

5. Conclusion

Simulation of crystal structures using empirical interatomic potentials might be a powerful means of understanding experimentally observed properties of materials. Such an approach is nevertheless insufficient to predict unknown structures and their properties, since the determination of empirical potentials essentially requires information on the resultant crystal structures. The present method of deriving interatomic potentials from *ab initio* cluster calculations is basically free from experimental information. Although there still remain some empirical factors, such as the choice of reasonable cluster or the final selection of a potential out of some parameter sets [58],

the present success demonstrates a promising step toward *prediction* of the properties of materials.

We have found that a pairwise interatomic potential works surprisingly well for silica. Physically this means that local packing of large oxygen ions essentially determines the structural properties of the crystals even in case of framework silica. It is natural to think that pairwise potentials will also be successful for silicates, which are more ionic and more closely packed, though prediction of relative stability of their polymorphs is much more difficult.

Recent dramatic advances in computational techniques and computer power have enabled us to simulate crystalline structures from first-principles by means of the electronic structure calculation of the whole system within the density functional theory. Even liquid and vitreous silica have come to be studied by the *ab initio* MD method or so-called Car-Parrinello method [59]. Thus the application of the classical MD method is to be shifted to study of dynamics with a larger system size and longer simulation time. For example, the simulation of the oxygen diffusivity mentioned in the previous section needs accumulation of positions of five hundred atoms over 120 ps at each pressure, for which the *ab initio* MD is too inefficient. On the other hand, a local structural deformation relevant for the diffusion could be simulated with a smaller cell and a shorter time scale. It is obviously fruitful to make proper use of these approaches, i.e. the classical MD supported by first-principles cluster calculations and the *ab initio* MD, in each problem of materials science.

The author thanks Y. Matsui, H. Aoki and M. Tsukada for fruitful discussions and collaboration.

References

1. Woodcock, L.V.., Angell, C.A., and Cheeseman, P. (1976) Molecular Dynamics Studies of the Vitreous State : Simple Ionic Systems and Silica, *J. Chem. Phys.,* **65,** 1565-1577.
2. Matsui, Y., and Kawamura, K. (1980) Instantaneous Structure of an $MgSiO_3$ Melt Simulated by Molecular Dynamics, *Nature,* **285,** 648-649.
3. Soules, T.F., and Busbey, R.F. (1981) Sodium Diffusion in Alkali Silicate Glass by Molecular Dynamics, *J. Chem. Phys.,* **75,** 969-975.
4. Matsui, Y., and Kawamura, K. (1984) Computer Simulation of Structures of Silicate Melts and Glasses, in I. Sunagawa (ed.), *Materials Science of the Earth's Interior,* Terra Scientific Publishing Company (TERRAPUB), Tokyo, pp.3-23.
5. Busing, W.R. (1981) WMIN, Oak Ridge National Laboratory, Report No. ORNL-5747, Oak Ridge.
6. Parker, S.C. (1983) Prediction of Mineral Crystal Structures, *Solid State Ionics,* **8,** 179.

7. Price, G.D., and S.C. Parker, S.C. (1984) Computer Simulations of the Structural and Physical Properties of the Olivine and Spinel Polymorphs of Mg_2SiO_4, *Phys. Chem. Minerals,* **10,** 209-216.
8. Matsui, M., and Busing, W.R. (1984) Computational Modeling of the Structure and Elastic Constants of the Olivine and Spinel Forms of Mg_2SiO_4, *Phys. Chem. Minerals,* **11,** 55-59.
9. Catlow, C.R.A., and Price, G.D. (1990) Computer Modelling of Solid-State Inorganic Materials, *Nature,* **347,** 243-248.
10. Catlow, C.R.A., Freeman, C.M., and Royle, R.L. (1985) Recent Studies Using Static Simulation Techniques, *Physica,* **131 B,** 1-12.
11. Wall, A., and Price, G.D. (1988) Computer Simulation of the Structure, Lattice Dynamics and Thermodynamics of ilmenite-type $MgSiO_3$, *Ana Mineralogist.,* **73,** 224-231.
12. Tsuneyuki, S., Matsui, Y., Tsukada, M., and Aoki, H. (1988) First-Principles Interatomic Potential of Silica Applied to Molecular Dynamics, *Phys. Rev. Lett.,* **61,** 869-872.
13. Tsuneyuki, S., Tsukada, M., Aoki, H., and Matsui, Y. (1990) Molecular Dynamics Simulation of Silica with a First-Principles Interatomic Potential, in F. Marumo (ed.), *Dynamical Processes of Material Transport and Transformation in the Earth's Interior,* Terra Scientific Publishing Company (TERRAPUB), Tokyo), pp. 1-21.
14. Lasaga, A.C., and Gibbs, G.V. (1987) Applications of Quantum Mechanical Potential Surfaces to Mineral Physics Calculations, *Phys. Chem. Minerals,* **14,** 107-117, and references therein.
15. Parrinello, M., and Rahman, A. (1981) Polymorphic Transitions in Single Crystals: A New Molecular Dynamics Method, *J. Appl. Phys.,* **52,** 7182-7190.
16. Nosé, S. (1984) A Unified Formulation of the Constant Temperature Molecular Dynamics Methods, *J. Chem. Phys.,* **81,** 511-519.
17. Levien, L Prewitt, C.T., and Weidner, D.J. (1980) Structures and Elastic Properties of Quartz at Pressure, *Am. Mineral.,* **65,** 920-930.
18. Peacor, D.R. (1973) High-Temperature Single-Crystal Study of the Cristobalite Inversion, *Z. Kristallogr.,* **138,** 274-298.
19. Tsuchida, Y. and Yagi, T. (1990) New Pressure-Induced Transfromations of Silica at Room Temperature, *Nature,* **347,** 267-269.
20. Levien, L. and Prewitt, C.T. (1981) High-Pressure Crystal Structure and Compressibility of Coesite, *Am. Mineral.,* **66,** 324-333.
21. Hill, R.J., Newton, M.D., and Gibbs, G.V. (1983) A Crystal Chemical Study fo Stishovite, *J. Solid State Chem.,* **47,** 185-200.
22. Sato, Y. (1977) Equation of State of Mantle Minerals Determined through High-Pressure X-Ray Study, in M.H. Manghnani and S. Akimoto (eds.), *High-Pressure Research — Applications in Geophysics,* Academic Press, New York, 307-323.
23. Park, K.T., Terakura, K., and Matsui, Y. (1988) Theoretical Evidence for a New Ultra-High-pressure Phase of SiO_2, *Nature,* **336,** 670-672.
24. Keskar, N.R., and Chelikowsky, J.R. (1992) Negative Poisson Ratios in Crystalline SiO_2 from First-Principles Calculations, *Nature,* **358,** 222-224.
25. Holmquist, S.B. (1961) Conversion of Quartz to Tridymite, *J. Am. Ceram. Soc.,* **44,** 82-86.
26. Kato, K., and Nukui, A. (1976) Die Kristallstruktur des monoklinen Tief-Tridymite, *Acta* Cryst., **B32,** 2486-2491.
27. Baur, W.H. (1977) Silicon-Oxygen Bond Lengths, Bridging Angles Si-O-Si And Synthetic Low Tridymite, *Acta* Cryst., **B33,** 2615-2619.
28. Matsui, Y. and Matsui, M. (1988) Molecular Dynamics Studies of Polymorphism of SiO_2 at High Pressure: A Possible New Cubic Polymorph with High Density, in S. Ghose, J.M.D. Coey and E. Salje (eds.), *Structural and Magnetic Phase Transitions in Minerals, Advances in Physical Geochemistry, vol. 7,* Springer-Verlag, New York, pp. 129-140.

29. Tsuchida, Y., and Yagi, T. (1989) A New Post-Stishovite High-pressure Polymorph of Silica, *Nature,* **340,** 217-220.
30. Kingma, K.J., Cohen, R.E., Hemley, R.J. and Mao, H.K. (1995) Transformation of Stishovite to a Dense Phase at Lower-Mantle Pressures, *Nature,* **374,** 243-245.
31. Cohen, R.E., First-Principles Predictions of elasticity and Phase Transitions in High Pressure SiO_2 and Geophysical Implications, in Y. Syono and M.H. Manghnani (eds.), *High-Pressure Research: Application to Earth and Planetary Sciences,* Terra Scientific Publishing Company (TERRAPUB), Tokyo, 425-431.
32. Scott, J.F. (1968) Evidence of Coupling between One- And Two-Phonon Excitations in Quartz, *Phys. Rev. Lett.,* **13,** 907-910.
33. Axe, J.D., and Shirane, G. (1970) Study of the α-β Quartz Phase Transformation by Inelastic Neutron Scattering, *Phys. Rev.,* **B1,** 342-348.
34. Dolino, G. (1988) Incommensurate Phase Transitions in Quartz and Berlinite, in S. Ghose, J.M.D. Coey and E. Salje (eds.), *Structural and Magnetic Phase Transitions in Minerals, Advances in Physical Geochemistry, vol. 7,* Springer-Verlag, New York, pp. 17-38.
35. Young, R.A. (1962) Mechanism of the Phase Transition in Quartz, U.S. Air Force Report No. AFOSR-2569.
36. Tezuka, Y., Shin, S., and Ishigame, M. (1991) Observation of the Silent Soft Phonon, in *B*-Quartz by Means of Hyper-Raman Scattering, *Phys. Rev. Lett.,* **66,** 2356-2359.
37. van Tendeloo, G., van Landuyt, J., and Amelinckx, S. (1976) The $\alpha \rightarrow \beta$ Phase Transition in Quartz and $AlPO_4$ as Studied by Electron Microscopy and Diffraction, *Phys. Stat. Sol. (a),* **33,** 723-735.
38. Wright, A.F., and Lehmann, M.S. (1981) The Structure of Quartz at 25 and 590°C Determined by Neutron Diffraction, *J. Solid State Chem.,* **36,** 371-380.
39. Tsuneyuki, S. (1990) Molecular Dynamics Study of Polymorphs of Silica with First-Principles Interatomic Potentials, PhD Dissertation, University of Tokyo.
40. Phonon dispersion by the present, interatomic potential together with thermal expansivity is also reported by Cowley, E.R., and Gross, J. (1991) Lattice Dynamics of a Pair-Potential Model of a-Quartz, *J. Chem. Phys.,* **95,** 8357-8361.
41. Dorner, B., Grimm, H., and Rzany, H. (1980) Phonon Dispersion Branches in *a* quartz, *J. Phys. C: Solid St. Phys.,* **13,** 6607-6612.
42. Barron, T.H.K., Huang, C.C., and Pasternak, A. (1976) Interatomic Forces and Lattice Dynamics of *a*-quartz, *J. Phys. C: Solid St. Phys.,* **9,** 3925-3940.
43. Tsuneyuki, S., Aoki, H., Tsukada, M., and Matsui, Y. (1990) Molecular-Dynamics Study of the *a* to β Structural Phase Transition of Quartz, *Phys. Rev. Lett.,* **64,** 776-779.
44. Tsuneyuki, S. (1992) Computer Simulation of the α to β Phase Transition of Quartz: Order-Disorder Type or Displacive Type, *Comments Cond. Mat. Phys.,* **16,** 125-136.
45. Hemley, R.J., Jephcoat, A.P., Mao, H.K., Ming, L.C., and Manghnani, M.H. (1988) Pressure-Induced Amorphization of Crystalline Silica, *Nature,* **334,** 52-54.
46. Tsuneyuki, S., Matsui, Y., Aoki, H., and Tsukada, M. (1989) New pressure-induced structural transformations in silica obtained by computer simulation, *Nature,* **339,** 209-211.
47. Matsui, Y., and Kawamura, K. (1987) Computer-Experimental Synthesis of Silica with the α-PbO_2 Structure, in M.H. Manghnani and Y. Syono (eds.) *High Pressure Research in Mineral Physics,* Geophysical Monograph **39,** (American Geophysical Union, Washington DC), 305-311.
48. Tsuneyuki, S., Aoki, H., and Matsui, Y. (1991) New Crystal Structures of SiO_2 Predicted by Molecular Dynamics Study, in M. Doyama, T. Suzuki, J. Kihara and R. Yamamoto (eds.), *Computer Aided Innovation of New Materials,* 381-384.
49. Matsui, Y. and Tsuneyuki, S. (1992) Molecular Dynamics Study of Rutile-$CaCl_2$-Type Phase Transition of SiO_2, in Y. Syono and M.H. Manghnani, (eds.), *High-Pressure Research: Application to Earth and Planetary Sciences,* Terra Scientific Publishing Company (TERRAPUB), Tokyo, pp. 433-439.

50. Parise, J.B., Yeganeh-Haeri, A., Widner, D.J., Jorgensen, J.D., and Saltzberg, M.A. (1994) Pressure-Induced Phase Transition and Pressure Dependnece of Crystal Structure in Low (α) and Ca/Al-Doped Cristobalite, *J. Appl. Phys.,* **75,** 1361-1367.
51. Stolper, E.M., and Ahrens, T.J. (1987) On the Nature of Pressure-Induced Coordination Changes in Silicate Melts and Glasses, *Geophys. Res.* Lett.,**14,** 1231-1233.
52. Williams, Q., and Jeanloz, R. (1988) Spectroscopic Evidence for Pressure-Induced Coordination Changes in Silicate Glasses and Melts, *Science,* **239,** 902-905.
53. Kushiro, I. (1976) Changes in Viscosity and Structure of Melts of $NaAlSi_2O_6$ Composition at High Pressures, *J. Geophys. Res.* **73,** 619-634.
54. Shimizu, N., and Kushiro, I. (1984) Diffusivity of Oxygen in Jadeite and Diopside Melts at High Pressures, *Geochim. Cosmochim. Acta,* **48,** 1295-1303.
55. Tsuneyuki, S., and Matsui, Y. (1995) Molecular Dynamics Study of Pressure Enhancement, of Ion Mobilities in Liquid Silica, *Phys. Rev. Lett.,* **74,** 3197-3200.
56. Angell, C.A., Cheeseman, P.A., and Tamaddon, S. (1982) Pressure Enhancement of Ion Mobilities in Liquid Silicates from Computer Simulation Studies to 800 Kilobars, *Science,* **218,** 885-887; (1983) Water-like Transport Property Anomalies in Liquid Silicates Investigated at High T and P by Computer Simulation Techniques, *Bull. Minéral.,* **106,** 87-97.
57. Angell, C.A., Cheeseman, P.A., and Kadyala, R.R. (1987) Diffusivity and Thermodynamic Properties of Diopside and Jadeite Melts by Computer Simulation Studies, *Chemical Geology,* **62,** 83-92.
58. Another set of potential parameters for SiO_2 is derived from a cluster calculation of H_4SiO_4 by van Beest, B.W.H., Kramer, G.J., and van Santen, R.A. (1990) Force Fields for Silicas and Aluminophosphates Based on Ab Initio Calculations, *Phys. Rev. Lett.,* **64,** 1955-1958; Kramer, G.J., Farragher, N.P., van Beest, B.W.H., and van Santen, R.A. (1991) Interatomic Force Fileds for Silicas, Alluminophosphates, and zeolites: Derivation Based on Ab Initio Calculations, *Phys. Rev.,* **B43,** 5068-5080.
59. Sarnthein, J., Pasquarello, A., and Car, R. (1995) Structural and Electronic Properties of Liquid and Amorphous SiO_2: An Ab Initio Molecular Dynamics Study, *Phys. Rev. Lett.,* **74,** 4682-4685; Model of Vitreous SiO_2 by an Ab Initio Molecular-Dynamics Quench from the Melt, *Phys. Rev.,* **B52,** 12690-12695.

MOLECULAR DYNAMICS SIMULATION OF SILICATE GLASSES

A. N. CORMACK AND YUAN CAO
Center for Glass Research, New York State College of Ceramics, Alfred University, Alfred, NY

1. Introduction

Because of its non-crystalline nature, the structure of glass has largely resisted attack from the usual range of experimental probes, (although recent studies have begun to break down this resistance). This breakdown has been substantially aided by the application of computer simulation methods, which have been able to probe the structure at the atomic level. In this chapter, the technique of molecular dynamics will be described and its application to the structure of silicate glasses discussed.

The principal benefit of molecular dynamics simulations derives from its atomic scale treatment : the models produce a picture of the atomic structure, which may be visualised directly using current state of the art imaging techniques, such as video production. This, of course, is in addition to the calculation of the standard range of structural information, such radial distribution functions, which can be measured directly. The problem with these measurements, obtained from neutron or x-ray scattering studies, is that they are essentially one dimensional, because of the isotropic nature of glass. A full three dimensional reconstruction of the atomic structure is not possible, therefore, so recourse to modeling is somewhat essential.

The substantial progress made in recent years by computer modeling may be ascribed to two reasons. Firstly, the great increase in computer power has made the necessary number crunching a lot easier : more calculations, on larger systems can be completed in shorter periods of time. Secondly, the heart of the model, the interatomic potential energy functions, from which the interatomic forces are calculated, have improved considerably. One can now make detailed quantitative comparisons with experimental measurements, instead of the somewhat qualitative comparisons of a few years ago. The increased confidence in the potentials has

B. Silvi and P. D'Arco (eds.), Modelling of Minerals and Silicated Materials, 227-271.

allowed one to explore fairly complicated chemistries : for example, mixed alkali aluminosilicate systems are now routine, although they contain four different cation species. Extension to systems with even more components is a straightforward exercise in number-crunching.

In the next section, the basic features of the structure of silicate glasses will be reviewed, followed by a description of the molecular dynamics technique. Then, its application to a number of systems will be discussed. The general theme will be how compositional changes alter the atomic structure, and how the changing structure controls an important transport property, the migration of alkali ions in the structure.

2. Silicate Glass Structures : Salient features

The basic structure of the parent glass, silica, SiO_2, has long been understood in terms of a three dimensional network of SiO_4 tetrahedra[1]. Spectroscopic and scattering (neutron and x-ray) studies indicate that the geometry of the tetrahedra is pretty much constant throughout the glass, as it is in the crystalline counterparts[2]. This geometry is often characterised as short range order (SRO) which relates the arrangement of the oxygens coordinated to the silicon ions, and, in aluminosilicates, to the aluminium ions as well. In silica, every tetrahedron is linked to four other tetrahedra, forming the network. Each oxygen is thus bonded to two silicon ions and is called a bridging oxygen (BO). The nature of how the tetrahedra are arranged spatially with respect to each other is called the Intermediate range order (IRO). More distant correlations are described in terms of the long range order (LRO). In crystalline materials, the LRO is usually associated with their periodicity.

In silica the SRO is well characterised, from high resolution scattering or diffraction experiments which also give information about the IRO[3]. From a practical point of view, however, considerable interest attaches to the changes in SRO and IRO which occur when additional network, creating non-bridging oxygens (NBO), because of the extra oxygen and the fact that the alkali cations do not enter the structure in tetrahedral coordination. That is to say, they do not contribute to network formation, but rather disrupt, or modify, it. The alkali cations are thus called network modifiers in contrast to the silicon ions which are called network formers. The addition of trivalent ions, such as Al or B, is usually considered to reduce the number of NBO, for stoichiometric reasons, provided they behave like network formers. The behaviour of these other cation species is of key interest. Is Al, for example, always a network former or might it be a modifier, under some conditions? How about calcium?

Other important questions concern the distribution of cations in the

structure, and whether the structure of alkali silicates is better described by an extension of Zachariasen's Continuous Random Network Model[1], or some other, such as the Modified Random Network Model, recently advocated by Greaves[4];that is to say, are the alkalis (and NBO) homogeneously distributed throughout the glass or are they segregated in an heterogeneous fashion? An important question is how to describe an alkali aluminosilicate which formally has no NBO present. Molecular dynamics simulations are able to address these questions directly, as we will show later.

A complete computer simulation procedure contains three parts : 1) derivation of interatomic potential parameters, 2) formation of simulated glass structures, and 3) analysis of the static and dynamic structural properties of the simulated glass. In the following sections these three parts will be discussed in detail.

3. Inter-Atomic Potential Models

Consider a system containing N atoms; the potential energy may be divided into various terms, such as individual, pairwise, three-body, etc.:

$$E = \sum_i E_i + \sum_i \sum_{j>i} E_{ij} + \sum_i \sum_{j>i} \sum_{k>j>i} E_{ijk} + \dots \quad (1)$$

The first term E_i, represents the effect of an external field on the i^{th} atom. The second term, E_{ij}, is the pair potential between the i^{th} and the j^{th} atoms, depending only on the magnitude of the pair separation. The third term, E_{ijk}, represents the three-body potential, which may be quite significant in the solid and liquid states, especially for describing covalent bonding characteristics. In oxides, higher order terms, four-body potentials and so on, are usually considered to be very small in comparison with the first three terms and are generally omitted.

The reliability of the results of computer simulation mainly depends on the accuracy of the interatomic potential models used in the calculation[5]. The interatomic potentials most often used are generally based on the Born model of the solid, which includes a long-range Coulombic interaction, and a short-range term to model the repulsion between electron charge clouds and the van der Waals dispersive interaction[6].

A number of functional forms for the short-range potentials have been used. In the earliest work[7, 8], only pair potentials were employed, but it was quickly realised that the covalent character of silica was too strong to be neglected. Central force models could not reproduce the tetrahedral geometry closely enough, so three-body terms were introduced to provide a measure of the directional nature of the covalent bonding[9]. These have taken a number of different forms as well.

The present authors have used short range interactions between Si-O and O-O modeled by four-range Buckingham potentials, with an O-Si-O three-body potential of the type used by Vessal *et al.*[10, 11]. These are expressed as

$$E_{ij}^{s} = A_i \exp(-\frac{r_{ij}}{\rho_1}) \qquad r_{ij} < r_1 \quad (2)$$

$$E_{ij}^{s} = A_1 r_{ij}^5 + B_1 r_{ij}^4 + C_1 r_{ij}^3 + D_1 r_{ij}^2 + E_1 r_{ij} + F_1 \qquad r_1 < r_{ij} < r_2 \quad (3)$$

$$E_{ij}^{s} = P_1 r_{ij}^3 + Q_1 r_{ij}^2 + R_1 r_{ij} + S_1 \qquad r_2 < r_{ij} < r_3 \quad (4)$$

$$E_{ij}^{s} = -\frac{C_{ij}}{r_{ij}^6} \qquad r_3 < r_{ij} < r_c \quad (5)$$

where r_{ij} is the distance between the i^{th} and the nearest image of the j^{th} ions, r_c is the cutoff of the pairwise short-range interactions, and the others are constants which need to be determined. In order to have, as a function of distance, continuous energy, and continuous first and second derivatives, the function is splined at r_1, r_2 and r_3. The function has a minimum at r_2.

The three-body interaction is described by the equation :

$$Fijk = \frac{1}{4} A_{ijk} B_{ijk}^2 \exp(\frac{r_{ij}}{\rho_1}) + \exp(\frac{r_{ik}}{\rho_2}) \qquad r_{ij} < t \quad \text{and} \quad r_{ik} < t \quad (6)$$

where $A_{ijk} = k_{ijk}/2(\phi_0 - \pi)^2$, $B_{ijk} = (\phi_0 - \pi)^2 - (\phi_\pi)^2$, ϕ is the calculated bond angle, ϕ_0 is the equilibrium bond angle, k_{ijk} is the three-body spring constant to be determined, and t is the three-body spline point. The three-body cut-off is represented by t_c. If either r_{ij} or r_{ik} is greater than t and less than t_c, the relevant exponential term in equation 6 is replaced with :

$$P(x) = G_1 + H_1 x + I_1 x^2 + J_1 x^3 + K_1 x^4 + L_1 x^5 \quad (7)$$

where $x = r^2 - t^2$ with r being either r_{ij} or r_{ik}. The application of the three-body potentials has allowed a successful simulation of the directionality of Si-O-Si bonding associated with its covalence, resulting in a good agreement with experimental data[9].

The short-range interactions between alkali/alkaline earth ions and oxygen ions were modeled by using a simple Buckingham potential :

$$E_{ij}^{s} = A_{ij} \exp(-\frac{r_{ij}}{\rho ij} - \frac{C_{ij}}{r_{ij}^6} \quad (8)$$

where A_{ij} and C_{ij} are constants to be determined.

Potential parameters may be derived in two main ways[12,13]. The most widespread is an empirical approach in which the parameters are found

by fitting to experimentally measured crystal properties. An alternative approach is to calculate the parameters. In recent years, this approach has gained favour because of advances in methodology.

Our preference is to use potential parameters obtained by fitting to the crystal properties and structures of appropriate binary oxide. The Si-O parameters were fit to the crystal structures and properties of β-cristobalite. The potential parameters for the short-range interaction between alkali/alkaline earth ions and oxygen ions were obtained by fitting to the appropriate crystal structures (anti-fluorite for alkali oxides and rock-salt for alkaline earth oxides). The fitting was accomplished by an inverse energy minimization technique[14]. The short-range interactions between cations are not explicitly considered because they are effectively screened by intervening oxygens. The parameters used in our work are listed in Table 1. Data in Table 1 are the same as those used by Huang[14] or those empirically derived by Lewis and Catlow[13].

TABLE 1. Short-Range Potential Parameters Used in Simulation

Parameter	O-SiO	Si-O	Al-O	Ca-O	Li-O	Na-O
A_{ij} / eV	3116130.6	1036.89	1012.6	1228.9	975.1	1226.8
r_{ij} /Å	0.1515	0.3259	0.3118	0.3327	0.2706	0.3065
C_{ij} /eVÅ^6	61.3916	0.0	0.0	0.0	0.0	0.0.
r_1 /Å	2.821	1.525	1.525			
r_2 /Å	3.666	2.525	2.525			
r_3 /Å	4.918	3.634	3.634			
r_c /Å	7.570	7.570	7.570	7.570	7.570	7.570
K_{ijk} /eVrad^{-2}		880.67				
r_1 /Å		0.3259				
r_2 /Å		0.3259	2.525			
t/Å		2.7				
t_c/Å		3.0				

4. Simulated Glass Formation

The algorithm for the formation of simulated glasses by molecular dynamics contains three steps : 1) initialization; 2) equilibration; and 3) production.

The initialization step establishes the thermodynamic states and assigns initial positions and velocities to each atom in the system. First of all, the number of atoms and the size of the simulation box are appropriately chosen. Too few atoms in a box will cause the size of the box to be too small

to extract useful structural information, whilst too many atoms in a box will require too much CPU time for calculation. In this work, the number of atoms in a simulation box ranges from about 700 to about 1100 atoms. The length of box is determined by the density and thermal expansion coefficient of the glasses. We note, in passing, that the continuing increase in computer power means that these limits will continue to increase.

Secondly, the initial positions for each atoms in the simulation box are assigned. Usually, the initial positions of Si, Al and a portion of O are assigned to the corresponding sites of the β-cristobalite structure, whilst the initial positions of Li, Na, Ca and some of the O are randomly distributed in the interstitial sites of the β-cristobalite structure (although it is, of course, possible to any initial distribution, including a completely random one). In the case of the alumino-silicate glasses, the initial positions of Si and Al are so selected that the Al-O-Al linkages are intentionally avoided. For those simulation processes that follow the melting process at 6000 K (i.e., those simulations at intermediate temperatures of 3000 K, 1500 K, and 300 K), the initial positions of the atoms in the simulation box were taken from the end of an earlier simulation.

The equilibration step allows the atoms to move from initial positions to other positions that are energetically more accessible. In other words, the structure develops over a time sufficient for the system to relax from the initial conditions, thus "forgetting" how it was prepared. The equilibration procedure is implemented by giving a kinetic energy corresponding to a given temperature. A Gaussian distribution of the velocities is obtained for each atom type in the simulation box according to the classical equation of motion $m_i\mathbf{r}_i = \nabla_i U$ for many interacting species. In the present authors' work, the initial structure is melted at either 6000 K or 8000 K according to the composition of the initial structure. The melting procedure is accomplished by allowing the system to relax for 10000 timesteps. Each timestep equals 2×10^{-15} seconds. In order to equilibrate the system at the target temperature, velocities of the ionic species are scaled every timestep during the first 3000 timesteps. The scaling is accomplished in such a way that the total kinetic energy of the atoms of each type will be equivalent to the target temperature and that the net momentum of the atoms of each type will be zero. During the second 3000 timesteps, the velocities are scaled every 40 timesteps in a similar manner. During the last 4000 timesteps, no scaling is applied and free relaxation is allowed. In order to obtain glass samples from the melts, a cooling or "quench" procedure which consists of a three-step cooling is applied. The melts are first cooled to 3000 K, then to 1500 K, and finally to 300 K. At each temperature, the same relaxation processes as described before are applied. The final configuration at 300 K is taken as the structure of the simulated glass.

The production step generates the equilibrium phase-space trajectory from which some properties can he evaluated. During the simulation, some representative thermodynamic properties, such as site potentials, kinetic energies, displacements, diffusion coefficients, and momenta, are averaged every 40 timesteps (and written to an output file for post analysis). In addition, when thought necessary, the positions and velocities of all atoms may be recorded every timestep, or every so many (e.g., 50) timesteps, for later extraction of dynamic structural information.

A significant problem to be overcome is the long run times that are needed to be able to observe true long-range diffusive motions in the simulation. At short run times, the dominant contribution to the displacement comes from Debye-Waller type thermal motion and not long range migration. Diffusion coefficients extracted from short run times will reflect this situation and thus will he in error. A new approach, called "fast-forwarding", has been developed by the present authors to obtain more detailed transport information from the MD simulations, within reasonable run times[15].

The basic method of this approach is to isolate the momentum among different kinds of atoms in the simulation box. Thus, in the room temperature structure, obtained in the usual way and which will contain the pathways followed by the migrating atoms at this temperature, one can give the mobile alkali ions a higher temperature. With this extra momentum they will move more rapidly through the structure which is maintained at room temperature. In this way, the alkalis will move longer distances in shorter times, permitting an accurate calculation of the diffusion coefficient.

In our work, the simulations were carried out to let alkali ions diffuse at 3000 K and 2500 K, respectively, while the structural relaxation of the other ions is limited to room temperature (through velocity scaling). The diffusion coefficient and diffusion activation energy of alkali ions may thus be calculated. This approach, although computationally "tricky", is, nevertheless, physically valid. Experimental support for this approach comes from NMR studies by Stebbins *et al.*[16], who found that alkali ion dynamics are effectively decoupled from the network.

5. Analysis of Static and Dynamic Properties

5.1. PAIR DISTRIBUTION FUNCTION AND TIME-SPACE CORRELATION FUNCTION

Two of the most useful structural properties that can be extracted from the molecular dynamics simulation are the radial distribution function (RDF) and pair distribution function (PDF). These two functions measure how atoms organize themselves around one another, i.e. represent "local struc-

ture". Specifically, they are proportional to the probability of finding two atoms separated by distance $r + \Delta r$. Since this information can also be extracted from x-ray and neutron diffraction experiments, it provides a way to compare directly and test the accuracy of molecular dynamics simulations. On the other hand, the PDF obtained from MD simulations can provide much more information than can be obtained from diffraction experiments, because the atomic structure is known[17]

The PDF can be expressed as follows :

$$g(r) = \frac{\langle N(r, \Delta r) \rangle}{\frac{1}{2} N \rho V(r, \Delta r)} \tag{9}$$

where $N(r, \Delta r)$ is the number of atoms found in a spherical shell of radius r and thickness Δr, with the shell centered on another atom; $V(r, \Delta r)$ is the volume of the shell; N is the total number of atoms; $r = N/V$ is the number density.

Writing the time average explicitly over a total of M time-steps gives :

$$g(r) = \frac{\sum_{k=1}^{N} N_k(r, \Delta r)}{M(\frac{1}{2} N \rho V(r, \Delta r)} \tag{10}$$

where N_k is the result of the counting operation at time t_k in the simulation run. In equation 10, the choice of Δr is a compromise : it must be small enough to resolve important features of $g(r)$, but also be large enough to provide a sufficiently large sampling population for statistically reliable results. In this work, values near $\Delta r \approx 0.025$Å, have been empirically found to balance these competing factors satisfactorily.

By accumulating PDFs for all the pairs in the system, the Radial Distribution Function (RDF) and the Correlation Function, $T(r)$, can be obtained. The relation between $g(r)$, RDF(r) and $T(r)$ can in principle be expressed as follows :

$$RDF(r) = 4\pi r^2 \sum_{i=1}^{N} \sum_{j=1}^{N} g_{ij}(r) \tag{11}$$

$$T(r) = 4\pi r \sum_{i=1}^{N} \sum_{j=1}^{N} g_{ij}(r) \tag{12}$$

(13)

The principal importance of $RDF(r)$ and $T(r)$ is comparability with x-ray and neutron diffraction data. Nevertheless, to make a quantitative

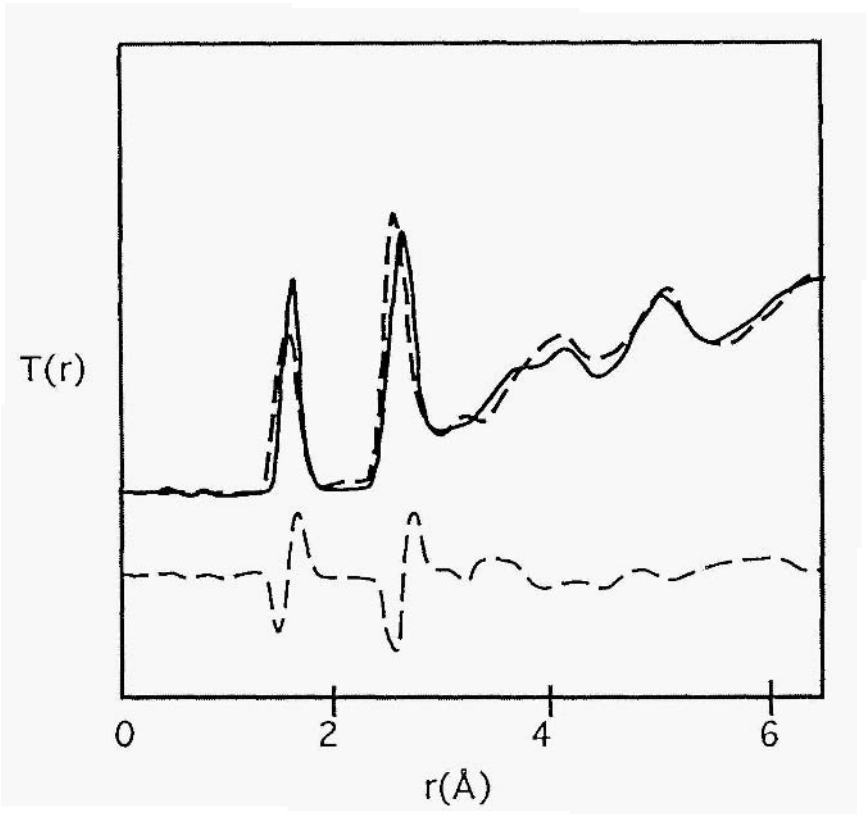

Figure 1. Comparison between calculated (dashed) and measured (solid) $T(r)$ for $32K_2O.68SiO_2$ glass. The difference is shown below.

comparison, one also has to include factors such as the scattering length (for neutron diffraction) and instrumental and thermal broadening[2]. This work can not be done without obtaining the appropriate technical data from the authors of the neutron diffraction experiments. A small number of these collaborations have been made; an example of such a comparison is given in figure 1 and a more complete discussion is available in ref. [17].

Dynamic structure information can be obtained from the Space-Time Correlation Function, $G(r, t)$. $G(r, t)$ expresses the probability that an atom is at position r at time t, given that an atom was at the origin $r = 0$ at initial time $t = 0$. $G(r, t)$ can be separated into two parts. Terms having $i = j$ yields the self space-time correlation function, for which the atom at

$(r,t)$is the same atom that occupied the origin at ($r = 0$, $t = 0$). Terms having $i \neq j$ yield the distinct space-time correlation function, for which the atom at (r, t)differs from the one that occupied the origin. The equations are as follows

$$G(r,t) = G_s(r,t) + G_d(r,t) \tag{14}$$

$$G_s(r,t) = \frac{1}{MNV(r,\Delta r)} \sum_k \sum_i \delta\left(r - |r_i(t_k) - r_i(t_k + t)|\right) \Delta r \tag{15}$$

$$G_d(r,t) = \frac{1}{M(N/2)V(r,\Delta r)} \sum_k \sum_i \sum_{j>i} \delta\left(r - |r_i(t_k) - r_i(t_k + t)|\right) \Delta r \tag{16}$$

where the index k runs over a total of M time origins. δ is the Dirac delta function. Its summation represents the usual time average over a system at equilibrium. $G_s(r,t)$ can be used to investigate the hopping behavior of the alkali migration in alkali silicate glasses, while $G_s(r,t)$may be used to investigate the site preference of the alkali ions in the mixed-alkali glasses and soda lime silicate glasses. A discussion will be given below.

5.2. Q_N DISTRIBUTION, RING SIZE DISTRIBUTION, AND VOID SIZE DISTRIBUTION

Q_n Species Distribution (QSD), Ring Size Distribution (RSD), and Void Size Distribution (VSD) are useful measures for characterising the mid-range structure of glasses. All these distributions are influenced by the number and spatial distribution of non-bridging oxygens. Determining which oxygens are bridging or not is frequently done using radial cut-off criterion : how many Si (or Al) there are within a specified distance of the oxygen.

Most of the MD work in the literature defines BO and NBO in this way[15,18, 19], that is, they define BO or NBO, based on the Si-O distance. Those oxygens with Si-O distance less than the cut-off are considered as bonded, whilst those oxygens with nearest Si-O distances longer than the cut-off are considered as not bonded. An alternative definition, which may be more reasonable than the simple cut-off criterion, is as follows.

NBO : oxygen which is bonded to only one Si or Al provided that each Si or Al is bonded to the four nearest oxygens;
BO : oxygen which is bonded to two Si or Al provided that each Si or Al is bonded to the four nearest oxygens;
TBO : oxygen which is bonded to three Si or Al provided that each Si or Al is bonded to the four nearest oxygens;

This may be considered a better scheme because it does not rely only on distance to determine the number of silicons bonded to each oxygen, but ensures that each of the Si is also properly co-ordinated.

The number, n, of bridging oxygens associated with the $[SiO_4]$ tetrahedron is an important parameter in defining glass structure. Q_n is defined as species with n bridging oxygens associated with it. For example, a Q_3 species of Si stands for a Si with 3 bridging oxygens (BO) and one non-bridging oxygen (NBO) in its tetrahedron. The calculation of QSD is quite straightforward as soon as BO and NBO are defined. The quantity, Q_n, represents the percentage of tetrahedra with n bridging oxygens. The Q_n distribution can be determine by NMR. Dupree *et al.*[20] proposed a binary model for Q_n distribution, which suggested that, with the increasing of alkali concentration (and the number of NBO), Q_4 species are continuously converted to Q_3 species until no Q_4 remains; after this point Q_3 are continuously converted to Q_2, and so on. Alternatively, Gurman[20] proposed a thermodynamic bond-ordering model, which applies configurational energy in the equilibrium of the Q_n species to account for the Q_n distribution. He argued that the proportions of different Q_n species are arranged by an ordering energy ΔE, which is due to the interaction between bridging and non-bridging oxygens. An equilibrium can be expressed as :

$$2Q_n \rightarrow Q_{n+1} + Q_{n-1}$$
$$[Q_{n+1}]\,[Q_{n-1}] / [Q_n]^2 = \exp[-2\Delta E/kT_g]$$

Infinite ΔE leads to the binary model, whilst $\Delta E = 0$ leads to a completely random distribution. Gurman found that the lithium silicate glasses have $\Delta E/kT = 1.5 \pm 0.5$[21]. However, some NMR data [20, 22, 23] from alkali-silicate glass systems support the binary model. On the other hand, other NMR data [24, 25, 26, 27] and a Raman investigation[28] support the bond-ordering model.

Ring size is usually defined as the number of tetrahedra involved in the smallest closed chains formed by BO and Si/Al in the glass network. Rings that can be decomposed into two or more smaller rings are not counted in the distribution. Although the RSD is not experimentally measurable for silicate glasses at present, most of the structural model in the literature are frequently discussed in terms of it. Therefore it becomes important for the simulations in analyzing the validity of those models. A complete calculation of RSD is somewhat tedious, and includes an exhaustive searching of all possible rings in the simulation box.

The VSD is important riot only for a discussion of the mid-range structures of glasses but also for many diffusion related properties and the transition range behavior of the glasses. Specifically, the VSD can be indirectly

derived from gas diffusion measurements[29]. Therefore it provides an effective way to compare the mid-range structures between the experimentally melted glasses and computer simulated glasses. The VSD calculation is performed by regarding the constituent atoms in the simulation box as rigid spheres. The radii of atoms are calculated from the positions of the first peak in the PDF, as well as the ionic radii of the corresponding cations and anions derived from crystals[30]. Mitra *et al.*[31] have proposed algorithms for calculating VSD.

5.3. DIFFUSION COEFFICIENT AND DIFFUSION ACTIVATION ENERGY

The standard way of calculating the diffusion coefficient is to measure the r.m.s. displacements over a period of time and then use equation 17 to extract D. As we have discussed, computational limits to the number of timesteps often cause problems.

An alternative approach was used by Cao and Cormack to calculate the diffusion coefficient, as was initially used by Huang[15]. The basic idea of this approach, as mentioned in the last section, is to keep the network temperature at room temperature while raising the temperature of the alkali ions to 3000 K or 2500K, thus allowing the alkali ions to diffuse at a "high temperature" while the network structure is relaxing at a "room temperature". With this approach, significant displacement of alkali ions can be observed within several thousands timesteps.

The diffusion coefficient D is evaluated by the mean-square displacement :

$$D = \frac{\sum_{i=1}^{N} \langle |r_i(\tau) - r_i(\tau_0)|^2 \rangle}{6N(\tau - \tau_0)} \tag{17}$$

where $r_i(t)$ is position vector of the diffusion species i at time t, and $r_i(t_0)$ is the position vector of the diffusion species i at time t_0. N is the number of the diffusing species. The diffusion activation energy can be determined using the Arrhenius relationship :

$$D = D_0 \exp(-\Delta E / RT) \tag{18}$$

After calculating two diffusion coefficients for each composition, where the temperature of alkali ions are raised to 2500 K and 3000 K respectively, with the network former ions are kept at room temperature, ΔE, the diffusion activation energy, can be calculated from equation 18.

5.4. VISUALIZATION OF GLASS STRUCTURES AND ANIMATION OF DIFFUSION PROCESSES

Visualization is probably the most effective and direct way to investigate the glass structures. Thanks to the development of the modern computer technology, several ways of three-dimensional visualization have been made possible through the application of some sophisticated software packages, such as InsightII (from Biosym, Inc.) and Cerius2 (from MSI).

To animate the alkali diffusion process in the glasses, the coordinates of each atom in the simulation box must be recorded each timestep, or each several timesteps, for thousand or tens of thousands of timesteps. Those time-dependent coordinates are then extracted and decomposed to multiple files, each file recording the coordinates of the atoms at a specific time for input into the graphical software, which can then be used to produce a 3-D solid model picture; these can be run together to produce a movie.

We now move to a discussion of some glass systems, to which MD simulations have been applied.

6. Alkali Silicates

There have been a number of simulations of alkali silicates, which is probably the most studied system from this point of view. The early studies showed that simulations demonstrated great potential for providing valuable atomic scale information about the structure of these glasses, although it was primarily qualitative in nature. There were, however, the same kind of discrepancies which were found in studies of silica described above, leading some question whether any useful quantitative information could be obtained.

The studies by Huang and Cormack[32, 33, 34] were probably the first to describe in detail the spatial distribution of alkalis. They showed that in sodium silicate and potassium silicate glasses, the alkali ions are not spread uniformly throughout the glass, but rather adopt an heterogeneous distribution leading to alkali-rich regions and separate silica-rich regions. Most, if not all, of the non-bridging oxygens are to be found in the alkali rich-regions, because the association of the NBO and alkalis. This association had long been postulated (on the basis of their opposite effective charge), and had also been reported in all of the earlier studies. These results, which have been supported by subsequent studies by other workers [35,36], indicate a structure of the glasses more in line with the Modified Random Network Model proposed by Greaves[4], rather than an extension of Zachariasen's Continuous Random Network Model. Indeed, recent EXAFS, Raman spectroscopy, and NMR studies all support this view[28, 37, 22, 23].

Huang and Cormack[33] also discussed the phase separation tendencies in alkali silicates in terms of the structural units which they found in their simulations. These units would not be present if the distribution of alkali ions was homogeneous. Some interest, therefore, attaches to the structure of lithium silicate glasses. With the small mass and the small ionic radius of Li ions, the physical properties of lithium silicate glass show some of the more interesting features in the group of alkali silicate glasses. The immiscibility gap in lithium silicate glass is known to be the most extensive in alkali silicate glasses[38, 39]. Raman spectroscopy[28] and EXAFS[37] have also suggested that regional alkali clustering is more prevalent in glasses containing smaller alkali cations. However, due to the complexity of the structure of alkali silicate glasses, little direct or unambiguous experimental evidence has been reported to show the distribution of alkali ions in the glass.

Lithium silicate glasses show the most disordered intermediate-range order of all alkali silicates, as shown in Fig. 2. This can be rationalized by the fact that the other alkalis have a considerably larger nearest neighbor oxygen distance (2.67 Å and 2.45 Å for K and Na, respect ively) than the corresponding distance for Li (2.0 Å), and can be ascribed to the stronger Li-O bonds. Therefore [SiO_4] tetrahedra are more distorted by Li ions, asymmetrically, leading to a greater effect on the intermediate range order of the Si-O network.

6.1. CLUSTERING OF ALKALIS AND NBO

Fig. 3 shows that Li ions are clustered in NBO-rich regions, a picture typical for alkali silicate glasses[32, 33], although the clustering is more complete in lithium silicate glass than in sodium and potassium silicate glasses. This result is consistent with the composition fluctuations which decrease in the order Li>Na>K [28, 37]. Even at low Li_2O content (5 mol% Li_2O), Li and NBO tend to cluster together. At high Li_2O content (35 mol% Li_2O), the Li-NBO clusters form percolated channels and isolated BO complexes. This is the picture envisaged in the the modified random network model[4]. For a composition of 15 mol% Li_2O, Cao and Cormack[40] found that the Li-NBO and BO complexes are clearly segregated, the composition of the Li-NBO region being nearly $Li_2O.2SiO_2$, in coincidence with the experimentally observed phase -separation boundary in lithium silicate glasses[39]. Although the veracity of this picture is supported by detailed comparisons with macroscopic experimental measurements (discussed earlier), there are a few discrepancies which suggest that there might be some improvements to the MD model (see fig. 1). These would not affect the basic picture or understanding of the atomic structure.

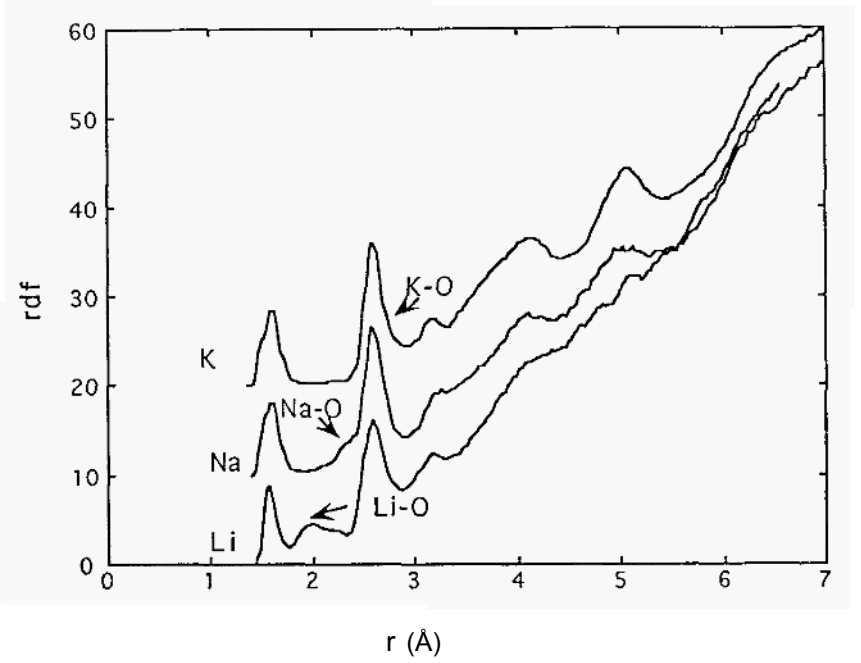

Figure 2. rdfs from $30R_2O.70SiO_2$ glasses (R=Li, Na, K).

Fig. 4 shows the displacements of Li ions in $0.3Li_2O.0.7SiO_2$ glass, after 5000 timesteps. Clearly, not all Li ions migrate over the same distance within the same timespan; there is considerable variation in the net displacement experienced by each lithium. Fig. 5 shows the displacement of an individual Li ion in $0.25Li_2O.0.75SiO_2$ glass. Fig. 6 shows a multi-exposure snapshot of the pathway of a migrating Li ion in glass. The timelapse between two Li positions is 20timesteps.

The BO/NBO transformation of the local environment during Li migration was investigated by Cao and Cormack[40] using animation techniques. They found that in some cases, at low alkali content, the migration of a lithium ion away from the site it had been occupying, caused the NBO adjacent to this site to transform into bridging oxygen, while a bridging oxygen adjacent to new site became an NBO. This transformation was not seen to occur every time a Li ion jumped, nor was it seen at higher concentrations because the co-operative nature of the Li ion migration (i.e. sites vacated by one ion would be shortly occupied by another ion).

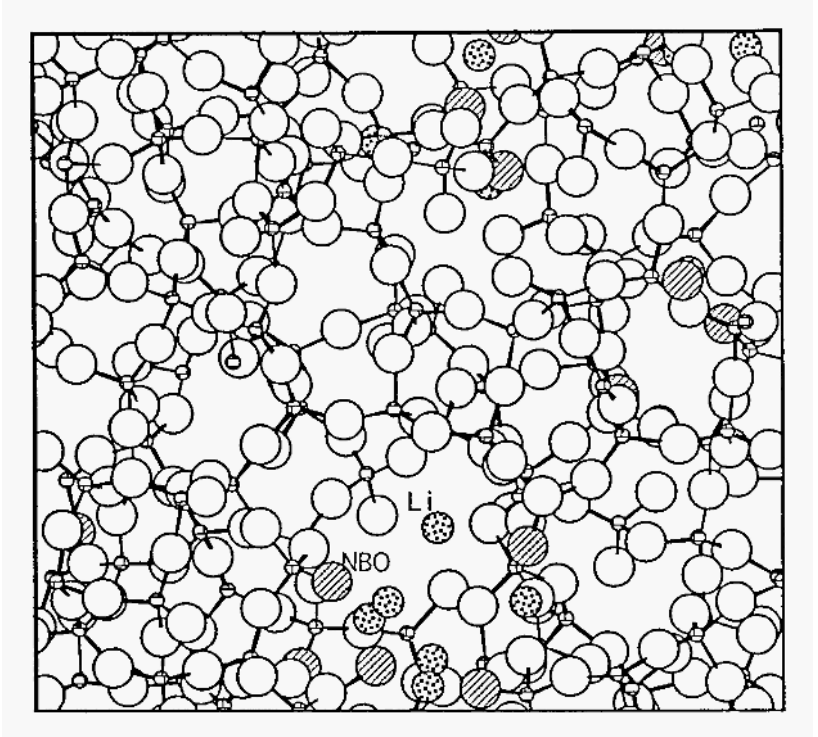

Figure 3. Structure of $0.05Li_2O.0.95SiO_2$ glass, showing clustering of Li and NBO.

7. Alumino-Silicate Glasses

The addition of aluminium to alkali silicate glasses produces some interesting behaviour. Alkali alumino-silicate glasses show at least one or more anomalous property change in the property vs. composition relation. Besides the extremum in the viscosity and electrical conductivity at Al/Alkali $\approx$ 1.0 which is observed in almost all the alkali alumino-silicate glasses, an anomalous property change at about Al/Alkali= 0.2 ~ 0.4 is observed in some alkali alumino-silicate glasses (see figure 7). While it has been generally agreed that there must be some fundamental structural changes associated with this somewhat drastic property change, the exact mechanism is a matter of disagreement. From a theoretical point of view, understanding the structure of this system is an important step towards understanding the structure of common, commercial glasses, such as the solid soda lime

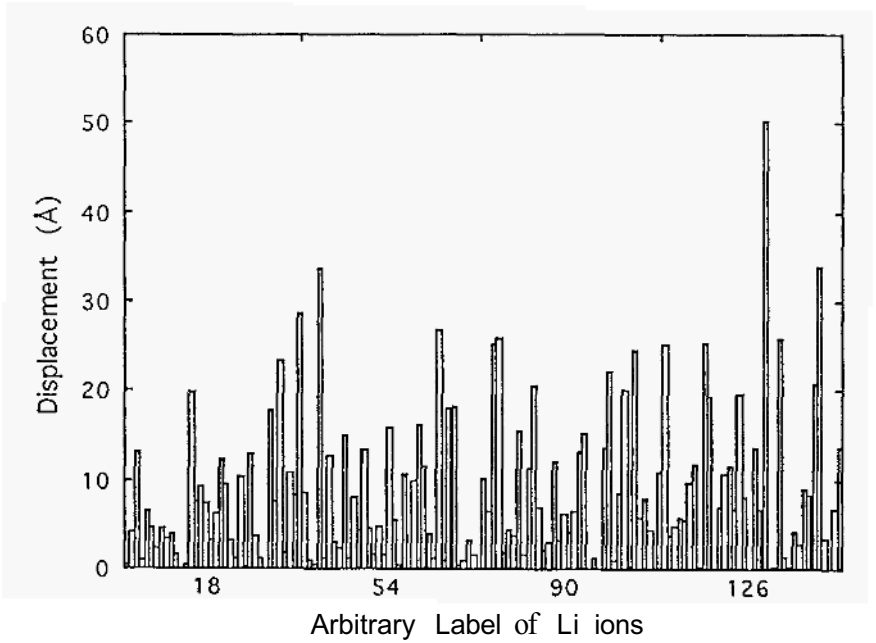

Figure 4. Displacement of Li ions after 5000 timesteps in $0.3Li_2.0.7SiO_2$ glass.

silicates. This phenomenon is discussed in greater detail below.

It is generally believed that the initial introduction of Al to alkali silicate glasses, up to Al/Alkali= 1.0, results in [SiO_4] tetrahedra, although the possibility of the existence of [AlO6] in the initial Al addition has also been suggested[41, 42]. For Al/Alkali$\geq$ 1.0, however, some disagreement exists. Two main models prevail : one suggests a change from [AlO_4] to [AlO_6] coordination for additional Al [41, 43, 44, 45, 46]. The other model proposes that Al remains tetrahedrally coordinated over whole composition range, and that tri-bonded oxygens appear at Al/Alkali$\geq$ 1.0 in order to maintain electrostatic neutrality [47]. This model is apparently supported by the EXAFS, XANES, Raman, and diffraction data of McKeown *et al.*[48, 49,50,51]. None of these experimental results, however, provides conclusive evidence in support of either model.

Another question which still remains is whether Loweinstein's "aluminium avoidance rule" [52]is obeyed in glasses, as it is in crystals. Molecular orbital calculations of de Jong and Brown[53] implied that Si-O-A1 bonds should be more stable than Si-O-Si or Al-O-Al bonds in glass. How-

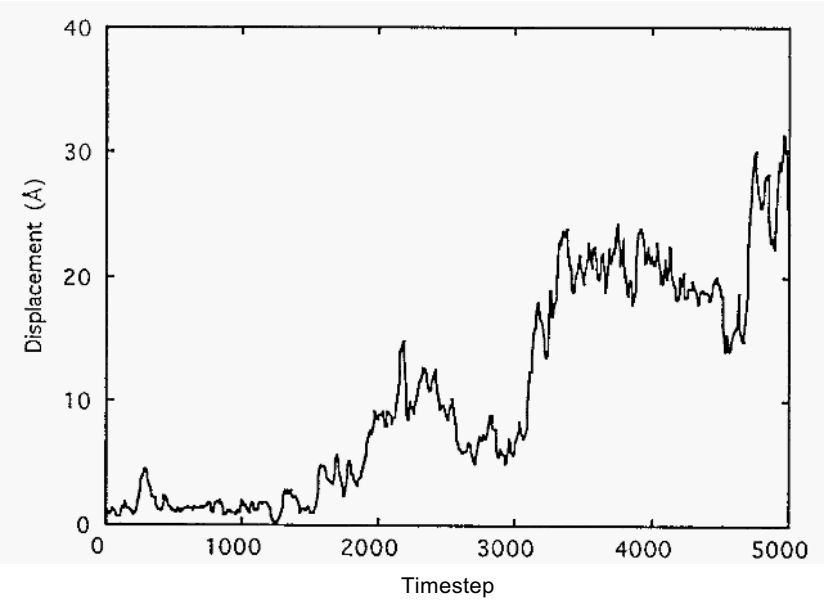

Figure 5. Displacement of arbitrary Li ion (#40 in figure 4).

ever, some experimental results indicate the presence of Al-O-Al bonds in glasses. Based on NMR analysis de Jong *et al.*[54] suggested the existence of Al-O-Al bonds in certain crystals and glasses. Klinowski *et al.*[55] demonstrated that the open structure of zeolites can absorb much of the strain associated with the Al-O-Al linkage, therefore, the presence of Al-O-Al bonds in glass seems reasonable because of its open structure. Navrotsky *et al.*[56] showed from their calorimetric data that the energy of the reaction :

$$1/2\,(\text{Al-O-Al}) + 1/2\,(\text{Si-O-Si}) \rightarrow \text{Al-O-Si}$$

should not be more than 5 – 10 kcal/mol, indicating no strong tendency toward Al-Si ordering in the glasses.

An earlier MD study by Zirl and Garofalini[57], by constraining the coordination of Al to $[AlO_4]$ over the whole composition range, reproduced the minimum inNa adiffusion activation at Al/Na= 1.0 in a series of $(4-x)Na_2O.xAl_2O_3.8SiO_2$ glasses. Cao and Cormack[58] also observed that Al remained as $[AlO_4]$ over the whole composition of a series of $Li_2O.xAl_2O_3.(3-x)SiO_2$ glasses, although they did not constrain the coordination of Al. They noted significant amounts of tri-bonded oxygens at high Al/R ratio and also the presence of Al-O-Al bonds. The minimum

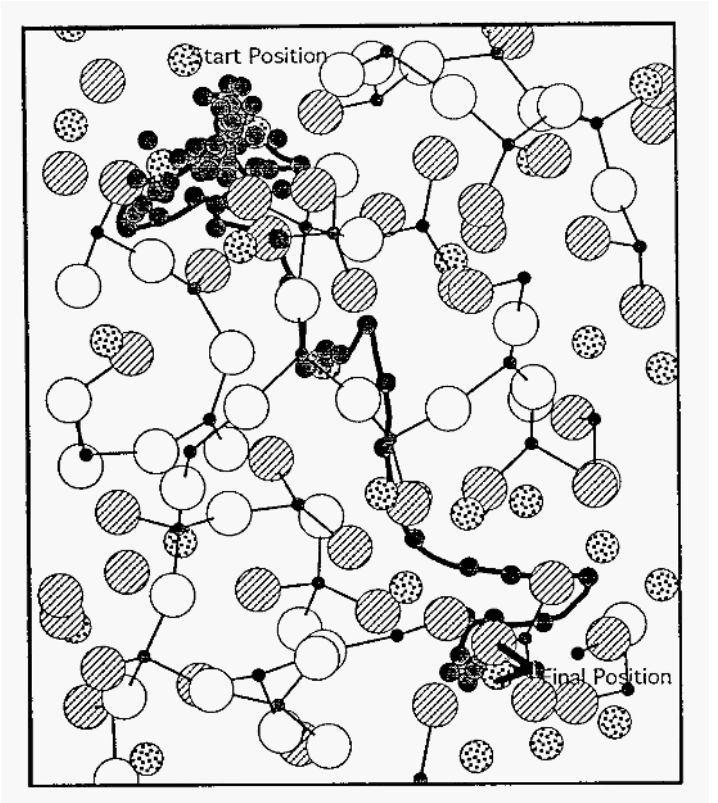

Figure 6. Li Migration path in $30Li_2O.70SiO_2$ glass at 1500K ; there are 50timesteps between each Li position.

in the diffusion activation energy was also successfully reproduced (figure 8).

7.0.1. *MID-RANGE STRUCTURES*

The mid-range order of the glass structure is characterized by the distribution of various rings in the network. The ring size distribution for a series of $Li_2O.xAl_2O_3.(3-x)$SiO2 glasses is shown in Fig. 9. As the Al/li ratio increases, the distribution it seen to shift to a smaller ring size. Note that the initial addition of Al to silicate glasses serves to eliminate the larger rings in the glasses, whilst the further addition of Al creates small rings. The ring size distribution at Al/Li= 0.0 is skewed to the right side, indicating the presence of large rings caused by the aggregated distribution of

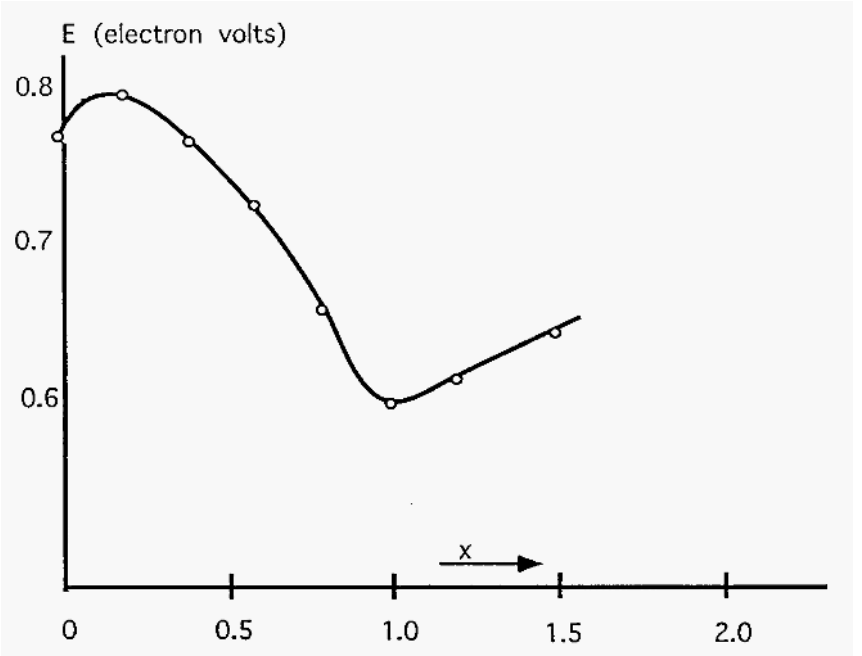

Figure 7. E *vs* . x in Na.xAl.$(4-x)$Si (J. Soc. Glass Tech. 1958).

Li ions in the glasses. At Al/Li= 0.5, the large rings (with more than 8 members) are almost eliminated because of the migration of Li ions from NBO-rich to $[AlO_4]$-rich regions[58]. The number of small rings does not change much, causing a sharper and more symmetric ring size distribution. This is consistent with the observation that the immiscibility in alkali silicate glasses is diminished with a small addition of Al to the glasses [59]. With increasing Al content (Al/li> 1.0), the ring size distribution becomes skewed to the left side, caused by the formation of tri-clusters, that is clusters containing three coordinated oxygen. The average ring size decreases linearly with increasing Al/Li ratio, which is quite reasonable considering that a NBO→BO or BO→TBO transformation is taking place, along with the replacement of Al to Si.

The participation of Si and Al in the differently sized rings is of interest, since it reflects the different $[SiO_4]$ and $[AlO_4]$ environments in the mid-range structure. A detailed analysis indicates a preference of Al for the

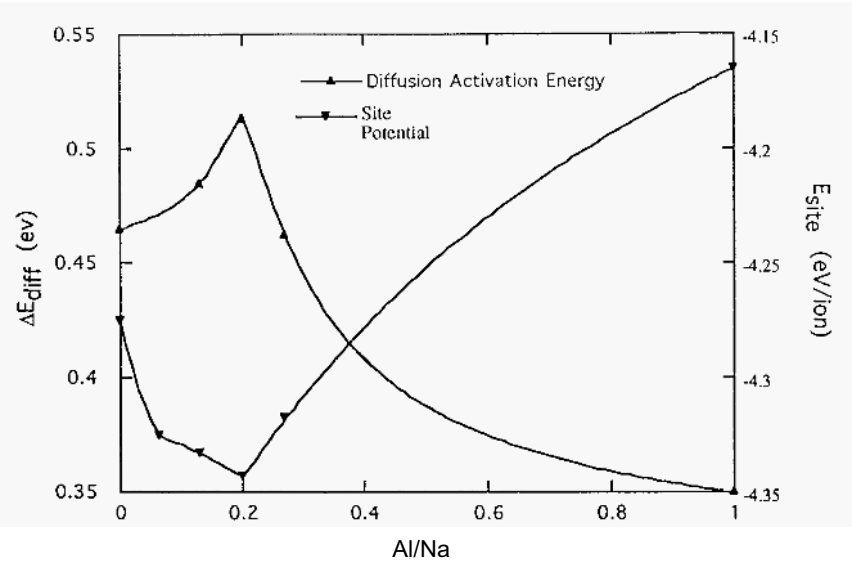

Figure 8. Na ion diffusion activation energy and site potential in $Na_2O.xAl_2O_3.(3-x)SiO_2$ glasses.

smaller rings, whilst Si opts for the later rings. This result is consistent with our results that tri-bonded oxygens are preferentially associated with Al. Zirl and Garofalini [57] also observed that Al is randomly incorporated into 4-member and 5-member rings, while a preferential replacement of Al is seen in the 3-member rings. At compositions with a high Al/Alkali ratio, the formation of Al-rich small rings and tri-clusters gives less freedom for $[SiO_4]$ and $[AlO_4]$ to be randomly arranged. This factor may contribute to the crystallization tendency of alkali alumino-silicate glasses at a high Al/Alkali ratio.

7.1. DIFFUSION PROPERTIES

Fig. 10 shows the Li diffusion activation energy in $Li_2O.xAl_2O_3.(3-x)SiO_2$ and $Li_2O.xAl_2O_3.(5-x)SiO_2$ glasses. A minimum is observed at Al/Li= 1.0 in both of the systems, consistent with the experimental results of Terai[60]. Meanwhile, it is observed that for both systems, the site potential of Li

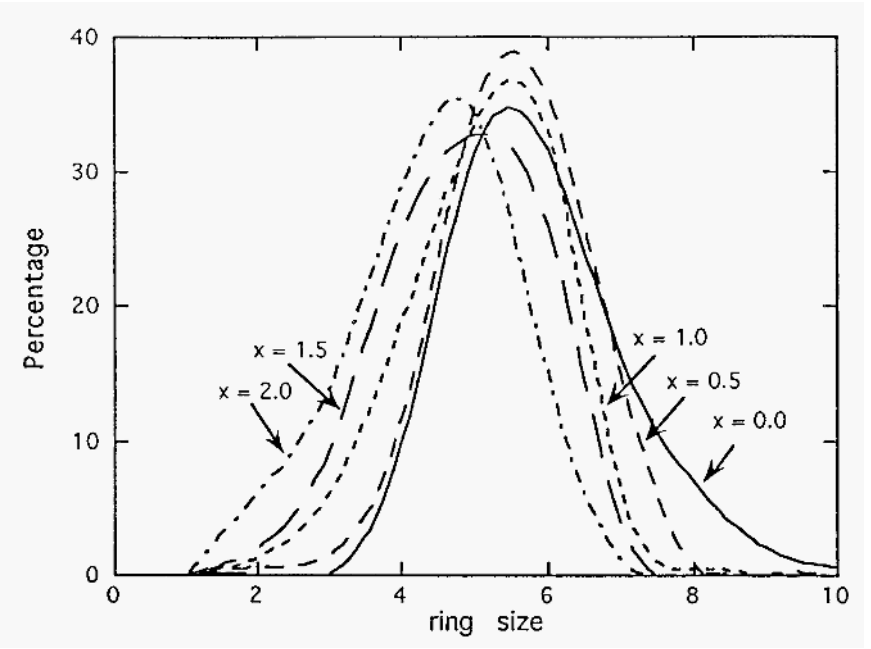

Figure 9. Ring size distribution in $Li_2O.xAl_2O_3.(3-x)SiO_2$ glasses.

increases significantly with Al/Li as Al/Li< 1.0, but, for the former system, remains almost unchanged as Al/Li> 1.0, whilst for the later system, it decreases as Ql/Li> 1.0.

According to Anderson and Stuart model[61], the alkali diffusion activation energy can be regarded as a sum of two terms. One is related to the Coulombic binding energy experienced by an ion, and the other represents a strain energy associated with the dilation of the diffusion doorway caused by the passage of an ion from one site to another. The introduction of Al to alkali silicate glasses causes two opposing effects in alkali diffusion. Firstly, it decreases the number of NBO, transforming the alkali diffusion paths from NBO-rich channels to $[AlO_4]$-rich channels. The result is that the fraction of NBO associated with Li in the first shell decreases drastically, as seen in Fig. 11. The binding energy for alkali diffusion is thus decreased. Additionally, as Al/Li< 1.0, only the numbers of the 7-, 8-, and 9- member rings decrease significantly, whilst the numbers of the 5- and 6-member rings remain almost constant (fig. 9). The increase in strain energy is therefore not significant in this composition range. These two factors con-

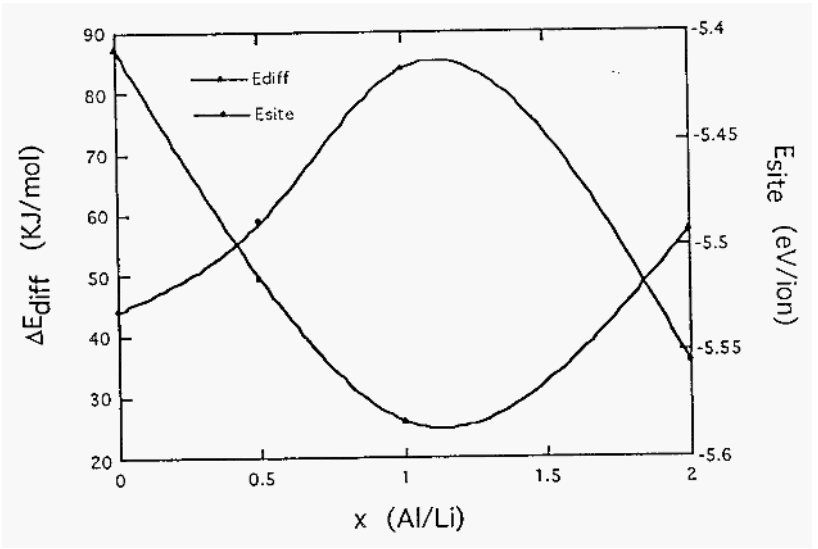

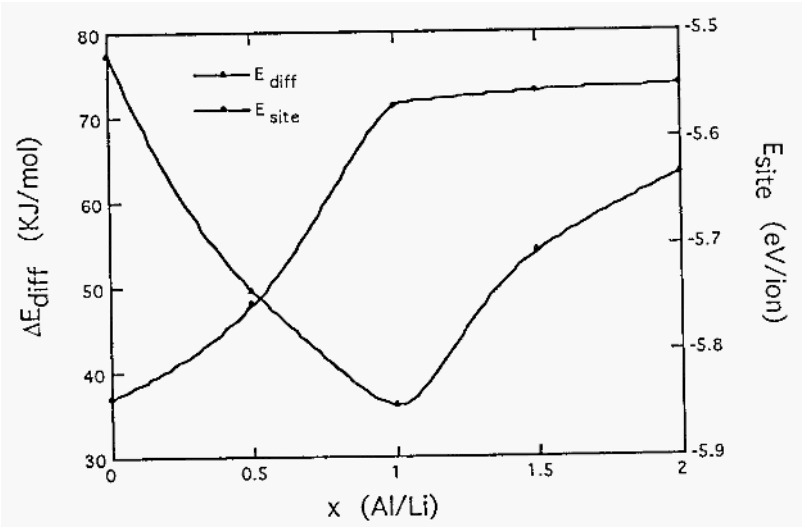

Figure 10. (a) Diffusion activation energy and alkali ion site potential in $Li_2O.xAl_2O_3.(5-x)SiO_2$ glasses. (b) Diffusion activation energy and alkali ion site potential in $Li_2O.xAl_2O_3.(3-x)SiO_2$ glasses.

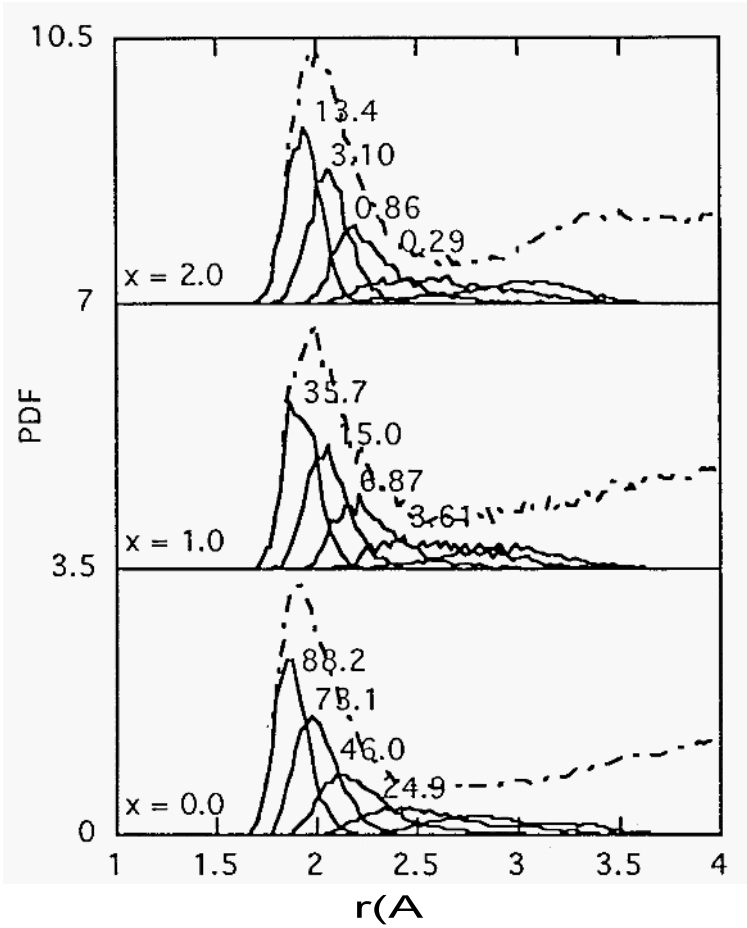

Figure 11. Sub-peaks in the first Li-O pdf in $Li_2O.xAl_2O_3.(5-x)SiO_2$ glasses. Numbers represent % NBO in each sub-peak.

tribute to the decrease in the Li diffusion activation energy for Al/Li< 1.0.

As Al/Li> 1.0, most of alkali ions are already associated with BO, and the decrease in the binding energy with increasing Al/Li is not significant. On the other hand, the ring size distribution shifts to smaller sizes, due to the formation of tri-clusters, as seen in Fig. 9. This reduces the concentration of favorable sites for Li diffusion, increasing the strain energy and

leading to a higher diffusion activation energy for Li.

7.2. THE ANOMALY AT AL/ALKALI= 0.2 ~ 0.4

As mentioned above, anomalous property changes have been observed for some alkali alumino-silicate glasses at Al/Li= 0.2 ~ 0.4. An interesting feature accompanying this anomaly is worth noting : The anomaly tends to be absent in those glass systems with high alkali concentrations or, if the alkali concentration is not high but the alkali concentration increases with Al/Alkali. It becomes significant and lasts to a higher Al concentration, or higher Al/Alkali, when the alkali concentration is low and/or decreases with Al/Alkali.

Several models have been proposed to interpret this phenomenon in various ways. Terai proposed that the anomaly is due to the decrease in Na concentration with the addition of Al[60]. This model, although successfully explaining the data presented in reference [60], can not account for data in some other glass systems. The anomaly can be observed in some alkali-poor glass systems when the alkali concentration increases with increasing Al/Alkali [62, 63]. LaCourse[64] attributed this anomaly to the "mixed-site effect". According to this model, alkali ions adjacent to NBO and those adjacent to $[AlO_4]$ interact with each other due to their different vibration frequencies, resulting in a higher diffusion activation energy. At higher Al_2O_3 contents the $[AlO_4]$ adjacent sites begin to dominate; thus, the interaction becomes negligible. According to this model, a stronger anomaly is expected at high alkali concentrations. Experimental results, however, yield the opposite trend. Hunold and Bruckner[65] and Shelby[66] proposed that the first Al^{3+} introduced into alkali silicate glass may appear as $[AlO_6]$. Further addition of Al enters increasingly as $[AlO_4]$ so the fraction of $[AlO_6]$ groups decreases. This model, too, is unable to account for the fact that the anomaly disappears at high alkali concentrations. Moreover, the existence of $[AlO_6]$ in the initial al addition has not been substained.

Cao and Cormack[58], from modeling a series of $Na_2O.xAl_2O_3.(3-x)SiO_2$ glasses in which they observed a maximum in the diffusion activation energy at A1/Na= 0.2, consistent with experimental results[63, 67], have proposed a new model. Based on the micro-heterogeneity of glass structures, the main idea of this model is that the anomaly is a result in the shift of the percolated alkali diffusion channels from NBO-rich regions to $[AlO_4]$-rich regions. An illustration of this model is shown in Fig. 12.

The anomaly observed in [60] is, in fact, a special case, in which the mechanism described above does not contribute anything. As discussed by Terai, the decreasing Na concentration with increasing Al/Alkali is the main reason for that anomaly.

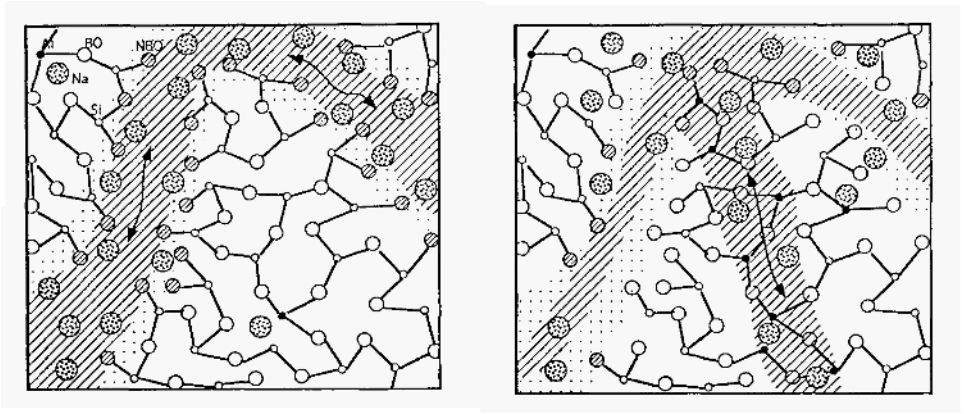

Figure 12. Illustration of Channel Shift Model. Alkali migration behaviour before and after $[AlO_4]$ channels are percolated.

The simulations strongly indicate, that, in alkali alumino-silicate glasses, Si is preferentially bonded to NBO, whilst Al is preferentially bonded to BO and TBO. Indeed, this feature is quite clear when the structure is visualized.

A number of authors have argued that there are no Al-O-Al bonds in alkali alumino-silicate glasses [62, 63, 68, 43], since, according to the aluminium avoidance principle well known in mineralogy [52], the Al-O-Al linkage is electrostatically unstable, thus unlikely. de Jong *et al.,* [54] however, suggested the existence of AI-O-A1 bonds in certain crystals and glasses as a result of NMR studies. Recently, Zirl *et al.*[57] found a significant number of Al-O-Al bonds in their MD simulation of sodium aluminium silicate glasses. Petrov *et al.*[69] also suggested the existence of Al-rich heterogeneous regions from Raman spectroscopy. Cao and Cormack also found significant numbers of Al-O-Al bonds in their MD simulation.

We note here that the existence of Al-O-Al bonds in glass is natural and necessary, since, besides the electrostatic effect, there is an entropy factor that makes the Al-O-Al linkage inevitable. As is well known, glass has a much higher entropy than do crystals, so instead of an ordered configuration which keeps the Al from linking together, a random configuration may, in fact, to be more favored by the glass structure.

The presence of Al-O-Al bonds inevitably leads to groups of $[AlO_4]$ tetrahedra and groups of $[SiO_4]$ tetrahedra. Further analysis of the struc-

ture of the [AlO_4] groups and the [SiO_4] groups reveals an interesting feature : with increasing Al/Na, theAl-O-Al bond angle decreases significantly, indicating that in alkali alumino-silicate glasses the [AlO_4] groups form their own separate environment, which is more compact than that of the [SiO_4] groups. This observation is consistent with the suggestion of Seifert *et al.*[70], of a bi-modal distribution of inter-tetrahedral angles in alkali alumino-silicate glasses inferred from a Raman spectroscopy only.

8. Mixed Alkali Effect in Alkali Silicate and Alkali Alumino-Silicate Glasses

The mixed-alkali effect has been observed and discussed for more than a century. It refers to a non-linear change of many physical properties, most notably the electrical the electrical conductivity, as a result of the addition of a second alkali ion to an alkali-containing glass. Quite a variety of models has been proposed, although none of these models has been universally accepted. Reviews given by Isard[71], Day[72], and LaCourse and Cormack[73] provide good summaries of these models.

The mixed-alkali effect in alkali alumino-silicate glasses is particularly interesting, because some models require a dependence on the existence of NBO[74, 75, 76]. At Al/Alkali= 1.0, lion-bridging oxygens (NBO) are, in principle, absent in the glass. Lapp and Shelby[77] studied the electrical conductivity of several series of lithium-sodium alumino-silicate glasses and demonstrated that, with the total alkali concentration kept constant, the mixed alkali effect increases with increasing Al concentration (i.e. with decreasing numbers of NBO). This result leads to the conclusion that the NBOs are not necessarily responsible for the effect, indicating that those models which require the existence of NBO are questionable.

Most of the current models of the mixed-alkali effect are based on the experimental observation of certain macroscopic properties, such as electrical conductivity, alkali ion diffusion and viscosity. However, the secret of the mixed-alkali effect must lie in the structure of the glass and in how the structure controls the mechanisms of alkali diffusion in the glass.

The simulations of sodium/potassium silicates by Huang and Cormack [15] were the first to reproduce the mixed alkali effect. Cao and Cormack[78] simulated two series of glasses, $x Li_2O.(1-x)Na_2O.3SiO_2$ and $x Li_2O.(1-x)Na_2O.Al_2O_3.2SiO_2$, in which the mixed alkali effect was also seen. Fig 13 shows the diffusion coefficient and diffusion activation energy of $x Li_2O.(1-x)Na_2O.3SiO_2$ (x = 0.0, 0.5, 1.0) and $x Li_2O.(1-x)Na_2O.Al_2O_3.2SiO_2$ (x = 0.0, 0.5, 1.0) glasses. The magnitude of the mixed-alkali effect, represented by the departure from additivity of diffusion activation energy, as shown in Fig 14, indicates that the mixed alkali-effect in alkali alumino-silicate

glasses is significantly stronger than in alkali silicate glasses, in accordance with the experimental results[77].

Interesting information is revealed from an analysis of the site potential of the alkali ions. in the $(0.5Li+0.5Na)_2O.3SiO_2$ glass, the site potential of Li decreases considerably (becomes more negative), compared to that in the $Li_2O.3SiO_2$ glasses, whilst the site potential of Na increases slightly (becomes less negative) compared to that in $Na_2O.3SiO_2$ glass. The average site potential deviates slightly negatively from additivity. The result is consistent with our previous study for the potassium-sodium glasses[15]. In $xLi_2O.(1-x)Na_2O.Al_2O_3.2SiO_2$ glasses the feature is slightly different, with the site potential of both Li and Na being lower in the mixed-alkali glass than in the single-alkali glass, leading to a stronger negative deviation of the average site potential from additivity, and accounting for the increased magnitude of the effect in alumino-silicate over silicates.

No significant difference is observed between the network structures of single alkali and mixed-alkali glasses, although differences in detail in the alkali-NBO rich regions are apparent. Fig. 15 shoes Li-O and Na-O PDFs of $xLi_2O.(1-x)Na_2O.3SiO_2$ and $xLi_2O.(1-x)Na_2O.Al_2O_3.2SiO_2$ glasses. Li-O peaks are seen to be sharper than Na-O peaks. The Li-O peaks are sharpened and the average Li-O bond-length becomes shorter in the mixed-alkali glass, compared to those in the single alkali glasses, whilst the first Na-O peaks in the mixed-alkali glass are broadened and the average Na-O bond-length elongated. This is the same as seen in Na/K silicates, in which the smaller ion finds a better environment. Fig. 16 shows the coordination shell of Li and Na in $xLi_2O.(1-x)Na_2O.3SiO_2$ and $xLi_2O.(1-x)Na_2O.Al_2O_3.2SiO_2$ glasses, significant differences between the mixed-alkali and the single-alkali glasses can be seen. The coordination shell of the smaller Li ions becomes more ordered in the mixed-alkali glasses than in the single-alkali glasses, whilst the coordination shell of the larger Na ions becomes less ordered. These results reflect the fact that Li ions, having stronger bond strengths, are able to get a better defined coordination shell than in the single alkali glass, at the expense of the environment of Na ions. They may also account for the decrease in the site potential of Li and the decrease in the site potential of Na.

Analysis of the PDF of alkali-alkali ions in $(0.5Li+0.5Na)_2O.3SiO_2$ and $(0.5Li+0.5Na)_2O.Al_2O_3.2SiO_2$ glasses reveals a random or stochastic distribution of the two types of alkali and indicates that the pairing of Li-Na ions is not preferential to that of Li-Li and Na-Na in either system so that such pairing of Li-Na ions is not preferential to that of Li-Li and Na-Na in either system so that such pairing is not a necessary part of a successful model of the mixed-alkali effect.

The reproductibility of the mixed-alkali effect in our MD simulation also

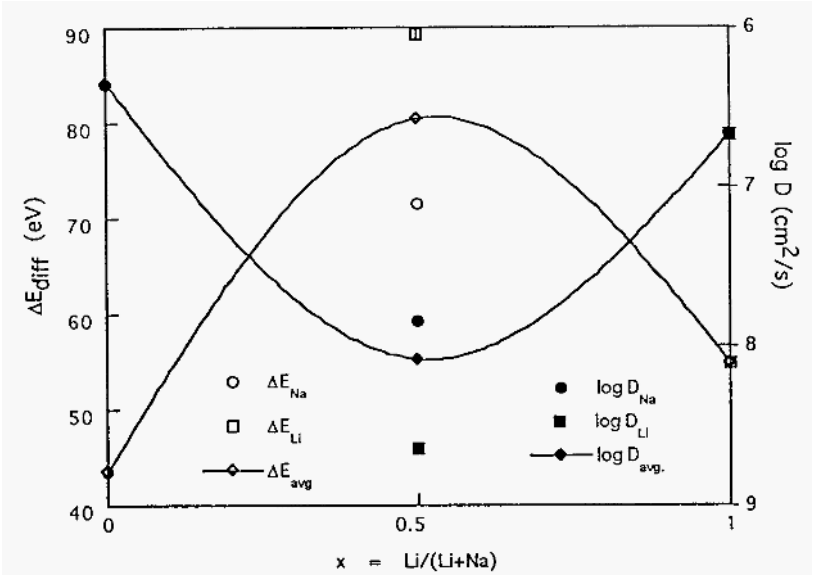

(a)

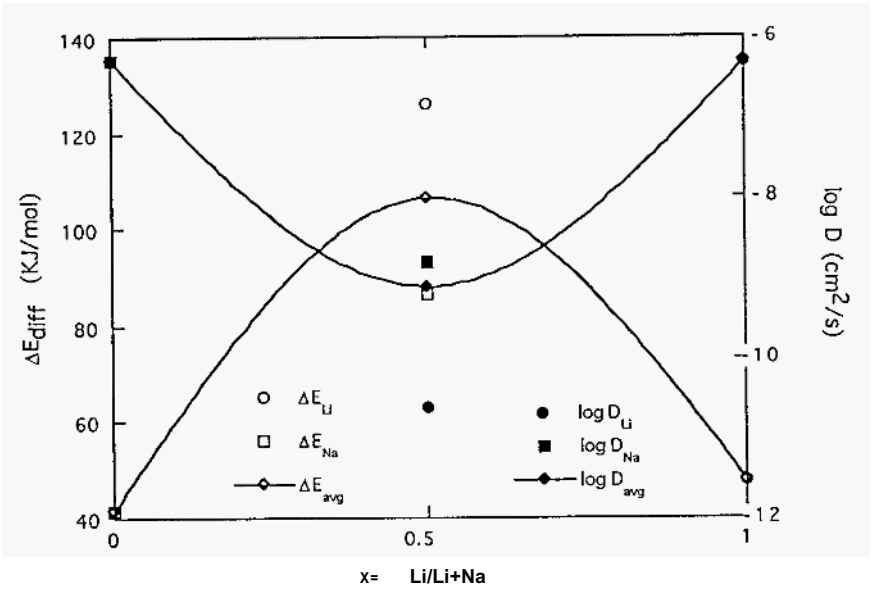

(b)

Figure 13. (a) Diffusion coefficient and activation energy for alkali ions in $x\mathrm{Li_2O}.(1-x)\mathrm{Na_2O}.3\mathrm{SiO_2}$ glasses. (b) Diffusion coefficient and activation energy for alkali ions in $x\mathrm{Li_2O}.(1-x)\mathrm{Na_2O}.\mathrm{Al_2O_3}\mathrm{SiO_2}$ glasses.

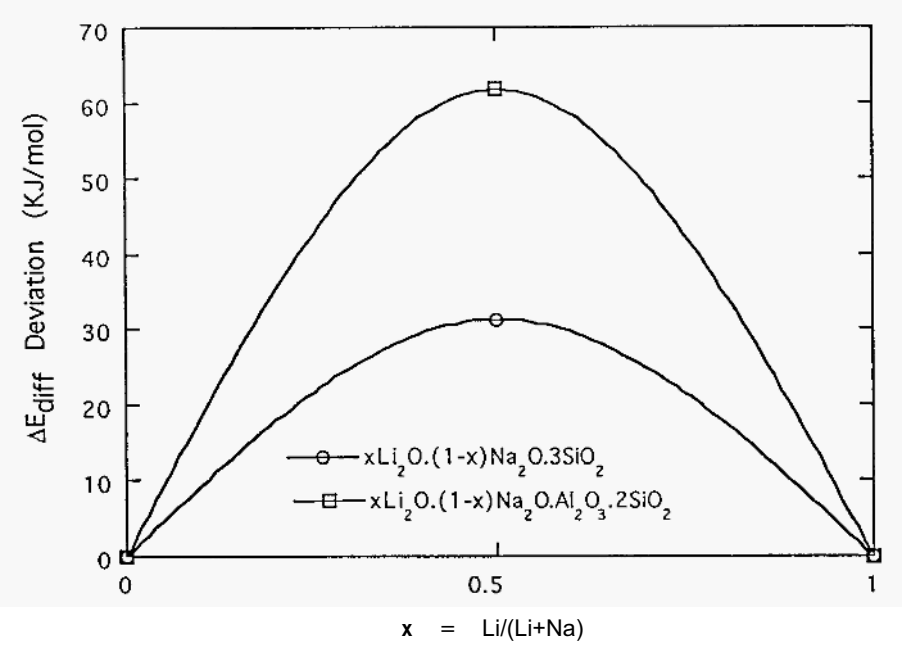

Figure 14. Deviation from additivity of diffusion activation energy in mixed alkali silicate and aluminosilicate glasses.

indicates that those theories based on interactions [78, 80, 81, 82] between dissimilar alkali ions can not be exclusively correct, for these interactions, although they may reasonably exist in nature, are not explicitly included in our calculations. Rather one should look to the glass structure itself for the origins of mixed-alkali effect.

As seen in Fig. 15, in either the mixed-alkali silicate or mixed-alkali alumino-silicate glasses, clearly distinguishable Li-O and Na-O PDF peaks and coordination shells are observed, indicating that Li and Na ions adopt distinctly separate environments in there glasses, in accordance with the defect model proposed by LaCourse[83].

The shortening of the Li-O bonds and the elongation of the Na-O bonds in the mixed-alkali silicate glasses is consistent with the model of Dietze [76], which rationalizes the mixed-alkali effect on the basis of different field strengths of two different ions, although our results do not appear to support this model as a whole. For example, the specific pairing of dissimilar ions is not seen. In fact, the sharpening of the Li-O peak and the broaden-

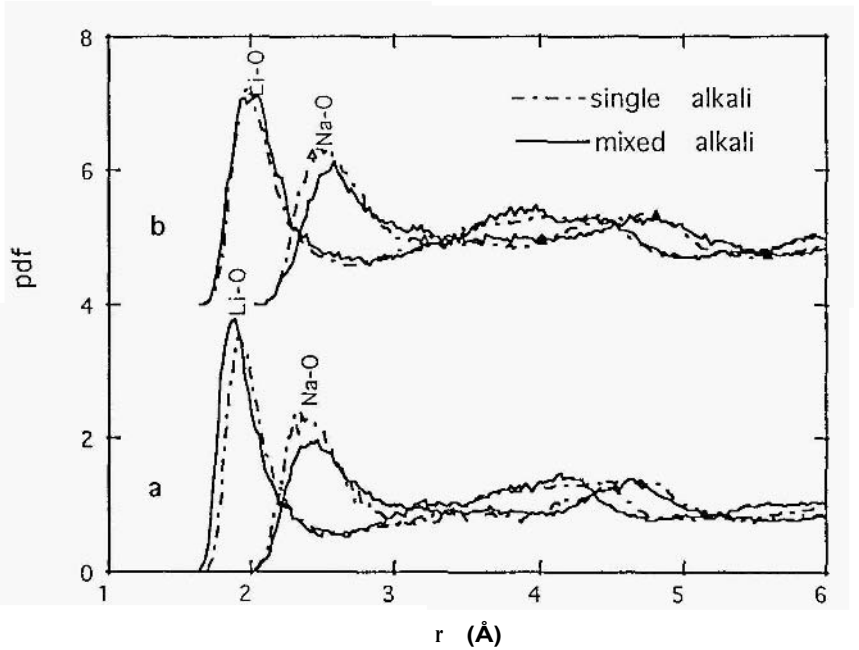

Figure 15. Li-O and Na-O pdfs in (a) single and (b) mixed alkali silicate and aluminosilicate glasses.

ing of the Na-O peak in the mixed-alkali glasses are more likely be a result of network relaxation, influenced by the differing field strengths, and not necessarily the direct interaction of dissimilar alkali ions.

The simulation results suggest the following interpretation. In both alkali silicate and alkali alumino-silicate glasses, alkali ions migrate along (percolated) alkali-rich channels, as postulated by the Modified Random Model. In the mixed-alkali glasses, dissimilar alkali ions share the same channels for their migration. However, because of the different sites adopted by the different alkali ions, ions of one type are more or less prohibited from occupying the sites of the other type, leading to longer effective jump distances and a lower diffusion coefficient. The more rigid the network, the harder it is for the network to accommodate ions of the "wrong" type because relaxation around the ions is more difficult. Obviously the network of the alkali alumino-silicate glasses, in which there is no NBO, is much more rigid than that of the alkali silicate glasses. Therefore, the site preference is stronger, and the mixed-alkali effect is more profound, in the mixed-alkali

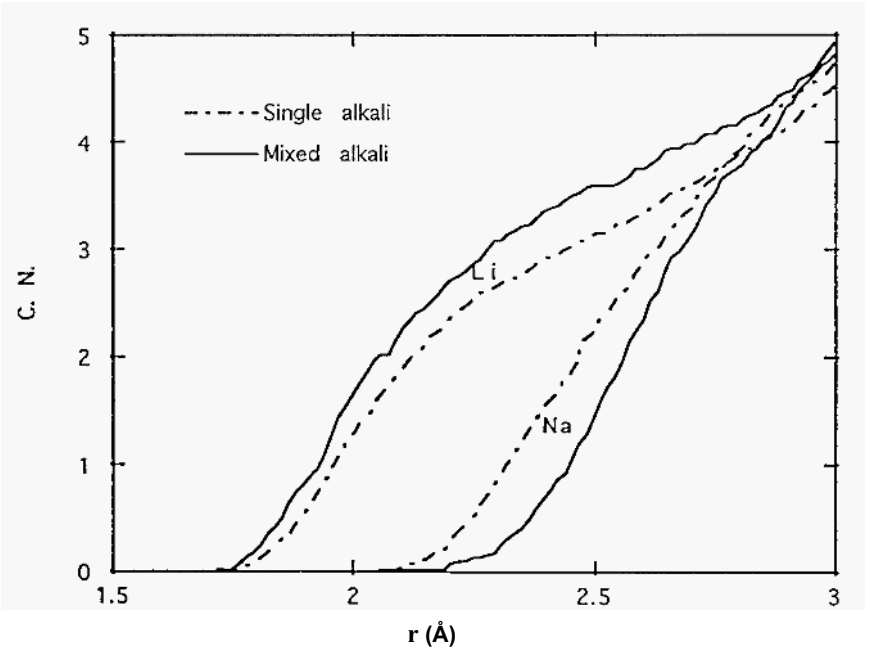

Figure 16. Coordination shell in single and mixed alkali silicate glasses.

alumino-silicate glasses than in the mixed-alkali silicate glasses.

9. Role of Calcium on Structures and Alkali diffusion of Soda Lime Silicate Glasses

Soda lime silicate glasses constitute one of the most important glass systems for commercial applications) mainly owing to their excellent resistance against aqueous and acid corrosion. The addition of calcium to sodium silicate glasses significantly decreases the soda extraction from the glasses by water or acid solutions) thus greatly increasing the chemical durability of the glasses [84]. Although the final stages of the corrosion are driven by surface chemistry occurring at the glass solution interfaces [85], the initial response of glass to water attack is mainly governed by the transport of alkali ions in the bulk. An understanding of the role of Ca on the structure and the diffusion properties of Na in soda lime silicate glasses is thus important.

Terai and Kitaoka [86]systematically investigated the effect of Ca on the

diffusion properties of Na in soda lime glasses. Mazurin and Brailovskaya [87] studied the electrical conductivity of soda lime silicate glasses with differing CaO contents. Both results show a significant impeding effect of Ca on the diffusion properties of Na in these glasses. Gaskell and co-workers [88, 89, 90] investigated the structures of $CaO.SiO_2$ glass by isotopically substituted neutron diffraction techniques and successfully obtained Ca-O and Ca-Ca pair distribution functions. The results lead to a Sterochemically Defined Model, in which the essential structure-forming operations of the crystal are considered to be applicable to glasses, especially at SRO scale. Veal *et al.* [91] studied the effect of Ca in soda lime silicate glasses by x-ray photoelectron spectroscopy. Their results indicated that Ca behaves like Na in converting bridging oxygens (BO) sites to non-bridging oxygens (NBO) sites. Brawer *et al.* [92] investigated the structures of a series of soda lime silicate glasses by Raman spectroscopy and showed that the addition of Ca-O to sodium silicate glasses acts to increase the disorder of the network slightly. Compared with alkali-silicate glasses, the structural studies reported on soda lime silicate glasses are relatively few, probably due to the complexity of the structures of these glasses.

MD simulations on soda lime silicate glasses are scarce. Abramo, Caccamo and Pizzimenti [93] studied the structure of $CaO.SiO_2$ glass by MD simulation and observed results that are favorably comparable with the neutron diffraction results by Gaskell [90]. Rosenthal and Garofalini [94] studied the structural role of Zn on silica and soda-silicate glasses. These studies, however, were restricted to static properties and local structures.

More recently, Cao and Cormack [95] have examined two series of soda lime silicates, and found that replacement of Na by Ca caused the distribution of the Si-O bond lengths to broaden, indicating that $[SiO_4]$ was distorted more by Ca than by Na. In addition, the Si-BO bond-length remained constant in all compositions, but the Si-NBO bond length became longer as Na is replaced by Ca, indicating the the Si-NBO bonding, which is equilibrated by the interactions of Si-O, Na-O, and Ca-O, is more affected by the stronger Ca-O interactions than by the Na-O interactions. This may be also because more NBO are found *to* be coordinated to Ca than Na (see below).

Figs. 17 and 18 show the PDFs of Na-O and Ca-O in $(0.3 - x)Na_2O$ $.xCaO$ $.0.7SiO_2$ glasses. The Ca-O peaks are significantly sharper than Na-O peaks in all the compositions, providing an additional indication that the Ca environment is much more ordered than the Na environment. To obtained more detailed information about the correlation between Ca, Na, and O, the first Ca-O peak and the first Na-O peak were deconvoluted into several sub-peaks. The first sub-peak represents the PDF between Ca/Na and its nearest O. The second sub-peak represents the PDF between Ca/Na

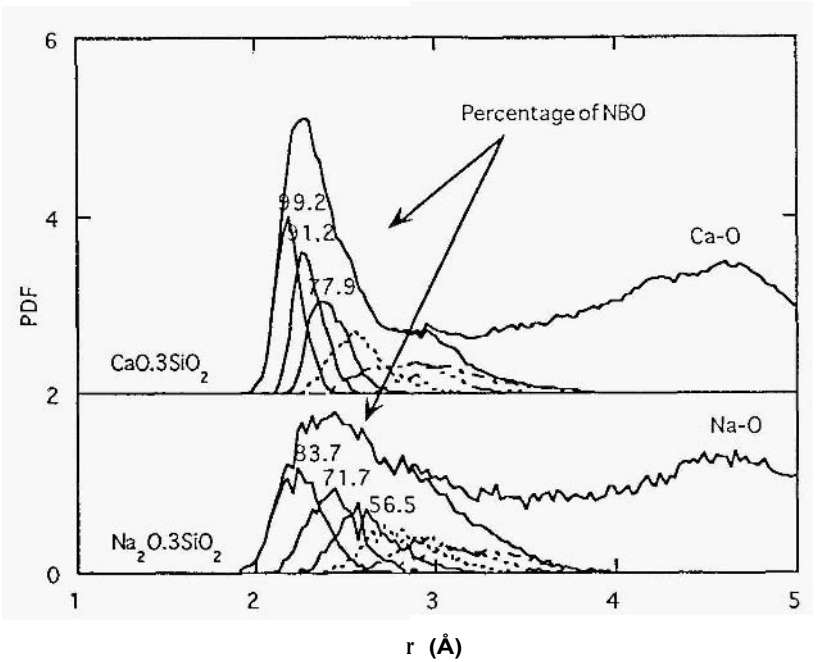

Figure 17. Subpeak deconvolution of Na-O and Ca-O pdf in $Na_2O.3SiO_2$ and $CaO.3SiO_2$ glasses. Numbers indicate % NBO in the first three subpeaks.

and its second nearest O, and so on. For both Na and Ca, the first sub-peak is seen to be always the sharpest and contains the highest percentage of NBO. This is quite reasonable, considering that alkali/alkaline-earth ions tend to be associated with NBO. The first two sub-peaks for Ca are significantly sharper than the other sub-peaks and the NBO percentage of these two-sub-peaks is as high as 95%. Therefore, it may be said that the nearest two oxygens associated with Ca are NBO.

An interesting feature is that, in the all compositions in $(0.3-x)Na_2O$ $.xCaO$ $.0.7SiO_2$ glasses, the percentage of NBO in the sub-peak for Ca is always significantly higher than the percentage of NBO in the corresponding sub-peaks for Na. It is, perhaps, even more interesting to see that in the glass where Ca and Na coexist ($x = 0.15$), the NBO percentage of the first sub-peak of Na is smaller than when only Na is present ($x = 0.0$), indicating that Ca competes more successfully for the coordination of NBO than does Na.

The Ca-Ca pair distribution function of the $0.5CaO$ $.0.5SiO_2$ and $0.3CaO$

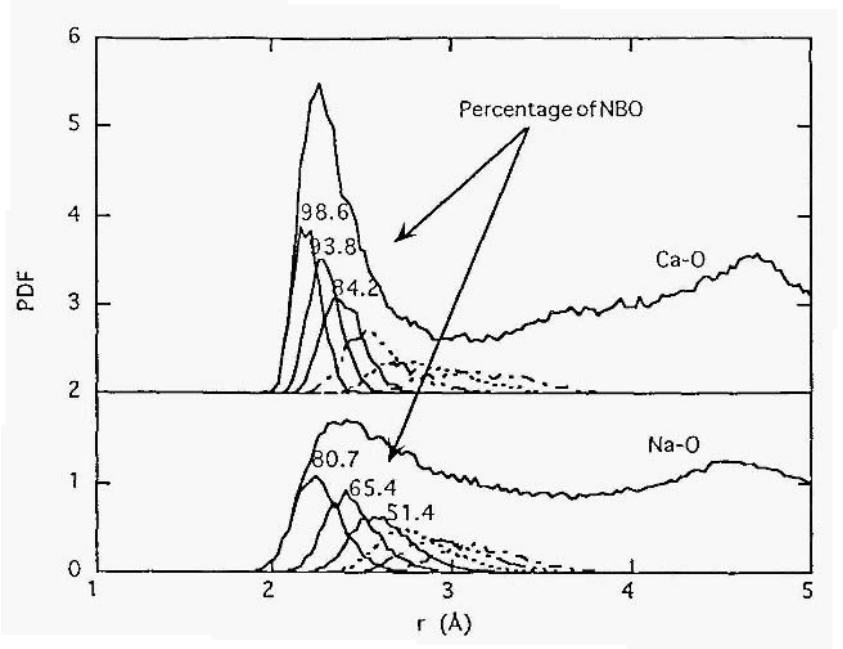

Figure 18. % NBO in subpeaks of Na-O and Ca-O pdfs in mixed Na, Ca silicate glass.

.0.7SiO_2 glasses show two peaks, at around 3.7 Å and at around 6.4 Å, in agreement with Gaskell's diffraction results [88, 89, 90] as well as the simulation results by Abramo *et al.* [93]. According to Gaskell, the similarity of the first Ca-O and Ca-Ca PDF between $0.5CaO.0.5SiO_2$ glasses and $0.5CaO.0.5SiO_2$ wollastonite is an indication that the local structures of Ca in the glasses is similar to those in wollastonite, which is composed of the trioctahedral strips of edge-sharing [CaO_6] octahedra. He, therefore, argued that in the medium-range structure of glasses, there must exist layered [CaO_6] octahedra. However, visual inspection of the simulated structure suggests that it is too distorted to be described as layered octahedra, although it is much more ordered, compared with the environment of Na. Cao and Cormack also observed that Ca ions are clustered in the large voids of Si-0 networks in the glasses, consistent with the observation reported by Abramo *et al.* [93]. Therefore, they proposed that Ca may be defined as a network binder, distinguishing it from either the network modifiers, such as Na, or the network former or intermediate, such as Si and Al.

Additional insight into the structure is found in the ring size distri-

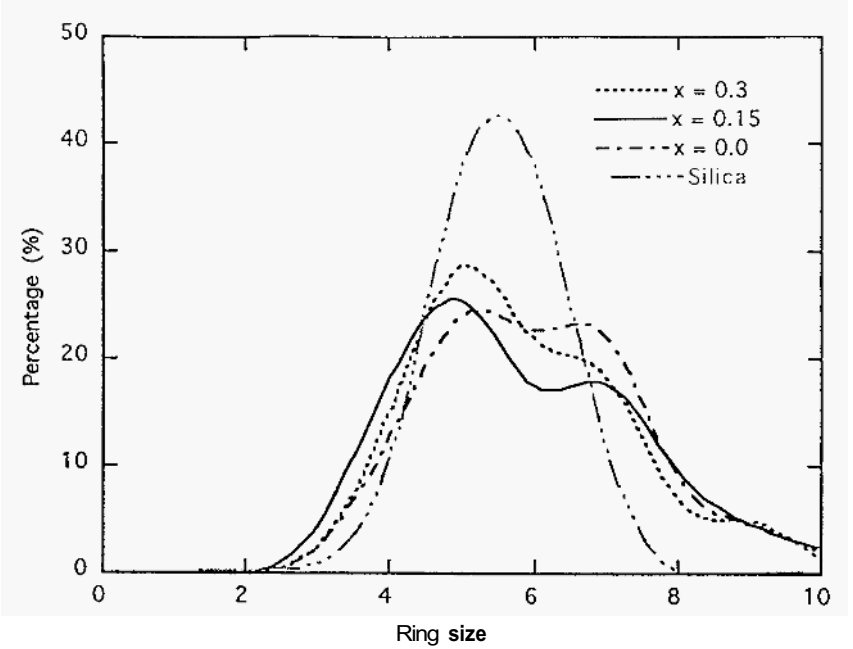

Figure 19. Ring size distribution in $(0.3-x)Na_2O.xCaO.0.7SiO_2$ glasses.

bution for $(1-x)Na_2O.xCaO.3SiO_2$ glasses shown in Fig. 19. Compared with the ring-size distribution of vitreous silica (which is obtained from the simulation results of our earlier work), bi-modal distributions are clearly observed in the ring-size distribution of soda lime silicate glasses, indicating that the introduction of Na or Ca to vitreous silica creates large rings in certain regions rather than expanding the ring size of the whole network homogeneously. In the other words, Na and Ca ions are segregated into particular regions rather than being randomly distributed. The mid-range structure of soda lime silicate glasses is thus heterogeneous.

9.1. EFFECT OF CA ON NA DIFFUSION

Fig. 20 shows the diffusion activation energy of Na ions in the two series of glasses, $0.2Na_2O.xCaO.(0.8-x)SiO_2$ (x= 0.0,0.1,0.2) and $(0.3-x)Na_2O.xCaO.0.77SiO_2$ (x= 0.0,0.075,0.15,0.225,0.3). It is seen that the diffusion activation energy of Na increases significantly as either Na or Si is replaced by Ca, consistent with the experimental results [86, 87]. There-

fore, the impeding effect of Ca on Na diffusion in soda lime silicate glasses is successfully reproduced by MD simulations. In addition, the increase of Na. diffusion activation energy is found to be significantly greater in $(0.3-x)Na_2O.xCaO.0.77SiO_2$ glasses than in $0.2Na_2O.xCaO.(0.8-x)SiO_2$ glasses, also consistent with experimental results [86, 87].

Several explanations for the effect of Ca on Na diffusion in soda lime silicate glasses have been put forward. Mazurin *et al.* [87] suggested that the replacement of Si by Ca produces weakly polarized oxygen ions, which interact more strongly with the neighboring Na ions and bind them more strongly in their equilibrium positions. Matusita, *et al.* [96] and LaCourse and Cormack [73] have suggested that the impeding effect of Ca on Na diffusion, like the mixed-alkali effect, is a general phenomenon in glass science, resulting from the ability of ions of different size, mass, and polarizability to generate and occupy sites of different local environments. An alternative approach is available, through the analysis of the mid-range structure and the dynamic properties of Na diffusion.

There are two main types of pathway for alkali diffusion in glasses : one through voids created during the glass formation, another through voids left by the other alkali ions which have diffused away during the diffusion process. Haven and Verkerk [97] observed that, in typical sodium silicate and soda lime silicate glasses, the Haven ratio lies in the range of 0.44-0.55, and argued that this was an indication that the above two mechanisms are the most promising for sodium diffusion in those glasses. This concept was later supported by Ingrain [98] and applied by Moynihan and Lesikar [99] to interpret the mixed-alkali effect. Undoubtedly, to understand the impeding effect of Ca on Na diffusion, it is important to know how Ca affects the free volume in the glasses and whether the Na sites are more or less accessible, given the presence of Ca in the glass. The information may be obtained by investigating the free-volume distribution and the distinct time-space correlation function of the Na ions.

Fig. 21 shows the free-volume distribution for $0.2Na_2O.xCaO.(0.8-x)SiO_2$ glasses (x= 0.0,0.1,0.2). Since the effective ionic radius for Na is 0.99 Å[30], only those voids that are larger than 0.99 A in radius can be effectively used by Na ions for diffusion. Considering that certain voids will shrink and expand during the thermal relaxation of the glass network, a lower limit to the void radius may be set at 0.8 Å, so that those voids smaller that this need not be considered. It was found that, as the Ca content in glass increases, although the number density of oxygen decreases thus leaving more total free volume in the glass, the number of effective voids decreases significantly (at x = 0.0,0.1, 0.2, the number density of oxygen is calculated to be 4.267 x 10-2/Å3,4.234 x 10-2/Å3,and 4.176 x 10-2/Å3 respectively. This results from the larger volume of [CaO_x] polyhedra com-

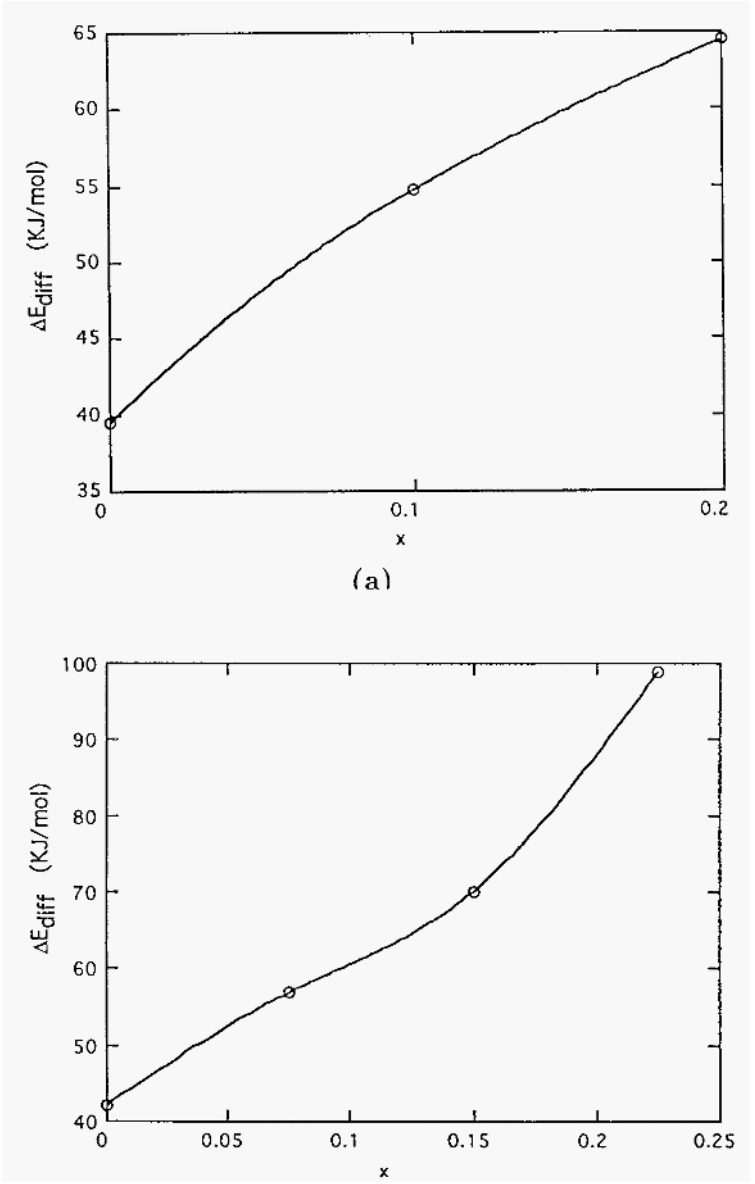

Figure 20. (a) Diffusion activation energy for Na in $0.2Na_2O.xCaO.(0.8-x)SiO_2$ glasses. (b) Diffusion activation energy for Na in $(0.3-x)Na_2O.xCaO.0.7SiO_2$ glasses.

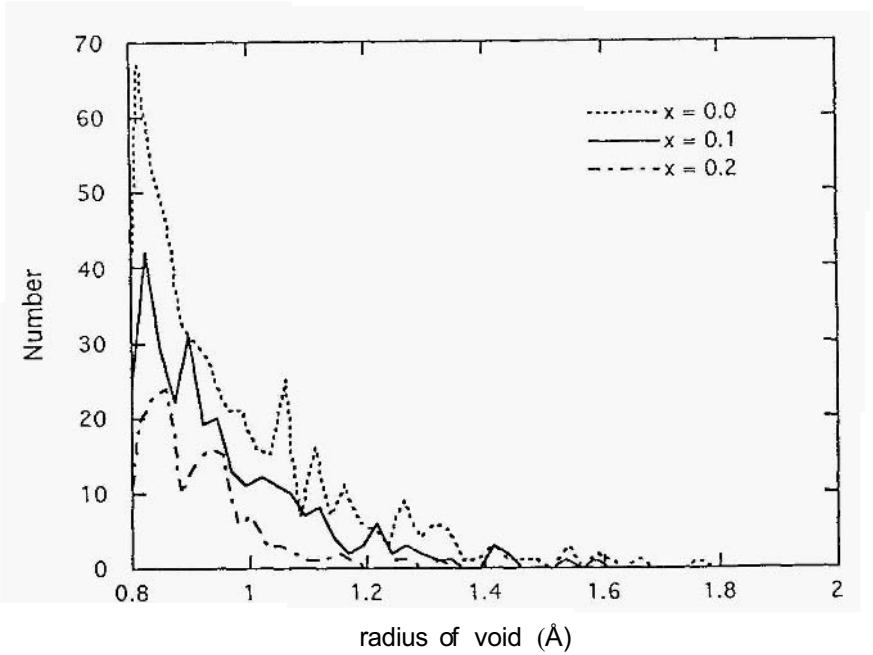

Figure 21. Free volume distribution in $0.2Na_2O.xCaO.(0.8-x)SiO^2$ glass.

pared with the volume of[SiO_4] tetrahedra in glasses. As discussed in the last section, the average Ca-O distance is about 2.4, significantly longer than the Si-O distance, which is about 1.6 Å. Meanwhile, the average coordination number of Ca is significantly larger than Si. Therefore, each [CaO_x] polyhedron occupies much more space than does an [SiO_4] tetrahedron. As a result, there actually are fewer effective voids left for Na ions as the content of Ca increases in glasses, thus reducing Na diffusion.

Fig. 22 shows the distinct time-space correlation function $g_{NaNa}(r, t)$ at $t = 5000$ timesteps. The peak strength is seen to decrease significantly as Si is replaced by Ca in the glasses, indicating that fewer Na sites are occupied by other Na ions as the Ca content increases in the glass. A similar phenomenon was seen in a study of the mixed-alkali effect. This phenomenon may be rationalised on the basis of the modified random network modem [4] : in both sodium silicate and soda lime silicate glasses, Na, Ca and NBO are clustered together to form channels (as in the mixed-alkali glasses). However, in soda lime silicate glasses, since the diffusion coefficient of Ca is much lower than Na, Ca actually "blocks" the pathways for Na diffusion

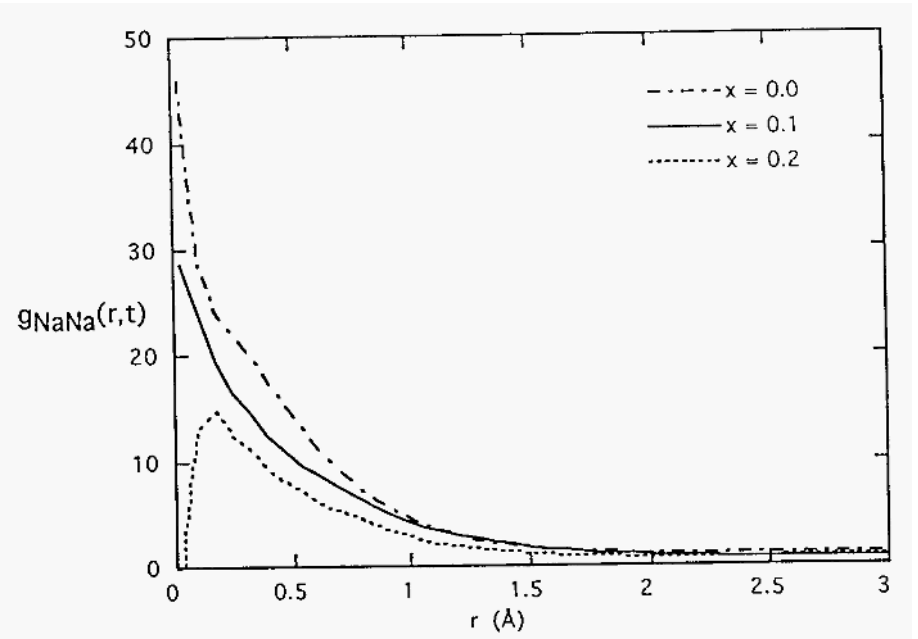

Figure 22. Distinct space-time correlation function for $0.2Na_2O.xCaO.(0.8-x)SiO_2$ glass.

in the channel. Therefore, while the Na-NBO channels become bigger with Si being replaced by Ca, the mean-distance between Na and Na becomes longer. In other words, the introduction of Ca diversifies the Na-NBO channel, thus making it more difficult for Na ions to access the site of other Na ions. The Na diffusion is thus effectively impeded.

The similarity of the time-space correlation functions for Na-Na pairs in the mixed-alkali glasses and in soda lime silicate indicates that the alkali diffusion behaviors in these glasses might have some common origins. Indeed, the blocking effect of alkali or alkali-earth ions on the diffusion of dissimilar alkali ions is obvious in both cases. In fact, the immobile Ca ions are able to block the pathway of Na diffusion more effectively than mobile alkali ions do. Therefore, it is reasonable to consider that the mechanism leading to the impeding effect of Ca on Na diffusion is the same as one leading to the mixed-alkali effect, as LaCourse and Cormack suggested [73].

10. Summary

Although the structure of glasses is not really accessible by experimental methods, molecular dynamics is a very useful alternative, as we have tried to demonstrate in this chapter. The simulations reproduce the broad macroscopic features found in these glasses, both structural and transport-related, providing a basis for the more detailed atomic scale features found in the simulated structures. An understanding of important aspects of alkali ion transport, such as the mixed alkali effect and anomalous behaviour in some alumino-silicates, can thus be approached from the atomistic pictures of the glasses produced by the simulations. Although there is room for improvements to the potential models available, it should be clear that the further application of computer simulation methods, such as molecular dynamics, promises to provide much needed advances in glass science and engineering.

References

1. Zachariasen, W.H. (1932) The Atomic Arrangement in Glasses, *J. Amer. Chem. Soc.,* **54,** 3841-3851.
2. Wright, A. C. (1993) Neutron and X-ray Amorphography, in: C. Simmons et al. (eds.), *Experimental Techniques in Glass Science,* pp. 205-314. Amer. Ceram. Soc., Westerville, OH.
3. Wright, A. C., Clare, A. G., Bachra, B., Sinclare, R. N., Hannon, A. C., Vessal, B. (1991) Neutron Diffraction Studies of Silicate Glasses, *Trans. Am. Crystallogr. Assoc.,* **27,** 239-254.
4. Greaves, G. N. (1989) EXAFS, Glass Structure and Diffusion, *Philos. Mag.,* **B 60,** 793-800.
5. Catlow, C.R.A. and Mackrodt, W.C. (1982) Computer Simulation of Solids, *Lecture Notes in Physics,* **166,** Springer-Verlag, Berlin
6. Catlow, C.R.A. and Cormack, A.N. (1987) Computer Modelling of Silicates, *Int. Rev. Phys. Chem.,* **6,** 227-250.
7. Woodcock, L.V., Angell, C.A. and Cheesman, P. (1976) Molecular Dynamics Studies of The Vitreous State: Simple Ionic Systems and Silica, *J. Chem. Phys.***65**, 1565-1577.
8. Soules, T.F. (1979) A Molecular Dynamics Calculation of The Structure of Sodium Silicate Glasses, *J. Chem.* Phys.,**71,**4570-4578.
9. Sanders, M.J., Leslie, M. and Catlow, C.R.A. (1984) Interatomic Potentials for SiO_2, *J.Chem.* Soc., *Chem. Comm*.1271-1273.
10. Vessal, B., Leslie, M., and Catlow, C. R. A. (1988) Effect of Pressure on the Structure of Simulated Silica Glass, *Info. Quart. MD and MC Simu.,* **28,** 39-43.
11. Vessal, B., Amini, M., Fincham, D. and Catlow, C. R. A. (1989) Water-like Melting Behavior of SiO_2 Investigated by the Molecular Dynamics Simulation Techniques, *Philos. Mag.,* **B 60,** 753-75.
12. Kendrick, J., and Mackrodt, W.C. (1983) Interatomic Potentials for Ionic Materials from First Principles Calculations, *Solid State Ionics,* **8**, 247-253.
13. Lewis, G.V. and Catlow, C.R.A. (1985) Potential Models for Ionic Oxides, *J. Phys. C: Solid State Phys.,* **18,** 1149-1161.
14. Huang, C. (1990) Characterization of the Structure and Transport Properties of Alkali Silicate Glasses by Computer Simulation, *PhD Thesis,* Alfred University.

15. Huang, C. and Cormack A. N. (1991) Computer Simulation Studies of the Structure and Transport Properties of Alkali Silicate Glasses, in L. D. Pye, W. C. LaCourse and H. J. Stevens (eds.), *Physics of Non-crystalline Solids,* Taylor & Francis, pp. 31-35.
16. Farnan, I., Grandinetti, P.J., Baltisberger, J.H., Stebbins, J.F., Werner, U. Eastman, M.A. and Pines, A. (1992) Quantification of the Disorder in Network-Modified Silicate-Glasses, *Nature,* **358,** 31-35.
17. Cao, Y., Cormack, A. N., Clare, A. G., Bachra, B., Wright, A. C., Sinclair, R. N., and Hannon, A. C. (1995) Points of Contact between Theory and Experiment: A Comparison of Molecular Dynamics And Neutron Diffraction, *J. Non-Cryst. Solid.,* **177,** 317-323.
18. Vessal, B., Greaves, G. N., and Marten, P. T. (1991) Computer simulation Study of the Mixed Alkali Silicate Glasses $Na_xRb_{1-x}SiO_{2.5}$, *Trans. Am. Crystallogr. Assoc.,* **27,** 323-329.
19. Melman, H. and Garofalini, S. H. (1991) Microstructural Evolution of Simulated Sodium Silicate Glasses, *J. Non-Cryst. Solid.,* **134,** 107-115.
20. Dupree, R., Holland, D., MacMillan, P. W. and Pettifer, R. F. (1984) The Structure of Soda-Silica Glasses: A MAS-NMR Study, *J. Non-Cryst. Solid.,* **68,** 399-410.
21. Gurman, S. J. (1990) Bond Ordering in Silicate Glasses: A Critique and A Resolution, *J. Non-Cryst. Solid.,* **125,** 151-160.
22. Dupree, R., Holland, D., and Williams, D. S. (1986) The Structure of Binary Alkali Silicate Glasses, *J. Non-Cryst. Solid.,* **81,** 185-200.
23. Grimmer, A. R., Magi, M., Hahnert, M., Stade, H., Samoson, A., Eieker, W. and Lippmaa, E. (1984) High-resolution Solid State ^{29}Si Nuclear Magnetic Resonance Spectroscopic Studies of Binary Alkali Silicate Glasses, *Phys. Chem. Glasses,* **25,** 105-112.
24. Stebbins, J. F. (1988) Effect of Temperature and Composition on Silicate Glass Structure and Dynamics: Si-29 NMR Results, *J. Non-Cryst. Solids,* **106,** 359-369.
25. Hater, W., Muller-Warmuth, W. Meiler, M. and Frischat, G. H. (1989) High Resolution Solid State NMR Studies of Mixed-alkali Silicate Glasses, *J. Non-Cryst. Solids,* **113,** 210-212.
26. Buckerman, W. Muller-Warmuth, W. and Frischat, G. (1992) A Further ^{29}Si MAS NMR Study on Binary Alkali Silicate Glasses, *Glasstech. Ber.,* **65,** 18-21.
27. Emerson, J. F., Stallworth, P. E. and Bray, P. J. (1989) High Field ^{29}Si NMR Studies of Alkali Silicate Glasses, *J. Non-Cryst. Solids,* **113,** 253-259.
28. Matson, D. W., Sharma, S. K. and Philpotts J. A. (1983) The Structure of High Alkali Silicate Glasses: A Raman Spectroscopic Study, *J. Non-Cryst. Solid.,* **58,** 323-352.
29. Shelby, J. E. (1993) Gas Diffusion Measurement in Glasses, in Experimental Techniques in Simmons, C. J. et al. (eds.), *Glass Science,* Amer. Ceram. Soc., Westerville, OH, pp 363-382.
30. Shannon, R. D. and Prewitt, C. T. (1969) Effective Ionic Radii in Oxides and Fluorides, *Acta. Crystallogr.,* **B 25,** 925-946.
31. Mitra, S. K. and Hockney, R. W. (1980) Distribution of Holes in Simulated Silicon Dioxide Glass, *J. Phys. C: Solid. St. Phys.,* **13,** L739-L741.
32. Huang, C. and Cormack A. N. (1991) Structural Difference and Phase Separation on Alkali Silicate Glasses, *J. Chem. Phys.,* **95,** 3634-3642.
33. Huang, C. and Cormack A. N. (1990) The Structure of Sodium Silicate Glass, *J. Chem. Phys.,* **93,** 8180-8186.
34. Huang, C. and Cormack A. N. (1992) Structure and Energetics in Mixed-Alkali-Metal Silicate Glasses from Molecular Dynamics, *J. Mater. Chem.,* **2,** 281-287.
35. Vessal, B., Greaves, G. N., Martin, P. T., Chadwick, A. V., Mole, R. and Houde-Walter, S. (1992) Cation Microsegregation and Ionic Mobility in Mixed Alkali Glasses, *Nature,* **356,** 504-506.
36. Melmam, H. and Garofalini, S. H. (1991) Microstructural Evolution of Simulated

Sodium Silicate Glasses, *J. Non-Cryst. Solids,* **134,** 107-115.
37. Greaves, G. N., Fontaine, A., Lagarde, P., Raoux, D. and Gurman, S. J. (1981) Local Structure of Silicate Glasses, *Nature,* **293,** 611-616.
38. Haller, W., Blackburn,D. H. and Simmons, J. H. (1974) Miscibility Gaps in Alkali Silicate Binaries – Detailed Thermodynamic Interpretation, *J. Am. Ceram. Soc.,* **57,** 120-126.
39. Uhlmann, D. R. and Kolbeck, A. G. (1976) Phase Separation and the Revolution in Concept of Glass Structures, *Phys. Chem. Glasses,* **17,** 146-158.
40. Cao, Y. and Cormack, A.N. (1995) Structure and Alkali Migration Behavior in Lithium Silicate Glasses, *J. Non-Crys. Solids.* (submitted)
41. Hunold, V. K. and Bruckner, R. (1980) Physikalische Eigenschaften und Struktureller Feinbau von Natrium Alumosilicatglasern und Schmelzen, *Glastech. Ber.,* **53,** 149-161.
42. Yoldas, B. E. (1971) The Nature of the Coexistence of Four- and Six-co-ordinated Al^{3+} in Glass, *Phys. Chem. Glasses,* **12,** 28-32.
43. Day, D. E. and Rindone, G. E. (1962) Properties of Soda Aluminosilicate Glasses: I. Refractive Index, Density, Molar Refractivity, and Infrared Absorption Spectra, *J. Am. Cer. Soc.,* **45,** 489-496.
44. Day, D. E. and Rindone, G. E. (1962) Properties of Soda Aluminosilicate Glasses: III. Coordination of Aluminum Ions, *J. Am. Ceram. Soc.,* **45,** 579-581.
45. Day, D. E. and Rindone, G. E. (1962) Properties of Soda Aluminosilicate Glasses: II. Internal Friction, *J. Am. Ceram. Soc.,* **45,** 496-497.
46. Hanada, T., Aikawa, T., and Soga, N. (1982) Coordination of Aluminum in Amorphous Sodium Aluminosilicate Films, *J. Non-Cryst. Solids,* **50,** 397-405.
47. Lacy, L. D. (1963) Aluminum in Glasses and in Melts, *Phys. Chem. Glasses,* **4,** 234-238.
48. McKeown, D. A., Waychunas, G. A., and Brown, G. E. (1985) EXAFS and XANES Study of the Local Coordination Environment of Sodium in A Series of Silica Rich Glasses and Selected Minerals within the Na_2O-Al_2O_3-SiO_2 System, *J. Non-Cryst. Solids,* **74,**325-48.
49. McKeown, D. A., Waychunas, G. A., and Brown, G. E. (1985) EXAFS Study of the Coordination Environment of Aluminum in a Series of Silica Rich Glasses and Selected Minerals within the Na_2O-Al_2O_3-SiO_2 System, *J. Non-Cryst. Solids,* **74,** 349-3xx.
50. McKeown, D. A., Galeener, F. L., and Brown Jr., G. E. (1984) Raman Studies of Al Coordination in Silica-rich Sodium Alumino-silicate Glasses and Some Related Minerals, *J. Non-Cryst. Solids,* **68,** 361-378.
51. McKeown, D. A. (1987) Radial Distribution Analysis of a Series of Silica-rich Sodium Alumino-silicate Glasses Using Energy Dispersive X-ray Diffraction, *Phys. Chem. Glasses,* **28,** 156-163.
52. Loweinstein, W. (1954) The Distribution of Aluminum in the Tetrahedra of Silicates and Aluminates, *Am. Mineral.,* **39,** 92-96.
53. De Jong, B. H. W. S. and Brown Jr., G. E. (1980) Polymerization of Silicate and Aluminate Tetrahedra in Glasses, Melts, and Aqueous Solution – I. Electronic Structure of $H_6Si_2O_7$, $H_6AlSiO_7^-$, and $H_6Al_2O_7^{2-}$, *Geochim. Cosmochim. Acta,* **44,** 491-510.
54. De Jong, B. H. W. S., Schramm, C. S., and Paraxial, V. E. (1983) Polymerization of Silicate and Aluminate Tetrahedra in Glasses, Melts, and Aqueous Solutions IV. Aluminum Coordination in Glasses and Aqueous Solutions and Comments on the Aluminum Avoidance Rule, *Geochim. Cosmochim. Acta,* **47,** 1223-1236.
55. Klinowski, J., Thomas, J. M., Fyfe, C. A. and Parzaile, V. E. (1981) Application of Magic Angle Spinning Silicon-29 Nuclear Magnetic Resonance. Evidence for Two Different Kinds of Silicon-Aluminum Ordering in Zeolite Structures, *J. Phys. Chem.,* **85,** 2590-2594.
56. Navrotsky, A., Persudeau, G., McMillan, P. and Courtures, J. P. (1982) A Thermodynamic Study of Glasses and Crystals Along the Joins Silica-Calcium Aluminate

and Silica-Sodium Aluminate, *Geochim. Cosmochim. Acta,* **46,** 2039-2047.
57. Zirl, D. M. and Garofalini, S. H. (1990) Structure of Sodium Aluminosilicate Glasses, *J. Am. Ceram. Soc.,* **73,** 2848-2856.
58. Cao, Y. and Cormack, A. N. (1994) Structural Interpretation on the Anomalous Property Changes in Sodium Alumino-silicate Glasses at Al/Na = 0.2 - 0.4, in: Diffusion, in Jain, H. et al. (eds.) *Amorphous Materials,* TMS, pp. 137-150.
59. Mazurin, O.V., Roskova, G. P., and Porai-Koshits, E. A. (1984) Immiscibility Diagrams of Oxide Glass-forming Systems, in Mazurin. O.V. et al. *Phase Separation in Glasses,* North-Holland, (eds.) pp. 103-142
60. Terai, R. (1969) Self-diffusion of Sodium Ions and Electrical Conductivity in Sodium Aluminosilicate Glasses, *Phys. Chem. Glass.,* **10,** 146-152.
61. Anderson, O.L. and Stuart, D. A. (1954) Calculation of Ionic Conductivity in Silica Glasses by Classical Methods, *J. Am. Ceram. Soc.,* **37,** 573-580.
62. Isard, J. O. (1959) Electrical Conductivity in Aluminosilicate Glasses, *J. Soc. Glass Technol.,* **43,** 113T-123T.
63. Tsekhosmski, V. A., Mazurin, O. V., and Evstrop'ev, K. K. (1963) Nature of the Conductivity of Alumino-silicate Glasses, *Sou. Phys. - Solid State,* **5,** 426-428.
64. LaCourse, W. C. (1976) Structural Influences on Diffusion in Glass - The Mixed Site Effect, *J. Non-Cryst. Solids,* **21,** 431-434.
65. Hunold, V. K., and Bruckner, R. (1980) Physical Properties and Structural Details of Sodium Aluminosilicate Glasses and Melts, *Glastech. Ber.,* **53,** 149-161.
66. Shelby, J. E. (1978) Viscosity and Thermal Expansion of Lithium Aluminosilicate, *Glasses, J Appl. Phys.,* **49,** 5885-5891.
67. Molot, V. (1993) The Effect of Composition on the Mechanical Properties of Aluminosilicate, Borosilicate, and Gallosilicate Glasses, *M.S. Thesis,* Alfred University.
68. Hsieh, C. H., Jain, H., Miller, A. C., and Kamitsos, E. I. (1994) X-ray Photoelectron Spectroscopy of Al- and B-substituted Sodium Tri-silicate Glasses, *J. Non-Cryst. Solid.,* **168,** 247-253.
69. Petrov, V. I., Bobovich, Y. S., Zhilin, A. A., Tsenter, N. Y., and Chuvaeva, T. I. (1990) Low Frequency Raman Study of the Submicroinhomogeneous Structure of Lithium Aluminosilicate Glasses, *Opt. Spectrosc.,* **68,** 216-218.
70. Seifert, F., Mysen, B. O., and Virgo, D.(1982) Three-dimensional Network Structure of Quenched Melts (Glass) in the Systems SiO_2-$NaAlO_2$, SiO_2-$CaAlO_4$, and SiO_2-$MgAl_2O_4$, *Am. Mineral.,* **67,** 696-717.
71. Isard, J. 0.(1969) The Mixed Alkali Effect in Glass, *J. Non-Cryst. Solids,* **1,** 235-261.
72. Day, D. E. (1976) Mixed Alkali Glasses - Their Properties and Uses, *J. Non-Cryst. Solids,* **21,** 343-372.
73. LaCourse, W. C. and Cormack, A. N. (1991) Structural Influences on the Mixed Alkali Effect in Glasses, *Tran. Am. Crystallogr. Assoc.,* **27,** 211-224.
74. Terai, R. (1971) The Mixed Alkali Effect in the Na_2O-Cs_2O-SiO_2 Glasses, *J. Non-Cryst. Solids,* **6,** 121-135.
75. Mazurin, O.V. (1965) Glass in A Direct Electrical Field, *Structure of Glass,* **4,** 5.
76. Dietzel, A. H. (1983) On the So-called Mixed Alkali Effect, *Phys. Chem. Glasses,* **24,** 172-180.
77. Lapp, J. S. and Shelby, J. E. (1987) The Mixed Alkali Effect in Lithium Aluminosilicate Glasses, *J. Non-Cryst. Solids,* **95-96,** 889-896.
78. Cao, Yand Cormack, A.N. (1995) Insights into the structure and transport properties of glasses from atomistic computer simulation, in:*Proc. XVI International Congress on Glass Meeting,* Beijing China, Oct. 1995.
79. Hendricksen, J. R. and Bray. P. J. (1972) A Theory for Mixed Alkali Effect in Glasses: Part I, *Phys. Chem. Glasses,* **13,** 43-49.
80. McVay, G. L. and Day, D. E. (1970) Diffusion And Internal Friction in Na-Rb Silicate Glasses, *J. Am. Ceram. Soc.,* **53,** 508-513.
81. Fleming, J. W., and Day, D. E. (1972) Relaxation of Alkali Mobility and Mechanical

Relaxation in Mixed-Alkali Silicate Glasses, *J.* Am. *Ceram. Soc.,* **55,** 186-192.
82. Hendricksen, J. R. and Bray. P. J. (1972) A Theory for Mixed Alkali Effect in Glasses: Part II, *Phys. Chem. Glasses,* **13,** 107-115.
83. Lacourse, W. (1987) A Defect Model for The Mixed-alkali Effect, *J. Non-Cryst. Solids,* **95-96,** 905-912.
84. Paul, A. (1977) Chemical Durability of Glasses: A Thermodynamic Approach, *J. Mater. Sci.,* **12,** 2246-2268.
85. Hench, L. L. (1975) Characterization of Glass Corrosion and Durability, *J. Non-Cryst. Solids 19,* 27-39.
86. Terai, R. and Kitaoka, T. (1968) The Effect of Various Divalent Ions on the Migration of Sodium Ions in the Silicate Glasses, *J. Ceram. Assoc. Jpn.,* **76,** 393-399.
87. Mazurin, **O.** V. and Brailovskaya, R. V. (1960) The Electrical Conductivity of Glasses of the $Na_2O.RO.SiO_2$ System, *Sov. Phys. - Solid State,* **2,** 1341-1345.
88. Gaskell, P. H. (1991) The Structure of Silicate Glasses – New Results from Neutron Scattering Studies, in L. D. Pye, W. C. LaCourse, and H. J. Stevens (eds), *Physics of Non-crystalline Solids,* Taylor and Francis pp. 15-21.
89. Gaskell, P. H. (1991) The Structure of Silicate Glasses and Crystals – Towards a Convergence of Views, *Trans Am. Crystallogr. Assoc.,* **27,** 95-112.
90. Gaskell, P. H., Eckersley, M. C., Barnes, A. C., and Chieux, P. (1991) Medium Range Order in the Cation Distribution of a Cation Silicate Glass, *Nature,* **350,** 675-677.
91. Veal, B.W., Lam, D.J., Pauliken, A.P. and Ching, W.Y. (1982) XPS Study of CaO in Sodium Silicate Glasses, *J. Non-Cryst. Solids,* **49,** 309-320.
92. Brawer, S.A. and White, W.B. (1977) Raman Spectroscopy Investigation of The Structure of Silicate Glasses (11). Soda-Alkaline Earth-Alumina Ternary and Quaternary Glasses, *J. Non-Cryst. Solids,* **23,** 261-278.
93. Abramo, M. C., Caccamo, C., and Pizzimenti, G., (1992) Structural Properties and Medium-range Orders in Calcium Metasilicate (CaSiO3) Glass: A Molecular Dynamics Study, *J. Chem. Phys.,* **96,** 9083-9091.
94. Rosenthal, A. B. and Garofalini S. H. (1987) Structural Role of Zinc Oxide in Silica and Soda-Silica Glasses, *J. Am. Ceram. Soc.,* **70,** 821-826.
95. Cao,Y. and Cormack, A.N. (1995) Computer Sirnulation Of Structure And Transport Properties In Silicate Glasses in: *Proceedings of the 3rd European Society of Glass Technology Meeting,* Wurzburg, Germany, May 1995
96. Matusita, K., Takayama, S., and Sakka, S. (1980) Electrical Conductivities of Mixed-Cation Glasses, *J. Non-Cryst. Solids,* **40,** 149-158.
97. Haven, Y. and Verkerk, B. (1965) Diffusion and Electrical Conductivity of Sodium Ions in Sodium Silicate Glass, *Phys. Chem. Glasses,* **6,** 38-45.
98. Ingram, M. D. (1980) Conduction and Dielectric Loss Mechanisms in beta-Alumina and Glass: A Discussion Based on the Paired Interstitialcy Model, *J. Am. Ceram. Soc.,* **63,** 248-263.
99. Moynihan, C. T. and Lesikar, A. V. (1981) Weak Electrolyte Models for the Mixed Alkali Effect of Glass, *J. Am. Ceram. Soc.,* **64,** 40-61.

This page intentionally left blank.

APPLICATION OF THE PARTIAL CHARGE MODEL TO THE AQUEOUS CHEMISTRY OF SILICA AND SILICATES

MARC HENRY
Institut Le Bel, Laboratoire de Chimie Moléculaire de L'Etat Solide,
4 Rue Blaise Pascal, 67070 Strasbourg Cedex, France.

1. Introduction

Aqueous solutions of silicates play an utmost important role in geochemistry, inorganic materials processing and chemical engineering [1].For practical applications, three main classes of products can be defined by looking at the molar ratio $R = SiO_2/Na_2O$:

i) Detergents when $R < 2.5$ (mainly ortho- and metasilicates).
ii) Adhesives, binders and de-flocculating agents when $2.5 < R < 3.8$ (polysilicates).
iii) Colloidal silica when $R > 3.3$.

From a scientific standpoint, depending mainly on the solution pH and silica concentration, we are faced with a very complex chemistry, ranging from monomeric species at high pH and low concentration up to three-dimensional reticulated gels at low pH and high concentration. At intermediate pH and concentration, the system can be either molecular (polysilicates) or colloidal (silica sols) with no clear-cut borderline between both domains. First attempts to derive the detailed molecular structure of these silicate solutions involve trimethylsilylation followed by chromatographic separation [2, 3] or reactions with molybdic acid [4]. With the growing development of high resolution NMR spectroscopies in the eighties, it is now possible to perform in situ experiments. This gives invaluable information on the connectivities of silicon atoms in the solution. Five main classes of ^{29}Si NMR signals have thus been identified and labelled Q_n, where Q stands for a fourfold coordinated silicon atom and n gives the number of siloxane bridges (Si-O-Si) per tetrahedron $(0 \leq n \leq 4)$ [5, 6]:

B. Silvi and P. D'Arco (eds.), Modelling of Minerals and Silicated Materials, **273-334.**

- Monomeric SiO_4 (Q^0)
- Terminal -SiO_4 (Q^1)
- Bridging =SiO_2 (Q^2)
- Capping or branching $\equiv SiO$ (Q^3)
- Cross-linking =Si= (Q^4)

A great number of NMR signals can be found in a typical aqueous silicate solution. Nevertheless it was possible using isotopic enrichment and 2D techniques at very high fields (500 MHz) to assign all the peaks from about twenty oligomeric species (figure 1) ranging from the monomer up to decamers [7, 16]. Characterization of colloidal or crystalline silica, was also possible using solid-state NMR with magic-angle spinning (MAS) with [17] or without cross-polarization (CP) [18]. Attempts to characterize aqueous silicate solutions by ^{17}O NMR spectroscopy have also been made [19]. Linewidths of the silicate anions are however rather broad (3-20 ppm), owing to the quadrupolar nature of the ^{17}O nucleus (I = 5/2). Moreover, the chemical shift range is rather small (about 50 ppm) resulting in considerable spectral overlap between terminal oxygen groups (Si-O- or SiOH: 35-55 ppm) and bridging groups (Si-O-Si: 45-85 ppm) [19].

The most fascinating aspects of the aqueous chemistry of silicates concern the major role plaid by the counter-cation, in relation with zeolites' synthesis [20]. Using inorganic bases such as NaOH or KOH, relative concentrations of polysilicate anions and NMR linewidths are changed, but no drastic changes occur [21]. This is not the case with tetraalkylammonium cations that seem to exert specific structure-forming effects. Thus with the tetramethylammonium cation (TMA) $[N(CH_3)_4]^+$, the solutions contain predominantly the cubic octamer $[Si_8O_{20}]^{8-}$ (Q_8^3) [21, 22, 23, 24]. The formation of such a species is however not instantaneous, as the first steps involve several other polysilicates: the dimer $[Si_2O_7]^{6-}$ (Q_2^1), the cyclic trimer $[Si_3O_9]^{6-}$ (Q_3^2) and the prismatic hexamer $[Si_6O_{15}]^{6-}$ (Q_6^3) [25]. The cubic octamer appears after several hours and becomes the predominant species after several weeks [25]. Moreover, in presence of a water-miscible organic solvent such as methanol or dimethylsulphoxide (DMSO), this cubic octamer accounts for about 98% of the total silicon concentration [26, 27]. Two kinds of crystals can be isolated from these TMA silicate solutions, the first one containing eight TMA ions [28], and the second one seven TMA and one sodium ions [29,30]. However, increasing the sodium to TMA ratio leads to the destruction of this double four-ring polysilicate [31]. The cubic octamer is not destroyed when the TMA cations are replaced by ethylenediamine (en) complexes such as $[Cu(en)_2]^{2+}$ [32] or $[Co(en)_3]^{3+}$ [33], the octamer being twice protonated in the latter case. A tricyclic heptasilicate $[Si_7O_{19}]^{6-}$ has also been isolated as a trimethylsilyl ester from these TMA solutions [34]. Attempts to crystallize this new polysilicate has lead

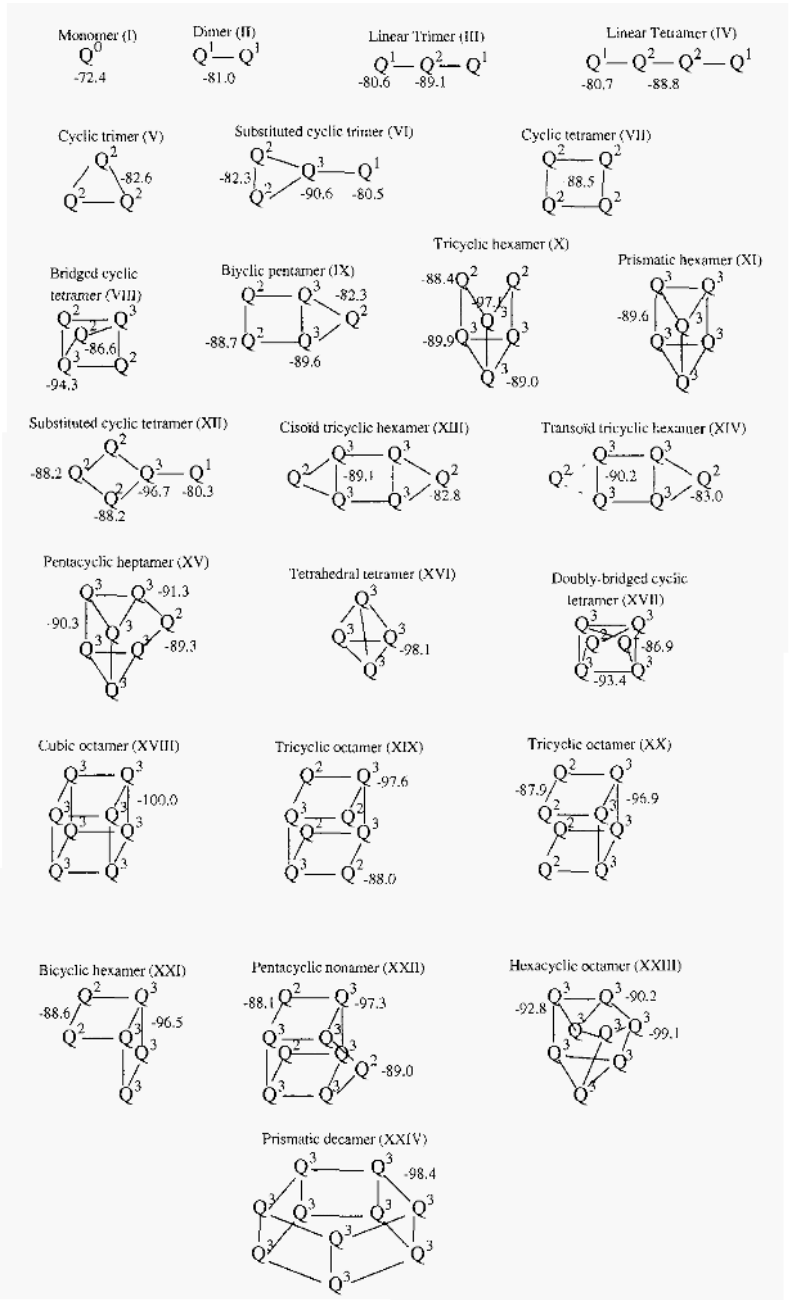

Figure 1. Structures and ^{29}Si NMR chemical shifts of polysilicates found at 22°C in 1.5 mol.l^{-1} aqueous solutions ($KOH:SiO_2$ = 1:1) after [14]. Polysilicates XVIII and XXIV are formed only in presence of tetra-alkylammonium ions.

to a clathrate hydrate-type material, containing the cubic octamer linked through hydrogen bonds to OH^- ions and water molecules [35]. With the tetraethylammonium cation (TEA), the polycondensation process leads to the prismatic hexamer $[Si_6O_{15}]^{6-}$ when the molar ratio TEA/Si is between 1 and 2.8, whereas the cubic octamer is formed for lower values (0.6-0.8) [36]. Single-crystals containing the prismatic hexamer can be obtained in the presence of a Ni^{2+} ethylenediamine complex [37]. 'The NMR spectra of tetrapropylammonium (TPA) and tetrabutylammonium (TBA) silicate solutions, resemble generally to those of sodium silicate solutions [38]. However, a double five-ring silicate $[Si_{10}O_{25}]^{10-}$ isolated as a trimethylsilyl ester can be crystallized from TBA solutions [39].

^{29}Si NMR spectroscopy has also provided some insights into the polycondensation mechanism of aqueous silicate solutions [40, 41, 42, 43, 44]. The first steps involve the polycondensation of the monomer Q^0, leading to the dimer, the linear trimer and the linear tetramer [43]:

$$Q^0 + Q^0 \leftrightarrow Q^1 - Q^1$$
$$Q^0 + Q^1 - Q^1 \leftrightarrow Q^1 - Q^2 - Q^1$$
$$Q^0 + Q^1 - Q^2 - Q^1 \leftrightarrow Q^1 - Q^2 - Q^2 - Q^1$$

In these schemes the active Q^0 monomer is the $[Si(OH)_3O]^-$ complex that is in equilibrium with two other forms [44]:

$$[Si(OH)_2O_2]^{2-} + 2H_2O \leftrightarrow [Si(OH)_3O]^- + H_2O + OH^- \leftrightarrow [Si(OH)_4]^0 + 2OH^-$$

The linear pentamer is never detected, owing to cyclization reactions of the linear trimer and tetramer according to:

$$Q^1 - Q^2 - Q^1 \leftrightarrow Q_3^2 \quad \text{and} \quad Q^1 - Q^2 - Q^2 - Q^1 \leftrightarrow Q_4^2$$

It should be noted that whereas the cyclic tetramer is inert on the NMR time scale, the end and middle groups of the linear trimer are under rapid exchange. This means that the cyclic trimer is quite labile undergoing a rapid ring opening and closing process in solution. Quite interesting is that all these species are found upon melting of $Na_2O.SiO_2.nH_2O$ (n = 9, 5) crystals that are known to contain only the $[SiO_2(OH)_2]^-$ monomer [45].

Subsequent additions of the monomer must then occur on these cyclic species leading to the substituted cyclic trimer and tetramer:

$$Q^0 + Q_3^2 \leftrightarrow Q_3^2Q^1 \text{and } Q^0 + Q_4^2 \leftrightarrow Q_4^2Q^1$$

The substituted cyclic trimer can lead through intramolecular rearrangments either to the cyclic tetramer or to the tetrahedral tetramer ($Q_4^2 \leftrightarrow$

$Q_3^2Q^1 \leftrightarrow Q_4^3$) whereas the substituted cyclic tetramer leads either to the bicyclic pentamer: $Q_4^2Q^1 \leftrightarrow Q_2^2Q_2^3Q^2$ or to the bridged cyclic tetramer $Q_4^2Q^1 \leftrightarrow Q^2Q^3Q^2Q^3Q^2$. Further addition of the monomer Q^0 leads to the various hexamers (prismatic Q_6^3, tricyclic cisoid and transoid $Q^2Q_4^3Q^2$, tricyclic $Q^2Q^3Q^2Q_3^3$ and bicyclic $Q_2^2Q_3^2Q_2^2$). Addition of another monomer to the prismatic or to the cisoid tricyclic hexamers leads to the pentacyclic heptamer $Q_4^3Q^3Q^2Q^3$ precursor of the cubic octamer Q_8^3 and of the pentacyclic nonamer $Q_8^3Q^2$.

If the solution chemistry of silicate ions is rather well understood from an experimental point of view, coherent theoretical justification of such a complex behavior is still lacking. *Ab initio* methods are well suited for the study of the Q^0 monomer $[SiO_4]^{4-}$ or $Si(OH)_4$. All-electron SCF molecular orbital calculations (SCF-MO) show that the charge distribution in the free orthosilicate anion $[SiO_4]^{4-}$ should be: $Si(core)^{10}\ 3s^{0.39}\ 3p^{1.06}$ (i.e. $q(Si) = +2.55$) and $O(core)^2\ 2s^{2.03}\ 2p^{5.62}$ (i.e. $q(O) = -1.65$) [46]. They also showed that the orthosilicate anion should not exist owing as 24 electrons are found in anti-bonding molecular orbitals [47]. Such a species is however commonly found in many natural silicates such as zircon, garnets, olivines, etc...[48]. Stabilization is then obviously needed from the molecular or crystalline environment. Determination of force constants in orthosilicate solutions or crystals leads to the following partial charges at the silicon atom [49] : +2.25 (Na_4SiO_4 aqueous solution), +2.66 (Be_2SiO_4), +2.56 (Mg_2SiO_4), +2.60 ($MgCaSiO_4$), +2.62 (γ-Ca_2SiO_4), +2.77 (β-Ca_2SiO_4), +2.73 (Sr_2SiO_4) and +2.69 (Ba_2SiO_4). Slightly smaller values are found from direct integration of the electron density determined from accurate single-crystal X-ray data: +2.11 (α-Mg_2SiO_4), +2.28 (α-Mn_2SiO_4), +2.43 (α-Fe_2SiO_4), +2.2 (α-Co_2SiO_4), and +2.4 (α-Ni_2SiO_4) [50, 51] Consequently, *ab initio* methods seem to give the right order of magnitude for the silicon partial charge but are clearly of no help for explaining the environment influence. This agreement is however probably quite fortuitous, as it is well known that partial charges are very sensitive to the basic sets employed in the calculations and particularly to the inclusion of *d*-orbitals. For instance, if silicon *d*-orbitals are allowed in the previous *ab initio* calculations, it is found that 2.82 electrons, to lower electrostatic repulsion, should flow from oxygen towards the diffuse silicon *d*-orbitals [47]. This now leads to a slightly negative partial charge at the silicon atom: $q(Si) = 2.55 - 2.82 = -0.27$. Neglect of electron correlation in early *ab initio* molecular orbital calculation is responsible for this incorrect result. Accordingly, *ab initio* molecular orbital calculations at the SCF level with configuration interaction (SCF-MO-CI) on the free orthosilicate ion $[SiO_4]^{4-}$ leads to $q(Si) = +0.952$, $q(O) = -1.238$ without silicon *d*-orbitals and to: $q(Si) = +0.452$, $q(O) = -1.113$ with inclusion of silicon *d*-orbitals [52]. The first set of val-

ues is close to that found using the self-consitent-field-Xa-scattered-wave (SCF-Xα-SW) method: q(Si) = +0.872, q(O) = -1.218 [53]. The influence of *d*-orbitals is also found at the SCF-MO-6-31G* level (split-valence plus polarization basis set) for the fully protonated form $Si(OH)_4$ with symmetry S_4 (orthosilicic acid) : q(Si) = +1.90, q(O) = -0.95 without d(Si), q(Si) = +1.12, q(O) = -0.72 with d(Si) and q(Si) = +1.34, q(O) = -0.81 with d(Si, O) [54].

Ab initio methods have also been applied to the dimer $[Si_2O_7]^{6-}$. At the SCF-MO level without silicon *d*-orbitals it is found that the silicon partial charge goes from +2.666 down to +2.653 as the Si-O-Si angle increases from 120° up to 180° [46]. The calculations also show that the silicon atom becomes more positive as the Si-O distance decreases and as polycondensation increases, and that bridging oxygen-atoms are less negative (about 0.13 electrons) than non-bridging ones [46]. Model clusters $H_4Si_2O_7M_2$ (M = H, Li, Na, K) have been studied at the SCF-MO-3-21G* level with inclusion of *d*-orbitals on silicon and oxygen [55]. It was found that the silicon-atom partial charge decreased regularly as one goes from hydrogen to potassium: +1.645 (H), +1.580 (Li), +1.534 (Na) and +1.491 (K). The same trend was found for the partial charge on the bridging oxygen-atom (Si-O-Si): -0.861 (H), -0.880 (Li), -0.886 (Na) and -0.890 (K) and on the non-bridging oxygen-atoms (Si-O-M) : -0.872 (Li), -0.928 (Na) and -0.967 (K. Interestingly, the M-O bond overlap population is not zero and decreases in the order: 0.509 (Li), 0.334 (Na) and 0.143 (K) leading to non-integral partial charges on the alkali metals: +0.583 (Li), +0.709 (Na) and +0.819 (K. Rather different charge distributions are found for the $[Si_2O_7]^{6-}$ dimer with the self-consitent-field-Xα-scattered-wave (SCF-Xα-SW) method. Without silicon *d*-orbitals it comes: q(Si) = +0.657, q(O) = -1.172 and $q(\mu_2\text{-O})$ = -0.285 against q(Si) = +0.148, q(O) = -1.036 and $q(\mu_2\text{-O})$ = -0.081 with inclusion of these d-orbitals [56]. To go one step further into the polycondensation process with *ab initio* methods, it becomes necessary to replace non-bridging oxygen atoms by hydrogen atoms to reduce the computation time. A pentamer model $Si(OSiH_3)_4$ with D_{2d} point-symmetry has thus been studied at the SCF-MO-STO-3G level leading to the following partial charge distribution: $q(SiO_4)$ = +1.471, $q(SiOH_3)$ = +0.880, $q(OSi_2)$ = -0.702 and q(H) = -0.176 or -0.185 [57]. Finally, when the system becomes too big for *ab initio* methods, the only alternative is to use semi-empirical methods such as CNDO (Complete Neglect of Differential Overlap), INDO (Intermediate Neglect of Differential Overlap), MNDO (Modified Neglect of Differential Overlap), EHT (Extended-Hückel Theory) or IEHT (Iterative Extended-Hückel Theory) [58]. Among these, the most widely used is surely the MNDO method that has been recently applied to various silicates and alumino-silicate oligomers [59]. It was found that the partial charge at the

silicon atom increased regularly as polycondensation goes on in the following way: +1.17 (Q^0), +1.35 (Q^1_2), +1.35 and +1.49 (resp. Q^1 and Q^2 in $Q^1_2Q^2$), +1.42 (Q^2_3), +1.49 (Q^2_4), +1.59 (Q^3_6) and +1.65 (Q^3_8).

Summarizing these results, it appears that experimental techniques such as NMR spectroscopy (both in the solution and in the solid-state), single-crystal X-ray diffraction or vibrational spectroscopy, provide a wide set of accurate data concerning crystalline or aqueous silicates. On the other hand, *ab initio* or semi-empirical methods are not yet able to take into account the influence of the crystalline or molecular environment dealing with models often very far from the chemical reality. Furthermore, to get correct charge distributions, one must use polarization basis sets containing *d*-orbitals even for light atoms [6O]. This has lead to a rather confusing controversy, where $(p-d)\pi$ bonding in the Si-O bond can be either completely negligible [61, 62] or completely necessary [63]. From a chemical point of view we thus need an empirical model, which allows, without considerable computational effort, to get accurate partial charge distributions in any crystalline or molecular environment without referring explicitly to *d*-orbitals. Empirical methods based on the partial charge idea fulfill these conditions. In these models the partial charge distributions are quickly computed knowing the electronegativities χ and chemical hardnesses, η of the constituent atoms. These two atomic quantities having long been rather ill-defined, a rather confusing proliferation of values exists in literature [64,65]. Renewed interested in electronegativity has come in 1978 from its identification with the electronic chemical potential of Density Functional Theory (DFT) [66]. Five years later, chemical hardness was identified as the resistance of the chemical potential to change in the number of electrons [67], and by now, these two parameters have a firmly established theoretical basis [68, 69, 70]. The basic formalism of partial charge models (PCM) can be derived either from classical electrostatics [71], MO theory [72] or point-charge approximation of the DFT equations [73], the extension to solid-state compounds being straightforward [74, 75]. It has already been used for studying the electronic properties of silica polymorphs [75] and zeolitic frameworks with the SiO_2 composition [76]. Concerning solution chemistry, by neglecting the external potential contribution to the electronegativity and by using the Allred-Rochow electronegativity scale, we have established a structure-independent PCM, which has been applied with success to the modelization of aqueous solution chemistry of cations [77] including actinide elements [78]. If the external electrostatic potential is taken into account, a structure-dependent PCM is obtained, and it was possible using the Sanderson electronegativity scale, to understand cement solution chemistry [79] as well as oxide solid-state chemistry [80]. We have also tried to use the Mulliken electronegativity scale in the framework of a

structure-dependent PCM to compute solid-state NMR chemical shifts [81]. In the following we will use a Mulliken-based structure-dependent PCM for understanding the chemical properties of silicates and silica, in solution as well as in the solid-state. However, instead of using an *ab initio* calibration that should be highly sensitive to the basis set, we have prefer to use empirical calibration against experimental data that seems more chemically sound.

2. The Model

2.1. PARTIAL CHARGE DISTRIBUTIONS

The basic equations of the model expressed in volts (with e the elementary charge and e0 the vacuum permittivity) are [71, 72, 73, 74, 75]:

$$\begin{cases} \chi_i = \langle \chi \rangle = \chi_i^0 + \eta_i e q_i + \dfrac{1}{4\pi\epsilon_0} \displaystyle\sum_{j=1}^{n} M_{ij} e q_j & \forall i = 1, \ldots, n \\ \displaystyle\sum_{i=1}^{n} q_i = z \end{cases} \tag{1}$$

Here χ_i represents the Mulliken electronegativity of the i^{th} atom in a compound having n atoms in its molecular structure (molecule or ion) or in its unit cell (network) and $\langle \chi \rangle$ the mean electronegativity to which all individual electronegativities ci have to equalize. The two remaining atomic parameters η_i and qi are respectively the chemical hardness (VC^{-1}) and the partial charge (no dimension) of atom i. M_{ij} (m^{-1}) is the Madelung contribution at site i coming from all sites j in the compound, and z the total algebraic charge on the compound ($z = 0$ for a molecule or a network). For a finite molecule or ion M_{ij} is simply given by $1/R_{ij}$, where R_{ij} is the distance between atom i and atom j. For a network, M_{ij} is a sum over the whole lattice of $1/R_{ik}$ terms, with R_{ik} distance between atom i and atoms k obtained by translating atom j along the three crystal axes. If **a, b, c** are the unit cell parameters, x_i and x_j the atomic coordinates of sites i or j :

$$M_{ij} = \sum_{\substack{\mathbf{l}=u\mathbf{a}+v\mathbf{b}+w\mathbf{c}\neq 0 \\ \mathbf{x}=x\mathbf{a}+y\mathbf{b}+z\mathbf{c}}} \frac{1}{|\mathbf{l} + \mathbf{x}_j - \mathbf{x}_i|} \tag{2}$$

This expression can however seldom be used because this sum is divergent. An alternative is to compute M_{ij} in the reciprocal space according to Bertaut's method [82] with optimized convergence and correction for series termination [83]. Here the atoms are replaced by spherical symmetric charge distributions that do not overlap. Let **a***, **b*** and **c*** be the reciprocal lattice parameters, R half the minimum interatomic distance in the

structure and V the volume of the unit cell. If the atomic charge is distributed within a sphere of radius R, with a normalized distribution function $f(r) = a(R - r)^n (n \geq 0)$, where r is the distance from the atomic center, the Madelung tensor can be computed as [83]:

$$M_{ij} = \frac{2\pi R^2}{V} \sum_{\substack{0<\alpha\leq 2\pi R|\mathbf{h}| \\ \mathbf{h}=h\mathbf{a}^*+k\mathbf{b}^*+l\mathbf{c}^* \\ \mathbf{x}=x\mathbf{a}+y\mathbf{b}+z\mathbf{c}}} \varphi(\alpha) \exp[2\pi \mathbf{h}(\mathbf{x}_j - \mathbf{x}_i)] - \frac{2g}{R}\delta_{ij} \qquad (3)$$

with $|\mathbf{h}|$ modulus of any reciprocal space vector such that $|h|+|k|+|l| \neq 0$, a a dimentionless summation index defined as $a = 2\pi|\mathbf{h}|R$ and δ_{ij} the Kroenecker symbol ($\delta_{ii} = 1$ and $\delta_{ij} = 0$ if $i \neq j$). In 3 the function $\varphi(\alpha)$ controls the rate of convergence and g is a constant. Both parameters depend on the choice of $f(r)$ as listed in table 1. If $f(r) = K^3 \exp(-K^2\pi r^2)$, a normalized Gaussian function, the atomic charge distributions are overlapping. In that case (Ewald method), the Madelung tensor can still be evaluated, but the summation has then to be performed both in the reciprocal and in the direct space [84]:

$$M_{ij} = \frac{\pi}{V} \sum_{\substack{\mathbf{h}=h\mathbf{a}^*+k\mathbf{b}^*+l\mathbf{c}^* \neq 0 \\ \mathbf{x}=x\mathbf{a}+y\mathbf{b}+z\mathbf{c}}} \frac{\exp[2\pi \mathbf{h}(\mathbf{x}_j - \mathbf{x}_i)]}{|\mathbf{h}|^2} \exp\left(\frac{\pi^2|\mathbf{h}|^2}{K^2}\right) + \sum_{\substack{\mathbf{l}=u\mathbf{a}+v\mathbf{b}+w\mathbf{c} \neq \mathbf{0} \\ \mathbf{x}=x\mathbf{a}+y\mathbf{b}+z\mathbf{c}}} \frac{\operatorname{erfc}\left(K|\mathbf{l}+\mathbf{x}_j - \mathbf{x}_i|\right)}{|\mathbf{l}+\mathbf{x}_j - \mathbf{x}_i|} - \frac{2K}{\sqrt{\pi}}\delta_{ij} \qquad (4)$$

with

$$\operatorname{erfc}(x) = \frac{2}{\sqrt{\pi}} \int_x^\infty \exp(-t^2)dt$$

Here the rate of convergence is governed by the value of the arbitrary parameter K. If it is small enough, the sum over (h,k,l) converges rapidly, but the sum over (u,v,w) is large. On the other hand, if K is large enough, the second sum becomes negligible, but the first sum converges slowly. An optimun choice has then to be made for each structure.

Knowing the Madelung tensor M_{ij} from equations (2-4) and some starting values for electronegativities Xi and chemical hardnesses η_i, it is rather easy to compute the n partial charges and the mean electronegativity $\langle\chi\rangle$ by solving the lineal (n+1)x (n+1)system (1)with standard techniques [85]. The Mulliken electronegativities and hardnesses are usually computed from valence-state ionization potential (IP_v) and electron affinity (EA_v)

TABLE 1. Atomic charge distribution functions $f(r)$ and $\phi(\alpha)$ and constants g for Eq. (3)

Atomic Shape	$f(r) r < R$	g	$\phi(\alpha)$
Uniform	$3/4\pi R^3$	3/5	$18(\sin\alpha - \alpha\cos\alpha)^2/\alpha^8$
Linear	$3(R-r)/\pi R^4$	26/35	$288(\alpha\sin\alpha + 2\cos\alpha - 2)^2/\alpha^{10}$
Parabolic	$15(R-r)^2/2\pi R^5$	25/28	$7200(\alpha\cos\alpha - 3\sin\alpha + 2\alpha)^2/\alpha^{12}$
Cubic	$15(R-r)^3/\pi R^6$	23/22	$259200(\alpha^2 + \alpha\sin\alpha + 4\cos\alpha - 4)^2/\alpha^{14}$

according to [86]:

$$\chi = \frac{IP_v + EA_v}{2e} \quad \text{and} \quad \eta = \frac{IP_v - EA_v}{2e^2} \tag{5}$$

If an element uses only s and p orbitals for chemical bonding, the pertinent parameters are the electronegativities $X(p)$, $X(s)$ and hardnesses $\eta(p)$, $\eta(s)$ of such orbitals [86]. Now, the electronegativity and hardness of an atom i on the Mulliken will depend on the amount of s orbital engaged in the chemical bond $(\%s)$, leading to:

$$\chi_i^0 = \chi(p) + [\chi(s) - \chi(p)](\%s) \quad \text{and} \quad \eta_i = \eta(p) + [\eta(s) - \eta(p)](\%s) \tag{6}$$

For transition metals, the participation of d orbitals must also be taken into account, and values have been tabulated for the first row series [87]. At first sight it seems that equations (1), (2-4) and (6) are all what we need to compute partial charge distributions. This is not the case and the main problem lies in the evaluation of the chemical hardnesses. This can be easily understood by applying (1) and (2-4) to a simple diatomic molecule A-B where B is more electronegative than A. If we apply the electronegativity equalization principle $\chi_A = \chi_B = (X)$, it comes with $q_A = -q_B = q$:

$$\begin{cases} \chi_A = \chi_A^0 + \eta_A e q_A + \dfrac{e q_B}{4\pi\epsilon_0 R_{AB}} \\ \chi_B = \chi_B^0 + \eta_B e q_B + \dfrac{e q_A}{4\pi\epsilon_0 R_{AB}} \Rightarrow eq = \dfrac{\chi_B^0 - \chi_A^0}{\eta_A + \eta_B - \dfrac{2}{4\pi\epsilon_0 R_{AB}}} \\ q_A + q_B = 0 \end{cases} \tag{7}$$

In this relation we see that the polarity of the bond will be governed by the difference in electronegativity of the two partners only if the sum of hardnesses is greater than $(2\pi\epsilon_0 R_{AB})^{-1}$. If for a diatomic molecule, it is rather easy to check this critical condition, it becomes increasingly difficult as the number of atoms increases, and very often incorrect charge distributions are

produced. This drawback can be easily overcome as a quantum-mechanical treatment shows that the hardness η of an atom is proportional to the average of the inverse of the electron-nucleus distance r : $\eta \propto \langle r^{-1} \rangle$ [88]. Consequently, the chemical hardness can he set proportional to the inverse of the atomic radius r_i : $\eta_i = (4\pi\epsilon_0 R_{AB})^{-1}$ [71, 89]. With this approximation the evaluation of hardnesses becomes as accessible as the covalent or ionic radii themselves. Moreover, as soon as the harmonic mean of two atomic radii is taken to be less than the internuclear distance, no problem of divergence will be met with equation (7).

2. 2. IONICITY INDEXES

The obvious application of the above model is to compute quite rapidly partial charge distributions in any crystalline or molecular environment. Useful comparisons can thus be made between a molecule in the gas phase, and the same molecule in a crystalline solid phase. We can even go one step further, by defining from these charge distributions some useful quantities. First, two kinds of energies can be derived from the charge distribution and the structure. Let $M_{ij}(p, K)$ be the Madelung tensor computed with a cut-off index $p(-p \leq h, k, l, u, v, w \leq +p)$, and a convergence modulator K, the corresponding molar Madelung energy $M_p(K)$, can be defined as :

$$\begin{aligned} M_p(K) &= \frac{e^2}{8Z\pi\epsilon_0} \sum_{i=1}^{n} \sum_{j=1}^{n} M_{ij}(p, K) q_i q_j \\ &= \frac{694.68}{Z} M_{ij}(p, K) \left[\text{Å}^{-1}\right] q_i q_j \text{kJ.mol}^{-1} \end{aligned} \tag{8}$$

with Z the number of formula units in the unit cell (by convention $Z = 1$ for a molecule). Taken alone this energy allows to compare closely related compounds such as isomers, conformers, polymorphs. . . , and check what should be the most stable configuration from a purely electrostatic point of view.

To compare compounds that are not closely related, we must obtain another kind of energy $E_p(K)$ by replacing in (8) the partial charges q_i and q_j on atoms i and j by the corresponding oxidation numbers z_i and z_j. With this full ionic energy $E_p(K)$ we can define an unambiguous ionicity index $I_p(K)$ as follows:

$$I_p(K) = \sqrt{\frac{M_p(K)}{E_p(K)}} \tag{9}$$

If $I_p(K)$ greater than 0.5, the structure under investigation should be a rather ionic one whereas lower values may indicate partial covalent character. We prefer to use this ionicity index instead of the Madelung constant,

because the SI unit of the Madelung tensor is m^{-1}. Consequently a reference distance R has to be found in the structure to get a dimensionless Madelung constant $A_p(K, R)$:

$$A_p(K,R) = \frac{4\pi\epsilon_0 R}{e^2} E_p(K) = \frac{R}{2Z} \sum_{i=1}^{n} \sum_{j=1}^{n} M_{ij}(p,K) z_i z_j \tag{10}$$

For highly symmetric structures involving only univalent ions, the choice of this R-value is generally obvious leading to consistent values among the literature. This is no more the case for other crystal lattices, leading to a rather confusing proliferation of data [90]. Our ionicity index being the ratio of two well-defined electrostatic energies does not suffer from all this confusion.

For a molecular compound, the Madelung constant is not a useful parameter, and we think that the best way to measure the overall polarity of the molecule is to localize the barycenter of positive and negative charges in the structure. With these two barycenters, an ionic dipolar moment can be computed by looking at the modulus of the vector joining them:

$$(\langle x\rangle, \langle y\rangle, \langle z\rangle)^{\pm} = \left(\frac{\sum_{i=1}^{n} q_i^{\pm} x_i}{\sum_{i=1}^{n} q_i^{\pm}}, \frac{\sum_{i=1}^{n} q_i^{\pm} y_i}{\sum_{i=1}^{n} q_i^{\pm}}, \frac{\sum_{i=1}^{n} q_i^{\pm} z_i}{\sum_{i=1}^{n} q_i^{\pm}} \right) \tag{11}$$

$$\Rightarrow \mu(\mathrm{D}) = 4.8\sqrt{(\langle x\rangle^{+} - \langle x\rangle^{-}) + (\langle y\rangle^{+} - \langle y\rangle^{-}) + (\langle z\rangle^{+} - \langle z\rangle^{-})}$$

Obviously, this moment does not include all the polarization effects induced by the charge distribution on the lone pairs contributions, and should be taken just as a molecular ionicity index and not as the true molecular dipolar moment.

2.3. CALIBRATION

As our aim is to modelize the aqueous chemistry of silica and silicates, we must now go on and show how to evaluate the electronegativity and hardnesses parameters for computing the charge distributions. We have also to provide a link between the structure and the pK_a values of the solute species that are by far the most important parameters for a solution chemist.

Concerning the calibration of electronegativities and hardnesses, we must refer to some known partial charge distributions and see what values should be used for the %s and atomic radius parameters to reproduce

the reference data. Looking for an experimental technique giving simultaneously accurate structural data, and electronic density maps, our only choice is to turn towards single-crystal X-ray diffraction. Our reference compound should then be crystalline silica. At atmospheric pressure silica exists in three crystalline forms: quartz below 867°C, tridymite between 870°C and 1470°C, and cristobalite from 1470°C up to the melting point of silica (1713°C). Moreover, each of these three polymorphs exists in a, low- (α) and high-temperature (β) modification that differs by slight rotations of the SiO_4 tetrahedra without change of the topology of the network. A microcrystalline polymorph named moganite having a structure closely related to quartz is also known. Under pressure, three other polymorphs have been recognized: keatite at moderate pressures and temperatures (P = 400 - 4000 bars, T = 300 - 60°C), coesite at high pressures (P = 20 — 70 kbars) and stishovite at very high pressures (P > 70 kbars). This last form has the 6-coordinated rutile structure while coesite and keatite are based on 4-connected frameworks of SiO_4 tetrahedra in which the smallest rings are respectively 4- and 8- membered (coesite) and 5-, 7- and 8-membered (keatite) [91]. Finally, other forms of silica can be obtained under hydrothermal conditions after removal of guest molecules that has favored the crystallization process. These are the so-called clathrasils and zeosils families that have zeolite-type frameworks.

2.3.1. *α-Quartz polymorph*

Among all these structures abundant data concern the quartz framework, whose basic structural units are three- and six-fold spirals of corner-connected SiO_4 tetrahedra that are all either left- or right-handed, the crystal being laevo- or dextro-rotary (fig.2). Accurate structure factors for synthetic low-quartz [92] have allowed the evaluation of the following partial charge distribution: $q(\mathrm{Si})$ = +1.0±0.1and $q(\mathrm{O})$ = -0.5±0.1 [93]. We can use these values to find what should be the bonding parameters of silicon and oxygen atoms in such a structure. Using the $P3_221$ space group with 3 SiO_2 units per unit cell leads to a 2x2 Madelung tensor having the following components: $M_{\mathrm{SiSi}}(3, 0.3)$ = 0.295653 Å^{-1}, $M_{\mathrm{OO}}(3,0.3)$ = 4.838378 Å^{-1} and $M_{\mathrm{SiO}}(3, 0.3)$ = 5.6284191 Å^{-1} (Ewald method). The Madelung constant of this network is thus found to be $A_3(0.3, R_{\min})$ = $8(M_{\mathrm{SiO}} - M_{\mathrm{SiSi}} - M_{\mathrm{OO}}/4)R_{\min}/3$ = 17.5922 with $R_{\min}$ = 1.60 Å. With this constant the charge distribution in low-quartz should be given by :

$$q = q(\mathrm{Si}) = -2q(\mathrm{O}) = \frac{e(\chi_{\mathrm{O}}^0 - \chi_{\mathrm{Si}}^0)}{e^2\eta_{\mathrm{Si}} + \dfrac{e^2\eta_{\mathrm{O}}}{2} - \dfrac{14.4A_3(0.3, 1.6)}{8 \times 1.60}} \qquad (12)$$

The covalent radii of silicon and oxygen being 0.73 Å and 1.18 Å respec-

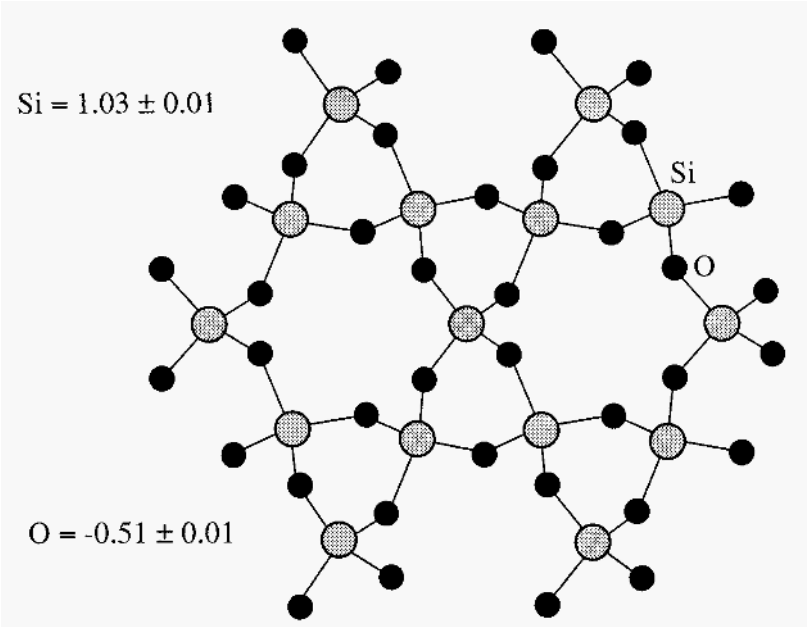

Figure 2. The three-fold and six-fold spirals of corner-sharing tetrahedra and computed charge distribution in α-quartz.

tively [94], typical hardnesses values should be : $\epsilon^2\eta(\mathrm{Si})$ = 12.20 eV and $\epsilon^2\eta(\mathrm{O})$ = 19.726 eV. For the electronegativities an evaluation of the *s*-character of the bonds is required, and a good rule of thumb is: $\%s = 1/G$, where *G* is the group number of the element [86]. For silicon e_{Xs}(Si) = 11.90 eV, e_{Xp}(Si) = 5.76 eV and *G* = 4 leading to $\%s$(Si) = 0.25 and e_X^0(Si) = 7.295 eV. For oxygen *G* = 6 (i.e. $\%s$ (O) =0.167), leading to e_X^0(O) = 12.55 eV as e_{Xs}(O) = 27.19 eV and ecp(O) = 9.63 eV [86]. However, it has also been suggested that if θ is the Si-O-Si bond angle the *s*-character should be given by [95]:

$$\%s(\mathrm{O}) = \frac{\cos\theta}{\cos\theta - 1} \tag{13}$$

In low-quartz θ = 143.67° leading to $\%s$(O) = 0.446, i.e. e_X^0(O) = 17.46 eV. Which value should we use? An empirical answer is brought if we compute what should be the electronegativity of the oxygen atom to reproduce the charge distribution derived from X-ray diffraction data. With *q*(Si) = +1.0±0.1 and e_X^0(Si) = 7.3 eV, (21) leads to e_X^0(O) = 9.6±0.2 eV, a value very close to the electronegativity of a pure *p*-orbital [86]. This result agrees with *ab initio* molecular-orbital studies that showed that geometrical data cannot be used to estimate the participation of *s* and *p* orbitals in bonding

[96]. Moreover, these studies have also shown that the *s*-orbital participation to the chemical bonding is always negligible except when a high local symmetry (T_d, D_{3h} or $D_{\infty h}$) is present. For these particular cases, the presence of only one totally symmetric valence-shell MO precludes a high *s*-orbital occupation [96]. Using these bonding parameters, table 2 gives the iono-covalent indexes of the low-quartz network averaged over 5 structures [92] (R = 1.57%), [97] (R = 1.60%), [98] (R = 1.70%), [99] (R = 2.13%) and [100] (R = 1.6%). The rather low values obtained for the ionicity index ($I_3(0.3)$ = 25.7%) and for the partial electrostatic energy M shows that covalent interactions should play a major role in that particular structure, in agreement with its rather low packing efficiency (≈55%). This ionicity is half that predicted from the electronegativity difference measured on the Pauling scale [101], as it is based of the whole network rather than on individual atomic properties.

TABLE 2. Iono-covalent indexes of α-quartz, coesite and stishovite structures computed with r = 118 and 73 pm for silicon and oxygen respectively and %s = 0.25, for four-fold coordinated silicon and %s = 0 for six-fold coordinated silicon and oxygen. (*) p = 3 and K = 0.3 Å^{-1}. (†) p = 4 and K = 0.2 Å^{-1}. (‡) p = 6 and K = 0.25 Å^{-1}.

Structure	α-quartz*	coesite†	stishovite‡
$e)\chi($ (eV)	7.41 ± 0.01	7.33 ± 0.01	5.57 ± 0.01
$M_p(K)$ (eV)	−10.4 ± 0.1	−10.0 ± 0.1	−21.8 ± 0.1
$I_p(K)$(%)	25.7 ± 0.1	25.3 ± 0.2	37.4 ± 0.1
$R_{\min}$ (pm)	160.7 ± 0.2	159.5 ± 0.1	175.7 ± 0.1
$A_p(R_{\min}, K)$	17.67 ± 0.01	17.50 ± 0.01	19.02 ± 0.01
q(O)	−0.51 ± 0.01	−0.50 ± 0.01	−0.75 ± 0.01
q(Si)	1.03 ± 0.01	1.01 ± 0.01	1.50 ± 0.01

2.3.2. *Coesite polymorph*

We can check the reliability of these electronegativities and hardness values by looking at other silica polymorphs where partial atomic charges have been measured through X-ray diffraction. This has been done for the two high-pressure polymorphs coesite and stishovite. The coesite polymorph is interesting because it displays two non-equivalent silicon atoms and five non-equivalent oxygen atoms. The basic structural feature of this structure is the occurrence of two kinds of four-membered rings linked at right angle to form a "double crankshaft" chain similar to that observed in the feldspars (fig. 3) [102]. These chains contain three non-equivalent oxygen atoms (O3, O4 and O5) with ∠SilOSi2 = 144.5° , ∠Si1O4Si2 = 149.5° and ∠Si1O5Si2

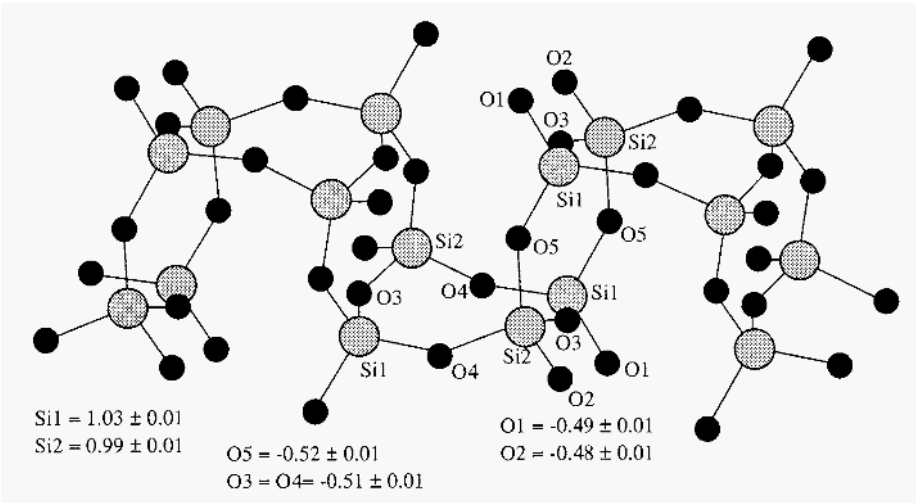

Figure 3. The "double crankshaft" chain running parallel to [101] and computed charge distribution in coesite.

= 137.2° and are cross-linked to each other by two other oxygen atoms O1 and O2 with ∠Si1O1Si1 = 180° and ∠Si2O2Si2 =142.6° . The net charge distribution found in a refined silica polymorph coesite (R = 3%) showed that the two silicon atoms are statistically identical (q(Si1) = +0.9(3) and q(Si1) = +0.8(3)) [103]. Concerning oxygen atoms, the charges on those belonging to the four-membered rings were slightly larger (q(O3)= -0.4(1), q(O4) = - 0.5(2) and q(O5) = -0.6(2)) than those on the remaining atoms (q(O1) = -0.3(1) and q(O2) = – 0.2(1)). Application of our model to four well-refined coesite polymorphs [102] (R = 1.09%), [104] (R = 1.7%), [105] (R= 2.7%) and [106] (R= 2.4%) leads to the same conclusions. On average the charges on the oxygen atoms are not significantly different from those found in *a*-quartz (table 2). The charges on four-membered ring oxygen atoms O3, O4 and O5 are also found to be significantly larger (0.03 e^-). Finally concerning their relative order, our model reads Si1 > Si2 > O2 > O1 > O3 = O4 > O5 that correlates very nicely with the experimental results.

2.3.3. *Stishovite polymorph*

The stishovite polymorph is also very interesting owing to the well-established six-fold coordination of the silicon atom (fig. 4). With this rutile-type structure oxygen atoms become threefold coordinated leading to a large

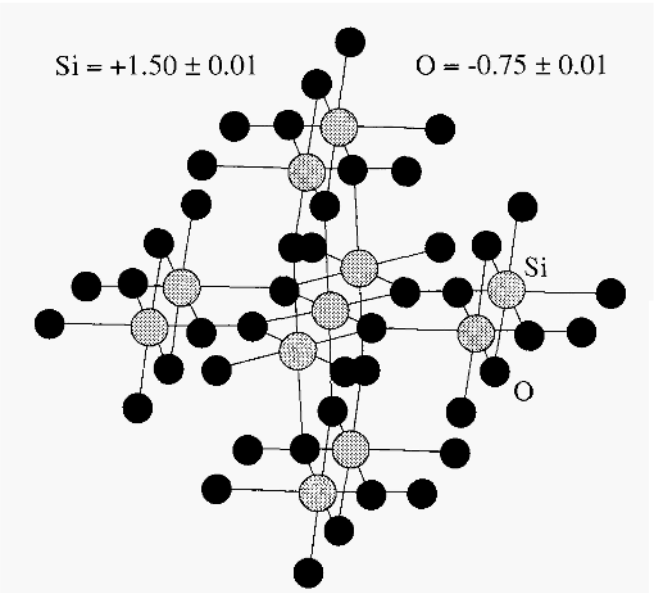

Figure 4. The linear rutile-type chains of edge-sharing octahedra and computed charge distribution in stishovite.

increase (about 15 pm) of the Si-O bond length. The net charge distribution found in a well-refined silica polymorph stishovite (R = 1.2%) leads to q(Si) = +1.71 0.30 and q(O) = +0.86 0.15 [107]. Application of our model to four well-refined stishovite polymorphs [107] (R = 1.2%), [108] (R = 0.74%), [109] (R = 1.5%) and [110] (R = 1.53%) leads to q(Si) = +0.90 0.01 and q(O) = -0.45 0.01 using the parametrization used for a-quartz and coesite. However, if we admit that a six-fold coordinated silicon atom uses only its p-orbitals for chemical bonding (i.e. $\%s(Si^{VI}) = 0$), table 2 shows that, within the experimental errors, the charge distribution is of the right order of magnitude.

2.3.4. *Solution chemistry*

We have now to look if such bonding parameters can be used to predict solution properties. Looking at some simple ionic species displaying a wide range of pK_a values, we have selected the oxy-ions gathered in table 3. Calculations of charge distributions in the fully deprotonated ion have been done with $\%s(O) = 0$, as found in crystalline silica, $\%s(X^{IV}) = 0.25$ and $\%s(X^{III}) = 0.15$. For the hardnesses standard covalent radii are used. The pK_a values have been taken from [111], with the exception of the value

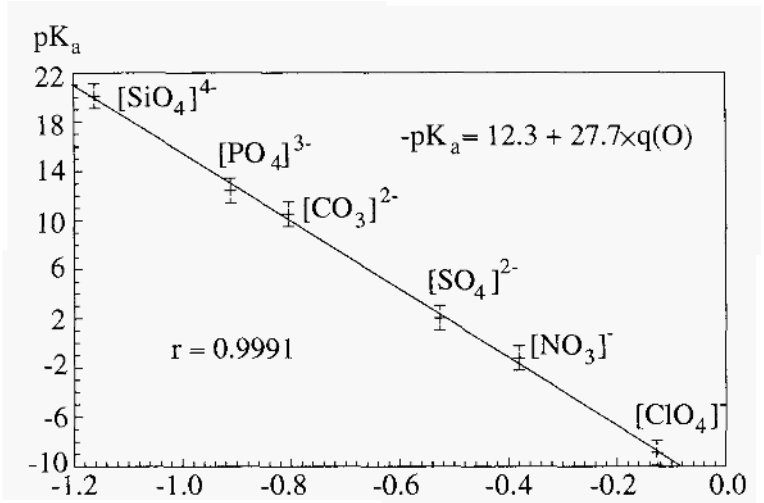

Figure 5. Acidity constant pK_a versus oxygen partial charge for some oxy-ions.

for the orthosilicate anion that have been estimated from the Ricci rule [112]. From very elementary electrostatic considerations, one expect that the most acid anions should be those displaying the least negative charge on oxygen. Moreover it follows from the Ricci rule, that pK_a values of species $[XO_u(OH)_v]^{(2u+v-z)-} \leftrightarrow H^+ + [XO_{u+1}(OH)_{v-1}]^{(2u+v+1-z)-}$ depend linearly on the formal oxidation state z of the central atom X: pK_a = 8+13u+9(v-z)±0.9.A linear relationship between the partial charge at the oxygen-atom in the $[XO_n]^{(2n-z)-}$ species and the pK_a is then anticipated, as from charge conservation $q(O) = -[q(X) + 2n - z]/n$. Figure 5 shows that this relationship holds over the whole range of pK_a investigated which covers as much as 28 pK_a units, leading to :

$$\log K_a = -pK_a = [12.3+27.7 \times q(O)] \pm 0.5 \qquad (14)$$

This fundamental relationship allows us to predict within one unit of pK_a the ability of an oxygen atom to be protonated, knowing its environment that can be either molecular or crystalline. For instance, according to (14) and table 2 an oxygen atom bridging two silicon atoms as found in the α-quartz structure should have a pK_a of about 1.6 that is very close to the experimental value 1.8 found for the isoelectric point of pure silica [113]. Equation (14) also tells us that the oxygen molecule O2 should be the strongest oxy-acid with pK_a = -12 ($q(O) = 0$), while the strongest base

TABLE 3. Selected ionic species for calibration of the charge-*p*Ka relationship. Charges have been computed with %*s* = 0 for oxygen atoms, %*s* = 0.25 and 0.15 for central atoms in T_d and *D*3h symmetry respectively.

[XOn]/[HXOn]	rX (pm)	*p K*a	*d*(X-O) pm	*q*(O) in [XOn]
$[ClO_4$ -/$HClO_4$	99	-9	143.4	-0.124
$[NO_3]$ - / H NO_3	75	-1.3	123.0	-0.379
$[SO_4$]2-/$[HSO^4]$-	104	+1.9	149.0	-0.525
$[CO_3]^2$ - / [HCO3] -	77	$10.4	129.0	-0.804
$[PO_4]^3$-/[HPO4]2-	110	+12.3	153.0	-0.910
$[SiO_4]$-/[HSiO3]3-	118	$20	160.0	-1.159

should be the free oxide anion 02- with pK_a = 43 (*q*(O) = -2). This last value is not unreasonable as in molten $LiOH/Li_2$ 0 mixtures that contain dimeric $[OHO]^{3-}$ species values as high as 35 have been invoked [114].

Let us consider now the various protonated forms of the oxide ion O^{2-} With *d*(O-H) = 96 pm, $\theta(H_2O)$ = 104.5° (C_{2v} geometry) and $\theta(H_3O)$ = 117° (C_{3v} geometry) it comes that *q*(O) = -0.92, -0.18 and +0.16 for OH–, H_2O and H_3O+ respectively if %s(H) = 1 and *r*(H) = 37 pm. With these values equation (14) predicts: *pK*a(OH-/H_2O) = 13.2, *pK*a(H_2O/H_3O+) = - 7.3 and *pK*a(H_3O+/H_4O_2+) = -16.7. The first two *pK*a having well-known experimental values of 15.7 (OH-/H_2O) and -1.7 (H_2O/H_3O+), our estimates are not unreasonable but a little bit too low. This difference may well reflect the very particular nature of the 0-H bond. If we think of a proton deeply buried into the electronic core of the oxygen atom, participation of the *s*-orbital oxygen is not unlikely. Taking the rule of thumb %*s* = 1/*G* where *G* is the group number in the periodic table, i.e. %*s* = 1/6 = 0.16 for oxygen [86], it comes: *q*(O) = -1.02, - 0.38 and -0.17 for OH–, H_2O and H_3O+ respectively always with *r*(O) = 73 pm, %s(H) = 1 and *r*(H) = 37 pm . The three last *pK*a of the O^{2-} ion are then predicted to be: 15.9, -1.8 and -7.8, in excellent accord for the first two values. The ionic dipolar moments corresponding to these polarities are then found to be $\mu(OH)$- = 4.61 D, $\mu(H_2O)$ = 2.82 D and $\mu(H_3O^+)$ = 0.81 D. Recalling that our values do not include the lone pairs contributions, these values are not unreasonable.

2.3.5. *Strategy, unreliability and accuracy*

Our bonding parameters for studying silicates and silica both in the solid state and in solution will thus be: %s(O) = %s(Si^{VI}) = 0, %s(OH, H_2O) = 0.16, %s(Si^{IV}) = 0.25, %s(H) = 1, *r*(H) = 37 pm, *r*(O) = 73 pm and *r*(Si) = 118 pm. To simplify our modelization of the molecular polysilicate anions,

the Si-O bond length has been kept fixed at 160 pm for both bridging and terminal oxygen atoms and the tetrahedral O-Si-O bond angles have all been set equal to arccos (-1/3) = 109.5°. Geometrical input was in the form of a point group symmetry with non-equivalent atom coordinates computed from a *Z*-matrix giving bond distances, bond angles and dihedral angles relative to three previously placed atoms [115]. For solid-state compounds, we have to defined the bonding parameters for the metal ions serving as counter- cations of the polysilicate species. Following the previous study, it has been decided to take %s(M) = 0.25 for fourfold coordinated non-alkaline cations and %s(M) = 0 for all other cases. For alkaline cations (Li, Na, K) %s(M) was set equal to 1. Concerning the atomic sizes, we have chosen to use the Pauling univalent metal radii [101] as a measure of hardnesses. Moreover, to avoid crystalline field effects, we limit ourselves to the study of silicates with metal cations displaying only a d^0 electronic configuration. These choices are obviously rather arbitrary, but the aim is to have a clear picture of the aqueous chemistry of silicates and silica, with the minimum amount of adjustable parameters.

With solid-state compounds, we have met the tricky problem of the reliability of a crystal structure. Some structural data lead to a highly unstable partial charge distribution. This means that very small changes (< 10%) of the atomic sizes induce large changes of the electronic density on a few atoms. As this problem occurs very often when the refinement factor *R* is higher than typically 5%, this factor is systematically given. In the following we have chosen to label such atoms as "unreliable". Let us notice however that an *R*-value greater than 5% does not necessarily mean that the charge distribution will be unstable This point must be checked for each particular structure. Finally, to get reproducible values against small variations of unit cell parameters or of atomic positions, the mean electronegativity $\epsilon\langle\chi\rangle$ and the Madelung energy $M_p(K)$ are reported with two significant digits, i.e., with an accuracy of ± 0.1 eV. Errors on the ionicity index $Ip(K)$, and on the partial charges are respectively 0.1% and ± 0.01e−. The accuracy of the minimum interatomic distance in the structure Rmin, and of the Madelung constant of the network $\Lambda_p(K, R\text{min})$ depends on the refinement factor, but for well-refined structures (R < 5%), typical errors are ± 1 pm for *R*min and ± 0.01 for $\Lambda_p(K, R_{\min})$.

3. Results

3.1. MONOMERS

The charge distribution found for the monomeric orthosilicate anion $[SiO_4]^{4-}$ is q(O) = -1.153 and q(Si) = +0.635 leading to a Madelung energy M = +17.9 eV and to μ = 0 D owing to the assumed T_d geometry. This high posi-

tive value shows that this ion is electrostatically unstable in the vacuum and needs some additional counter-cations to be stabilized. Accordingly, highly alkaline solutions contain the di-protonated form $[SiO_2(OH)_2]^{2-}$ and not the naked monomer [116]. In the solid state charge compensation can be realized by combining mono-, di-, tri- or tetravalent metal cations in such a way that the total sum charge is +4. These crystalline phases containing the monomeric orthosilicate anion are generally named "nesosilicates" from the greek "$\nu\eta\sigma o\zeta$" that means "insular". Besides synthetic compounds six main groups of non-hydrated nesosilicate minerals having no additional anions can be recognized : olivine, monticellite, larnite, phenacite, garnets and zircon.

3.1.1. *A_4SiO_4 compounds*

Three crystal structures of synthetic M_4SiO_4 compounds (M = K [117], Na [118] and Li [119]) are available and our results are gathered in table 4. We see that the mean electronegativity and the ionicity of the network decrease from Li to K, leading to an increase of the Madelung energy. In all cases this energy is strongly negative meaning that all these compounds are electrostatically stable in contrast to the free anion. The most ionic conipound is the lithium one with the following mean values $\langle q(\mathrm{Li})\rangle$ = +0.65, $\langle q(\mathrm{Si})\rangle$ = +0.54 and $\langle q(\mathrm{O})\rangle$ = - 0.85. If we compare these charges with those found for the free orthosilicate anion, we see that the oxygen charge has been strongly reduced, in agreement with the well-known negative second electron affinity of oxygen. This reduction is apparently more pronounced in the sodium ($\langle q(\mathrm{O})\rangle$ = -0.76, $\langle q(\mathrm{Na})\rangle$ = +0.64) and potassium ($\langle q(\mathrm{O})\rangle$ = -0.72, $\langle q(\mathrm{K})\rangle$ = +0.43) compounds. We have however to be careful with such a conclusion as in the potassium phase the K1 and K4 atoms are found to be unstable. This could be correlated with the rather high *R*-value (8%) of this compound. The two other phases appeared to have only stable atoms.

3.1.2. *$M2SiO_4$ compounds*

Table 5 compares the iono-covalent indexes of four crystalline phases (forsterite Mg_2SiO_4 [120, 121], γ-Ca_2SiO_4 [122], Sr_2SiO_4 [123] and Ba_2SiO_4 [124]) having the same framework typical of the olivine group of minerals (fig 5a). All these structures have stable partial charge distributions. As with M_4SiO_4 phases we notice the significant decrease in overall ionicity in going from Mg to Ba. It is interesting to notice the much higher ionicity of forsterite relative to K_4SiO_4 in spite of very similar electronegativities for Mg and K. The reluctance of oxygen atom to have a partial charge lower than -1 is here clearly demonstrated. Accordingly as one goes from Mg to Sr, the positive charge on the metal atom increases meaning that more elec-

TABLE 4. Iono-covalent indexes of M_4SiO_4 orthosilicates with M = Li, *N*a and K. (*) $p = 4$. (‡) $p = 3$. The number of non-equivalent, sites in the structure is indicated in parentheses after the partial charges ranges.

Element M	Li*	Na*	K‡
Space group	$P2_1/m$	$P\bar{1}$	$P2_1/c$
R (%)	6	5.47	8
$e\chi^0$(M) (eV)	3.01	2.84	2.42
r (pm)	123	157	202
$e(\chi)$ (eV)	3.1	2.5	1.6
$M_p(0.2)$ (eV)	-32.6	-22.2	-18.2
$I_p(0.2)$ (%)	37.7	31.7	29.2
R_{min} (pm)	158.1	163.0	162.9
$A_p(0.2, R_{min})$	25.19	24.90	24.19
q(Si)	+0.47...+0.65 (7)	0.46	+0.46
q(O) range	-0.92...-0.80 (21)	-0.77...-0.73 (4)	-0.74...-0.71 (4)
q(M) range	+0.40...+0.81 (19)	+0.58...+0.72 (4)	+0.33...+0.78 (4)

trons are given to the SiO_4 moiety. Instead of going onto oxygen-atoms that have already negative charges close to -1 in forsterite, the electronic density flows along the Si-O bond towards the silicon atom that behave as an acceptor by reducing its partial charge. This mechanism cannot be invoked to explain the rather low ionicity of the barium phase as the positive charges on barium atoms are lower than those on magnesium atoms in forsterite. Here it is probably a size effect coming from the poor overlap between the rather diffuse 6*p*-orbitals of barium and rather contracted 2*p*-orbitals of oxygen. This very poor overlap means that Ba→O electronic transfers are much less efficient than Mg→O ones thereby reducing electronic density on oxygen atoms. This mechanism may also explain why K_4SiO_4 is much less ionic than Li_4SiO_4 although potassium is less electronegative than lithium. It is also interesting to compare the partial charge distribution found in forsterite with that deduced from X-ray data [120]. The charges on the magnesium atoms are very similar in both cases (+1.7-+1.8) and we confirm the higher ionicity of site M2 relative to site M1. The charge distribution with in the SiO_4 tetrahedron is however quite different. A much higher ionicity of the Si-O bond is derived from radial electron distribution curves : q(Si) = +2.11, q(O) = -1.40, q(O1) = -1.29 and q(O2) = -1.52 [120]. Such a high asymmetry seems to us very unlikely as we cannot see how a good orbital overlap between silicon and oxygen atoms could lead to such a charge separation. A more reasonable view is provided by our partial charge scheme that does not put a high negative burden on oxygen

atoms.

TABLE 5. Iono-covalent, indexes of olivine structures M_2SiO_4 (M = Mg, Ca, Sr, Ba).

Element M	Mg*	Ca*(γ-form)	Sr‡	Ba‡
Space group	*Pbnm*	*Pbnm*	*Pmnb*	*Pmcn*
R (%)	2.33 and 2.09	7 5.2	2.5	
$e\chi^0(M)$ (eV)	2.37	2.11	1.95	1.81
r (pm)	140	174	191	198
$e\langle\chi\rangle$ (eV)	2.0	0.4	0.0	0.3
$M_p(0.25)$ (eV)	-58.1	-51.9	-44.7	-34.6
$I_p(0.25)$ (%)	48.2	46.5	43.4	38.7
R_{min} (pm)	161.6	163.3	160.3	161.4
$A_p(0.25, R_{min})$	28.05	27.22	26.36	25.88
q(O) in 8*d*	-0.99	-0.98	-0.96	-0.87
q(O1) in 4*c*	-1.02	-1.03	-0.97	-0.88
q(O2) in 4*c*	-1.00	-0.99	-0.90	-0.82
q(Si)	+0.61	+0.52	+0.53	+0.42
q(M1)	+1.61	+1.66	+1.42	+1.37
q(M2)	+1.77	+1.80	+1.85	+1.64

At least three modifications of di-calcium silicate are known. Besides the γ-form that has the olivine structure studied just above, the crystal structure of larnite (β-Ca_2SiO_4) which crystallizes in the $P21/n$ space group has been refined to R = 4.8% [125]. Application of our model to this phase shows that it is less ionic than the room temperature stable γ-form. The main difference lies in the oxygen charge distribution (table 6). In the γ-form all oxygen atoms bear almost the same charge of -1.00, whereas in the β-form charges are very similar except for one atom 01 that has an ionic charge much less (about 10%) than the others. This observation may be related to the hydraulic activity of the β-form : whereas the γ-form reacts very slowly with water, the β-form appears to be much more reactive [125]. It is thus very tempting to attribute this difference in reactivity to the more asymmetric charge distribution in the β-polymorph.

With phenacite Be_2SiO_4 we can investigate the effect of using a rather small counter-cation that adopts the same coordination number as silicon. As shown in table 6, the effect is rather spectacular as the partial charge at the silicon is almost multiplied by two leading to a strongly negative Madelung energy, i.e., to a very stable compound. Interestingly enough, the charges on the oxygen atoms are all close to -1 and thus very similar to those found on other M_2SiO_4 compounds. Consequently we can say that the

additional electrostatic stabilization relative to other silicates comes from the higher ionicity of the Si-O bond, induced by the presence of fourfold coordinated beryllium atoms.

TABLE 6 Iono-covalent indexes of minerals larnite (β-Ca_2SiO_4), phenacite (Be2SiO4), monticellite ($CaMgSiO_4$) and $NaYSiO_4$. (*) p = 3 and K = 0.25 Å-1. (†) p = 3 and K = 0.20 Å-I. (‡) p = 4 and K = 0.20 Å-1.

Element M	Larnite*	Phenacite†	Monticellite‡	$NaYSiO_4$‡
Space group	$P2_1/n$	$R\bar{3}$	$Pnma$	$Pc2_1n$
R (%)	4.8	2.1 and 4.1	6.8	3.9
$e\chi^0$(M) (eV)	2.11	3.78	2.37 and 2.11	2.84 and 3.41
r (pm)	174	106	140 and 174	157 and 162
$e\langle\chi\rangle$ (eV)	0.4	4.7	0.8	2.4
$M_p(K)$ (eV)	-49.5	-59.0	-58.3	-36.9
$I_p(K)$ (%)	45.4	46.4	48.7	38.3
R_{min} (pm)	160.9	162.9	161.2	161.7
$A_p(K, R_{min})$	26.81	30.66	27.61	28.25
q(O)	O3=-1.00	O1=-0.97	O3=-1.06	O1=O2=-0.84
q(O)	O2=O4=-0.99	O4=-0.96	O2=-1.02	O3=-0.82
q(O)	O1=-0.91	O3=O2=-0.94	O1=-0.96	O4=-0.81
q(Si)	+0.48	+1.03	+0.61	+0.60
q(M)	Ca1=+1.68	Be2=+1.38	Mg=+1.45	Na=+1.03
q(M)	Ca2=+1.73	Be1=+1.39	Ca=+2.03	Y=+1.67

Finally with monticellite $CaMgSiO_4$ and $NaYSiO_4$ we have two different metal cations in an olivine-type network. Table 6 shows that in both cases the least electronegative atoms Ca and Na are fully ionized leading to Na^+ and Ca^{2+} cations. The main difference comes from the much lower ionicity induced by the presence of half-ionized yttrium atoms and reflected by the significantly reduced oxygen partial charges. A very similar partial charge distribution ($\langle q(Y)\rangle$ = +1.64, q(Li) = +0.92, $\langle q(O)\rangle$ = -0.84, q(Si) = +O.82) and ionicity $I_4(0.2)$ = 39.4% is obtained with the $LiYSiO_4$ compound that crystallize in the $P2_1/b$ space group but with R = 11.7% only [130].

3.1.3. *Garnets and zircons*

Garnets have cubic structures with the general composition $(M^{2+})_3(M^{3+})_2(SiO_4)_3$ in which M^{2+} = Fe, Ca, Mg, Mn and M^{3+} = Al, Fe, Cr, V. Among the various classes of garnets : pyrope $Mg_3Al_2(SiO_4)_3$, grossular $Ca_3Al_2(SiO_4)_3$, almandite $Fe_3Al_2(SiO_4)_3$, andradite $Ca_3Fe_2(SiO_4)_3$, spessartite $Mn_3Al_2(SiO_4)_3$, goldmanite $Ca_3V_2(SiO_4)_3$, uvarovite $Ca_3Cr_2(SiO_4)_3$,

we will he concerned only with refined structures of pyrope [131] and grossular [132] which do not contain transition metal elements. Table 7 shows that the prominent feature of' these garnets is their strongly negative Madelung energy. In contrast to phenacite, this high lattice energy cannot be attributed to the ionicity of the Si-O bond but rather to the six-fold coordinated aluminum atom and to the eight-fold coordinated magnesium or calcium atoms. In agreement with the previous observations, the phase with the largest metal atom (grossular) has less ionic Si-O and Al-O bonds. Concerning this grossular phase it has to he pointed out that the charges have been computed with r(Ca.) = 164 pm arid not r(Ca) = 174 pm as before, as this last value would lead to : q(Ca) = $2.33, q(Al) = +1.28, q(Si) = +0.77 and q(O) = -0.99. Decreasing by 6% the atomic, size of the calcium atom prevents to get an ionic charge greater than 2 for this element.

Another phase that has regularly eight-fold coordinated metal cations is zircon $ZrSiO_4$ [133]. Here the charge compensation for the orthosilicate anion is insured by a 1:1 stoichiometry. This leads to a strong reduction of the negative partial charge on oxygen atoms compared to other orthosilicates. The increased difficulty of getting the full ionic charge for the compensating metal cation as one goes from the monovalent up to the tetravalent ones is thus clearly demonstrated. Values of table 7 also apply to the compound $HfSiO_4$ that is completely isostructural of ZrSiO4 [134] and with very closely related bonding parameters $\chi^0(\mathrm{Hf})$ = 4.6 eV and r(Hf) = 144 pm. With thorium, two polymorphs having the stoichiometry $ThSiO_4$ are known: thorite that is isostructural with zircon and huttonite that is isostructural with monazite. Comparison of thorite and zircon shows that the lower electronegativity of thorium leads to a small increase of the negative charge on oxygen atoms and to a sinall decrease of the silicon partial charge. As a whole the structure appears to be more ionic as the thorium partial charge is close to +2. Exactly the same thorium partial charge (+1.93) is found in the other $ThSiO_4$ polymorph huttonite (R = 5.1% in the $P21/n$ space group) which displays edge-sharing ThO_9 polyhedra instead of edge-sharing ThO_8 polyhedra, [135]. Huttonite is however found to be a little bit less ionic than thorite (M_p,(0.25) = -31.6 eV, I_3(0.25) = 33.9% and A_3(0.25, 158.4) = 30.31) owing to slightly more covalent Si-O bond ($\langle q(\mathrm{O})\rangle$ = -0.68 and q(Si) = +0.78).

3.1.4. *Hydroxylated orthosilicate anions*

As numerous hydrated silicate phases are known we want to say something about the effect of protonation and hydration on the charge distribution in the orthosilicate anion. The task is however not easy owing either to the non-localization of the protons in the framework or to ill-refined crystal structures. Here, the most useful data come from single-crystal neutron

TABLE 7. Iono-covalent indexes of minerals pyrope ($Mg_3Al_2(SiO_4)_3$), grossular ($Ca_3Al_2(SiO_4)_3$), zircon ($ZrSiO_4$) and thorite ($ThSiO_4$). (*) $K = 0.15$ Å^{-1}. (†) $K = 0.25$ Å^{-1}. (‡) $K = 0.20$ Å^{-1}.

Element M	Pyrope*	Grossular*	Zircon†	Thorite‡
Space group	*Ia3d*	*Ia3d*	$I4_1/amd$	$I4_1/amd$
R (%)	1.5	3.6	2.8	4.8
$e\chi^0$(M) (eV)	3.99 and 2.37	3.99 and 2.11	4.5	3.74
r (pm)	126 and 140	126 and 164	145	165
$e(\chi)$ (eV)	3.1	2.1	5.0	4.0
M_3(K) (eV)	-154	-150	-31.9	-32.6
I_3(K) (%)	43.9	43.7	33.3	34.4
R_{min} (pm)	163.5	164.6	163.0	163.5
$A_3(K, R_{min})$	90.64	89.73	32.60	31.32
q(O)	-0.91	-0.91	-0.66	-0.69
q(Si)	+0.88	+0.78	+0.88	+0.83
q(M)	Al = +1.62	Al = +1.33	Zr = +1.76	Th = +1.93
q(M)	Mg = +1.66	Ca = +1.99		

diffraction studied that are not so abundant as X-ray ones.

The monoprotonated form of the orthosilicate anion $[SiO_4(OH)]^{3-}$ is found in four crystalline phases $Na_3HSiO_4.nH_2O$ that differs only by their hydration state (n = 0, 1, 2 and 5) [136]. Among these the structures of the n = 5 phase [137] and n = 2 phases [138] have been solved by X-ray diffraction. Figure 5a shows the computed charge distribution in the monomer extracted from the hydrogen-bonded network of the pentahydrate phase [137]. These values have been computed using exactly the same bonding parameters as before namely : %s = 0 for oxygen (r = 73 pm), %s = 0.25 for silicon (r = 118 pm) and %s = 1 for hydrogen (r = 37 pm). We have not set the %s-orbital participation of the OH group to 0.16 as in the water molecule as this renders this group more basic than terminal oxo groups. This probably means that the oxygen-atom s-orbital should be used only when it is bonded exclusively to hydrogen as in OH^-, H_2O or H_3O^+. For non-symmetric M-O-H bonds, a decrease of the s-orbital participation in chemical bonding is not unreasonable, as it has been shown through *ab initio* calculations that a high symmetry favors s-orbital participation [96]. The charge distribution of figure 6a is however not really satisfactory. The terminal oxo groups are predicted to be too acidic (pK_a = 11.8 against 16 according to the Ricci rule) and the hydrogen-atoms bear a negative partial charge. A clue is however provided by the crystal structure of the

pentahydrate phase that appears to be built of strongly hydrogen-bonded $[Si_2O_6(OH)2]^{6-}$dimers H11. . .O3 = 151 pm) associated into layers through hydrogen bonding with water molecules (137. . .O4 = 160 pm and H2. . .O2 = 161 pm) [137]. These layers are further associated by sodium ions to form the 3-D network. Figure 6b shows what happens to the charge distribution when an hydrogen-bonded dimer is considered. The hydrogen atom is now positively charged and the terminal oxo groups have a predicted pK_a of 16.2 a much correct value. Looking now at the solid state (figure 6c), we see that the charge distribution is again completely changed. The charge on the hydrogen bridge has been doubled while the silicon-atom partial charge has increased by 10%. The big difference comes however from the oxygen atoms. The two terminal oxo groups, which are now extensively engaged into hydrogen bonding with water molecules to build a 2-D layer, are less negatively charged than the two other oxygen atoms that insure the dimer cohesion. The effect of the network is also to provide a strong electrostatic stabilization as the Madelung energy that had a positive value in the monomer or the dimer, has now a strongly negative value. Notice also the strong perturbation of the electronic charge distribution on the water molecules, induced by the insertion of $Na_6[Si_2O_6(OH)_2]$ species into the Hydrogen-bonded network of water. Concerning these sodium atoms that have been omitted from the drawing for clarity but which have been taken into account for the charge calculation, a small adjustment of the atomic size of sodium has been made. As using r(Na) = 157 pm as in Na_4SiO_4 leads here to q(Na) > +1, we have reduced this value down to 132 pm to get for the most ionic sodium q(Na) > +1. Looking at the mean electronegativity difference between these two phases (~ 3 eV) this 20% reduction of the sodium atomic size just means that faced with a rather electronegative network the sodium-atom becomes harder. Moreover, this value is not unrealistic, as the ionic radius of the Na+ ion is quoted to be comprised between 99 and 138 pm depending on its coordination number [139].

The crystal structure of the dihydrate form $Na_3HSiO_4.2H_2O$ that also belongs to the *Pbca* space group [138], is not as reliable as that of the pentahydrate phase despite a much better *R* factor (3.9%). This structure has a water molecule that displays a very wide bond angle (H2-05-H3 = 166°) and a very acute hydrogen bridge angle (O5-H3... .O1 = 68°). This anomaly is immediately seen in the charge distribution as the H3 hydrogen atom bears a negative partial charge of -0.09 that is far below that of other hydrogen atoms (mean at +0.09). Extraction of the $[SiO4(OH)]^{3-}$ monomer from the network leads to : q(Si) = +0.51, q(O) = -0.88, q(OH) = -0.82 and q(H) = -0.05 with μ = 0.36 D. The difference observed for the OH group may come from the slightly lower Si-O-H bond angle (122°) as the Si-O

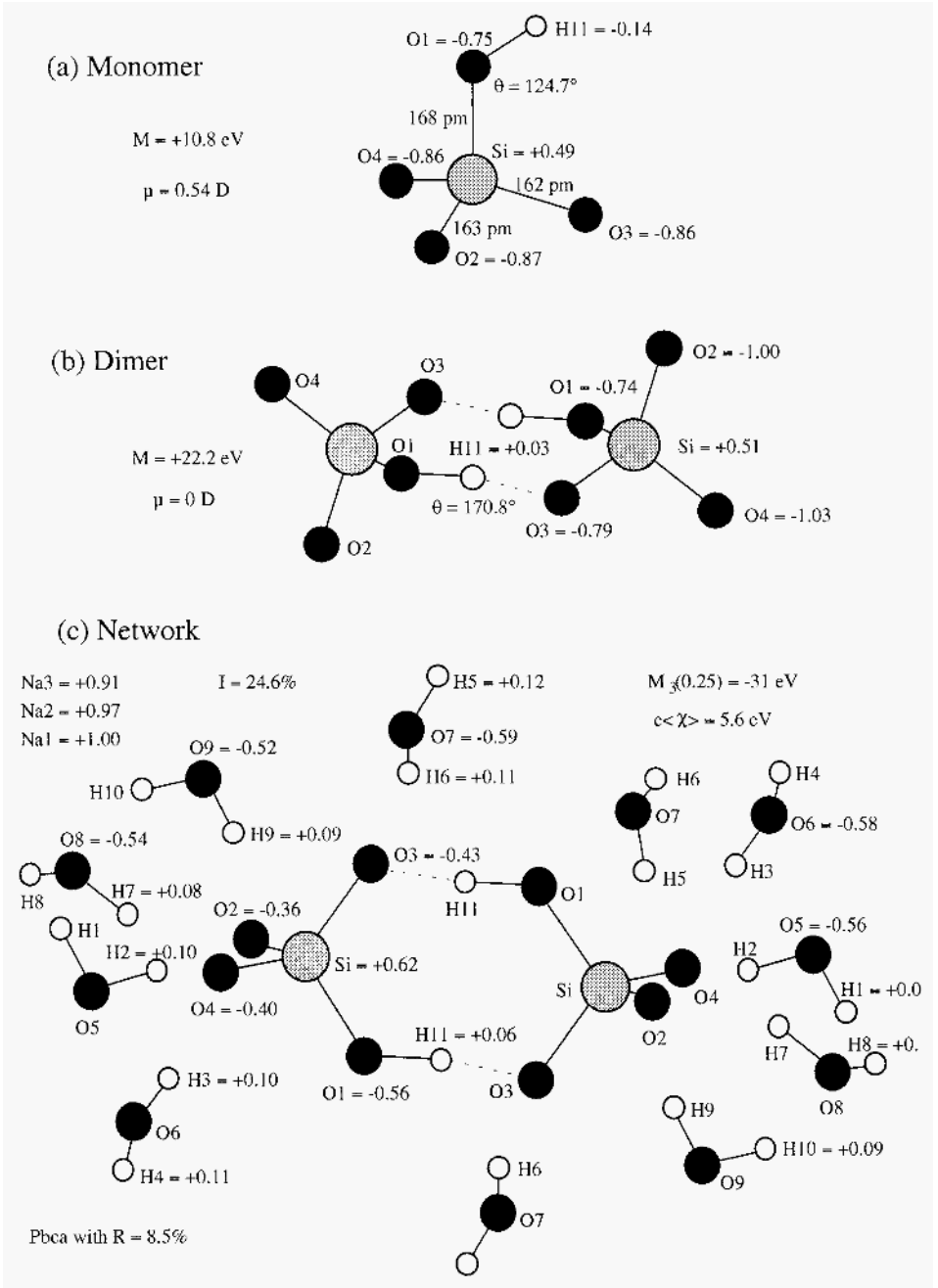

Figure 6. Partial charge distributions in the crystalline hydrogen-bonded $Na_3SiO_3(OH).5H_2O$ phase. (a) Extraction of the naked $[SiO_3(OH)]^{3-}$ ion. (b) Extraction of the naked hydrogen-bonded $[Si_2O_6(OH)_2]^{6-}$ dimer. (c) Full network structure.

bond distances are virtually the same as in the pentahydrate phase. In contrast to this latter phase, no dimers are found here. Instead, the monomer is hydrogen-bonded to two water molecules through atom 03 (03. . .O5 = 258 pm and 03.. .06 = 27.5 pm), and these solvates $[SiO_4(OH)]^{3-}.2H_2O$ are further associated into hydrogen-bonded linear chains through atom O6 (O3. . .H4 = 171 pm, H4-O6-H5 = 99 and H5. . .O2 = 175 pm). Association of these chains with sodium atoms leads to the formation of the 3-D network. Owing to the wrong localization of hydrogen H3, we will not, report the network partial charge distribution.

The di-protonated form $[SiO_2(OH)_2]^{2-}$ is also found in crystalline sodium-based hydrates $Na_2H_2SiO_4.nH_20$ with n = 8, 7, 5, 4 and 0. Among phases where the hydrogen-atom positions have been determined, that with $n = 0$ (space group $P2_1/c$ with R = 7.1%) [l40] leads to a very unlikely hydrogen-atom charge distribution ranging from -0.27 (H6) to +0.08 (H2) and with a very low silicon-atom charge (+0.01). The n = 5 hydrate whose structure has been solved by neutron diffraction [141] is much more reliable. Figure 7a shows the charge distribution and geometry is in the monomer that have been extracted from the network. As with the $[SiO_4(OH)]^{3-}$ monomer, we get negative partial charge on hydrogen atoms and too much acidic (pK_a = 5.4) oxo groups. The Madelung energy is here only slightly positive owing to the presence of two protons around the orthosilicate anion. Turning on the hydrogen-bond interactions is a little bit tricky as the monomers are associated into infinite chains rather than isolated dimers. Figure 7b shows the charge distribution computed on, a chain fragment involving three silicon tetrahedra. As before, the partial charge on hydrogen bridges becomes positive while the terminal oxo group becomes more basic (pK_a = 9.6). Increasing the chain length up to 15 tetrahedra leads to the following averaged value : q(Si) = +0.57, q(H1) = +0.07, q(H2) = +0.10, q(02) = -0.57, q(O4) = q(O3) = -0.65 and q(O1) = -0.85). This last value gives pK_a = 11.2 against 12 according to the Ricci rule. Finally if we add water molecules and sodium ions (figure 7c) we find that the 01 atom which is engaged into two strong hydrogen bonds inside one chain (01. . . H5 = 161 pm and 01. . . H8 = 169 pm) and two weaker ones between such chains (01.. .H4 = 182 pin and 01.. .H10 = 193 pin) becomes less negative than OH groups. Again to avoid sodium-atom charges greaterr than +1, its atomic size must be set equal to 125 pm, a value slightly lower than before owing to the higher framework's electronegativity.

Such chains are not found in the octahydrate crystal structure, which contains isolated $[SiO_2(OH)_2]^{2-}$ ions solvated by water molecules [136]. These solvates are further cross-linked through hydrogen bonding between OH groups and water molecules (01. . . H6 = 187 pm) leading to a 3-D network displaying edge-linked chains of $[Na(OH2)_6]+$ cations. Figure 8 gives

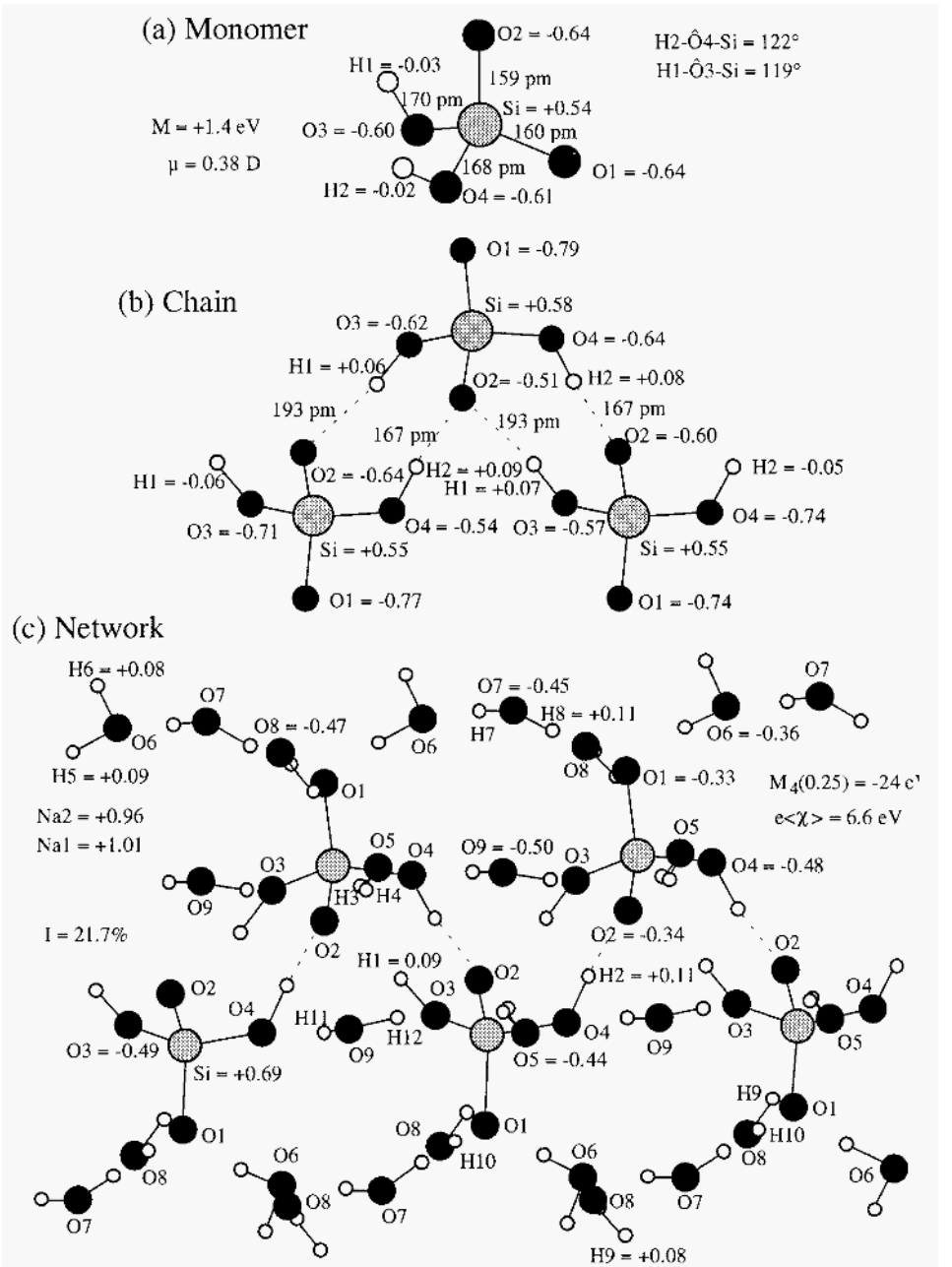

Figure 7. Partial charge distributions in the crystalline hydrogen-bonded $Na_2SiO_2(OH)_2.5H_2O$ phase. (a) Extraction of the naked $[SiO_2(OH)_2]^{2-}$ ion. (b) Extraction of a small portion of the naked $[SiO_2(OH)_2]^{2-}$ infinite chain. (c) Full network structure.

the charge distribution computed with the same sodium radius as in the pentahydrate phase (125 pm). If we compare the partial charge distributions in the penta- and hexahydrate, phases we find very similar. values for the naked $[SiO_2(OH)_2]^{2-}$ anions. Strong differences are however observed when this ion is associated to himself giving chains (fig. 7b) or solvated by water molecules (fig. 8b). In the solvate case the Si-O bond polarity is much reduced whereas it is increased for the chain case. This decrease of polarity upon hydrogen bonding with water molecules is obviously associated with the fact that water molecules have a much higher mean electronegativity than $[SiO_2(OH)_2]^{2-}$ anions. As association with water molecules leads to very low pKa values for oxo groups (pK_a = -3), we can conclude with confidence that in highly alkaline solutions where it is found pK_a = 12.7 [116], the $[SiO_2(OH)_2]^{2-}$ anion should be extensively hydrogen-bonded to OH^- under dilute conditions or even to himself in concentrated solutions.

TABLE 8. Refinement factor R(%), mean electronegativities $e\langle\chi\rangle$ (eV); atomic sizes r(M) (pm), Mulliken electronegativities $e\chi^0_M$ (eV), Ewald summation indexes p, Ewald summation parameters K ($Å^{-1}$), Madelung energies M (eV), ionicity indexes I (%), minimum interatomic distances Rmin (pm) and Madelung constants $A(R_{min})$ of the eleven pyrosilicates displayed in figure 8. (*) Mg values (r(Ba) = 198 pm, exo (Ba) = 1.81 eV). (†) Ba values (r(Cu) = 135 pm, eX^0 (Cu) = 1.48 eV). (‡) Ba values (r(Be) = 106 pm, $e_X{}^0$ (Be) =3.78 eV).

M	Space Group	R	$e\langle\chi\rangle$	$r(M)$	$c\chi^0_M$	p	K	$M_p(K)$	I	R_{min}	$A(R_{min})$
Sc	$C2/m$	2.3	3.4	144	5.62	4	0.25	-17.8	21.2	161	44.05
Er	$P2_1/b$	6.2	2.5	158	2.04	4	0.25	-88.7	43.2	155	51.04
Yb	$C2$	5.3	0.6	170	1.85	4	0.25	-143	54.7	161	53.48
Gd	$Pna2_1$	7.3	2.4	162	2.02	4	0.20	-81.3	41.7	158	51.35
Y	$Pnam$	7.7	3.2	162	3.41	4	0.20	-70.5	38.8	161	52.34
Ca, Mg	$P42_1m$	3.2	1.1	140*	2.37*	3	0.25	-91.9	45.5	160	49.24
Sm	$P4_1$	4.4	2.4	162	1.96	3	0.12	-75.4	40.2	158	50.98
Li	$P42_1m$	11.6	3.5	123	3.01	4	0.20	-55.2	36.2	162	47.44
Ca	$P2_1/a$	3.3	0.7	174	2.11	3	0.20	-90.6	45.4	159	48.72
Ba, Cu	$Pnma$	3.1	1.4	192	1.81	4	0.25	-83.3	43.2	161	49.89
Ba, Be	$Pnma$	6	3.0	180	1.81	4	0.25	-74.2	40.0	159	51.45

3.2. LINEAR OLIGOMERS

3.2.1. *Dimers*

After this very detailed and useful study of the orthosilicate anion, it is time to see what our model predicts for condensed species. The very first step

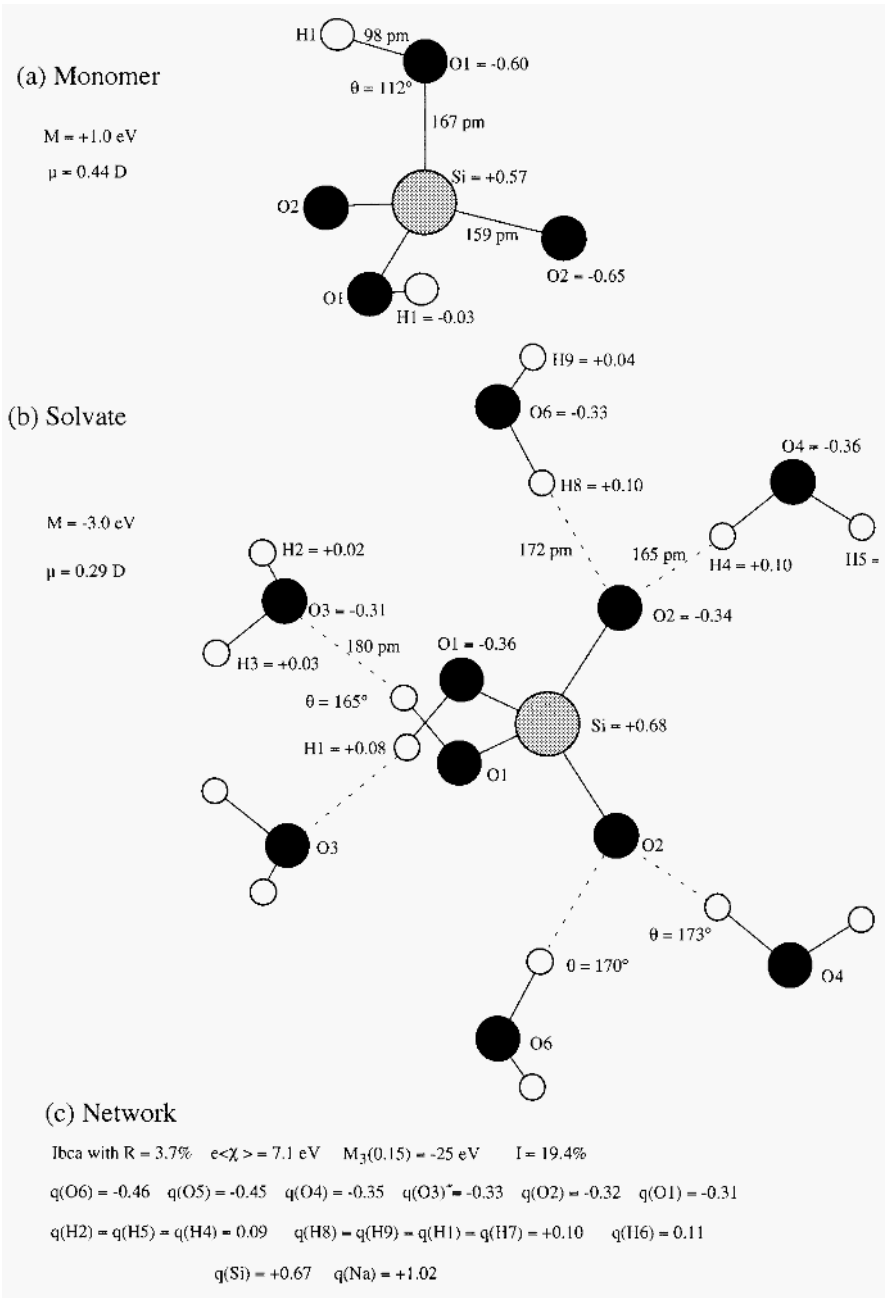

Figure 8. Partial charge distributions in the crystalline hydrogen-bonded $Na_2SiO_2(OH)_2.8H_2O$ phase. (a) Extraction of the naked $[SiO_2(OH)_2]^{2-}$ ion. (b) Extraction of the solvated $[SiO_2\ (OH)_2]^{2-}.6H_2O$ monomer. (c) Full network characteristics.

of such condensation reactions being the dimerization of the orthosilicate anion, we will begin by looking simple dimeric models where the Si-O-Si bond angle is changed from 90° up to 180°. At this stage we have considered two main geometries : the fully eclipsed conformation where all the oxygen-atoms are face to face, and the fully decaled conformer where all dihedral angles are equal to 60° or 180°. Figure 9 shows how the Madelung energy changes with Si-O-Si bond angle.The occurence of a shallow minimum (< 8 KJ.mol^{-1}) between 130° and 140° for both the decaled and eclipsed conformations is a nice result, because this is just the typical range found experimentally in a great number of silicates. Moreover, the steep increase in energy below 130° which contrast with the more smoother one above 140° agrees with the fact that bond angles less than 130° are hardly observed while those greater than 140° are not uncommon. The difference in energy needed to increase the Si-O-Si bond angle from 130° up to 180° is found to be 44 KJ.mol^{-1} a very reasonable value. Looking at crystal structures containing this dimer, figure 10 shows that the smallest Si-O-Si bond angle is found in barylite $BaBe_2Si_2O_7$ (θ = 129°), while the highest valueoccurs in thortveitite $Sc_2Si_2O_7$ (θ = 180"). Concerning the conformation of the pyrosilicate anion, the difference found between the eclipsed and decaled conformation is only 20 KJ.mol^{-1} meaning that both conformers should be observed in natural products. Figure 10 shows that this is indeed the case. A decaled conformation is found when the bond angle is higher than 170° (M = Sc, Er nd Yb). All other pyrosilicates having θ < 160° show an eclipsed conformation. As figure 9 shows that the decaled conformation should be always more stable than the eclipsed one, there is probably some screening effect provided by the counter-cation. If we extract the various dimers of figure 10 from their crystalline environment and perform the partial charge calculation without any counter-cations we find the following averaged values :$\langle q(\mathrm{Si})\rangle$ = +0.52, $\langle q(\mathrm{Oterm.})\rangle$ = -1.05, $\langle q(\mathrm{Obridge})\rangle$ = -0.70 and $\langle M\rangle$ = +46.1 eV. If we compare these values to those found in figure 10, we can see that consideration of the dimer alone is justified only for the bridging oxygen-atom that is found to be always less negatively charged than the terminal oxygen-atoms. For these latter, their partial charges are deeply affected by the chemical nature of the facing counter-cation whose ionic charge can be either very low (M = Li) or conversely as high as +3.0 (M = Yb). This variability of the oxygen-atom partial charge is responsible for the wide dispersion of the silicon-atom partial charge that vary between +0.31 (M = Sc) up to +0.98 (M = Yb). Consequently, both the problems of the conformation and of the Si-O-Si bond angle in pyrosilicate strucures cannot he decorrelated from the cation effect. Presence of these cations that insures a strong negative value to the Madelung energy, must then he absolutely considered to explain the solid-state properties of pyrosilicates.

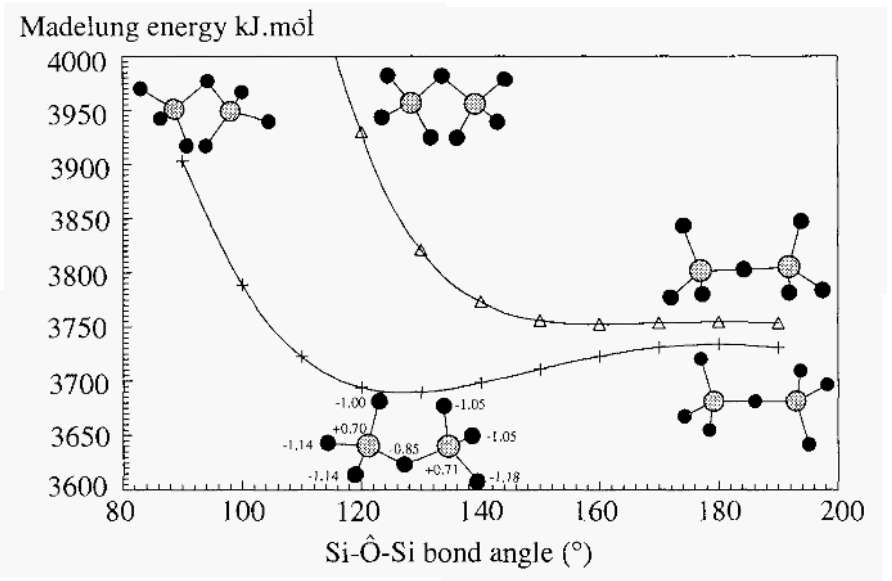

Figure 9. Predicted variation of the Madelung energy as a function of the SiOSi bond angle for two extreme conformations of the $[Si_2O_7]^{6-}$ dimer having all dihedral angles equal to 60° (lower curve ≡ decaled) or 120° (upper curve ≡ eclipsed).

Concerning the solution, we notice that, like the monomer, the unprotonated dimer cannot be found in aqueous solutions as terminal oxo groups are predicted to be highly basic (pK_a = 16.8). This conclusion is supported by experiments that shows that the dimer is extensively protonated when 11 < pH < 12.2 [116]. The bridging oxygen-atom is predicted to he much more acidic (pK_a = 7.1) displaying a difference of about 10 *pK* units relative to terminal oxo groups, and thus only these latter can be protonated.

3.3. TRIMERS AND TETRAMERS

Further condensation of the silicate anion can occur either by association of a monomer with a dimer : $[Si_2O_7]^{6-} + [SiO_4]^{4-} + 2\ H+ \rightarrow [Si_3O_{10}]^{8-} +$ H2O leading to a linear trimer, or between two dimers : $2\ [Si_2O_7]^{6-} + 2\ H+ \rightarrow [Si_4O_{13}]^{10-} +$ H2O leading to a linear tetramer. Both anions have been isolated in crystalline matrices. The linear trimer is found in the compound

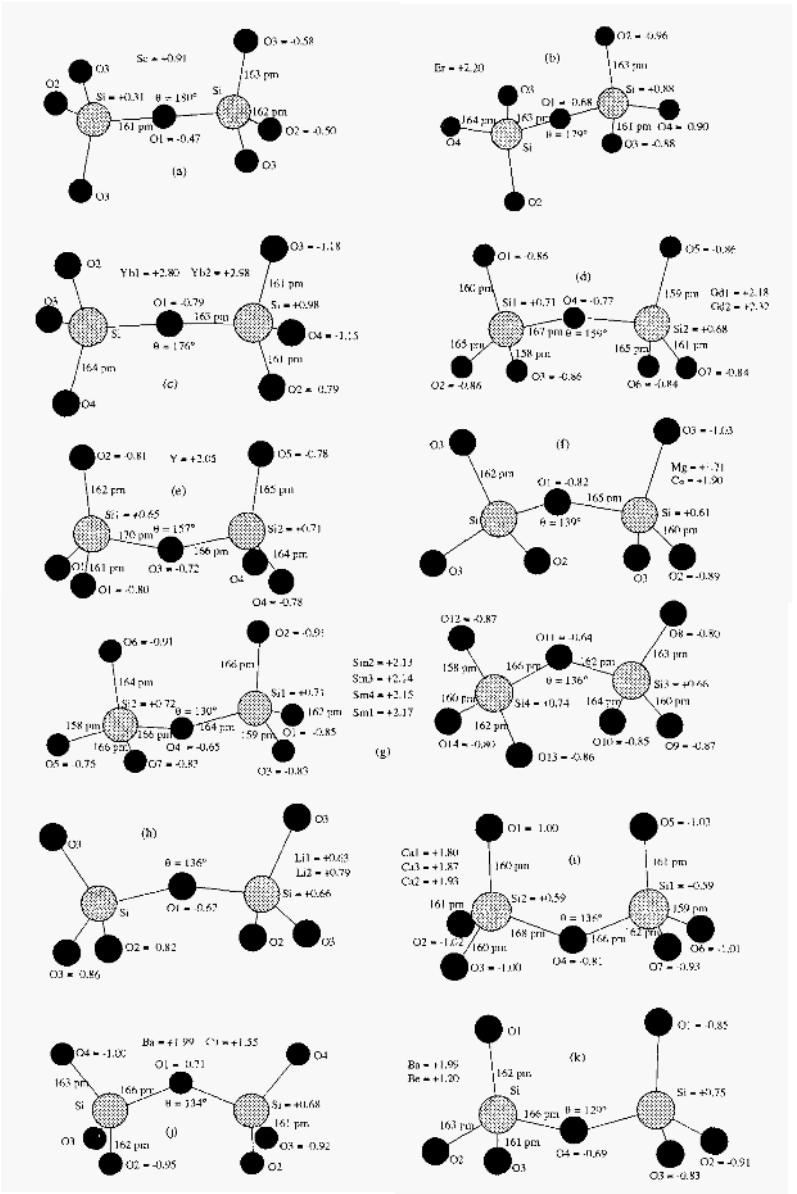

Figure 10. Partial charges distributions in selected anhydrous pyrosilicates structures. (a) Thortveite $Sc_2Si_2O_7$ [141], (b) $Er_2Si_2O_7$ [143], (c) $Yb_2Si_2O_7$ [144], (d) $Gd_2Si_2O_7$ [145], (e) d-$Y_2Si_20_7$ [146], (f) Akermanite $Ca_2MgSi_2O_7$ [147], (g) $Sm_2Si_2O_7$ [148], (h) $Li_6Si_2O_7$ [149], (i) Rankinite $Ca_3Si_2O_7$ [150], (j) $BaCu_2Si_2O_7$ [151], (k) Barylite $BaBe_2Si_2O_7$ [152].

$Na_2Ca_3[Si_3O_{10}]$ that has been obtained through hydrothermal synthesis in the CaO-SiO_2-$NaOH$ system [153]. Figure 11a shows the conformation found for this anion. It consists of two eclipsed tetrahedra (Si2) arranged in decaled conformation relative to the central one (Sil). Ionic charges for the counter-cations are rather close to their formal oxidation states explaining the high ionicity (42%) and the very negative Madelung energy (-110.4 eV). Extracting the anion from the network, leads to a rather similar charge distribution : q(O2) = q(O3) = -1.11, q(O5) = -0.99, q(O4) = -0.88, q(O1) = -0.75, q(Si2) = +0.54, q(Sil) = +0.62, μ = 0.09 D and M = +75.7 eV. Oxygen-atom O3 is the most affected by the cation removal, while the least affectcd is the bridging oxygen-atom O1.

TABLE 9. Refinement factor R(%), mean electronegativities $e\langle\chi\rangle$ (eV); Ewald summation indexes p, Ewald summation parameters K (Å-1), Madelung energies M (eV), ionicity indexes I (%), minimum interatomic distances Rmin (pm) and Madelung constants $A(R_{min})$ of synthetic or natural silicates containing various polysilicate anions (figs 11-18). Kilchoanite = $Ca_6Si_4O_{14}$, Benitoite = $BaTiSi_3O_9$ (rBa = 177 pm), Wadeite ≡ $K_2ZrSi_3O_9$ (rK = 150 pm), Tugtupite ≡ $Na_8(Al_2Be_2Si_8O_{24})Cl_2$ (rNa = 140 pm), $Ba_2Cu_2[Si_4O_{12}]$ (rBa = 190 pm), Beryl ≡ $Al_2Be_3(SiO_3)_6$, Tourmaline = $NaMg_3B_3Al_6Si_6O_{27}(OH,F)_4$, Buergerite ≡ $NaFe^{3+}_3B_3Al_6Si_6O_{30}F$, Blue dioptase $Cu_6[Si_6O_{18}].6H_2O$, Black dioptase ≡ $Cu_6[Si_6O_{18}]$.

Silicate	Space Group	R	$e\langle\chi\rangle$	p	K	$M_p(K)$	I	R_{min}	$A(R_{min})$
$Na_2Ca_3Si_3O_{10}$	$B2/b$	3	1.3	4	0.20	-110.4	42.0	159	69.42
Kilchoanite	$I2cm$	8.9	0.6	5	0.16	-92.5	43.2	155	51.04
$Ag_2Si_2O_7$	$C2/m$	4.8	1.6	3	0.15	-45.8	45.5	160	45.46
Benitoite	$P\bar{6}c2$	4.9	3.6	3	0.25	-102.3	39.6	160	72.67
Wadeite	$P6_3/m$	3	4.3	3	0.25	-54.6	29.4	159	70.06
Tugtupite	$I\bar{4}$	2.3	4.3	3	0.20	-102.5	34.9	158	92.57
$Ba_2Cu_2[Si_4O_{12}]$	$I4/mmm$	3	2.0	3	0.20	-66.4	40.4	157	44.37
Beryl	$P6/mcc$	2	5.8	3	0.20	-202.2	39.3	159	145.7
Tourmaline	$R3m$	6.9	4.7	4	0.25	-361.3	42.4	136	190.0
Buergerite	$R3m$	4.6	5.5	4	0.15	-293.2	37.1	137	201.7
Blue dioptase	$R\bar{3}$	3.68	4.7	4	0.15	-42.9	40.6	95	17.06
Black dioptase	$R\bar{3}$	7.9	3.4	4	0.15	-37.9	43.0	162	23.12

Figure 11b show a skewed conformation for such a trimer found in the mineral kilchoanite that is best formulated as $Ca_6(SiO_4)(Si_3O_{10})$ [154]. Besides this skewed trimer an isolated monomer is found which displays a partial charge distribution very similar to that found in orthosilicate structures. The calcium-atoms have nearly their full ionic charge but in contrast to the

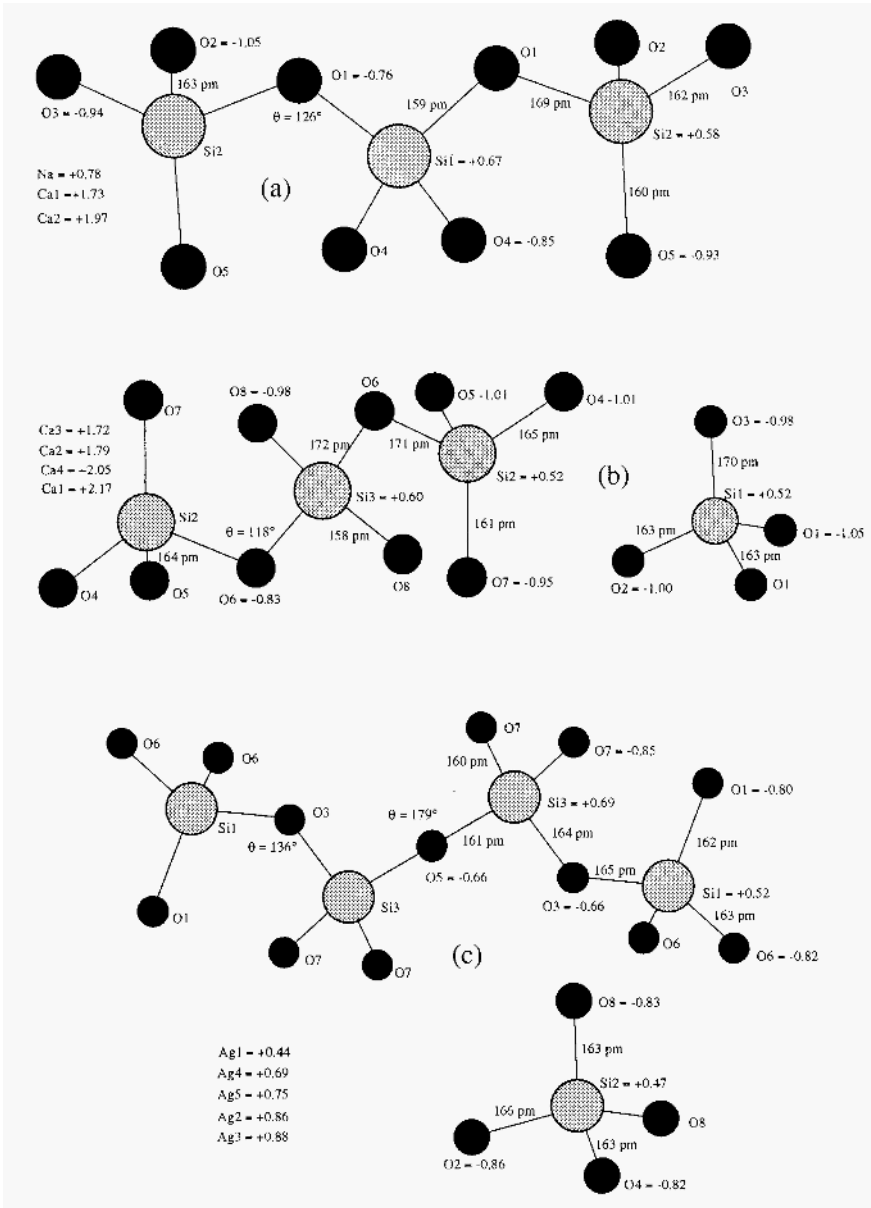

Figure 11. Partial charge distributions in linear polysilicates. (a) $[Si3O10]^{8-}$ trimer found in Na2CasSi3O10. (b) $[SiO4]^{4-}$ monomer and $[Si3O10]^{8-}$ trimer found in kilchoanite $Ca_6Si_4O_{14}$. (c) $[SiO_4]^{4-}$ monomer and $[Si_4O_{13}]^{8-}$ tetramer found in $Ag_2Si_2O_7$.

previous structure, extraction of the anion from the network strongly affects the bridging oxygen-atom: q(O4) = -1.12, q(O5) = q(08) = -1.04, q(O7) = -0.94, q(O6) = -0.66, q(Si2) = +0.48 and q(Si3) = +0.61. This demonstrates that within this structure, the bridging atom develops preferential interactions with the calcium atoms. As a whole this skewed anion is much more polar (μ = 0.8 D) and much less stable than the straight conformer (M = +81.9 eV). By changing the various dihedral angles in this kind of anion, we have observed that the conformation found in $Na_2Ca_3[Si_3O_{10}]$ is the one with the smallest Madelung energy, i.e,. the more favorable from an electrostatic point of view. The most striking feature of these two structures is however the rather low Si-O-Si bond angle observed (126° for the straight conformer and 118° for the skewed one). These low values tend to show that the widening above 130° of the Si-O-Si bond angle in the dimer has for main origin the steric, repulsion between highly negative terminal oxo groups. In a trimer where there is more degrees of freedom, these repulsive interactions are probably more easily accommodated, allowing a closing of the Si-O-Si bond angle.

The possibility of dimerizing two dimers is clearly shown in the crystal structure of the compound $Ag_6Si_2O_7$ that is best written as $Ag_{18}(SiO_4)_2(Si_4O_{13})$ [155]. Figure 11c shows that two dimers in decaled conformation and with Si-O-Si = 136° are associated into a linear tetramer by a quasi-linear oxygen-bridge (Si-O-Si = 179°). As in kilchoanite an isolated $[SiO_4]^{4-}$ monomer coexists with the tetramer. Extraction of the tetramer from the network shows that it has a null dipolar moment with the following charge distribution : q(O6) = -1.11, q(O1) = -1.02, q(O7) = -0.96, q(O5) = -0.73, q(O3) = -0.68, q(Si1) = +0.54 and q(Si2) = +0.66, leading to a highly repulsive Madelung energy M = +104.8 eV. Atoms that are mainly affected by cations' removal are the linear bridge (05) and all the terminal oxygen-atoms. Consequently silver atoms should play an important role in the stabilization of this structure. This agrees with the rather wide range of charge found for these latter: +0.44.. .+ 0.88.

In all cases (dimers, trimers or tetramer) we found that the bridging oxygen-atoms should be less negatively charged (and thus more acidic) than the terminal ones. Concerning the silicon-atom charge, it was found to increase from the monomer $\langle q(Q^0)\rangle$ = +0.48, to the dimer $\langle q(Q^1)\rangle$ = +0.52. This last value is also found for the silicon-atom charge of the Q^1 end-groups both in the trimers and tetramer. The charge on the middle silicon-atom is also systematically higher : $\langle q(Q^2)\rangle$ = +0.65 than the charge on the Q^1 group.

3.3.1. *Higher oligomers and chains*

The ultimate term of the linear condensation of monomers and/or dimers is the metasilicate chain $[SiO_4]_\infty$ found in the pyroxene family $XYSi_2O_6$ (X, Y = Mg, Fe, Ca . . .) and in wollastonite $Ca_3Si_3O_9$. If evidence of such chains in the solid-state is beyond any doubt, our results clearly show that such chain-formation should not occur in the solution. If we look how the relative Madelung energies of the free anions changes as the condensation degree n in $[Si_nO_{3n+1}]^{(2n+2)-}$ increases we get : E($[SiO_4]^{4-}$) = +18 eV, E($[Si_2O_7]^{6-}$) = +46 eV, E($[Si_3O_{10}]^{8-}$) = +78 eV and E($[Si_4O_{13}]^{10-}$) = +105 eV. As in solution these anions are decorrelated from their counter-cations owing to the high dielectric constant of water, it should become increasinglye difficult to form such linear polysilicates. More particularly, the failure to detect the linear pentamer in silicate solutions by ^{29}Si NMR spectroscopy is easily explained by this high increase of the Madelung energy with n. This result no more holds as soon as the cation is associated with the polysilicate, as evidenced by our solid-state calculations that give rise systematically to a strongly negative Madelung energy. Fortunately, an alternative way of condensation is provided in solution through the formation of cycles. The question is then raised of the possible partial removal of the negative burden put on a linear polysilicate structure, through cyclization that leads to water elimination.

3.4. CYCLIC OLIGOMERS

3.4.1. *Cyclic trimers*

As shown above cyclization of the linear silicates in solution is expected. Accordingly several of the silicate structures thus far established contain anion groups in which the silicon atoms are associated together in rings of various degrees of complexity. Figure 12 gives the charge distributions found in three silicate minerals that are known to contain discrete Si_3O_9 groups. All trimers are found to be in Planar conformation with Si-O-Si and O-Si-O bond angles close to 130° and 109° respectively. As for linear oligomers the charges found on the bridging oxygen-atoms are systematically much lower than those on the terminal atoms. The trimer extracted from benitoite $BaTiSi_3O_9$ [156] has a null dipolar moment and the following charge distribution q(02) = -0.95, q(O1) = -0.70, q(Si) = +0.60 leading to M = +11.3 eV. If we compare this last value with that found for a linear $[Si_3O_{10}]^{8-}$ trimer (+78 eV) we see that a mere cyclization stabilizes the system by more than 65 eV! The trimer of wollastonite [157] is more polar (μ = 0.5 D) with a lower Madelung energy (M = +9.5 eV). These values should however be taken with caution, as the Madelung summation process leads to an unrealistic charge distribution for that structure. This is

the reason why we do not report in figure lab the full network charges but just that found on the extracted trimer isolated from its counter-cations. Two slightly different trimers are found in wadeite $K_2ZrSi_3O_9$ [158]. For the first one based on silicon-atom Sil, extraction leads to μ = 0.2 D with q(O3) = -0.97, q(O4) = -0.91, q(O1) = -0.68 and q(Si) = +0.56 leading to M = +12.1 eV. The second one has the same polarity μ = 0.2 D with q(O5) = 0.98, q(O6) = -0.92, q(O2) = -0.68 and q(Si) = $0.58 leading to M = +11.8 eV. Omitting the wollastonite trimer to compute mean values characterizing the free isolated trimer $[Si_3O_9]^{6-}$ leads to: $\langle q(\mathrm{Oterm})\rangle$ = -0.95, $\langle q(\mathrm{Obridge})\rangle$ = -0.69, (q(Si)) = +0.58 and M = +12 eV. With these mean values the pK_a of terminal oxo groups is estimated at 14.0 against 6.8 for the bridging oxygen-atoms.

3.4.2. *Cyclic tetramers*

Figure 13 shows the charge distributions found in five solid phases that are known to contain discrete Si_4O_{12} groups. As there is more flexibility in a tetramer than in a trimer, it is not surprising to find non-planar cycles. As already noticed for linear oligomers and cyclic trimers, the bridging oxygen-atoms are again less negatively charged than the terminal oxygen- atoms. In tugtupite $Na_8(Al_2Be_2Si_8O_{24})Cl_2$, the tetramer display a fully eclipsed conformation (double boat-shaped) of the four silicon tetrahedra (fig. 13a) [159]. Extraction of the tetramer from the network shows that it has a null dipolar moment with q(O3) = q(O2) = -0.98, q(O1) = -0.66 and q(Si) = +0.62 leading to M = +16.0 eV. Compared to the corresponding linear tetramer $[Si_4O_{13}]^{10-}$, this corresponds to an electrostatic stabilization of about 90 eV. A similar conformation apparently more stable (M = +13.0 eV) is found in the mineral kainosite $Ca_2Y_2Si_4O_{12}CO_3.H_2O$ [160]. This extra stability coming from two very short terminal Sil-03 bonds (149 pm), its charge distribution will not be reported here. In synthetic barium copper silicate [161], the extracted tetramer (fig.13b) has also a null dipolar moment but is fully planar with q(O1) = -1.02, q(O2) = -0.72 and q(Si) = +0.77. This charge distribution and planar structure confers a higher stability to this tetramer as M = +12.4 eV, a value very close to that typical of a planar trimer. In papagoite $Ca_2Cu_2Al_2(SiO_4)4(OH)_6$, [162] we find a chair-shaped anion (fig. 13c) having μ = 0 D and M = +16.4 eV. This value is of the same order of magnitude as that found for the double boat-shaped conformer. Finally, the double chair-shaped conformer having a null dipolar moment has been characterized in the synthetic potassium metasilicate $K_4(HSiO_4)_4$ (fig. 13d) [163]. It appears to be more stable (-2.2 eV) than the double-boat conformer, but less stable than the planar one (+1.4 eV). Si_4O_{12} rings have also initially been found in two minerals : axinite $H(Fe,Mn)Ca_2Al_2BSi_4O_{12}$ and taramellite $Ba_4(Fe,Ti,Mg)_4B_2Si_8O_{29}Cl$. Fur-

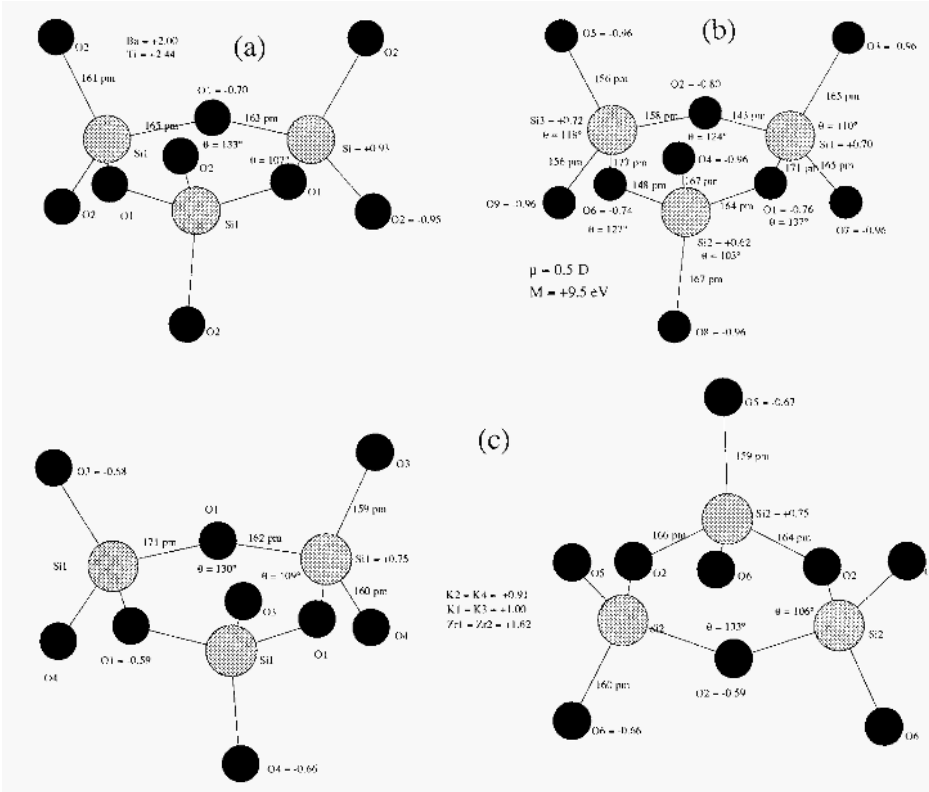

Figure 12 Partial charge distributions in cyclic trimers $[Si3\ O_9]^{6-}$ found in polysilicates minerals. (a) Benitoite $BaTiSi^{3-}$ O9. (b) Wollastonite $Ca_3Si_3O_9$ (charges given are those on the $P2_1/a$ network-extracted trimer). (c) Wadeite $K_2ZrSi_3O_9$.

ther refinements of these crystal structures have shown that axinite mineral contains a complex borosilicate $[B_2Si_8O_{30}]^{22-}$ heteropolyanion built with four Si_2O_7 dimers fused by two BO_4 tetrahedra [164]. Similarly, taramellite contains another kind of borosilicate polyanion $[B_2Si_8O_{27}]^{16-}$ built with two facing Si_4O_{12} rings fused by two BO_4 tetrahedra, [165]. Such heteropolyanions will not be considered here.

Averaging the charge distributions found in these cyclic tetramers leads to the following typical values : $\langle q(\mathrm{Oterm})\rangle$ = -0.93, $\langle q(\mathrm{Obridge})\rangle$ = -0.70, $\langle q(\mathrm{Si})\rangle$ = +0.76 and and M = +14.7 eV. Cyclic trimers a,nd tetramers should then be very similar regarding solution properties (pK_a = 13.5 and 7.1 for terminal and bridging oxygen-atoms respectively). Accordingly, both

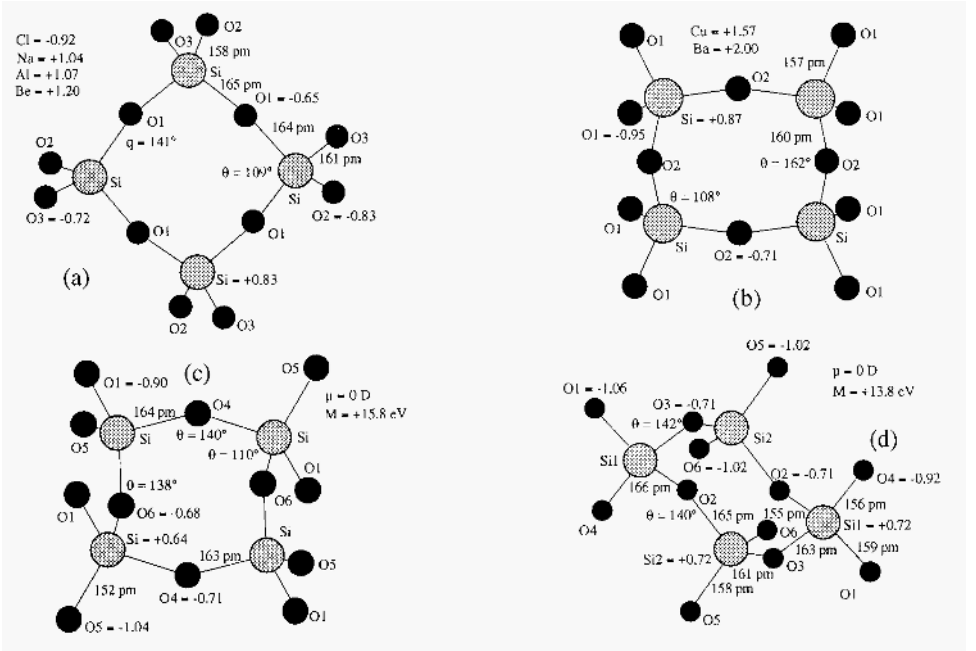

Figure 13 Partial charge distributions in cyclic tetramers $[Si_4O_{12}]^{8-}$ found in polysilicates minerals and synthetic phases. (a) Tugtupite $Na_8(Al_2Be_2Si\ O_{24})Cl_2$. (b) Synthetic barium copper silicate $Ba_2Cu_2\ [Si_4O_{12}]$. (c) Papagoite $Ca_2Cu_2Al_2\ (SiO_3)_4(OH)_6$ (charges given are those on the *C2/m* network-extracted tetramer with R = 3.4%). (d) Synthetic potassium metasilicate $K_4(HSiO_3)_4$ (charges given are those on the $P2_1/n$ network-extracted tetramer with R = 9.5%).

species have been well characterized through ^{29}Si NMR spectroscopy [40, 41, 42, 43, ?].

3.4.3. *Cyclic hexamers*

If cyclic trimers or tetramers are detected in alkaline silicate solutions, this is not the case of larger rings that can be characterized only in the solid state. Owing to the highly repulsive Madelung energies of silicated chains with $n > 4$, formation of a large ring through consecutive addition of monomers on a growing chain followed by cyclization seems very unlikely. The only possibility that remains is through reactions involving already condensed species (dimers, trimers and/or tetramers). For example dimerization of two linear trimers could lead to hexameric $[Si_6O_{18}]^{12-}$ rings found in many precious minerals.

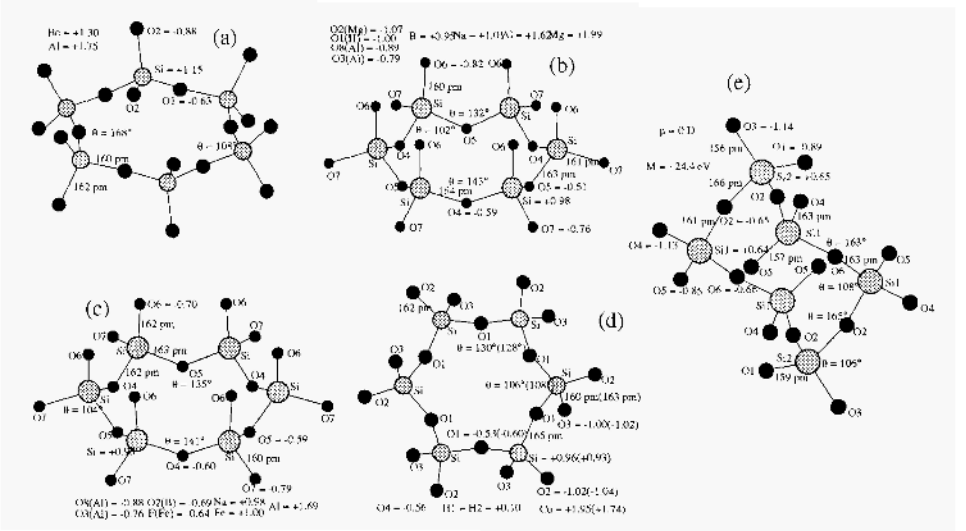

Figure 14. Partial charge distributions in cyclic hexamers $[Si_6O_{18}]^{12-}$ found in polysilicates minerals. (a) Beryl $Al_2Be_3(SiO_3)_6$. (b) Tourmaline (dravite) $NaMg_3B_3Al_6Si_6O_{27}(OH,F)_4$. (c) Buergerite $NaFe_3^{3+}B_3Al_6Si_6O_{30}F$. (d) Dioptase $Cu_6[Si_6O_{18}].6H_2O$ and $Cu_6[Si_6O_{18}]$ (data in parentheses). (e) Imandrite $Na_{12}Ca_3Fe_2(Si_6O_{18})_2$ (charges given are those on the *Pmnn* network-extracted hexamer with R = 8.5%).

A perfect planar and hexagonal ring is found in beryl $Al_2Be_3(SiO_4)_6$ [166] and in bazzite a light blue natural silicate whose exact chemical corn-position has not yet been established owing to its extreme rarity [167]. Figure 14a show the ring geometry of these two minerals. Extraction of the hexameric ring having a null dipolar moment from the networks leads to the following charge distribution for beryl (bazzite values in parentheses) : q(O2) = - 1.01(-1.00), q(O1) = -0.65(-0.66) and q(Si) = +0.67(+0.66) with M = +22.2 eV(+22.4 eV), showing that both rings are effectively very sim-ilar. Influence of the counter-cation is here particularly marked at both the terminal oxygen-atoms and central silicon-atoms. Quite impressive is the very nagative Madelung energy of this structure (table 9) which is twice that found in benitoite and 30% above that of garnets.

This Madelung energy is still higher in tourmaline $NaMg_3B_3Al_6Si_6O_{27}$ (OH,F) [168] and in its iron analog buergerite $NaFe_3^{3+}B_3Al_6Si_6O_{30}F$ [169]. In these two minerals the hexamer ring is not fully planar (fig. 14b and 14c). Its geometry is not really affected by substitution of magnesium by

iron and hydroxyl groups by fluorine. Neglecting the counter-cations we compute for these two rings (buergerite values in parentheses) : q(O7) = -1.13(- 1.13), q(O6) = -0.82(-0.82), q(O4) = q(O5) = -0.68(-0.70) and q(Si) = +0.63(+0.65) with a dipolar moment of 0.5 D(0.6 D) and a Madelung energy of +24.3 eV(+23.9 eV). As in trimers and tetramers, we notice that rings are destabilized by small departures from the fully coplanar arrangement of oxygen and silicon-atoms. On going from the network to the free state we see that, in contrast to the beryl structure, all the atoms are rather strongly affected by the counter-cation removal. This suggests that the ditrigonal distortion of the hexamer ring should be somewhere related to the influence of the counter-cation.

The distortion of the hexameric ring is still more marked in two forms of dioptase : blue dioptase $Cu_6(Si_6O_{18}).6H_2O$ [170] and black dioptase $Cu_6(Si_6O_{18})$ [171] (fig. 14d). Extraction of the ring (having a null dipolar moment) from the $Cu_6(Si_6O_{18}).6H_2O$ network leads to (anhydrous dioptase values in parentheses) : q(O2) = -1.03(-1.02), q(O3) = -0.96(-0.96), q(O1) = -0.63(-0.66), q(Si) = +0.63(+0.64) and M = +25.1 eV(+25.1 eV). Here it is clearly the bridging oxygen-atoms that are most affected, reinforcing the idea of the cation influence in the distortion. Both rings are less stable than those found in beryl or tourmalines. Table 9 shows that both structures have Madelung energies that are about 10% of that found for the tourmaline network. This again illustrates the crucial importance of the counter-cations for the stabilization of intrinsically unstable polysilicate anions.

In lovozerite $Na_2ZrSi_6O_{15}.3H_2O$.ca.1/2NaOH [172] and imandrite $Na_{12}Ca_3Fe_2(Si_6O_{18})_2$ [173], the hexameric ring is not planar at all but rather chair-shaped (fig. 14e). Owing to cationic disorder in both structures we cannot report solid-state partial charge distributions. Extraction of the ring from the imandrite network shows that it has a null dipolar moment and is slightly less stable than the ring found in tourmalines, but more stable than the one found in dioptase. The presence of two rather short terminal Si-O bonds in this ring (156 and 157 pm) probably linked with the rather high refinement factor (R = 8.5%) could explain this extra stability relative to the dioptase ring. Reported coordinates for O2 oxygen-atom in lovozerite being obviously wrong, we cannot compare the two hexameric rings extracted from lovozerite and imandrite.

Averaging our values for the network-extracted hexameric rings leads to: $\langle q(\mathrm{Oterm})\rangle$ = -0.99, $\langle q(\mathrm{Obridge})\rangle$ = -0.66, (q(Si)) = +0.65 and M = +23.9 eV. The lower electronic density and thus higher acidity of bridging oxygen-atoms (pK_a = 6.0 against 15.1 for terminal ones) is again evidenced. The pK_a gap between these two kinds of oxygen appears however to be larger in hexameric rings (ΔpK_a = 9) than in tetrameric (ΔpK_a = 6.5) or trimeric

rings (ΔpK_a = 7).

3.4.4. *Higher Cyclic oligomers*

Cyclization can also occur between two linear tetramers or between three trimers leading to still larger rings (octamers and nonamers respectively). If such very large rings have never been characterized in solution they have been found in some natural minerals. A cyclic octamer $[Si_8O_{24}]^{16-}$ has been found in the very complex mineral muirite $Ba_{10}(Ca, Mn, Ti)_4Si_8O_{24}$ $(Cl, OH, O)_{12}.4H_2O$ [174]. Owing to the occurrence of oxygen disorder in the structure, we cannot report solid-state partial charge distributions. Figure 15a gives the partial charge distribution found €or this slightly polar hut almost planar octameric ring (two equivalent positions separated by 72 pm are available for oxygen-atom O2). As expected charges on bridging oxygen-atoms are much smaller than charges on terminal ones and the overall electrostatic stability is less than for hexameric rings. Making the average between bridging oxygen-atoms O1 and O2 leads to $\langle q(\mathrm{Obridge})\rangle$ = -0.61 (i.e. pK_a = 4.6). With q(Oterm) = -1.00 (i.e. pK_a = 15.4) we see that the pK_a gap has still increased (ΔpK_a = 11) relative to the hexamers. As with linear oligomers, we notice that increasing the ring size systematically increases the Madelung energy that is found to be M = +31 eV.

Eudialyte $Na_{12}Ca_6Fe_3Zr_3Si_{24}O_{66}(Cl,OH)_8$ has still a. more complex structure with two kinds of cyclic polysilicates : $[Si_3O_9]^{6-}$ trimers and $[Si_9O_{27}]^{18-}$ nonamers [175]. In the crystal structure two slightly non-equivalent anions of each kind are found whose partial charge distributions are given in figure 15b. Charges on the trimers are very similar to that found on previously studied compounds. The nonamers are obviously built from three linear trimers with three very closed terminal oxygen-atoms O17 and O18 forming a perfect equilateral triangle. For the first time, we find terminal oxygen-atoms (O17 and O18) which are much acidic than bridging ones (ΔpK_a > 5.5). It is however evident that such a result is the consequence of the extremely short O-O distances quite similar to that found for very strong and linear O-H-O bridges. It is thus highly probable that O17 and O18 are in fact OH groups very strongly associated through hydrogen-bonding. Omitting these three particular oxygen atoms, the charge average for other atoms leads to: $\langle q(\mathrm{Oterm})\rangle$ = -1.02, $\langle q(\mathrm{Obridge})\rangle$ = -0.72 and $\langle q(\mathrm{Si})\rangle$ = +0.64 with $\langle M\rangle$ = +35 eV. If we cannot compare these values to that of other rings, owing to very particular geometry of these nonamers, we see that the Madelung energy has nevertheless still increased. This increase is however rather moderate, and this probably means that huge rings with n > 9 are not strictly forbidden from an electrostatic point of view. As such rings cannot be obtained from the closure of a long linear chain, but rather through the simultaneous aggregation of small oligomers having

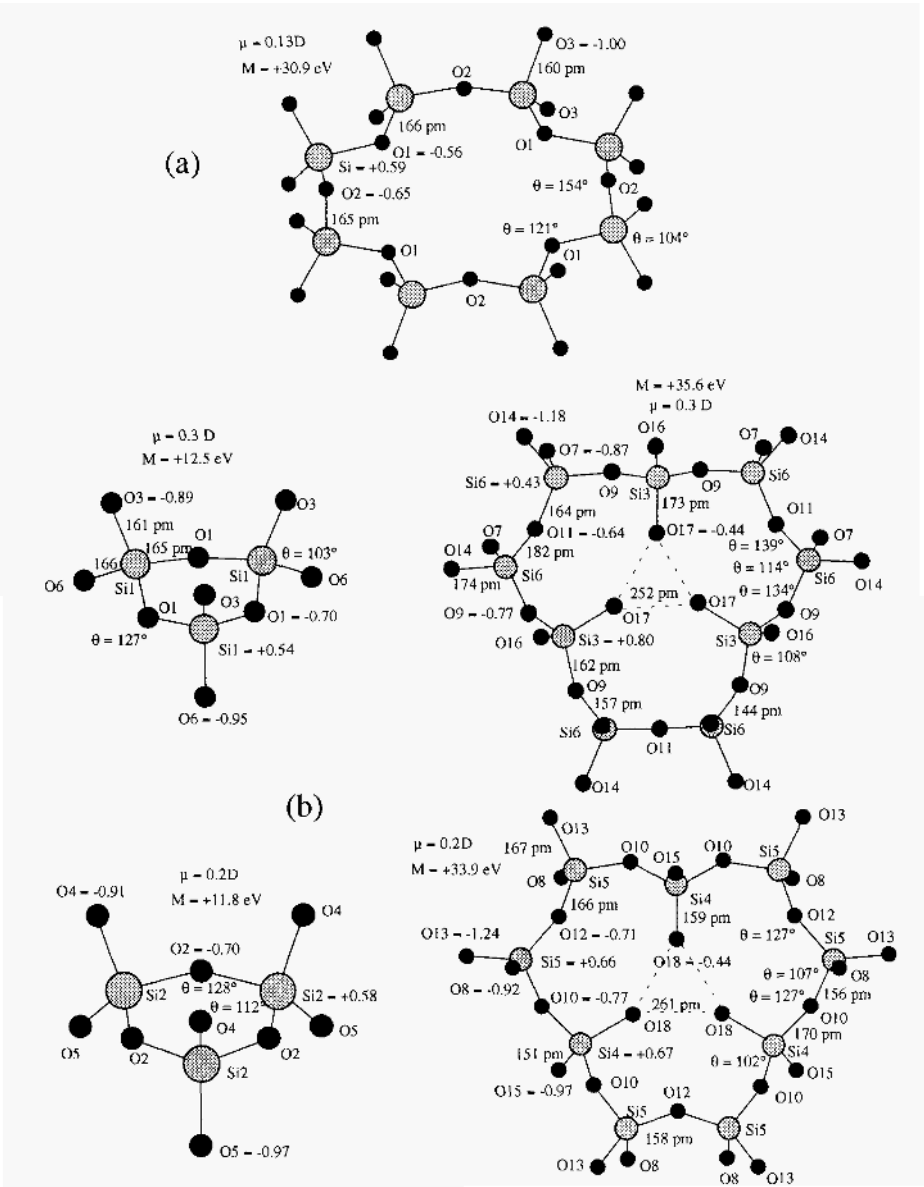

Figure 15. Partial charge distributions in cyclic polysilicates found in minerals. (a) muirite $Ba_{10}(Ca,Mn,Ti)_4Si_8O_{24}(C1,OH,O)_{12}.4H_2O$ (*P4/mmm* with R = 6.5%) and (b) eudialyte. $Na_{12}Ca_6Fe_3Zr_3Si_{24}O_{66}(Cl,OH)_8$ (*R3m* with R = 15%). Charges given are those on the network-extracted oligomers.

$n < 5$, their formation should not be favored for entropic reasons. If we admit that the encounter of four chemical species is statistically improbable and that chains with $n > 5$ cannot be formed, the larger ring that could be obtained should be a dodecamer formed through condensation of three linear tetramers. Thus for different reasons, there are also limitations on the growth a single huge polysilicate ring. Polycyclization leading to cages is however still possible and will be studied right now.

3.5. POLYCYCLIC OLIGOMERS

3.5.1. *Oligomers having the Si_3O_9 ring*

The smallest polycyclic oligomer that can be formed is a tetramer $[Si_4O_{10}]^{4-}$ by capping a Si_3O_9 ring with a SiO_4 monomer (fig. 16a). The resulting arrangement has for the first time a negative Madelung energy and thus does not need counter-cations to be stabilized. Accordingly, such a species has been evidenced in solution through 29Si NMR [44] but have never been observed, to our knowledge, in the solid state associated with a counter-cation. Interestingly, this very compact tetramer that can be viewed as a small portion of a silica network has a very small pK_a gap: pK_a(Oterm) = 7.6 and pK_a(Obridge) = 6.2, which is just the range found for surface silanol groups [176]. The bridging oxygen-atoms are still found to have less electronic density than the terminal ones.

The next possibility is the fusion of two Si_3O_9 rings to form a $[Si_6O1]^{8-}$ prismatic hexamer. Such a species has been isolated in the solid-state using a Ni^{2+}-ethylenediamine (en) complex counter-cations [37]. Figure 16b gives the charge distribution on the network-extracted hexamer. After averaging similar oxygen-atoms, it comes $\langle q(\mathrm{Oterm})\rangle$ = -0.78 (pKa = 9.3) and $\langle q(\mathrm{Obridge})\rangle$ = -0.60 (pK_a = 4.3), i.e. a larger pKa gap (ΔpK_a = 5) compared to the tetrahedral tetramer (ΔpK_a = 1.5). That this species can be crystallized only in the presence of a very large counter-cations having a rather low charge density could be related to the slightly positive value found for the Madelung energy.

3.5.2. *Oligomers having the Si4O12 ring*

By fusing two Si_4O_{12} rings, it is possible to obtain a $[Si_8O_{20}]^{8-}$ cubic octamer. Such a. species has been characterized in the thorium silicate mineral ekanite $ThK(Ca,Na)_2Si_8O_{20}$ [177] and shown in figure 16c. The Madelung energy and the pK_a gap obtained (ΔpK_a = 6.5) are in concordance with what have been observed on going from the tetrahedral tetramer to the prismatic hexamer. Owing to its higher Madelung energy, this anion has been characterized in the solid state in several compounds. Figure 17 shows the charge distributions in four cubic octamers extracted

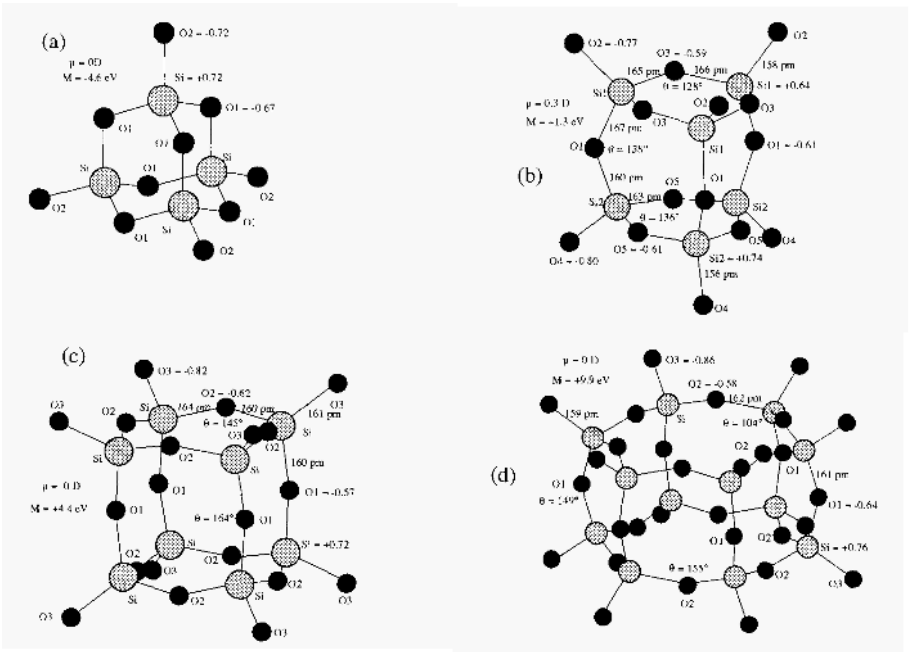

Figure 16. Partial charge distributions in various polycyclic polysilicates. (a) Tetrahedral tetramer of *Td* symmetry $[Si_4O_{10}]^{4-}$. (b) Prismatic hexamer $[Si_6O_{15}]^{6-}$ found in the synthetic compound $[Ni(en)_3]Si_2O_5.8{,}7\ H_2O$ ($P6_3$ with R = 9.1%). (c) Cubic octamer $[Si_8O_{20}]^{8-}$ found in the mineral ekanite $ThK(Ca,Na)_2Si_8\ O_{20}$ (*P4*/*mcc* with R = 5.8%). (d) Prismatic dodecamer $[Si_{12}O_{30}]^{12-}$ found in the mineral milarite $KCa_2(Be_2Al)Si_{12}O_{30}.H_2O$ (*P6*/*mcc* with R = 2.9%).

from silicates synthetized using low charge-density counter-cations such as $[N(CH_3)_4]^+$, $[Cu(en)_2]^{2+}$ or $[Co(en)_3]^{3+}$. The most stable octamer is found in the $[N(CH_3)_4]_8[Si_8O_{20}]$ $64{,}8H_2O$ compound [28] (fig. 17a). In spite of its monoclinic symmetry, this octamer has a very regular partial charge distribution and geometry. Terminal oxygen-atoms have pK_a = 11.2 against 6.0 for bridging atoms leading to ΔpK_a = 5.2. Two octamers have exactly the same Madelung energy in spite of their different space-group symmetry : $[Cu(en)_2]_4[Si_8O_{20}].38H_2O$ [32] (fig. 17b) and $Na[N(CH_3)_4]_7[Si_8O_{20}].54H_2O$ [30] (fig. 17c). Finally, the least stable octamer is found in the clathrate-hydrate type compound $[N(CH_3)_4]_{16}$ $[Si_8O_{20}]$ $[OH]_8.116H_20$ [35] (fig.17d). If we take the average over these five cubic octamers it comes $\langle q(\mathrm{Oterm})\rangle$

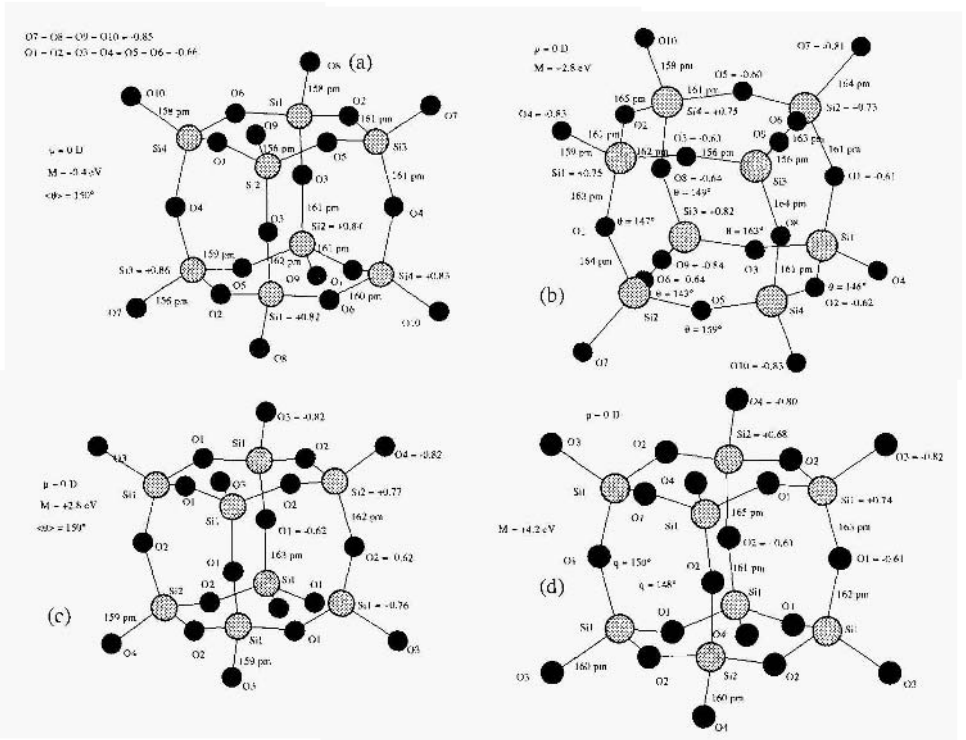

Figure 17. Partial charge distributions in various $[Si_8O_{20}]^{8-}$ cubic octamers from (a) $[N(CH_3)_4]_8Si_8O_{20}.64{,}8\ H_2O$ (Pi with R = 7.3%). (b) $[Cu(en)_2]_4[Si_8O_{20}].38H_2O$ (*P*I with *R* = 8,9%). (c) $Na[N(CH_3)_4]_7[Si_8O_{20}].54H_2O$ (*R*3 with *R* = 7.8%). (d) $[N(CH_3)_4]_{16}[Si_8O_{20}][OH]_8.116H_{2O}$ (*R*3 with *R* = 10.4%).

= -0.83 (pKa = 10.7), $\langle q(\mathrm{Obridge})\rangle$ = -0.63 (pK_a = 5.2), $\langle q(\mathrm{Si})\rangle$ = +0.77 and $\langle M\rangle$ = +2.8 eV. We thus have ΔpK_a = 5.5, a value very similar to that found in the prismatic hexamer. These pKa values agree with the observation that the cubic octamer can be protonated [33]. We have investigated this protonated octamer as the position of the hydrogen-atoms is not reliable in this structure that must then be revised.

Another kind of cage is found in the minerals milarite $kCa_2(AlBe_2)Si_{12}O_{30}.H_2O$ and osumilite $(K,Ca,Na)(Mg,Fe^{2+})_2(Al,Fe^{3+})_3Si_{12}O_{30}.H_2O$. This cage is displayed in figure 16d and can be built by fusing two Si_6O_{18} hexameric rings or alternatively two Si_4O_{12} rings with two Si_2O_7 dimers. A water molecule is apparently trapped inside the cavity, but the positions of the hydrogen-atoms have not yet been determined. Charge distribution

computed from the network-extracted cage [178] shows that it has the highest Madelung energy with the biggest pK_a gap (ΔpK_a= 11.5 - 4.3 = 7.2).

4. Discussion and conclusion

In conclusion we will summarize our results and compare them with literature when possible. Figure 18 shows that a good description of chemical bonding in orthosilicate structures cannot be reached by looking at just one iono-covalent index. For instance the most ionic compounds are found to be $CaMgSiO_4$ and Mg_2SiO_4, which however have not the lowest Madelung energy found for garnets. Similarly the most positively charged silicon atom is found in phenacite and not in olivine or garnet frameworks. Looking at the mean electronegativity of the framework the following order is found : Z > Ph > T > H > P > Li > N > Y > G > F > K > M > L > C > B > S.As a high framework electronegativity means a high refractive index [75], it is not surprising to find in the first places, zircon and phenacite that can both be used as a substitute for diamond in jewelry. To compare our results with other theories, we have to extract the monomers from their network leading to the following averaged value : $\langle q(\mathrm{Oterm})\rangle$ = -1.12, $\langle q(\mathrm{Si})\rangle$ = +0.48 and $\langle M\rangle$ = +18 eV. Recalling that our calibration has been made on accurate X-ray measurements performed on the a-quartz structure, we noticed that these values are very close to those obtained by *ab initio* molecular orbital calculations at the SCF level with configuration interaction and inclusion of silicon *d*-orbitals [52], and to those obtained with the SCF-Xa-SW theory [53].

Concerning the $[Si_2O7]^{6-}$ dimers we have found on average after extraction from the network $\langle q(\mathrm{Oterm})\rangle$ = -1.05, $\langle q(\mathrm{Obridge})\rangle$ = -0.70, $\langle q(\mathrm{Si})\rangle$ = +0.52 and $\langle M\rangle$ = +46 eV. These values are again rather close to those obtained with the SCF-Xa-SW theory, but now without the inclusion of silicon *d*-orbitals [56]. That the Si-O-Si bond angle cannot be less than ca 130° in a $[Si_2O_7]^{6-}$ dimer, has been very simply interpreted as a steric effect between highly negatively charged terminal oxo-groups. Consequently, there is no need to introduce silicon d-orbitals, nor arguments based on π-bonding between oxygen and silicon to explain this experimental fact. Concerning the various conformations observed in the solid-state for this dimer, this is clearly a counter-cation problem that cannot be handled by looking at isolated species in the vacuum.

At a more qualitative level we have found in agreement with ab *initio* methods that bridging oxygen-atoms are systematically less negatively charged (i.e. more acidic) than terminal ones, and that charges at the silicon atoms decreased as the Si-O-Si bond angle was increased. For condensed species we have found, in agreement with the MNDO method [59],

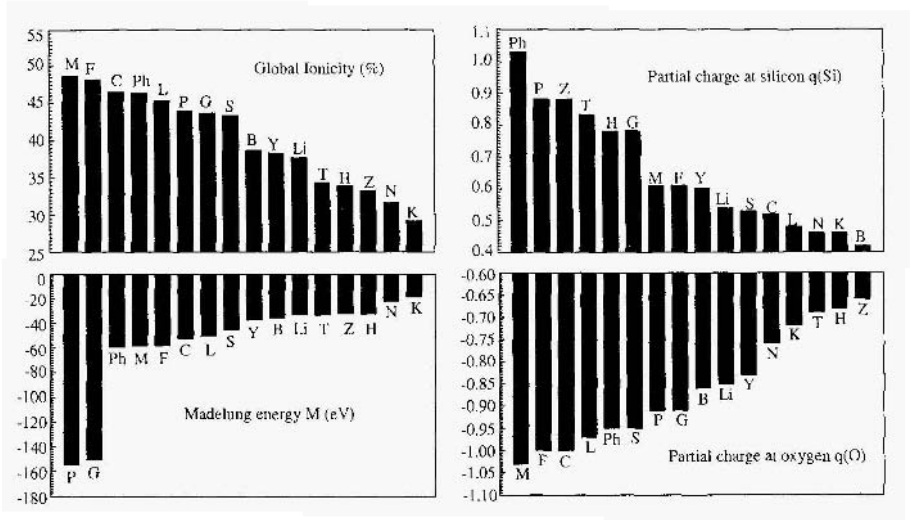

Figure 18. Classification of sixteen orthosilicate structures according to their ionicities, madelung energy and partial charge at oxygen or silicon. Li ≅ Li_4SiO_4, N E Na_4SiO_4, K ≡ K_4SiO_4, F ≅ Forsterite (Mg_2SiO_4), C E γ-Ca_2SiO_4, S ≡ β-Sr_2SiO_4, B ≡ Ba_2SiO_4, L ≅ Larnite (β-Ca_2SiO_4), Ph ≡ Phenacite (Be_2SiO_4), M E Monticellite ($CaMgSiO_4$), Y ≡ ($NaYSiO_4$), P E Pyrope ($Mg_3Al_2Si_3O_{12}$), G ≅ Grossular ($Ca_3Al_2Si_3O_{12}$), Z E Zircon ($ZrSiO_4$), T ≡ Thorite ($ThSiO_4$), H≅ Huttonite ($ThSiO_4$).

that the charge at the silicon atom increases as polycondensation goes on : $q(Q^0) < q(Q^1) < q(Q^2) < q(Q^3) < q(Q^4)$. Figure 19 shows that our mean charges correlate rather nicely with the experimental ^{29}Si solution NMR chemical shifts given in figure 1. The parabolic correlation observed also agrees with semi-empirical calculation of the paramagnetic screening constants of the ^{29}Si nucleus in tetracoordinated silicon compounds [179].

We can thus conclude that our model leads to the same qualitative conclusions as *ab initio* or semi-empirical met hods with incommensurably less computational effort (all the calculations reported here have been done on a 486DX2 personal computer cadenced at 66 MHz under the Windows© environment with 32 Mo RAM). On the other hand it correlates very nicely with experiments and has provided very interesting results not attainable by more sophisticated methods.

i) We can handle in a straightforward manner the crucial problem of the counter-cation, including the association through hydrogen bonding. This should have important implications for the interpretation of chemical shifts and electrical field gradients at the nucleus in solid-state

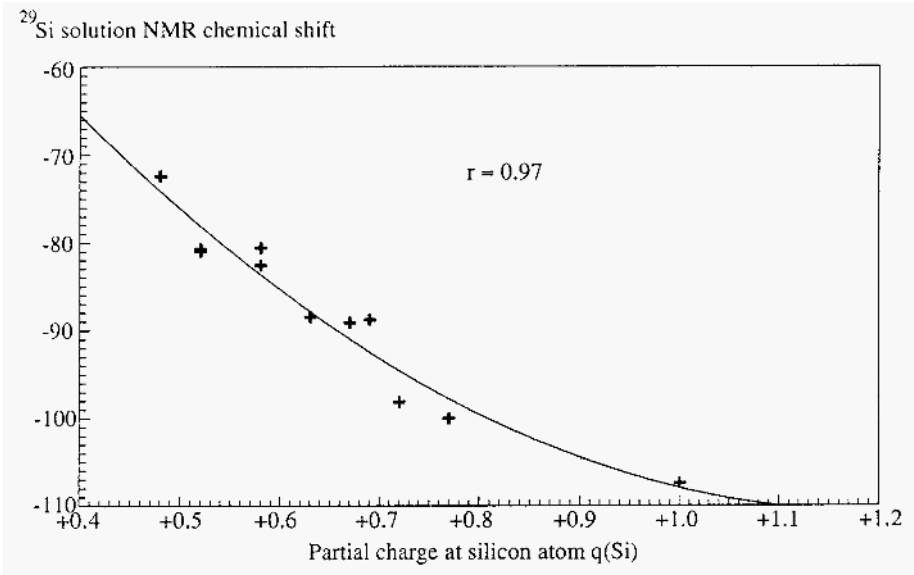

Figure 19. Parabolic variation of the ^{29}Si solution NMR chemical shift, with partial charge at the silicon atom.

NMR. Severe limitations are however expected in the case of solids having disordered atoms, solid-substitutions or ill-defined hydrogen-atoms positions. To have a chance to correlate structural data to solid-state NMR chemical shifts, one must have a refinement factor R less than typically 5%. Even if it is very difficult to fulfill these conditions for most of the silicate minerals, we think that for very well defined structural types and provided that both NMR and X-ray or neutron diffraction measurements have been performed on the same product, good correlations should be observed.

ii) Our model interprets quite satisfactorily most of the important aspects of silica, solution chemistry. Concerning hydrolysis phenomena, it is able to predict the pK_a values of various chemical species. More particularly, the experimental increase of pK_a values on going from the monomer $[SiO_4]^{4-}$ to crystalline SiO_2 has been quantitatively reproduced. Concerning the pK_a gap existing between a terminal oxygen-atom and an oxo-bridge, it was shown that Si-O-Si bridges were much

more acidic than terminal Si-O bonds. Geometry have been proved to have a deep influence on pK_a values. When oxo-bridges and terminal oxygen-atoms are close in space, the ΔpK_a is low and can increase by several units as spatial separation goes on. Occurence of hydrogen bonding can pertub this simple picture, and here again the geometries of the bridges have a deep influence on the pKa values. For condensation reactions, our model has shown that the growth of a long arid single polysilicate chain should occur only in the presence of a stabilizing counter-cation, whose main role is to reduce the negative burden borne by the growing chain. In solution cations are extensively solvated and interact with the oligomers only through much weaker hydrogen bonds. Consequently, chain-growth is stopped at an early stage ($n \leq 4$) and intramolecular cyclization occurs to stabilize the system. The preferential formation of cage-like oligomers in the presence of low charge-density counter-cations has be interpreted in the same lines. In the presence of cations that are well solvated by water molecules (alkaline and alkaline-earth cations), there is no need to form rather stable polycyclic species as hydrogen bonding with surrounding water molecules provides enough stabilization. A complex mixture of rings and linear species is thus obtained whose detailed composition is mainly governed by temperature and silicon concentration. This is no more the case in the presence of low charge-density cations which, owing to their organic shell, are rather hydrophobic. Faced with a more organic, environment that is unable to remove the negative burden put on the polysilicate, the only alternative is to form as much rings as possible. This leads to a strong reduction of the number of terminal oxygen-atoms, and reduces considerably the electrostatic pressure on the polysilicate. In that case, instead of a complex mixture of rings and chains, the system adopts the polycyclic structure which fits to the best extent with the surrounding medium. As the local structure of this latter is highly dependent on the extent of the hydrocarbon chain-length n, it is possible to change the polycyclic silicate shape by playing with the length and/or the geometry of the hydrocarbon chain. This kind of calculations should thus have important consequences in the field of zeolites and microporous materials synthesis. To prepare future work in this field and to underline the generality of this argument we have nicknamed the formation of polycyclic oligomers under the influence of a low charge-density cation the “Yin-Yang effect”. This allows to remember that in the presence of good electron acceptors (naked cations, hydrogen bonds,. . .) the system can be space- expanded revealing its “Yang” face. When the medium is not a good electron acceptor (complexed or hydrophobic cations) the system tends to be space-condensed

revealing its "Yin" face.

iii) Our model should also be of considerable help in crystal structure analysis. It can detect very rapidly and unambiguously an ill-placed atom or any charge unbalance in the structure. Localization of hydrogen bridges is also straighforward, as short O-O contacts leads to rather low oxygen-atom partial charges. Another powerful feature is the possibility of comparing within the same theoretical framework, a small portion of the network to the whole solid phase. It is thus possible to analyze on a quantitative and accurate basis, how a molecule or an ion is affected by a crystalline environment. All we have to look is which atoms have had their partial charge mostly affected by the extraction process. This knowledge could be of considerable help in deciding whether a molecular fragment detected in the solid-state has a chance to exists as such in the mother solution from which crystal growth has occured. Again, this could have very important consequences in the field of microporous materials synthesis.

In conclusion this model appears to be well suited to follow within the same theoretical framework very complex processes such as hydrolysis, condensation, nucleation and growth. It can bring about a quantitative theoretical answer to an experimental problem by looking at what is found in the beaker and not by looking at a model often very far from chemical reality. It is obviously not restricted to silicates and silica and work is in progress to study transition-metal polyoxometallates, phosphate-based solid phases or actinides' solution chemistry. As it allows to go from the molecule to the network, it has been initially tailored for sol-gel chemistry. We think, however, that other fields of materials synthesis could be concerned by such an approach, and quite interesting implications to understand complex geochemical or biological problems are foreseen in a very next future.

References

1. Iler, R.K. (1979) *The chemistry of silica*, John Wiley and Sons, New-York.
2. Dent-Glasser, L.S. and Lachowski, E.E. (1980) Silicate Species in Solution. Part 1. Experimental Observations, *J. Chem. Soc. Dalton Trans,* 393-398.
3. Dent-Glasser, L.S. and Lachowski, E.E. (1980) Silicate Species in Solution. Part 2. The Structure of Oligomeric Species, *J. Chem. Soc. Dalton Trans*, 399-402.
4. Hoebbel, D. and Wieker, W. (1973) On Condensation Reactions of the Monomeric Silicic Acid, *Z. Anorg. Allg. Chemie,* **400**, 148-160.
5. Marsmann, H.C. (1974) ^{29}Si NMR Studies on Aqueous Silicate Solutions, *Z. Naturforsch*., **29B**, 495-499.
6. Engelhardt, G., Zeigan, D., Jancke, H., Hoebbel, D., and Wieker, W. (1975) ^{29}Si-NMR Spectrocopy of Silicate Solutions. II. On the Dependence of the Structure of Silicate Anions in Water Solutions from the Na:Si Ratio, Z. *Anorg. Allg. Chemie*, **418**, 17-28 (1975).

7. Harris, R.K., Jones, J., and Knight, C.T.G. (1980) Silicon-29 NMR Studies of Aqueous Silicate Solutions. Part II. Isotopic Enrichment., *J. Mol. Struct*., **69**,95-103.
8. Harris, R.K., and Newman, R.H. (1977) ^{29}Si NMR Studies of Aqueous Silicate Solutions, *J. Chem. Soc. Faraday Trans*, **73**,1204-1215.
9. Harris, R.K., Knight, C.T.G., and Hull, W.E. (1981) Nature of Species Present in an Aqueous Solution of Potassium Silicate, *J. Am. Chem. Soc* ., **103**,1577-1578.
10. Harris, R.K., Knight, C.T.G., and Hull, W.E. (1982) in J.S. Falcone (ed.), *Soluble ,Silicates, Am. Chem. Soc. Symp. Ser* ., **194**, 79.
11. Harris, R.K., and Knight, C.T.G. (1983) Silicon-29 NMR Studies of Aqueous Silicate Solutions. Part 5.- First-order Patterns in Potassium Silicate Solutions Enriched with Silicon-29, *J. Chem. Soc. Faraday Trans. II,* **79**,1525-1538.
12. Harris, R.K., and Knight, C.T.G. (1983) Silicon-29 NMR Studies of Aqueous Silicate Solutions. Part 6.- Second-order Patterns in Potassium Silicate Solutions Enriched with Silicon-29, *J. Chem. SOC. Faraday Trans. II,* **79**,1539-1561.
13. Harris, R.K., O'Connor, M.J., Curzon, E.H., and Howarth, O.W. (1984) Two-Dimensional Silicon-29 NMR Studies of Aqueous Silicate Solutions, *J. Magn. Reson*., **57**,115-122.
14. Knight, C.T.G. (1988) A Two-dimensional Silicon-29 Nuclear Magnetic Resonance Spectroscopic Study of the Structure of the Silicate Anions present in an Aqueous Potassium Silicate Solution, *J. Chem. Soc. Dalton Trans*., 1457-1460.
15. Knight, C.T.G., Kirkpatrick, R. J., and Oldfield, E. (1989) Silicon-29 Multiple Quantum Filtered N.M.R. Spectroscopic Evidence for the Presence of Only Six Single Site Silicate Anions in a Concentrated Potassium Silicate Solution, *J. Chem. Soc*. *Chem. Commun.,* 919-921.
16. Kinrade, S.D., and Swaddle, T.W. (1988) Silicon-29 NMR Studies of Aqueous Silicate Solutions. 1. Chemical Shifts and Equilibria, *Inorg. Chem*., **27**,4253-4259.
17. Maciel, G.E., and Sindorf, D.W. (1980) Silicon-29 Nuclear Magnetic Resonance Study of the Surface of Silica Gel by Cross Polarization and Magic-Angle Spinning, *J. Am. Chem. Soc.* , **102**,7606-7607.
18. Lippmaa, E., Magi, M., Samoson, A., Engelhadt, G., and Grimmer, A.-R. (1980) Structural Study of Silicates by Solid-state High-Resolution ^{29}Si NMR, *J. Am. Chem. Soc*., **102**,4889-4893.
19. Knight, C.T.G., Thomson, A.R., Kunwar, A.C., Gutowsky, H.S., Oldfield, E., and Kirkpatrick, R. J. (1989) Oxygen-17 Nuclear Magnetic Resonance Spectroscopic Studies of Aqueous Alkaline Silicate Solutions, *J. Chem. Soc. Dalton Trans., 275-281.*
20. *Occelli, M.L., and Robson, H.E.(eds.) (1989) Zeolites Synthesis,* Am. Chem. Soc. Symp. 398, American Chemical Society, Washington DC.
21. Engelhardt, G., and Michel D. (1987) *High-Resolution Solid-state NMR of Silicates and Zeolites,* John Wiley and Sons, pp. 75-105.
22. Hoebbel, D., and Wieker, W. (1971) On the Constitution of Tetramethylammonium Silicates with Composition 1.0 $N(CH_3)_4OH$.1.0 SiO_2. 8.0-8.3 H_2O, *Z. Anorg. Allg. Chemie*, **384**,43-52 (1971).
33. Harris, R.K., and Knight, C.T.G. (1982) Silicon-29 NMR Studies of Aqueous Silicate Solutions. Part, IV. Tetraalkylammonium hydroxide solutions, *J. Mol. Struct.,* **78**,273-278.
24. Hoebbel, D., Garzo, G., Engelhardt, G., and Vargha, A. (1982) On the Condensation and Distribution of Silicate Anions in Aqueous Tetramethylammonium Silicate Solutions, *Z. Anorg. Allg. Chemie,* **494**,31-42.
25. Knight, C.T.G., Kirkpatrick, R.J., and Oldfield, E. (1986) The Unexpectedly Slow Approach to Thermodynamic Equilibrium of the Silicte Anions in Aqueous Tetramethylammonium Silicate Solutions, *J. Chem. Soc. Chem. Commun.* , 66-67.
26. Groenen, E.J.J., Kortbeek, A.G.T.G., Mackay, M., and Sudmeijer, O. (1986) Double-ring silicate anions in tetraalkylammonium hydroxide/silicate solutions; their possible role in the synthesis of silicon-rich zeolites, *Zeolites*, **6**,403-411,

27. Knight, C.T.G. (1989) High-field Silicon-29 Nuclear Magnetic Resonance Spectroscopic Studies of dilute Methanolic Tetramethylammonium Silicate Solutions, *Zeolites*, **9**,448-450.
28. Smolin, Yu.I., Chepelev, Yu.F., Pomec, R., ,Hoebbel, D., and Wieker, W. (1979) Crystal structure determination of the tetramethylammonium silicate 8[N(CH3)4] Si_8 O_{20}.64,8 H_2O à -10O^c*irc*C, *Kristallografia*, **24**,38-44 (1979).
29. Shepelev, Yu.F., Smolin, Yu.I., Ershov, A.S., Rademacher, O., and Scheler, G. (1987) Crystal structure determination of the sodium-tetramethylammonium silicate Na.7[$N(CH_3)_4$]Si_8O_{20}.54H_2O à-12O^c*irc*C, *Kristallografia*, **32**,1399-1403 (1987).
30. Wiebcke, M., and Koller, H. (1992) Single-Crystal X-ray Diffraction and Variable-Temperature MAS NMR Study on the Heterogeneous Network Clathrate Na.7[$N(CH_3)_4$]Si_8O_{20}.54 H_2O, *Acta Cryst.*, **B48**,449-458.
31. Engelhardt, G., and Rademacher, O. (1984) Structure-forming Effects of Cations in Sodium Tetramethylammonium Silicate Solutions. A Silicon-29 NMR Study, *J. Molecular Liquids,* **27**,125-131.
32. Smolin, Yu. I., Shepelev, Yu.F., and Boutikova, I.K. (1972) Crystal structure determination of 4[CU($NH_2CH_2CH_2NH_2)_2$].Si_8O_{20}.38 H_2O, *Kristallografiya*, **17**,15-21 (1972).
33. Smolin,
Yu. I., Shepelev, Yu.F., Pomec, R., Hoebbel, D., and Wieker, W. (1975) Silicate complex [$Si_8O_{18}(OH)_2$] in the crystal 2[$Co(NH_2CH_2CH_2NH_2)_3$].$Si_8O_{18}(OH)_2$.16,4 H_2O, *Kristallografiya*, **20**,917-924 (1975).
34. Hoebbel, D., and Wieker, W. (1974) On the Constitution of a Silicate with the Anion $[Si_7O_{19}]^{10-}$, *Z. Anorg. Allg. Chemie*, **405**,267-274.
35. Wiebcke, M., and Hoebbel, D. (1992) Structural Links between Zeolite-type and Clathrate Hydrate-type Materials : Synthesis and Crystal Structure of $[NMe_4]_{16}[Si_8O_{20}][OH]_8.116H_2O$, *J. Chem. Soc. Dalton Trans.*, 2451-2455.
36. Hoebbel, D., Garzo, G., Engelhardt,, G., Ebert, R., Lippmaa, E., and Alla, M. (1980) On the Constitution of Silicate Anions in Tetraethylammonium Silicates and their Aqueous Solutions, *Z. Anorg. Allg. Chemie*, **465**,15-33.
37. Smolin, Yu. I. (1970) New silicate complex Si6O15 in the crystal [Ni(en)3]Si2O5. 8,7 H_2O, *Kristallografiya*, **15**,31-37.
38. Hoebbel, D., Vargha, A., Engelhardt, G., and Ujszasky, K. (1984) On the Anion Constitution of Tetrabutylammonium Silicates and their Aqueous Solutions, *Z. Anorg. Allg. Chemie*, **509**,85-94.
39. Hoebbel, D., Wieker, Franke, W.P., and Otto, A. (1975) On the Constitution of the New Silicate Anion $[Si_{10}O_{25}]^{10-}$, *Z. Anorg. Allg. Chemie*, **418**,35-44.
40. Engelhardt, G., and Hoebbel, D. (1984) ^{29}Si N.M.R. Spectroscopy reveals Dynamic SiO_4 4- Group Exchange between Silicate Anions in Aqueous Alkaline Silicate Solutions, *J. Chem. Soc., Chem. Commun.,* 514-516.
41. Harris, R.K., Jones, J., Knight, C.T.G., and Newman, R.H. (1984) Silicon-29 NMR Studies of Aqueous Silicate Solutions. Part 7 : Exchange Rates between Anions, *J. Molecular Liquids,* **29**,63-74.
42. Creswell, C.J., Harris, R.K., and Jageland, P.T. (1984) Exchange Rates between Silicate Anions in Alkaline Aqueous Solutions, *J. Chem. Soc., Chem. Commun.*, 1261-1263.
43. Knight, C.T.G., Kirkpatrick, R. J., and Oldfield, E. (1988) Two-Dimensional Silicon-29 Nuclear Magnetic Resonance Study of Chemical Exchange Pathways in Potassium Silicate Solutions, *J. Magn. Reson.,* **78**,3 1-40.
44. Kinrade, S.D., and Swaddle, T.W. (1988) Silicon-29 NMR Studies of Aqueous Silicate Solutions. 2. Transverse ^{29}Si Relaxation and the Kinetics and Mechanism of Silicate Polymerization, *Inorg. Chem.,* **27**,4259-4264.
45. Koller, H., Engelhardt, G., and Felsche, J. (1990) ^{29}Si NMR Studies of the Transformation of Silicate Anions in the System $Na_2O.SiO_2.nH_2O$ (n = 9, 5) in Crystals, melts and Solution, *J. Chem. Soc., Chem. Commun.,* 371-372.

46. Tossell, J.A. (1973) Molecular Orbital Interpretation of X-ray Emission and ESCA Spectral Shifts in Silicates, *J. Phys. Chem. Solids,* **34**,307-319.
47. Collins, G.A.D., Cruickshank, D.W.J., and Breeze, A. (1972) Ab Initio Calculations on the Silicate ion, Orthosilicic Acid and their L2,3 X-ray Spectra, *J. Chem. Soc. Faraday Trans. II,* **68**,1189-1195.
48. Wyckoff, R.W.G. (1968) *Crystal Structures Second edition, Vol.4,* John Wiley and Sons, New-York, pp.157-215.
49. Handke, M. (1984) Force Constants and Chemical bond Character in (SiO_4) and (GeO_4) Anions in Orthosilicates and Orthogermanates, *J. Molecular Structure,* **114**,187-190.
50. Fujino, K., Sasaki, S., Takéuchi, Y., and Sadanaga, R. (1981) X-ray Determination of Electron Distributions in Forsterite, Fayalite and Tephroite, *Acta Cryst.,* **B37**, 513-518.
51. Tamada, O., Fujino, K. and Sasaki, S. (1983) Structures and Electron Distributions of α-Co_2SiO_4 and α-Ni_2SiO_4 (Olivine Structure), *Acta Cryst.,* **B39**,692-697.
52. Julg, A,, Ozias, Y., and Pellegatti, A. (1985) An *Ab Initio*-C.I. Comparative Study of some First and Second Row Tetraoxy-ions, New. *J. Chem.,* **9**,675-680.
53. Tossell, J.A. (1975) The Electronic Structures of Silicon, Aluminum, and Magnesium in Tetrahedral Coordination with Oxygen from SCF-Xa MO Calculations, *J. Am. Chem. Soc.,* **97**,4840-4844.
54. Sauer, J. (1983) Molecular Structure of Orthosilicic Acid and Importance of $(p-d)\pi$ Bonding. An Ab Initio Molecular Orbital Study, *Chem. Phys. Letts.,* **97**,275-278.
55. Uchino, T., Sakka, T., Ogata, Y., and Iwasaki, M. (1992) Changes in the Structure of Alkali-Metal Silicate Glasses with the type of Network Modifer Cation : An ab initio Molecular Orbital Study, *J. Phys. Chem.,* **96**,2455-2463.
56. Lopez, J.P., Yang, C.Y., and Helms, C.R. (1987) Electronic Structure of Clusters Modeling Silica, *J. Comput. Chem.,* **8**,198-203 (1987).
57. Wolff, R., Radeglia, R., and Sauer, J. (1986) Charge Differences between silicon Atoms in Aluminosilicates and their Relation to ^{29}Si NMR Chemical Shofts. A Quantum-mechanical Study, *J. Molecular Structure,* **139**,113-124.
58. Clark, T. (1985) *A Handbook of Computational Chemistry,* John Wiley and Sons, New York.
59. Mortlock, R.F., Bell, A.T., Chakraborty, A.K., and Radke, C.J. (1991) Effect of Silicate Ratio on the Distribution of Silicate and Aluminosilicate Anions in TPA Aluminosilicate Solutions, *J. Phys. Chem.,* **95**,4501-4506.
60. Hehre, W.J., Radom, L., Schleyer, P., and Pople, J.A. (1986) *Ab Initio Molecular Orbital Theory,* Wiley-Interscience, New-York, pp. 336-341 (1986).
61. Oberhammer, H., and Boggs, J.E. (1980) Importance of (p - $d)\pi$ Bonding in the Siloxane Bond, *J. Am. Chem. Soc.,* **102**,7241-7244.
62. Ernst, C.A., Allred, A.L., Ratner, M.A., Newton, M.D., Gibbs, G.V., Moskowitz, J.W., and Topiol, S. (1981) Bond Angles in Disiloxane : A Pseudo-Potential Electronic Structure Study, *Chem. Phys. Letts.,* **81**,424-429.
63. Janes, N., and Oldfield, E. (1986) Oxygen-17 NMR study of Bonding in Silicates : The d-Orbital Controversy, *J. Am. Chem. Soc.,* **108**,5743-5753.
64. Pritchard, H.O., and Skinner, H.A. (1955) The Concept of Electronegativity, *Chem.* Revs.,**55**,745-786.
65. Batsanov, S.S. (1968) The Concept of Electronegativity : Conclusions and Prospects, *Russ. Chem. Revs,* **37**,332-351.
66. Parr, R.G., Donnelly, R.A., Levy, M., and Palke, W.E. (1978) Electronegativity : The density functional viewpoint, *J. Chem. Phys.* **68**,3801-3807.
67. Parr, R.G. and Pearson, R.G. (1983) Absolute Hardness : Companion Parameter to Absolute Electronegativity, *J. Am. Chem. Soc.,* **105**,7512-7516.
68. Sen, K.D., and Jorgensen, C.K. (1987) *Electronegativity, Structure and Bonding, 66,* Springer-Verlag, Berlin, Heidelberg.
69. Pearson, R.G. (1993) *Chemical Hardness, Structure and Bonding, 80, Springer-*

Verlag, Berlin, Heidelberg (1993).
70. Pearson, R.G. (1991) Density Functional Theory : Electronegativity and Hardness, *Chemtracts Inorg. Chem.*,**3**,317-333.
71. Davis, D.W., Shirley, D.A., and Thomas, T.D. (1972) X-Ray Photoelectron spectroscopy of Fluorinated Benzenes, *J. Am. Chem. Soc.,* **94**,6565-6575.
72. Pearson, R.G. (1985) Absolute Electronegativity and Absolute Hardness of Lewis Acids and Bases, *J. Am. Chem. Soc.,* **107**,6801-6806.
73. Mortier, W.J., Ghosh, S.K., and Shankar, S. (1986) Electronegativity Equalization Method for the Calculation of Atomic Charges in Molecules, *J. Am. Chem. Soc.,* **108**,43 15-4320.
74. Parry, D.E. (1974) Determination of Atomic Partial Charges using X-ray Photoelectron Spectroscopy : Application to Crystalline Solids, *J. Chem. Soc. Faraday Trans. 2,* **70**,337-345.
75. van Genechten, K.A.,, Mortier, W.J. and Geerlings, P. (1987) Framework Electronegativity : a Novel Concept in Solid-state Chemistry, *J. Chem. Phys.,* **86**,5063-5071.
76. van Genechten, K.A., and Mortier, W.J. (1988) Influence of the Structure Type on the Intrinsic Framework Electronegativity and the Charge Distribution in Zeolites with SiO_2 Composition, *Zeolites,* **8**,273-283.
77. Henry, M., Jolivet, J.P., and Livage, J. (1992) Aqueous Chemistry of Metal Cations : Hydrolysis. Condensation and Complexation, in *Chemistry, Spectroscopy and Applications of Sol- Gel Glasses, Structure and Bonding,* **77**,153-207.
78. Henry, M., and Merceron, T. (1994) An Independent Method for Data Selection of Long-Life Radionuclides (Actinides and Fission Products) in the Geosphere, *Radiochimica Acta.,* **M25**,1-5 (1994).
79. Henry, M., and Taulelle, F. (1994) The use of the Partial Charge Model and Multinuclear NMR Techniques in Aqueous Chemistry, in P. Colombet and A.R. Grimmer (eds.), in *Applications of NMR Spectroscopy to Cement Science,* Gordon and Breach Science Pub., Switzerland, Chap. V, pp. 361-402.
80. Henry, M. (1994) Partial Charge Distributions in Crystalline Materials through Electronegativity Equalization, in J. Rouxel, M. Tournoux and R. Brec (eds.), *in Soft Chemistry Routes to New Materials-Chimie Douce,* Mater. Sci. Forum, pp. 152-153, 355-358.
81. Gérardin, C., Henry, M., and Taulelle, F. (1993) Evaluation of Chemical Shifts in Solid-state NMR by Electronegativity Equalization Principle, in J.A. Tossell (ed.), *in Nuclear Magnetic Shieldings and Molecular Structure,* NATO-AS1 Series C, 386, 566, Kluwer, Dordrecht.
82. Bertaut, F. (1952) The Electrostatic Energy of Ionic Networks, *J. Phys. Rad.,* **13**,499-505.
83. Jones, R.E., and Templeton, D.H. (1956) Optimum Atomic Shape for Bertaut Series, *J. Chem. Pkys.,* **34**,1062-1063 .
84. Fischer, R., and Ludwiczek, H. (1975) Computer Programs for the Calculation of Madelung Constants and their Recalculation for Spinel Type, *Monatsh. Chem.,* **106**,223-228.
85. Press, W.H., Tenkolsky, S.A., Vetterling, W.T., and Flannery, B.P. (1992) *Numerical Recipes in C, the Art of Scientific Computing, second edition,* Cambridge University Press, Cambridge, pp.32-105,
86. Bratsch, S.G. (1988) Revised Mulliken Electronegativities, *J. Chem. Educ.,* **65**,34-41.
87. Basch, H., Viste, A., and Gray, H.B. (1965) Valence Orbital Ionization Potentials from Atomic Spectral Data, *Theoret. Chim. Acta (Berl.),* **3**,458-464.
88. Gasquez, J.L., and Ortiz, E. (1984) Electronegativities and hardnesses of open shell atoms, *J. Chem. Phya.,* **81**,2741-2748.
89. Komorowski, L. (1987) Empirical Evaluation of Chemical Hardness, *Chem. Phys. Letts.,* **134**,536-540.

90. Quane, D. (1970) Crystal Lattice Energy and the Madelung Constant,, *J. Chem. Educ.,* **47**,396-398,
91. Wells, A.F. (1984) *Structural Inorganic Chemistry 5th edition*. Clarendon Press, Oxford, pp.1004-1009.
92. Le Page, Y., and Donnay, G. (1971) Refinement of the crystal structure of low-quartz, *Acta Cryst.,* **B32**,2456-2459.
93. Stewart,, R.F., Whitehead, M.A., and Donnay, G. (1980) The Ionicity of the Si-O bond in low-quartz, *American Mineralogist,* **65**,324-326.
94. Sutton, L. (1958, 1965) *Tables of Interatomic Distances and Configurations in Molecules and Ions, Spec. Publ. n° 11 and 18.* The Chemical Society, London.
95. Radelia, R., and Engelhardt, G. (1985) Correlation of Si-O-T (T = Si or Al) Angles and ^{29}Si Chemical Shifts in Silicates and Aluminosilicates. Interpretation by Semi-Empirical Quantum-Chemical Considerations, *Chem. Phys. Letters,* **114**,28-30.
96. Magnusson, E. (1984) sp Hybridization Reconsidered : The Composition of Orbitals in Main-Group Hydrides, *J. Am. Chem. Soc.,* **106**,1177-1191 (1984).
97. Levien, L., Prewitt, C.T., and Weidner, D.J. (1980) Structure and Elastic properties of quartz at pressure, *American Mineralogist,* **65**,920-930.
98. Ogata, K., Takeuchi, Y., and Kudoh, Y. (1987) Structure of alpha-quartz as a Function of Temperature and Pressure, *Z. Krist.,* **179**,403-413, (1987)
99. Lager, G.A., Jorgensen, J.D., and Rotella, F.J. (1982) Crystal structure and thermal expansion of alpha-quartz SiO_2 at low temperature, *J. Appl. Phys.,* **53**,6751-6756.
100. Will, G., Bellotto, M., Parrish, W., and Hart, M. (1988) Crystal structure of quartz and magnesium germanate by profile analysis of synchrotron-radiation high-resolution powder data, *J. Appl. Cryst.,* **21**,182-191.
101. Pauling, L. (1967) *The Chemical Bond,* Cornell University Press, London, pp. 69-73.
102. Geisinger, K.L., Spackman, M.A. and Gibbs, G.V. (1987) Exploration of structure, electron density distribution, and bonding in coesite with Fourier and pseudoatom refinement methods using single-crystal X-ray diffraction data, *J. Phys. Chem.,* **91**,3237-3244 (1987).
103. Gibbs, G.V., and Hill, R.J. (1978) Net charge distributions and radial dependence of the valence electrons on the Si and 0 atoms in coesite, *GAC/MAC Abstracts with Programs,* **10**,407 (1978).
104. Levien, L., and Prewitt, C.T. (1981) High-pressure crystal structure and compressibility of coesite, *Amer. Min.,* **66**,324-333 (1981).
105. Smyth, J.R., Smith, J.V., Artioli, G., and Kvick, Å (1987) Crystal structure of coesite, a high-pressure form of SiO_2, at 15 and 298K from single-crystal neutron and X-ray diffraction data : test of bonding models, *J. Phys. Ckem.,* **91**,988-992 (1987).
106. Gibbs, G.V., Prewitt, C.T., and Baldwin, K.J. (1977) A study of the crystal chemistry of coesite, *Z. Krist.,* **145**,108-123 (1977).
107. Hill, R.J., Newton, M.D., and Gibbs, G.V. (1983) A crystal chemical study of stishovite, *J. Solid State Chem.,* **47**,185-200 (1983).
108. Spackman, M.A., Hill, R.J. and Gibbs, G.V. (1987) Exploration of structure and bonding in stishovite with Fourier and pseudoatom refinement methods using single-crystal and powder X-ray diffraction data, *Phys. Chem. Miner.,* **14**,139-150 (1987).
109. Sugiyama, M., Endo, S., and Koto, K. (1987) The crystal structure of stishovite under pressure up to 6 GPa, *Mineralogical Journal,* **13**,455-466 (1987).
110. Sinclair, W., and Ringwood, A.E. (1978) Single crystal analysis of the structure of stishovite, *Nature,* **272**,714-715 (1978).
111. Janz, G.J. and Tomkins, R.P.T.. (1972) *Non-aqueous electrolytes handbook,* Academic Press, New-York, pp. 215.
112. Ricci, J.E. (1948) The aqueous ionization constants of inorganic oxygen acids, *J. Am. Chem. soc.,* **70**,109-113 (1948).

113. Yoon, R.H., Salman, T., and Donnay, G. (1979) Predicting points of zero charge of oxides and hydroxides, *J. Colloid Interface Sci.,* **70**,483-493 (1979).
114. Jorgensen, C.K. (1963) *Inorganic Complexes,* Academic Press, London, p.25.
115. Nordlander, J.E., Bond IV, A.F., and Bader, M. (1985) ATCOOR : A program for calculation and utilization of molecular atomic coordinates from bond parameters, *Computers and Chemistry,* **9**,209-235 (1985).
116. S. Sjöberg, Ohman, L.O., and Ingri, N. (1985) Equilibrium and Structural Studies of Silicon(IV) and Aluminium(III) in Aqueous Solutions. 11. Polysilicate Formation in Alkaline Aqueous Solutions. A Combined Potentiometric and ^{29}Si NMR Study, *Acta Chem. Scand.,* **A39**,93-107.
117. Bernet, K., and Hoppe, R. (1990) Crystal Structure of K_4SiO_4, *Z. Anorg. Allg. Chem.,* **589**,129-138.
118. Baur, W.H., Halwax, E., and Voellenke, H. (1986) Comparison of the crystal structures of sodium orthosilicate Na_4SiO_4 and sodium orthogermanate Na_4GeO_4, *Monatsh. Chem.,* **117**,793-797 (1986).
119. Tranqui, D. Shannon, R.D., Chen, H.Y., Iijima, S., and Baur, W.H. (1979) Crystal structure of ordered Li_4SiO_4, *Acta Cryst.,* **B35**,2479-2487.
120. Fujino, K., Sasaki, S., Takéuchi, Y., and Sadanaga, R. (1981) X-ray determination of electron distributions in forsterite, fayalite and tephroite, *Acta Cryst.,* **B37**,513-518 (1981).
121. Van der Wal, R.J., Vos, A., and Kirfel, A. (1987) Conflicting results for the deformation of Forsterite, *Acta Cryst.,* **B43**,132-143 (1987).
122. Czaya, R. (1971) Refinement of the structure of *gamma*-Ca2SiO4, *Acta Cryst.,* **B27**,848-849 (1971).
123. Catti, M., Gazzoni, G., and Ivaldi, G. (1983) Structures of twinned β-Sr_2SiO_4 and of $Sr_{1.9}Ba_{0.1}SiO_4$, *Acta Cryst,* **C39**,29-34 (1983).
124. Grosse, H.P., and Tillmanns, E. (1974) Barium orthosilicate Ba_2SiO_4, *Cryst. Struct. Comm.,* **3**,599-601 (1974).
125. Jost, K.H., Ziemer, B., and Seydel, R. (1977) Redetermination of the structure of β-dicalcium silicate, *Acta Cryst.,* **B33**,1696-1700 (1977).
126. Downs, J.W., and Gibbs, G.V. (1987) An exploratory examination of the electron density and electrostatic potential of phenakite, *American Mineralogist,* 72,769-777.
127. Zachariasen, W.H. (1971) Refined crystal structure of Phenacite Be_2SiO_4, *Kristallografiya,* **16**,1161-1166.
128. Onken, H. (1965) Refinement of the crystal structure of monticellite, *Tscher. Mineral. Petrog. Mitt.,* **10**,34-44 (1965).
129. Merinov, B.V., Maksimov, B.A., Ilyukhin, V.V., and Belov, N.V. (1979) The refinement of the crystal structure of Na,Y-orthosilicate NaYSiO4, *Dokl. Acad. Nauk. SSSR* ,**248**,1108-1111.
130. Nikolsky, Y.V. (1976) The crystal structure of LiYSiO4, *Dokl. Acad. Nauk. SSSR,* **230**,331-333.
131. Sawada, H. (1993) The crystal structure of garnets(I) : the residual electron density in pyrope, *Z. Krist.,* **203**,41-48.
132. Hazen, R.M., and Finger, L.W. (1978) Crystal structures and compressibilities of pyrope and grossular up to 60 kbar, *American Mineralogist,* **63**,297-303 (1978).
133. Finger, L.W. (1974) Refinement of the crystal structure of zircon, *Carnegie Inst. Washington Yearbook,* **73**,544-547.
134. Fuhrmann, J., and Pickardt, J. (1986) On the formation of $HfSiO_4$ single crystals by chemical transport reactions, *Z. Anorg. Allg. Chem.,* **532**,171-174.
135. Taylor, M., and Ewing, R.C. (1978) The crystal structure of the $ThSiO_4$ polymorphs : huttonite and thorite, *Acta Cryst.,* **B34**,1074-1079.
136. Schmid, R.L., Felsche, J., and McIntyre, G.J. (1984) Location and anisotropic refinement of deuterium atoms in deuterium sodium silicate-deuterium oxide (1/8) $Na_2D_2SiO_4.8D_2O$ by neutron diffraction; hydrogen bonding at 173K, *Acta Cryst.,* **C40**,733-736.

137. Smolin, Yu. I., Shepelev, Yu. F., and Butikova, I.K. (1973) Crystal structure determination of a sodium silicate hydrate $Na_3HSiO_4.5\ H_2O$, Kristallografiya,**18**,281-386.
138. Schmid, R.L., Szolnai, L., Felshe, J., and Huttner, G. (1981) The structure of trisodium hydrogensilicate dihydrate : high-temperature form, *Acta Crys t.* , **B37**,789-792.
139. Shannon, R.D. (1976) Revised effective ionic radii and systematic studies of interatomic distances in halides and chalcogenides, *Acta Cryst.,* **A32**,751-767.
140. Glasser, L.S.D., and Jamieson, P.B. (1976) Sodium silicate hydrates. V. The crystal structure of $Na_2O.SiO_2,(H_2O)$, *Acta Cryst.,***B32**,705-710.
141. Williams, P.P., and Glasser, L.S.D. (1971) Sodium silicate hydrates. IV. Location of hydrogen atoms in $(Na_2O)(SiO_2)(H2O)_6$ by neutron diffraction, *Acta Cryst.,* **B27**,2269-2275.
142. Bianchi, R., Pilati, T., Diella, V., Gamaccioli, C.M., and Mannucci, G. (1988) A re-examination of t hor tveitite, *American Mineralogist*, **73** ,60 1-607.
143. Smolin, Yu.I., and Shepelev, Yu. F. (1968) Structure determination of erbium pyrosilicate, *Izvs. Akad. Nauk SSSR, Neorg. Mater.,* **4**,1133-1136.
144. Smolin, Yu.I., Shepelev, Yu.F., and Butikova, I.K. (1971) Crystal structure of ytterbium Pyrosilicate, *Zhur. Struk. Khim.,* **12**,272-276.
145. Smolin, Yu.I., and Shepelev, Yu. F. (1967) The determination of the structure of gadolinium pyrosilicate, *Izvs. Akad. Nauk SSSR, Neorg. Mater.,* **3**,1034-1038.
146. Dias, H.W., Glasser, F.P., Gurwardane, R.P., and Howie, R.A. (1990) The crystal structure of 6-yttrium pyrosilicate, *Z. Krist.,* **191**,117-123.
147. Kitama, M., and Li, N. (1981) The crystal structure of synthetic akermanite, $Ca_2MgSi_2O_7$, *Neues Jb. Miner.,*1-10 (1981).
148. Smolin, Yu.I., Shepelev, Yu.F., and Butikova, I.K. (1970) The crystal structure of the low-temperature form of samarium pyrosilicate, *Kristallografiya,* **15**,256-261.
149. Voellenkle, H., Wittmann, A., and Nowotny, H. (1969) The crystal structure of the compound $Li_6Si_2\ O_7$, *Monatsh. Chem.,* **100**,295-303.
150. Saburi, S., Kusachi, I.,Henmi, C., Kawahara, A., and Kawada, I. (1976) Refinement of the structure of rankinite, *Mineralogical Journal*, **8,** 240-246.
151. Janczak, J., Kubiak, K., and Glowiak, T. (1990) Structure of barium copper pyrosilicate at 300K, *Acta Cryst.* , **C46**,1383- 1385.
152. Robinson, P.D., and Fang, J.H. (1977) Barylite, $BaBe_2Si_2O_7$: its space group and crystal structure, *American Mineralogist,* **62**,167-169.
153. Kouznetsova, T.P., Nevskii, N.N., Ilioukhine, V.V., and Belov, N.V. (1980) Crystal structure determination of a Na,Ca-triorthosilicate $Na_2Ca_3[Si_3O_{10}]$, *Kristallografiya,* **25**,855-857.
154. Taylor, H.F.W. (1971) The crystal structure of Kilchoanite, $Ca_6(SiO_4)(Si_3O_{10})$, with some comments on related phases, *Mineralogical Magazine,* **38**,26-31.
155. Heidebrecht, K., and Jansen, M. (1991) $Ag_{18}(SiO_4)_2(Si_4O_{13})$, the first silver silicate with mixed anions, *Z. Anorg. Allg. Chem.,* **597**,79-86, (1991);606,242.
156. Fisher, K. (1969) Crystal structure determination of benitoite $BaTi(Si_3O_9)$, *Z. Krist.,***129**,232-243.
157. Wyckoff, R.W.G. (1968) *Crystal Structures, ,Second edition, Vol. 4,* Interscience Publishers, New-York, pp. 265-266,
158. Blinov, V.A., Shumyatskaya, N.G., Voronkov, A.A., Ilyukhin, V.V., and Belov, N.V. (1977) Refinement of the crystal structure of wadeite $K_2Zr(Si_3O_9)$ and its relation to kindred structural types, *Kristallografiya,* **22**,59-65.
159. Hassan, I., and Grundy,, H.D. (1991) The crystal structure and thermal expansion of tugtupite $Na_8(Al_2Be_2Si_8\ O_{24})Cl_2$, *Canadian Minerologist,* **29**,385-390.
160. Rumanova, I.M., Volodina, G.F., and Belov, N.V. (1966) Crystal structure of the rare-earth ring silicate kainosite, *Kristallografiya,* **11**,549.
161. Janczak, J., and Kubiak, R. (1992) Structure of cyclic barium copper silicate $Ba_2Cu_2[Si_4O_{12}]$ at 300 K, *Acta Cryst.,* **C48**,8-10.
163. Groat, L.A., and Hawthorne, F.C. (1987) Refinement of the Structure of Papagoite,

$CaCuAlSi_2O_6(OH)_3$, *Mineral. Petrol.***37**,89-96.
163. Hilmer, W. (1965) The crystal structure of potassium acid metasilicate K4 $(HSiO_3)_4$, *Acta Cryst.,***17**,1063-1066, (1964);**18**,574.
164. Takeuchi, Y., Ozawa, T., Ito, T., Araki, T., Zoltai, T., and Finney, J.J. (1974, 1975) The $B_2Si_8O_{30}$ groups of tetrahedra in axinite and comments on the deformation of Si tetrahedra in silicates, *Z. Krist.,* **140, 289-312**, (1974),**141,471-472.**
165. Mazzi, F., and Rossi, G. (1980) The crystal structure of taramellite, *American Mineralogist,* **65**,123-128 (1980).
166. Morosin, B. (1972) Structure and thermal expansion of Beryl, *Acta Cryst.,* **B28**,1899- 1903.
167. Peyronel, G. (1956) The crystal structure of Baveno Bazzite, *Acta Cryst.,***9**,181-186.
168. Buerger, M.J., Burnham, C.W., and Peacor, D.R. (1962) Assessment of the several structures proposed for tourmaline, *Acta Cryst.,***15**,583-590.
169. Barton Jr., R. (1969) Refinement of the crystal structure of Buergerite and the absolute orientation of tourmalines, *Acta Cryst.,***B25**,1524-1533.
170. Belov, N.V., Maksimov, B.A., Nozik, Y.Z., and Muradyan, L.A. (1978) The refinement of the crystal structure of dioptase $Cu_6(Si_6O_{18})$ $(H_2O)_6$ by the X-ray and neutron diffraction methods, *Doklady Akademii Nauk SSSR,* **239**,842-845.
171. Breuer, K.-H.,Eysel. W., and Muller, R. (1989) Structural and chemical varieties of dioptase $Cu_6[Si_6O_{18}].6H_2O$. II Structural properties, *Z. Krist.,*187,15-23.
172. Ilyukhin, V.V., and Belov, N.V. (1960) The crystal structure of Lovozerite, *Doklady Akademii Nauk SSSR,* **131**,176-179.
173. Chernitsova, N.M., Pudovkina Z.V., Voronkov, A.A., Ilyukhin, V.V., and Pyatenko, Y.A. (1980) Imandrite $Na_{12}Ca_3Fe_2(Si_6O_{18})_2$ - a representative of a new branch in the lovozerite structural family, *Doklady Akademii Nauk SSSR,* **252**,618-621.
174. Khan, A.A., and Baur, W.H. (1971) Eight-Membered Cyclosilicate Rings in Muirite, *Science,* **173**,916-918.
175. Golyshev, V.M., Simonov, V.I., and Belov, N.V. (1971) Crystal Structure of Eudialite, *Kristallografiya,* **16**,93-98.
176. Gatehouse, B.M., Guddat, L.W., and Roth, R.S. (1987) *J. Solid State Chem.,* **71**,390-395.
177. Richard, P., and Perrault, G. (1972) Structure cristalline de I'ekanite de St-Hilaire, *Acta Cryst.,* **28**,1994-1999.
178. Hawthorne, F.C., Kimata, M., Cerny, P., Ball, N., Rossman, G.R., and Grice, J.D. (1991) The crystal chemistry of the milarite-group minerals, *American Mineralogist,* **76**,1836-1856.
179. Engelhardt, G., and Michel, D. (1987) *High-Resolution Solid-state NMR of Silicates and Zeolites,* John Wiley and Sons, New-York, pp. 122-134.

INDEX

$Ag_6Si_2O_7$, 310
$Al_2Be_3(SiO_3)_6$ beryl
  interatomic distance, 308
  Madelung energy, 308
  mean electronegativity, 308
  partial charge distribution, 315
$Al_2Be_3(SiO_4)_6$ beryl, 314
Al_2O_3 corundum, 94
  bulk modulus, 95
  Rh_2O_3 phase transition, 95,97
  structure, 97
Al_2O_3 Rh_2O_3
  bulk modulus, 97
Al-O-Al bond, 244, 252
alkali alumino-silicate glasses, 250, 253
alkali diffusion, 248, 262, 263
alkali diffusion channel, 251, 257
alkali ion site potential, 254
alkali silicate glasses, 239,246,251, 253, 258
aluminium avoidance principle, 252
alumino-silicate glasses, 242, 243
animation, 239
aqueous chemistry of silicates, 274
atomic charge, 192
atomic diffusion, 220, 222
attractor, 186

Ba_2Cu_2 [Si_4 O_{12}
  partial charge distribution, 314
Ba_2Cu_2[Si_4 O_{14}
  interatomic distance, 308
  Madelung energy, 308
  mean electronegativity, 308
Ba_2SiO_4, 293
  iono-covalent indexes, 295
$Ba_4(Fe,Ti,Mg)_4B_2Si_8O_{29}Cl$ taramellite, 313
$BaBe_2Si_2O_7$ barylite, 305
  partial charge distribution, 307
$BaCu_2Si_2O_7$
  partial charge distribution, 307
basin, 186
basin population, 189
basis set, 116
  for $MgCO_3$ and $CaCO_3$, 117
basis set superposition error, 67
$BaTiSi_3O_9$ benitoite, 311
  interatomic distance, 308
  Madelung energy, 308
  mean electronegativity, 308
  partial charge distribution, 312
Be_2SiO_4 phenacite, 295
  iono-covalent indexes, 296
BeF_2 (a-quartz)
  cohesive energy, 68
bond cristical point, 160
bond ellipticity, 166, 192
bond path, 160
Born criteria, 19
Born-Oppenheimer approximation, 4
bridging oxygen, 228,236,237,241
bulk modulus, 119

$Ca_2Cu_2Al_2(SiO_4)_4(OH)_6$ papagoitee, 313
  partial charge distribution, 314
$Ca_2MgSi_2O_7$ akermanite
  partial charge distribution, 307
Ca_2SiO_4

iono-covalent indexes, 295
β-Ca_2SiO_4 larnite, 295
iono-covalent indexes, 296
γ-Ca_2SiO_4, 293
$Ca_2Y_2Si_4O_{12}CO_3.H_2O$ kainosite, 313
$Ca_3Al_2(SiO_4)_3$ grossular, 297
$Ca_3Si_2O_7$ rankinite
partial charge distribution, 307
$Ca_3Si_3O_9$ wollastonite, 311
partial charge distribution, 312
$Ca_6Si_4O_{14}$ kilchoanite
interatomic distance, 308
Madelung energy, 308
mean electronegativity, 308
$CaCO_3$ aragonite
elastic constants, 140
entropy, 151
heat capacity, 149
interatomic potential, 137
structure, 149
vibrational frequencies, 137
vibrational frequency density, 150
$CaCO_3$ calcite
atomic charges, 153
bulk modulus, 123
cohesive energy, 130
density of states, 132
elastic constants, 121, 129
electron density, 133, 135
entropy, 148
equation of state, 122
force constants, 129
heat capacity, 147
interatomic potential, 135,137
Mulliken population, 132
structure, 121, 123, 124
thermal expansion coefficient, 147
vibrational frequencies, 129,135
vibrational frequency density, 146
$CaCO_3$ calcite
Grüneisen parameters, 145
heat capacity, 144
thermal expansion coefficient, 144
vibrational frequencies, 145
$CaMgSiO_3$ perovskite, 98
equation of state, 99
$CaMgSiO_4$ monticellite
iono-covalent indexes, 296
CaO, 91,93
B1 B2 phase transition, 94
$CaO/Na_2O/SiO_2$ glass, 260, 262, 264, 265
CaO/SiO_2 glass, 260
$CaSiO_3$ perovskite, 44, 46
bulk modulus, 52
channel shift model, 252
charge density, 86
clinopyroxene, 53
closed-shell interaction, 161
clustering of alkali, 240
clustering of Ca ions, 261
Continuous Random Network Model, 229
core basin, 188
core-pseudopotential, 4–6
Coulomb interaction, 7, 84, 85, 204, 205, 229
covalent potential, 118, 229
critical exponent, 186
critical point, 186
$Cu_6(Si_6O_{18})$ black dioptase, 316
$Cu_6(Si_6O_{18})$.GH2O blue dioptase, 316
$Cu_6[Si_6O_{18}]$ black dioptase
interatomic distance, 308
Madelung energy, 308
mean electronegativity, 308
$Cu_6[Si_6O_{18}]$ dioptase
partial charge distribution, 315
$Cu_6[Si_6O_{18}].6H_2O$ blue dioptase

interatomic distance, 308
Madelung energy, 308
mean electronegativity. 308
cyclic polysilicates, 317

deformation electron density, 157–159
density functional, 64, 65
diffusion activation energy, 238,247, 249, 251, 264
diffusion coefficient, 233, 238
dispersion interaction, 229
displacive phase transition, 219
distorted ion model, 67
disynaptic, 188
domain, 187
dynamical system, 186

elastic constants, 11, 19
electron density, 64, 65, 83
laplacian, 159–161
electron gas model, 64, 65, 83, 85
electron localization function (ELF), 183, 184, 193
electronegativity, 195
electronegativity equalization, 280
principle, 282
electronegativity scale
Allred-Rochow, 279
Mulliken, 280
Pauling, 287
electrostatic perturbation, 66
enthalpy, 31
enthalpy of reaction, 27
entropy, 31
entropy of reaction, 27
Er2Si2O7
partial charge distribution, 307
eudialyte, 317
partial charge distribution, 318
exchange-correlation, 7, 84
functional, 86
potential, 4

fluctuation of basin populations, 189
force, 7
Hellman-Feynmann, 43
force constant, 277
free energy, 27
free volume distribution, 265

garnet, 296
glass simulation, 232
Gordon-Kim model, 87
Grüneisen parameter, 119
gradient dynamical system. 186
grossular $Ca_3Al_2(SiO_4)_3$
iono-covalent indexes, 298

$H_2Si_2O_7$
electron density
laplacian, 168, 169
H_2SiO_3, 162, 163
H_4SiO_4, 162
$H_6Si_2O_7$, 162
H_8SiO_6, 162, 163
$H_{10}Si_2O_{10}$, 162, 163
$H_{12}SiO_8$, 162, 163
$H(Fe,Mn)Ca_2Al_2BSi_4O_{12}$ axinite, 313
hardness, 281
heat capacity, 31
IIfSiO4, 297
hydrogen-bonded networks, 300
hydroxylated orthosilicate anions, 298
hyperbolic point, 186

intermediate range order, 228
internal energy, 31
ion mobility, 220
ionic self energy, 66
ionicity index, 283, 287
irreducible domain, 187

K_2O/SiO_2 glass, 235

$K_2ZrSi_3O_9$ wadeite, 311
interatomic distance, 308
Madelung energy, 308
mean electronegativity, 308
partial charge distribution, 312
$K_4(HSiO_3)_4$
partial charge distribution, 314
K_4SiO_4, 293
iono-covalent indexes, 294
kinetic energy, 7, 84, 86
density, 161, 181
Kinetic energy density
definite positive, 183

Lagrangian, 43
$Li_2O/Al_2O_3/SiO_2$ glass, 244
$Li_2O/Na_2O/A1_2O_3/SiO_2$ glass, 255
$Li_2O/Na_2O/SiO_2$ glass, 253–255
$Li_2O/Na_2O/SiO_2$ glass, 254
$Li_20/Na_20/Al_2O_3/SiO_2$ glass, 254
Li2O/SiO2 glass, 241, 242
Li_4SiO_4, 293
iono-covalent indexes, 294
$Li_6Si_2O_7$
partial charge distribution, 307
lithium silicate glasses, 240
local density approximation, 84
localization attractor, 187
localization basin, 187
localization domain, 189
long range order, 228
lovozerite, 316

Madelung constant, 284
Madelung energy, 322
Madelung tensor, 281
mantle (upper/lower boundary), 45
mean electronegativity, 280, 322
mechanical stability, 19
Mg_2SiO_4
iono-covalent indexes, 295
Mg_2SiO_4 forsterite, 293
Mg_2SiO_4 spinel
cohesive energy, 68
electron distribution, 69
Mg_2SiO_4 spinel $MgSiO_3$ perovskite
phase transition, 73
$Mg_3Al_2(SiO_4)_3$ pyrope, 297
iono-covalent indexes, 298
$MgCaSi_2O_3$ perovskite-like, 105
$MgCO_3$ magnesite
atomic charges, 153
bulk modulus, 123, 124
cohesive energy, 130
density of states, 132
elastic constants, 121, 128, 129
electron density, 133, 135
equation of state, 122
force constants, 129
Mulliken population, 132
structure, 121, 123
vibrational frequencies, 129
MgO, 91, 92
B1 B2 phase transition, 94
$MgSiO_3$ clinoenstatite, 54
bulk modulus, 58
compressibility, 56
structure, 55
$MgSiO_3$ enstatite, 44, 51
$MgSiO_3$ perovskite, 44, 46, 49, 98
bulk modulus, 47, 51
cohesive energy, 68
elastic constants, 47, 51
electron distribution, 69
equation of state, 99
phonon modes, 102, 103
shear modulus, 50
stability, 47
thermal expansion, 100, 101
mid-range order, 245
milarite, 321
mixed alkali effect, 253, 254, 256, 257, 263
Modified Random Network Model, 229

molar Madelung energy, 283
Molecular Dynamics, 41, 42, 208
monosynaptic, 188
MPIB model, 88, 89
muirite, 317
  partial charge distribution, 3 18
Murnaghan equation of state, 125

$Na_2O/Al_2O_3/SiO_2$ glass, 253
$Na_3HSiO_4.nH_2O$, 298
$Na_3HSiO_4.2H_2O$, 299
$Na_4ClSi_3Al_3O_{12}$
  cohesive energy, 68
Na_4SiO_4, 293
  iono-covalent indexes, 294
$Na_6[Si_2O_6(OH)_2]$, 299
$Na_8(Al_2Be_2Si_8O_{24})Cl_2$ tugtupite, 313
  interatomic distance, 308
  Madelung energy, 308
  mean electronegativity, 308
  partial charge distribution, 314
$Na_{12}\ Ca_3\ Fe_2(Si_6O_{18})_2$ imandrite, 316
$NaFe_3^{3+}B_3Al_6Si_6O_{30}F$ buergerite, 315
  interatomic distance, 308
  Madelung energy, 308
  mean electronegativity, 308
  partial charge distribution, 315
$NaMg_3B_3Al_6Si_6O_{27}(OH,F)_4$ tourmaline, 315
  partial charge distribution, 315
$NaMg_3B_3Al_6Si_6O_{27}(OH,F)_4$ tourmaline
  interatomic distance, 308
  Madelung energy, 308
  mean electronegativity, 308
$NaYSiO_4$
  iono-covalent indexes, 296
NMR spectroscopy, 274
non-bridging oxygen, 228,236. 237, 240, 241, 253, 259, 260
Nosé thermostat, 208

one-electron approximation, 4
orthosilicate
  ionicity, 323
orthosilicates, 277
osumilite, 321
oxygen
  atomic radius, 195
  basin populations, 194
  charge, 278
  covalent radius, 285
  diffusion, 221

pair distribution function, 233,234, 260, 261
Parrinello-Rahman constant pressure algorithm, 208
partial charge distribution, 280
partial charge model, 279
Pauli kinetic energy density, 183
periodic Hartree-Fock, 116
phase transition, 27
phonon density of states, 27
phonon spectrum, 26, 28
PIB model, 88
pK_a, 289, 324
Poincaré-Hopf theorem, 187
Poisson ratio, 13
polycyclic Polysilicates
  partial charge distribution, 320
polysynaptic, 188
potential parameters, 205,207,231
pyrosilicate
  atomic size, 303
  ionicity indexes, 303
  mean electronegativity, 303
pyroxene, 52

Q^n distribution, 236
quasi-harmonic model, 118. 119

radial distribution function, 233

radial electron localization function, 185
reducible domain, 187
reduction of localization domains, 189
relative fluctuation of basin populations, 190
repellor, 186
rigid ion
  dynamical matrix, 90
rigid ion model, 118
ring size distribution, 236,237,245, 262

$Sc_2Si_2O_7$ thortveite
  partial charge distribution, 307
$Sc_2Si_2O_7$ thortveitite, 305
separatrix, 186
shared interaction, 161
shell-model
  dynamical equations, 90
short range interaction, 230
short range order, 228
^{29}Si
  NMR chemical shift, 275
  NMR spectroscopy, 276
^{29}Si NMR chemical shift, 324
$[SiO_2(OH)_2]^{2-}$, 293
$[SiO_4]^{4-}$, 293
$[Si_2O_6(OH)_2]^{6-}$, 299
$[Si_2O_7]^{6-}$
  Madelung energy, 306
Si_3O_9 ring, 319
Si_4O_{12} ring, 319
$[Si_8O_{20}]^{8-}$ octamers
  partial charge distribution, 321
silicate glass, 228
silicon
  atomic radius, 195
  cationic radius, 195
  charge, 278
  covalent radius, 285
SiO, 162
  interatomic potential, 201
SiO bond
  character, 175
  critical point, 171
  electron density laplacian, 172
  electronic properties, 164
  length, 170
SiO_2, 162
  α-quartz coesite phase transition, 27
  α-quartz stishovite phase transition, 27, 72
  stishovite $CaCl_2$ structure phase transition, 72, 194
  thermal properties, 25
SiO_2 α to β quartz phase transition, 212
SiO_2 α-cristobalite, 190
  cohesive energy, 68
  elastic constants, 13
  electron distribution, 69
  localization basins, 193
  structure, 13, 210, 211
  Poisson ratio, 13
SiO_2 α-PbO2, 25, 217
SiO_2 α-quartz, 8, 26, 190, 285
  amorphization, 16, 21
  bulk modulus, 10, 70
  cohesive energy, 68
  elastic constants, 13
  iono-covalent indexes, 287
  localization basins, 193
  phonon dispersion, 213
  SiOSi angle, 70
  structure, 10, 13, 210, 211
  thermal expansion, 214
  twinning, 215
SiO2 β-cristobalite
  structure, 13
SiO_2 β-quartz, 8
  bulk modulus, 10

structure, 10, 13
SiO_2 β-tridymite
structure, 13
SiO_2 *Cmcm*, 218
SiO_2 $Pa\bar{3}$, 8, 9, 212
bulk modulus, 10
structure, 10, 13, 210
SiO_2 $CaCl_2$, 8, 9, 190
bulk modulus, 10
localization basins, 193
structure, 10, 13
SiO_2 CaF_2, 8, 190
bulk modulus, 10
localization basins, 193
structure, 10, 13
SiO_2 coesite, 26,162,221,287,288
bonding, 165
electron density, 164, 167
iono-covalent indexes, 287
structure, 210, 211
SiO_2 stishovite, 8, 9, 26, 190, 221, 288,289
bulk modulus, 10
cohesive energy, 68
electron distribution, 69
iono-covalent indexes, 287
localization basins, 193
structure, 10, 13, 210, 211
$Sm_2Si_2O_7$
partial charge distribution, 307
soda lime silicate glasses, 258
sodalite
cohesive energy, 68
solution chemistry of silicates, 277, 289
space-phase distribution, 182
space-time correlation function, 234–236
spherical ion model, 67
Sr_2SiO_4, 293
iono-covalent indexes, 295
SSMEG model, 88
stable manifold, 186
synaptic order, 187

tetrabutylammonium cation, 276
tetraethylammonium cation, 276
tetramethylammonium cation, 274
tetrapropylammoniuni cation, 276
$ThK(Ca,Na)_2Si_8O_{20}$ ekanite, 319
Thomas-Fermi model, 87
three-body potential, 229, 230
$ThSiO_4$ thorite, 297
iono-covalent indexes, 298
time-space correlation function, 265, 266
TiO_2 rutile
cohesive energy, 68
two-body potential, 3, 116, 204, 205, 229, 230

unstable manifold, 186

VIB model, 88, 89
vibrational energy, 25
visualization, 239
void size distribution, 237
von Weizsäcker functional, 183
VSEPR model, 191, 196
VSMEG model, 88

Wigner function, 182

$Y_2Si_2O_7$
partial charge distribution, 307
$Yb_2Si_2O_7$
partial charge distribution, 307
Yin-Yang effect, 325

zircon, 296
$ZrSiO_4$ zircon, 297
iono-covalent indexes, 298